MARTIN MARIETTA ENERGY SYSTEMS LIBRARIES

3 4456 0275047 7

ORNL/TM-10705

ornl

OAK RIDGE
NATIONAL
LABORATORY

MARTIN MARIETTA

Ceramic Technology for Advanced Heat Engines Project Semiannual Progress Report for April 1987 Through September 1987

Prepared for
U.S. Department of Energy
Assistant Secretary for Conservation and Renewable Energy
Office of Transportation Systems
Advanced Materials Development Program

OAK RIDGE NATIONAL LABORATORY
CENTRAL RESEARCH LIBRARY
CIRCULATION SECTION
4500N ROOM 175
LIBRARY LOAN COPY
DO NOT TRANSFER TO ANOTHER PERSON
If you wish someone else to see this report, send in name with report and the library will arrange a loan.

CERAMIC TECHNOLOGY PROJECT
DOE/ORNL

OPERATED BY
MARTIN MARIETTA ENERGY SYSTEMS, INC.
FOR THE UNITED STATES
DEPARTMENT OF ENERGY

Printed in the United States of America. Available from
National Technical Information Service
U.S. Department of Commerce
5285 Port Royal Road, Springfield, Virginia 22161
NTIS price codes—Printed Copy: A20 Microfiche A01

This report was prepared as an account of work sponsored by an agency of the United States Government. Neither the United States Government nor any agency thereof, nor any of their employees, makes any warranty, express or implied, or assumes any legal liability or responsibility for the accuracy, completeness, or usefulness of any information, apparatus, product, or process disclosed, or represents that its use would not infringe privately owned rights. Reference herein to any specific commercial product, process, or service by trade name, trademark, manufacturer, or otherwise, does not necessarily constitute or imply its endorsement, recommendation, or favoring by the United States Government or any agency thereof. The views and opinions of authors expressed herein do not necessarily state or reflect those of the United States Government or any agency thereof.

ORNL/TM-10705

Metals and Ceramics Division

CERAMIC TECHNOLOGY FOR ADVANCED HEAT ENGINES PROJECT
SEMIANNUAL PROGRESS REPORT FOR
APRIL 1987 THROUGH SEPTEMBER 1987

D. R. Johnson
Project Manager

Date Published: March 1988

NOTICE: This document contains information of a preliminary nature. It is subject to revision or correction and therefore does not represent a final report.

Prepared for
U.S. Department of Energy
Assistant Secretary for Conservation and Renewable Energy
Office of Transportation Systems
Advanced Materials Development Program
EE 04 00 00 0

Prepared by the
OAK RIDGE NATIONAL LABORATORY
Oak Ridge, Tennessee 37831
operated by
MARTIN MARIETTA ENERGY SYSTEMS, INC.
for the
U.S. DEPARTMENT OF ENERGY
under Contract DE-AC05-84OR21400

MARTIN MARIETTA ENERGY SYSTEMS LIBRARIES
3 4456 0275047 7

REPORTS PREVIOUSLY ISSUED

ORNL/TM-9325	Period March 1983–September 1983
ORNL/TM-9466	Period October 1983–March 1984
ORNL/TM-9497	Period April 1984–September 1984
ORNL/TM-9673	Period October 1984–March 1985
ORNL/TM-9947	Period April 1985–September 1985
ORNL/TM-10079	Period October 1985–March 1986
ORNL/TM-10308	Period April 1986–September 1986
ORNL/TM-10469	Perod October 1986–March 1987

CONTENTS

SUMMARY 1

0.0 PROJECT MANAGEMENT AND COORDINATION 3

1.0 MATERIALS AND PROCESSING 5

INTRODUCTION 5

1.1 MONOLITHICS 7

1.1.1 Silicon Carbide 7

Synthesis of High-Purity Sinterable Silicon Carbide Powders (SOHIO) 7

Turbomilling of SiC Whiskers (University of Southern Illinois) 9

1.1.2 Silicon Nitride 13

Sintering of Silicon Nitride (AMTL) 13

Synthesis of High Purity Sinterable Si_3N_4 Powders (Ford) 21

1.2 CERAMIC COMPOSITES 27

1.2.2 Silicon Nitride Matrix 27

SiC-Whisker-Toughened Silicon Nitride (Garrett Ceramic Component Division) 27

Silicon Nitride-Metal Carbide Composites (GTE) . . . 50

Development of Toughened Si_3N_4 Composites by Glass Encapsulated Hot Isostatic Pressure (Norton) 60

1.2.3 Oxide Matrix 87

Dispersion-Toughened Oxide Composites (ORNL) 87

Processing of Improved Transformation-Toughened Ceramics (Norton) 95

Sol-Gel Oxide Powder (ORNL) 112

Processing and Characterization of Transformation-Toughened Ceramics with Strength Retention to Elevated Temperatures (Ceramatec) 114

Injection Molded Composites (ORNL) 126

1.2.4 Silicate Matrix 127

Low Expansion Ceramics for Diesel Engine Applications (VPI) 127

1.3 THERMAL AND WEAR COATINGS 166

1.3.1 ZrO_2 Base Coatings 166

Development of Adherent Ceramic Coatings to Reduce Contact Stress Damage of Ceramics (GTE Laboratories) 166

1.4 JOINING 183

1.4.1 Ceramic-Metal Joints 183

Joining of Ceramics for Heat Engine Applications (ORNL) 183

2.0 MATERIALS DESIGN METHODOLOGY 191

INTRODUCTION 191

2.2 CONTACT INTERFACES 193

2.2.2 Dynamic Interfaces 193

Studies of Dynamic Contact of Ceramics and Alloys for Advanced Heat Engines (Battelle) 193

2.3 NEW CONCEPTS 200

Advanced Statistical Concepts of Fracture in Brittle Materials (GE) 200

3.0 DATA BASE AND LIFE PREDICTION 209

INTRODUCTION 209

3.1 STRUCTURAL QUALIFICATION 211

Microstructural Analysis of Structural Ceramics (NBS) 211

Physical Properties of Structural Ceramics (ORNL) . . 218

Effect of Translucence of Engineering Ceramics on Heat Transfer in Diesel Engines (ITI) 220

3.2 TIME-DEPENDENT BEHAVIOR 222

Characterization of Transformation-Toughened Ceramics (AMTL) 222

Fracture Behavior of Toughened Ceramics (ORNL) . . . 228

Cyclic Fatigue of Toughened Ceramics (ORNL) 232

3.3 ENVIRONMENTAL EFFECTS 247

Static Fatigue Behavior of Toughened Ceramics (University of Illinois) 247

Environmental Effects in Toughened Ceramics (University of Dayton) 254

3.4 FRACTURE MECHANICS 371

Improved Methods for Measuring the Fracture Resistance of Structural Ceramics (University of Washington) 371

Testing and Evaluation of Advanced Ceramics at High Temperature in Uniaxial Tension (North Carolina A&T University) 372

Standard Tensile Test Development (NBS) 382

3.5 NONDESTRUCTIVE EVALUATION DEVELOPMENT 387

Nondestructive Characterization (ORNL) 387

Computed Tomography (ANL) 397

4.0 TECHNOLOGY TRANSFER 405

Technology Transfer (ORNL) 405

IEA Annex II Management (ORNL) 406

Standard Reference Materials (NBS) 414

CERAMIC TECHNOLOGY FOR ADVANCED HEAT ENGINES PROJECT SEMIANNUAL PROGRESS REPORT FOR APRIL 1987 THROUGH SEPTEMBER 1987

SUMMARY

The Ceramic Technology For Advanced Heat Engines Project was developed by the Department of Energy's Office of Transportation Systems (OTS) in Conservation and Renewable Energy. This project, part of the OTS's Advanced Materials Development Program, was developed to meet the ceramic technology requirements of the OTS's automotive technology programs.

Significant accomplishments in fabricating ceramic components for the Department of Energy (DOE), National Aeronautics and Space Administration (NASA), and Department of Defense (DOD) advanced heat engine programs have provided evidence that the operation of ceramic parts in high-temperature engine environments is feasible. However, these programs have also demonstrated that additional research is needed in materials and processing development, design methodology, and data base and life prediction before industry will have a sufficient technology base from which to produce reliable cost-effective ceramic engine components commercially.

An assessment of needs was completed, and a five-year project plan was developed with extensive input from private industry. The objective of the project is to develop the industrial technology base required for reliable ceramics for application in advanced automotive heat engines. The project approach includes determining the mechanisms controlling reliability, improving processes for fabricating existing ceramics, developing new materials with increased reliability, and testing these materials in simulated engine environments to confirm reliability. Although this is a generic materials project, the focus is on the structural ceramics for advanced gas turbine and diesel engines, ceramic bearings and attachments, and ceramic coatings for thermal barrier and wear applications in these engines. This advanced materials technology is being developed in parallel and close coordination with the ongoing DOE and industry proof-of-concept engine development programs. To facilitate the rapid transfer of this technology to U.S. industry, the major portion of the work is being done in the ceramic industry, with technological support from government laboratories, other industrial laboratories, and universities.

This project is managed by ORNL for the Office of Transportation Systems, Heat Engine Propulsion Division, and is closely coordinated with complementary ceramics tasks funded by other DOE offices, NASA, DOD, and industry. A joint DOE and NASA technical plan has been established, with DOE focus on automotive applications and NASA focus on aerospace applications. A common work breakdown structure (WBS) was developed to facilitate coordination. The work described in this report is organized according to the following WBS project elements:

0.0 Management and Coordination

1.0 Materials and Processing

- 1.1 Monolithics
- 1.2 Ceramic Composites
- 1.3 Thermal and Wear Coatings
- 1.4 Joining

2.0 Materials Design Methodology

- 2.1 Modeling
- 2.2 Contact Interfaces
- 2.3 New Concepts

3.0 Data Base and Life Prediction

- 3.1 Structural Qualification
- 3.2 Time-Dependent Behavior
- 3.3 Environmental Effects
- 3.4 Fracture Mechanics
- 3.5 NDE Development

4.0 Technology Transfer

This report includes contributions from all currently active project participants. The contributions are arranged according to the work breakdown structure outline.

0.0 PROJECT MANAGEMENT AND COORDINATION

D. R. Johnson
Oak Ridge National Laboratory

Objective/scope

This task includes the technical management of the project in accordance with the project plans and management plan approved by the Department of Energy (DOE) Oak Ridge Operations Office (ORO) and the Office of Transportation Systems. This task includes preparation of annual field task proposals, initiation and management of subcontracts and interagency agreements, and management of ORNL technical tasks. Monthly management reports and bimonthly reports are provided to DOE; highlights and semiannual technical reports are provided to DOE and program participants. In addition, the program is coordinated with interfacing programs sponsored by other DOE offices and federal agencies, including the National Aeronautics and Space Administration (NASA) and the Department of Defense (DOD). This coordination is accomplished by participation in bimonthly DOE and NASA joint management meetings, annual interagency heat engine ceramics coordination meetings, DOE contractor coordination meetings, and DOE Energy Materials Coordinating Committee (EMaCC) meetings, as well as special coordination meetings.

1.0 MATERIALS AND PROCESSING

INTRODUCTION

This portion of the project is identified as project element 1.0 within the work breakdown structure (WBS). It contains four subelements: (1) Monolithics, (2) Ceramic Composites, (3) Thermal and Wear Coatings, and (4) Joining. Ceramic research conducted within the Monolithics subelement currently includes work activities on green state ceramic fabrication, characterization, and densification and on structural, mechanical, and physical properties of these ceramics. Research conducted within the Ceramic Composites subelement currently includes silicon carbide and oxide-based composites, which, in addition to the work activities cited for Monolithics, include fiber synthesis and characterization. Research conducted in the Thermal and Wear Coatings subelement is currently limited to oxide-base coatings and involves coating synthesis, characterization, and determination of the mechanical and physical properties of the coatings. Research conducted in the Joining subelement currently includes studies of processes to produce strong stable joints between zirconia ceramics and iron-base alloys.

A major objective of the research in the Materials and Processing project element is to systematically advance the understanding of the relationships between ceramic raw materials such as powders and reactant gases, the processing variables involved in producing the ceramic materials, and the resultant microstructures and physical and mechanical properties of the ceramic materials. Success in meeting this objective will provide U.S. companies with new or improved ways for producing economical highly reliable ceramic components for advanced heat engines.

1.1 MONOLITHICS

1.1.1 Silicon Carbide

Synthesis of High-Purity Sinterable Silicon Carbide (SiC) Powders
H. A. Lawler and B. L. Mehosky [Standard Oil Engineered Materials Company (Carborundum)]

Objective/Scope

The objective of this program is to develop a volume scaleable process to produce high purity, high surface area sinterable silicon carbide powder.

The program is organized in two phases. Phase I, completed in July, 1986, included the following elements:

- Verify the technical feasibility of the gas phase synthesis route.
- Identify the best silicon feedstock on the basis of performance and cost.
- Optimize the production process at the bench scale.
- Fully characterize the powders produced and compare with commercially available alternatives.
- Develop a theoretical model to assist in understanding the synthesis process, optimization of operating conditions and scale-up.

Phase II, authorized in August, 1986, will scale the process to five to ten times the bench scale quantities in order to perform confirmatory experiments, produce process flowsheets and to perform economic analysis.

Technical Progress

Task 8. Process Scale-up

Based upon the results of Phase I, a scaled-up reactor was designed and fabricated. During this reporting period all of the major components and ancillary equipment were received.

Prior vendor testing was performed on the power supply, the plasma torch, the high frequency starter system and bag house. These major components, along with the 8" diameter by 6' long 316 stainless steel reactor vessel, the tail gas scrubber and gas induction system, were "skid" or "rack" mounted to an integral structural steel framework which can be relocated in its entirety if required.

Piping and electrical connections both for power and instrumentation/control were completed. Drawings were revised to reflect the "As Built" system and a Preoperation Safety Review was conducted followed by a "What If?" safety meeting. Minor corrective measures were implemented.

Commissioning activities were delayed several times due to an initial facility redesign to remove the recycle quench gas system, a delay in the delivery of the bag house and an underestimation of the construction time required for a facility of this size.

In September the initial start-up attempt was unsuccessful due to defective modules in the control computer. During a second attempt the power supply suffered a failure of a rectifying diode causing further diode and conductor insulation damage. Aside from the power supply failure, the system performed well.

Following repair of the power supply, startup was again attempted. The plasma torch would not remain in operation when the high frequency starter signal was discontinued.

The probable causes of this malfunction are presently under investigation, however, nothing definitive has been identified to date. The commissioning delay has resulted in the additional slippage of Task 9 and 10.

Status of Milestones

Although ORNL had previously granted a no-cost contract extension to December 31, 1987, it is now apparent that additional time will be required. The nature of this additional extension is presently under discussion.

A breakdown of the major Phase II tasks and milestones is shown in Figure 1.

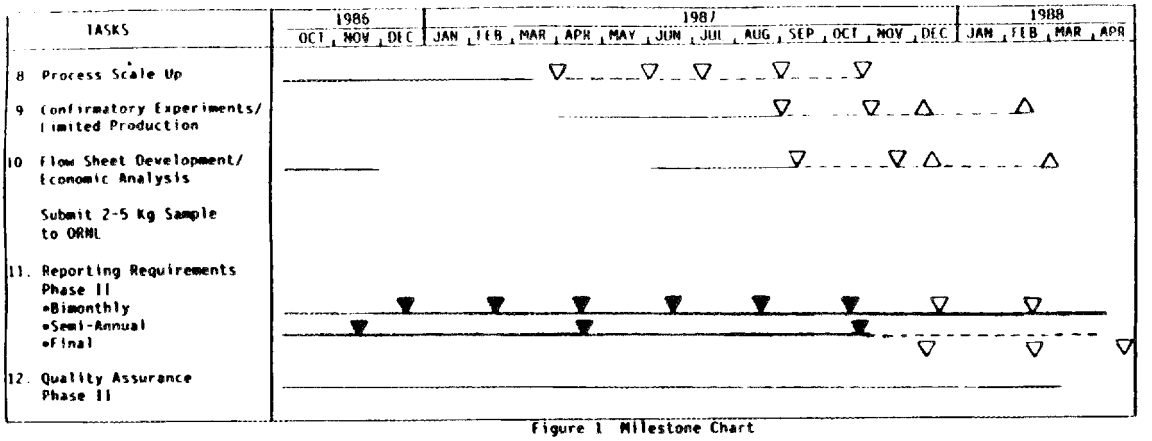

Figure 1 Milestone Chart

Publications

None during this reporting period.

Turbomilling of SiC Whiskers-- D. E. Wittmer
(Associate Professor, SIU-C, Carbondale, IL)

Objective/scope

The goal of this research is to determine the feasibility of using turbomilling as a technique to improve the reliability of SiC whisker containing composites. The research is directed at determining the effect of turbomilling on particulate impurties in the whiskers, reduction of whisker aspect ratio, and dispersion and homogenization of whisker/ceramic matrix composites.

Technical progress

Summary

The objectives of the initial research for this program were to determine the feasibility of using turbomilling[1-2] techniques to:

1. Reduce particulate impurities in SiC whiskers,
2. Create uniform reduction of aspect ratio to improve pressureless sintering characteristics, and
3. For dispersion and homogenization of SiC whisker/Alumina composites with high whisker loading and higher solids content.

Turbomilling without media was somewhat successful in breaking up agglomerates in both American Matrix* and Tateho* whiskers, but had little effect on the particulate impurities for the solids loading used. When premilled 30-mesh SiC was used as a coarse addition, the American Matrix whiskers were significantly reduced in aspect ratio after 1 hour and were ground to almost all particulate after 2 hours. The Tateho whiskers were reduced in aspect ratio after 1 hour and showed much less particulate after 2 hours. In both cases the coarse SiC grinding media added some fine particulate impurity to the whiskers, which presents a separation problem.

The dispersion and homogenization of 30 vol. % SiC whiskers in RCHP Alumina* by turbomilling for 30 min. using partially stabilized zirconia* (PSZ) media appears to have been very successful. There was no evidence of whisker agglomerates in the alumina particulate matrix as examined by scanning electron microscopy (SEM). This powder has been submitted for hot-pressing to determine the effects of these techniques on the physical properties of the composite.

---

* American Matrix Co., Knoxville, TN
* Tateho Chemical Co. through ICD Group Inc., N.Y.,N.Y.
* Reynolds Metals Co., Bauxite, AR
* Toyo Soda Mfg. Co., Ltd., Toyko, Japan

Due to the early success of this program, further expansion of the scope of the program was requested. The proposed expansion will examine the dispersion/ homogenization of SiC whisker/ceramic matrix composites in further detail, the use of higher whisker loadings to reduce aspect ratios in the absence of coarse grinding particulate, and involves development of turbomill prototypes.

Preliminary Results and Discussion

Five separate turbomilling runs were made with and without coarse alpha-SiC angular grain and rounded PSZ beads. The first two runs were made to determine the effects of dispersion of whisker agglomerates and reduction of whisker aspect ratio with out media, while the second two runs were made to determine the effects of milling media on the dispersion of whisker agglomerates, reduction of whisker aspect ratio and comminution of the particulate impurities. The final run used the turbomill as a means of dispersing, deagglomerating, and homogenizing a 30 vol. % Tateho whisker/RCHP Alumina composite.

Dispersion and Aspect Ratio Reduction Without Milling Media

Attempts at dispersion and aspect ratio reduction by turbomilling Tateho and American Matrix whiskers alone were not very successful due to the limited amount of whiskers that were available. For comparison, the first two runs consisted of 400 grams of each whisker added to 2.5 liters of water and 100 ml. of a 10% solution of Marasperse N-22. This amounted to only 13% total solids. The turbomilling conditions throughout the run were 1600 r.p.m., 28 in-lbs. of torque, and .78 h.p. for both runs. The r.p.m. were reduced to 400 during sampling, which consisted of syphoning 50 ml. of whisker slurry at 15 min. intervals over a 2 hour run at about the center position of the mill body. These samples were then analyzed by SEM to determine the effect on whisker agglomeration.

After 1 hour there was some evidence of dispersion and aspect ratio reduction for both whiskers, but no evidence of separating hard agglomerates or grinding of hard agglomerates or particulate impurities. At the end of 2 hours there did not appear to be much change from the 1 hour sampling. Upon discharging the mill, neither whisker source would pour through a 60 mesh screen without severe agitation. Fracture of whiskers was more evident for the American Matrix whiskers than for the Tateho whiskers. This could be a result of the higher shear modulus suspected for the Tateho whiskers and the large amount of the segmented alpha phase in the American Matrix whiskers.

---

* Marasperse N-22 is a sodium lignosulfonate made by Reed Lignin, Rothschild, WI

Dispersion and Aspect Ratio Reduction with Milling Media

The next two runs consisted of the addition of 800 grams of 30-mesh alpha SiC grain (Norton Co.*, green high purity grade) to 400 grams of whisker, 2.5 liters of distilled water and 125 ml. of a 10 % Marasperse N-22 solution, which gave a 2:1 coarse to fine ratio and a total solids content of 31.6 wt./o.

After 15 minutes, noticeable dispersion and some fracture of the American Matrix whiskers was observed, while at 30 min. there was considerable fracture of the whiskers into small segments and very few long whiskers. The 1 hour sample showed only a small volume of low aspect ratio whiskers and small fracture segments, until at 2 hours very little whiskers remained and some coarse SiC from the milling media was present. Microtrack* particle size analyses with a 37 micron column were also run on each sample. The breakpoint in average whisker size as estimated from a change in estimated surface area and whisker diameter was 1 hour, which was in agreement with SEM results.

For the Tateho whiskers there was very little particulate contamination or signs of small whisker fragments for milling times up to 1 hour. There was evidence that significant deagglomeration of the whiskers started between 15 and 30 min. of milling time with little effect on the aspect ratio. For times over 1 hour there was increased observation of whisker aspect ratio reduction and particulate contamination from the milling media. However, even after 2 hours there was a significant volume of high aspect ratio whiskers remaining. (Although in both cases the slurry passed through a 325-mesh screen during discharging of the mill.) This is most likely due to the small diameter of these whiskers (0.5 to 1 micron) compared to the larger diameter (2 to 5 micron) American Matrix whiskers. The results of particle size analyses also indicated a break point at 1 hour of milling.

It should be mentioned that the American Matrix whiskers were a grade 2 material and not their better grade 1. American Matrix has indicated that grade 1 whiskers would be available for expansion of this program.

Dispersion/Homogenization of SiC/Alumina Composite

Since the coarse SiC grinding media appeared to contaminate the whiskers with fine particulate the decision was made to use a rounded PSZ bead (1 to 2 mm.) for milling the 30 vol.% SiC whisker/alumina composite. The run consisted of 800 grams of PSZ beads, 300 grams of composite powder that had not been premixed, 2.5 liters of water and no dispersant for 60 min. The idea was to deagglomerate the whiskers during milling but reagglomerate the whiskers with well dispersed alumina by allowing uniform flocculation. After 30 min. into the run the rotor assembly developed a fracture in the upper drive

---

* Norton Co., Worcester, M.A.
* Leeds and Northrup Instruments, North Wales, PA

shaft and the run was halted at that point. (This was the original rotor assembly that was constructed in 1981.) A wet sample was taken at this point and processed the same as reported previously. The SEM photomicrographs showed that the whiskers were homogeneously dispersed in the alumina and no whisker agglomerates were evident.

This is considerable improvement over state of the art, which consists of wet or dry milling for up to 24 hours for equivalent deagglomeration. After turbomilling, the slurry was passed through a 100-mesh screen with no assistance and the milling media showed virtually no weight loss. After dewatering by sedimentation, the supernatant liquid was removed by syphon and the % solids was determined to be about 50%. This slurry was dried in an oven at 70 to 100°C and lightly ground with a mortar and pestle. This powder is presently being hot-pressed to determine the effect of turbomilling on the physical properties.

Status of milestones

The single deliverable for this program was a feasibility report. The feasibility of using turbomilling as a technique for improved processing of SiC whisker containing composites has been demonstrated and is reported in this semi-annual report. The deliverable date for this milestone was at the end of the contract period, but due to the early success of the initial research, increased funding and expansion of the research tasks and milestones has been requested.

Turbomilling Feasibility Report	October 1987

Publications

None.

References

1. Wittmer, D. E., "Use of Bureau of Mines Turbomill to Produce High-Purity Ultrafine Nonoxide Ceramic Powders", BuMines RI 8854, 1983, pp. 12.

2. Hoyer, J. L. and A. V. Petty, "High Purity, Fine Ceramic Powders Produced in the Bureau of Mines Turbomill", Ceramic Proceedings, Vol. 6, 9-10, 1985, pp. 1342-1355.

1.1.2 Silicon Nitride

Sintering of Silicon Nitride

G. E. Gazza (Army Materials Technology Laboratory)

Objective/scope

The program is concentrating on sintering compositions in the Si_3N_4- Y_2O_3-SiO_2 system using a two-step sintering method where the N_2 gas pressure is raised to 7-8 MPa during the second step of the process. During the sintering, dissociation reactions are suppressed by the use of high N_2 pressure and cover powder of suitable composition over the specimens. Variables in the program include the sintering process parameters, source of starting powders, milling media and time, and specimen composition. Resultant properties determined are room temperature modulus of rupture, high temperature stress-rupture, oxidation resistance, and fracture toughness. Successful densification of selected compositions with suitable properties will lead to densification of injection molded or slip cast components for engine testing.

Technical progress

Sintering

Compositions focused on at this point in the program for extensive evaluation are 88.0m/0 Si_3N_4-4.0m/o Y_2O_3-8.0m/oSiO_2 and 85.8m/o Si_3N_4-4.73m/o Y_2O_3-9.47m/o SiO_2, designated as composition numbers 40 and 39, respectively. Also, it was observed that the presence of W (added as WC or WO_3) or Mo (added as Mo_2C or MoO_3) promoted densification of these compositions. Such observations have been noted in past Si_3N_4 densification studies when W was present as an inadvertant, uncontrolled impurity, usually introduced during milling of starting powders with WC milling media. Subsequent studies focused on the effect of the W impurity on the oxidation and high temperature creep/stress-rupture behavior of Si_3N_4 rather than specifically defining its role in promoting densification of the material. Due to the deleterious influence found on the properties of Si_3N_4 associated with the presence of W (1,2), it is regarded as an impurity to be avoided in the processing of Si_3N_4 compositions. However, in this study, it was decided to explore the use of Mo_2C and MoO_3 which have been found to be effective in promoting densification. Since these compounds have a lower theoretical density than WC, there is less tendency to segregate when used as an additive to the compositions of interest. Also, molybdenum silicide (Mo_xSi_y) forms as a distributed phase with good oxidation resistance. The use of Mo_2C rather than Moo_3 is preferred due to the volatility of the latter compound. It was found that sintering temperatures could be significantly reduced for the compositions of interest, i.e., 39 and 40, if 1.0m/o of Mo_2C was added to the sintering composition. Also, if the Mo_2C particles were fine enough and well distributed, their presence as reacted Mo_xSi_y particles in the body would not serve as fracture origins as found for coarser Fe-base impurity inclusions by Pasto (3).

From a stability standpoint, it was anticipated that the Mo_xSi_y particles would remain discrete and stable in contact with grain boundary $Y_2Si_2O_7$ phases with SiO_2 serving as a stable boundary phase.

Sintering of compositions identified as 39 and 40 containing 0.35-1.10m/o Mo_2C or 1.0-2.2m/o MoO_3 was accomplished using RBSN crucibles and Si_3N_4 cover powder. Two-step sintering cycles were used where the first step, at temperature T_1, and pressure p_1, was held for 60 minutes. The second step, at temperature T_2, and pressure p_2, was held for thirty minutes. T_1/T_2 temperatures ranged from 1850/1860 to 1950/1960 while nitrogen gas pressures, p_1/p_2, were typically 1.5 MPa/8 MPa. Sintered discs were approximately 1.75" diameter x 0.25"-0.375" thick. The discs were machined into bars 0.060" thick x 0.080" wide x 1.125" long. The bars are being used for determination of room temperature modulus of rupture, intermediate temperature (700-1000C) and high temperature (1200-1300C) stress-rupture, and fracture surface examination by SEM.

Room temperature modulus of rupture (MOR)

Room temperature MOR values were determined for machined specimens in the as-sintered condition, after heat treatment of specimens in air or under 7 MPa nitrogen gas, and for stress-rupture survivors to determine retained strength. Heat treatment time was 48-150 hours when fired in air and 12-15 hours when fired in high pressure nitrogen. A temperature of 1200C was used in air heat treatment while 1400C was used in nitrogen. Before testing of specimens sintered at various temperatures between 1850C and 1960C, it was felt that the lower sintering temperatures would produce the highest strength specimens due to finer microstructures. However, from data obtained thusfar, MOR values for specimens sintered at 1850-1900C fell in the 475-575 MPa range while those sintered at 1925-1960C fell in the 650-750 MPa range. Compositions containing 1m/o Mo_2C additions had the highest strengths with values falling off as Mo_2C levels were reduced. Compositions 39 containing 1.1m/o Mo_2C and sintered at temperatures between 1925C and 1960C had a mean strength value of 730 MPa. Long term (150 hours) heat treatment (1200C) in air or shorter term (12-15 hours) at 1400C in nitrogen appears to strengthen these materials but more data must be generated to confirm this effect.

Room temperature MOR testing of stress-rupture survivors to determine retained strength showed apparent significant increases in strength values. A dozen values were obtained with specimens that had been stress-rupture tested at 1200C and 1250C for between 200-400 hours under 300 MPa stress. Specimens exhibited a permanent strain of 0.1-0.25% (depending on temperature and time under stress) from stress-rupture testing and associated errors in MOR testing are probable. However, from curved beam analysis (4), it is shown that if the beam curvature/specimen thickness ratio is large (>40), the error is determined to be small (<1%).

Values of retained MOR for compositions 39 and 40 with 1m/o Mo_2C had risen into the 800-900 MPa range (830 MPa mean) with one value of 1030 MPa recorded.

Stress-rupture testing

Some specimens machined from sintered discs are being tested to determine their behavior in stress-rupture at both intermediate temperatures (700-1000C) and high temperatures (1200-1300C). Four point loading stresses of 300MPa and 400MPa are being used for 400-500 hours at temperature. Prior oxidation results and stress-rupture tests at 900C and 1200C for 200 hours showed no anomalous oxidation behavior at intermediate temperature and good oxidation resistance at both 900C and 1200C. Stress-rupture parameters have been extended to 400-500 hours of test time using the following temperature-stress conditions for specimens sintered using different temperatures:

(1) 1200C-1250C-1300C for 150,150,100 hours, respectively, with 300 MPa stress.

(2) 1200C-1250C-1250C for 150,150,100 hours, respectively, with 300,400,400 MPa stress respectively.

(3) 900C-1250C for 150,150, hours, respectively, with 300,400, MPa stress.

(4) 700C-900C-1100C-1300C for 24,24,24,150, hours, respectively, with 300MPa stress.

(5) 1200C-1250C for 150,250, hours, respectively, with 300 MPa stress.

Most specimens have survived these stress-rupture conditions with residual machining marks still evident on surfaces, i.e., having a thin, coherent oxide layer. Specimens which did not survive were found by subsequent fractographic examination by SEM to have an abnormally large defect as the fracture origin. The defects were either large isolated pores (as shown in Figure 1), pore clusters, or agglomerate/impurity where EDXA indicated the presence of Cl. With increasing hold times at high temperature and stress, stress-rupture survivors exhibited more permanent strain. For bars surviving the stress-rupture conditions shown above, a permanent residual strain of approximately 0.15-0.3% was observed for 1250C and 1300C survivors. Lesser amounts of strain were noted with decreasing temperature and time. Long term, high temperature applications for this material appears limited to 1200C, possibly 1250C.

Sintered bars with the best properties observed to date will be stress-rupture tested at 1200C under 300 MPa for 750 hours.

Microscopy

Sintered bars were polished and etched for microscopic examination by SEM to compare grain size and distribution produced by the various sintering parameters. The use of starting silicon nitride powder with broad particle size distribution and the use of higher sintering temperatures produced microstructures which were more bimodal, i.e., having larger, high aspect ratio grains in a finer grain matrix. Preserving all phases after etching is still presenting problems and continues to be studied. A polished and etched (molten KOH) surface of composition 39 with 1m/o Mo_2C addition as shown in Figure 2. The $Y_2Si_2O_7$ phase has been etched away leaving the outline of the Si_3N_4 grains. The small white area is a Mo_xSi_y particle. This material was sintered at a 1925/1935C, 60/30 min., 1.5/8 MPa N_2 cycle. A comparison of structural features, i.e., grain size, morphology, for specimens sintered at 1870/1880C and 1925/1935C is shown in Figures 3a and 3b, respectively. The fractographs reveal a somewhat coarser microstructure developed at the higher sintering temperatures with higher aspect ratio grains. As previously mentioned, the strength of specimens sintered at temperatures between 1850C-1900C was considerably lower than those sintered at temperatures of 1925C-1960C.

The size and distribution of Mo_xSi_y particles in the Si_3N_4 microstructure is shown in Figure 4 (white areas). These particles are similar to the specimen grain size (in the 1-2um range). Fracture surface analysis indicates that Mo is confined to the particle areas shown. Thusfar, they do not appear to serve as principal fracture origins in specimens used for MOR tests.

Status of milestones

(a) Two compositions of interest (identified as 39 and 40 in the Sintering Section of this report) are being evaluated for final scale-up. These compositions will contain distributed Mo_xSi_y particles with fine (1-2um) particles size.

(2) 75-100 RT MOR tests have been conducted with as-sintered bars, post heat treated bars, and bars surviving stress-rupture tests. The bars were machined from composition 39 and 40 discs sintered at temperatures ranging from 1850C to 1960C.

Stress-rupture tests are continuing at both intermediate and high temperature regimes with test times increasing from 200 hours to 400-500 hours and then, 750 hours under 300 MPa stress. Some of the stress-rupture tests include intermediate temperature STSR in the cycle.

(c) Numerous fractographs of MOR specimens are being examined to determine relative size and morphology of Si_3N_4 grains and minor phases. Fracture origins are being determined. Polished and etched surfaces are being examined for grain size measurements and for compositional analysis of minor phases.

References

1. N.J. Tighe, S.M. Wiederborn, T.J. Chuang, and C.L. McDaniel, "Creep Cavitation and Crack Growth in Silicon Nitride", Proceedings of the International Conference on Plastic Deformation in Ceramics", Penn. State Univ., University Park, PA, 21-22 July 1983.

2. S.M. Wiederhorn and N.J. Tighe, "Structural Reliability of Yttria-Doped Hot-Pressed Silicon Nitride at Elevated Temperatures", Jour. of the American Ceramic Soc., 66, [12], 884-889, Dec. 1983.

3. A.E. Pasto, "Causes and Effects of Fe-Bearing Inclusions in Sintered Si_3N_4", Jour. Amer. Ceramic Soc., 67, [9], C178-C180, Sept. 1984.

4. F.I. Baratta, W.T. Matthews, and G.D. Quinn, "Errors Associated with Flexure Testing of Brittle Materials", MTL TR87-35, July 1987.

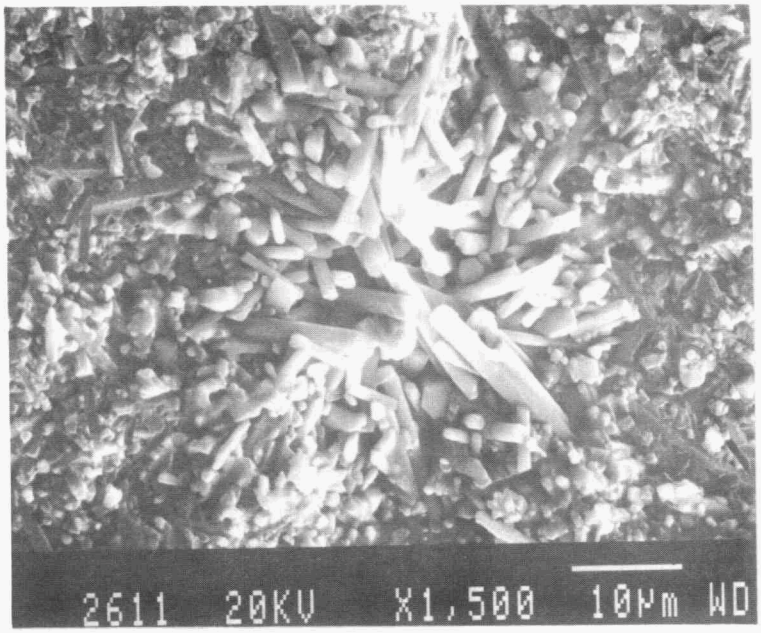

Figure 1. Large pore as fracture orgin of composition 39 specimen with 1m/o Mo_2C sintered at 1925/1935C for 60/30 min. under 1.5/8 MPa N_2 gas pressure (1500X).

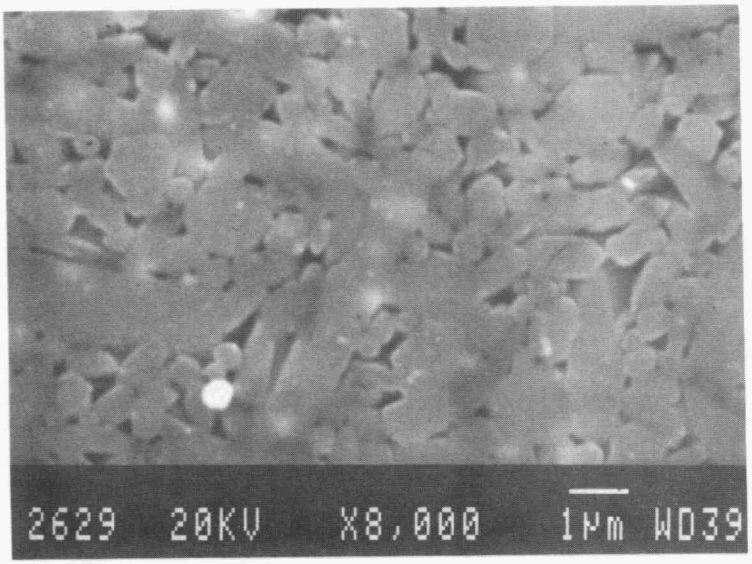

Figure 2. Polished and etched (molten KOH) surface of composition 39 with 1m/o Mo_2C.Silicate phase is etched away (8000X).

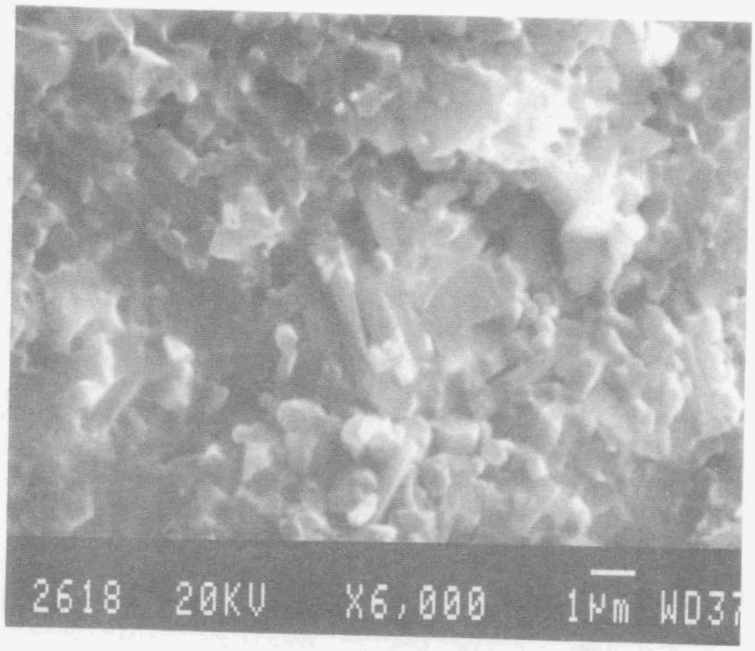

(a)

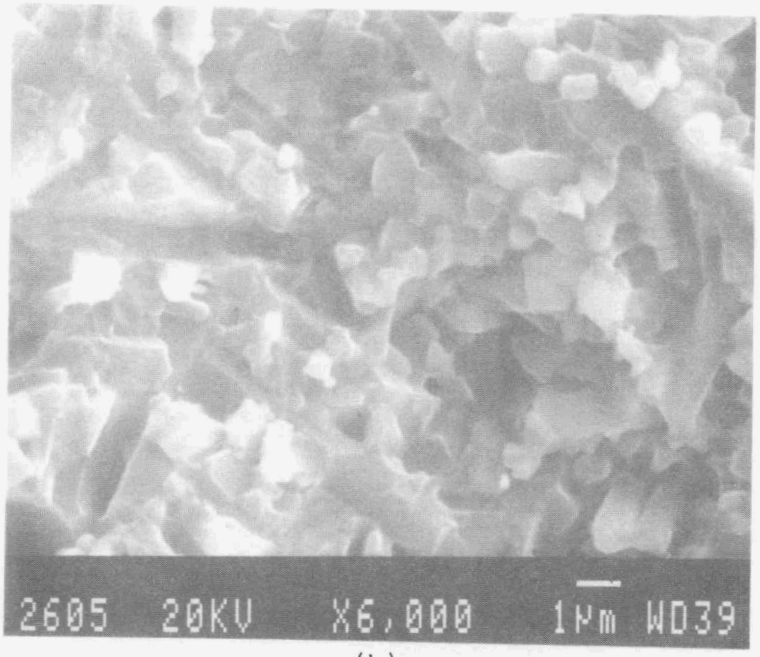

(b)

Figure 3. SEM fractographs of specimens sintered at (a) 1870/1880C and (b) 1925/1935C for 60/30 minutes under 1.5/8 MPa N_2 gas pressure (6000X).

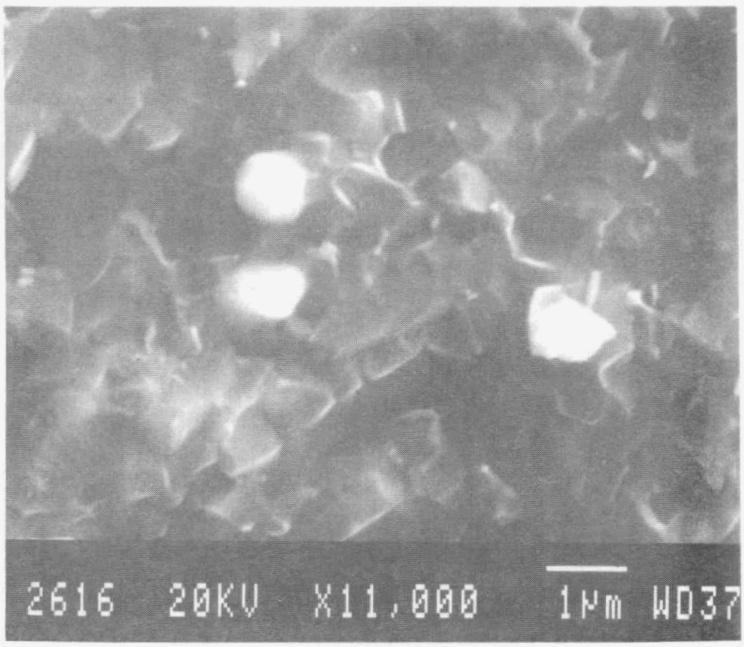

Figure 4. SEM fractograph of specimen sintered at 1870/1880C showing particles (white areas) of Mo_xSi_y in the microstructure (11,000X).

Synthesis of High Purity Sinterable Si_3N_4 Powders -- G. M. Crosbie, J. M. Nicholson, R. L. Predmesky, and E. D. Stiles (Research Staff, Ford Motor Company, Dearborn, Michigan)

Objective/scope

The goal of this task is to achieve major improvements in the quantitative understanding of how to produce sinterable Si_3N_4 powders having highly controlled particle size, shape, surface area, impurity content and phase content. Through the availability of improved powders, new ceramic materials are expected to be developed to provide reliable and cost-effective structural ceramics for application in advanced heat engines.

Of interest to the present powder needs is a silicon nitride powder of high cation and anion purity without carbon residue.

The process study is directed towards a modification of the low temperature reaction of $SiCl_4$ with liquid NH_3 which is characterized 1) by absence of organics (a source of carbon contamination), 2) by pressurization (for improved by-product extraction efficiency), and 3) by use of a non-reactive gas diluent for $SiCl_4$ (for reaction exotherm control).

Technical progress

Introduction

Silicon nitride based ceramics are often considered to represent the toughest of the high-temperature (above 1000°C) monolithic ceramics intended for advanced heat engine use. Also, due to a desirable combination of lower temperature properties (wear resistance, low density, high hardness, and toughness), the nitride ceramics are already finding commercial applications in certain passenger vehicles.

Ceramic reliability and cost depend on powder qualities and subsequent processing. Because powders can limit the capability to achieve unique sintered properties and to fabricate complex shapes, the availability of appropriate powders is critical to advanced ceramics research. In the case of silicon nitride ceramics, the powder purity is especially important, since a low solubility in silicon nitride for many impurities leads to high concentrations of those impurities in grain boundary phases. Also, carbon residues (which are found in some otherwise high purity powders) are considered to be detrimental to second phase oxynitride development, thermal stability, and mechanical properties.

Previous work

The primary points of reference for the previous process work are the 1986 Automotive Technology Development Contractors' Coordination Meeting proceedings paper[1] and the previous semiannual report.[2]

In the previous work, we prepared a novel process flowsheet for preparation of Si_3N_4 with a block flow diagram and a mathematical model of mass and heat balances. We observed that the cooling from latent heat of vaporization of NH_3 more than offsets the heat of reaction at 0°C and 75 psig.

Powder characteristics met or were approaching target values. Key results were achieved in the areas of phase and microstructure, and carbon

purity. Si_3N_4 powder was produced with phase content, particle size andshape which are close to those characteristics considered desirable for pressureless sinterability. An overpressure sintering to 83% T.D. was obtained.

Specifically, the powder derived by thermal decomposition of an intermediate imide product (from reaction of $SiCl_4$ with liquid NH_3 at 0^oC and 75 psig) was principally alpha silicon nitride (as determined by x-ray diffraction, which has little sensitivity to amorphous phases) with crystallite size of 0.2 to 0.3 um and primarily equi-axed particle shape.

The process was identified to have features which are important for scale-up. Key features of near-neutral heat balance and liquid-like materials handling were demonstrated.

Also, improvements were achieved in yield, laboratory production rate, cation purity, and alpha/beta ratios.

Summary of current period work

In this period, we prepared a pilot plant design for the "vapor-chloride - liquid ammonia" process, carried out additional process development including the "liquid chloride - liquid ammonia" direct reaction, campaigned runs to test process stability, carried out sintering tests, and reported on a new analytical method. These are described below.

Pilot plant design

A design for a 100 kg/month Si_3N_4 pilot plant was developed in cooperation with a chemical engineering consulting firm. The detailed pilot plant design is for the "vapor chloride - liquid ammonia" process for imide preparation. Numerous suggestions for redesign of the reactor and auxiliaries were made which are being incorporated in the next phase scale-up at Ford.

A detailed piping and instrumentation diagram for a silicon diimide route pilot plant was completed as part of this subcontracted engineering study. The design specifies equipment and costs for a 100 kg/mo. (as nitride) plant. This monthly production rate is based on 8 hour days and 20 days per month operation. The study also provided for detailed checking of the overall flowsheet calculations and for input of new ideas for scaled lab production by the vapor-liquid process. Open issues in the design were identified which will be addressed in further lab work.

Tests of factors other than imide synthesis
with "liquid chloride - liquid ammonia" route

In the laboratory, additional process development was carried out to test process factors other than imide formation, which had been the previous focus. In these tests, the imide was prepared by the "liquid chloride - liquid ammonia" reaction, along the lines of Billy[3] and Morgan,[4] but with operation under pressure (rather than extremely low temperature) to keep the ammonia liquid. The expected exotherm of the liquid-liquid reaction was confirmed, but controllable at 10 g scale. These tests showed that oxygen contamination is not exclusively due to the

carrier gas of the "vapor chloride - liquid ammonia" process. Tests for effectiveness of rinsing out of by-product Cl by decantation were carriedout in a series of six runs. Various minor modifications were made which apparently resulted in a reduction in oxygen contamination from 12.8 wt.% to 7.4 wt.%, as reported in the last semi-annual report.[2]

Scaled Production

We then campaigned scaled runs with the "liquid $SiCl_4$ - liquid NH_3" reaction to produce powder batches for sintering tests with minor modification of the apparatus. In seven of the eight runs made in a two-month period, we obtained product masses averaging 7.6 grams. We began sintering of these powders to 1800°C at atmospheric pressure.

We were consistently succeeding in completing powdermaking runs tested in this campaigning period. This consistency reflects the relatively minor nature of changes made and the operability in spite of an exotherm at lab scale of the liquid chloride - liquid ammonia reaction under 60 to 110 psig (0.52 to 0.86 MPa).

The process changes included a new valving scheme for the $SiCl_4$ line purging and a change in return flow management for the condenser return stream. In seven of the eight runs made in April and May 1987, we obtained product masses averaging 7.6 gram. Product masses ranged from 3.9 to 11.2 gram. (In the eighth run, a valving sequence change was made which resulted in a 2.9 g batch.) This relative measure of production consistency is an important accomplishment.

Sintering

With the powder production, we began again sintering of die pressed samples from our own powders. The sintering tests are marginally feasible with 9-11 gram quantities of powder. In sinterability tests (in 1986) of our powder, we had used nitrogen overpressure sintering. Now, we are developing cycles for pressureless sintering, with a sintering cycle developed in a baseline study with commercial powders. In the baseline study with a composition of 10 wt.% Y_2O_3 and 2.25 wt.% Al_2O_3, we were able to reproduce both densities of 96-97% T.D. and grain boundary phases developed in three separate sintering runs.

For the one pair of samples tested from our own powder from this period, we observed by x-ray diffraction phase problems that are expected with oxygen excess: oxynitride phase. Density value was 67% (well below overpressure sintered of 83% with vapor chloride process powder with 8 wt.% Y_2O_3 and no added Al_2O_3). Diametral sintering shrinkage was 16%, which continues to indicate sintering activity, in spite of problems with final value.

What was unexpected in the pressureless sintering run was that a control sample of the composition that was reproducible in baseline tests dropped from 96 to 91 % density and shifted to a less desirable grain boundary phase. Factors changed were the presence of the other samples and smaller size of the test pieces. This departure may be due to smaller size (than previous baseline tests) or interaction in sintering in the atmosphere shared with a dissimilar material.

Agitation testing

We then moved away from campaigning runs in order to return to process flowsheet development. We began tests of agitation duringrinsing. In order to decrease water vapor permeability and oxygen contamination of the powder product, the imide synthesis and thermal decomposition systems were re-designed to eliminate 95% of the polymer tubing previously present. Also, a non-alumina decomposition vessel was installed. The benefits of these changes are pending.

In laboratory demonstration tests, we continued to operate the reaction system under pressure but without agitation. As we move to larger quantities, agitation appears to be a greater need.

The simplest implementation of agitation on the flow system was tried: gas bubble agitation from the bottom of the vessel during rinsing. In one test so far, no indication of greater NH_4Cl recovery was observed. It appears unlikely that this method will be sufficient for removal of chloride from the liquid $SiCl_4$ - liquid ammonia imide.

A mechanically agitated pressure vessel was specified and an order initiated. The mechanical agitation is expected to increase bubble residence time in operation of the gaseous $SiCl_4$-liquid NH_3 reaction route and allow greater mass rates. The agitation is also expected to improve chlorine extraction.

System rebuild

To address persistent oxygen contamination around the 10 wt.% level, several changes were made to the experimental apparatus to reduce inward leakage. (It now appears that in spite of a pressure differential, there can be diffusion of H_2O through polymeric tubing and gaps in fitted joints, due to the chemical driving force for reaction of water with $SiCl_4$ and ammonia.) Both the imide synthesis and thermal decomposition systems were re-designed to eliminate 35 feet (10.7 m) of Teflon^R tubing previously present. Also, the number of fittings was reduced by about 30%. The condenser was also rebuilt after long use. These changes should reduce inward permeation of gases and liquids against the pressure.

A non-alumina decomposition vessel was installed as part of the enclosed system. There is some evidence of correlation of higher aluminum concentrations with higher oxygen contamination levels. (Earlier, we had tried to monitor weight gain/loss of the decomposition vessel, but results were inconsistent.) The choice of non-alumina vessel may also reduce alumina transport to the powder in view of the Cl species which are known to remain due to incomplete rinsing of NH_4Cl.

This equipment was used in early October to complete a powdermaking run by the liquid $SiCl_4$ - liquid NH_3 route. The resulting powder characteristics are still pending. The shake-down period was longer than anticipated. The types of problems encountered in incomplete runs included 1) compression fittings that leaked after the cool-down for a run, in spite of ambient temperature vacuum and overpressure testing, 2) multiple valve stem leaks on new valves in the NH_3 metering line, and 3) valve seizure due to corrosion in a nine-month old $SiCl_4$ line valve.

Novel characterization method to discern amorphous species

An analytical method was developed (by K. R. Carduner, Ford Research) for quantitatively evaluating crystalline and amorphous contents of silicon nitride powders by ^{29}Si MAS-NMR (Magic Angle Spinning Nuclear Magnetic Resonance).

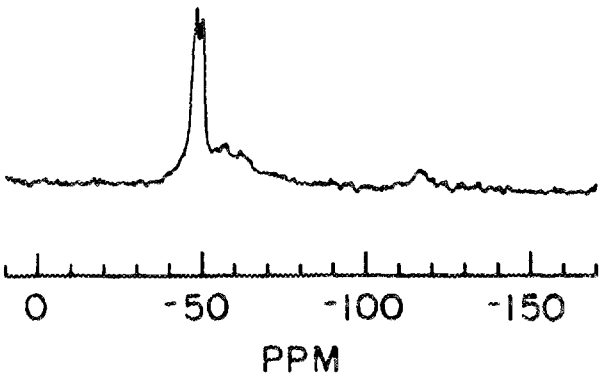

Figure 1. Magic Angle Spinning - Nuclear Magnetic Resonance (MAS-NMR) spectrum of synthesized powders (courtesy K. R. Carduner, et. al, Ref. 5). The two peaks corresponding to alpha Si_3N_4 have a broad shoulder representing amorphous silicon nitride. To the right, a broad peak for amorphous silicon oxynitrides appears. By x-ray diffraction methods, it would not be feasible to distinguish the amorphous oxynitrides from amorphous silicon nitride.

In the powder synthesis project Task 2, titled "Characterization," there is stated a need "... to develop or demonstrate new and improved quantitative techniques ...." A technique was developed which can readily distinguish the individual concentrations of different amorphous and crystalline chemical species in silicon nitride powders. The alpha Si_3N_4 has two peaks and the beta has only one. Amorphous silicon nitride is a broad peak at the Si_3N_4 position. In the sample from this work shown in Fig. 1, a second broad peak is apparent, which corresponds to the amorphous silicon oxynitrides. By x-ray diffraction methods, it would not be feasible to distinguish the amorphous oxynitrides from amorphous silicon nitride.

A manuscript describing the quantitative method is in press.[5] The manuscript also relates that certain commercial Si_3N_4 powders which appear to be entirely crystalline by x-ray diffraction actually have 20 to 30% amorphous content as determined by magic angle spinning NMR (MAS-NMR).

Status of milestones

The milestones for the contract extension periods are on schedule.

Publications

G. M. Crosbie, "Si_3N_4 Powder Synthesis," presented at the Am. Ceramic Soc. Annual Meeting, Pittsburgh, Pa., April 26-30, 1987.

G. M. Crosbie, "Silicon Nitride Powder Synthesis," pp.255-265 in: *Proc. of the 24th Automotive Technology Development Contractors' Coordination Meeting*, Soc. of Automotive Engineers, Warrendale, Pa., 1987. (P-197)

L. M. Sheppard, "Vapor-Phase Synthesis of Ceramics," *Advanced Materials & Processes inc. Metal Progress*, April 1987, pp. 53-58. (A review article.)

K. R. Carduner, R. O. Carter III, G. M. Crosbie, M. E. Milberg, T. J. Whalen, L. C. Westwood, E. N. Boulos, and M. F. Best, "Analytical Applications of Solution and Solid State ^{29}Si NMR," submitted for presentation at the Pittsburgh Conference to be held in New Orleans, February 22-26, 1988.

K. R. Carduner, R. O. Carter III, M. E. Milberg, G. M. Crosbie, "Determination of Silicon Nitride Crystallinity and Silicon Phase Composition of Silicon Nitride Powder by ^{29}Si MASNMR," to appear in *Analytical Chemistry*, November-December, 1987.

G. M. Crosbie, J. M. Nicholson, R. L. Predmesky, and E. D. Stiles, "Silicon Nitride Powder Synthesis Program," presented at the 25th Automotive Technology Development Contractors' Coordination Meeting, Dearborn, Michigan, Oct. 26-29, 1987.

References

1. G. M. Crosbie, "Silicon Nitride Powder Synthesis," pp.255-265 in: *Proc. of the 24th Automotive Technology Development Contractors' Coordination Meeting*, Soc. of Automotive Engineers, Warrendale, Pa., 1987. (P-197).

2. G. M. Crosbie, "Synthesis of High Purity Sinterable Si_3N_4 Powders," pp. 17-23 in *Ceramic Technology for Advanced Heat Engines Project Semiannual Report for October 1986 Through March 1987*, ORNL/TM-10469, Oak Ridge National Laboratory, Oak Ridge, Tenn., August 1987.

3. M. Billy, "Preparation et Definition du Nitrure de Silicium," *Ann. Chim. (Paris)* 4 [13] 795-851 (1959).

4. P. E. D. Morgan, "Production and Formation of Si_3N_4 from Precursor Materials," Final Report, March 1973 - December 1973, NTIS AD-778-373, March 1974, (Sponsored by Office of Naval Research).

5. K. R. Carduner, R. O. Carter III, M. E. Milberg, G. M. Crosbie, "Determination of Silicon Nitride Crystallinity and Silicon Phase Composition of Silicon Nitride Powder by ^{29}Si MASNMR," to appear in *Analytical Chemistry*, November-December, 1987.

1.2 CERAMIC COMPOSITES

1.2.2 Silicon Nitride Matrix

SiC-Whisker-Toughened Silicon Nitride

Hun Yeh (Garrett Ceramic Components Division) and Jim Schienle (Garrett Turbine Engine Company)

Objective/scope

The objective of this program is to develop the technology base for fabricating ceramic composites consisting of silicon carbide whiskers dispersed in a dense silicon nitride matrix. A goal of this research is to develop a ceramic composite with significantly improved fracture toughness over the unreinforced silicon nitride matrix without a degradation of other properties. Garrett Ceramic Components Division (GCCD), Garrett Processing Company (formerly AiResearch Casting Company), as prime contractor, is responsible for developing the fabrication techniques. Garrett Turbine Engine Company (GTEC), as a major subcontractor, is responsible for mechanical property and microstructural evaluations. Allied-Signal Engineered Materials Research Center (ASEMRC) provides analytical assistance.

Technical progress

(a) Processing

In the last reporting period, two new sets of four composite billets (10 to 40 wt. percent ACMC* SC-9 SiC whisker (SiCw)) were coprocessed through slip casting. One set of the two was subsequently processed through presintering (1000°C/argon/1 hr), encpasulation in niobium and HIP'ing (1750° F/28 ksi/4 hr). All four billets achieved near-theoretical densities and uniform whisker dispersion (October 1986 -March 1987 Semiannual Report). Consequently, in this reporting period it was decided to complete processing the second set of billets through HIP'ing using the procedures/parameters identical to those used for the first set. Again, near-theoretical densities were achieved in all four billets. Table 1 lists the density results of both HIP runs.

Both sets of composite billets were machined into text bars for flexural strength and chevron toughness tests. The results are presented in the next section.

Two additional composite billets (10 and 40 wt. percent ACMC SC-9 SiC whiskers) were hot isostatically pressed using the ASEA glass encapsulation/HIP method. Both billets achieved

*Advanced Composite Materials Corp. (Formerly a division of ARCO)

TABLE 1

DENSITY RESULTS FOR 1750°C/28 ksi/4 hr HIP CYCLE

Percent SiC	HIP Run 1	HIP Run 2
10	3.23	3.24
20	3.23	3.24
30	3.23	3.23
40	3.20	3.24

3.24 g/cc. Characterization results will be reported in the final report. This activity is beyond the scope of the program. The purpose of this study is to compare the Nb metal encapsulation/HIP used in the program with ASEA glass/HIP, which has a higher potential for net shape mass production.

(b) Mechanical Testing

Flexural strength (MOR) and chevron toughness tests were conducted at room temperature, 1000°C and 1200°C on the test bars machined from the two sets of densified composite billets described in the last section.

Flexural strength testing was performed on 0.025-in. by 0125-in. by 2.0-in test bars (chamfered) using four-point bending. Chevron toughness testing was performed on 0.25-in by 0.25-in by 2-in. chevron notched bars in three-point bending. All fractured MOR specimens were examined optically at 40x. A selected number of specimens were examined under an SEM for more detailed analysis. The results of these two tests are discussed in the following paragraphs. Due to the limited numbers of test bars that can be machined from each billet, only a limited number of tests were performed for each SiC whisker loading and test temperature combination.

- Flexural Strength and Fractorgraphy of HIP Run 1 Specimens

The strength results are summarized in Table 2 and Figure 1. At room temperature, the 10 percent and 30 percent SiC composites exhibited average strengths above 100 ksi (109.0 ksi and 102.7 ksi, respectively). The 20 percent and 40 percent SiC composites exhibited lower strengths (80.0 ksi and 69.6 ksi, respectively). Optical analysis of the failure origins revealed that all specimens of the 10 percent, 20 percent, and 30 percent SiC compositions failed from grayish areas. The 40 percent SiC composites exhibited the same grayish areas on the

TABLE 2

FLEXURAL STRENGTH TEST RESULTS

(Number in parenthesis indicates number of tests)

Average	Strength* ± Standard Deviation (ksi)		
Percent SiC	Room	1000°C	1200°C
HIP Run 1			
10	109 ± 13.9 (10)	108.2 + 4.5 (5)	63.4 ± 4.5 (5)
20	80 ± 17.9 (10)		36.9 ± 3.5 (4)
30	102.7 ± 11.8 (10)		40.3 (1)
40	69.6 ± 7.1 (10)		27.4 (1)
HIP Run 2			
10	97.3 ± 10.4 (5)	92.1 ± 8.3 (5)	61.4 ± 11.3 (5)
20	102.8 ± 8.8 (5)	116.4 ± 12.5 (5)	38.9 ± 3.3 (5)
30	88.0 ± 19.6 (5)	97.8 ± 28.2 (5)	38.2 ± 3.0 (5)
40	51.7 ± 27.9 (5)	93.2 ± 15.4 (5)	34.6 ± 3.4 (5)

*Four-point bending; outer and inner spans 1.5-in. and 0.75-in., respectively; 0.025-in x 0.125-in. x 2.0-in. test bars.

fracture surfaces, but failed from flaws light in color relative to the matrix. SEM analysis was used to further characterize the fracture origins. A high and low strength specimen for each whisker loading was examined. The results are summarized in Table 3. Figures 2 through 9 are SEM micrographs for specimens listed in Table 3.

The SEM results did not find the grayish areas to be associated with a particular flaw type. The origins for 10 percent, 20 percent and 30 percent SiC composites were associated with either high concentrations of Y and Al (Y_2O_3 and Al_2O_3 are used as sintering aids) or Fe, Cr, and Mo (frequently observed contaminants of the Si_3N_4 powder used in this study). In many cases, both type of concentrations were associated with large Si_3N_4 grains (energy dispersive and wavelength dispersive X-ray analysis indicates the grains are Si and N rich). Since no large Si_3N_4 grains were detected by SEM in green, as-cast composite material, the large Si_3N_4 grains most likely grew during densification. The green composites did have concentrations of sintering aids and the contaminants observed in dense composites. The 40 percent SiC composite failure origins were low density regions that exhibited acicular Si_3N_4 grain growth.

At 1200°C, all four composite compositions exhibited strength loss relative to the room temperature strengths. The 1200°C strength for

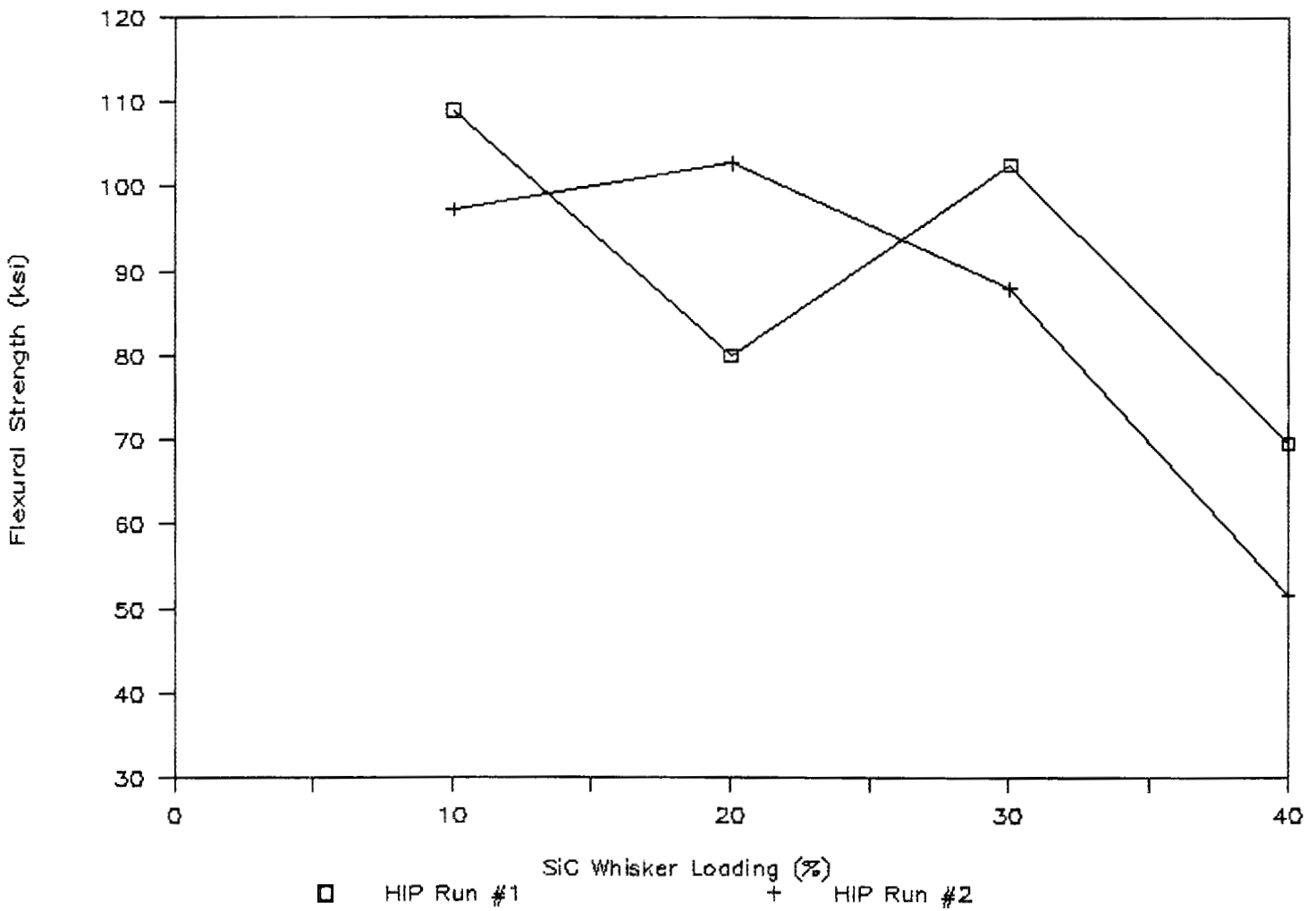

Figure 1. Room Temperature Strengths for Composites from HIP Runs 1 and 2 as a Function of SiC Whisker Loading

TABLE 3

SUMMARY OF SEM FRACTOGRAPHY RESULTS OF ROOM TEMPERATURE MOR TESTS *

Percent SiC	MOR (ksi)	Origin
10	84.1 (min)	Concentration of Y (Figure 2)
10	123.6 (max)	Porosity inside 15 micron Si_3N_4 grain (trans-granular); Fe detected around grain (Figure 3)
20	63.9	5 micron pore inside 50 micron Si_3N_4 grain (transgranular); concentrations of Y and Al around the inside grain (Figure 4)
20	97.9	70 micron grain on bar surface (transgranular); concentrations of Y and Al around and inside grain (Figure 5)
30	93.9	30 micron grain (transgranular) with concentrations of Fe around and inside grain (Figure 6)
30	114.9	Concentration of Fe, Cr, and Mo (Figure 7)
40	57.9	Low density region (Figure 8)
40	76.6	Low density region (Figure 9)

*Specimens from HIP Run 1

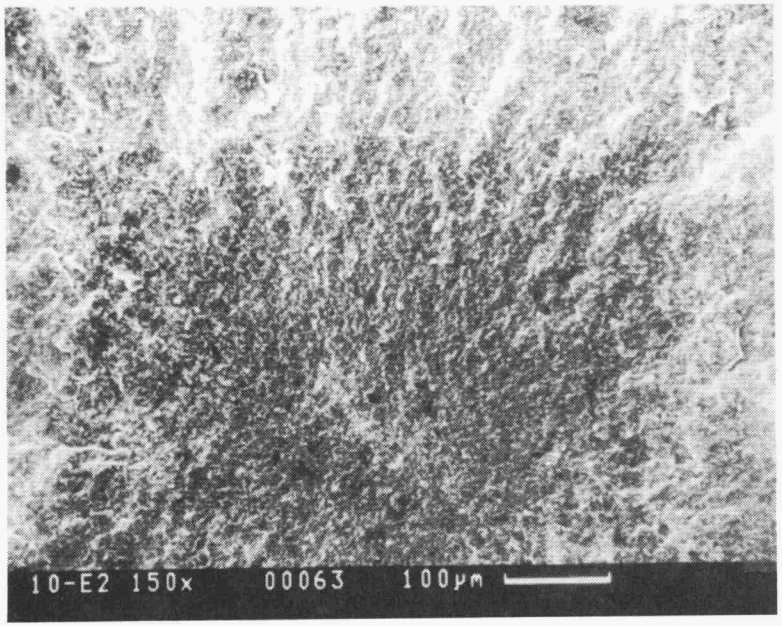

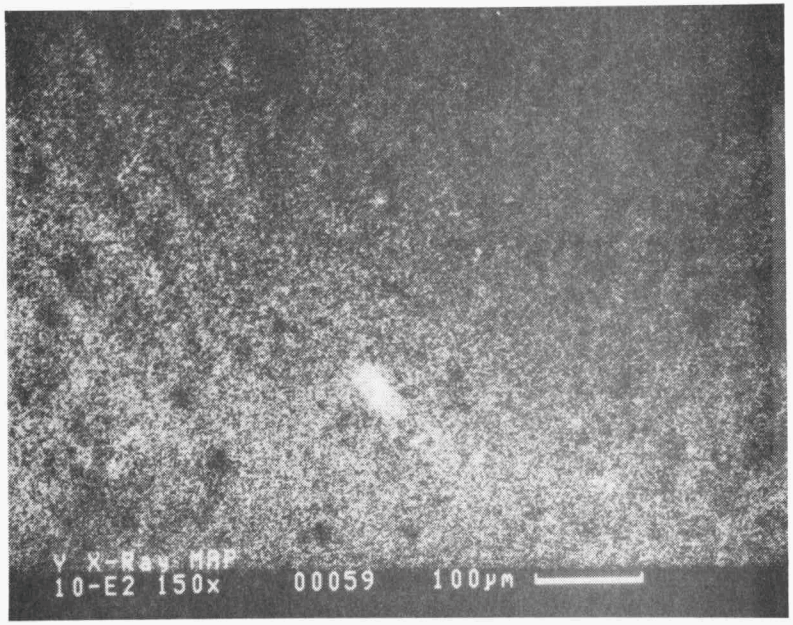

Figure 2. Y Rich Failure Origin (10 Percent SiC Whisker Loading Composite)

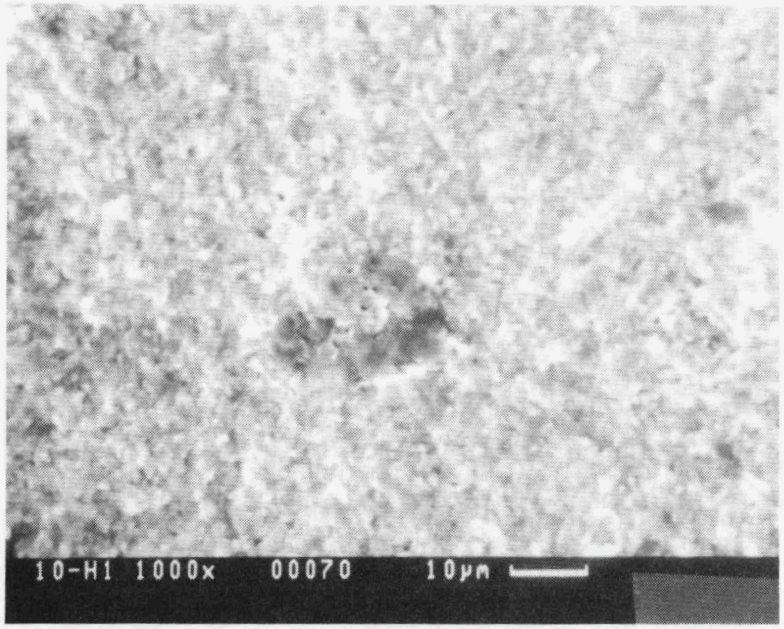

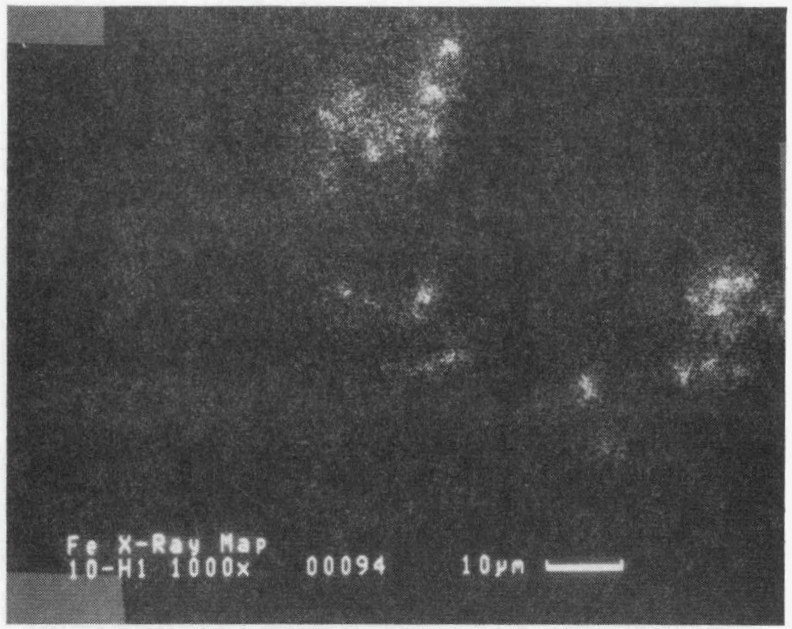

Figure 3. 15 Micron Si_3N_4 Grain Exhibiting Transgranular Fracture from Porosity Inside; Fe Contamination Around Grain (10 Percent SiC Whisker Loading Composite)

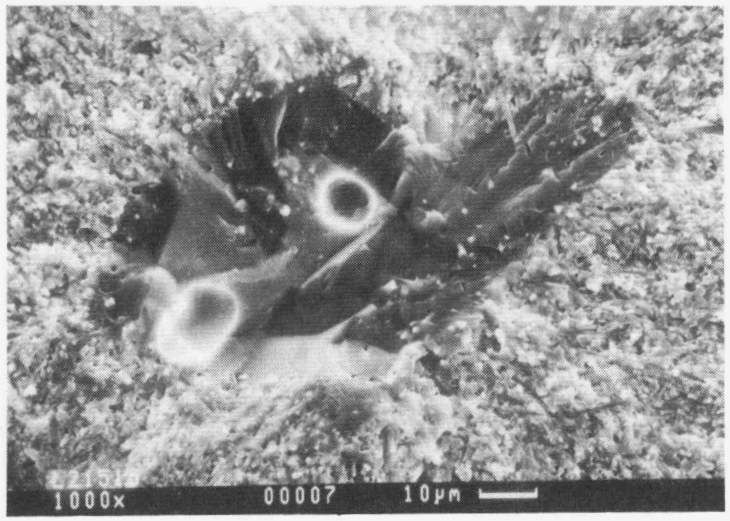

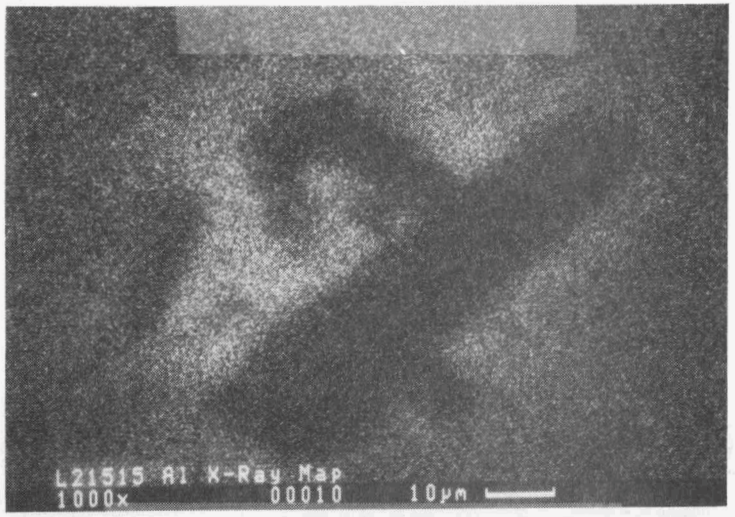

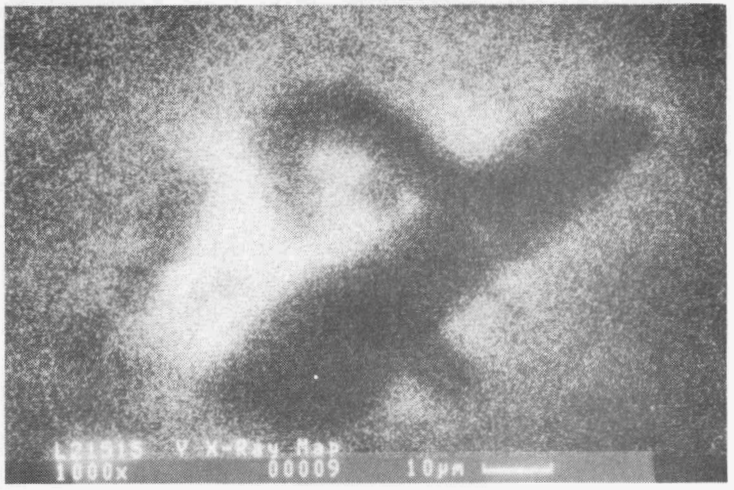

Figure 4. 50 Micron Si_3N_4 Grain Exhibiting Transgranular Fracture from 5 Micron Pore Inside; Concentrations of Y and Al Around and Inside Grain (20 Percent SiC Whisker Loading Composite)

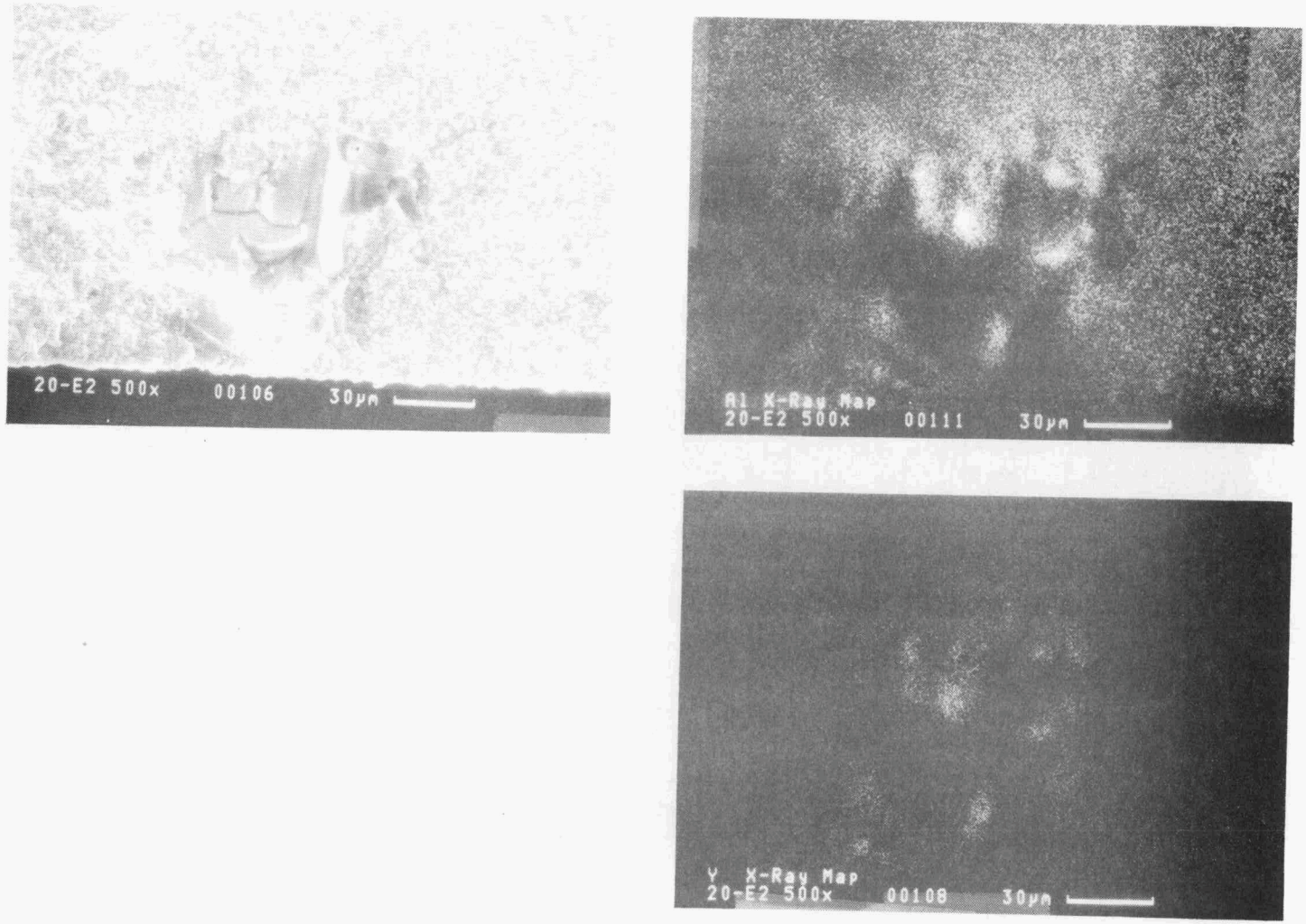

Figure 5. 70 Micron Si_3N_4 Grain with Concentrations of Y and Al Around and Inside Grain (20 Percent SiC Whisker Loading Composite)

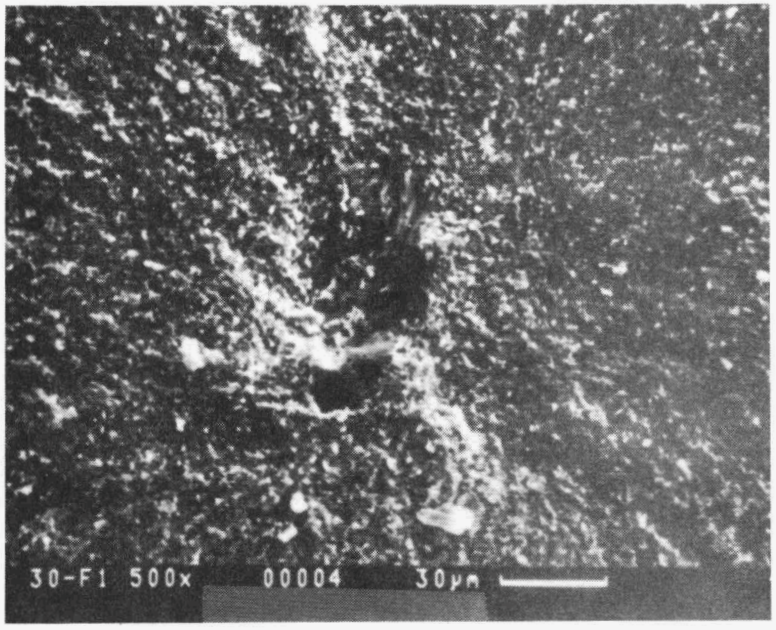

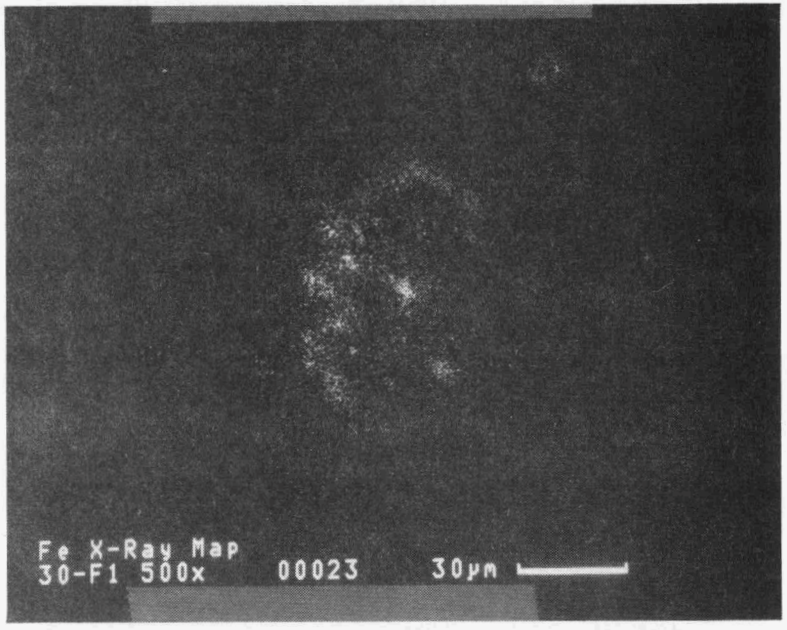

Figure 6. 30 Micron Grain with Concentrations of Fe Around and Inside (30 Percent Whisker Loading Composite)

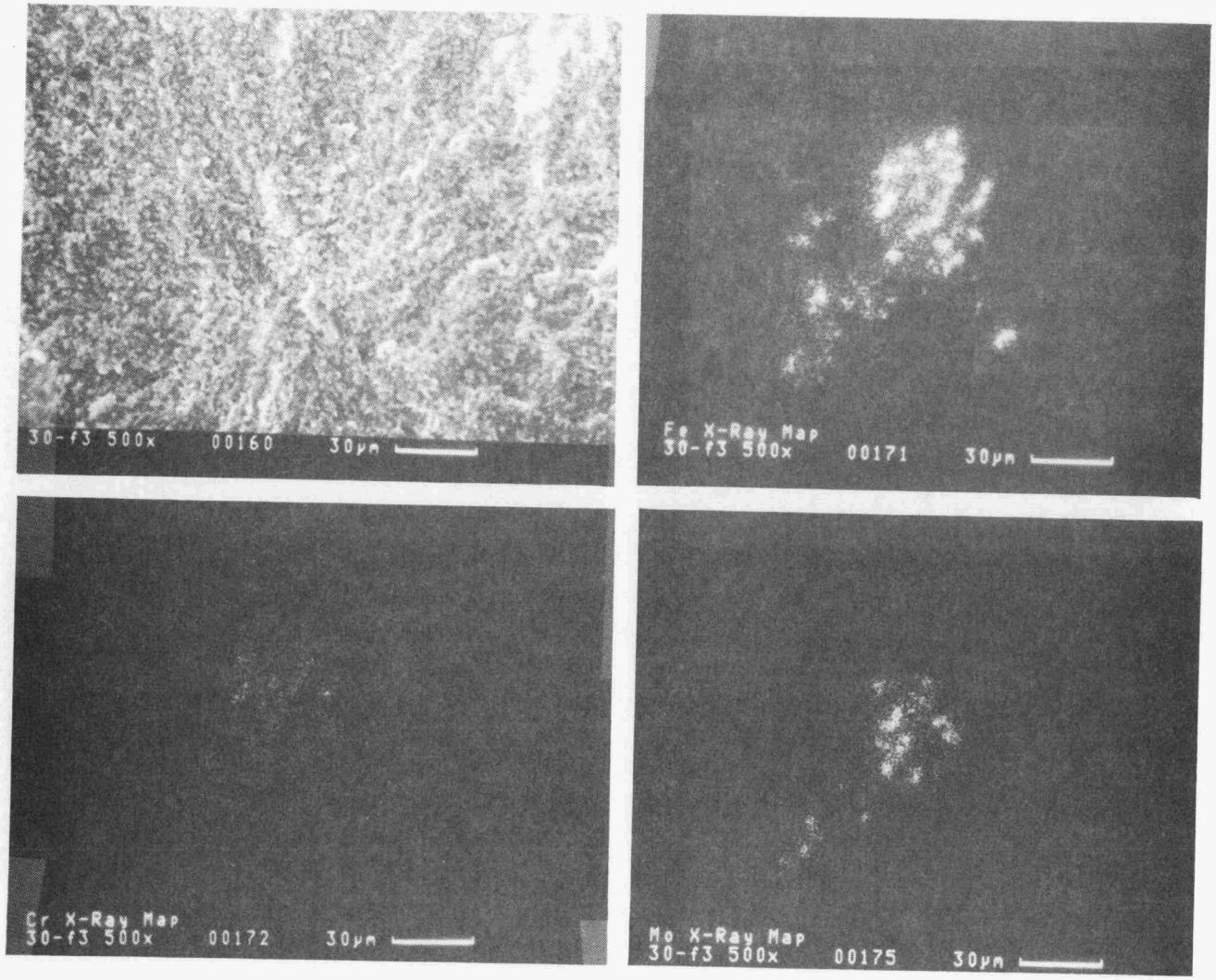

Figure 7. Concentration of Fe, Cr, and Mo (30 Percent Whisker Loading Composite)

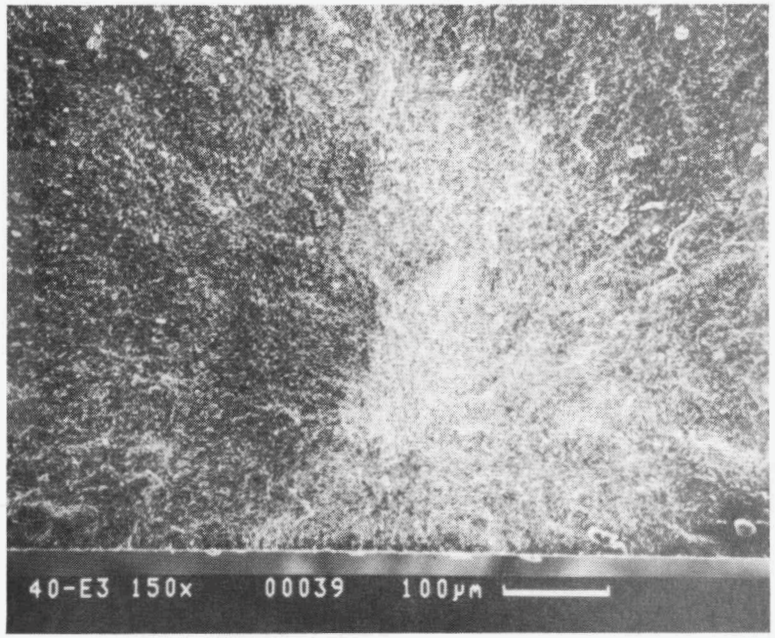

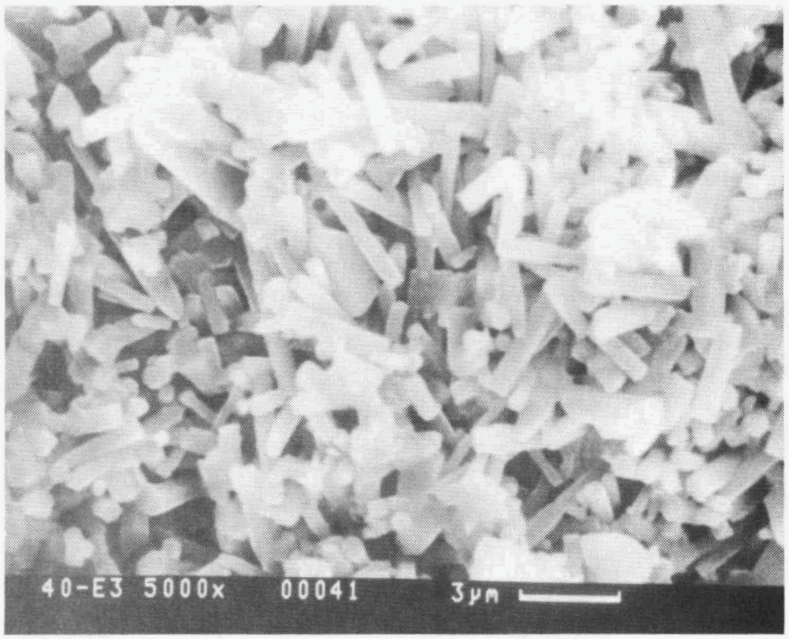

Figure 8. Low Density Region Exhibiting Acicular Si_3N_4 Grains (40 Percent SiC Whisker Loading Composite

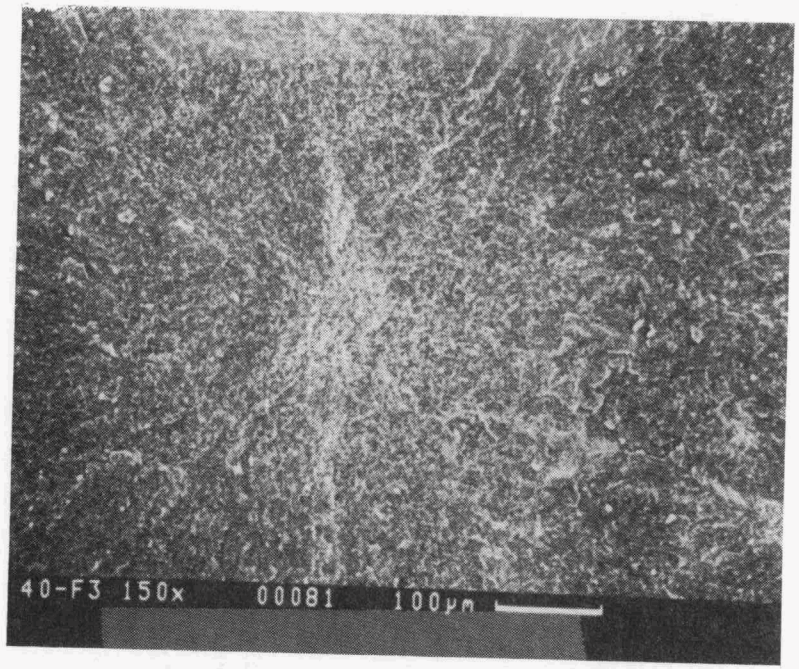

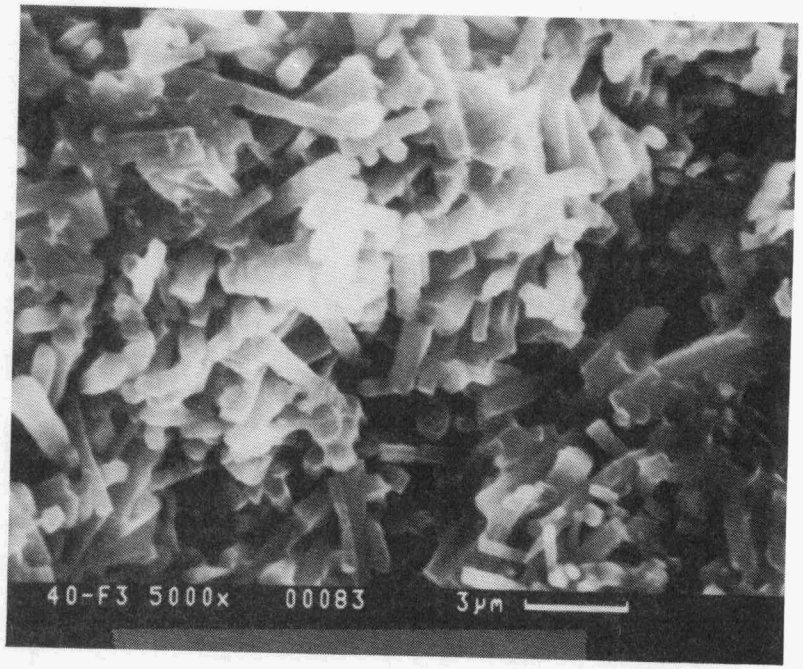

Figure 9. Low Density Region Exhibiting Acicular Si_3N_4 Grains (40 Percent SiC Whisker Loading Composite)

the 10 percent SiC composite was 63.4 ksi, characteristic of the GCCD Code 2 matrix, typically 60 ksi. However, composites with larger whisker loading exhibited significantly lower strengths. The 20, 30, and 40 percent SiC composites exhibited averaged strengths of 39.6 ksi, 40.3 ksi, and 27.4 ksi, respectively. The failure origins for the 10 percent SiC composites were the grayish areas, which were also observed in the room temperature test specimens. For the 20 percent, 30 percent and 40 percent SiC composites, the fracture surfaces appeared smooth and featureless, and did not exhibit a distinct failure origin.

Additional specimens of the 10 percent SiC loading were available for intermediate temperature testing (1000°C). At 1000°C, the 10 percent SiC composite exhibited complete strength retention, 108.2 ksi compared to 109.0 ksi at room temperature. The fracture origins were similar to those observed in 10 percent SiC composites tested at room temperature and 1200°C.

- Flexural Strength and Fractography of HIP Run 2 Specimens

The room temperature strengths for HIP Run 2 specimens were lower than that for HIP Run 1 specimens, with the exception of the 20 percent SiC composition (Table 2). As observed for the HIP Run 1 specimens, the origins of the 10 percent, 20 percent and 30 percent SiC composites were predominantly the grayish areas. However, the 40 percent SiC composites also failed from these areas. In 40 percent SiC specimens from HIP Run 1, the failure origins were areas of low density.

At 1000°C, the 10 percent SiC composites exhibited complete strength retention relative to the room temperature strength (Table 2). The 20, 30, and 40 percent SiC composites exhibited increased strength relative to the room temperature strength. The strength increase for the 40 percent SiC composite was almost twofold. The reason for the strength increase requires more detailed study.

At 1200°C, the composites exhibited the same trends in strength observed for HIP Run 1 specimens (Table 2). The 10 percent SiC composite had an average strength of 61.4 ksi, which is typical of the Code 2 matrix. The 20, 30, and 40 percent SiC composites exhibited lower strengths, 38.9 ksi, 38.2 ksi, and 34.6 ksi, respectively.

- Fracture Toughness Test

The scatter in toughness results for a given composite and at a given temperature is very narrow (Table 4). The differences in toughness between the two HIP run billets, where tests at the same temperatures were performed, are also very small. Therefore, the following discussions concern the combined toughness results from the two HIP runs, although they are listed separately by the run number in Table 4.

TABLE 4

FRACTURE TOUGHNESS RESULTS

(Numbers in parenthesis indicate number of tests)

Percent SiC	Average Room	Average Toughness* ± Standard Deviation (ksi*in 1/2) 1000°C	1200°C
HIP Run 1			
10	5.92 ± 0.85 (5)		
20	6.12 ± 0.57 (5)	6.01 (1)	5.03 ± 0.07 (2)
30	6.51 ± 0.21 (5)	6.44 ± 0.13 (2)	5.83 ± 0.07 (2)
40	5.73 ± 0.42 (4)	6.91 ± 0.80 (2)	4.02 (1)
HIP Run 2			
10		5.62 ± 0.05 (2)	4.77 (1)
20		6.42 ± 0.78 (3)	
30		6.22 ± 0.52 (3)	
40		6.59 ± 0.02 (3)	

The room temperature fracture toughness (K_{IC}) results are plotted in Figure 10. The K_{IC} increased as a function of SiC loading from 5.92 ksi in. at 10 percent SiC up to 6.51 ksi in.$^{1/2}$ at 30 percent SiC. At 40 percent SiC, the K_{IC} dropped off to 5.73 ksi in.$^{1/2}$ The results indicated 30 percent whisker loading is optimum for fracture toughness. The toughness for the 30 percent SiC composite is a 21 percent increase over the sintered monolithic GCCD Code 2 matrix (5.37 ksi in.$^{1/2}$). This toughness is a slight improvement over the program's previous best, 6.45 ksi in.$^{1/2}$ (June-July 1986 Bimonthly Report), obtained from a composite containing 20 percent SiC whisker (ACMC SC-9) and HIP'ed at 1800°C. The fact that the new 20 percent SiC loaded material HIP'ed at 1750°C for 4 hr, exhibited a toughness lower than the similar material HIP'ed at 1800°C for 2 hr (6.12 vs 6.45 ksi in.$^{1/2}$) suggests that additional improvements in the 30 percent SiC composite might be obtained by HIP'ing at 1800°C for 2 hr.

For the 10 percent, 20 percent, and 30 percent SiC composites, the toughness at 1000°C is approximately the same as at room temperature. The toughness of the 40 percent SiC composite increased slightly at 1000°C relative to the room temperature toughness. At 1200°C, the toughness decreases for all compositions.

- <u>X-Ray Diffraction and Metallographic Analyses</u>

X-ray diffraction (XRD) analysis was performed on HIP Run 1 specimens of each whisker loading (10, 20, 30, and 40 percent SiC). The

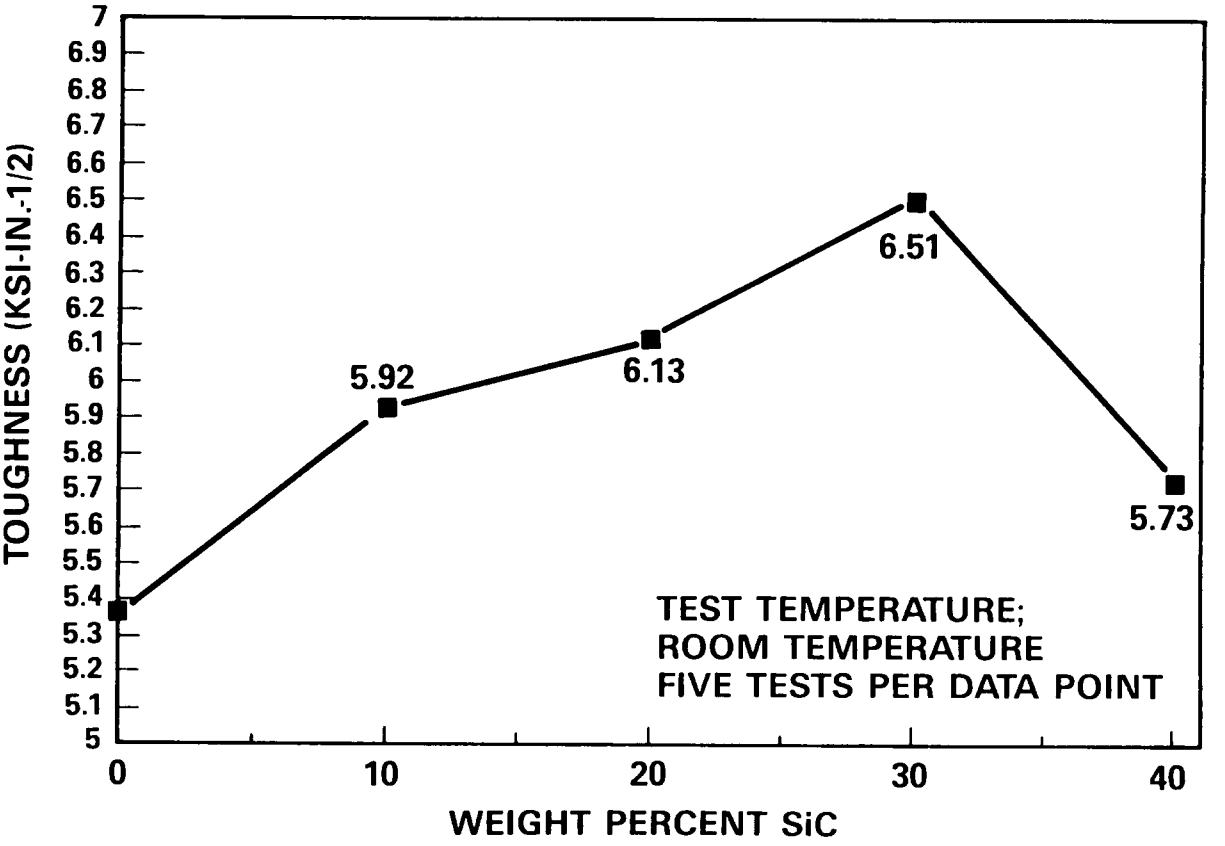

CHEVRON NOTCH THREE POINT BEND TEST

SPAN: 1.5 IN.

SPECIMEN:

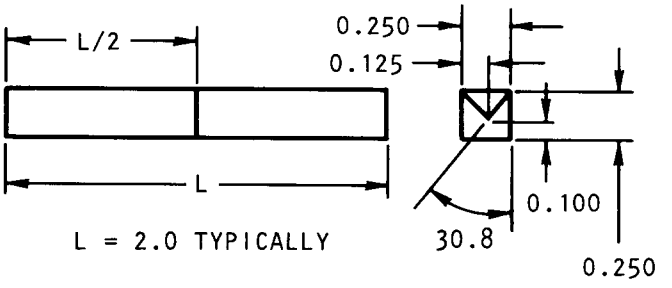

TOLERANCE ±0.001

NOTES: 1. ALL DIMENSIONS ARE IN INCHES
2. EDGES ARE NOT CHAMFERED

Figure 10. Room Temperature Toughness vs Whisker Loading

XRD patterns loading revealed only the expected beta Si_3N_4 and SiC phases.

Metallographic analysis was performed on HIP Run 1 composites of each whisker loading to evaluate whisker integrity through processing, and whisker distribution and orientation. Photographs of the polished sections are shown in Figures 11 through 14. The results indicate that, within the detectability of an optical microscope, the whiskers maintained integrity through processing, still exhibiting high aspect ratio characteristics. Also, the whiskers are relatively well dispersed and randomly oriented. However, regions of unreinforced matrix up to 20 microns in diameter were observed.

- Elastic and Thermal Properties

The elastic properties, thermal diffusivity, and thermal expansion coefficient of composite specimens from HIP Run 1 were measured.

The elastic properties of the composites were determined by measuring the shear and compressional velocities of an ultrasonic wave through composite test bars. Two specimens for each whisker loading (10, 20, 30, and 40 percent) were evaluated. Measurements were taken parallel and perpendicular to the test bar length to evaluate anisotropy effects. The results are shown in Table 5. No significant differences in the Young's moduli, shear moduli, and Poisson's ratio measured parallel and perpendicular to the test bar lengths were observed, indicating all of the composites are isotrophic. The effects of whisker loading on the Young's and shear moduli are illustrated in Figures 15 and 16. Both the Young's and the shear moduli increase linearly up to 30 percent SiC loading. The Young's moduli for the 30 percent and 40 percent SiC are equivalent, possible due to the lower density of the 40 percent SiC composite (3.20 g/cc compared to 3.23 g/cc for the 10 percent, 20 percent and 30 percent SiC composites).

The thermal diffusivity was measured as a function of whisker loading using thermal wave analysis. A 5 watt argon laser was used to probe the thermal wave generated. Two specimens of each whisker loading were evaluated. The results are shown in Table 6 and Figure 17. The thermal diffusivity increases with whisker loading up to 30 percent SiC, and then drops off at 40 percent SiC. The drop in diffusivity observed for the 40 percent SiC may be attributed to its lower density.

Thermal expansion coefficient measurements on baseline as well as composites were made in an air atmosphere on a dilatometer, running from room temperature to 1400°C at a rate of 3°C/min, followed by a return to room temperature. Thermal expansion coefficients were calculated based on the slopes of the dilatometer outputs. Change of slope or discontinuity on the dilatometer output curves was observed in most samples. Table 7 summarizes the results.

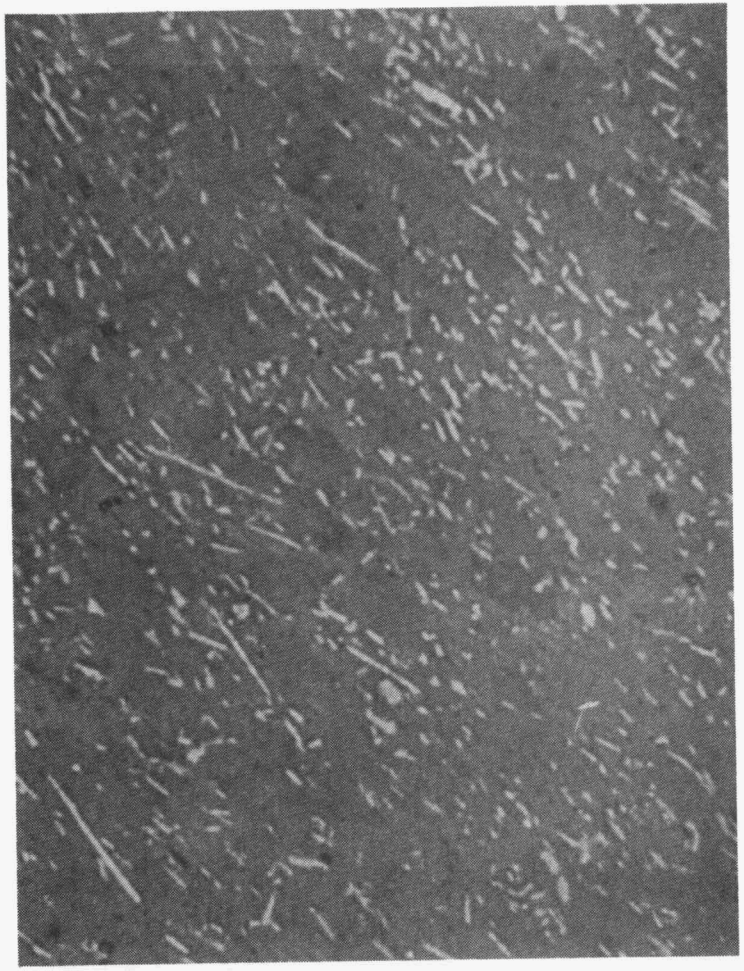

Figure 11. Polished Section of 10 Percent SiC Composite Exhibiting Good Whisker Distribution and Orientation

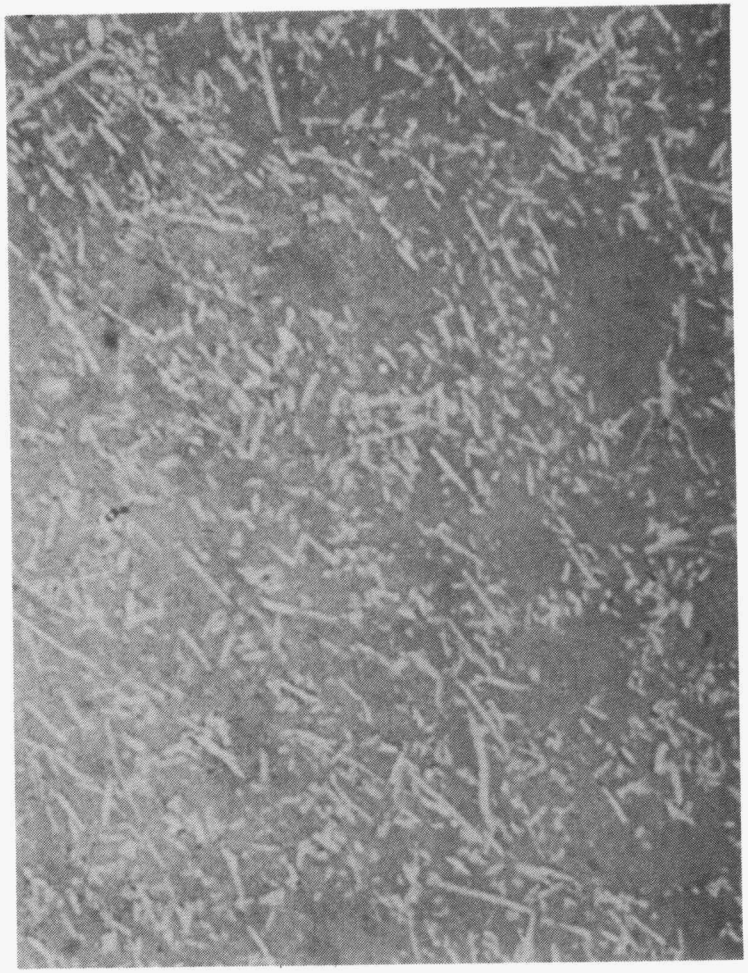

Figure 12. Polished Section of 20 Percent SiC Composite Exhibiting Good Whisker Distribution and Orientation

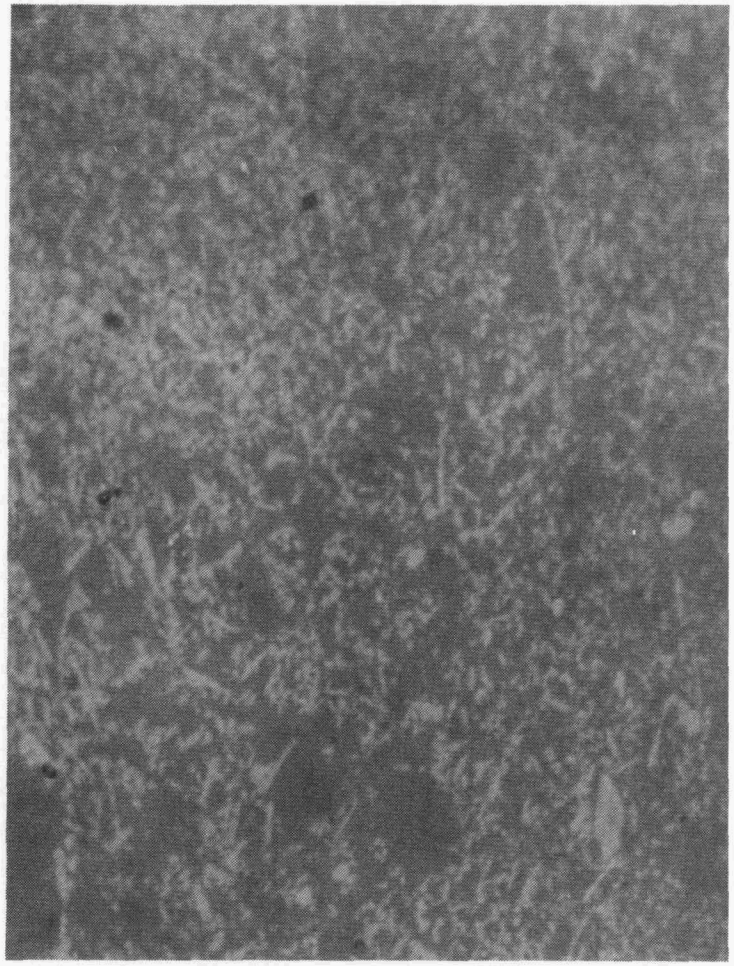

Figure 13. Polished Section of 30 Percent SiC Composite Exhibiting Good Whisker Distribution and Orientation

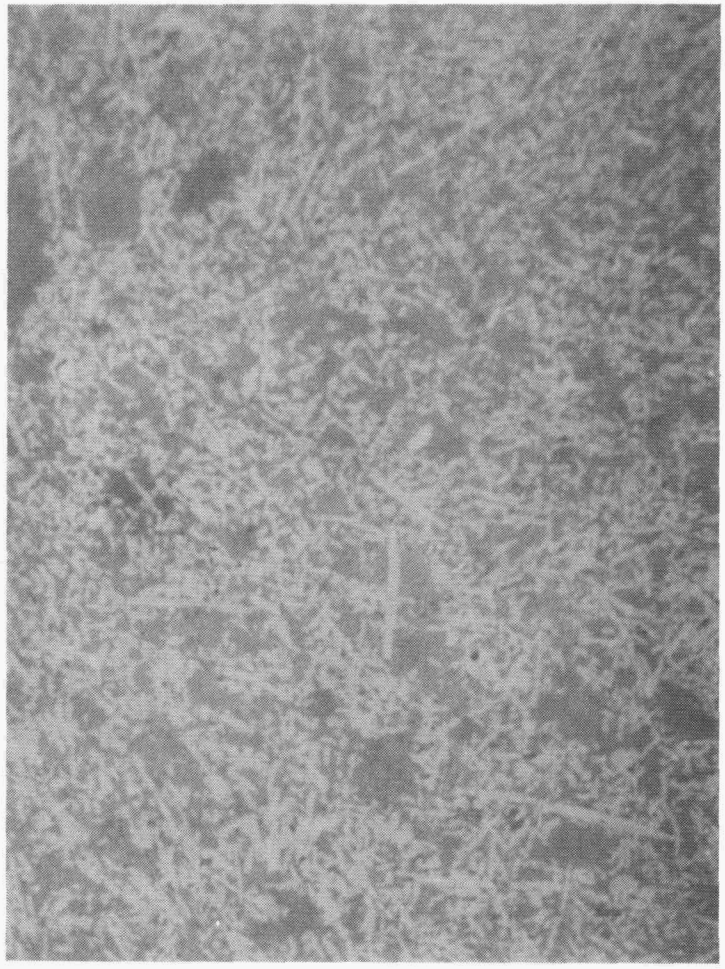

Figure 14. Polished Section of 40 Percent SiC Composite Exhibiting Good Whisker Distribution and Orientation

TABLE 5

ELASTIC PROPERTIES OF SiCw/Si_3N_4 COMPOSITES

Percent SiC	Young's Modulus (msi)	Shear Modulus (msi)	Poisson's Ratio
10	45.1 44.4	18.0 17.5	0.26 0.27
10	44.8 44.4	17.7 17.5	0.26 0.27
20	46.8 46.8	18.7 18.7	0.25 0.25
20	46.8 46.5	18.7 18.6	0.25 0.26
30	48.7 48.6	19.6 19.6	0.24 0.24
30	48.3 48.0	19.4 19.3	0.24 0.25
40	48.7 48.7	20.0 19.7	0.22 0.23
40	48.4 48.4	19.7 19.6	0.23 0.23

TABLE 6

THERMAL DIFFUSIVITY OF SiCw/Si_3N_4 COMPOSITES

Percent SiC	Thermal Diffusivity (cm/sec)
10	0.090 0.095
20	0.101 0.096
30	0.107 0.098
40	0.106 0.097

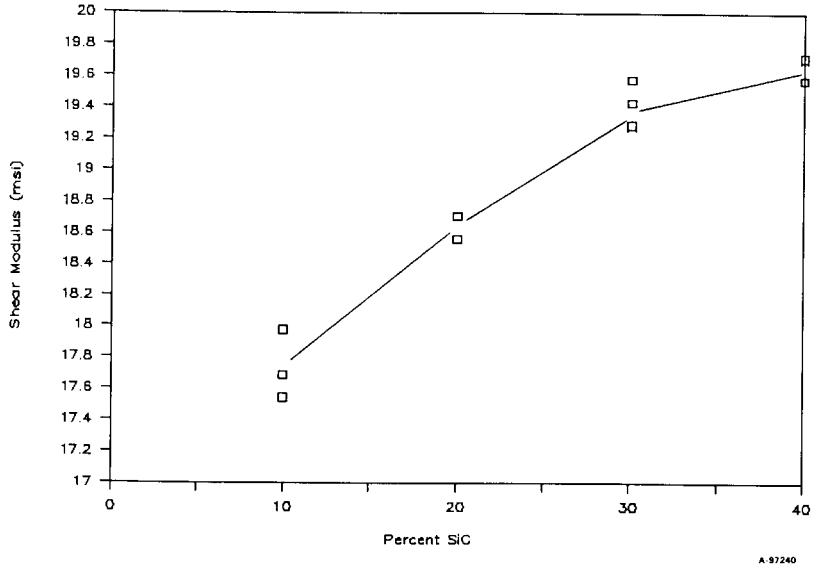

Figure 15. Young's Modulus vs Percent SiC

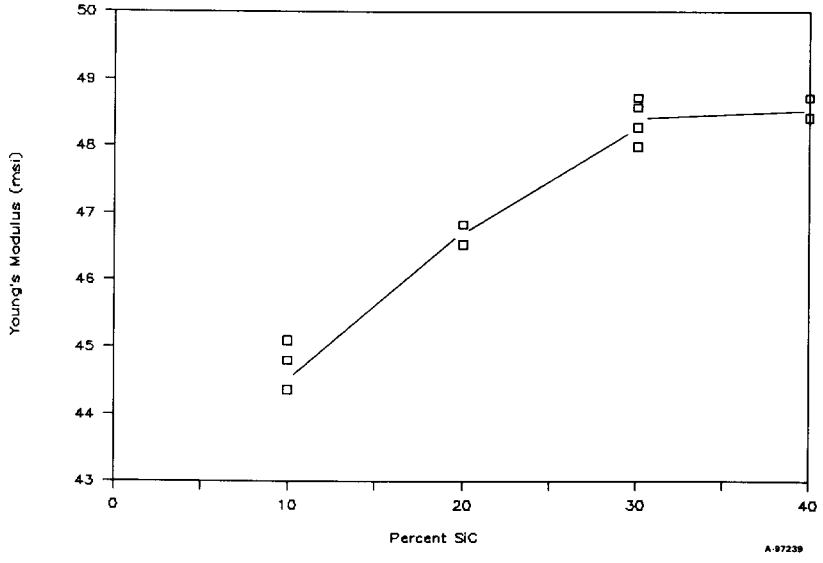

Figure 16. Shear Modulus vs Percent SiC

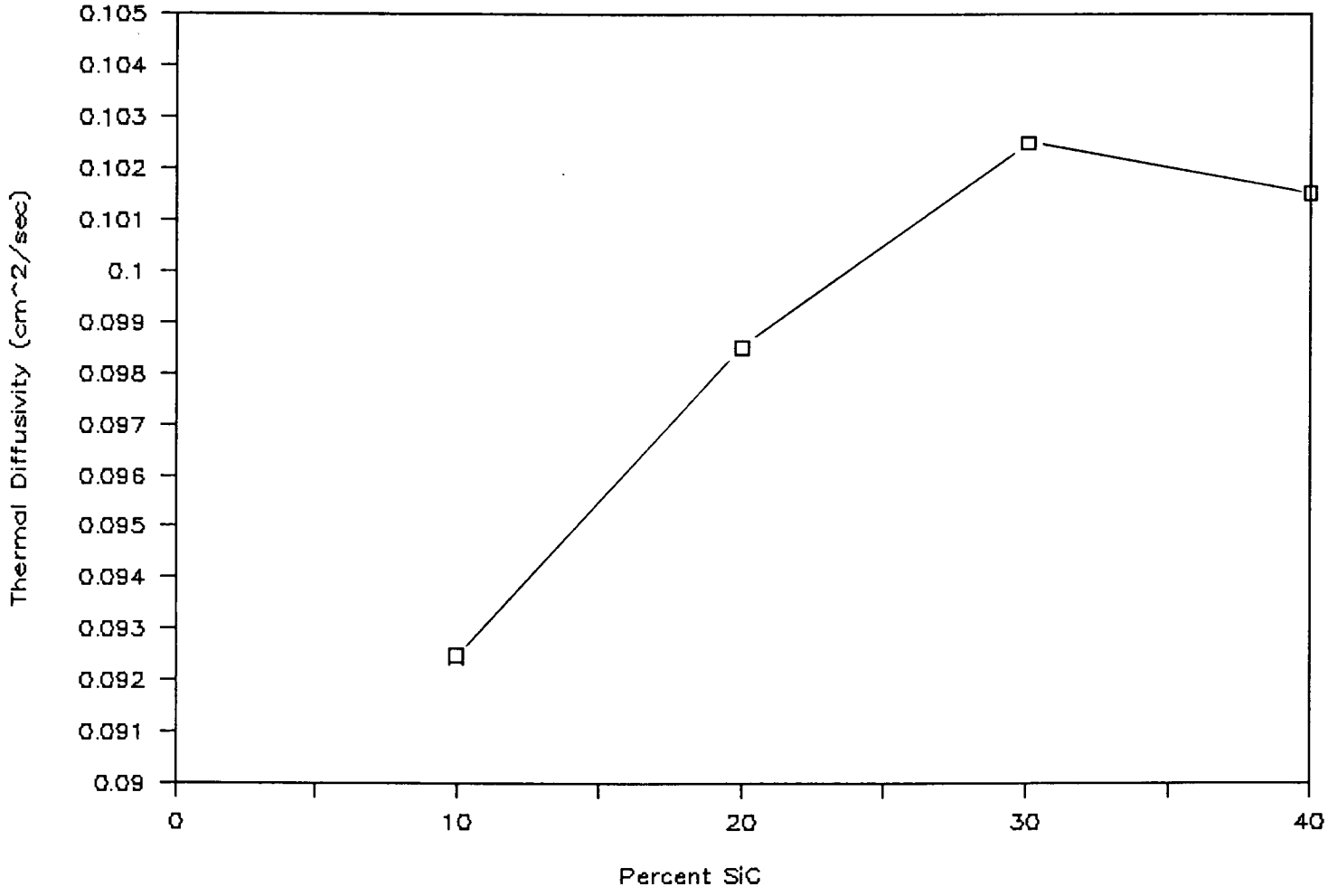

Figure 17. Thermal Diffusivity vs Percent SiC

TABLE 7

THERMAL EXPANSION COEFFICIENT

Composition (Wt. Percent SiCw)	Thermal Expansion Coefficient (ppm/°C)
0	2.9 (100-950°C); 3.4 (1050-1300°C)
10	3.1 (100-930°C); 4.0 (1000-1250°C)
20	3.2 (100-750°C); 4.4 (1000-1300°C)
30	3.3 (100-800°C); 4.0 (900-1200°C)
40	4.2 (100-1200°C)

Additional baseline material properties were obtained and are listed in the following:

MOR at 1200°C	60.7 ksi
Young's modulus	301 GPA
Sheer modulus	117.5 GPA
Poisson's ratio	0.278
Thermal diffusivity	0.169 cm^2/sec

Status of milestones

Milestone 5 is complete. Milestone 7 (final report) is in process.

Publications

None.

Silicon-Nitride–Metal Carbide Composites

S. T. Buljan (GTE Laboratories, Inc.)

Objective/Scope

The objective of this program is to develop silicon nitride-based composites of improved toughness, utilizing SiC and TiC as particulate or whisker dispersoids, and to develop and demonstrate a process for near net shape part fabrication. Near net shape process development will explore forming by injection molding and consolidation by hot isostatic pressing or conventional sintering.

Technical Progress

Thermal Expansion Measurements

Measurements of thermal expansion of AY6 (Si_3N_4 6 w/o Y_2O_3 + 1.5 w/o Al_2O_3) and an AY6 + 30 v/o SiC whisker (SC-9) composite were made over the range from 25°C to 1400°C using a Theta dilatometer. Polycrystalline Al_2O_3 was used for calibration of the equipment. Essentially no difference in thermal expansion was observed for the two materials over the range 25 - 1400°C (Figure 1). The thermal expansion coefficients are reported in Table 1.

Table 1: Thermal Expansion Coefficients of AY6 and an AY6 - 30 v/o SiC Whiskers Composite

Temperature (°C)	AY6 + 30 v/o Arco ($\times 10^{-6}$/°C)	AY6 $\times 10^{-6}$/°C)
200	2.91	2.53
400	3.21	3.11
600	3.51	3.64
800	3.83	4.08
1000	4.16	4.42
1200	4.51	4.67
1400	4.86	4.87

Thermal Conductivity Measurements

The thermal conductivities of AY6 and an AY6 + 30 v/o SiC whisker composite were measured by Fiber Materials, Inc. using measurements of enthalpy/specific heat and laser flash diffusivity to calculate the conductivity. Enthalpy was measured with a Bunsen-type ice calorimeter and the specific heat determined graphically from the smoothed enthalpy data. Thermal diffusivity was measured on disk-shaped samples using the laser pulse method. The laser pulse direction corresponds to the axis of hot pressing for both materials.

Thermal conductivity was calculated from the data using the following equation:

$$\lambda = \alpha \rho C_p \qquad (1)$$

where λ = thermal conductivity
α = thermal diffusivity
C_p = specific heat
ρ = density

Table 2 shows the thermal diffusivity, specific heat and the calculated thermal conductivity values for both AY6 and the SiC whisker composite. As reported by FMI, the data shown are accurate within ±2.5%. Figure 2 illustrates thermal conductivity as a function of temperature. At room temperature, the addition of SiC whiskers increases the thermal conductivity by 25% compared to AY6, but at temperatures greater than 1000°C, the difference is reduced to approximately 15%.

Table 2: Thermal Diffusivity, Specific Heat and Thermal Conductivity of AY6 and an AY6 + 30 v/o SiC Whiskers Composite

Material	Temperature °C	°F	Thermal Diffusivity $cm^2\ s^{-1}$	Specific Heat $cal\ g^{-1}C^{-1}$	Thermal Conductivity $w\ cm^{-1}C^{-1}$	$Btu\ in\ hr^{-1}ft^{-2}F^{-1}$
AY6	28	82	0.1246	0.150	0.2523	174.9
+	98	208	0.1043	0.185	0.2605	180.6
30 v/o	264	508	0.0754	0.232	0.2361	163.7
SiC(SC9)	431	807	0.0636	0.250	0.2147	148.9
Whiskers	656	1213	0.0492	0.264	0.1754	121.6
	821	1509	0.0464	0.270	0.1691	117.2
	986	1806	0.0369	0.273	0.1360	94.3
	1110	2930	0.0351	0.274	0.1298	90.0
	1200	2192	0.0335	0.275	0.1243	86.2
AY6	28	82	0.0958	0.150	0.1940	134.5
	99	211	0.0811	0.185	0.2026	140.5
	264	508	0.0625	0.232	0.1959	135.8
	429	805	0.0492	0.250	0.1661	115.2
	653	1207	0.0422	0.264	0.1504	104.3
	819	1506	0.0366	0.270	0.1332	92.4
	985	1805	0.0343	0.273	0.1264	87.6
	1106	2022	0.0310	0.274	0.1147	79.5
	1200	2192	0.0288	0.275	0.1070	74.2

Oxidation Resistance Evaluation

The oxidation of an AY6 + 30 v/o SiC whiskers composite has been evaluated relative to standard hot pressed AY6 for up to 1000 hours of exposure to ambient air at 1200°C. The results (Figure 3) show that the long term (>500 hour) oxidation resistance

of the composite is equivalent to AY6. The small difference is most likely related to dilution of the (Al_2O_3 + Y_2O_3) sintering aid by substitution of SiC for the blended AY6 powder. At shorter times (<200 hrs.), a nine-bar data set shows AY6 to have slightly better oxidation resistance compared to the composite. The data show that the oxidation of AY6 is not adversely affected by the addition of ARCO SC-9 SiC whiskers.

The oxidation of SiC (SC-9) whiskers was examined separately. The whiskers were oxidized in Al_2O_3 crucibles at 1200°C. in static air and exhibited parabolic oxidation behavior (Figure 4). Phase analysis (XRD) of the oxidized whiskers showed an increase in the amount of amorphous phase with increasing oxidation time at a lattice spacing corresponding to SiO_2 (tridymite), which is consistent with the oxidation temperature employed. It was further noted that, while the SiC whiskers in the as-received state exhibited predominantly α phase peaks, the relative intensity of β phase peaks increased with increasing oxidation time. This may result from preferential oxidation of the α phase.

Oxidation rate constants for whiskers, base line silicon nitride and the composite, as well as the expectation value calculated for 30 v/o SiC whisker composites, are given in Table 3. Calculated and measured values for the 30 v/o SiC (whisker) containing composite are in good agreement.

The effect of oxidation at 1200°C up to 500 hours on modulus of rupture has also been evaluated (Table 4). While at room temperature, small variations in strength are observed; the MOR at elevated temperature is unaffected by oxidation. Based on these data, i.e., weight gain and MOR, the effects of oxidation on AY6 and AY6 +30 v/o SiC whisker-containing composites are statistically equivalent.

Table 3: Oxidation Rate Constants of Investigated Materials

Material	K_p ($Kg/m^2 \cdot sec^{-1/2}$)
SiCw (SC-9)	3.47×10^{-13}
AY6	5.89×10^{-12}
AY6 + 30 v/o SiCw (SC-9)	4.51×10^{-12}
Rule of Mixtures	
$0.7\ K_p'^{AY6} + 0.3\ K_p'^{SiCw}$	4.23×10^{-12}

Table 4: Relative Strength of Oxidized Silicon Nitride-Based Ceramics

Material	Relative Modulus of Rupture 25°C	1000°C	1200°C
AY6-As Ground	1.00	0.98	0.81
AY6-Ground/Annealed*	0.98	-	-
AY6-Ground/Oxidized**(100 hrs.)	0.93	0.97	0.81
AY6-Ground/Oxidized**(500 hrs.)	0.98	1.01	0.74
AY6 + 30 v/o SiCw***-As Ground	1.00	1.03	0.93
AY6 + 30 v/o SiCw-Ground/Annealed	0.95	-	-
AY6 + 30 v/o SiCw-Ground/Oxidized** (100 hrs.)	1.06	1.08	0.87
AY6 + 30 v/o SiCw-Ground/Oxidized** (500 hrs.)	0.98	1.06	0.88

*1200°C/60 Min./Ar
**1200°C/Ambient Air
***ARCO SC-9

Creep Measurements

Four-point creep tests (ambient air atmosphere) were conducted to compare monolithic AY6 to an AY6 + 30 v/o SiC whisker (SC-9) composite. Figure 5a compares the strain-time relationships of AY6 to the composite at 1200°C, 30 ksi applied stress. This whisker-containing composite has appreciably higher resistance to creep under these conditions compared to the monolith. One AY6 bar exhibited substantial subcritical crack growth, as opposed to the expected grain boundary sliding controlled creep. This crack growth was observed to be initiated from a grinding flaw in the chamfer. The conditions of this test are in a regime where creep and crack growth from existing flaws are competitive mechanisms of failure for Si_3N_4. To further evaluate these phenomena, test bars of both materials were precracked with 100 N Knoop indentations, which, from experience, produce a surface flaw of approximately 125 μm in depth. The samples were then annealed at 1200°C in argon to relieve indentation stresses and subsequently creep tested at 1200°C/30 ksi. The indented AY6 bar fractured 20 minutes after the test load was applied, while the indented SiC whisker-containing composites showed essentially the same steady state creep rate as had been measured for the unindented composite (Figure 5b). These data again indicate that the addition of SiC whiskers to Si_3N_4 decreases the materials' susceptibility to slow crack growth and demonstrates that the flaw sensitivity of the composite is greatly reduced under operating conditions which may be encountered in adiabatic engine applications.

The effect of dispersoid morphology was also evaluated (Figure 5c). The resistance to creep of AY6 was appreciably reduced by the addition of 30 v/o SiC particulates ($\approx$8 μm). Figure 5d compares results for AY6 and the SiC whisker composite at 1200°C/30 ksi to those obtained for the composite at 1200°C/40 ksi. The creep rate of the composite at the higher stress is equivalent to that of the monolith at the lower stress. These results indicate that at 1200°C the AY6 + 30 v/o SiC whisker composite can be

subjected to 30% higher stress than the monolith, at which point both have equivalent resistance to creep.

Injection Molding/HIP Processing

Previous results have shown that a systematic and reproducible warpage occurred in both bars and CATE blades produced by injection molding and HIPing whisker-containing composite materials. These results suggest that whisker alignment causes differential shrinkage and part distortion. In order to examine the extent of this effect and eliminate compositional concerns, an experimental batch of composite powder was prepared using comminuted SiC whiskers. Test bars of material containing 30 v/o of milled whiskers showed relatively little distortion relative to whisker composites. Dimensional measurements of composites with milled and unmilled whiskers were made to evaluate densification shrinkages. Table V shows that, although both materials densified to 99% of theoretical density, the whisker-containing samples showed substantially lower shrinkage in bar length and higher shrinkages in width and height. The sample containing milled whiskers showed essentially isotropic shrinkage.

Table V: Linear Shrinkage of Injection-Molded and HIPed AY6 - 30 v/o SiC Composites Containing Milled and Unmilled Whiskers

Dimensions	Unmilled Whiskers	Milled Whiskers
Length	18.2%	21.7%
Width	23.2%	21.6%
Thickness	26.0%	21.5%

These data present the strongest evidence to date in identifying whisker alignment during injection molding as a major cause of distortion during densification of molded composites. Additional effort in this area will now concentrate on microscopy to determine the degree of alignment at the surface and within the bulk of molded parts.

The mechanical properties of injection-molded and HIPed composite materials produced from powders containing thirty volume percent SiC whiskers (SC-9) which were blended with a premilled batch of AY6 at Advanced Composite Materials Corp. (formerly ARCO) were also investigated.. Fractions of the composite blend were hot pressed as disks or injection-molded as bars and sprues and HIPed. Both processes produced densified bodies with densities greater than 99% of theoretical. Fracture toughness measurements, controlled surface flaw-MOR technique, showed the toughness of the hot pressed material to be approximately 30% higher than the HIPed counterpart, while the moduli of rupture were essentially equivalent (Table 6). Previous results have shown that the fracture toughness of Si_3N_4-SiC whisker composites is controlled by both the SiC whisker content and the grain size of the Si_3N_4 matrix. Increased Si_3N_4 grain size leads to increased fracture toughness. Densification of the composite by HIPing requires a considerably shorter schedule. Reduced residence time at densification temperatures results in a finer grain matrix and reduced fracture toughness. The decreased fracture toughness with essentially no change in modulus of rupture suggests that HIPing reduces the size of prcessing flaws. In order to develop tougher HIPed materials, modified cycles will be explored.

Table 6: Comparison of Mechanical Property Data of Hot-Pressed and Injection-Molded/HIPed AY6 + 30 v/o SiC Whisker Composites

Material	Temp (°C)	Time (min)	Pressure (ksi)	Density (% theo.)	K_{IC} $MPa \cdot m^{1/2}$	MOR (MPa)
Hot Pressed	1725	400	3.6	99.6	6.1 ± 0.6	796 ± 41
IM/HIP						
Sprue	1750	60	30	99.2	4.2	818 ± 112
Bar	1750	60	30	99.4	3.9	762 ± 40

Status of Milestones

Milestones 122.305, 122.306, and 122.307 were completed on schedule. Execution of the program is on schedule.

Publications

S.T. Buljan and G. Zilberstein, "Microstructure Development in Si_3N_4-Based Composites, Mat. Res. Soc. Symp. Proc., Vol. 78, 1987, pp. 273-281.

R.J. Nixon, S. Chevacharoenkul, M.L. Huckabee, S.T. Buljan and R.F. Davis, "Deformation Behavior of SiC Whisker-Reinforced Si_3N_4", Mat. Res. Soc. Symp., Vol. 78, 1987, pp. 295-302.

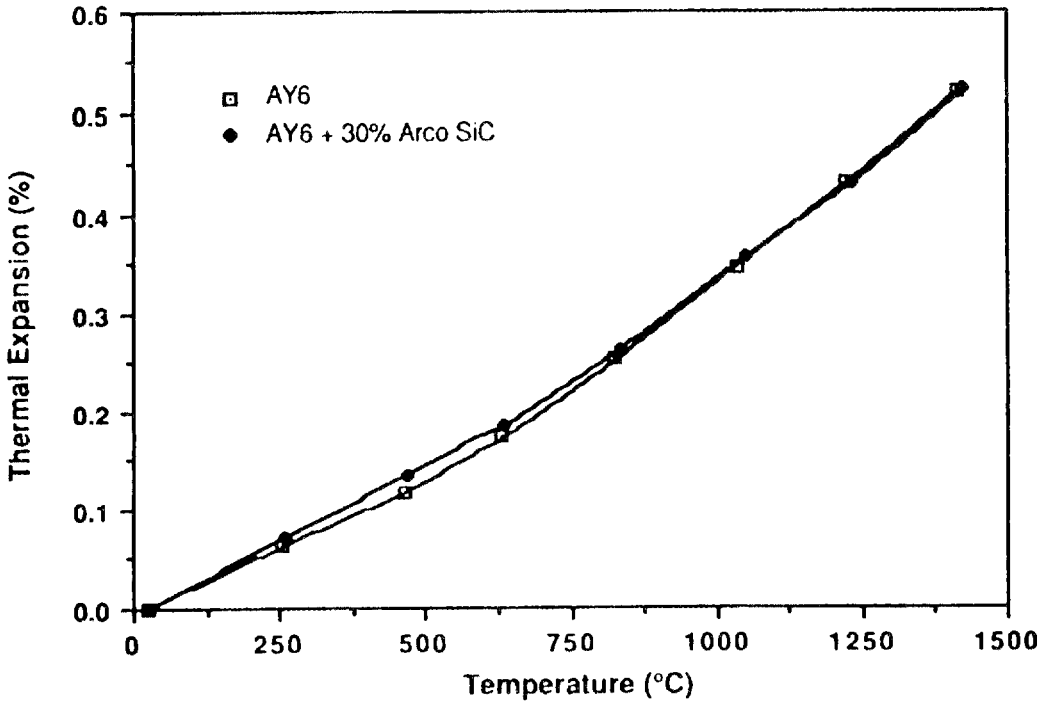

Figure 1: Thermal Expansion of AY6 and AY6 + 30 v/o SiC Whiskers for the Temperature Range 25°C to 1400°C

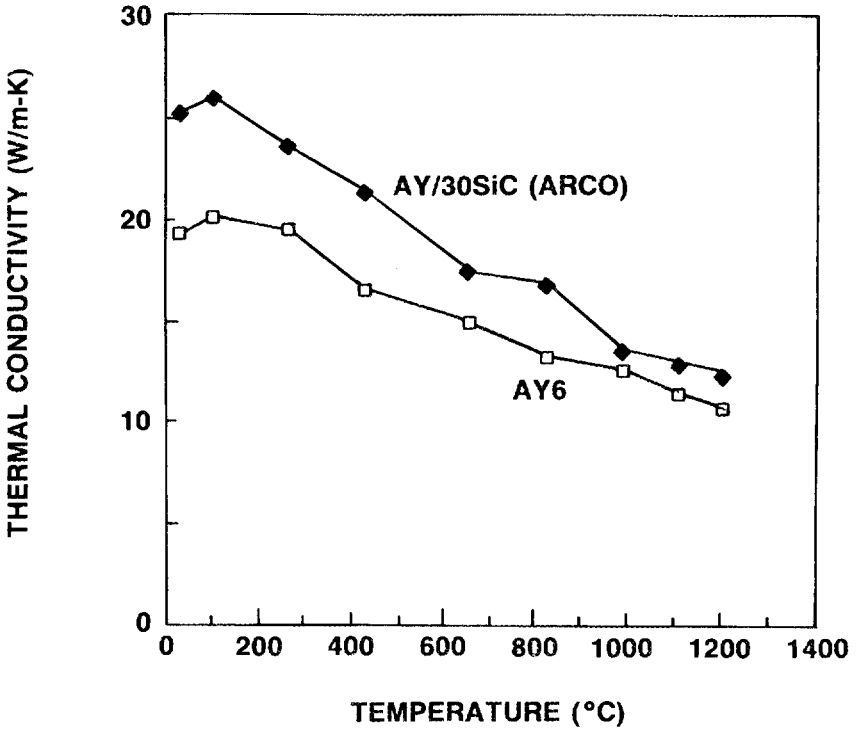

Figure 2: Thermal Conductivity of Si_3N_4-Based Ceramics from Room Temperature to 1200°C

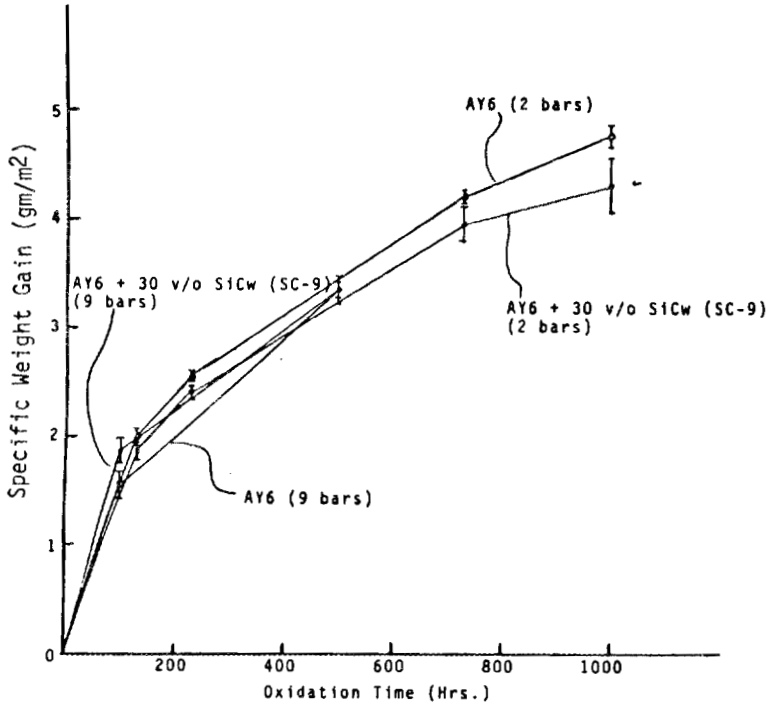

Figure 3: Ambient Atmosphere Oxidation at 1200°C of AY6 + 30 v/o SiCw (SC-9) Composite

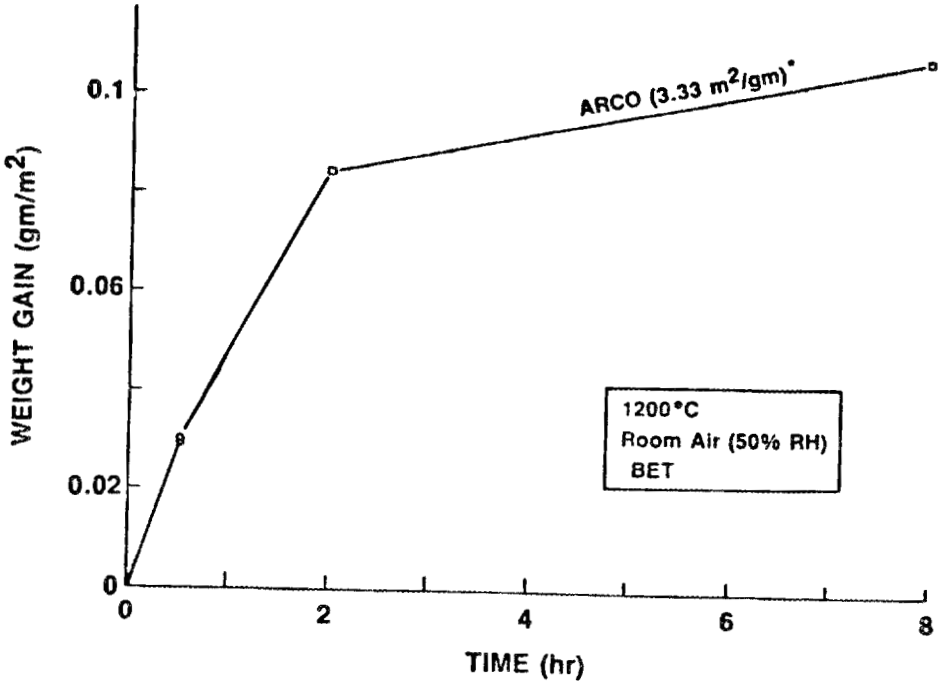

Figure 4: Static Air Oxidation of ARCO (SC-9) SiC Whiskers

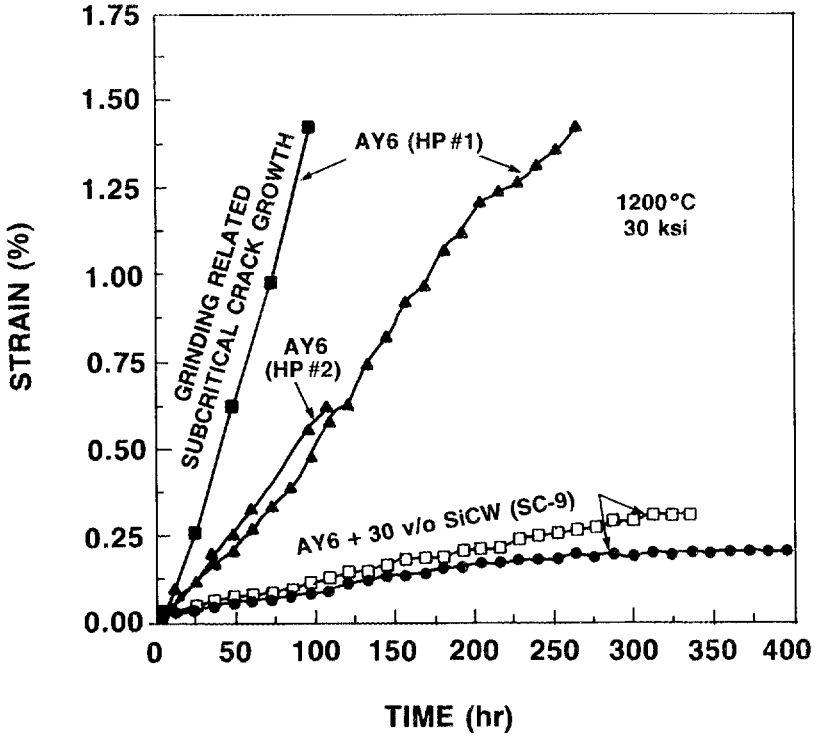

Figure 5a: Results of Four-Point Creep Evaluation for Monolithic AY6 and AY6-30 v/o SiCw Composite

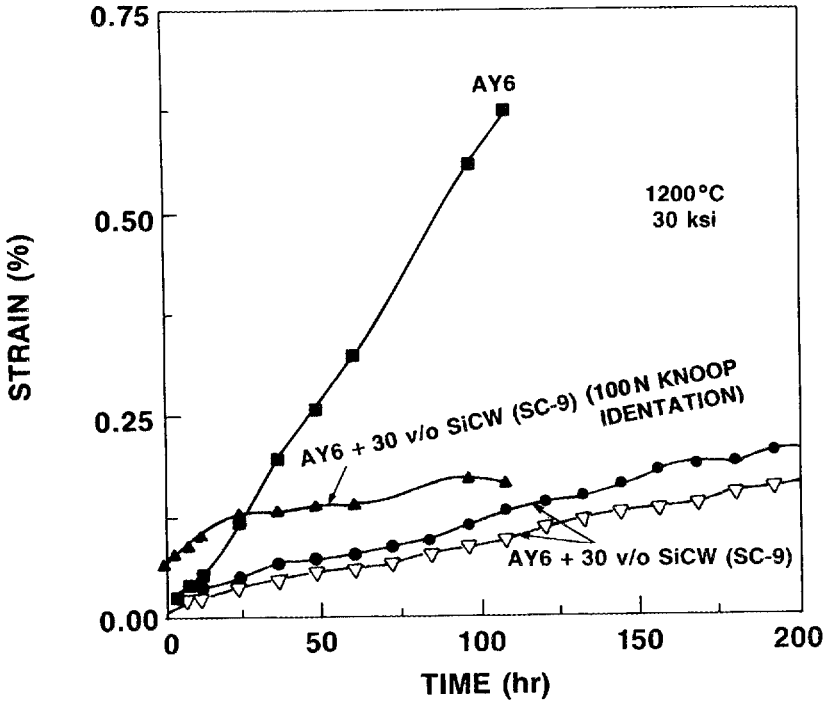

Figure 5b: Comparison of AY6, AY6-30 v/o SiC Whisker Composite and Precracked Composite in Four-Point Creep

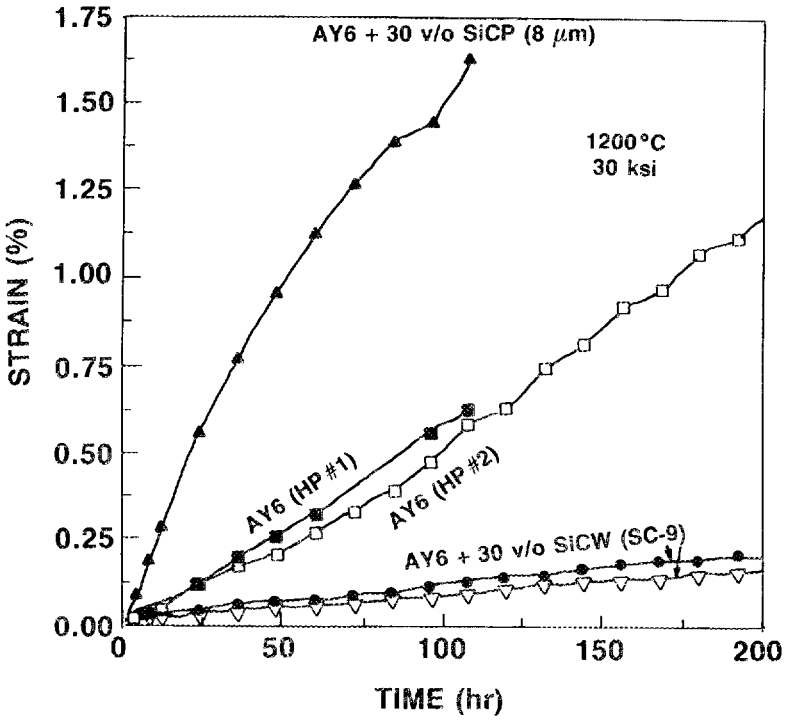

Figure 5c: Effect of SiC Dispersoid Morphology (Equiaxed Particle (P) vs Whisker (w) on the creep of Si_3N_4-Based Materials

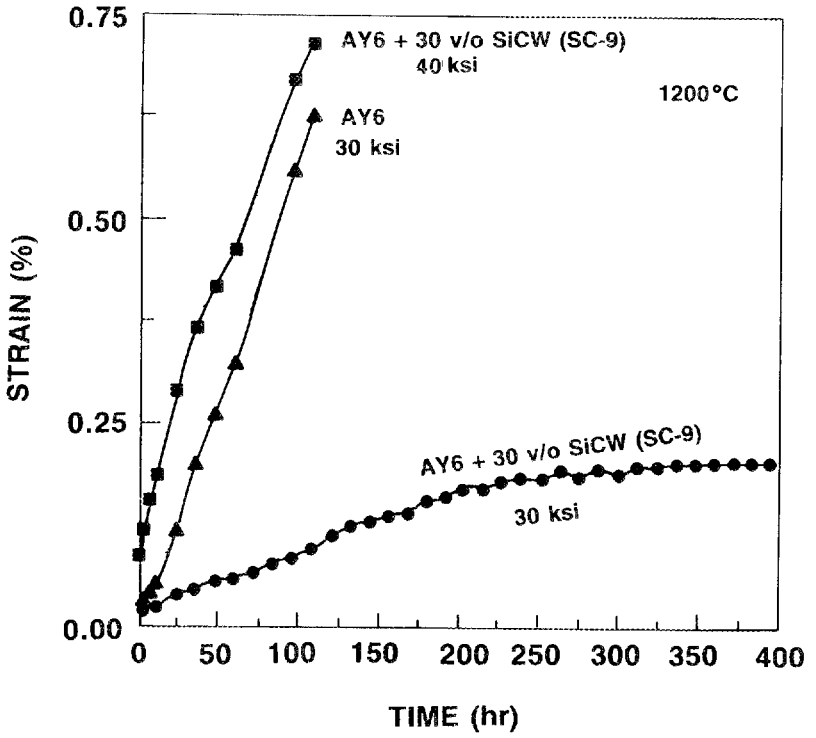

Figure 5d: Four-Point Creep at 1200°C of AY6 and AY6-30 v/o SiC Whisker Composite

Development of Toughened Si_3N_4 Composites by Glass Encapsulated Hot Isostatic Pressure

Normand D. Corbin and Craig A. Willkens (Norton Company)

OBJECTIVE/SCOPE

This one-year effort is to develop fully dense Si_3N_4 matrix SiC whisker composites which show enhanced properties over monolithic Si_3N_4 materials. Composites will be prepared by an RBSN approach followed by high pressure HIPing. The emphasis of this study is on utilizing the ASEA HIP process which has the potential for producing near-net shaped complex geometries.

In addition, evaluations will be conducted to determine the role of whisker aspect ratio, coatings on whiskers, nitridation environments and HIP parameters on composite properties.

TECHNICAL HIGHLIGHTS

1.0 Evaluation Procedures

Microstructure Evaluations - A technique to enhance composite microstructures by utilizing a multiple etching technique on polished specimens has been developed. Molten potassium hydroxide is used to remove the intergranular phase and highlight the grain boundaries. After this treatment, samples were plasma etched in a halocarbon gas with 5% oxygen.[1] This later treatment preferentially attacks silicon nitride leaving the SiC whiskers in relief. The resulting microstructure can then be analyzed for both matrix grain size and reinforcement diameter using SEM photomicrographs. This technique will be used to quantify microstructures to relate to fracture toughness.

Specimen preparation procedures for optical microscopy and TEM analysis have been described earlier.[2]

Composition Evaluations - The bulk oxygen content of densified composites was determined by a combustion/IR method.[3] Using this information the bulk matrix composition can be calculated by assuming; 1) all oxygen detected in the composite is in the matrix, 2) the Y_2O_3 content remains unchanged during processing and 3) silicon carbide acts as an inert material. This allows the determination of mole fraction Si_3N_4-SiO_2-Y_2O_3 and the SiO_2/Y_2O_3 ratio. This method is preferred because the SiO_2 content is sensitive to composite processing and the presence of surface oxides on both powders and whiskers. Intergranular phase volume fraction can be by assuming only Y_2O_3

and SiO_2 are present and using their respective crystalline densities. In fact, a small quantity of nitrogen is dissolved into the phase[4] and the majority of the phase is amorphous.[5] However our calculations are good first approximations for comparison purposes.

Details for determining surface composition using Scanning Auger (SAM) and Electron Spectroscopy for Chemical Analysis (ESCA) have been reported earlier.[2]

Property Evaluations - In addition to the U.S. Army Standard for MOR evaluations[6] we also use a 4-point Norton Company testing configuration. Specimen size is 3.1x3.0mm with chamfered edges and a 320 grit surface finish. The test fixture has a 25.4mm lower by 12.7 mm upper span. Cross-head speed is .51mm/min. Composite strength and control flaw fracture toughness measurements are obtained with this configuration. This configuration is used when the densified composite tile is too small for the preferred Army standard. Best-to-date samples are tested using the Army standard 3mmx4mmx45mm bar.

The methods used for determining fracture toughness are controlled flaw[7], indentation[8] and double torsion. Indentation toughness values for our composites are considerably lower than controlled flaw toughness values. Comparison of results for NC-132 by Anstis[8] to that of Chantikul[7] reveals that they also obtain a lower value when the indentation method is used (4.0 vs. 5.0 MPa$\sqrt{m}$). The reason for the difference in values is unclear.

Room and elevated temperature fracture toughness measurements were conducted using a double torsion method. The main elegance of this particular test method is the crack length independence to the stress intensity in the central half of the specimen. Specimen size was a flat plate nominally 25mm wide by 1mm thick by 50mm long. Surface finish was prepared using a 320 grit wheel. The tolerance on the plate width and the center placement of the starter notch is critical to guarantee crack propagation down the center of the specimen width. The machined slit width was made with a 150 micrometer slitting wheel saw. A tapered machined notch with a slope of 1 to 4 was used to notch the specimen. After notching, the specimen is precracked at room temperature to generate a sharp crack prior to testing. This sharp crack is necessary for reliable and reproducible measurements. Without this precrack, 10 to 15 percent higher fracture toughness values result due to the blunt notch. The loading rate for precracking is nominally 5 micrometers per minute. The sharp crack must extend beyond the root of the tapered notch by 5 to 7 mm. After precracking has occurred, the specimen is unloaded immediately and the loading rate is

increased to 0.5mm/min displacement rate for testing on a screw driven testing machine until failure. The maximum load to failure is used to calculate the fracture toughness. The equation modified by Fuller[9] was used to calculate the fracture toughness.

High temperature stress rupture is conducted in air using 3mmx4mm bars and the 20/40mm 4-point span configuration per the U.S. Army standard. Testing conditions are similar to that described by Quinn.[10,11]

2.0 Reinforcements

Volume Fraction - The influence of whisker content on composite strength and toughness at room temperature are shown in Figure 1. Strength and toughness increase when adding 20 volume percent Tateho SiC whiskers to the monolith. Above 20 volume percent no increase in properties are observed. It is expected that crack deflection mechanisms play a role in toughening this material. As reported by Faber[12], this process is optimized at 20 volume percent loading for rod shaped particles. In addition, minimal fiber pullout or crack wake bridging is anticipated due to the random orientation of the reinforcements. The material shown in Fig. 1 is considered to be a whisker-added only product which has not had the interface region optimized for enhanced toughness. Future materials are expected to show further toughness enhancement due to interface modifications, higher (40 v/o) whisker loadings, and whiskers with optimized l/d ratios.

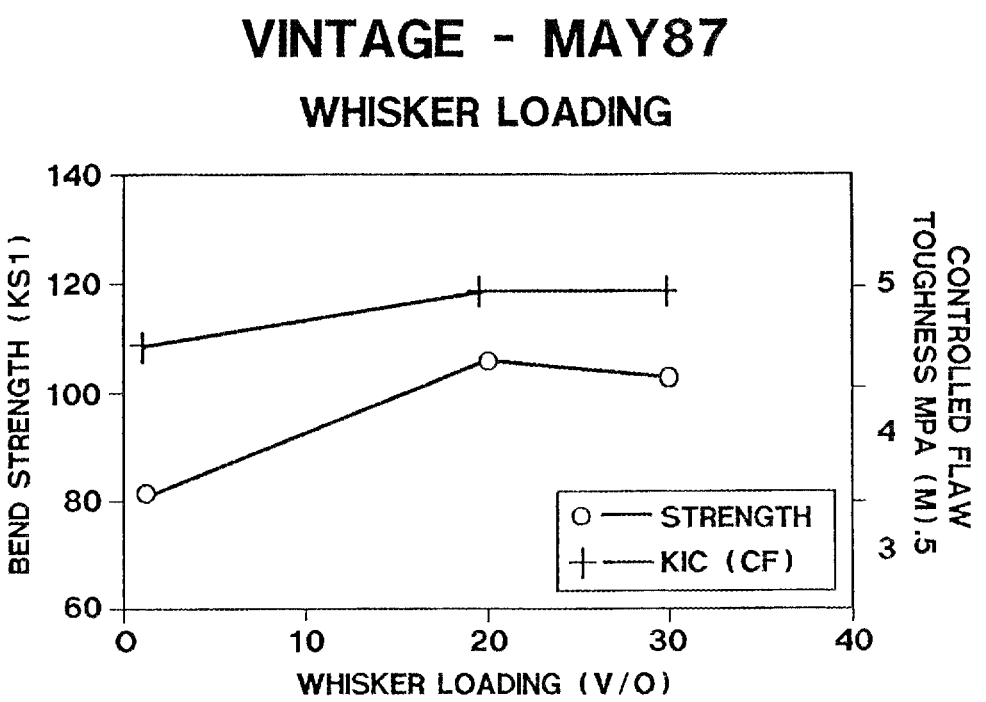

FIGURE 1

Whisker Coatings - As discussed in the last semi-annual report[2] we have an effort to improve composite fracture toughness by optimizing the whisker/matrix interface. This effort utilizes CVD to deposit thin coatings on the SiC whiskers. The coating of fine materials by CVD is very difficult due to the large surface area associated with these materials and mean free path considerations which can limit infiltration of gas species into whisker bundles[13]. As a result an effort to optimize the coating process by working closely with the vendor is underway. To date seven lots of CVD coated whiskers have been prepared with mixed results. There has been more success in applying coatings to Tateho SCW #1 grade material than Tateho T44 grade. The reason for this is unclear but may be related to the carbon rich surface previously detected on the T44 product.[2] Analysis of the various coatings show the dual BN/SiC coating to be most successful in terms of composition and morphology at this time. A difficulty which remains is in controlling the stoichiometry of the SiC (C-rich) and BN (B-rich) layers. We are working closely with the vendor to improve the CVD process parameters to improve coating composition. Chemical analysis on coated whiskers show a significant amount of oxygen (4-8% w/o) associated with the BN coated materials. Both BN and Si_3N_4 coated materials (1.0 vs. >4.0) have a much higher nitrogen content than the uncoated product signifying that nitrogen containing species are present.

Composites were prepared using the coated whiskers to determine their effect on fracture toughness. Both SRBSN processed and Si_3N_4 powder processed composites were evaluated. In the SRBSN matrix the BN and BN/SiC coated whiskers result in improved indentation fracture toughness over other materials evaluated (Fig. 2). Si_3N_4 powder processed materials are currently under evaluation. Analysis by TEM of a coated whisker composite revealed that the coating appears to have dissolved into the matrix resulting in a large quantity of intergranular phase.

Aspect Ratio - The purpose of the program task on aspect ratio is to determine the effect of whisker length and diameter on composite toughness. We have approached this task in two ways. First, we are continuing to evaluate different whisker sources with inherently different diameters. Second, recognizing the difficulty of making direct comparisons using different sources, we are using techniques to separate different size fractions within a given whisker source. The goal is to understand the direct and indirect effects that whiskers with different diameters, lengths and loadings have on the microstructure and relate these to toughening mechanisms such as crack deflection, bridging, and pullout.

Table 1 lists the various SiC whisker sources that have been evaluated. The vast majority of these sources are from Japan. Huber has recently curtailed whisker development and the former Arco product is not commercially available. The American Matrix product is the only known commercially available domestic source. The sizes listed are only qualitative comparisons based on visual observations of SEM photos, and final composite photos.

Four different whisker sources (Tateho SCW #1, Tateho T44, Huber and ARCO), were characterized using x-ray diffraction and TEM. The x-ray diffraction was performed on the as received whiskers. The whiskers examined by TEM were in densified matrices.

The crystalline structure of all the whiskers was similar by x-ray diffraction. The whiskers are a mixture of alpha and beta silicon nitride. The x-ray diffraction results differed by the amount of amorphous phase present, most likely due to an amorphous coating on the whiskers. The ARCO and Tateho whiskers had larger amorphous peaks.

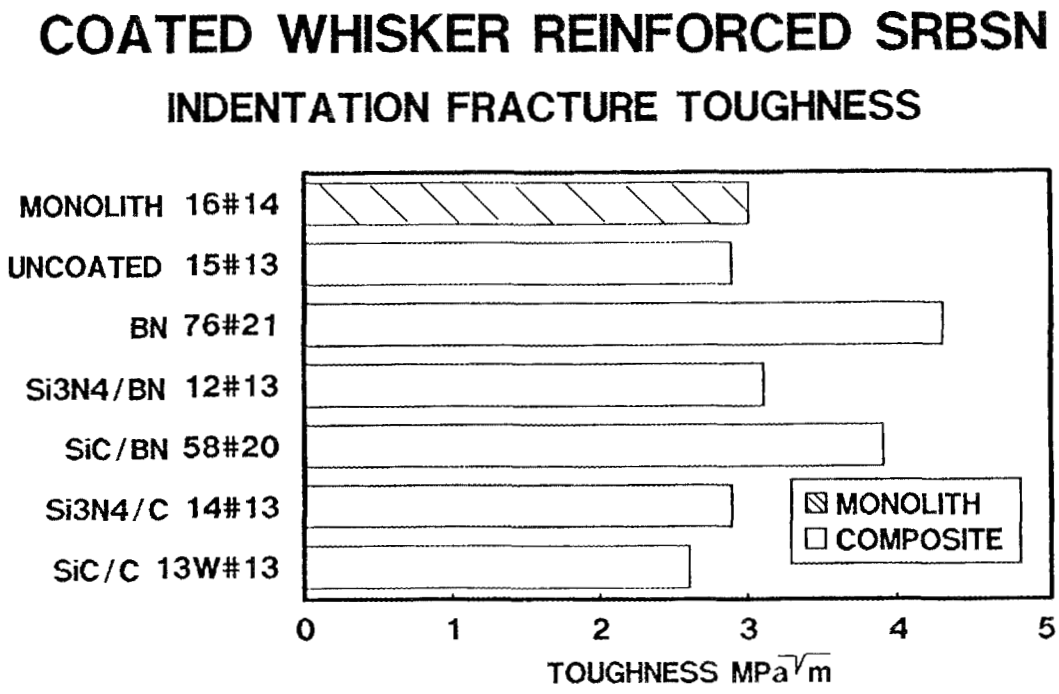

FIGURE 2

TABLE 1

SiC WHISKERS EVALUATED

SOURCE	GRADE	LOT[1]	CHEMISTRY[2]	ESTIMATED DIAMETER RANGE (um)	ESTIMATED DIAMETER AVERAGE (um)
Tateho (Japan)	#1 - 0.6	7/86	-	0.2 to 1.0 (narrow)	0.5
Tateho (Japan)	T44	11/86 3/87	0-0.40 N-0.90 Ca-0.80	0.1 to 0.8 (narrow)	0.4
Huber (U.S.)	XPWZ	1/87, 5/87	0-0.10 N-0.90	0.2 to 2 (broad)	0.6
Tokai (Japan)	Toka-Whisker	7/87, 7/86	0-0.18 N-0.64	0.1 to 1.0 (broad)	0.5
American Matrix (U.S.)	-	3/87	0.-0.96 N-0.09 Ca-0.11	0.2 to 6.0	2.0
American Matrix (U.S.)		7/87	-	-	-
Tateho (Japan)	SCW #1	12/85	0-0.38 N-1.00	0.2 to 0.8	0.4
Kobe Steel (Japan)	-	2/87	0-1.20 N-0.70 Ca-0.03	0.1 to 2.0	0.6
Nikkei (Japan)	-	2/87	0-2.90 N-0.90	0.1 to 0.8	0.4
Kanebo (U.S.)	-	2/86, 5/87	0-0.25 N-0.1 0		
Arco (U.S.)	SC-9	7/85	0-1.18 N- Ca-0.12	0.2 to 2.0	0.6
Mitsui-Toatsu (Japan)	-	12/85	0.-0.85 N-2.10 Ca-0.11	0.2 to 2.0	0.7

1- Internal code
2- 0, N by Leco combustion
   Ca by emission spectroscopy
3- Visual qualitative comparison

The Tateho whiskers appeared similar to the ARCO materials as reported by Nutt.[14] The whiskers contained many planar faults and twins perpendicular to the growth axis. The planar faults and twins of a Tateho SCW #1 whisker are presented in Figure 3a. The core of the whiskers was either solid silicon carbide with some cavities or completely hollow. The cavities could be due to the evolution of gas bubbles during whisker growth.[14] The cross sections of the whiskers contained many partial dislocations extending out from the whisker core. The main difference between the Tateho SCW #1 and T44 whiskers was that a large percentage of the Tateho SCW #1 whiskers were hollow and only a very small percentage of the Tateho T44 whiskers were hollow. The whisker size had a very broad distribution and the diameter of the Tateho whiskers varied with the length of the whisker. A micrograph of the Tateho SCW #1 whiskers in silicon nitride is presented in Figure 3b. The dark core region was initially hollow and now contains the intergranular phase of the matrix.

The ARCO whiskers are similar to those reported on by Nutt.[14] They contained the same types of defects as the Tateho whiskers, such as the stacking faults and dislocations. The ARCO whiskers had a solid core region that contained cavities and dislocations extending out in a radial direction. The whisker size and shape varied similar to that of the Tateho whiskers.

To our knowledge the Huber whiskers were not prepared by the rice hull process. They did not contain the typical planar faults and twins perpendicular to the growth axis as observed with rich hull derived materials. The whiskers contained a high density of dislocations and faults. The faults were stepped and irregularly spaced instead of planar and irregularly spaced as observed for Tateho and ARCO materials. Most of the Huber whiskers had a solid core with cavities. The whisker size distribution was broad and the diameter of the whiskers varied over the length of the whisker. The structure of a Huber whisker is presented in Figure 3c.

A large number of different whisker sources have been evaluated in SiC-w/Si_3N_4 composites. Whiskers are first evaluated "as-received", in a standard matrix, at a loading of 20 v/o. Evaluation includes examining the microstructure for uniformity and fracture toughness measurements by the indentation and controlled flaw methods. Figures 4 and 5 show microstructures for selected composites. Observations of all whisker sources revealed that the American Matrix product has a relatively large diameter. Nikkei and the Tateho SCW #1 product have the smallest diameters. The other sources fall in between, some having broader size distributions (eg. Huber, Kobe). The differences in diameter are evident from the

FIGURE 3A

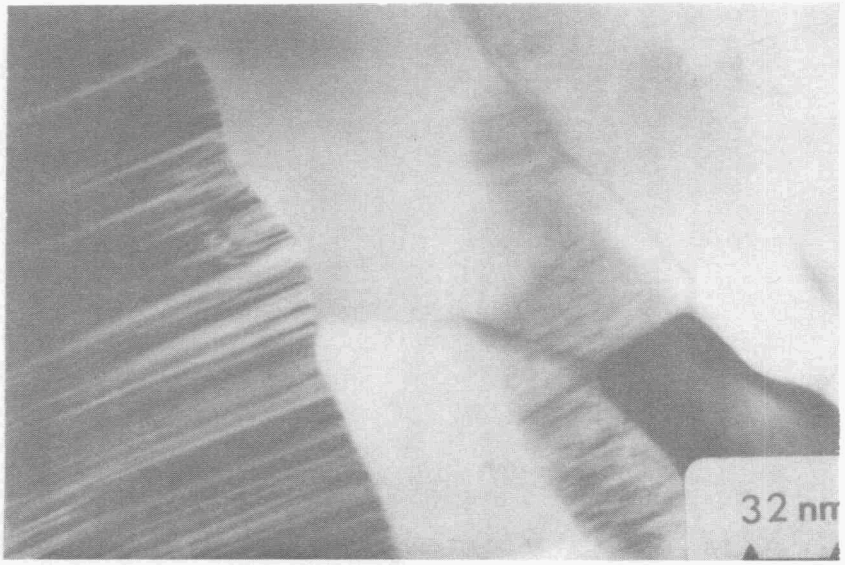

FIGURE 3B

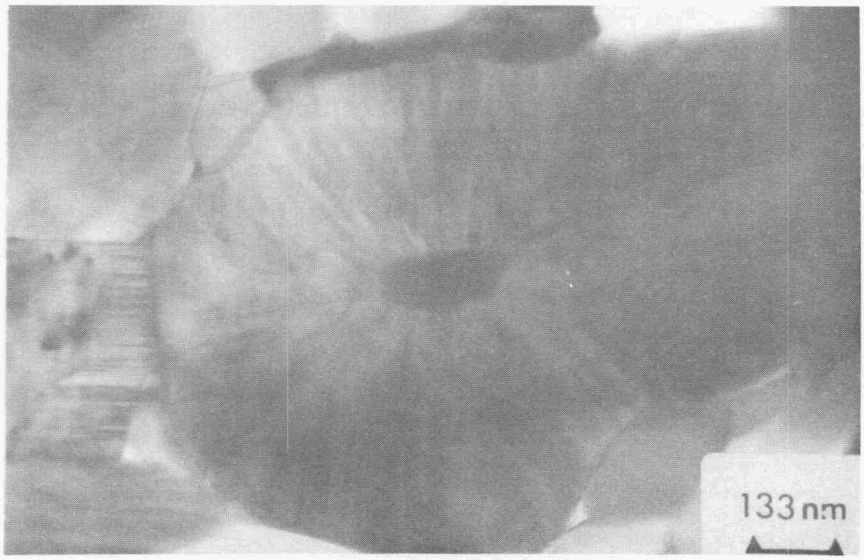

FIGURE 3C

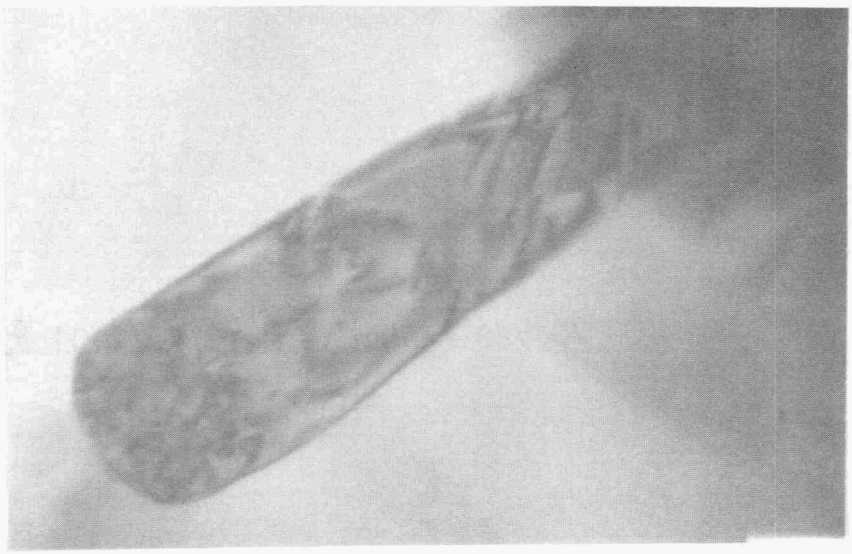

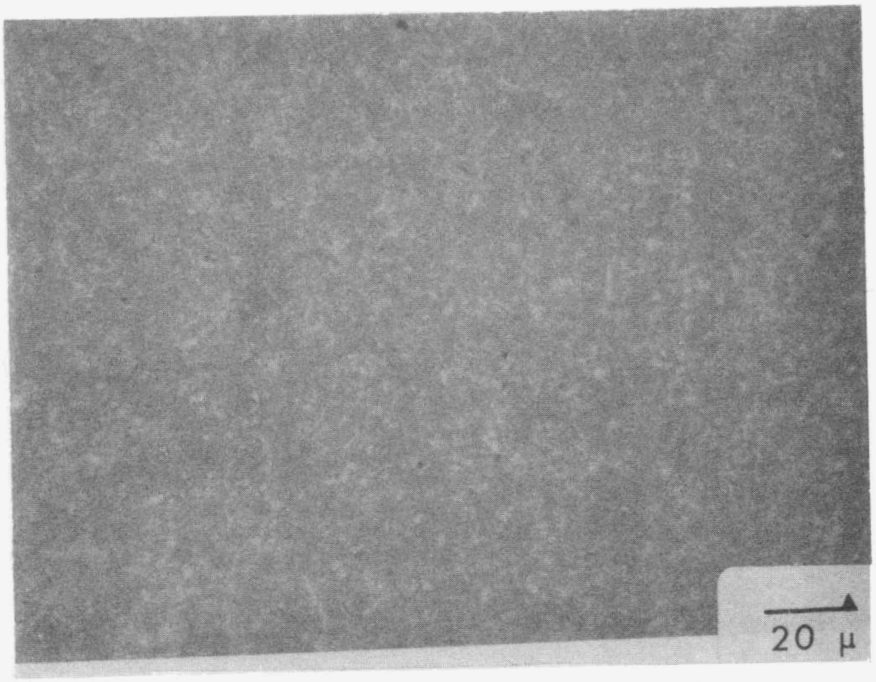

20 v/o NIKKEI SiC, (2104 #21)

FIGURE 4

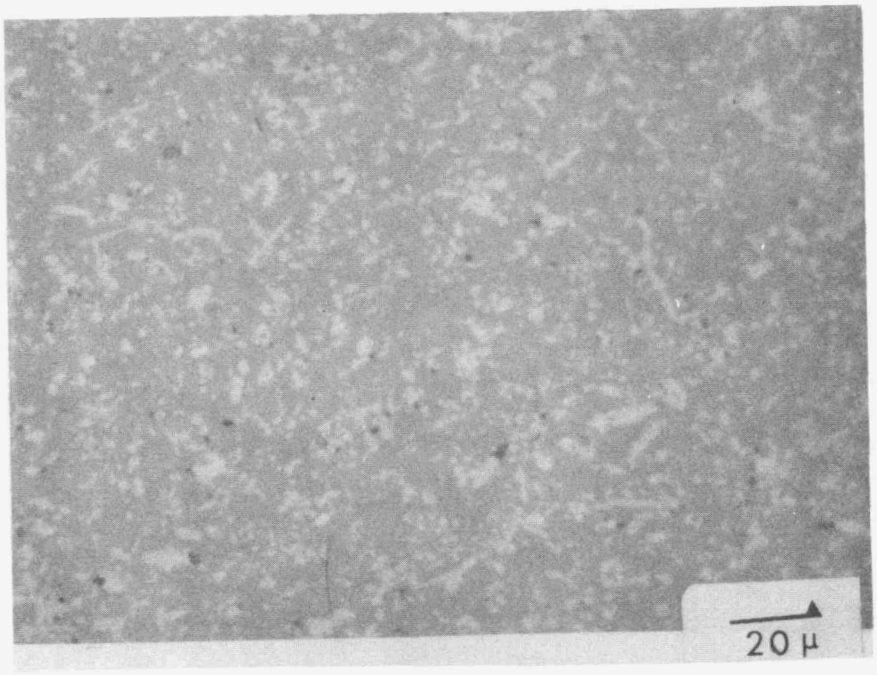

20 v/o AMERICAN MATRIX, (2101 #26)

FIGURE 5

polished sections. Also, as the diameter increases the total number of whiskers for a given volume fraction loading decreases dramatically and the spacing between whiskers increases.

The fracture toughness values are plotted in Fig. 6 as measured by the controlled flaw technique. Compared to a similar monolith, the composites showed toughness values that were 20 to 40% higher. There was no overwhelming effect of whisker diameter with toughness for this particular loading in this matrix. The best direct comparison is the Tateho T44 grade (0.4μm) and the Tateho "thick" grade (0.6μm). The "thick" grade did give a slightly higher toughness value (5.5) as compared to the T44 grade (5.0).

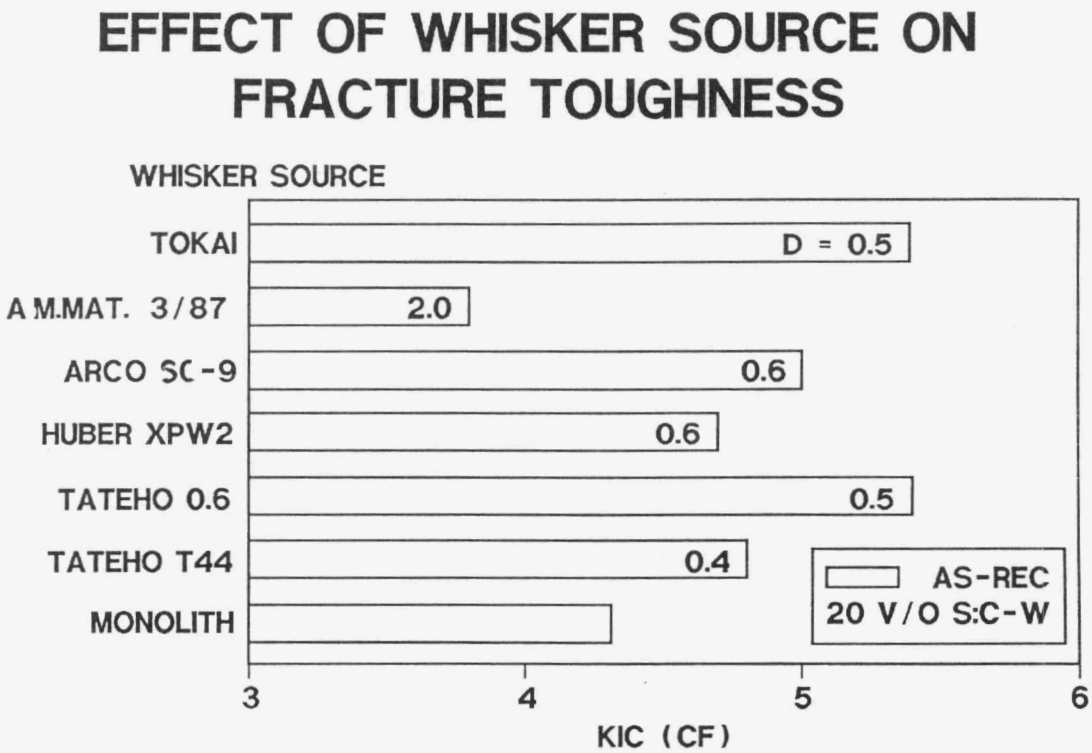

FIGURE 6

The American Matrix composite was interesting in that the composite made with "as-received" whiskers had a low strength (35ksi, 240 MPa) and low toughness (3.8). However, after a length reduction treatment, the strength was dramatically increased (96 ksi, 660 MPa) and toughness significantly increased (4.7) as shown in Fig. 7. The strength increase was probably due to the breakdown of very coarse whiskers and particulate. Whiskers up to 20μm diameter and 400μm long have been observed in the as-received product.

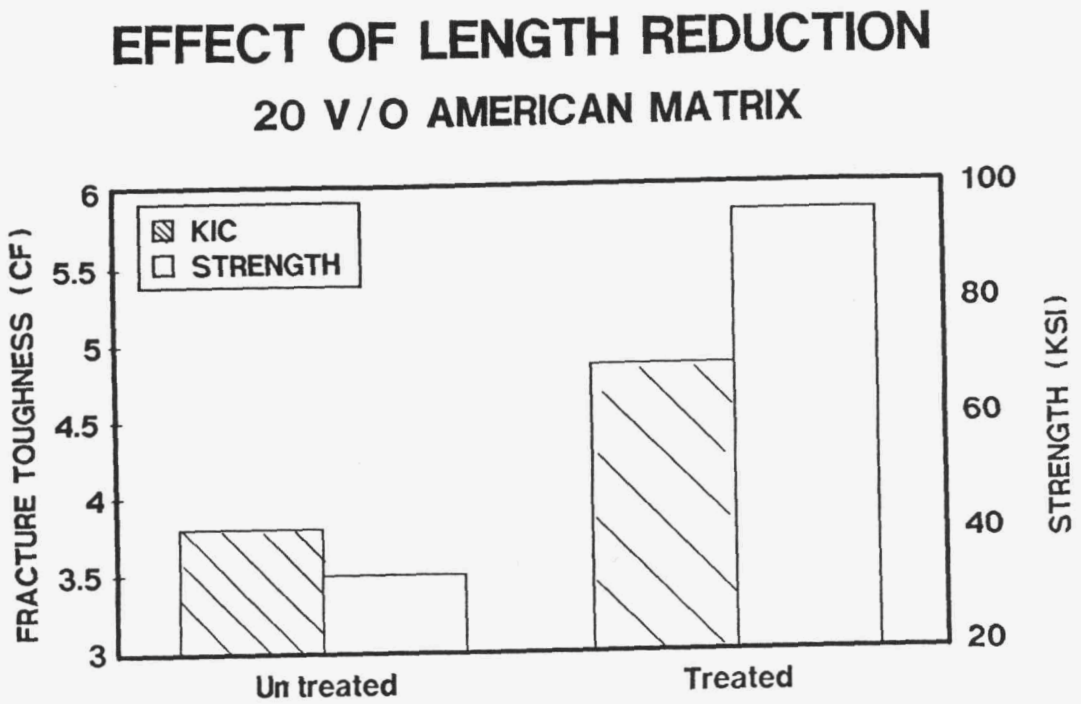

FIGURE 7

Fracture surfaces of composites made with various whisker sources are shown in Figures 8. In general, there is very little whisker pullout observed, typically less than 0.5μm. No large differences were noted for the varying whisker diameters in terms of pullout.

Fine particle classification techniques are currently being applied to allow for whisker size effects to be studied within a given whisker source. Figure 9 shows an example in which Huber SiC-whiskers were separated into a coarse fraction and fine fraction. Huber was chosen because it has a relative broad diameter size distribution. These two extremes are currently being evaluated as a composites. The classification technology has also been used to remove coarse particulates.

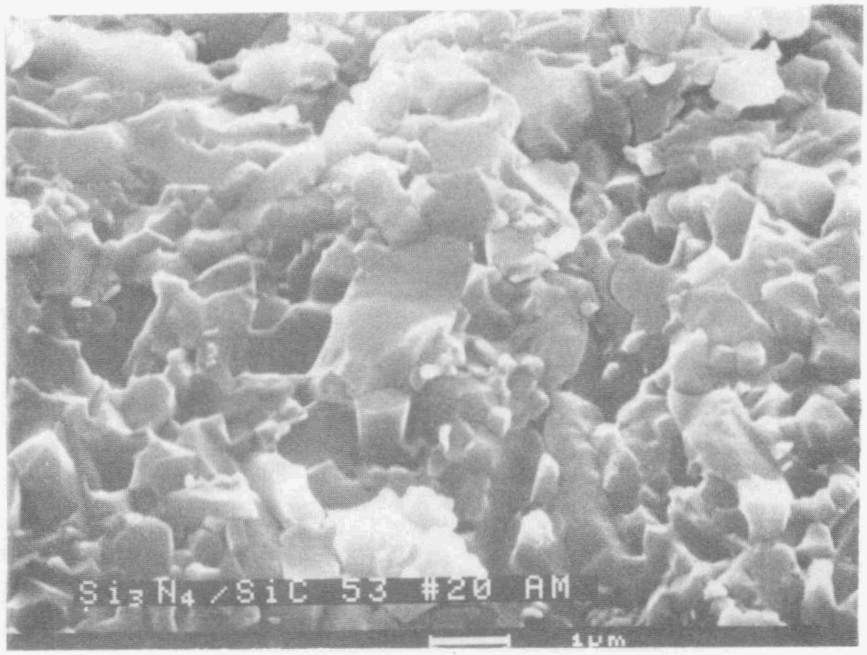

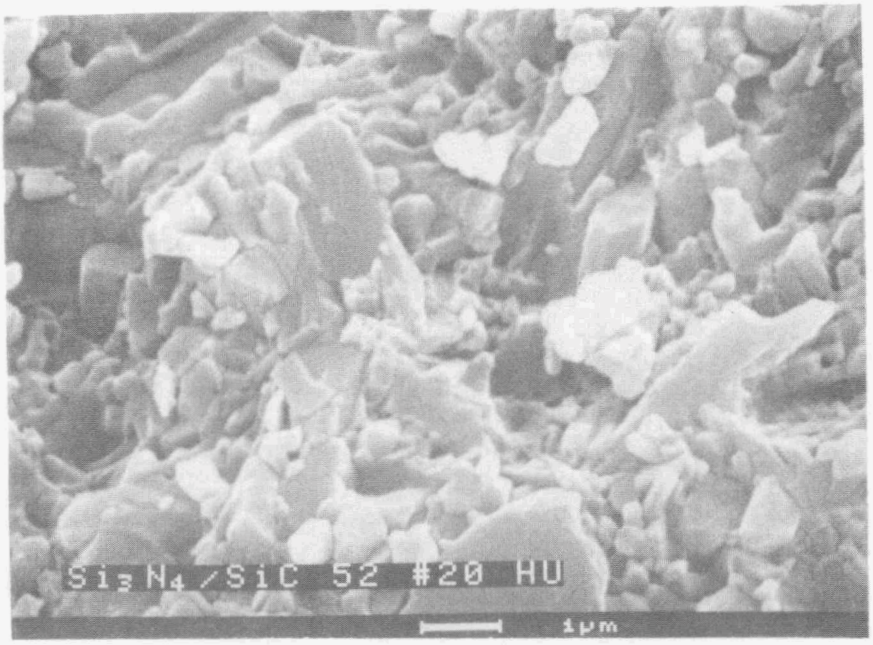

FRACTURE SURFACE OF CIP/HIP 20 v/o SiC-w/SRBSN
(4 w/o Y_2O_3)
TOP: AMERICAN MATRIX LOT 3/87 (FIRST ITERATION)
BOTTOM: HUBER XPW2 GRADE, LOT 1/87

FIGURE 8

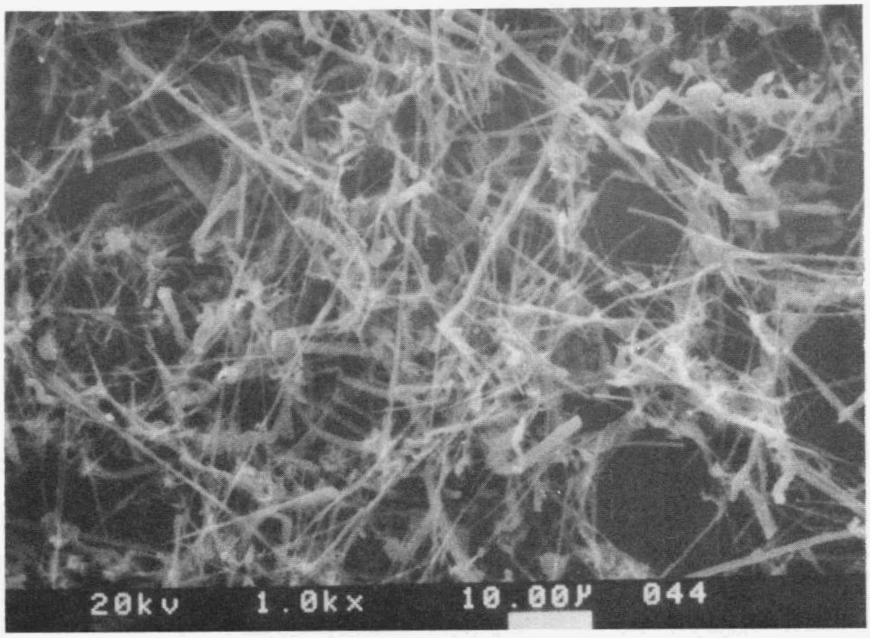

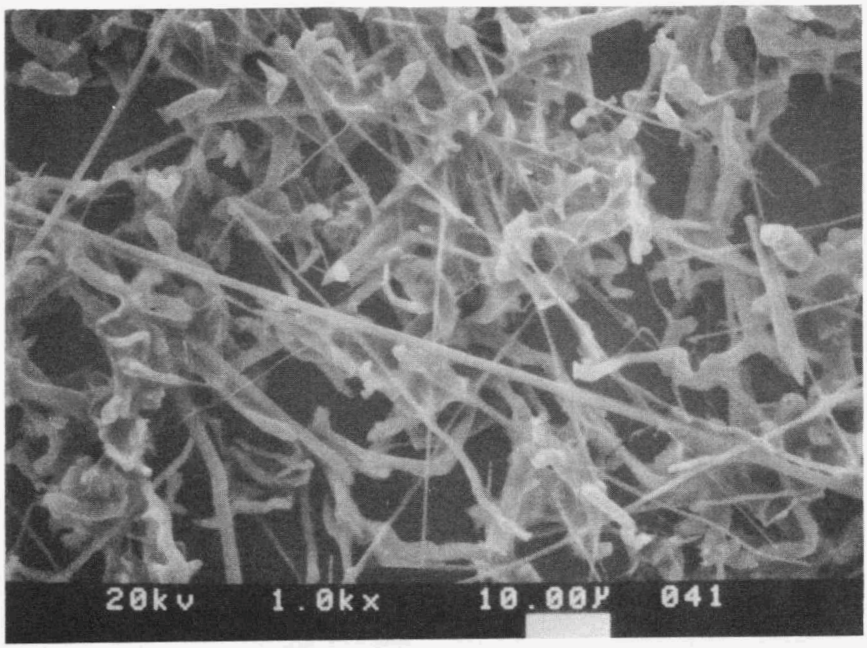

CLASSIFIED HUBER GRADE XPW2 LOT 5/87
TOP: FINE FRACTION
BOTTOM: COARSE FRACTION

FIGURE 9

3.0 Green Body

Forming - General powder processing and forming was discussed in the last Semiannual report[2].

Nitridation - The nitriding cycle limits are being explored in greater depth to determine their role on final composite properties. Previously the standard 36-hour cycle was shown to produce a composite with a higher final oxygen content and higher fracture toughness value than a more severe nitriding cycle.[2] Composites made from the same powder lot were prepared using shorter nitriding cycles (16 hours, 8 hours). All were fully nitrided with >80% alpha contents. The SiC whiskers seem to behave as a thermal diluent allowing the use of these fast reaction rates. The oxygen content after nitriding varied with the cycle (Table 2). Mechanical properties are currently being determined.

TABLE 2

	After Nitridation		
Cycle Time	Oxygen Content	Alpha Si_3N_4	Free Silicon
36-Hour	1.96%	87%	<0.1%
16-Hour	1.97%	89%	<0.1%
8-Hour	2.30%	87%	<0.1%

4.0 Densification

HIP Parameters - The HIP parametric study has been completed. The composite materials used 3μm silicon powder as the matrix precursor with 20 v/o Tateho (T44) SiC whiskers. Monoliths and composites were processed identically. Table 3 lists the density, strength, toughness and hardness values obtained for composites and monoliths. In all cases, samples are greater than 99% dense. Composite fracture toughness is essentially unchanged by the different HIP processing conditions evaluated. This is observed by both measurement techniques. Fracture toughness of materials prepared in the standard cycle shows the composite to have a higher fracture toughness than the monolith (4.8 vs. 3.3).

When comparing materials processed using the same HIP parameters, the composite strength is improved over the monolith. Fracture surface evaluations of composites prepared in the standard cycle revealed that failure origins consist of localized coarse grained regions ranging from 40μm to 7μm. EDAX analysis was unsuccessful in determining any localized compositional variations or if the coarse grains were SiC.

TABLE 3

HIP PARAMETRIC STUDY RESULTS

Specimen Code	Composites	density (g/cc)	MOR (MPa)[2]	K_{IC} (MPa m) Cont. Flaw[2]	K_{IC} (MPa m) Indentation[3]	Hardness (GPa)[4]
(30 #20)	Standard Cycle	3.22	587 ± 90	4.8 ± .2	3.6 ± .1	16.7 ± .2
(30 #16)	Standard Cycle(+A)	3.22	615 ± 49	4.3 ± .6	4.1 ± .1	16.1 ± .4
(30 #17)	Standard Cycle(+B)	3.19	435 ± 135	4.2 ± .7	3.7 ± .1	16.4 ± .3
(30 #18)	Short Cycle	3.20	788 ± 245	4.9 ± .1	3.9 ± .2	15.4 ± .1
Monoliths						
(37 #20)	Standard Cycle	3.23	507 ± 69	3.3 ± .5	2.7 ± .2	15.1 ± .2
(37 #18)	Short Cycle	3.23	603 ± 11	4.6 ± .1	3.9 ± .2	17.5 ± .3

1) Per MIL-STD-1942, 3x4x38mm span, 4-point (2-3 bars)
2) Chantikul Method, 10 kg indent (2-3 bars)
3) Anstis Method, 10 kg indent (5 indents measured)
4) At 10 kg using Vickers indent

Standard Cycle 1790°C, 1 hr. soak, 207 MPa pressure
Short Cycle 1890°C, .25 min., 207 MPa pressure
A= proprietary high temperature soak
B= proprietary extended soak time

Sintering Aid - An effort is being conducted to determine the influence of sintering aid content and composition on composite fracture toughness. Our primary emphasis is with compositions in the Y_2O_3-SiO_2-Si_3N_4 chemical system due to its favorable high temperature properties.[15] The phase field of particular interest is Si_3N_4-Si_2ON_2-$Y_2Si_2O_7$ because it is known to contain the most stable high temperature, intergranular compositions.[16] In silicon nitride based materials, many properties are strongly influenced by the resulting intergranular phase which contains the sintering aid components along with impurities associated with starting materials. The quantity, composition and crystallinity of the intergranular phase needs to be addressed in order to prepare materials with the desired properties. Intergranular phase composition (Y_2O_3/SiO_2) and content (volume fraction) are under evaluation. Composition and volume fraction is determined by the method described earlier.

In Fig. 10 the effect of total composite oxygen content on indentation toughness can be seen. Toughness increases to 4.5 MPa$\sqrt{m}$ at ~4 w/o oxygen and then levels off. There appears to be an optimum fraction to obtain highest toughness in this material. In Fig. 11 the volume percent of intergranular phase is related to toughness. The resulting plot is very similar to that for the oxygen content. Evaluations are underway to determine the effect of grain boundary composition, matrix microstructure, and grain boundary crystallinity on toughness.

When considering the volume fraction of intergranular phase, it is of value to note how the volume fraction will decrease when SiC is added. For example; a standard Si_3N_4 monoliths containing 4 w/o Y_2O_3 will contain 7.3 v/o inter granular (Y_2O_3 + SiO_2) phase. When 40 v/o SiC is added the intergranular content decreases to 4.4 v/o. This reduction in the intergranular phase (sintering aid content) can significantly alter both the sintering behavior of the materials and their properties.

5.0 Composite Property Progress

During our program we periodically prepare large batches of composite material using what we consider to be promising composition and processing conditions at that time. Enough material is fabricated to allow for extensive evaluations. Of particular interest are; high temperature strength at 1370°C, stress-rupture life at 1370°C, Weibull modulus and high temperature K_{IC}. The first set of materials was prepared shortly after initiation of our program (October 1986). Since then two additional lots of material have been prepared and evaluated (May 1987 and July 1987 vintages).

INDENTATION KIC VS BULK OXYGEN

20% - 40% TATEHO SiC-w

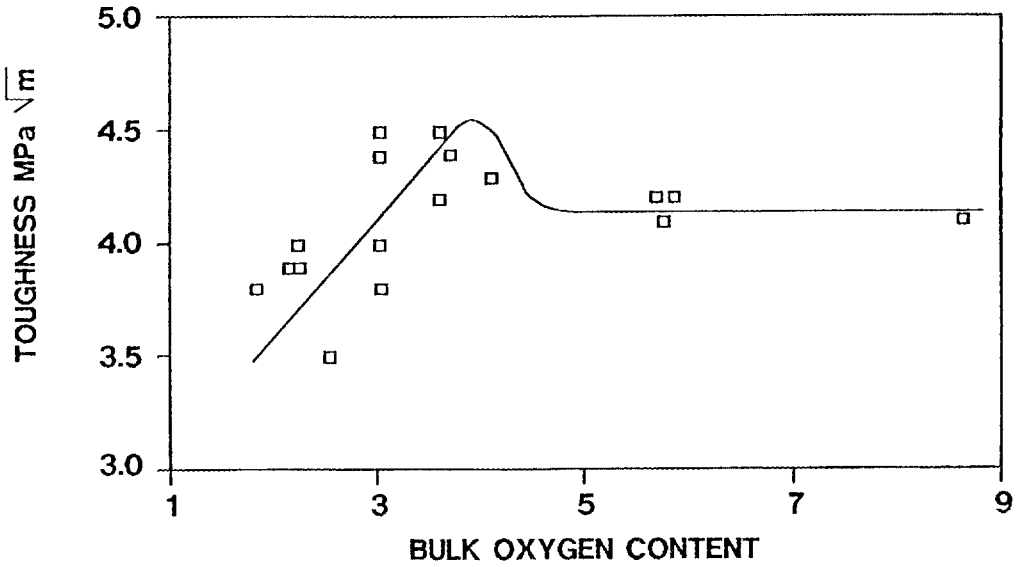

FIGURE 10

INDENTATION KIC vs v/o SIO2+Y2O3

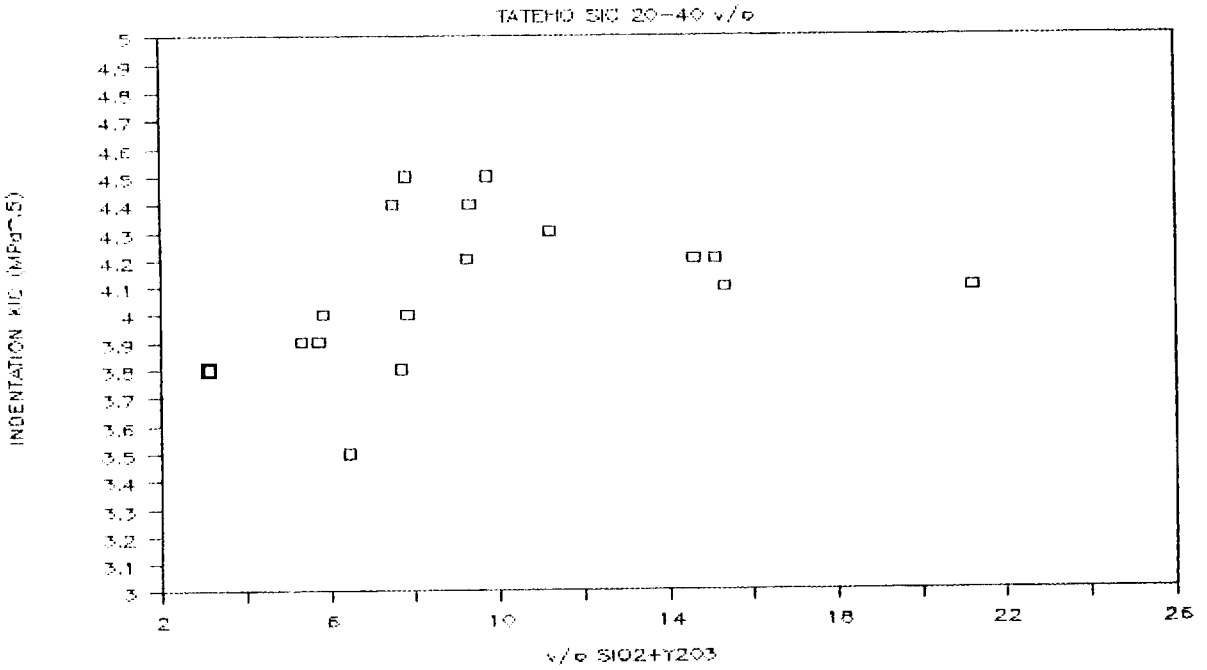

FIGURE 11

A comparison of composite compositions and room temperature properties are given in Table 4. Of major note is the steady improvement in material strength (593-823 MPa). This has been accomplished by processing the whiskers to remove large (+75μm) SiC grit from the whisker materials. These grits were the critical flaw in early materials. The Weibull modulus has also been improved and is now above our program goal of 15. Composite fracture toughness for these materials are improved 20 to 30% as compared to monolithic Si_3N_4 materials. We consider these to be "whisker added only" composites which have not had their interfaces nor whisker orientation optimized which are felt necessary to significantly increase toughening by crack bridging and whisker pullout mechanisms. Future large batch materials will be processed to enhance crack bridging and pullout mechanisms.

Figure 12 compares the high temperature strength of the three composite materials. For all materials the average strength at 1370°C in air is between 483-427 MPa (70-62 ksi). This is surprisingly high considering the larger quantity of sintering aid (10% Y_2O_3) present in the Huber reinforced material.

TABLE 4

LARGE BATCH COMPOSITE MATERIAL

FABRICATION DATE SAMPLE CODE	OCT 86 (2N #10)	MAY 87 (2081 #22)	JULY 87 (3083 #25)
Silicon Powder	3μm	milled	milled
Additive (w/o)[1]	4% Y_2O_3	4% Y_2O_3	10% Y_2O_3
SiC(w) source	Tateho SCW#1	Tateho T44	Huber
v/o SiC(w)	20	30	30
Hardness (GPa)	17.5 ± .3	15.3 ± .2	16.5 ± .1
Strength (MPa)[2]	583 ± 72	707 ± .110	823 ± 67
Weibull Modulus[3]	6.8 (12)	16.4 (8)	
Indentation Toughness[4] (MPa $\sqrt{m}$)	3.7 ± .4	3.9 ± .1	3.9 ± .1
Control Flaw Toughness[5] (MPa $\sqrt{m}$)	5.0 ± .1	4.9 ± .2	4.7 ± .8
Total Oxygen	1.8	2.1	4.0
Minor phases	Apatite $Y_2Si_2O_7$	α Si_3N_4 Y_2SiO_5	Si_2ON_2 $Y_2Si_2O_7$

1) as weight percent in matrix
2) MIL STD-1942 (MR), 3x4mm X-section
3) #of bars in parenthesis
4) Anstis method 10 kg indent
5) Chantikul method 10 kg indent

FIGURE 12

STRENGTH VS TEMPERATURE

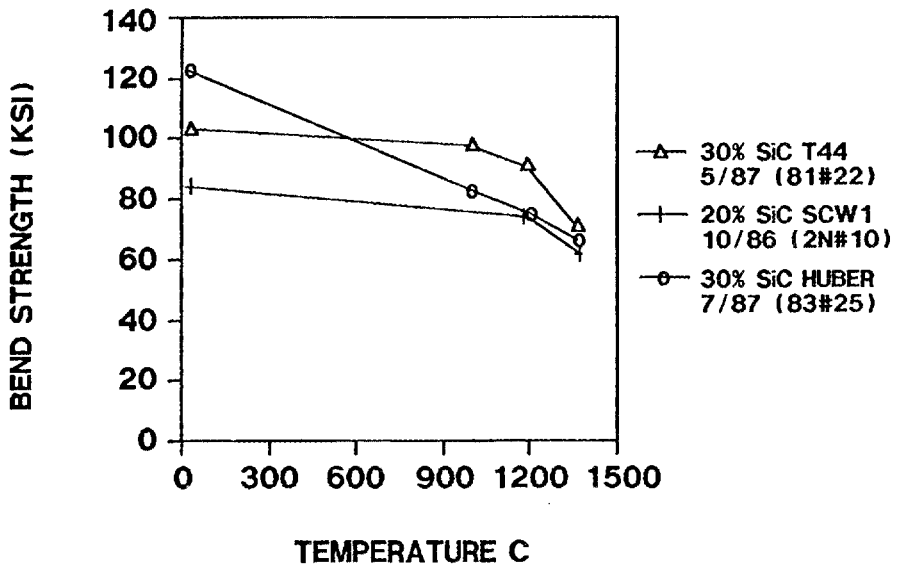

High temperature fracture toughness of the Huber whisker reinforced material was evaluated by a double torsion method. The results are presented in Fig. 13. NC132 was used as a standard material for this test, and had a room temperature fracture toughness of 6.0 which remained constant to 1200°C. Fracture toughness for the composite decreases with increasing temperature.

The decrease in toughness was unexpected since studies on hot pressed $Si_3N_4/SiC(w)$ composites showed an increase with temperature [17]. The decrease in toughness at 1000°C and 1200°C would partially explain the decrease in strength at these temperatures. The mechanism for the reduction in toughness is unclear at this time but is expected to be related to the high sintering aid content for this particular material (10 w/o Y_2O_3). Further evaluations are underway.

At 1370°C the high temperature stress rupture life for the May '87 material is over 200 hrs. at 200 MPa of stress. (After 200 hrs. samples are removed for evaluation). During testing the specimen had undergone some creep resulting in a bowed bar. X-ray diffraction analysis of this specimen revealed that the apatite phase (Y_{15} $(SiO_4)_9N_3$) had crystallized from the amorphous phase during testing. The effect of crystallization on composite properties will be addressed as a result of this information.

FIGURE 13

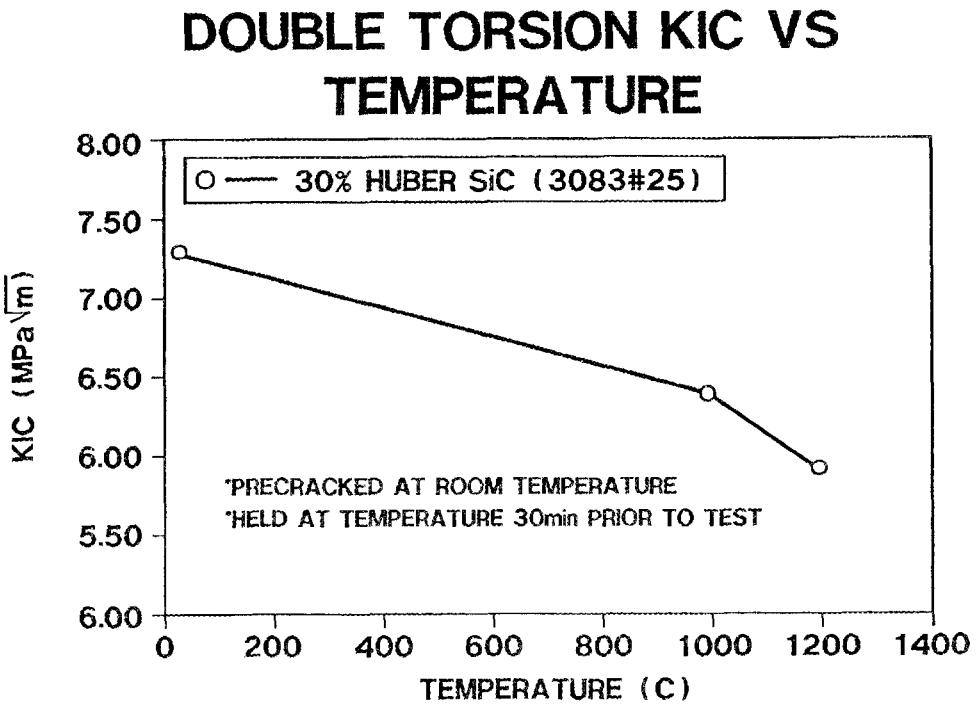

6.0 Toughening Issues

Microstructural Influences - There are similar requirements for preparing a tough Si_3N_4 monolith and a tough whisker reinforced Si_3N_4 composite. Both require elongated microstructures and interface optimization. The elongated microstructures of monolithic Si_3N_4 are grown "in-situ" whereas for composites they are artificially introduced by adding whisker shaped reinforcements. Tough Si_3N_4 monoliths result from the development of a tortuous crack path due to preferential failure in the intergranular phase around the elongated β-Si_3N_4 grains.[18] Crack interface grain bridging as observed in Al_2O_3 may also be significant.[19] For SiC whisker reinforced Si_3N_4, interface failure between the matrix and reinforcement is desired to obtain increases in toughness.

Considering that tough Si_3N_4 monoliths (including Sialons) can be prepared one could ask; Why reinforce Si_3N_4? The answer involves the desire to prepare a silicon nitride based material which can withstand high temperatures (>1400°C), be fabricated into complex shapes, and have high toughness. Tough silicon nitride monoliths are prepared by utilizing

large quantities of sintering aid (sialon up to 20 v/o) which promote grain grown and result in thick intergranular regions or by hot pressing which promotes grain growth perpendicular to the applied pressure direction. Neither of these methods are appropriate for preparing the desired high temperature, complex shaped toughened material required for applications such as the advanced gas turbine. High sintering aid contents limit uses to below 1200°C while hot pressing is limited to simple shapes. Silicon nitrides prepared for use at high temperatures require small quantities of sintering aid resulting in the use of high pressures and temperatures to promote densification. The result is a strong high temperature material with low fracture toughness. The low toughness is a result of relatively small and nearly equiaxed grains and a small quantity of intergranular phase. To improve the fracture toughness of this high temperature material, the elongated microstructure has to be artificially introduced.

To optimize the toughness of the HIPed material, we have to consider the microstructural interrelationships which occur in a composite. Key parameters which can be interrelated are listed in Table 5. The starred parameters remain essentially unchanged during processing all others have been observed to vary with processing. As an example, the thickness of the intergranular phase (T_{IG}) is effected by many parameters as highlighted below.

$$T_{IG} = V_{IG}/SA$$

T_{IG} = thickness of intergranular phase
V_{IG} = volume of intergranular phase
SA = wetted surface area of grains and whiskers

V_{IG} is a function of:
- Volume fraction SiC(w)
- SiO_2 content = f(silicon surface area, and processing)
- Y_2O_3 content

SA is a function of:
- Si_3N_4 grain size = f(whisker spacing)
- SiC(w) size = f(diameter, length)
- wetting angle of liquid on SiC and Si_3N_4

It is anticipated that intergranular phase content and composition will have an influence on composite K_{IC}.

A TEM evaluation was conducted on two Tateho SiC whisker reinforce composites having different fracture toughness. The

TABLE 5

MICROSTRUCTURAL FEATURES IN Si_3N_4/SiC COMPOSITES

SiC WHISKER	Si_3N_4 MATRIX	INTERGRANULAR PHASES
DIAMETER*	VOL. FRAC.*	Y_2O_3*
VOL. FRAC.*	SIZE	VOL. FRAC.
LENGTH	SHAPE	SiO_2
TOTAL#		THICKNESS
SPACING		CRYSTALLINE
ASPECT RATIO		AMORPHOUS
ORIENTATION		DISTRIBUTION

*Processing Independent Variable

major difference between the two samples was the crystallinity of the intergranular phases. One material contained all amorphous intergranular phase and the other contained both crystalline and amorphous intergranular phases. A continuous glassy film was observed in most of the grain boundaries and interfaces of both materials. The whiskers appeared well bonded to the matrix, and there were no voids present at the interface regions.

A sample containing 4% yttria and 20% Tateho SCW#1 whiskers (2N#10) had a toughness of 5.0 and contained the smallest amount of glassy phase in the grain boundaries. The glassy grain boundary film thickness was approximately 7.5nm and it surrounded most of the silicon nitride grains and whiskers. Also a large percentage of the whiskers were hollow and the intergranular phase filled the hollow cores of the whiskers, decreasing the amount of intergranular phase in the grain boundaries. The microstructure of this sample is presented in Fig. 14a.

A sample containing 4% yttria and 40% Tateho T44 whiskers (IM5#19) was injection molded and had a toughness of 6.3. It has a relatively uniform distribution of glassy phase in the boundaries and multigrain junctions. The glassy film thickness was on the order to 10nm and it formed a continuous film surrounding all of the grains and whiskers. The multigrain junctions varied in size, but compared to previous samples the glassy phase was more homogeneously distributed. The general microstructure of this sample is given in Fig. 14b.

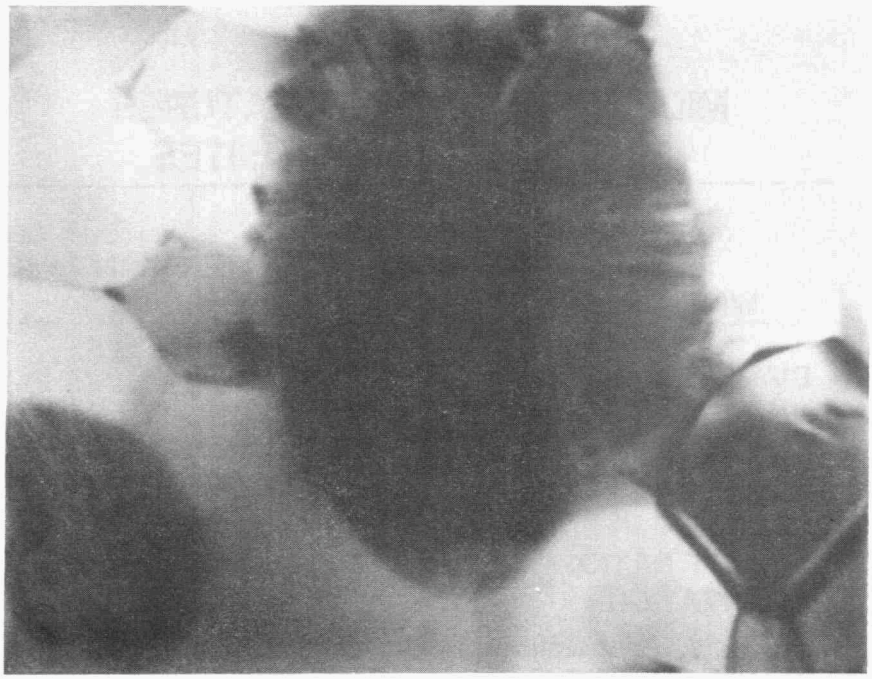

FIGURE 14A 100KX

FIGURE 14B 100 KX

Quantified relationships between microstructural features and fracture toughness will follow.

Compositional Influences - It is anticipated that the intergranular phase will play a key role in toughening Si_3N_4/SiC(w) composites. We are currently quantifying the composition of this matrix by the procedure previously described. Crystallinity of the intergranular phases is being determined by XRD and TEM analysis.

TEM observations have shown that some of the glassy phase in specimen 2N#10 crystallized during processing. Yttrium disilicate and the apatite phase were observed in the boundaries and at multigrain junctions. In sample IM5#19 crystalline intergranular phases were not observed. This specimen contained some faulted grains which are thought to be silicon oxynitride[20]. It appears that subtle changes in matrix composition can significantly change the crystallinity and phase content of the intergranular phase. At this time, the effect of crystallinity and phases on fracture toughness is not fully understood.

SUMMARY

During the past six months of our program, we have focussed our efforts on improving composite strengths, evaluating whisker sources, determining high temperature properties and evaluating CVD coated whiskers. The largest influence on composite fracture toughness appears to be interface related. This is observed by the improved toughness when BN coated whiskers are used and the sensitivity of toughness to composite oxygen content.

The ASEA HIP technology has allowed us to routinely prepare fully dense materials. The processing/blending methods developed prior to this reporting period has been successfully applied to uniformly distribute a large variety of SiC whisker sources into the SRBSN matrix. Composite toughness was not greatly influenced by the whisker sources. However, it was found that treatments of the whiskers prior to incorporation into the matrix can result in a significant improvement in K_{IC} (as received American Matrix whiskers 3.8, treated whiskers 4.8). The actual cause for this increase is under evaluation.

Both BN and a dual coating of BN with SiC on SiC whiskers has resulted in an increased fracture toughness over uncoated whisker reinforced materials (+48%). The application of coatings with stoichiometric compositions and microstructural uniformity is difficult. We are working with our vendor to refine the coating process to improve stoichiometry and minimize gas-phase nucleation.

Our evaluation of the effect of sintering aids have shown that fracture toughness is sensitive to the bulk oxygen content of the composites. Highest toughness is obtained when ~4.0 w/o oxygen is present. The oxygen content can be used to determine the volume fraction intergranular phase and its composition (SiO_2/Y_2O_3).

Large batches of material were prepared for extensive property evaluations. Room temperature strength of 842 MPa and 1370°C strength of 480 MPa have been obtained. The stress rupture life at 1370°C was greater than 200 hrs. with stress levels at and below 200 MPa. In general, composite toughnesses are 20-40% higher than similarly processed monoliths (SRBSN).

STATUS OF MILESTONES

The first three milestone have been completed.

1. Prepare and evaluate composites which utilize the first lot of CVD coated whiskers. Determine the effect of coatings on toughness - MAR 31, '87.
2. Determine HIP and nitridation processing parameters (time, temp., pressure) which reuslt in highest strength and K_{IC} for uncoated whisker reinforced Si_3N_4 - MAY 31, '87.
3. Prepare and evaluate composites which utilize whiskers of different aspect ratio, and composites which contain the 2nd lot of CVD whiskers. Determine optimum whisker l/d and coatings for improved toughness. Optimize SiC whisker distribution and green density. - SEP 31, '87.
4. Submit draft of final report to ORNL - NOV 31, '87.

PUBLICATIONS None.

REFERENCES

1. Siebein, K. N., and Lovington, W.M., "Plasma Etching of Si3N4," Presented at the 20th Annual International Metallographic Society Meeting, Montery, CA, July 1987.
2. Corbin, N.D., and Willkens, C.A., "Development of Toughened Si3N4 Composites by Glass Encapsulated Hot Isostatic Pressure," to be publsihed in Ceramic Technology for Advanced Heat Engines Project Semiannual for October 1986 to March 1987. Oak Ridge National Laboratory, Oak Ridge, TN.
3. Leco Model #TC-136, Saint Joseph, MI.

4. Ruhle, M., and Petzow G., "Microstructure and Chemical Composition of Grain Bundaries in Ceramics," In: Surfaces and Interfaces in Ceramics, Editor, Pask Plenum (1981) p167-175.

5. Clark, D.R., "The Microstructure of Nitrogen Ceramics," In: Progress in Nitrogen Ceramics, editor F.L. Riley, Martinus Nijhoff, Boston, (1983), p341-358.

6. MIL-STD-1942 (MR), Flexural Strengths of High Performance Ceramics at Ambient Temperature, November 21, (1983).

7. Chantikul, P. Anstis, G., Lawn, B., and Marshall, D., "A Critical Evaluation of Indentation Techniques for Measuring Fracture Toughness: II, Strength Method," Journal of the American Ceramic Society, Vol. 64, #9, P.539-543, Sept. 1981.

8. Antis, G., Chantikul, P., Lawn, B., Marshall, D., "A Critical Evaluation of Indentation Techniques for Measuring Fracture Toughness: I, Direct Crack Measurements," Journal of the American Ceramic Society, Vol. 64, #9, p.533-538, Sept. 1981.

9. Fuller, E.R., "An Evaluation of Double Torsion Testing Analysis," Presented at the 11th National Symposium on Fracture Mechanics, Blackburg, VA, June (1987).

10. Quinn, G.D., "Guide to the Construction of a Simple 1500°C Test Furnace," U.S. Army Materials Technology Laboratory, AMMRC TR83-1, January 1983, NTIS ADA 125636.

11. Quinn, G.D., "Characterization of Turbine Ceramics after Long-Term Environment Exposure," U.S. Army Materials Technology Laboratory, AMMRC TR80-15, April 1980, AD A117463.

12. Faber, K.T., Evans, A.G., "Crack Deflection Processes - I. Theory," Acta. Metall. Vol. 31, No. 4, p565-576, (1983).

13. Zachrich, D., "Personal Communication," Norton Company, Diamond Technology Center, Salt Lake City, UT, Sept. 21, 1987.

14. Nutt, S.R., "Defects in Silicon Carbide Whiskers," J. Amer. Ceram. Soc., Vol. 67, No. 6, June, p428-431, (1984).

15. Gazza, G.E., "Effect of Yttria Additions on Hot Pressed Si_3N_4," Am.Cer.Soc.Bull., Vol. 54, No. 9, p778-81, (1975).

16. Lange, F.F., Sighal, S.C., and Kaznicki, "Phase Relations and Stability Studies in the Si_3N_4-SiO_2-Y_2O_3 Pseudoternary System," J.Amer. Ceram. Soc., Vol. 60, No. 5-6, May-June, p249-252 (1977).

17. Buljan, S., Baldoni, J., and Huckabee, M.L., "Si_3N_4-SiC Composites," Am. Ceram. Soc. Bull., Vol. 66, No. 2, 347-52 (1987).

18. Rice, R.W., "Fracture Energy of Si_3N_4," J.Mat.Sci., Vol. 20, p1392, (1985).

19. Swanson, P.L., Fairbanks, C.J., Lawn, B.R., Mai, Y.W., Hockey, B.J., "Crack-Interface Grain Bridging as a Fracture Resistance Mechanism in Ceramics: I, Experimental Study on Alumina, J. Amer. Ceram. Soc., Vol. 70, No. 4, p279-89 (1987).

20. Lou, L.K.V., Mitchell, T.E., and Heuer, A.H., "Impurity Phases in Hot Pressed Silicon Nitride," J. Amer. Ceram. Soc., Vol. 61, No. 9-10, Sept.-Oct. p392-396, (1978).

1.2.3 Oxide Matrix

Dispersion Toughened Oxide Composites

T. N. Tiegs, K. C. Liu, and J. W. Geer (Oak Ridge National Laboratory)

Objective/scope

This work involves development and characterization of SiC whisker-reinforced oxide composites for improved mechanical performance. To date, most of the work has dealt with alumina as the matrix because it was deemed a promising material for initial study. However, a new effort in SiC whisker-reinforced sialon is being initiated. Emphasis in the new system will be on pressureless sintering and control of the whisker-matrix interface properties.

Technical progress

SiC Whiskers

As shown previously, considerable variation in fracture toughness of alumina-SiC whisker composites is observed when using whiskers from various sources.[1] We have found that the surface chemistry of the whiskers and ultimately its effect on the whisker-matrix interface are of great importance.[1,2] In addition to the effect of surface chemistries, the whiskers from various sources also vary in size. If crack bridging is considered to be one of the major toughening mechanisms, then the toughness should increase as whisker diameter increases. Figure 1 shows the various whiskers used in alumina-20 vol % SiC composites as a function of their whisker diameter and toughness. As shown, a good correlation exists between increasing whisker diameter and toughness.

The increase in fracture toughness with whisker diameter of alumina composites is limited by microcracking of the matrix due to the thermal expansion mismatch between alumina and silicon carbide. Microcracking is dependent on the diameter of the whisker and would result in a loss of fracture strength. To determine the effect of varying the whisker diameter, SiC particulate can be used to simulate the stresses around the whiskers. Alumina-20 vol % SiC particulate composites were fabricated and the fracture strengths calculated. The mean particulate diameters ranged from 0.6 to 16.9 μm. A summary of the results are illustrated in Fig. 2. As shown, increases in the fracture strength were observed with increasing mean particulate size into the 2–2.5-μm region. A reduction in strength was observed with increasing SiC particulate size. Evidently the initiation of extensive microcracking of the alumina matrix is occurring with SiC particulate sizes larger than 3–4 μm. Further analysis of these specimens using scanning electron microscopy and ultrasonic attenuation is currently in progress.

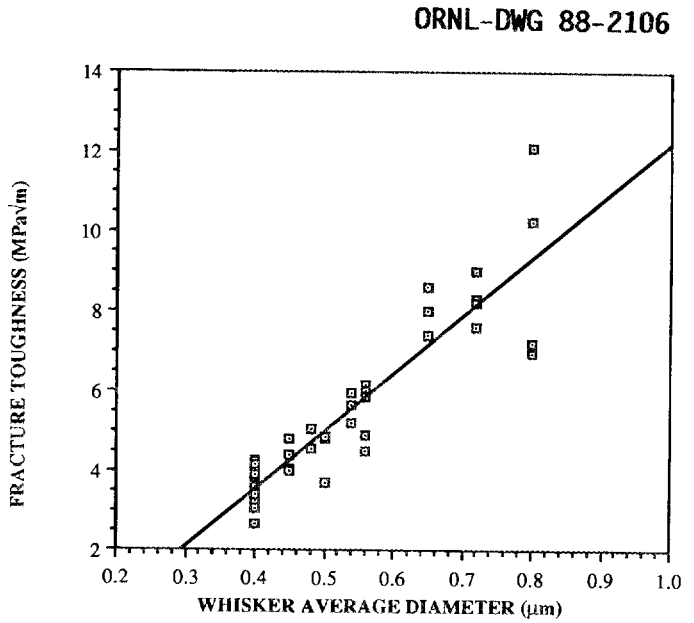

Fig. 1. Fracture toughness of alumina-20 vol % SiC whisker composites appear to increase with increasing whisker diameter.

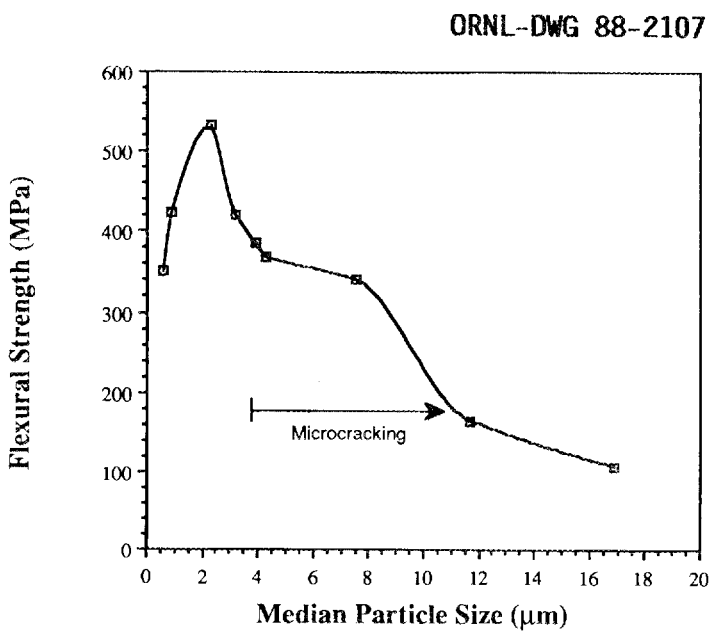

Fig. 2. Loss of strength at large SiC particulate sizes indicates matrix microcracking.

Pressureless Sintering of Alumina Matrix Composites

Additional work on pressureless sintering of alumina-SiCw composites has been done with the goal to densify material with 20 vol % SiCw to 95% T.D. The effects of whisker aspect ratio and amount of liquid phase were examined.

The effect of whisker aspect ratio on sintering was investigated by milling the whiskers for various times to change the length distribution and then examining the changes in green and fired densities. The composites were fabricated with low amounts of sintering aids (2 wt % Y_2O_3 and 0.5 wt % MgO) to help delineate the effects whisker ratio from the liquid phase sintering.

The resulting whisker length distributions obtained by the milling procedure are illustrated in Fig. 3. As shown, the whisker lengths are reduced considerably during milling. As the whisker lengths are reduced, the composite green densities increase slightly but not dramatically for both the 10 and 20 vol % composites. However, when the same composites are sintered, the effect of the lower aspect ratio is clearly evident, especially for the composite with 20 vol % SiCw (Fig. 4). As shown, the sintered densities are improved with lower aspect ratios at all sintering temperatures, indicating that inhibition to particle rearrangement and shrinkage is reduced as the whisker aspect ratio is lowered.

To determine the effect of liquid phase sintering aids, specimens were prepared with increasing amounts of Y_2O_3 to create more liquid phase at the sintering temperature. The whiskers were milled 32 h to produce a whisker size distribution similar to that in Fig. 3.

The results for the liquid phase sintering are summarized in Fig. 5. As shown, the sintered densities generally increase with both the temperature and Y_2O_3 content. However, at the higher temperatures and Y_2O_3 contents (i.e., >10 wt % Y_2O_3 and >1750°C), the densities are observed to remain constant or slightly decrease. This effect is believed to be due to excessive liquid phase formation which leads to increased volatilization of gaseous species.

The most important effect of varying the temperature and the Y_2O_3 content is to change the amount of liquid phase present. Using available phase diagrams, the amount of matrix liquid phase at the sintering temperatures was calculated. A good correlation between the quantity of liquid phase and the final density is shown in Fig. 6. As indicated, the amounts of liquid phase can be quite excessive with quantities up ~80%. In addition, the densities do not improve with liquid phase contents >30–40%.

Pressureless Sintering of Mullite Matrix Composites

Additional work on pressureless sintering of mullite-SiC whisker composites has been done with the goal to densify material to 95% T.D. While hot pressing of the mullite-SiC whisker composites produces dense materials with attractive mechanical properties, the ability to pressureless sinter the composites is desirable for some potential applications. Pressureless sintering is also necessary to provide complex and near-net-shape fabrication capability for these composites.

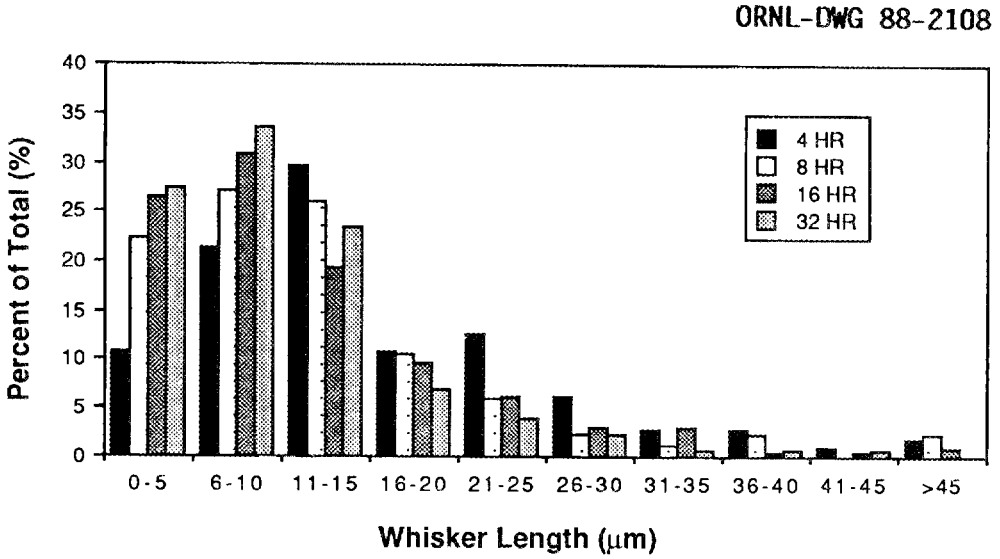

Fig. 3. Whisker length distribution of milled whiskers used in sintering study.

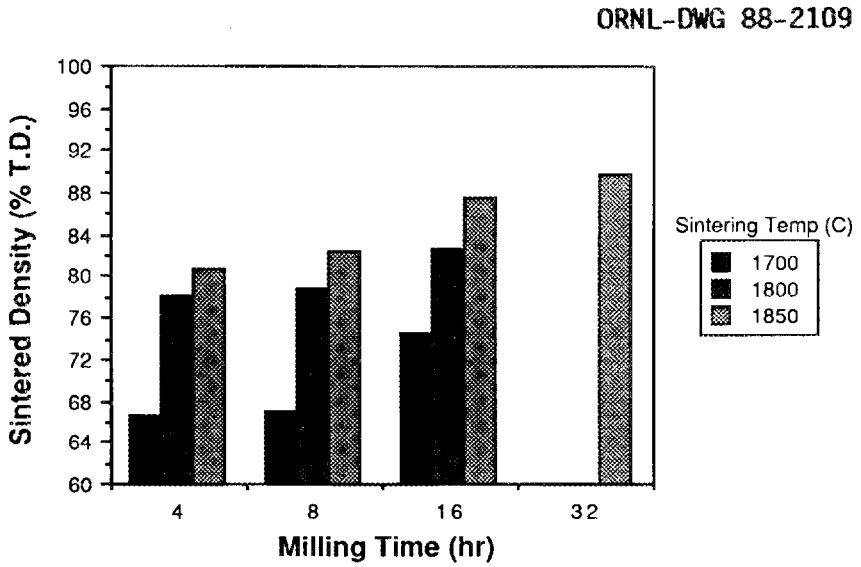

Fig. 4. Sintered densities of alumina-20 vol % SiCw composites with different whisker aspect ratios.

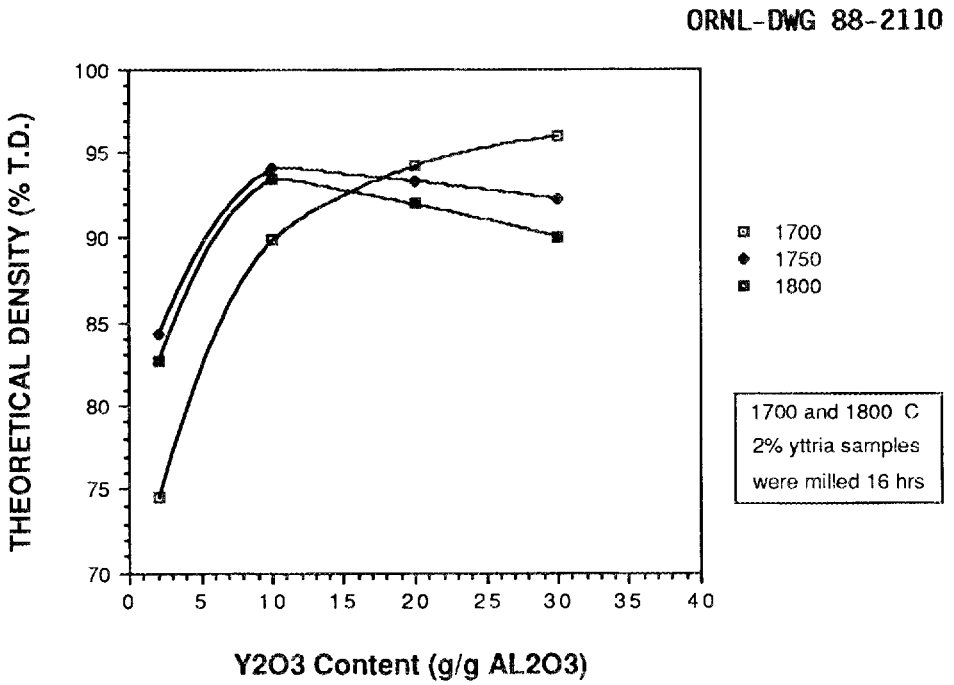

Fig. 5. Sintered densities of alumina-20 vol % SiCw composites with different Y_2O_3 contents.

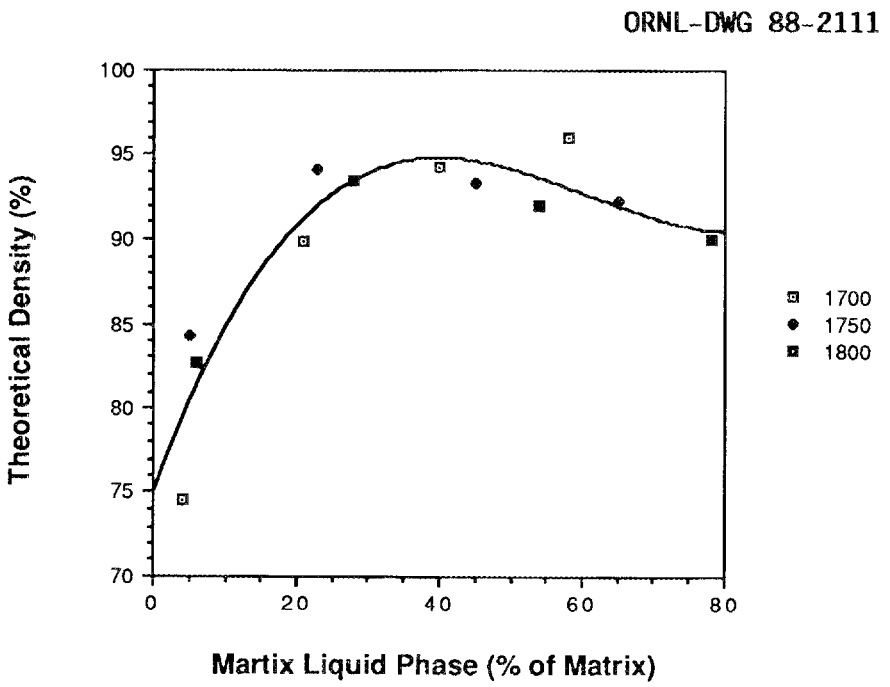

Fig. 6. Sintered densities of alumina-20 vol % SiCw composites with different amounts of liquid phase.

Previous results have shown that SiC whiskers inhibit sintering by interfering with particle rearrangement and shrinkage.[3] To promote densification, liquid phase sintering aids are used. Figure 7 shows the contrast in densification behavior of mullite-10 vol % SiC whisker composites with and without sintering aids. As indicated, the sintering aids are necessary to achieve acceptable densities at appropriate whisker contents. Because of the inhibiting effect of the whiskers, the ability to densify the composites is highly dependent on the whisker content. As the whisker content approaches 20 vol %, the sintering is severely inhibited (Fig. 8). For the present time, high density mullite-SiC whisker composites (>94% T.D.) are generally limited to compositions with up to 10 vol % whiskers.

Stress-Strain Behavior of Alumina-SiC Whisker Composites

The stress-strain behavior of an alumina-20 vol % SiC whisker composite was determined on test bars under four-point loading. The test results are summarized in Table 1. As shown, the strain to failure of these composites is about 0.15%.

Status of milestones

Milestone 123105 was completed. Results have been published in current and previous[1] semiannual progress reports.

Publications

T. N. Tiegs and P. F. Becher, "Thermal Shock Behavior of an Alumina-SiC Whisker Composite," *J. Am. Ceram. Soc.* **70**(5), C-109–11 (1987).

References

1. T. N. Tiegs, L. A. Harris, and J. W. Geer, "Dispersion Toughened Oxide Composites," pp. 86–93 in *Ceramic Technology for Advanced Heat Engines Project Semiannual Progress Report for October 1986 Through March 1987*, ORNL/TM-10469 (August 1987).

2. T. N. Tiegs, P. F. Becher and L. A. Harris, "Interfaces in Alumina-SiC Whisker Composites," in *Proc. Ceramic Microstructures: Role of Interfaces*, ed. J. A. Pask and A. G. Evans, in press.

3. T. N. Tiegs and P. F. Becher, "Sintered Al_2O_3-SiC-Whisker Composites," *Am. Ceram. Bull.* **66**(2), 339-42 (1987).

Table 1. Summary of results on stress-strain behavior of alumina-20 vol % SiC whisker composite

Specimen	Fracture strength[a] (MPa)	Strain to failure (%)	Elastic modulus (GPa)
1	488	0.126	386.5
2	648	0.166	390.1
3	792	0.198	401.2
4	717	0.179	400.9
5	575	0.146	393.3
Average	644 ± 119	0.163 ± 0.028	394.4 ± 6.5

[a]Four-point bend test, inner span = 20 mm, outer span = 40 mm; nominal specimen dimensions 4.8 × 5.2 × >40 mm; stress rate = 69 MPa/s.

ORNL-DWG 88-2112

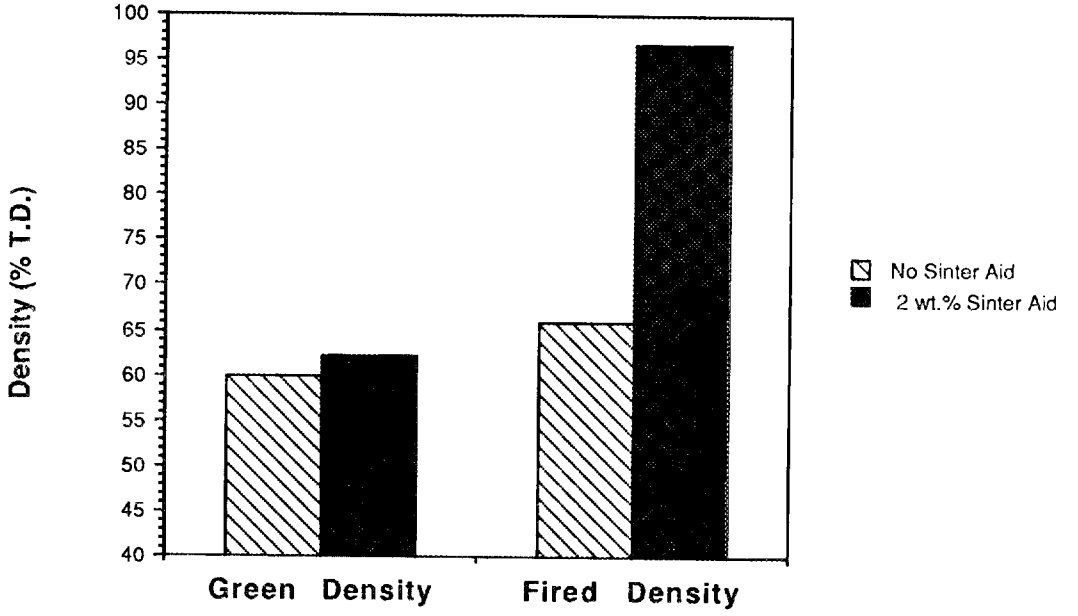

Fig. 7. Effect of sintering aid addition on densification of mullite-10 vol % SiC whisker composites. Sintered at 1600°C.

ORNL-DWG 88-2113

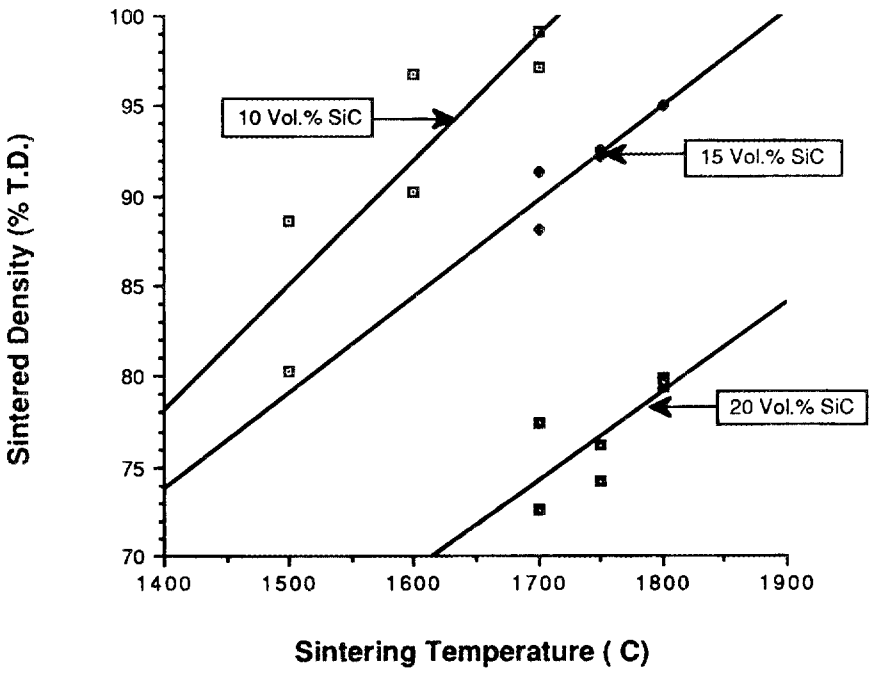

Fig. 8. Effect of whisker content and sintering temperature on density of mullite-SiC whisker composites. All composites contain 2 wt % sintering aids.

Processing of Improved Transformation-Toughened Ceramics

J. J. Blum, C. E. Knapp, and G. A. Rossi (Norton Company)

Objective/scope

The objective of this program is the production of zirconia toughened ceramics (ZTC) which exhibit mechanical properties (strength and toughness) superior to those of the "state of the art" toughened ceramics, particularly at high temperature and after prolonged aging at high temperature. In addition, such ceramics should possess low thermal conductivity to minimize energy losses in heat engine applications.

The scope includes the powder synthesis and characterization, shape forming, pressureless sintering, characterization of the sintered ceramics, and reporting of results.

Our research will concentrate on three classes of zirconia toughened ceramics (ZTC), i.e. Mg-PSZ, (MgO-partially stabilized zirconia), Y-TZP (Y_2O_3)-tetragonal zirconia polycrystals), and ZTA (zirconia toughened alumina). Most of the work will be done using rapidly solidified (R/S) powders, which offer several important advantages over the chemically derived (C/D) powders. However, the C/D powders or their mixtures will be used for testing new compositions, since melting/rapid solidification of small batches is expensive and impractical.

The ceramics should be made by pressureless sintering, but hot isostatic pressing will be used to evaluate the potential of each composition, before processing optimization is complete.

The goals of this program are minimum values of strength and toughness at RT and at 1000°C; in addition, the ceramics should meet the same requirements for RT strength and toughness after aging in air at 1000°C for 1000 hrs.

Technical progress

During the last six months our efforts have concentrated on the following three areas:

A. Enhancement of the strength of the Y-TZP (Y_2O_3-stabilized Tetragonal Zirconia Polycrystals) ceramics made with the rapidly solidified (R/S) powders, through improvements in powder processing, shape forming and firing cycle.

B. Improvement of our understanding of the microstructure/-property relationship in the Y-TZP's made with the R/S powders.

C. Development of Y-ZTA (Y_2O_3-stabilized Zirconia Toughened Alumina) ceramics and of Ce-ZTA (CeO_2-stabilized Zirconia Toughened Alumina) ceramics with and without HfO_2 additions.

1. Improved Y-TZP ceramics (4.5 w/o Y_2O_3) made with the rapidly solidified (R/S) powders

Since our last semi-annual report we have been using our R/S material which has been comminuted using a newly developed, proprietary process. To determine the densification parameters for this new powder, dilatometer bars were CIPed. In order to find the conditions at which shrinkage is completed, the samples were fired at 3°C/min. up to hold temperature, then held for long times (5-7 hrs.).

Based on the results obtained, it was concluded that firing at 1500°C for 1.5 hrs. yielded the best microstructure (small grain size, tight distribution).

To maximize the properties which could be achieved from this new powder, it was decided to use the method described by Lange [1] to prepare samples. In this technique slurries are not dried, but flocced, decanted, and redispersed to increase the solids loading. The resultant slip is then pressure cast.

In order to better understand our slip characteristics the relative acoustic mobility (RAM), which is related to zeta potential, as a function of pH was measured on our Pen-Kem 7000 instrument. The results are presented in Figure 1. As can be seen, the isoelectric point was about pH=6.5.

Following the procedure described above, the slips were about 55-65 wt.% solids. Billets were pressure cast and then cold isostatically pressed (CIPed). All of the samples were fired to 1500°C/1.5 hr.

As we have improved our powder making process, the resulting billets have shown an increase in strength as shown in Table 1.

TABLE 1

Powder Lot	No. of Samples	Avg. Strength*	Std. Deviation
1	11	870 MPa	255 MPa
2	8	1060 MPa	241 MPa
3	24	1074 MPa	218 MPa

*(4 pt. bending)

As can be seen from the Table, the average strengths have been increasing while the width of the distribution (standard deviation) has been decreasing. The data for Lots 1 and 3 are plotted in a Weibull manner in Figure 2. This leads to a Weibull modulus of 4.0 for Lot 1 and 6.2 for Lot 3.

The processing of the billets has been the same for Lots 1-3. We believe that the improvements in the strengths shown in Table 1 and Figure 2 are due to our continuing efforts to minimize contamination of the powder. We have had some fractography done on our highest strength lot.

Fractography was performed on nine of the weakest samples. The fracture origin of the weakest sample (710 MPa) was a void which appeared to be the remnant of a thread-like piece of lint (see Fig. 3). Several of the fracture origins in the other weak samples were fairly large (60 microns) voids. These may be the result of contamination, e.g. abraded plastic from our containers. In one case (strength=1041 MPa) was there evidence of Al_2O_3 contamination. The inclusion was small, about 5 microns long, and had grains slightly larger than the ZrO_2 matrix (see Fig. 4).

2. <u>Improved understanding of the microstructure/property relationship in the Y-TZP ceramics made with the R/S powders</u>

It is well known that the Y-TZP ceramics suffer degradation upon annealing at low temperature (200-300°C) in a humid atmosphere. It has been reported that such degradation, which starts at the surface where t-ZrO_2 transforms to m-ZrO_2 and then propagates towards the interior of the piece due to the associated microcracking, can be minimized by keeping the grain size below a critical level and by increasing the Y_2O_3 content. However, it is also known that the toughness decreases by decreasing grain size and increasing the Y_2O_3 concentration. A compromise must therefore be found in order to produce a strong and tough ceramic fairly insensitive to the low temperature degradation.

Lange [2] has shown that phase partitioning occurs upon annealing at high temperature in the two phase field of the ZrO_2-Y_2O_3 phase diagram, i.e. t-ZrO_2 and c-ZrO_2. The phase partitioning is accompanied by a redistribution of the Y_2O_3 among the tetragonal (low yttria) and cubic (high yttria) grains. The low yttria t-ZrO_2 grains then become prone to the spontaneous transformation to m-ZrO_2 which causes cracking.

We have tried to determine the extent of the yttria redistribution in a sample of Y-TZP which had been deliberately overfired and showed the presence of large (> 2 um)

grains, suspected to be cubic. The Y_2O_3 concentration was measured with an SEM technique on nine grains, of which one was much larger than the others surrounding it. The results are shown in Table 2 below.

TABLE 2

Y_2O_3 distribution in a Y-TZP sample overfired at 1600°C

Grain #	w/o Y_2O_3	Grain Size (um)
1	6.6	3.2
2	3.6	0.7
3	4.3	0.8
4	3.3	1.1
5	3.7	1.0
6	3.9	0.7
7	3.6	1.5
8	3.4	1.0
9	4.1	0.6
overall	3.9	---

The data shown above indicate that some Y_2O_3 redistribution seems to be occurring, with the large grain (#1) becoming Y_2O_3 enriched and the smaller surrounding grains (#2-9) becoming somewhat depleted. It should be noted that the high Y_2O_3 concentration of grain #1 is below that predicted by the equilibrium phase diagram. (We know that the rapidly solidified powder used to make the sintered billets has a very uniform Y_2O_3 distribution, which was measured by analytical electron microscopy [3]).

In another more complete experiment a series of square billets of Y-TZP were sintered simultaneously at 1450°C for 2 hrs. to a density of about 99% of TD. The R/S powder used contained 4.0 w/o Y_2O_3 and had been previously classified to eliminate the particles larger than 1 um. The sintered billets were then annealed isothermally at 1500°C for different times, i.e. 1, 4, 6 and 8 hrs. The billet aged for 8 hrs. was all cracked when cooled down to room temperature, while the others were good. MOR bars (3 x 3 x 30 mm) were then cut out of the aged billets and tested for strength. The fracture toughness was also measured with the micro-indentation method. Table 3 shows the results obtained.

TABLE 3

Relationship between strength and toughness for Y-TZP ceramics sintered at 1450°C and aged at 1500°C for different times

Billet #	Aging Time	AGR	Avg. MOR	# Bars	K_{IC}
1	Not Aged	.36	985	5	5.7
2	1	.52	792	5	9.5
3	4	.68	820	3	12.3
4	6	.72	841	3	12.9

NOTE: Aging time in hrs; AGR = Average Grain Radius in um; MOR (4 pt. bending) values in MPa; K_{IC} values in MPa.m$^{1/2}$.

Figs. 5 through 8 show the microstructures (SEM) of the four billets previously mentioned.

Fig. 9 shows the hystograms of the grain size distribution for the four billets described in Table 3.

The as-fired surface of the four billets was also analyzed by XRD, in order to determine the relative ratios of the phases present. Table 4 shows the results.

TABLE 4

Phase composition by XRD on the as-fired surface of billets described in Table 3

Billet #	m-ZrO_2	t-ZrO_2	c-ZrO_2
1	2%	Balance	N.D.
2	1%	"	"
3	13%	"	11%
4	15%	"	15%

NOTE: N.D. = Not Detected

From these data it appears that phase partitioning has occurred due to aging.

In conclusion, this experiment has shown that aging at high temperature causes phase partitioning, an increase in grain size and a considerable increase in toughness. No direct proportionality between strength and toughness was found, as predicted by the Griffith equation. Since the billets had the same previous history, it seems unlikely that they have different flaw size distributions, which would have explained the lack of proportionality between strength and toughness.

Since a higher percentage of m-ZrO_2 was found after aging, microcracking associated with the t/m transformation may explain the drop in strength in the aged samples.

3A. CeO_2-ZrO_2 toughened Al_2O_3 with and without HfO_2 addition

The results obtained on these materials are not reported because they are considered patentable information. A patent disclosure and application are now being written.

3B. Y_2O_3-ZrO_2 toughened Al_2O_3 ceramics made with R/S powders

A batch of submicron powder was made by milling a rapidly solidified crude with composition 0.9 w/o Y_2O_3, 24.0 w/o ZrO_2 and 75.1 w/o Al_2O_3.

Square billets were die pressed, cold isostatically pressed and sintered at 1600°C for 1 hr. 3 x 3 x 30 mm MOR bars were obtained as well as rectangular samples (50 x 25 x 1 mm) for K_{IC} measurement with the double torsion method.

Table 5 shows the results of strength and K_{IC} vs. temperature.

TABLE 5

MOR (4 pt.) and K_{IC} (DT) vs. T for sintered Y-ZTA ceramics

	25°C	SD%	600°C	SD%	1000°C	SD%
MOR (MPa)	587(4)	10.0	---	---	426(4)	4.0
K_{IC}(MPa.m$^{\frac{1}{2}}$)	---	---	---	---	4.4(3)	6.2

NOTE: Numbers in parenthesis are samples tested.

It appears that the Y-ZTA ceramics, like the Ce-ZTA materials, are promising candidates for heat engine applications.

4. Aging at 1000°C/1000 hrs.

The Y-TZP ceramics made with the R/S powder and the Ce-ZTA made with the colloidal method are being aged. Two types of Y-TZP have been prepared by sintering, i.e. a low purity material with 4.5 w/o Y_2O_3 and a higher purity one with 5.4 w/o Y_2O_3.

Status of milestones

Table 6 shows the milestone list for 1987.

TABLE 6

Milestone #	Description	Date
1	Identify M_s and A_s temperatures of Y-TZP ceramic using low temperature (Liquid N_2) dilatometry.	Mar. 31
2	Final evaluation of the Mg-PSZ ceramics made with the R/S powders.	Mar. 31
3	Develop ceramic fixture for measurement of hot fracture toughness with double torsion technique.	Apr. 30
4	Evaluate influence of microstructure of Y-TZP ceramics made with the R/S powders on MOR and K_{IC} at RT and HT.	Jun. 30
5	Evaluate MOR and K_{IC} at RT and HT for ZTA ceramics made with C/D and R/S powders, i.e. ZrO_2/Al_2O_3, Y-TZP/ Al_2O_3, Ce-TZP (HfO_2)/Al_2O_3.	Jul. 31
6	Select final composition and best processing method for final optimization.	Jul. 31
7	Optimize composition, processing, firing schedule to achieve program objectives.	Oct. 31
8	Measure thermal conductivity and thermal expansion coefficient of ceramic with optimized composition.	
9	Write final report to document results of the research contract.	Nov. 30

No more work will be done for milestone #2, because all billets came out cracked, despite our best efforts. All other milestones are on schedule.

Publications

None

References

[1] F. F. Lange, B. I. Davis, and E. Wright, J Am Ceram Soc, 69, 66-69, (1986).

[2] F. F. Lange, "Transformation-Toughened ZrO_2: Correlations between Grain Size and Composition in the System ZrO_2-Y_2O_3", J Am Ceram Soc, 69 (3), 240-42, (1986).

[3] K. N. Siebein, R. R. Biederman and G. A. Rossi, "Microchemical Analysis of Y_2O_3-Doped ZrO_2 Powders", Advances in Ceramics, Vol. 21 pp. 801-809, (1987).

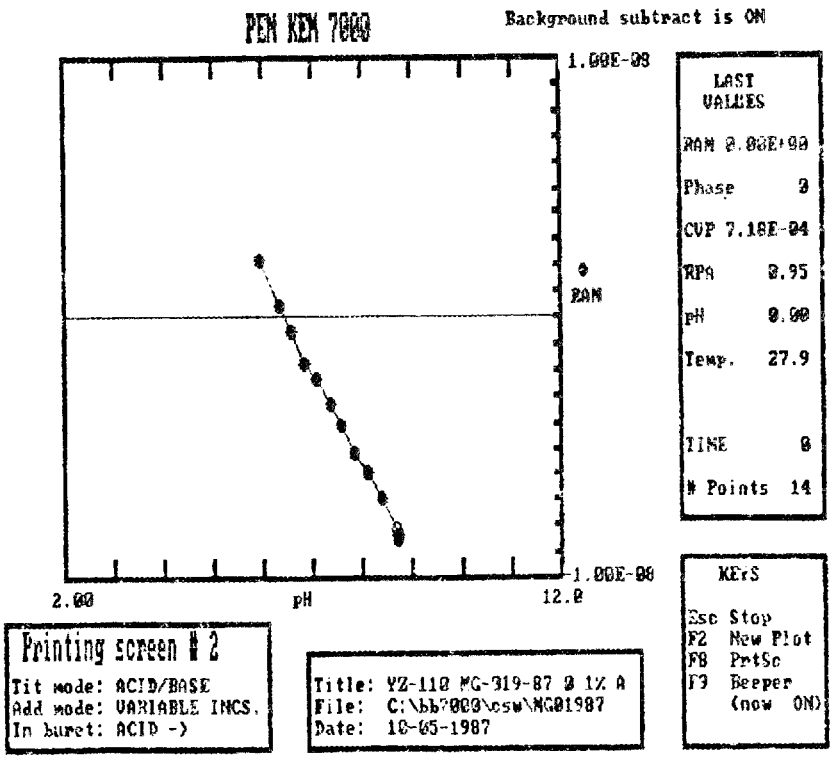

Fig. 1: Relative acoustic mobility vs. pH for R/S Y-TZP powder.

Weibull Plot for YZ-110
Pressure Cast/Sintered at 1500°C

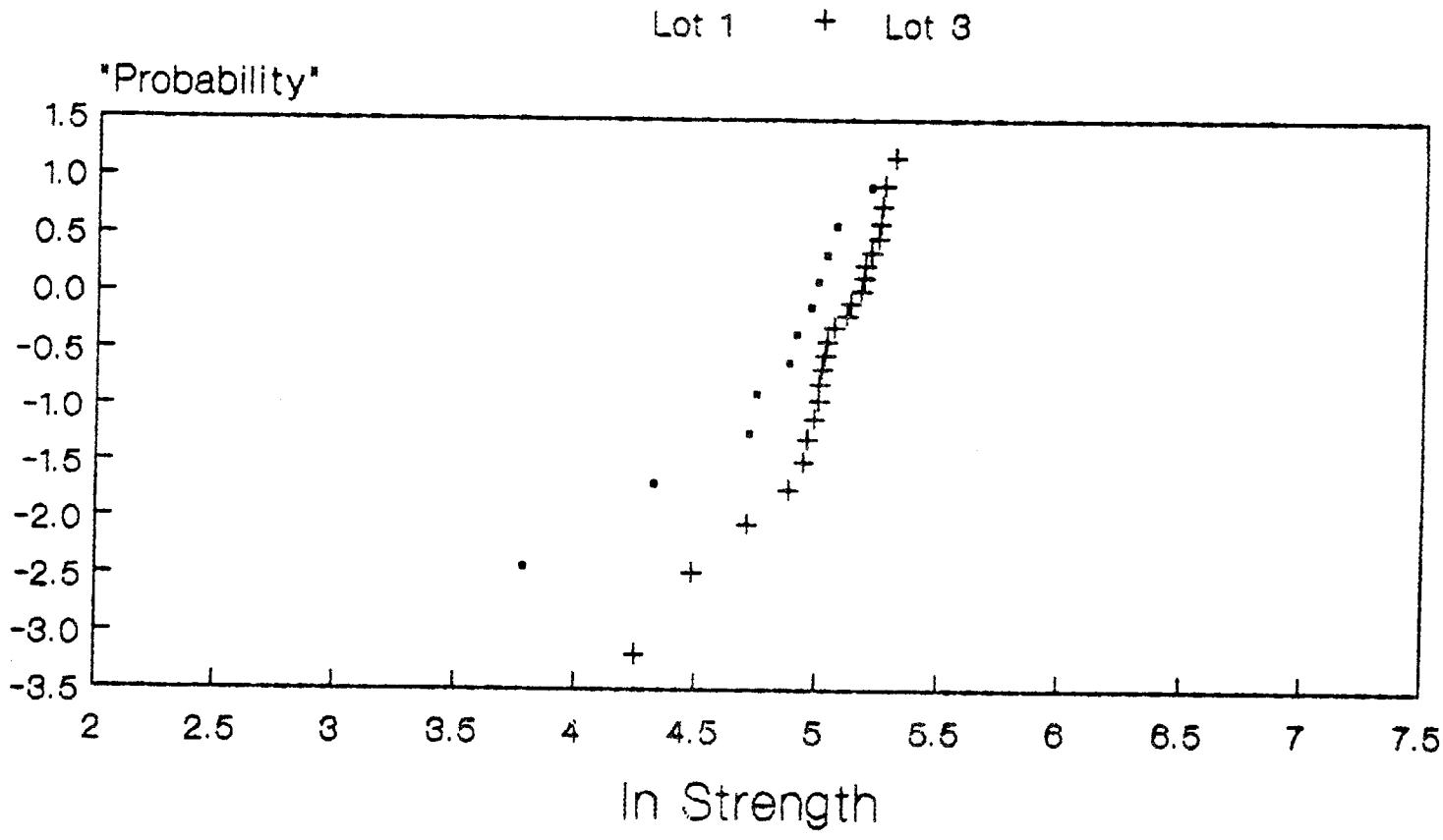

Fig. 2: Weibull Modulus plots for two batches of pressure cast and sintered Y-TZP ceramics.

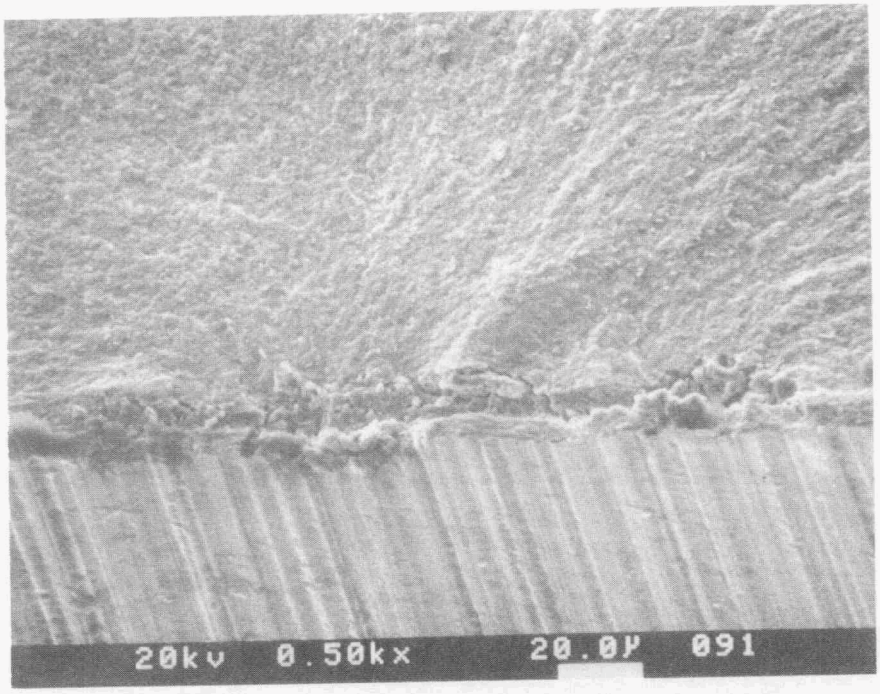

Fig. 3: SEM fractograph of MOR bar (710 MPa) containing lint derived strength reducing flaw

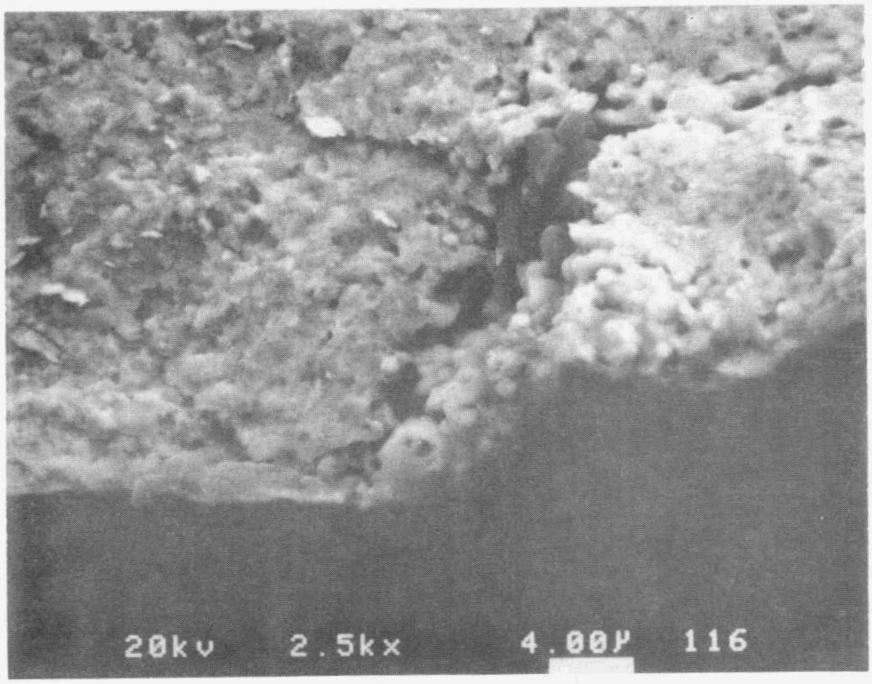

Fig. 4: SEM fractograph of MOR bar (1041 MPa) containing alumina inclusion

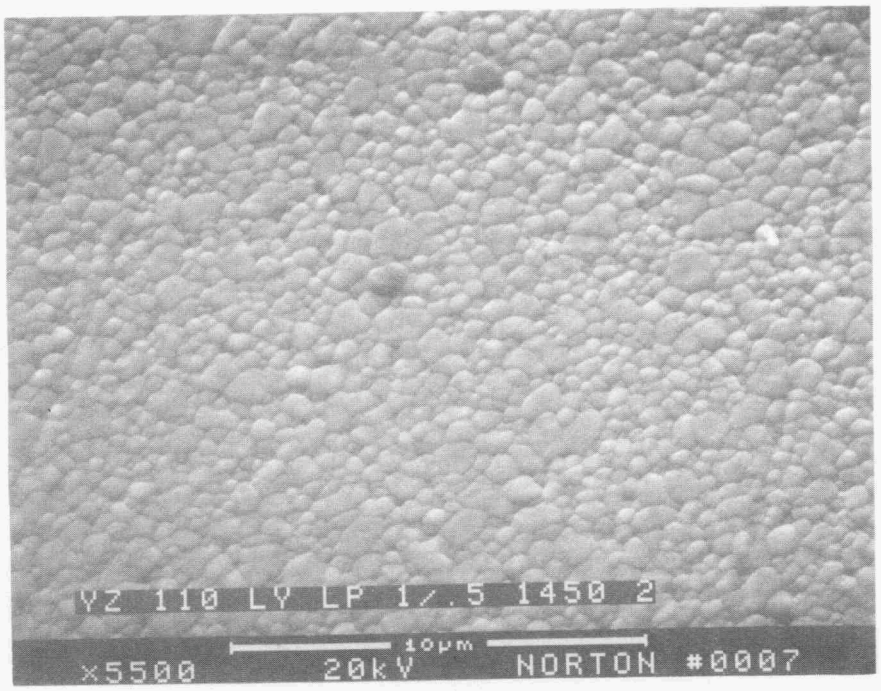

Fig. 5: Microstructure (SEM) of Y-TZP (4 w/o Y_2O_3) ceramic sintered at 1450°C/2 hrs.

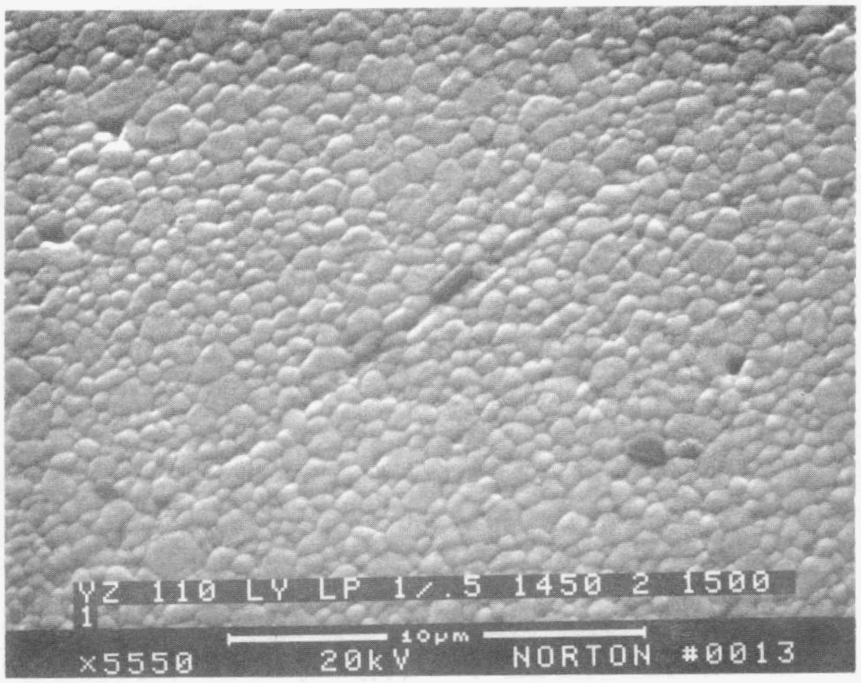

Fig. 6: Microstructure (SEM) of Y-TZP (4 w/o Y_2O_3) ceramic after aging at 1500°C/1 hr.

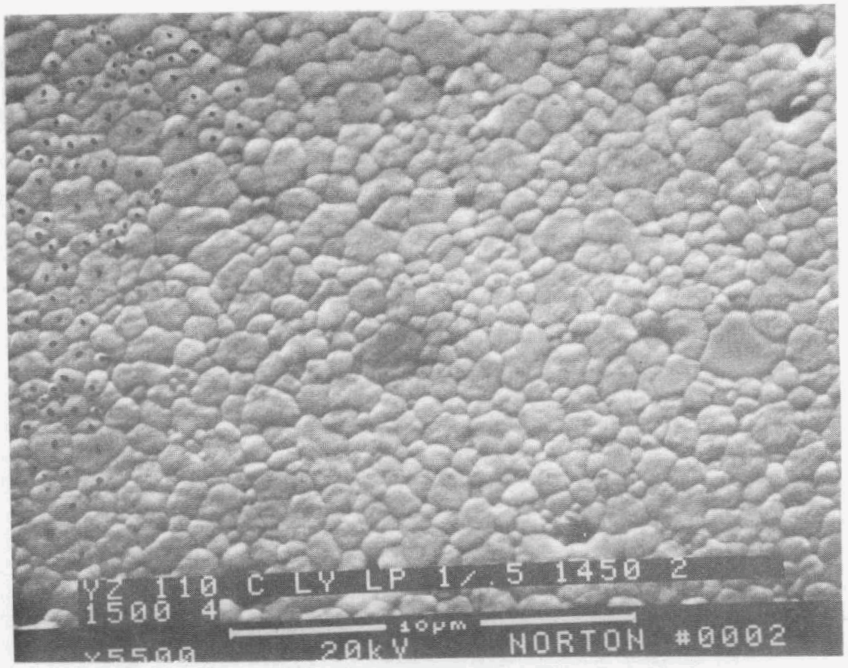

Fig. 7: Microstructure (SEM) of Y-TZP (4 w/o Y_2O_3) ceramic after aging at 1500°C/4 hrs.

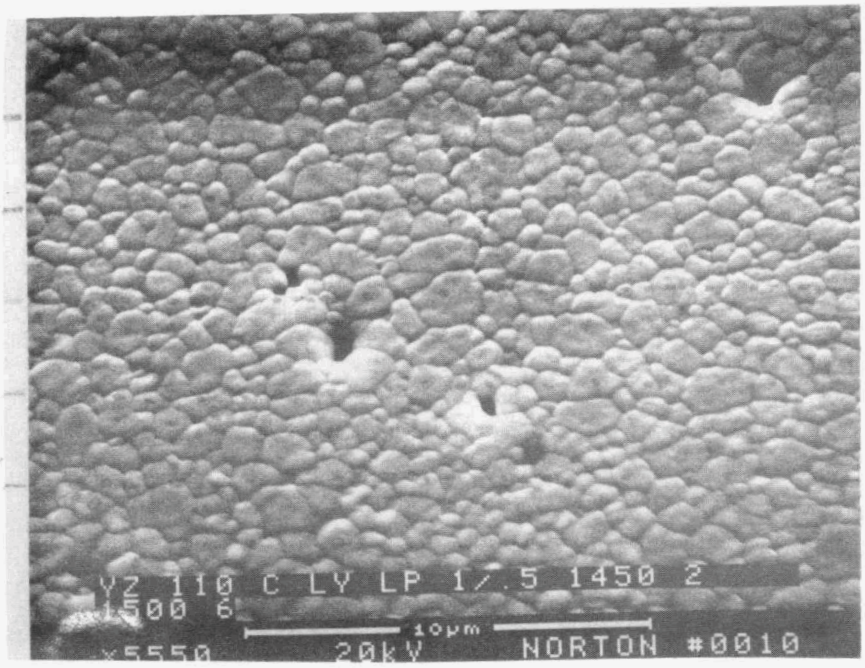

Fig. 8: Microstructure (SEM) of Y-TZP (4 w/o Y_2O_3) ceramic after aging at 1500°C/6 hrs.

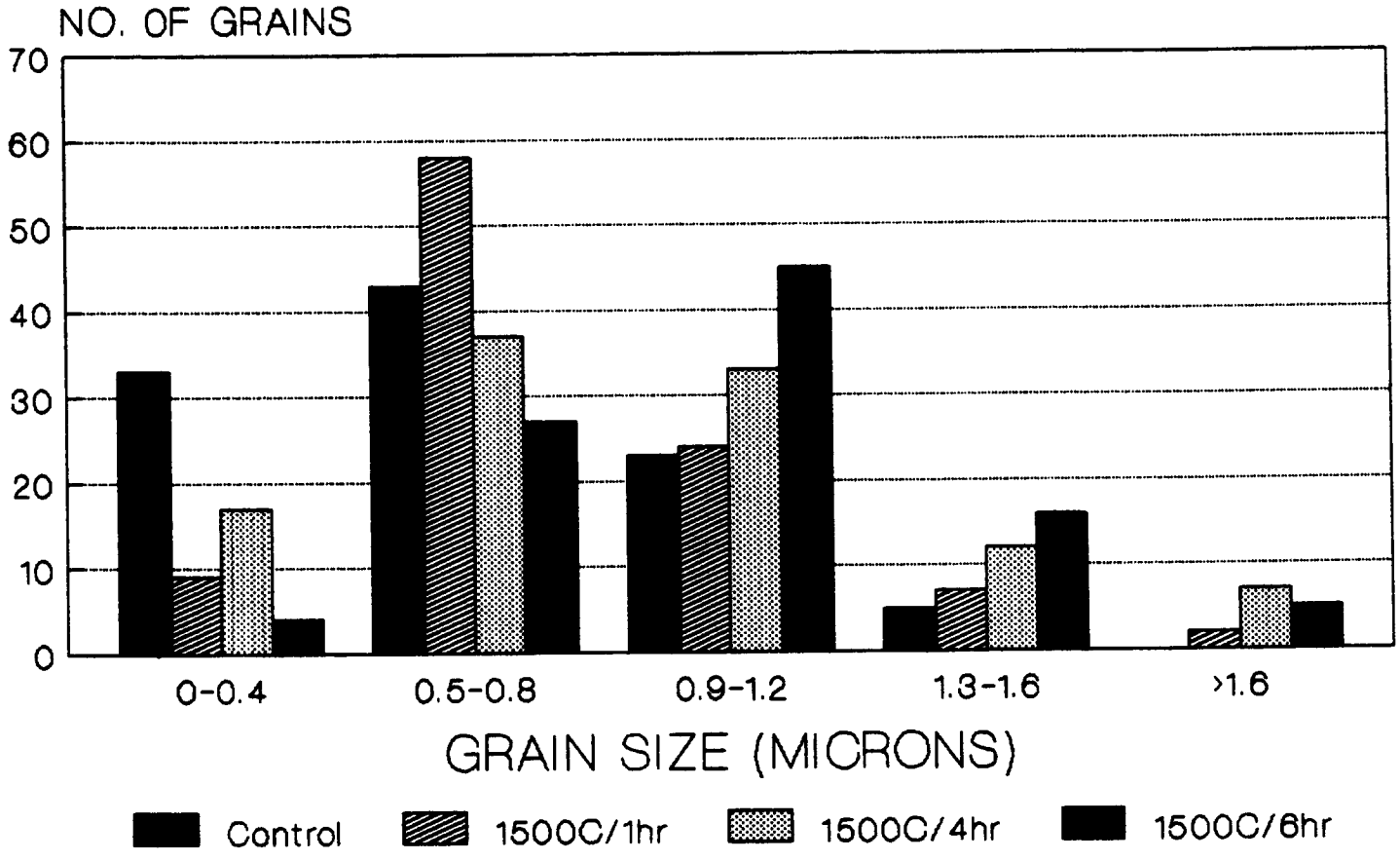

Fig. 9: Hystograms showing grain size distributions for samples shown in Figs. 5, 6, 7, and 8.

Sol-Gel Oxide Powder

W. D. Bond, P. F. Becher, and T. N. Tiegs (Oak Ridge National Laboratory)

Objective/scope

Sol-gel processes have can potentially synthesize materials that can be processed at modest temperatures; simultaneously, highly uniform composition is obtained in dense, fine-grain ceramics which incorporate dispersed second phases to increase fracture toughness. This research emphasizes the determination of the feasibility of sol-gel processes for (1) synthesizing powders of phase-stabilized zirconia and alumina and (2) synthesis of Al_2O_3-SiO_2 gels for conversion to mullite ($3Al_2O_3 \cdot 2SiO_2$) by reaction sinstering. Sol-gel processes take advantage of the high degree of homogeneity that can be achieved by mixing on the colloidal scale and by the surface properties of the colloidal particles. The excellent bonding and sintering properties of colloids are a result of their very high specific surface energy.

Technical progress

Our investigations continued to emphasize the effects of the sol-gel process liquid (water vs ethanol) on particle agglomeration in alumina-zirconia and in alumina-silica powders. The powder particles are less tightly agglomerated when the mixed oxide sols (Al_2O_3-ZrO_2 or Al_2O_3-SiO_2) were chemically gelled in water-ethanol solutions and then washed in dry ethanol. Typical tap densities of calcined powders (600°C) derived from aqueous and from ethanol processing routes are given in Table 1. Processing in ethanol significantly reduces the tap density of powders. In addition, the gel powders prepared by ethanol processing were visibly more fluffy and were crushed more easily than the gels obtained from aqueous sol-gel processing.

Studies of the properties of Al_2O_3-SiO_2 sols were also continued. Transmission electron microscopy investigations show the Al_2O_3 and SiO_2 colloids are well mixed (10 nm scale). The sols have a reasonable stability over the pH range 3.5 to 8.5 but are most stable at pH values 3.5 to 4.5.

Table 1. Tap densities of calcined powders derived from sol-gel processing with water and with ethanol

Powder	Tap density, g/cm³	
	Water processing	Ethanol processing
$Al_2O_3 \cdot 20$ vol % ZrO_2	0.51	0.36
$3\ Al_2O_3 \cdot 2\ SiO_2$	0.59	0.32
ZrO_2	1.30	0.56

We also initiated work on the preparation of ZrO_2-NiO gel powders which are to be used in the basic studies on the ZrO_2NiO phase diagram. The gel powders were prepared from hydrosols of the mixed oxides. Nickel oxide sols were prepared by a precipitation-peptization method and then blended with ZrO_2 sol that was prepared by hydrothermal reaction at 200°C. Gel powders containing 7, 10, and 16 mol % NiO in zirconia were prepared.

Status of milestones

Work on Al_2O_3-SiO_2 gel powder synthesis variables (Milestone 12 33 04) was completed.

Publications

None

Processing and Characterization of Transformation-Toughened Ceramics with Strength Retention to Elevated Temperatures

R. A. Cutler, J. J. Hansen, D. W. Prouse (Ceramatec, Inc.) A. V. Virkar and D. K. Shetty (University of Utah).

Objective/Scope

Previous work[1] has shown that it is possible to increase the strength of Al_2O_3-ZrO_2 ceramics by incorporating transformation-induced residual stresses in sintered specimens consisting of three layers. The outer layers contained Al_2O_3 and unstabilized ZrO_2, while the central layer contained Al_2O_3 and partially stabilized ZrO_2. When cooled from the sintering temperature, some of the zirconia in the outer layers transformed to the monoclinic form while zirconia in the central layer was retained in the tetragonal polymorph. The transformation of zirconia in the outer layers led to the establishment of surface compressive stresses and balancing tensile stresses in the bulk. In theory, the residual stresses will not decrease with temperature until the monoclinic to tetragonal transformation temperature is reached since monoclinic and tetragonal ZrO_2 polymorphs have nearly the same coefficients of thermal expansion. The demonstration of the retention of residual stresses with temperature is a primary purpose of this project.

Previous work was accomplished using dry pressing techniques. The development of slip casting technology for layered composites will allow for better dispersion of zirconia in alumina and thereby facilitate higher volume monoclinic ZrO_2 in outer layers without strength degrading microcracking. A comparison between slip casting and dry pressing techniques will be made to identify higher strength materials for more detailed characterization during the second year of the project.

Technical Highlights

Indentation/Strength Measurements

Three layer composites with compressive residual stresses extending approximately 375 microns into the surface[2,3] were shown to display superior damage resistance to monolithic ceramics[4]. Improved damage resistance would aid in cylinder liners where contact damage can create substantial surface flaws. The indentation/strength[3] behavior of three layer composites were compared to monolithic ceramics to determine if the three layer Al_2O_3-ZrO_2 ceramics would retain their improved strength under severe contact damage conditions.

Polycrystalline alumina, Al_2O_3-15 vol. % ZrO_2, and a three layer composite (outer layer thickness of 375 microns) that consisted of two outer layers of the same

composition as the above monolithic Al_2O_3-ZrO_2 ceramic and an inner layer of Al_2O_3-15 vol. % ZrO_2 (with 2.6 mole % Y_2O_3 additive) were fabricated into test bars (4.5 x 5 x 50 mm) as described previously[2,3]. The sintered bars were chamfered and then isostatically hot pressed (HIPped) at 1525°C for 30 minutes with 200 MPa Ar over pressure. The sintered and HIPped specimens had densities greater than 99.8 % of theoretical. Specimens for indentation and strength testing were used in the as-sintered and HIPped condition. A Vickers diamond pyramid indenter with an apex angle of 136° was attached to a universal testing machine. The specimens were indented at constant cross head speed (0.5 mm/minute) to the selected maximum load and immediately unloaded at the same cross head speed. A drop of dry mineral oil was placed at the site of the indentation prior to loading to minimize post-indentation subcritical crack growth from moisture. Selected specimens were tested using a drop of a saturated lead acetate solution[5] instead of the mineral oil. The lead acetate penetrated the crack and it could be used to assess crack size and shape by SEM fractography. Strengths of the indented specimens were assessed in four-point bending (40 mm support span and 20 mm loading span).

When a stress-free monolithic ceramic is indented with a Vickers indenter, the radius, c_o, of the half-penny surface crack generated by the indentation satisfies the following equilibrium relation[6]:

$$c_o = \{\delta(E/H)^{1/2}P/K_{Ic}\}^{2/3} \qquad (1)$$

where δ is a nondimensional constant dependent on the indenter geometry, E is elastic modulus, P is indentation load, K_{Ic} is fracture toughness, and H is indentation hardness. Anstis et al.[7] have determined a value of 0.016 for δ based on calibration of the indentation load/crack length parameter, $Pc_o^{-3/2}$, relative to known properties, K_{Ic}, E, and H of a number of ceramics.

Upon application of a tensile stress, σ, to a monolithic ceramic with an indentation flaw, the half-penny crack grows stably under equilibrium according to the following equation:

$$K_{Ic} = \delta(E/H)^{1/2}(P/c^{3/2}) + \Omega(2/\pi^{1/2})\sigma c^{1/2} \qquad (2)$$

where Ω is a free surface correction factor for the stress intensity[7]. The crack length, c_m, at instability (i.e.. $d\sigma/dc = 0$ and $d\sigma^2/dc^2 < 0$) is given by

$$c_m = \{4\delta(E/H)^{1/2}P/K_{Ic}\}^{2/3} \qquad (3)$$

When a three layer composite ceramic is indented at the same load P, if the resulting indentation flaw (assumed to be half-penny shaped) is contained well within

the outer layer of uniform compressive stress, σ_c, the equilibrium condition for crack growth is given by:

$$K_{Ic} = \delta(E/H)^{1/2}(P/c^{3/2}) + \Omega(2/\pi^{1/2})\sigma c^{1/2} - \Omega(2/\pi^{1/2})\sigma_c c^{1/2} \quad (4)$$

Applying the conditions for instability, the crack length at instability is again given by Equation (3). Simple indentation fracture mechanics, therefore, predicts that while the initial (after indentation) crack length of the three layer composite will be less than the corresponding monolithic specimen with no residual stress, the crack length at the time of fracture will be identical in both cases. The analysis does, however, predict an enhanced strength due to the compressive residual stress. The fracture stress, σ_f, for the three layer specimens is given by

$$\sigma_f = [CK_{Ic}^{4/3}/(E/H)^{1/6}P^{1/3}] - \sigma_c \quad (5)$$

where C is a constant that combines all the nondimensional parameters and was found to be equal to 2.02 by Chantikul et al.[6].

A number of indentation/strength tests were performed on monolithic and three layer specimens to examine the predictions of Equation (5). Figures 1 and 2 show fracture stresses of the three layer Al_2O_3-15 vol. % ZrO_2, monolithic Al_2O_3-15 vol. ZrO_2 (outer layer material) and monolithic Al_2O_3 plotted as functions of P and $P^{-1/3}$. A plot of σ_f versus $P^{-1/3}$ should yield a linear relationship where the intercept gives the residual stress and the slope can be used to determine K_{Ic}. Figure 2 shows such plots for alumina, outer layer monolithic Al_2O_3-15ZrO_2, and three layer Al_2O_3-15ZrO_2 composite specimens . The monolithic specimens gave linear plots of σ_f vs $P^{-1/3}$ in agreement with Equation (5). Linear regression of the data gave slopes corresponding to K_{Ic} values of 3.79 and 4.53 MPa·m$^{1/2}$ for alpha alumina and Al_2O_3-15 vol. % ZrO_2 monolithic specimens, respectively. Both monolithic materials had intercepts near zero, showing that they were free of residual stresses. Monolithic specimens of the inner layer Al_2O_3-15ZrO_2 (2.6 mole % Y_2O_3) showed identical indentation response as the outer layer material[8].

In contrast to the monolithic specimens where all of the specimens failed from the indent, three layer specimens indented at low loads often failed from other surface flaws. Only those three layer specimens which fractured through the indent are included in Figure 2. At low loads it was not always possible to be sure that the indent was the cause of failure due to the number of fragments at the initiation location. Figure 2 clearly shows that the three layer composites retain their strength superiority, as compared to the monolithic outer layer, at all loads. Due to the nature of the test (i.e., using

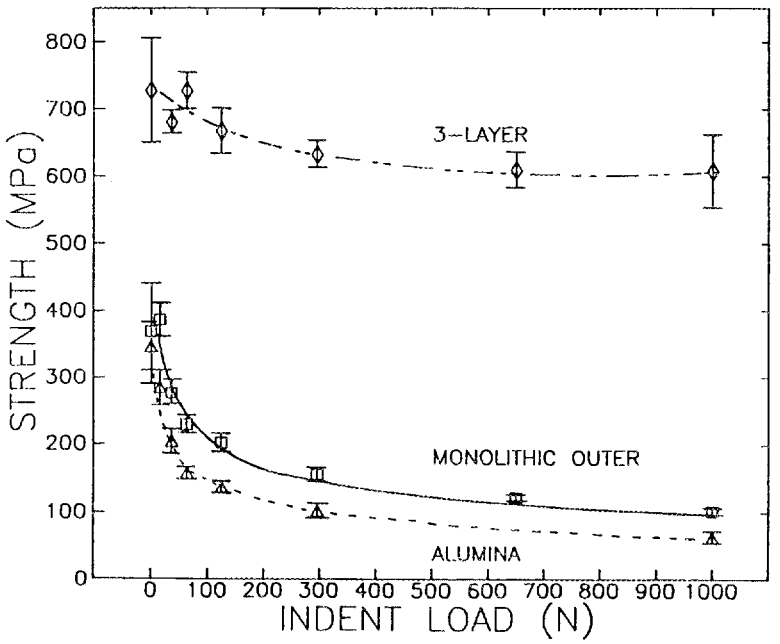

Figure 1. Indentation load dependence of fracture stresses for alumina as well as monolithic and three layer Al_2O_3-15ZrO_2 ceramics.

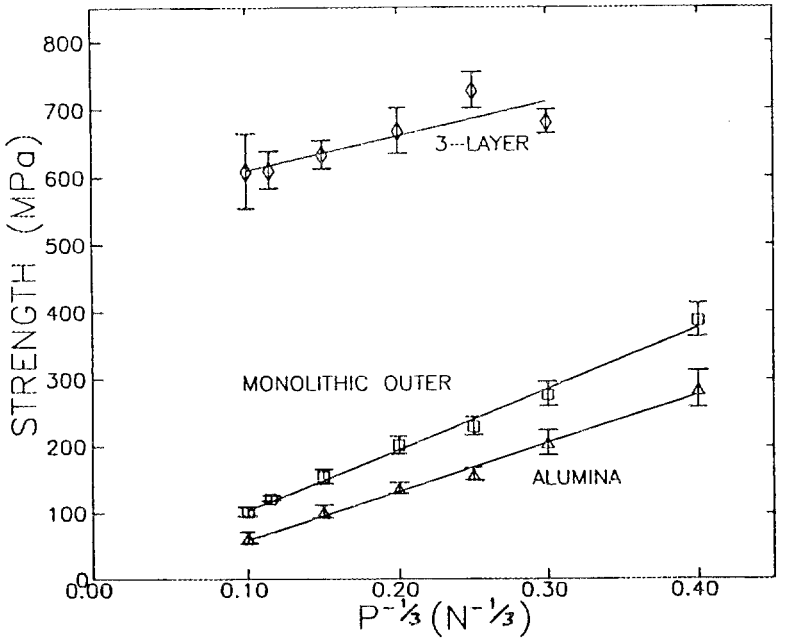

Figure 2. Fracture stress vs. inverse cube root load plots of data in Figure 1 above.

unpolished specimens) and the subsequent uncertainty regarding the fracture origins, it is not possible to draw conclusions with respect to the shallower slope (i.e., apparently superior strength response) of the three layer specimens. The intercept of the three layer specimens is approximately 550 MPa, which is higher than the 400 MPa measured by strength testing but is consistent with the residual strength calculated using strain gage and x-ray techniques[2,3].

Scanning electron micrographs of fracture surfaces of monolithic and three layer Al_2O_3-15 vol. % ZrO_2 specimens indented at 1000N prior to strength testing are shown in Figure 3 using both secondary electron and back scattered imaging modes. The lead marking the cracks created during indentation is clearly visible in the back scattering mode (see Figure 3). The monolithic inner material (Figure 3(a)) shows a half penny shaped crack approximately 825 microns in length, c. The monolithic outer layer material (Figure 3(b)) shows two radial cracks (c approximately 850 microns) which have joined during crack extension. The initial depth of the cracks is approximately 415 microns. The three layer composite (Figure 3(c)) has much shallower cracks (crack depth of approximately 100 microns). Higher magnification photos (Figures 3(d) and 3(e)) clearly show Palmqvist cracks (c of approximately 110 microns) extending approximately 100 microns in depth. Lateral cracks parallel to the surface (approximately 100 microns below the surface) extending over a millimeter in length are visible in the three layer composites. The Palmqvist cracks do not extend below the lateral cracks. Further work is needed to see if lateral cracks develop during wear or erosion.

These tests clearly show that three layer composites have damage resistance equal to or superior to their residual stress when indented at loads up to 1000N. This should allow them to show superior resistance to contact damage in applications such as cylinder liners.

Characterization of Three Layer Composites

In previous analyses[1-3], it was assumed that the residual compressive stress in three layer composites is given by

$$\sigma_c = -d_2 E \Delta\varepsilon_o / d(1-\nu) \qquad (6)$$

where d_2 is the thickness of the inner layer, d is the total thickness of the bar, $\Delta\varepsilon_o$ is the free expansion of the outer layers per unit length when they are not constrained by the inner layer, and ν is Poisson's ratio. The term $(1-\nu)$ is due to the assumed equibiaxial state of stress and strain parallel to the layers. This assumption was checked by mounting strain gauges parallel (longitudinal direction) and perpendicular (transverse direction) to

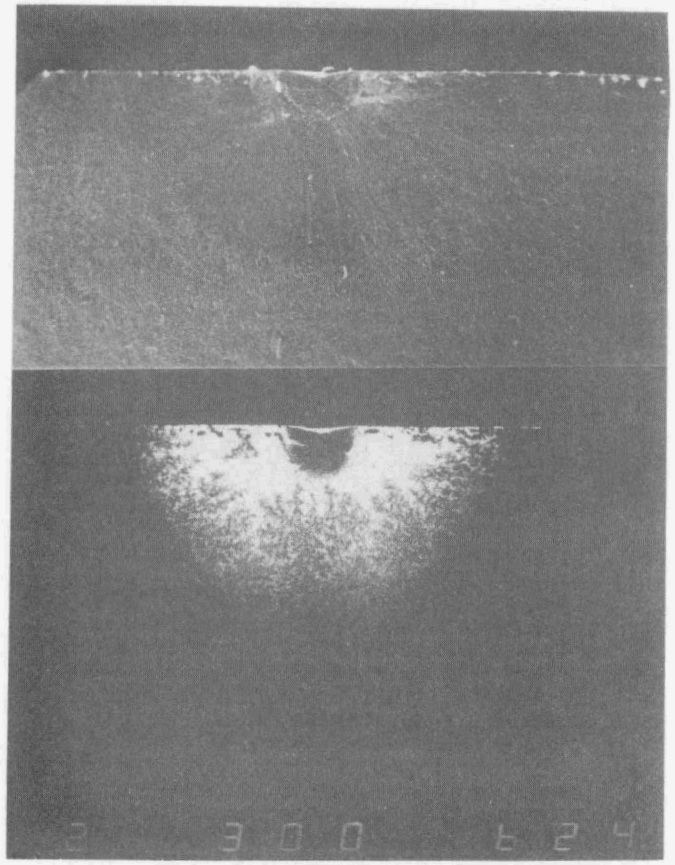

(a)

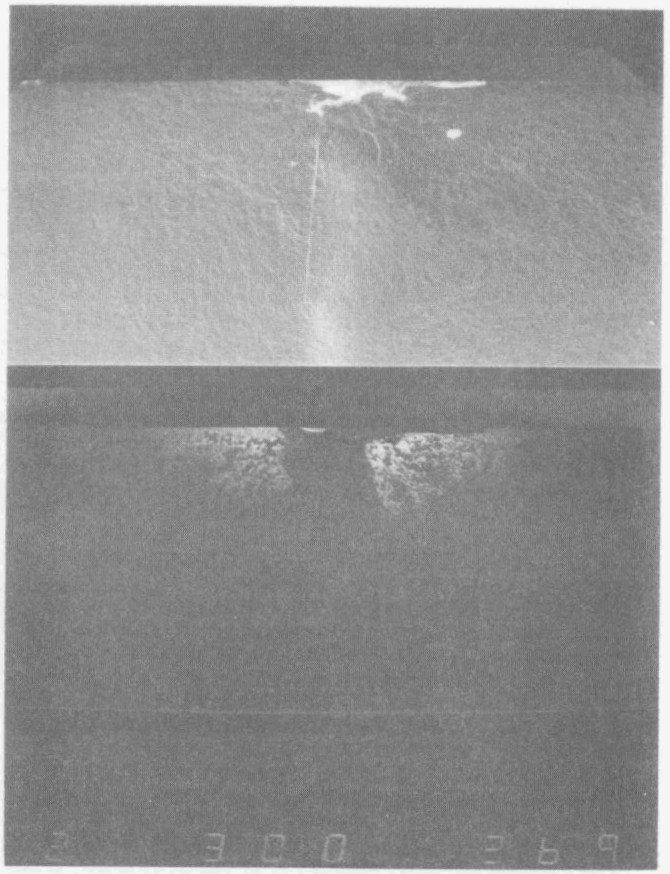

(b)

Figure 3: Scanning electron micrographs of fracture surfaces of Al_2O_3-$15ZrO_2$ bars indented at 1000N using lead acetate to show indentation cracks[5]. Secondary electron and back scattered imaging were used for top and bottom photos, respectively, in each micrograph. (a) Inner layer material showing half penny crack approximately 825 microns (30X), (b) Outer layer material showing radial cracks which have joined after crack extension (30X).

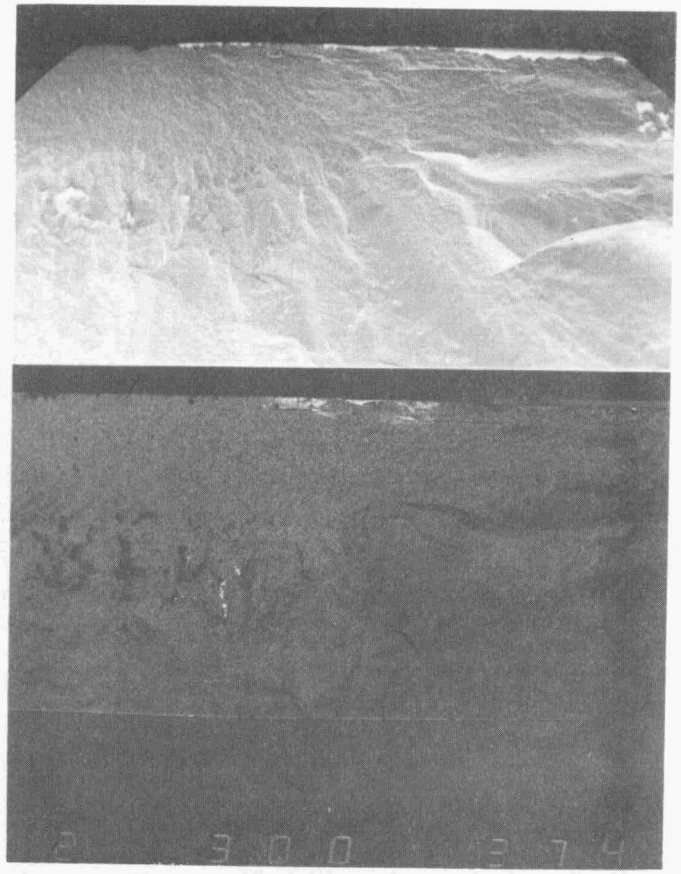

(c)

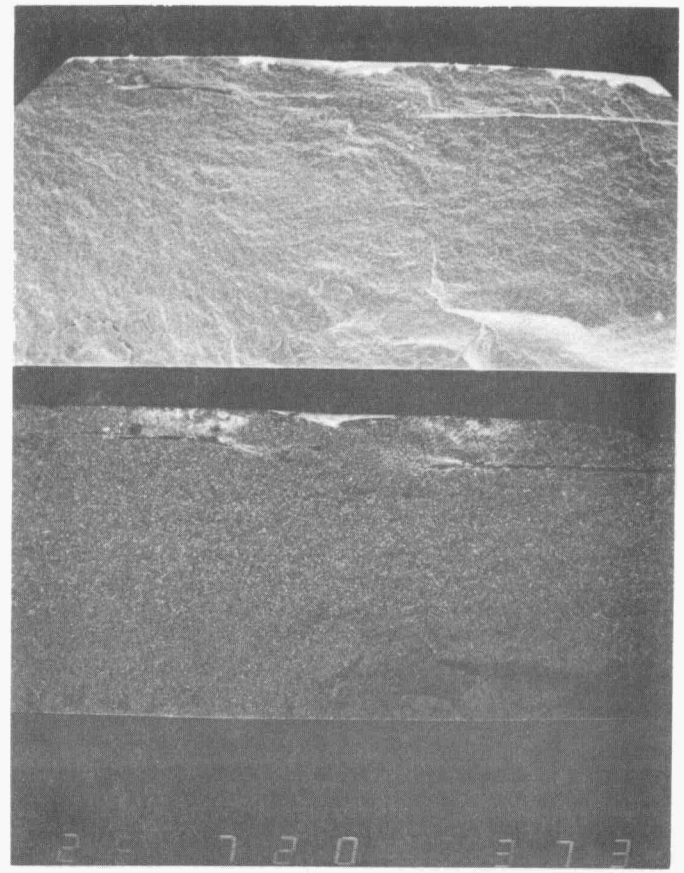

(d)

Figure 3 (continued): (c) Three layer composite showing Palmqvist cracks extending approximately 100 microns in depth, as well as lateral cracks (30X), (d) Same as Figure 3(c) except higher magnification (72X).

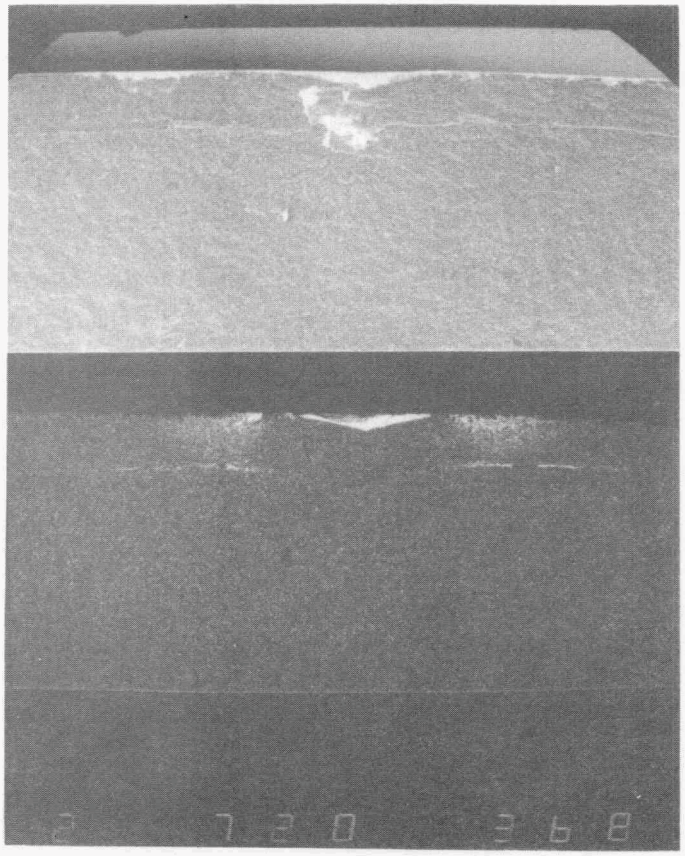

Figure 3 (continued). (e). A second three layer composite (compare with Figure 3(d) clearly showing Palmqvist cracks and lateral cracks (parallel to tensile surface) (72X).

the long axis of a strength bar and determining strain by preferentially removing the outer layer on the side opposite the strain gage, as reported previously[1-3]. These data showed increasing strain with increasing outer layer depth removed for the strain gages mounted parallel and orthogonal to the long axis of the strength bar (see Figure 4). Both gages showed a distinct slope change at the interface as explained by Virkar et al.[9]. The transverse gauge measured up to 20% less strain than the longitudinal gage. When the same experiment was conducted for a square geometry, both gages showed identical strain behavior (see Figure 5), as expected. The implication of these experiments is that the assumption of equibiaxial strain is a good assumption even for strength bars.

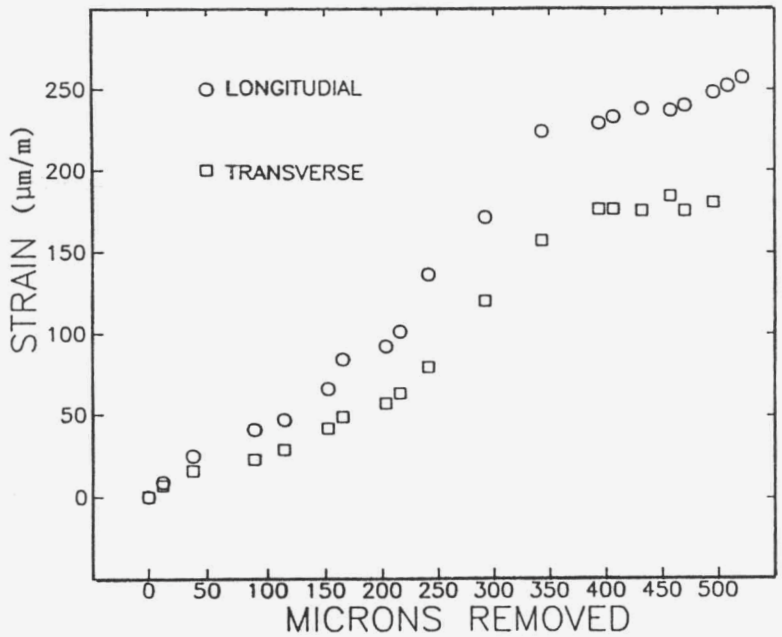

Figure 4. Measured strain as a function of outer layer thickness removed for strain gages placed parallel and perpendicular to length of Al_2O_3-$15ZrO_2$ three-layer strength bar.

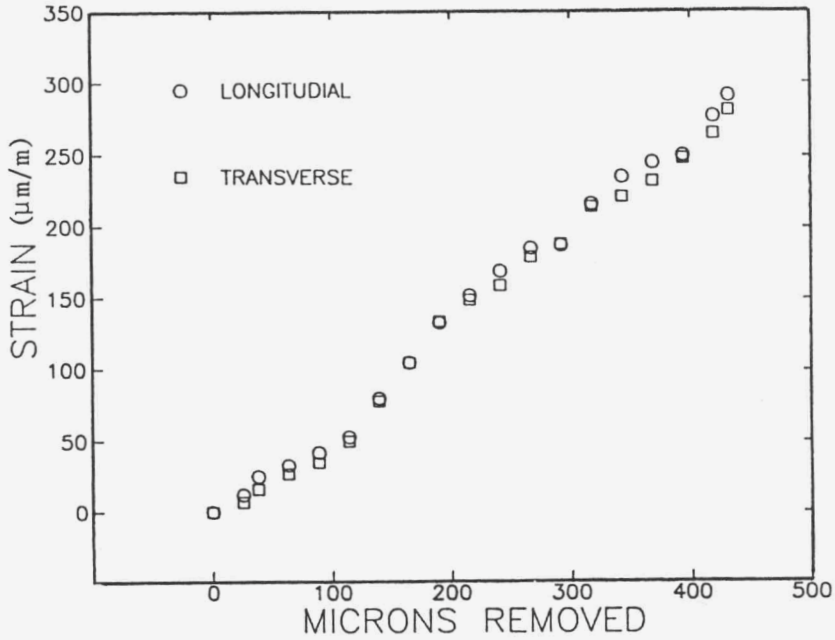

Figure 5. Measured strain as a function of outer layer thickness removed for orthogonal strain gages placed in center of top layer of Al_2O_3-$15ZrO_2$ three-layer square.

Previous work on three layer composites has assumed equal Young's modulus for inner and outer layers. This was verified by mounting strain gages on monolithic inner and outer layer specimens and testing in bending. Young's modulus was 348 GPa for the outer layer and 370 GPa for the inner layer bars. These values are in good agreement with the value of 365 GPa previously assumed[2].

Improved Processing

Monolithic and three layer Al_2O_3-20 vol. % HfO_2 and Al_2O_3-20 vol. % $HfO_2 \cdot 50ZrO_2$ composites were fabricated using HfO_2 and $ZrO_2 \cdot HfO_2$ powders (with and without 3 mole % Y_2O_3) supplied by Teledyne Wah Chang Albany. Powder processing and sintering conditions were identical to those reported for Al_2O_3-15 vol. % ZrO_2 three layer composites[2]. The reason for substituting HfO_2 for ZrO_2 was to increase the monoclinic to tetragonal transformation temperature since previous results for three layer Al_2O_3-15ZrO_2 composites suggested that this transformation was the main reason for the strength degradation observed as a function of temperature in layered composites[2]. Three layer composites were also made using HfO_2 and $HfO_2 \cdot ZrO_2$ powders for the outer layers and 15 vol. % ZrO_2 in the central layer.

The densities of all sintered and HIPped monolithic and three layer composites were greater than 98% of theoretical. The ZrO_2, $HfO_2 \cdot ZrO_2$ or HfO_2 in the inner layers were always 100% tetragonal as identified by x-ray diffraction. HfO_2 in the outer layers was 98.3 to 100 % monoclinic and $HfO_2 \cdot ZrO_2$ was 95.4 to 97.3% monoclinic. Strengths for monolithic inner and outer Al_2O_3-20 vol. % HfO_2 and Al_2O_3-20 vol. % $HfO_2 \cdot ZrO_2$ specimens varied between 312 and 366 MPa. There was no indication that the inner material was stronger than the outer layer monolithic composite. This is in contrast to monolithic inner and outer Al_2O_3-15 vol. % ZrO_2 specimens which have typical strengths of 550 and 450 MPa, respectively. For three layer composites where HfO_2 (or HfO_2-ZrO_2) was used in the outer layer and ZrO_2 in the inner layer, the strengths increased 230 to 290 MPa as compared to the monolithic outer materials, to give strengths of approximately 600 MPa. When the inner material contained partially stabilized HfO_2 (or $HfO_2 \cdot ZrO_2$) the strengths of three layer composites only increased 50-80 MPa as compared to the monolithic materials. Thermal expansion measurements will be made to explain these differences. Elevated temperature testing of Al_2O_3-20HfO_2 three layer composites containing Al_2O_3-15ZrO_2 in the inner layer had a mean strength of 325 MPa at 1000°C. This elevated temperature strength was only 50 MPa higher than the monolithic outer layer specimens. It is believed that microcracking in the outer layers is contributing to the poor strength of the bars made

using HfO_2, although cracks were not obvious on fracture surfaces based on scanning electron microscopy. Future experiments will use finer HfO_2 at lower volume fractions to limit particle coarsening during sintering. Although the preliminary results for hafnia substitutions for zirconia do not show any improvement over current three layer composites, this is a sound approach for improving high temperature strength.

A substantial effort was also devoted to slip casting Al_2O_3-15 vol. % zirconia composites since previous results had shown that strengths greater than 1 GPa were attained for three layer composites made using this technique[4]. Previous slip casting was hindered by plates cracking during drying after removal of parts from the plaster mold. Dispersants investigated included nitric acid at pH between 2.5 and 4.0[10], sodium hexametaphosphate at 0.3 wt. % (based on total solids) and an ammonium polyelectrolyte at 0.5%. With the addition of 0.35 to 0.5 % binder it was possible to obtain uncracked sintered plates using either HNO_3 or sodium hexametaphosphate. Sintered densities of monolithic or three layer plates, however, were below 94% of theoretical when using these dispersants. The ammonium polyelectrolyte dispersant gives high sintered densities but water removal without cracking is difficult for three layer composites. It is believed that high strength slip cast bodies can be obtained by further characterizing the rheology of the individual slips and by varying drying procedures. Further efforts in this direction are underway.

Status of Milestones

On schedule

Publication

A paper entitled "Measurement of Residual Stresses in Oxide-ZrO_2 Three Layer Composites" by A. V. Virkar, J. F. Jue, J. J. Hansen and R. A. Cutler was accepted by the Am. Ceram. Soc. for publication. This work was partially supported by the present contract.

References

1. A. V. Virkar, J. L. Huang, and R. A. Cutler, "Strengthening of Oxide Ceramics by Transformation Induced Stresses," J. Am. Ceram. Soc.. 70[3] 164-170(1987).

2. R. A. Cutler, J. J. Hansen, A. V. Virkar, D. K. Shetty, and R. C. Winterton, "Strength Improvement in Transformation Toughened Ceramics Using Compressive Residual Surface Stresses," Advanced Structural Ceramics, Vol. 78, ed. by P. F. Becher, M. V. Swain, and S. Somiya (Materials Research Society, Pittsburgh, PA, 155-163, 1987).

3. R. A. Cutler, J. D. Bright, A. V. Virkar and D. K. Shetty, "Strength Improvement in Transformation Toughened Alumina by Selective Phase Transformation," J. Am. Ceram. Soc., 70 10 (1987).

4. R. A. Cutler, J. J. Hansen, D. W. Prouse, A. V. Virkar, and D. K. Shetty, "Processing and Characterization of Transformation Toughened Ceramics with Strength Retention to Elevated Temperatures," in Ceramic Technology for Advanced Heat Engines Project Semiannual Technical Progress Report (Oct. 1986-Mar. 1987), Oak Ridge National Laboratory, Oak Ridge, Tenn.

5. S. L. Jones, C. J. Norman and R. Shahani, "Crack-Profile Shapes Formed Under a Vickers Indent Pyramid," J. Mater. Sci. Letters, 6 721-723 (1987).

6. B. R. Lawn, A. G. Evans and D. B. Marshall, "Elastic/Plastic Indentation Damage in Ceramics: The Median/Radial Crack System," J. Am. Ceram. Soc.. 63[9-10] 574-581 (1981).

7. P. Chantikul, G. R. Anstis, B. R. Lawn and D. B. Marshall, "A Critical Evaluation of Indentation Techniques for Measuring Fracture Toughness: II, Strength Method," J. Am. Ceram. Soc., 64[9] 539-543(1981).

8. R. A. Cutler, J. J. Hansen, A. V. Virkar, and D. K. Shetty, "Processing and Characterization of Transformation Toughened Ceramics with Strength Retention to Elevated Temperatures," in Ceramic Technology for Advanced Heat Engines Project Bimonthly Technical Progress Report (June-July 1987), Oak Ridge National Laboratory, Oak Ridge, Tenn.

9. A. V. Virkar, J. F. Jue, J. J. Hansen and R. A. Cutler, "Measurement of Residual Stresses in Oxide-ZrO_2 Three Layer Composites," to appear in Communications of the Am. Ceram. Soc.

10. S. Baik, A. Bleir and B. F. Becher, "Preparation of Al_2O_3-ZrO_2 Composites by Adjustment of Surface Chemical Behavior," Better Ceramics Through Chemistry II ed. by C. J. Brinker, D. E. Clark and D. R. Ulrich, (MRS, Pittsburgh, PA 1986).

Injection Molded Composites

M. A. Janney (Oak Ridge National Laboratory)

Objective/scope

The goals of this activity are twofold: (1) to evaluate the ability of advanced ceramic-ceramic composites to be injection molded and processed using standard wax- and/or polymer-based binder systems; and (2) to develop advanced complex-shape-forming technologies that will eliminate some of the problems associated with wax- and polymer-based binder systems such as long binder removal times, cracking, and low green strength.

Technical progress

Work during this period has focused on the development of a new advanced forming technique that would be a replacement for wax- or polymer-based injection molding. Such a process has been developed and complex parts have been formed using the process. However, because of patent considerations, we cannot at this time disclose the nature of the process or any of its particular embodiments.

1.2.4 Silicate Matrix

Low Expansion Ceramics for Diesel Engine Applications

J. J. Brown, R. E. Swanson (VPI & SU), and F. A. Hummel (Consultant)

Objective/scope

The major objective of this research is to investigate selected oxide systems for the development of a low expansion, high thermal shock resistant ceramic. Specifically, it is the goal of this study to develop an isotropic, ultra-low expansion ceramic which can be used above 1200°C and which is relatively inexpensive.

Technical progress

This research program includes the synthesis, property characterization, and fabrication of candidate low thermal expansion ceramics from four systems based upon aluminum phosphate, silica, mullite, and zircon. In the first two systems, the goal is to stabilize low thermal expansion, high temperature, high crystal symmetry phases via solid solution formation. In mullite, deviation from stoichiometry and solid solution formation are utilized to reduce the thermal expansion. In zircon, the crystal anisotropy and thermal expansion are reduced via solid solution formation. Based upon earlier data of the investigators, compositional ranges are evaluated by fabricating experimental specimens and determining phase content plus microstructure, thermal expansion, solidus temperature, and density. Those compositions which exhibit acceptable sintering, phase composition, and expansion characteristics are studied in more detail, including flexure strength, creep, thermal conductivity, and crystal structure. Finally, those ceramic compositions exhibiting the best combination of properties are evaluated as to their fabrication behavior in the form of specimens having masses up to about 0.5 kg.

Aluminum Phosphate System

Three materials, $AlPO_4$, BPO_4, and β-eucryptite ($Li_2O \cdot Al_2O_3 \cdot 2SiO_2$), have been targeted as comprising a system that has potential for ultra-low expansion. β-eucryptite is of interest in that it has an overall negative coefficient of thermal expansion up to 1000°C.[1] Work has previously been conducted with β-eucryptite to bring its coefficient nearer to zero. Increasing the SiO_2 content as a solid solution in β-eucryptite was successful in bringing the coefficient closer to zero.[2]

Experimental

The starting materials for β-eucryptite synthesis are lithium carbonate (Li_2CO_3), aluminum hydroxide [$Al(OH)_3 \cdot nH_2O$], and silica gel (SiO_2), weighed to give a ratio of 1:1:2 $Li_2O/Al_2O_3/SiO_2$ after weight loss. The raw materials are calcined at 200°C for 24h before weighing and mixed under acetone using a mortar and pestle. The samples of β-$LiAlSiO_4$ are fired at 800°C for 48h, reground and mixed dry with a mortar and pestle, and fired at 1800°C in an alumina crucible for 48-72h. X-ray diffraction (XRD) analyses indicate that this heat treatment gives a material which contains small amounts of impurities.

The starting materials used in preparing $AlPO_4$ are aluminum hydroxide and dibasic ammonium phosphate [$(NH_4)_2HPO_4$], weighed to give a 1:1 Al_2O_3 to P_2O_5 ratio after weight loss. The raw materials for each batch are mixed under acetone using a mortar and pestle, and fired in alumina crucibles at 175°C for 2h and 400°C for 12h. After regrinding and mixing dry with a mortar and pestle, the samples are fired at 1080-1100°C for 48-72h. XRD analysis confirms that this heat treatment consistently gives $AlPO_4$.

BPO_4 is prepared from boric acid (H_3BO_3) and dibasic ammonium phosphate, weighed to give a B_2O_3 to P_2O_5 ratio 1:1 after weight loss, and processed as described for $AlPO_4$.

Bar samples used in coefficient of thermal expansion (CTE) determinations are pressed in stainless steel dies using distilled water as a binder, and sintered on alumina plates. Bar compositions

and heat treatments are shown in Table 1. XRD analysis and optical microscopy are used to determine phase composition of the samples.

Results and Discussion

Dilatometric analyses of the $AlPO_4$ samples prepared are shown in Figure 1. The CTE values listed in Table 1 are the slopes of straight lines drawn between expansions at room temperature and 1000°C, and are not indicative of linear expansion.

Composition $Li_{0.55}AlP_{0.45}Si_{0.55}O_4$ (YS-1), with a CTE of 1.09 x $10^{-7}/°C$, exhibited the lowest positive thermal expansion. Composition $Li_{0.45}AlP_{0.55}Si_{0.45}O_4$ (YS-2) exhibited low negative expansion. XRD patterns of both samples following thermal expansion measurement indicated that β-$LiAlSiO_4$ solid solution was the major phase present with only small amounts of $AlPO_4$, Al_2O_3, and $Al(PO_3)_3$. The presence of Al_2O_3 in both samples may indicate the incomplete solid reaction and/or the volatilization of P_2O_5, producing a final ratio depleted in $AlPO_4$.

The expansion behavior of sample YS-1 was similar to that of a 50% $AlPO_4$/50% β-eucryptite specimen reported by Hummel and Langensiepen.[3] However, upon refiring sample YS-1 at 1250±30°C for 72h, the bar softened and adhered to the alumina plate. This unexpected phenomenon should be studied further.

Two bar specimens of initial composition $Li_{0.55}AlP_{0.45}Si_{1.5}O_4$ were synthesized using a variation in $AlPO_4$ starting materials. One bar (YS-4) was prepared using Li_2CO_3, Al_2O_3, SiO_2 gel, and $AlPO_4$ synthetized in the lab, whereas the other bar (YS-4) was prepared from Li_2CO_3, Al_2O_3, SiO_2 gel, $Al(OH)_3 \cdot nH_2O$, and $(NH_4)_2HPO_4$. Although the final samples showed similar thermal expansion behavior, XRD patterns indicated more complete phase formation and, therefore, probable increased reactivity in the sample synthesized with aluminum hydroxide plus dibasic ammonium phosphate rather than aluminum phosphate as a starting material.

Adding BPO_4 to the $AlPO_4$- β-eucryptite system resulted in surface melting of bar specimens YS-5 through YS-8 after final firing at

Table 1. $AlPO_4$ sample processing and thermal expansion results

Sample No.	Composition (mol%) $AlPO_4$	BPO_4	β-$LiAlSiO_4$	Heat Treatment*	Raw Materials	Expansion (αx $10^{-7}/^oC$) 25-1000°C
YS-1	45	-	55	1	Li_2CO_3,Al_2O_3,SiO_2 gel, and $AlPO_4$ synthesized in lab	1.09
YS-2	55	-	45	1	Same as YS-1	-2.95
YS-3	45	-	55($LiAlSi_{1.5}O_4$)	2	Same as YS-1	-5.87
YS-4	45	-	55($LiAlSi_{1.5}O_4$)	2	Li_2CO_3,Al_2O_3,SiO_2 gel,$Al(OH)_3 \cdot nH_2O$, $(NH_4)_2HPO_4$	-6.15
YS-5	45	5	50	3	Li_2CO_3,Al_2O_3,SiO_2 gel and $AlPO_4$,BPO_4 synthesized in lab	-10.13
YS-6	45	5	50	3	Li_2CO_3,Al_2O_3,SiO_2 gel, $Al(OH)_3 \cdot nH_2O$, $(NH_4)_2HPO_4$ and BPO_4 synthesized in lab	-9.41
YS-7	50	5	45	3	Same as YS-5	-14.76
YS-8	50	5	45	3	Same as YS-6	-8.65

* Heat treatments: temp/time(°C/h)

1 = 100/1, 400/5, 800/14, 1100/48

2 = 175/3, 400/19, 800/24, 1150/70

3 = 175/11, 400/24, 800/24, 1120/74, 800/10, 400/22

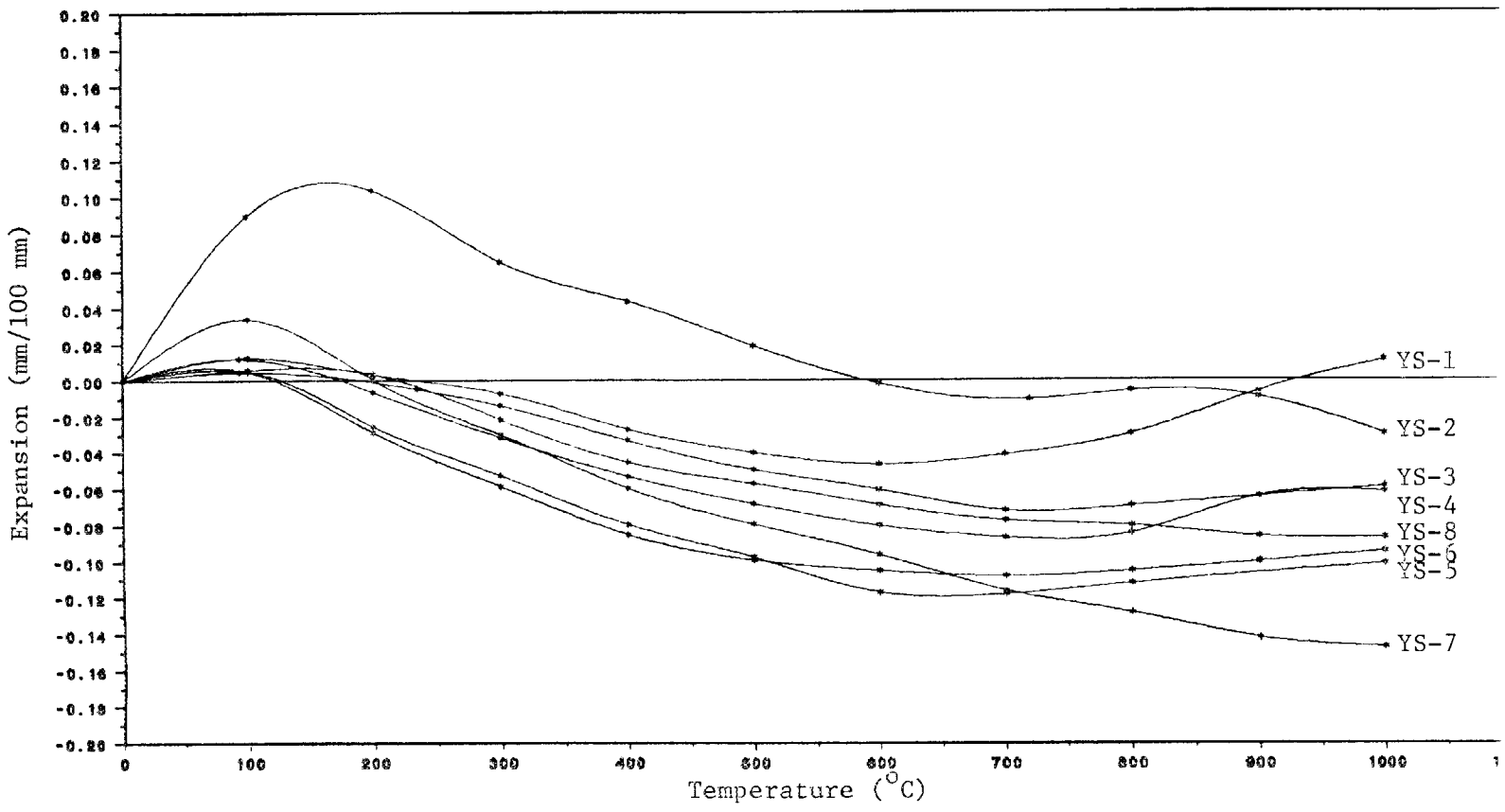

Figure 1. Thermal expansion of $AlPO_4$ samples.

1120°C for 74h. The surface melting was more pronounced in the samples containing 50 mol% β-eucryptite when compared to samples containing 45 mol% β-eucryptite. Microscopic examination of the samples under orthogonal polarized light indicated the presence of glass. This was unexpected considering the melting points of the three constituent materials, i.e., $T_m > 1800°C$ for $AlPO_4$, $T_d = 1400°C$ for β-eucryptite, and $T_m = 1300°C$ for BPO_4.

Further work should concentrate on identifying a $Li_{1-x}AlP_xSi_{1-x}O_4$ single phase solid solution (where x is probably between 0.45-0.70) which will have an expansion near zero between room temperature and 1200°C (or above). Differential thermal analysis (DTA) and other analytical methods should be used to determine the temperature or temperature range at which the systems begin to melt or soften. The effect of BPO_4 on β-eucryptite and $AlPO_4$ solid solution and its thermal expansion should be examined around 1200°C.

Silica System

The ultra-low thermal expansion of the high temperature form of cristobalite (β-cristobalite) has long been recognized. Like most polymorphs of silica, cristobalite also shows a displacive type transformation at low temperatures. Upon transformation, a discontinuous change in expansion curves occurs and a large volume expansion results. Therefore, the potential of β-cristobalite in structural ceramic applications depends on the stabilization of the high cristobalite structure.

The high-low transformation of cristobalite differs from most phase transformations in that (1) nucleation and growth are not involved, (2) the transformation temperature is not fixed, and (3) the amount of the transformed phase is independent of the degree of supercooling. These characteristics can be linked to the commonly observed structural collapse in most framework silicates with open structures.[4-7] For open structures, a metastable low energy configuration can be achieved by adjusting the position of secondary coordination to provide closer packing and to generate new symmetries.

In cristobalite, the high-low transformation can occur over a wide range from 120-272°C with a much higher probabiliy of transformation above 225°C.[8] This can be attributed to both impurity contents and the degree of disorder of the high cristobalite structure. The structure of low cristobalite is well established with a tetragonal symmetry $P4_32_1$.[9] However, the structure of high cristobalite can only be known as an averaged domain structure.[10-12] Each domain cannot extend to more than a few unit cells. Therefore, the high cristobalite structure can be regarded as a variable structure from a unit cell viewpoint with one domain slightly different from the other. Since energy content varies with structural configurations, the variable high-low transformation temperatures are likely to depend on the energy content characteristic of the high cristobalite structure. In fact, it had been found that each individual crystallite crushed from a bulk cristobalite sample has its own characteristic transformation temperature upon heating.[13] Moreover, in single crystal studies of cristobalite, variations in transformation temperature of up to 10°C were found in different positions of the same crystal.[14] The transformation temperature seems to follow a statistical distribution. Both impurities and heat treatment can affect the distribution.

The purpose of this study is to investigate the high-low transformation of cristobalite by forming solid solutions of cristobalite with isostructural compounds and to determine the extent to which the transformation temperature can be lowered. In the present work, phase diagrams are constructed for the high silica portion of the two binary systems SiO_2-$AlPO_4$ and SiO_2-BPO_4. The solubility limits and eutectic temperatures are determined. Transformation parameters including enthalpies and temperatures are also measured.

Experimental

Sample compositions were prepared from silicic acid, $AlPO_4$, and BPO_4. $AlPO_4$ was made by reacting $Al(OH)_3 \cdot nH_2O$ and $(NH_4)_2HPO_4$, and BPO_4 by H_3BO_4 and $(NH_4)_2HPO_4$. XRD examinations of the synthetic

compounds showed pure phases and good crystallinity. Compositions listed in Tables 2 and 3 were mixed and calcined at 1000°C for 2h for those containing $AlPO_4$, and 10h at 800°C for those containing BPO_4. The calcined samples were sealed in platinum tubes and heat-treated at various temperatures for 72h and then quenched in a water bath.

Phases in the reacted samples were identified by XRD and petrographic analyses. The transformation parameters of cristobalite were measured by differential scanning calorimetry (DSC) at a heating rate of 20°C/min. Indium was used as a standard to calibrate the reaction heat and temperature.

Table 2. Composition and heat treatment of the SiO_2-$AlPO_4$ system

Sample No.	Composition (wt%) SiO_2	$AlPO_4$	Heat Treatment Temperature (°C)
TS-26	95	5	1415, 1430, 1450, 1480, 1605, 1620
TS-28	90	5	1415, 1450, 1480, 1605, 1620
TS-29	85	15	1415, 1450, 1480, 1605, 1620
TS-45	82	18	1415, 1450, 1480, 1605, 1620
TS-46	79	21	1415, 1450, 1480, 1605, 1620
TS-51	75	25	1480, 1590, 1650
TS-52	70	30	1480, 1590, 1650
TS-53	60	40	1480, 1590, 1650

Table 3. Composition and heat treatment of the SiO_2-BPO_4 system

Sample No.	Composition (wt%) SiO_2	BPO_4	Heat Treatment Temperature (°C)
TS-47	97	3	940, 970, 980, 1000, 1020
TS-48	93	7	940, 970, 980, 1000, 1020
TS-49	90	10	940, 970, 980, 1000, 1020
TS-32	88	12	940, 980, 1000
TS-50	86	14	940, 980, 1000

Results and Discussion

SiO_2-$AlPO_4$ System. Phase identification for this system was largely based on petrographic and DSC analyses, since XRD patterns for the low cristobalite phase of SiO_2 and $AlPO_4$ are extremely similar. It becomes very difficult to separate these two phases by XRD techniques when only a small amount of $AlPO_4$ is present. Nevertheless, the cristobalite phase of $AlPO_4$ appears to be more discernible by petrographic and DSC analyses. $AlPO_4$ shows a higher relief than SiO_2 cristobalite in petrographic analyses. In addition, the $AlPO_4$ cristobalite has a high-low transformation around 210°C, while the high-low transformation for pure SiO_2 cristobalite is in general above 250°C.

Phase analyses for different compositions at different temperatures are listed in Table 4. Studies are concentrated on the SiO_2 cristobalite solid solution range. For the temperature range studied, the system appears to be a binary eutectic as shown in Figure 2. The solubility limit of $AlPO_4$ in SiO_2 is approximately 15% at 1605°C. Results from other studies showed the eutectic temperature to be at about 1420°C.[15] However, samples from the present study require temperatures in excess of 1480°C to initiate sintering.

Small particle size and low birefringence of SiO_2 cristobalite can sometimes lead to errors in examining glassy phases. Compositions TS-51, T-52, and T-53 are mainly used to check the eutectic temperature, although their $AlPO_4$ content is far beyond the solid solution range.

Table 4. Phase analyses of the SiO_2-$AlPO_4$ system

Sample No.	Temperature (°C)	Phase Present
TS-26	1415	α-cristobalite(ss)
	1450	α-cristobalite(ss)
	1480	α-cristobalite(ss)
	1605	α-cristobalite(ss)
	1620	α-cristobalite(ss)
TS-28	1415	α-cristobalite(ss), $AlPO_4$(ss)
	1450	α-cristobalite(ss), $AlPO_4$(ss)(trace)
	1480	α-cristobalite(ss)
	1605	α-cristobalite(ss)
	1620	α-cristobalite(ss), glass (trace)
TS-29	1415	α-cristobalite(ss), $AlPO_4$(ss)
	1450	α-cristobalite(ss), $AlPO_4$(ss)
	1480	α-cristobalite(ss), $AlPO_4$(ss)
	1605	α-cristobalite(ss)
	1620	α-cristobalite(ss), glass
TS-45	1415	α-cristobalite(ss), $AlPO_4$(ss)
	1450	α-cristobalite(ss), $AlPO_4$(ss)
	1480	α-cristobalite(ss), $AlPO_4$(ss)
	1605	α-cristobalite(ss), glass
	1620	α-cristobalite(ss), glass
TS-46	1415	α-cristobalite(ss), $AlPO_4$(ss)
	1450	α-cristobalite(ss), $AlPO_4$(ss)
	1480	α-cristobalite(ss), $AlPO_4$(ss)
	1605	α-cristobalite(ss), glass
	1620	α-cristobalite(ss), glass
TS-51	1480	α-cristobalite(ss), $AlPO_4$(ss)
	1590	α-cristobalite(ss), $AlPO_4$(ss)
	1650	α-cristobalite(ss)(trace), glass
TS-52	1480	α-cristobalite(ss), $AlPO_4$(ss)
	1590	α-cristobalite(ss), $AlPO_4$(ss)
	1650	α-cristobalite(ss)(trace), $AlPO_4$(ss)(trace), glass
TS-53	1480	α-cristobalite(ss), $AlPO_4$(ss)
	1590	α-cristobalite(ss), $AlPO_4$(ss)
	1650	$AlPO_4$(ss), glass

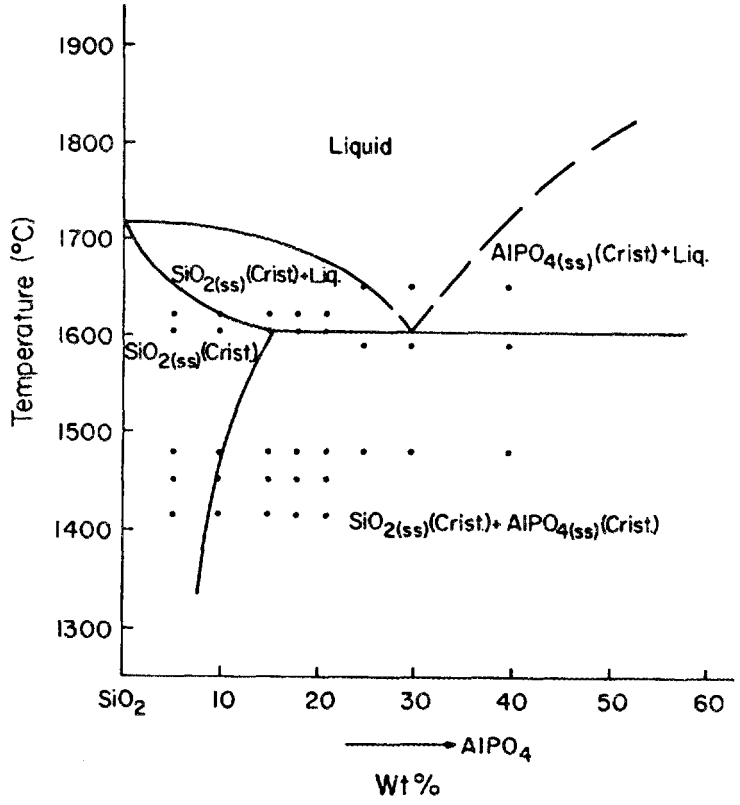

Figure 2. Phase diagram of the high SiO_2 portion of the SiO_2-$AlPO_4$ system.

The high-low transformation parameters of cristobalite solid solution at different firing temperatures and $AlPO_4$ content are shown in Table 5. Data are listed for single phases only since the transformation parameters are independent of second phases. In general, both $\Delta H_{\alpha\beta}$ and $\Delta S_{\alpha\beta}$ show a decrease with firing temperature and $AlPO_4$ content. The maximum decrease occurs at the solubility limit of $AlPO_4$ (15% $AlPO_4$ at 1605°C), indicating a minimum difference between the high and low cristobalite structure for the SiO_2-$AlPO_4$ system. The $\Delta H_{\alpha\beta}$ and $\Delta S_{\alpha\beta}$ for pure cristobalite at 1605°C are also listed in Table 5 for comparison.

The transformation temperature is determined by the temperature at which the free energy of high cristobalite equals that of low cristobalite. In other words, it is determined by the relative change

in enthalpy $\Delta H_{\alpha\beta}$ and entropy $\Delta S_{\alpha\beta}$. The inversion temperature is fairly constant around 244°C, probably because the relative change in enthalpy happens to be proportional to the relative change in entropy. However, introducing $AlPO_4$ to the SiO_2 cristobalite lattice appears to reduce the energy difference between the high and low cristobalite phases.

Table 5. Transformation parameters of cristobalite solid solution in the SiO_2-$AlPO_4$ system

Sample No.	Firing Temperature(°C)	$T_{\alpha\beta}$ (°C)	$\Delta H_{\alpha\beta}$(J/g)	$\Delta S_{\alpha\beta}$ (J/g·K)
TS-26	1415	246.5	18.24	0.035
	1480	244.3	16.6	0.032
	1605	243.3	8.33	0.016
	1620	244.3	10.28	0.02
TS-28	1480	247.36	14.55	0.028
	1605	244.6	11.21	0.022
	1620	246	11.64	0.022
TS-29	1605	248	7.86	0.015
Pure SiO_2	1605	268.84	19.89	0.037

<u>SiO_2-BPO_4 System</u>. Phase analyses of the heat-treated samples are shown in Table 6. For the compositions studied, the SiO_2-BPO_4 system appears to be a binary eutectic as shown in Figure 3. The solubility limit of BPO_4 in SiO_2 is located at 10% BPO_4 at 980°C. These results were verified after doubling the heat treatment time (150 hours) for all compositions at 980°C.

Table 6. Phase analyses for the SiO_2-BPO_4 system

Sample No.	Temperature (°C)	Phase Present
TS-47	940	α-cristobalite(ss)
	980	α-cristobalite(ss)
	1000	α-cristobalite(ss)
	1020	α-cristobalite(ss)
TS-48	940	α-cristobalite(ss),
	980	α-cristobalite(ss)
	1000	α-cristobalite(ss), glass (trace)
	1020	α-cristobalite(ss), glass (trace)
TS-49	940	α-cristobalite(ss), BPO_4(ss)
	980	α-cristobalite (ss)
	1000	α-cristobalite(ss), glass (trace)
	1020	α-cristobalite(ss), glass
TS-32	940	α-cristobalite(ss), BPO_4(ss)
	980	α-cristobalite(ss), glass (trace)
	1000	α-cristobalite(ss), glass
TS-50	940	α-cristobalite(ss), BPO_4(ss)
	980	α-cristobalite(ss), glass, BPO_4(ss) (trace)
	1000	α-cristobalite, glass

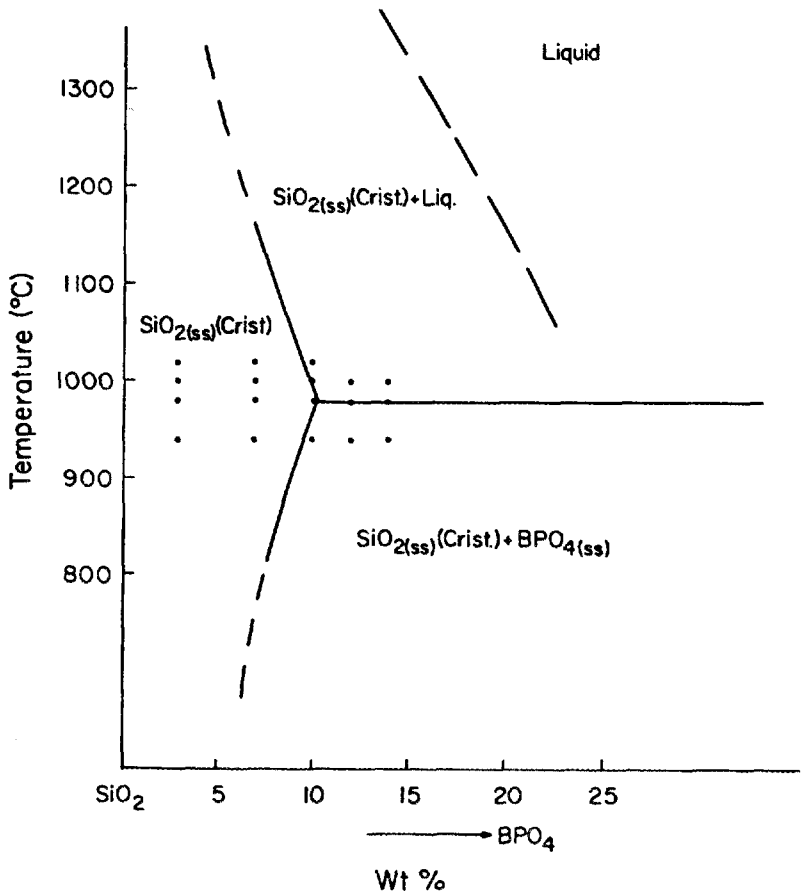

Figure 3. Phase diagram of the high SiO_2 portion of the SiO_2-BPO_4 system.

The transformation parameters of the BPO_4-substituted cristobalite solid solution are listed in Table 7. Introducing BPO_4 to the cristobalite lattice also causes decreases in $\Delta H_{\alpha\beta}$ and $\Delta S_{\alpha\beta}$. Minimum values of $\Delta H_{\alpha\beta}$ and $\Delta S_{\alpha\beta}$ are obtained at the solubility limit. Compared to the $AlPO_4$-substituted cristobalite, the BPO_4-substituted cristobalite shows lower transformation temperatures. This is because the $\Delta H_{\alpha\beta}$ is smaller for BPO_4-substituted cristobalite than for $AlPO_4$-substituted cristobalite, while the $\Delta S_{\alpha\beta}$ remains approximately the same for both. It also means the energy difference between the high and low cristobalite phase is smaller for the BPO_4-substituted cristobalite. A goal to be achieved is either the elimination of the energy gap or further lowering of the transformation temperature.

Table 7. Transformation parameters of cristobalite solid solution for the SiO_2 system

Sample No.	Firing Temperature(°C)	$T_{\alpha\beta}$ (°C)	$\Delta H_{\alpha\beta}$ (J/g)	$\Delta S_{\alpha\beta}$ (J/g·K)
TS-47	940	226.5	15.8	0.032
	980	226.3	16.3	0.033
	1000	229	14.54	0.029
	1020	235	15.97	0.031
TS-48	940	184	10.68	0.023
	980	184	8.57	0.019
	1000	185	10.73	0.023
TS-49	980	183	6.58	0.014

Thus far, only binary systems have been investigated. It is likely that the energy difference and the transformation temperature can be further decreased by introducing more than one compound to the cristobalite lattice. Therefore, the high silica portions of the following three ternary systems will be investigated: SiO_2-TiO_2-$AlPO_4$, SiO_2-TiO_2-BPO_4, and SiO_2-$AlPO_4$-BPO_4. In addition, the formation temperature versus transformation temperature of cristobalite solid solution will be studied to determine whether a correlation exists.

Mullite System

The thermal expansion behavior of various mullite solid solutions is being investigated. It was previously reported that TiO_2, $AlPO_4$, and BPO_4-modified mullite showed that only TiO_2 (3-4 wt%) gave a lower CTE ($4.5 \times 10^{-6}/°C$) than stoichiometric mullite ($5.3 \times 10^{-6}/°C$).[16] Presently, the thermal expansion behavior of P_2O_5, B_2O_3, Ga_2O_3, GeO_2, $CrPO_4$, $GaPO_4$, WO_3, Cr_2O_3, $BAsO_4$, $AlAsO_4$, and $GaAsO_4$-modified mullite is being studied. Additionally, a processing technique using hydrolysis of alkoxide to develop the mullite solid solution with TiO_2 is being investigated.

Experimental

Starting materials in the solid-state reaction studies include reagent-grade silicic acid, aluminum oxide, aluminum hydroxide, dibasic ammonium phosphate, boric acid, gallium oxide, germanium oxide, chromium oxide, tungsten oxide, and arsenic pentoxide. $CrPO_4$

and $GaPO_4$ are prepared by mixing the desired composition of oxide powders in acetone for thirty minutes whereas $BAsO_4$, $AlAsO_4$, and $GaAsO_4$ are prepared by dry mixing the oxide powders. The oxide mixtures are heat treated in covered alumina crucibles following the firing schedules shown in Table 8.

Table 8. Solid-state synthesis of selected half breed SiO_2 compounds

Compound*	Starting Compounds	Heat Treatment Temp/Time (°C/h)
$CrPO_4$	$Cr_2O_3 + 2(NH_4)_2HPO_4$	100/2 + 400/2 + 600/10 + 1080/48
$GaPO_4$	$Ga_2O_3 + 2(NH_4)_2HPO_4$	100/2 + 400/2 + 600/10 + 1048/48
$BAsO_4$	$2H_3BO_3 + As_2O_5$	100/2 + 200/16 + 400/8 + 600/8 + 700/8
$AlAsO_4$	$Al_2O_3 + As_2O_5$	200/16 + 400/8 + 600/8 + 700/8 + 900/12
$GaAsO_4$	$Ga_2O_3 + As_2O_5$	200/16 + 400/8 + 600/8 + 700/8 + 900/12

* With the exception of $CrPO_4$, all compounds are isostructural with silica.[17]

Subsequent to each firing step, the samples are removed from the furnace and thoroughly mixed using a mortar and pestle. Phases in the reacted samples are identified by XRD following each of the last two firings. A general processing technique adopted to synthesize and fabricate the bars of modified mullites by solid-state reaction is outlined in Figure 4.

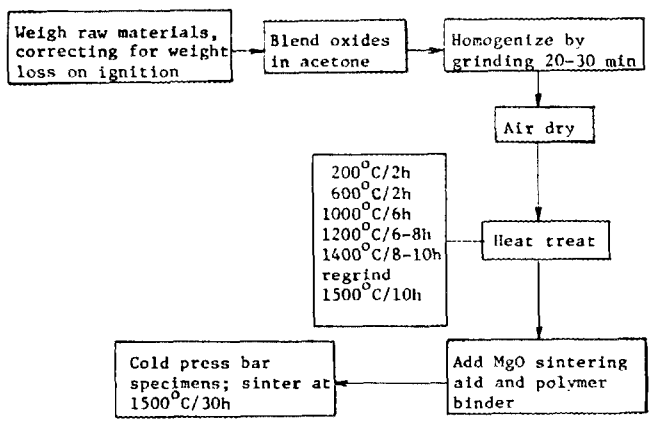

Figure 4. Chemically modified mullite processing by solid-state reaction.

A process using hydrolysis of metal alkoxides[44] (sol-gel) was applied to the mullite-TiO_2 system in an effort to obtain a high degree of reaction, high homogeneity, narrow particle size distribution, low sintering temperatures, and possible increased solubility of selected cations in mullite. The starting materials used for synthesis were tetraethyl orthosilicate $[Si(OC_2H_5)_4]$, aluminum isopropoxide $[Al(OC_3H_7)_3]$, and titanium (IV) isopropoxide $[Ti(OC_3H_7)_4]$. The general expression of compositional variation of mullite with Ti^{+4} is $3(Al_{1-1/3x}, Ti_{1/4x}, \square_{1/12x})_2O_3 \cdot 2SiO_2$. The procedures adopted to synthesize modified mullite solid solution with TiO_2 by sol-gel processing are outlined in Figure 5.

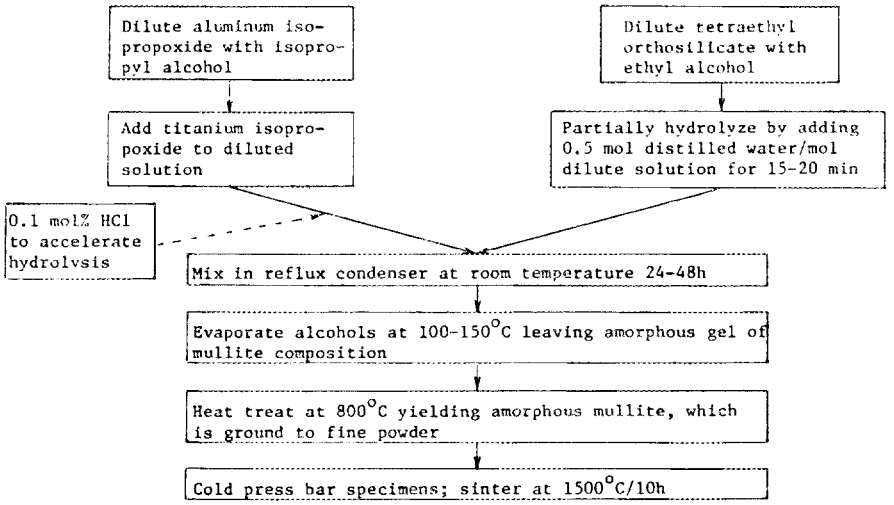

Figure 5. Sol-gel processing of modified mullite

Phases in all the reacted samples are identified by XRD and optical microscopy, and a fused silica dilatometer is used to measure the linear aggregate thermal expansion. Precise lattice expansion as a function of temperature of a Ga-modified mullite sample was measured on the high temperature XRD at the High Temperature Materials Laboratory (HTML) user center at Oak Ridge National Lab. Variation of the lattice constants was determined up to 1200°C at intervals of

200°C. A scanning rate of 2°(2θ)/min was used. Platinum was used as the internal standard to correct for the machine which was assumed to have a constant 2θ error.

Results and Discussion

Because of mullite's orthorhombic structure, the thermal expansion properties are characterized by three independent principal linear thermal expansion coefficients, α_a, α_b, α_c. Axial expansion of a Ga-modified mullite sample $3(Al_{0.833}Ga_{0.167})O_3 \cdot 2SiO_2$ was measured by high temperature XRD, and Figure 6 shows lattice parameters as a function of temperature.

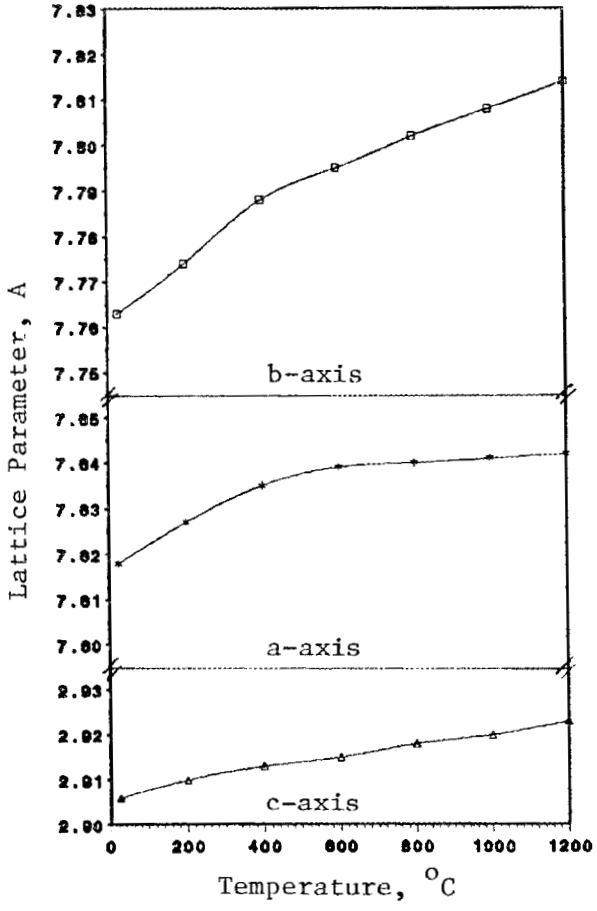

Figure 6. Axial expansion for Ga-modified mullite.

It can be seen that the three parameters vary somewhat non-linearly with temperature. Expansion of the Ga-modified mullite cell was greatest along the b-axis and smallest along the a-axis. It can also be seen that greater expansion takes place along all three axes at low temperatures.

The results for the sol-gel studies and substitution of the phases listed in Table 8 for SiO_2 in mullite will be reported at a later date.

Zircon-Based System

According to F. A. Hummel's classification,[18] low thermal expansion materials may be grouped as materials having thermal expansion less than $20 \times 10^{-7}/^{o}C$. Only three low expansion oxide materials were known before World War II, i.e., fused silica glass ($\alpha = 5.0 \times 10^{-7}$),[19] Vycor glass ($\alpha = 8.0 \times 10^{-7}$),[19] and cordierite ($\alpha = 14 \times 10^{-7}$).[20,21] Since then, much research has been done to develop other low thermal expansion materials and to analyze their behavior based on phase relations, stability, crystallization, and crystal chemistry. Many new materials having low α over different temperature ranges were reported;[22-38] however, the correlation of low thermal expansion behavior with other material characteristics remains unclear.

It may be possible to classify low thermal expansion materials into three groups. The first group consists of systems which have strong covalent molecular bonding characteristics. This crystal structure is typified by the diamond structure.[39] Strong bond strength correlates to low thermal expansion, whereas weak bond strength corresponds to high thermal expansion. All glasses containing 85-100% SiO_2 (except those such as alkali-containing systems),[19] copper aluminosilicate glasses,[23,24] and some glass-ceramics[25,26] have low α . The low thermal expansion exhibited by these systems compared to other glasses may be due to the bond angle bending and stretching during heating and to the bond strength between Si-O. Most of the low thermal expansion materials are grouped in a third group where low

CTE results from the anisotropic characteristic occurring in systems such as hexagonal,[2,22,35,37,38,40] orthorhombic,[29,34] monoclinic,[27] and tetragonal[31] with different lattice parameters.

Among the third group, compounds such as sodium dizirconium triphosphate, $NaZr_2(PO_4)_3$ [the NZP structure[37] which can be said be a structural derivative of zircon $ZrZr_2(SiO_4)_3$], have attracted much attention since the work by Alamo and Roy.[37] Additional research studies have been published on the effects of other elemental substitutions for chemically modified systems.[35,38,41] In this study, efforts are being made to substitute other cations for Na^+ in the NZP structure without changing its skeletal framework. The linear aggregate thermal expansion of the NZP-type systems was studied using classical dilatometry. For the systems showing low thermal expansion, axial thermal expansion measurements were conducted using high temperature XRD.

Experimental

During sample preparation, the raw materials were heat treated at 1100°C for 24h, and at 1300°C for 4 h. The samples were then reground and sintered at 1300°C for 8h. To aid sintering, 1 to 2 wt% ZnO was added to the reground powder.

XRD patterns were obtained to determine the phases present after sintering. A fused silica dilatometer was used to measure CTE at a heating rate of 5 to 8°C/min from room temperature to 1000°C. Thermal expansion values were corrected by adding the thermal expansion of fused silica ($5.0 \times 10^{-7}/°C$).

Lattice parameter measurements were conducted at the HTML at Oak Ridge National Lab. High temperature XRD was performed up to 1400°C using a Scintag θ-θ goniometer equipped with a Buehler high temperature attachment. Platinum powder was mixed as an internal standard. The diffraction patterns were obtained in a 2θ range at 18° to 42° with a scanning rate of 2° 2θ/min. Six major peaks were selected to calculate the lattice parameter, i.e., (110), (113), (024), (116), (214) and (300).

Results and Discussion

Experimentally determined linear aggregate CTE values for the samples studied are given in Table 9, and the thermal expansion curves from R.T. to 1000°C are shown in Figures 7 through 12. For the alkali-modified phases (Group A Table 9), thermal expansion showed negative values for specimens with substitutions of Li, Na, and K (JK-111 through JK-113). The systems modified with the heavy elements Rb and Cs exhibited very low positive CTE values of $2x10^{-7}$ and $5x10^{-7}/°C$, respectively. The thermal expansion results for systems modified by elements which have electron valence of +2 are shown in Figures 7 and 8. Of the systems modified with alkaline earth metals (Figure 8), only JK-122 (substituted by CaO) showed negative expansion values, with the remaining systems showing CTE values of $15x10^{-7}$ through $22x10^{-7}/°C$ (absolute values). Of the transition metal substitutions (Figure 9), sample JK-125 (substituted by MnO) showed a very low CTE value of $4x10^{-7}/°C$. The CTE values for JK-126 and JK-128 (replaced by NiO and ZnO, respectively), decreased up to 550°C, and then increased.

For the substituted systems having +3 electron valence, only JK-131 (by Y_2O_3) was included in the low thermal expansion group. Other systems showed similar behavior of increasing thermal expansion with increasing temperature, and they ranged from $24x10^{-7}$ to $29x10^{-7}/°C$. Figure 10 shows the detailed expansion behavior of Group D which includes systems substituted with elements with +3 electron valence.

Thermal expansion behavior of systems grouped as E and F, which have electron valences of +4 and +5, respectively, are shown in Figures 11 and 12, respectively. Among the systems of Group E, substitution of elements from IVA group (Ti, Zr, Hf) resulted in a slight decrease in thermal expansion above 950°C. Two systems from Group E, JK-141 and JK-145 (by TiO_2 and CeO_2, respectively) showed the low expansion values of $20x10^{-7}$ and $11x10^{-7}/°C$, respectively. Systems from Group F, except for the substitution by V_2O_5 (which has a low melting temperature of 690°C,[42] showed low α_c. JK-152 (by Nb_2O_5) had

Table 9. Phase analyses and thermal expansion results for the zircon system

Group	Sample Designation	Composition (Moles)	Phase	Linear Aggregate Thermal Expansion (αx10^{-7}/°C)	Temp. Range(°C)
A	JK-111	$4ZrO_2$-$3P_2O_5$-$1Li_2O$	$LiZr_2(PO_4)_3$	-22	150-1000
	JK-112	$4ZrO_2$-$3P_2O_5$-$1Na_2O$	$NaZr_2(PO_4)_3$	-32	R.T.-1000
	JK-113	$4ZrO_2$-$3P_2O_5$-$1K_2O$	$KZr_2(PO_4)_3$	-23	R.T.- 950
	JK-114	$4ZrO_2$-$3P_2O_5$-$1Rb_2O$	$RbZr_2(PO_4)_3$	2	R.T.-1000
	JK-115	$4ZrO_2$-$3P_2O_5$-$1Cs_2O$	$CsZr_2(PO_4)_3$	5	R.T.-1000
B	JK-121	$4ZrO_2$-$3P_2O_5$-$1MgO$	$[Mg_{0.5}, \square_{0.5}]Zr_2(PO_4)_3$	16	R.T.-1000
	JK-122	$4ZrO_2$-$3P_2O_5$-$1CaO$	$[Ca_{0.5}, \square_{0.5}]Zr_2(PO_4)_3$	-18	R.T.-1000
	JK-123	$4ZrO_2$-$3P_2O_5$-$1SrO$	$[Sr_{0.5}, \square_{0.5}]Zr_2(PO_4)_3$	22	R.T.-1000
	JK-124	$4ZrO_2$-$3P_2O_5$-$1BaO$	$[Ba_{0.5}, \square_{0.5}]Zr_2(PO_4)_3$	15	R.T.- 950
C	JK-125	$4ZrO_2$-$3P_2O_5$-$1MnO$	$[Mn_{0.5}, \square_{0.5}]Zr_2(PO_4)_3$	4 -3	R.T.-1000 R.T.- 550
	JK-126	$4ZrO_2$-$3P_2O_5$-$1NiO$	$[Ni_{0.5}, \square_{0.5}]Zr_2(PO_4)_3$	25	550-1000
	JK-127	$4ZrO_2$-$3P_2O_5$-$1CuO$	$[Cu_{0.5}, \square_{0.5}]Zr_2(PO_4)_3$	40 -1	R.T.-1000 R.T.- 550
	JK-128	$4ZrO_2$-$3P_2O_5$-$1ZnO$	$[Zn_{0.5}, \square_{0.5}]Zr_2(PO_4)_3$	15	550- 900
D	JK-131	$12ZrO_2$-$9P_2O_5$-$1Y_2O_3$	Refer to Discussion	14	R.T.-1000
	JK-132	$12ZrO_2$-$9P_2O_5$-$1La_2O_3$	"	25	R.T.-1000
	JK-133	$12ZrO_2$-$9P_2O_5$-$1Al_2O_3$	"	24	R.T.-1000
	JK-134	$12ZrO_2$-$9P_2O_5$-$1Cr_2O_3$	"	29	R.T.-1000
E	JK-141	$8ZrO_2$-$6P_2O_5$-$1TiO_2$	$[Ti_{0.25}, \square_{0.75}]Zr_2(PO_4)_3$	20	R.T.- 980
	JK-142	$8ZrO_2$-$6P_2O_5$-$1ZrO_2$	$[Zr_{0.25}, \square_{0.75}]Zr_2(PO_4)_3$	39	R.T.- 980
	JK-143	$8ZrO_2$-$6P_2O_5$-$1HfO_2$	$[Hf_{0.25}, \square_{0.75}]Zr_2(PO_4)_3$	42	R.T.-1000
	JK-144	$8ZrO_2$-$6P_2O_5$-$1SiO_2$	$[Si_{0.25}, \square_{0.75}]Zr_2(PO_4)_3$	23	R.T.-1000
	JK-145	$8ZrO_2$-$6P_2O_5$-$1CeO_2$	$[Ce_{0.25}, \square_{0.75}]Zr_2(PO_4)_3$	11	R.T.-1000
F	JK-151	$2ZrO_2$-$3P_2O_5$-$1V_2O_5$	$VZr(PO_4)_3$	20	400- 800
	JK-152	$2ZrO_2$-$3P_2O_5$-$1Nb_2O_5$	$NbZr(PO_4)_3$	-4	R.T.- 800
	JK-153	$2ZrO_2$-$3P_2O_5$-$1Ta_2O_5$	$TaZr(PO_4)_3$	11	R.T.-1000

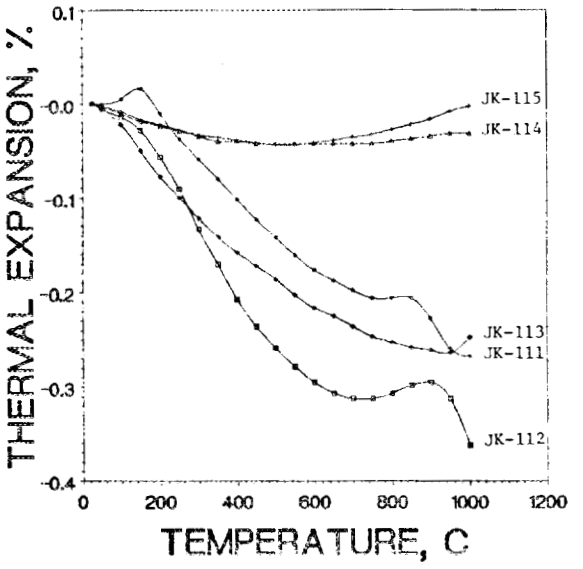

Figure 7. Thermal expansion behavior of the alkali-modified phases (Group A).

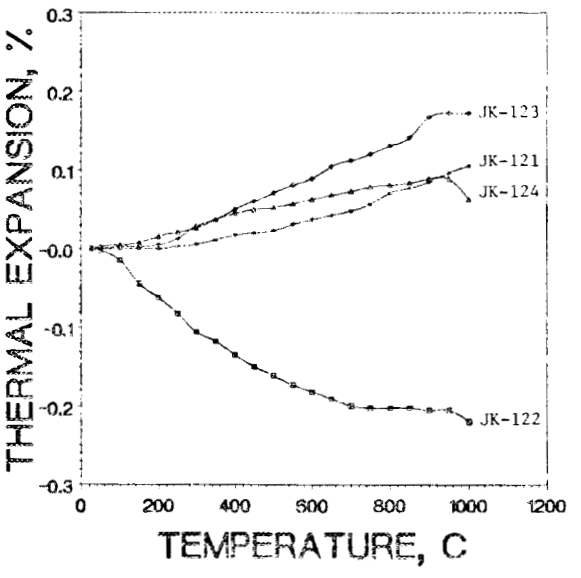

Figure 8. Thermal expansion behavior of systems modified with alkaline earth metals (Group B).

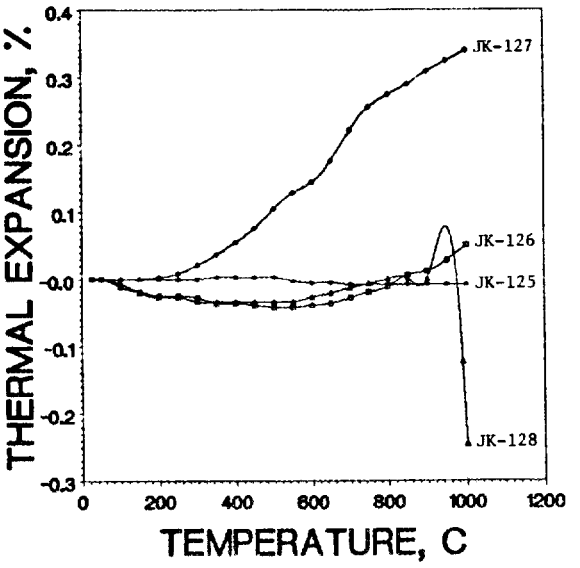

Figure 9. Thermal expansion behavior of the transition metal substitutions (Group C).

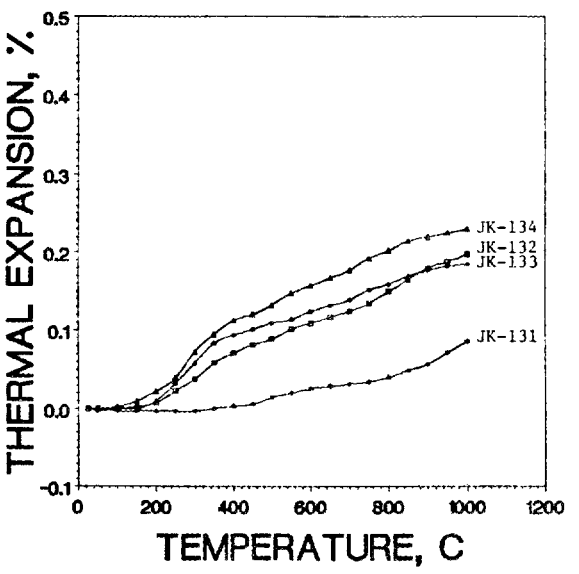

Figure 10. Thermal expansion behavior of the substituted systems with +3 valence (Group D).

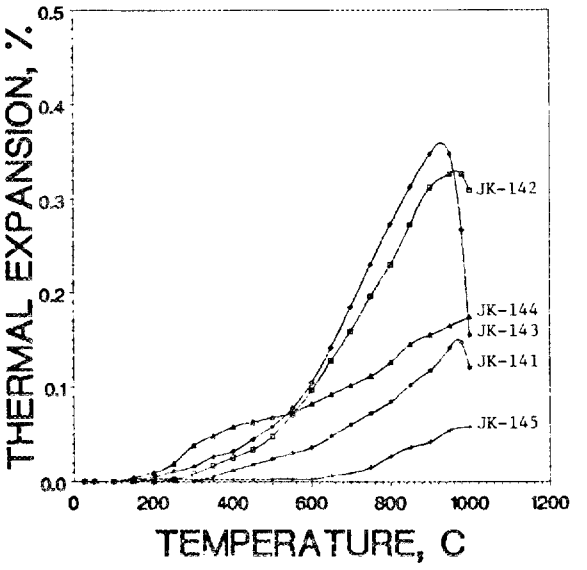

Figure 11. Thermal expansion behavior of the substituted systems with +4 valence (Group E).

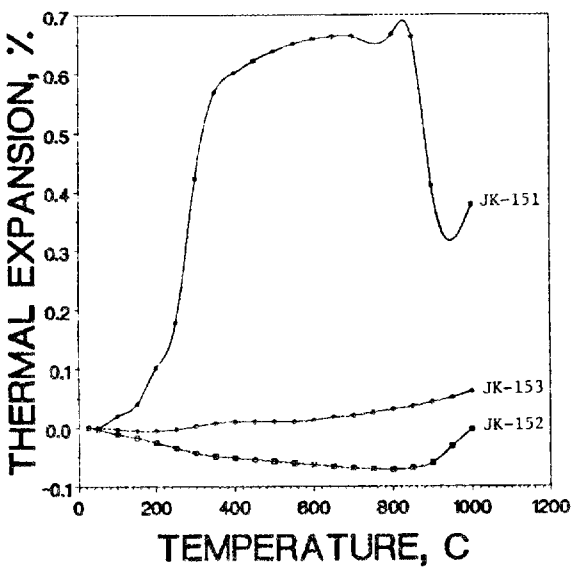

Figure 12. Thermal expansion behavior of the substituted systems with +5 valence (Group F).

low thermal expansion values of $-4x10^{-7}$ and $11x10^{-7}/^{o}C$, respectively.

Axial thermal expansion measurements of the systems exhibiting CTE less than $20x10^{-7}/^{o}C$ are given in Table 10. Detailed axial thermal expansion behaviors from R.T. to 1400°C are shown in Figures 13 through 17. Among the systems considered, JK-114 (by Rb_2O) and JK-115 (by Cs_2O) showed the lowest axial thermal expansion values (Figure 13). Except for the substitution of elements with electron valence of +5, all the systems exhibited anisotropic expansion characteristics, i.e., during heating the a-axis contracted while the c-axis expanded.

Table 10. Lattice parameters and axial thermal expansion coefficients for the systems with low CTE

Sample No.	Lattice Parameters (Å at 25°C) a_o	c_o	Axial Thermal Expansion ($\alpha x10^{-7}/^{o}C$) a-axis	c-axis	Temp. Range (°C)
JK-114	8.64973	24.42959	-12	30	R.T.-1400
JK-115	8.58474	24.95697	-9	23	R.T.-1400
JK-121	8.90407	26.84166	-22	58	R.T.-1400
JK-122	8.78421	22.69170	-38	79	R.T.-1400
JK-124	8.39028	24.89218	-67	279	R.T.-1400
JK-125	8.87921	21.80763	-96	250	R.T.-1400
JK-126	8.21981	25.15314	-89	188	R.T.-1400
JK-131			-31	46	R.T.-1400
JK-141	8.25130	24.69185	-30	44	R.T.-1400
JK-145	8.30818	24.74959	-29	39	R.T.-1400
JK-152	8.25497	23.92264	24	-61	R.T.- 600
			-25	79	600-1400
JK-153	8.39493	23.85328	38	-36	R.T.- 600
			-35	78	600-1400

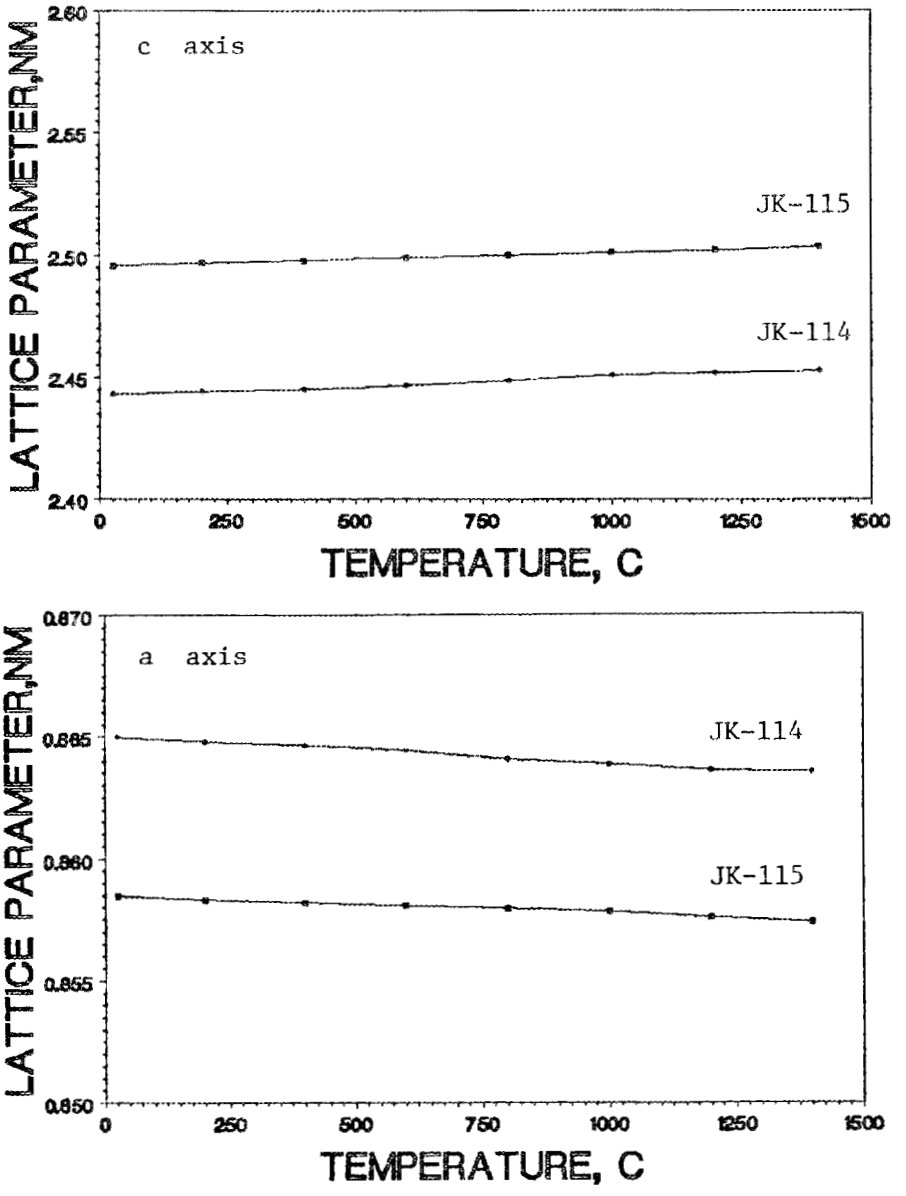

Figure 13. Axial thermal expansion behavior of JK-114 (Rb_2O) and JK-115 (Cs_2O).

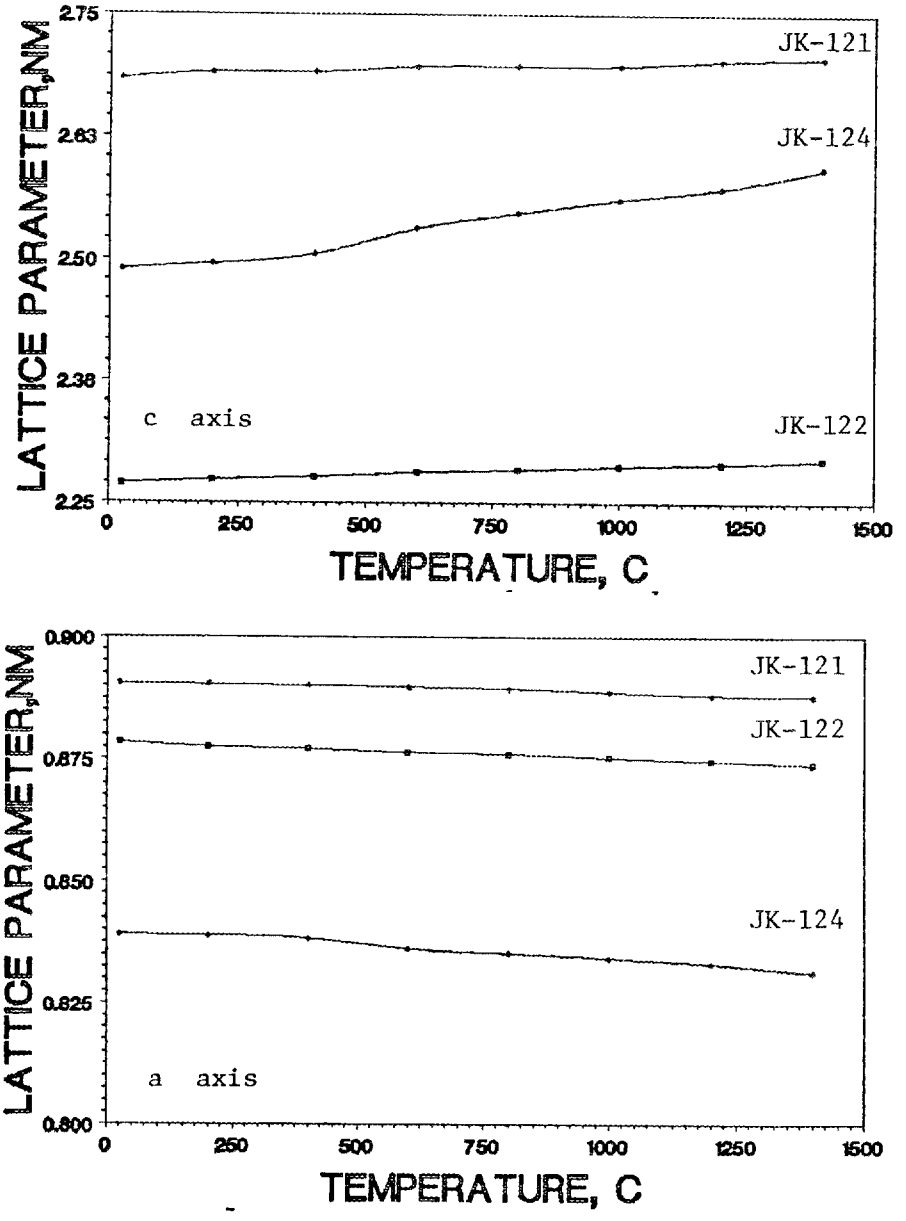

Figure 14. Axial thermal expansion behavior of JK-121 (MgO), JK-122 (CaO), and JK-124 (BaO).

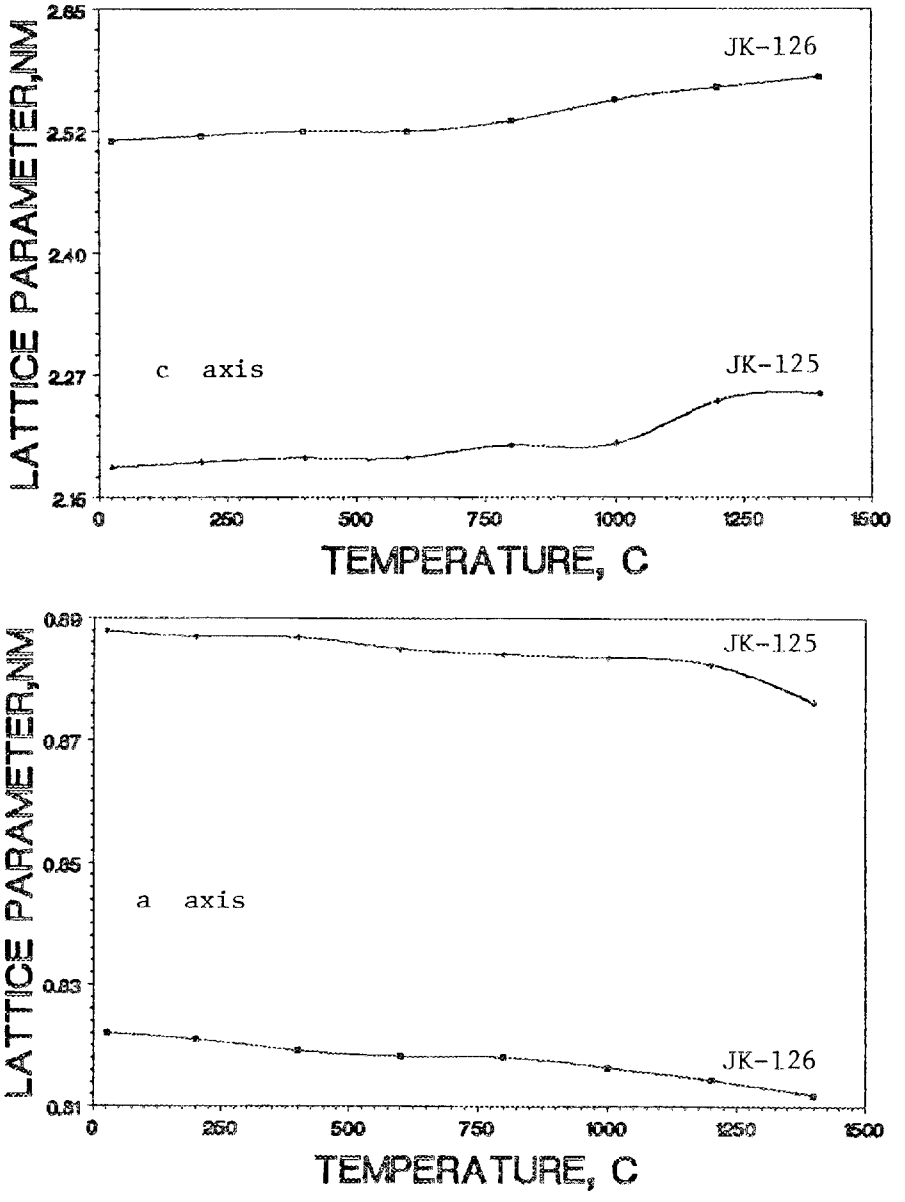

Figure 15. Axial thermal expansion behavior of JK-125 (MnO) and JK-126 (NiO).

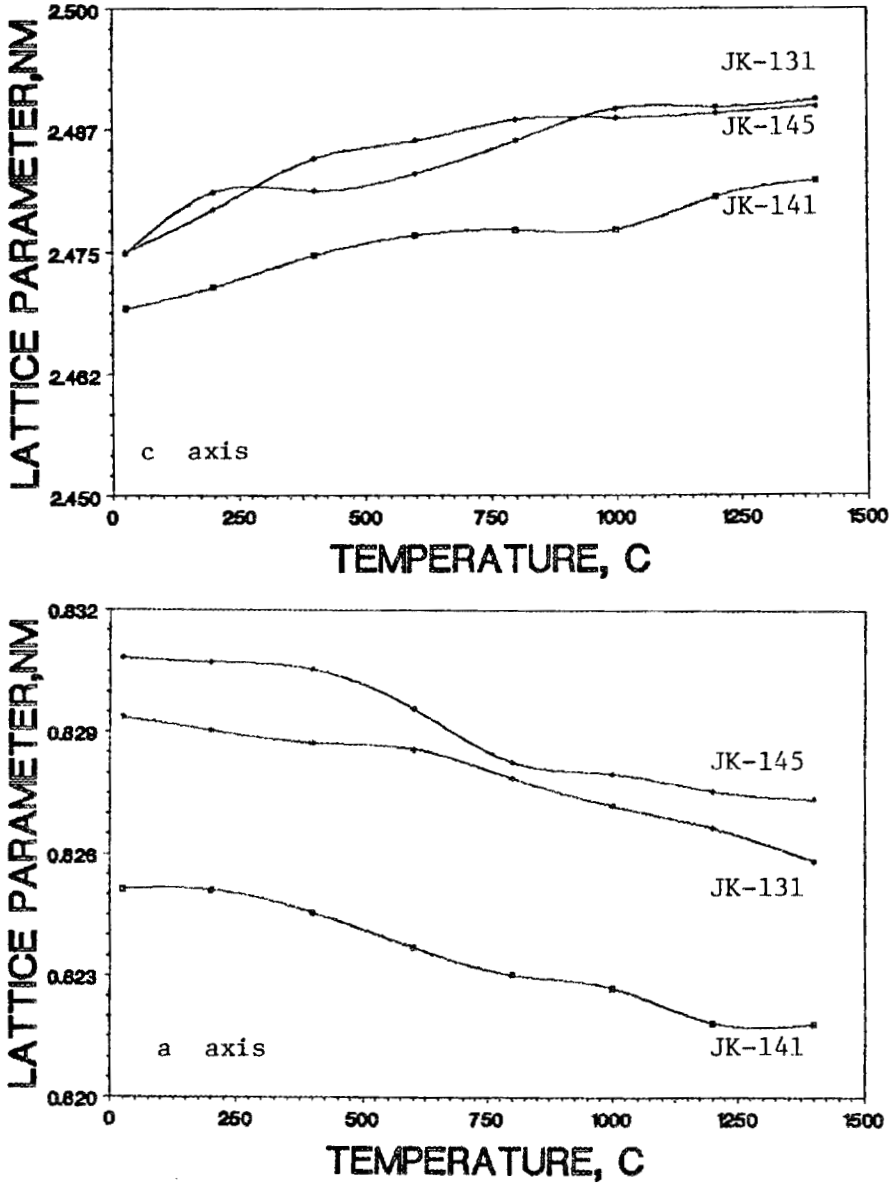

Figure 16. Axial thermal expansion behavior of JK-131 (Y_2O_3), JK-141 (TiO_2), and JK-145 (CeO_2).

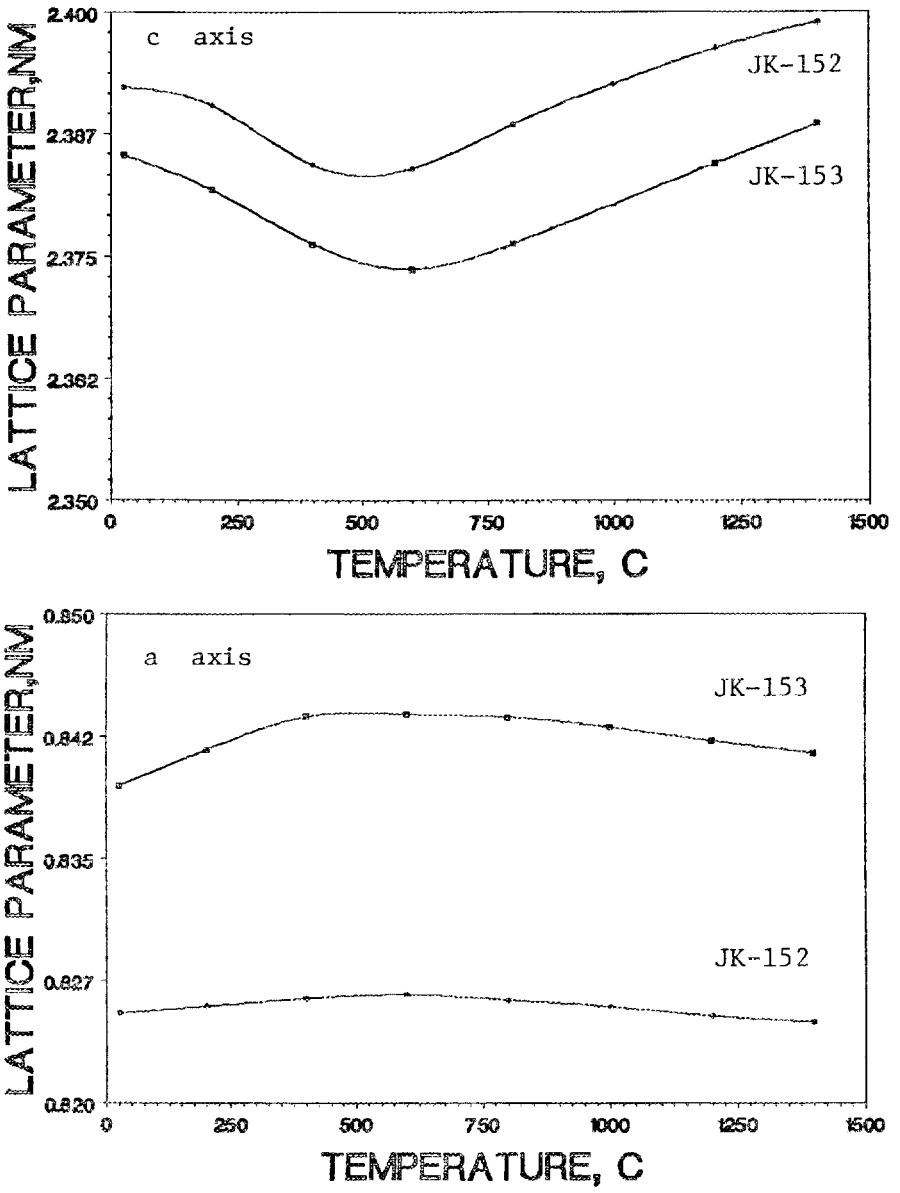

Figure 17. Axial thermal expansion behavior of JK-152 (Nb_2O_5) and JK-153 (Ta_2O_5).

In Figures 14 and 15, the changes in lattice parameters are plotted for the systems replaced by elements with a valence of +2. JK-125 (by MnO) and JK-126 (by NiO) by substitution of transition elements and JK-124 (by BaO) showed very large anisotropy, which can be explained as the large change in the high temperature region above 600°C. The results in Figure 16 for powders prepared by substitution of Y_2O_3, TiO_2 and CeO_2 and showed similar values of -29 to $-31 \times 10^{-7}/^{o}C$ for the a-axis, and 39 to $46 \times 10^{-7}/^{o}C$ for the c-axis. In Figure 17, the results are shown for the systems of JK-152 (by Nb_2O_5) and JK-153 (by Ta_2O_5). The lattice parameter increases up to 600°C, but above 600°, the a-axis is decreased. Conversely, c-axis decreases up to 600°C, but at temperatures above 600°C, it increases.

Substitution of cations with electron valence of +1, +2 and +4 probably replace Na^+ ion in the NZP structure. The NZP structure includes 8 Na^+ ions in the unit cell, as shown in Figure 18.[38,41] Elements which have valences of +1, +2, and +4 can be considered to substitute the position of Na cation fully, half of the Na^+, and one-fourth of Na cation with the crystal chemical form of $[M^{I}]Zr_2(PO_4)_3$, $[M^{II}{}_{0.5}, \square_{0.5}]Zr_2(PO_4)_3$ and $[M^{IV}{}_{0.25}, \square_{0.75}]Zr_2(PO_4)_3$, respectively. But the crystal structure of Group D might be thought of as $[M^{III}{}_{0.25}, (M^{III}{}_{0.08}, \square_{0.67})]Zr_2(PO_4)_3$, where elements with +3 valence might be expected as interstitials after filling one-fourth of the Na^+ sites. Substitution by elements with electron valence of +5 has been confirmed by other work.[43] The crystal form can be written as $M^{V}Zr(PO_4)_3$ or $M^{V}[Zr_{0.5}, \square_{0.5}]_2(PO_4)_3$.

The materials having NZP structure are already known to have anisotropic thermal characteristics,[37,38] and anisotropic behavior was confirmed by our high temperature XRD investigation. As suggested earlier, those materials with expansion anisotropy (one or two positive axial thermal expansions and one or two negative axial thermal expansion) are related to low thermal expansion. From previously reported axial thermal expansion results for the NZP-type compound,[37,38] and from our results, we realize that the c-axis expands with increasing temperature while the a-axis contracts, except for the

few cases such as JK-152 (by Nb_2O_5) and JK-153 (by Ta_2O_5). The a-axis contraction can be considered as the increasing distortion of the PO_4 tetrahedra with increasing temperature accompanying a decrease in bond angle in the O-P-O. This has been suggested previously.[38] This type of contraction may be related to an open structure and the cation in the $O-X^+-O$ occurring in the tetrahedral or octahedral structure of oxide systems, which will be based on crystal chemical equilibrium from thermodynamic equilibrium.

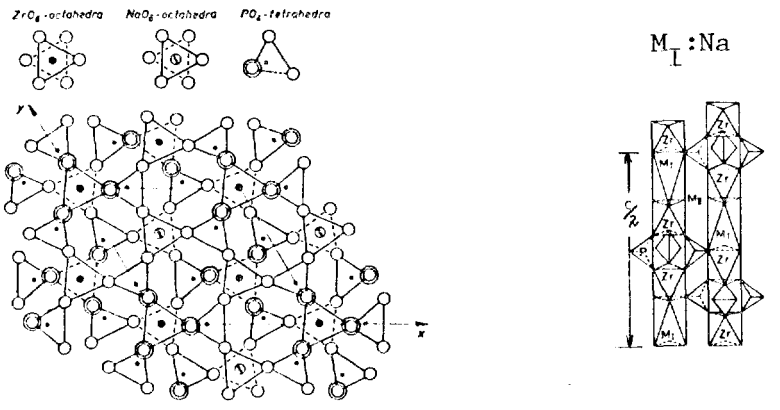

Figure 18. Schematic of the structure of $NaZr_2(PO_4)_3$
(Taken from references 44 and 47)

It is possible that positive thermal expansion is due to the expansion of bond length, and that the negative expansion is due to the contraction of bond angle. In some of the systems, such as JK-126 (by NiO), JK-128 (by ZnO), and JK-152 (by Nb_2O_5), linear aggregate thermal expansion behavior showed both characteristics of contraction and expansion up to 1000°C. A decrease in CTE probably indicates a temperature range in which bond angle contraction is dominant in the thermal expansion behavior, whereas a positive CTE corresponds to bond length expansion upon heating.

Status of Milestones

Status of milestones is presented in Table 11 and Figure 19. An automatic thermal expansion measurement system has been received and installed.

Publications

None this period.

Table 11. Key to major milestones

VPI 1.1	Process selection for phosphate- and silicate-based systems (Oct. 31, 1986)
VPI 1.2	Process selection for mullite- and zircon-based systems (Oct. 31, 1986)
VPI 2.1	Complete literature review (Oct. 31, 1986)
VPI 3.1	Complete upgrade of characterization facility (Dec. 31, 1986)
VPI 3.2	Complete upgrade of specimen fabrication, processing facilities (June 30, 1987)
VPI 4.1	Complete initial screening of phosphate-based systems (Dec. 31, 1987)
VPI 4.2	Complete initial screening of silicate-based systems (Dec. 31, 1987)
VPI 4.3	Complete initial screening of zircon-based systems (Dec. 31, 1987)
VPI 4.4	Complete initial screening of mullite-based systems (Dec. 31, 1987)
VPI 5.1	Complete second-stage property and characterization evaluation of phosphate-based systems (Sept. 30, 1988)
VPI 5.2	Complete second-stage property and characterization evaluation of silicate-based systems (Oct. 31, 1988)
VPI 5.3	Complete second-stage property and characterization evaluation of mullite-based systems (Nov. 30, 1988)
VPI 5.4	Complete second-stage property and characterization evaluation of zircon-based systems (Dec. 31, 1988)
VPI 6.0	Complete scale-up specimen fabrication of most promising low-expansion ceramics (Feb. 28, 1989)

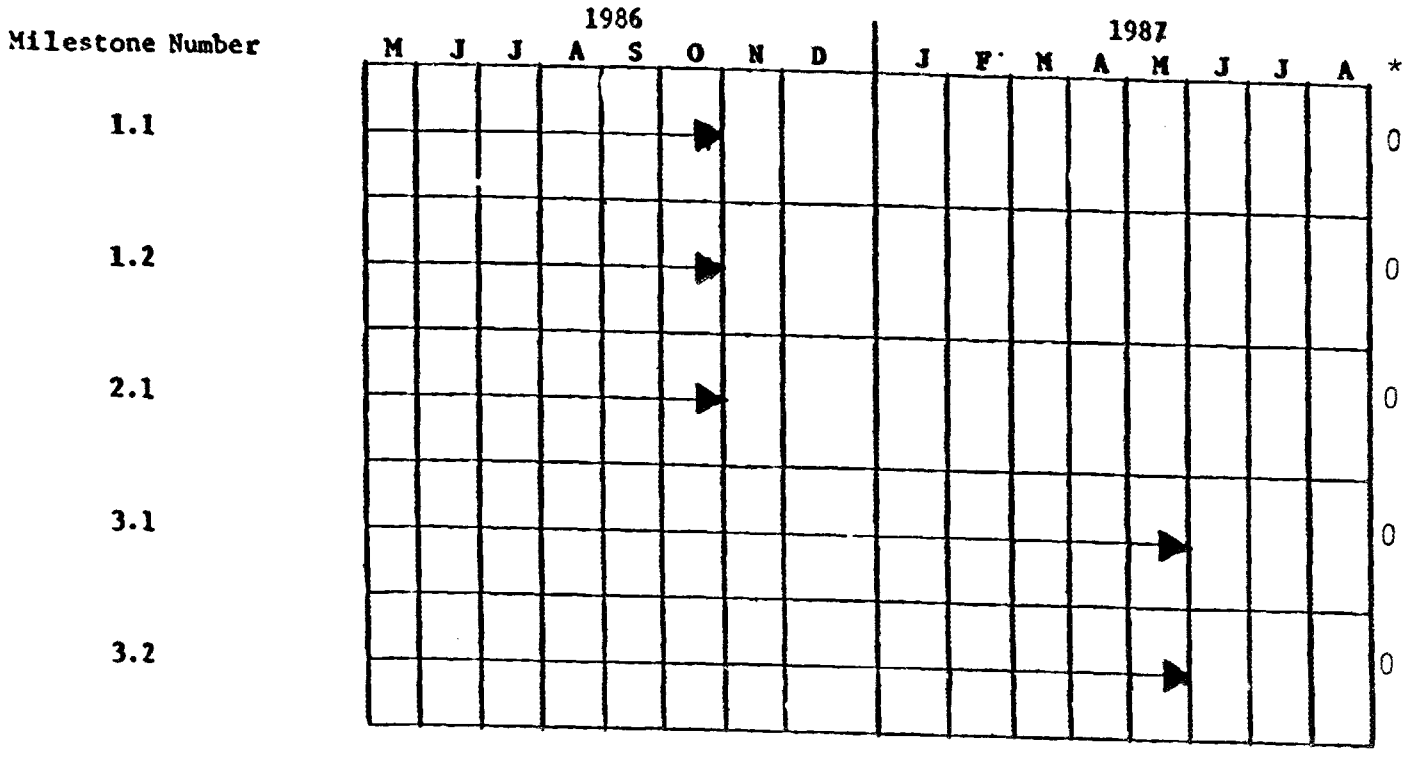

*On, ahead of, or behind schedule.

Figure 19. Milestone status.

References

1. F. A. Hummel, "Thermal Expansion Properties of Some Synthetic Lithia Minerals," *J. Am. Ceram. Soc.*, 34 [8] 235-239 (1951).

2. J. S. Moya, A. G. Verduch, and M. Hortal, "Thermal Expansion of Beta-Eucryptite Solid Solutions," *Trans. J. Brit. Ceram. Soc.*, 73 [6] 177-78 (1974).

3. F. A. Hummel and J. B. Langensiepen, "Elimination of $\alpha \gtrless \beta$ Cristobalite Inversion of $AlPO_4$," *Korean Cer. Inds. Ass.*, 11 [4] 4-5 (1986).

4. H. D. Megaw, "Crystal Structures and Thermal Expansion," *Mat. Res. Bull.*, 6, 1007-18 (1971).

5. D. Taylor, "The Thermal Expansion of the Sodalite Group of Minerals," *Miner. Mag.*, 36, 761-69 (1968).

6. D. Taylor and C. M. B. Henderson, "The Thermal Expansion of the Leucite Group of Minerals," *Amer. Miner.*, 53, 1476-89 (1968).

7. D. Taylor, "The Thermal Expansion Behavior of the Framework Silicates," *Miner. Mag.*, 38, 593-604 (1972).

8. R. B. Sosman, *The Phase of Silica*, Rutgers University Press, New Brunswick, New Jersey, 1964.

9. W. A. Dallase, "Reinvestigation of the Structure of Low Cristobalite," *Z. Kristollogr.*, 121, 369-77 (1965).

10. W. L. Wyckoff, "The Crystal Structure of the High Temperature Form of Cristobalite (SiO_2), *Amer. J. Sci.*, 9, 448-59 (1925).

11. W. Nieuwenkamp, "On the Structure of High-Cristobalite," *Z. Kristollogr.*96, 454-58 (1937).

12. A. F. Wright and A. J. Leadbetter, "The Structure of the β-Cristobalite Phases of SiO_2 and $AlPO_4$," *Philosophical Mag.*, 31 [6], 1391-401 (1975).

13. A. J. Leadbetter and T. W. Smith, "The α-β Transition in the Cristobalite Phases of SiO_2 and $AlPO_4$: II Calorimetric Studies," *ibid.*, 33 [1], 113-19 (1976).

14. D. R. Peacor, "High-Temperature Single-Crystal Study of Cristobalite Inversion," *Z. Kristollogr.*, 138, 272-98 (1973).

15. W. F. Horn and F. A. Hummel, "The System $AlPO_4$-SiO_2," *Glass and Ceram. Res. Bull.*, 26, 47-59 (1979).

16. J. J. Brown, R. E. Swanson, and F. A. Hummel, "Low Expansion Ceramics for Diesel Engine Applications," in *Ceramic Technology for Advanced Heat Engines Project Semiannual Progress Report for October, 1986 through March, 1987*, Oak Ridge National Laboratory, Oak Ridge, Tenn., (in publication).

17. J. P. Attfield, A. W. Sleight, and A. K. Cheetham, "Structure Determination of α-$CrPO_4$ from Powder Synchrotron X-ray Data," *Nature*, Vol. 332, 14, August, 620-2 (1986).

18. F. A. Hummel, "A Review of Thermal Expansion Data of Ceramic Materials, Especially Ultra-low Expansion Compositions," *Interceram.*, 33 [6], 27-30 (1984).

19. W. H. Dumbaugh, Jr., and J. W. Malmendier, "Refractory Glasses," *High Temperature Oxides, Part IV*, Edited by A. M. Alper, 1 - 14, Academic Press, New York and London, 1971.

20. M. E. Milberg and H. D. Blair, "Thermal Expansion of Cordierite," *J. Am. Ceram. Soc.*, 60 [7-8], 372-373 (1977).

21. R. Roy, D. K. Agrawal, J. Alamo, and R. A. Roy, "A New Structural Family of Near-zero Expansion Ceramics," *Mat. Res. Bull.*, 19 [4], 471-477 (1984).

22. H. Schulz, "Thermal Expansion of Beta Eucryptite," *J. Am. Ceram. Soc.*, 57 [7], 313-318 (1974).

23. A. Makishima, T. Ustugi, and T. Sakaino, "Grüneisen's Constant of Low Expansion Aluminosilicate Glass Containing Copper Oxide," *ibid*, 62 [3-4], 224 (1979).

24. K. Matusita and J. D. MacKenzie, "Low Expansion Copper Aluminosilicate Glasses," *J. Non-Cryst. Solids*, 30 [3], 285-292 (1979).

25. G. H. Beall and H. L. Rittler, "Glass-ceramics Based on Pollucite," *Advances in Ceramics*, Vol. 4, 301-312, American Ceramic Society, 1982.

26. K. Matusita, J. D. MacKenzie, K. Kamiya, and S. Sakka, "Low Expansion Glass-ceramics Prepared from Cu_2O-Al_2O_3-SiO_2 Glasses, *ibid*, 277-286.

27. W. R. Manning, O. Hunter, Jr., F. W. Calderwood, and D. W. Stacy, "Thermal Expansion of Nb_2O_5, *J. Am. Ceram. Soc.*, 55 [7], 342-347 (1972).

28. D. W. Richerson and F. A. Hummel, "Synthesis and Thermal Expansion of Polycrystalline Cesium Minerals," *ibid*, 55 [5], 269-273 (1972).

29. C. E. Holcombe, Jr., "Thermal Expansion Coefficients for Low Expansion Oxides," *Am. Ceram. Soc. Bull.*, 59 [12], 1219 (1980).

30. H. P. Kirchner, K. M. Merz, and W. R. Brown, "Thermal Expansion of Uranium Pyrophosphate and of Ceramic Bodies in the System UO_2-UP_2O_7," *J. Am. Ceram. Soc.*, 46 [3], 137-141 (1963).

31. W. Ostertag, G. R. Fischer, and J. P. Williams, "Thermal Expansion of Synthetic β-Spodumene and β-Spodumene-Silica Solid Solutions," *ibid*, 51 [11], 651-654 (1968).

32. G. F. Hawkins and E. G. Wolff, "Isotropic Zero CTE Materials," *Thermal Expansion*, No. 7, 103-118, Edited by D. C. Larsen, Plenum Press, New York and London, 1979.

33. K. R. Laud, F. A. Hummel, "Subsolidus Relations in the System ZrO_2-ThO_2-P_2O_5," *J. Am. Ceram. Soc.*, 54 [8], 407-409 (1971).

34. I. Yamai and T. Oota, "Low Thermal Expansion Polycrystalline Zirconyl Phosphate Ceramic," *ibid* 68 [5], 273-278 (1985).

35. G. E. Lenain, H. A. McKinstry, S. Y. Limaye, and A. Woodward, "Low Thermal Expansion of Alkali-Zirconium Phosphates," *Mat. Res. Bull.*, 19 [11], 1451-1456 (1984).

36. D. E. Harrison, H. A. McKinstry, and F. A. Hummel, "High Temperature Zirconium Phosphates," *J. Am. Ceram. Soc.* 37 [6], 277-280 (1954).

37. J. Alamo and R. Roy, "Ultralow Expansion Ceramics in the System Na_2O-ZrO_2-P_2O_5-SiO_2," *ibid*, 67 [5[, C78-80 (1984).

38. T. Oota and I. Yamai, "Thermal Expansion Behavior of $NaZr_2(PO_4)_3$-Type Compounds," *ibid*, 69 [1], 1-6 (1986).

39. E. Bruton, *Diamonds*, 300-307, N.A.G. Press Ltd., London,1970.

40. P. Predecki, J. Haas, J. Faber, Jr., and R. L. Hitterman, "Structural Aspects of the Lattice Thermal Expansion of Hexagonal Cordierite," *J. Am. Ceram. Soc.*, 70 [3], 175-182 (1987).

41. L. Hagman and P. Kierkegaard, "The Crystal Structure of $NaMe^{IV}_2(PO_4)_3$; Me^{IV} = Ge, Ti, Zr," *Acta Chem. Scan.*, 22 [6], 1822-1832 (1968).

42. J. F. Lynch, C. G. Ruderer, and W. H. Duckworth, *Engineering Properties of Selected Ceramic Materials*, Table 5.4.7-1, Am. Ceram. Soc., Inc., Columbus, OH, (1966).

43. M. Nagai, S. Fujitsu, T. Kanazawa, H. Yanagida, "The Dependence of Structure and Conductivity in Three-dimensional Phosphate Ionic Conductors on Composition," *J. Mat. Sci.* 16 [6], 1633-1642 (1981).

44. Bulent E. Yoldas et al, *Low Temperature Formation of Mullite*, U. S. Pat. Appl. U. S. 867,727 (Oct. 10, 1986).

1.3 THERMAL AND WEAR COATINGS

1.3.1 ZrO_2 Base Coatings

Development of Adherent Ceramic Coatings to Reduce Contact Stress Damage of Ceramics
V. K. Sarin (GTE Laboratories)

Objective/Scope

The objective of this program is to develop oxidation-resistant, high toughness, adherent coatings for silicon based ceramic substrates, namely, reaction bonded Si_3N_4 (RBSN), sintered SiC (SSC), and HIPed Si_3N_4 (AY6[H]) for use in an advanced gas turbine engine. The program will utilize a singular coating technique, chemical vapor deposition (CVD), to develop appropriate coating configurations to accommodate as many of the mechanical, thermal and chemical requirements demanded of the application as possible.

Technical Highlights

Substrate Characterization

Acquisition, fabrication, and mechanical property characterization of substrate materials has been completed. The contract statement of work has been modified in agreement with ORNL to use HIPing rather than injection molding and sintering as the consolidation technique for monolithic Si_3N_4. The characterization included measurements of Knoop hardness, fracture toughness, and strength at room temperature, as well as strength at 1000°C and 1375°C.

Results of the mechanical property determination at room temperature are summarized in Table 1. The Knoop hardness and indentation fracture toughness were measured on the top face and edge of polished test bars (2" x 1/4" x 1/8"). For hardness determination, ten indentations using a 1 kg load were made on a sample of each material. The Knoop hardness was then calculated using the equation

$$KHN = 139.53\ p/l^2$$

where: KHN = Knoop hardness number, kg/mm^2
p = load, g
l = measured length of long diagonal, µm

The fracture toughness was determined by indenting samples with five Vickers indents each using a 1 kg load. The lengths of the cracks emanating from the corners of the indentations were measured, and fracture toughness was calculated using the equation

$$IFT = 0.113\ (KHN)\ (D)^{1/2}/(1 + C_L/2D)^{3/2}$$

where: IFT = indentation fracture toughness, $MN/m^{3/2}$
D = average Vickers diagonal, µm
C_L = total crack length, µm

The IFT values reported for RBSN are higher due to inherent porosity. On the other hand, the IFT of AY6(H) is lower than usually measured for AY6 sintered (SSN) as a result of the finer grain size obtained with the HIPing process.

Table 1: Room temperature mechanical properties of substrate materials.

Substrate	Property		
	KHN (kg/mm^2)	IFT ($MN/m^{3/2}$)	MOR (MPa)
RBSN			272.7±36.8
top face	1004±57	3.5±0.3	
edge	958±82	4.0±0.6	
SSC			401.2±55.2
top face	2579±93	2.2±0.2	
edge	2438±47	2.3±0.2	
AY6(H)			821.5±117.1
top face	1348±15	3.4±0.2	
edge	1337±17	3.3±0.3	

A conventional four point MOR test was used to determine the strength. Twenty test bars of each material were tested at room temperature, and five were tested at each high temperature (1000°C and 1375°C). The average strength values are reported in Table 2. A comparison of the room temperature strength of each material is given in the form of a Weibull plot (see Fig. 1). The Weibull moduli of RBSN, SSC, and AY6(H) are 7.6, 7.6, and 6.8, respectively.

Thermodynamic Modeling

Thermodynamic modeling is being used as a guide for the selection of CVD process parameters. Additionally, modeling to assess the stability of the substrates in the CVD gaseous environment for the temperature range over which the coating may be grown has also been investigated. Results indicate that all three substrates are stable under the anticipated coating process conditions.

Table 2: Room temperature and high temperature strength of substrate materials as determined by a four point bend test. Dimensions of test bars: 2" x 1/4" x 1/8".

Substrate	MOR (MPa)		
	room temperature[1]	1000°C[2]	1375°C[2]
RBSN	272.7±36.8	271.8±12.9	254.2±15.7
SSC	401.2±55.2	352.1±20.4	415.6±68.4
AY6(H)	821.5±117.1	608.4±21.9	120.7±7.7

[1]Reported MOR values are average of 20 measurements.
[2]Reported MOR values are average of 5 measurements.

Thermodynamic modeling of the $AlCl_3$ - NH_3 - H_2 - Ar system for growth of AlN has been completed. A modified NASA chemical equilibrium computer program (1) was used to predict sets of operating conditions at which AlN would form. These results were then used to compute the yield of AlN from $AlCl_3$ so that sets of operating conditions at which a high yield was thermodynamically possible could be identified. Yield values for one pressure and temperature are shown in Fig. 2. They indicate that yield is maximized by using large ratios of NH_3 to $AlCl_3$ in the inlet gas (see region V on Fig. 2). Similar behavior is obtained for the range of pressures and temperatures studied (0.1 atm $< P <$ 1.0 atm, 1073°K $< T <$ 1273°K). The trend indicated by these calculations was used to design a matrix for the initial CVD experiments. The region in which these experiments were conducted is indicated by cross-hatched area (Fig. 2). These gave dense coatings of AlN, with coating thickness increasing as the ratio $NH_3/AlCl_3$ increased. Figure 3 shows some experimental growth rates calculated from weight gain of the substrate. Maximum calculated growth rates at equilibrium are also shown (see insert on Fig. 3). These were obtained from the equilibrium fluxes of reactants to the substrate surface. The actual growth rates are much smaller than the theoretical ones, indicating kinetic limitations. Subsequent sets of operating conditions for AlN CVD were chosen based on information provided by the model.

In preparation for growing a graded intermediate layer between AlN and the protective Al_2O_3 + ZrO_2 layer, a thermodynamic analysis of the formation of aluminum oxynitride ($Al_xO_yN_z$) was done. The extent of oxidation of AlN was calculated as a function of the amount of oxygen in the gas for three oxygen sources - CO_2, H_2O, and air. The calculations considered all possible gaseous and solid species containing the elements present in the starting material. The results obtained at one pressure and temperature are plotted in Fig. 4. The ratio of N to Al (z/x) is shown for various oxygen moles (n_o). At very low n_o values, z/x is nearly 1.0, indicating no oxidation. As n_o increases, z/x declines by a small amount until n_o

reaches 10^{-1}. At this point, further increases in n_O result in extensive oxidation. The predicted behavior is independent of the source used for oxygen. Similar trends are calculated at other pressures and temperatures. Using these predictions, an experimental matrix for forming $Al_xO_yN_z$ is being constructed.

The model has also been utilized to predict operating conditions under which both Al_2O_3 and ZrO_2 will form from a mixture of $AlCl_3$, $ZrCl_4$, CO_2 and H_2. Although Ar is generally used as a carrier gas in the experiments, the presence of such an inert gas does not influence the thermodynamic calculations. CVD phase diagrams showing the various phases present in the system and their regions of stability are shown in Fig. 5 for a fixed value of initial mole fraction of CO_2 ($x^o_{CO_2}$) and two values of initial mole fraction of $AlCl_3$ ($x^o_{AlCl_3}$) These diagrams indicate that both Al_2O_3 and ZrO_2 are stable over a wide range of conditions. No solid solution forms between Al_2O_3 and ZrO_2 (2), so each is a separate phase with unit activity. At high $x^o_{ZrCl_4}$ values and high temperatures, Al_2O_3 becomes unstable and only ZrO_2 is predicted to form. The single phase region of stability of ZrO_2 increases as $x^o_{AlCl_3}$ decreases. At very small $x^o_{AlCl_3}$ values, free carbon is predicted to form together with ZrO_2. In addition, free carbon is stable with both Al_2O_3 and ZrO_2 at low temperatures and high $x^o_{ZrCl_4}$ values. For all conditions shown in Fig. 5, Al_2O_3 is present as α-Al_2O_3 and ZrO_2 is monoclinic below 1478°K (ZrO_2[m]) and tetragonal above 1478°K (ZrO_2[t]) in accordance with the phase transformation for pure ZrO_2 (3). The results shown in Fig. 5 are not strongly influenced by pressure changes. For example, a decrease in pressure from 100 torr to 10 torr shifts the phase boundary between Al_2O_3 + ZrO_2(t) and ZrO_2(t) from $x^o_{ZrCl_4} = 5.5 \times 10^{-2}$ to 4.8×10^{-2} at 1573°K and $x^o_{AlCl_3} = 10^{-3}$. An increase in $x^o_{CO_2}$ gives more free carbon and, at some conditions, the formation of ZrC.

The predicted ratio of ZrO_2 to Al_2O_3 in the solid is shown for a range of temperatures and initial compositions in Fig. 6. For large excess of CO_2 and H_2 (e.g., low values of $x^o_{AlCl_3}$ and $x^o_{ZrCl_4}$), conversion of both $AlCl_3$ and $ZrCl_4$ to the corresponding oxides is predicted to be complete and hence the ratio Zr/Al in the solid is the same as in the initial gas mixture. As the temperature increases, $ZrCl_4$ and the subchlorides of $AlCl_3$ (AlCl and $AlCl_2$) become more stable, resulting in incomplete conversion of the metal chlorides to metal oxides and a ZrO_2/Al_2O_3 ratio that deviates from the ratio $x^o_{ZrCl_4}/x^o_{AlCl_3}$.

The model predictions have been used to select CVD process parameters for growing Al_2O_3 + ZrO_2 composite layers. Initial experimental results showed the formation of a mixture of Al_2O_3 and ZrO_2. The coatings are currently being analyzed to determine the composition and the phases formed.

Finite Element Modeling (FEA)

Finite element analysis is being used to predict residual thermal stresses in the coating and substrate. The model is based on uncoupled, quasi-static thermoelastic theory, and it is assumed that material properties are independent of temperature. So far, the model has been used to predict residual stresses in AlN coatings on pure Si_3N_4 and SiC substrates. Initial calculations for 10 μm thick AlN coatings on Si_3N_4 substrates gave residual stresses which oscillated between

elements, regardless of mesh pattern. This was found to be caused by the large aspect ratios of the elements. Consequently, a technique for varying the mesh size (4) was incorporated. A schematic of the resulting mesh and of the substrate coating system is shown in Fig. 7.

Since the system is symmetric, calculations are done on only one quarter of the material. Predicted normal stresses at various distances into the coating are listed in Table 3. Three sets of stresses were calculated for a SiC substrate since a range of thermal expansion coefficient values for SiC is reported in the literature. The calculations predict better coating stability on SiC than on Si_3N_4 due to the smaller thermal mismatch. The stress values calculated for a Si_3N_4 substrate exceed the room temperature MOR of AlN (400-450 MPa) by nearly a factor of two, suggesting high inherent residual stress and therefore cracked coatings. However, none of the AlN coatings have been found to contain inherent cracks in the as-grown condition. It is believed that the formation of an interfacial layer between the substrate and coating, which has not been considered in the theoretical model, considerably reduces the inherent residual stress levels in the AlN coating. The chemical composition of the interfacial zone is being analyzed.

Table 3: Residual stress values of an AlN coating on monolithic SiC and Si_3N_4 substrates. Coating thickness is assumed to be 20 μm. Thermal expansion coefficient of AlN = 4.9×10^{-6}/°C.*

Distance from Substrate (μm)	Normal Stress in x Direction (see Fig. 7) (MPa)			
	SiC[1]	SiC[2]	SiC[3]	Si_3N_4[4]
6	339.6	68.18	-210.5	801.7
8	337.5	65.94	-209.9	--
10	335.4	65.69	-209.3	795.0
12	333.4	65.45	-208.8	791.7
14	--	--	--	788.4

*The model does not consider interfacial composition or reactions between substrate and coating.
[1]thermal expansion coefficient = 4.3×10^{-6}/°C
[2]thermal expansion coefficient = 4.9×10^{-6}/°C
[3]thermal expansion coefficient = 5.6×10^{-6}/°C
[4]thermal expansion coefficient = 2.7×10^{-6}/°C

FEA calculations are also being used to predict edge effects. Figure 8 shows the distribution of residual stresses for a sintered Si_3N_4 substrate from the edge to a distance of 100 μm into the material. Since the normal stress in the coating is

greatest at the center, σ_{xx} approaches σ_l for large x/h values (see Fig. 8). The results indicate that the coating is in tension (stress > 0) and the substrate is in compression (stress < 0). The smaller residual stress values at the edge indicate that failure of the coating should originate at the center. However, these results are not directly applicable, since the actual samples will have rounded edges with a uniform coating coverage.

Experimental Results

Development of CVD conditions for application of the coating is under way. Dense, adherent layers of AlN in the 5 - 10 μm thickness range are being deposited reproducibly on all substrates. The adherence is assessed by measuring the critical load required for coating failure using a variable load scratch tester (using a Revetester). Results indicate that as-grown AlN coatings are strongly adherent on both Si_3N_4 and SiC substrates. Average critical loads obtained for AlN on RBSN, SSC, and AY6(H) are reported in Table 4. For comparison purposes, values for TiC-coated Si_3N_4 composites (SNAT and SNT(5)) and cemented carbide (WC-Co) have also been listed. It should be noted that both of these coated systems have been successfully tested under severe machining conditions. Failure of the AY6(H) and RBSN systems occurred catastrophically at the critical load reported, whereas AlN on SSC began flaking at much lower loads. Hence, a precise critical load for SSC is difficult to determine. Photomicrographs of typical scratches are shown in Fig. 9. Failure of the coating is clear on RBSN and SSC. However, on AY6(H), failure appears to originate in the substrate (see cracks in substrate in Figure 9c). This suggests a very strongly adherent coating.

Table 4: Comparison of critical loads required for coating failure for various coating/substrate systems.

Coating	Substrate	Critical load, N
AlN	AY6(H)	77
AlN	SSC	53*
AlN	RBSN	50
TiC	WC-Co	50
TiC	SNT	30
TiC	SNAT	21
TiC	AY6(H)	< 10

*Load at catastrophic failure. Flaking of coating occurred at lower loads.

The influence of a post-coating anneal on adherence is also being investigated. Coated samples are heated in flowing N_2 at a constant temperature for one hour and then analyzed with the scratch tester. Results for AY6(H) samples coated at 950°C indicate an increase in adherence, with the increase peaking at an anneal temperature of approximately 1450°C. This is believed to be due to chemical interactions between coating and substrate with the possible formation of an interfacial layer. Analyses of the interfacial composition are currently being done to confirm this hypothesis.

Optimization of the AlN growth process is under way. Operating conditions which will give uniform layers are being identified for each substrate. In addition, substrate weight gain is being correlated with coating thickness to give a nondestructive method of evaluating thickness.

Composite layers of Al_2O_3 + ZrO_2 have been grown in an effort to identify ranges of acceptable operating conditions for composite formation. Preliminary results gave a distribution of both Al_2O_3 and ZrO_2 throughout the coating. These coatings are currently being analyzed to determine their composition.

Acknowledgments

Finite element analysis done by Prof. T.L. Sham, Rensselaer Polytechnic Institute; contributing GTE employees: C. D'Angelo, S. Mackel, D.W. Oblas, A.E. Pasto, H.E. Rebenne, and F. Sivo.

References

1. G. Gordon and B. McBride, NASA Report SP-273, Washington, DC (1976).

2. Allen M. Alger, ed., "Phase Diagrams: Materials Science and Technology," Vol. 2, Academic Press, New York (1970).

3. I. Barin, O. Knacke, and O. Kubaschewski, "Thermochemical Properties of Inorganic Substances," Springer-Verlag, Berlin (1977).

4. H. Tiersten, Journal of Mathematical Physis., Vol. 9, pp. 1445-1450 (1968).

5. V.K. Sarin and S.T. Buljan, in "High Productivity Machining," V.K. Sarin, ed., p. 105, American Society for Metals, USA (1985).

Status of Milestones

First milestone due in September 1987 was completed on time. Second milestone due in December 1987 is on schedule.

Communications/Visits/Travel

V.K. Sarin and D.W. Oblas attended Coatings for Advanced Heat Engines Workshop sponsored by DOE, Castine, ME, July 27-30. V.K. Sarin gave a talk at the workshop entitled "Ceramic Coatings to Reduce Ceramic-Ceramic Contact Stress."

Problems Encountered

None.

Publications

None.

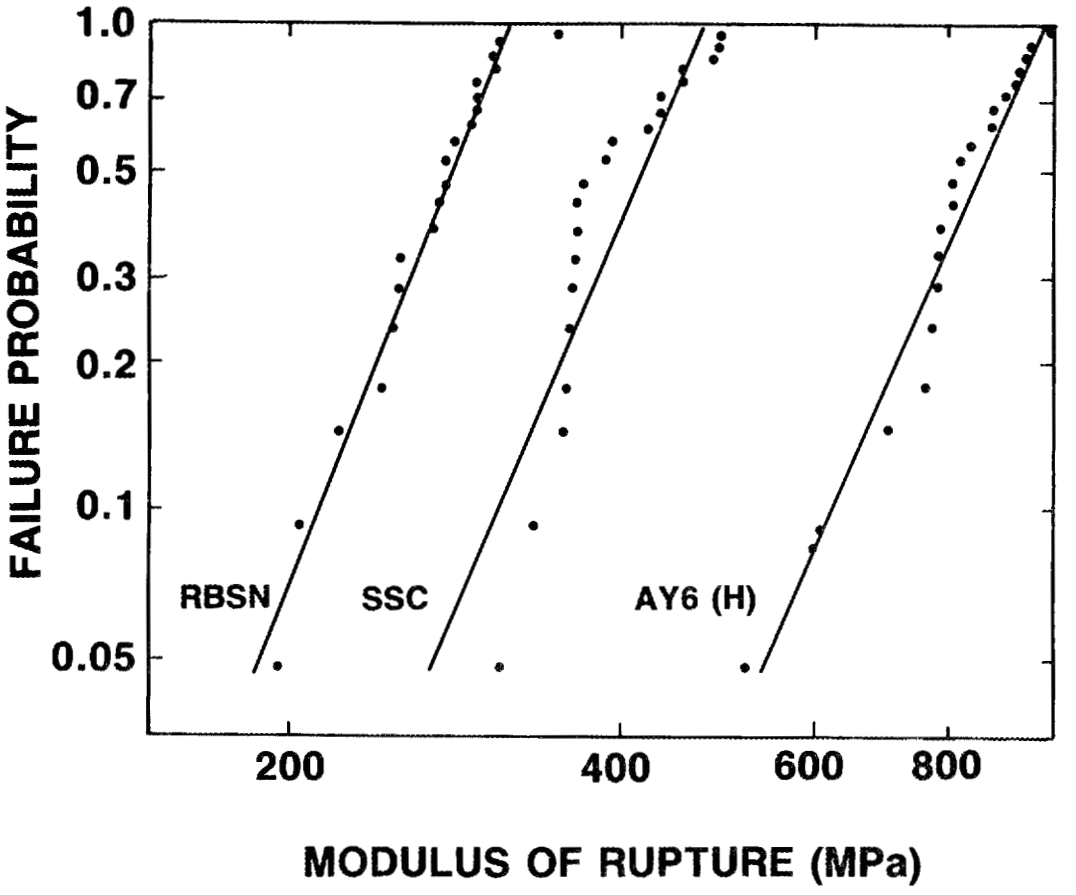

Figure 1: Weibull plot comparing room temperature strengths of reaction bonded Si_3N_4 (RBSN), sintered SiC (SSC), and HIPed Si_3N_4 (AY6[H]).

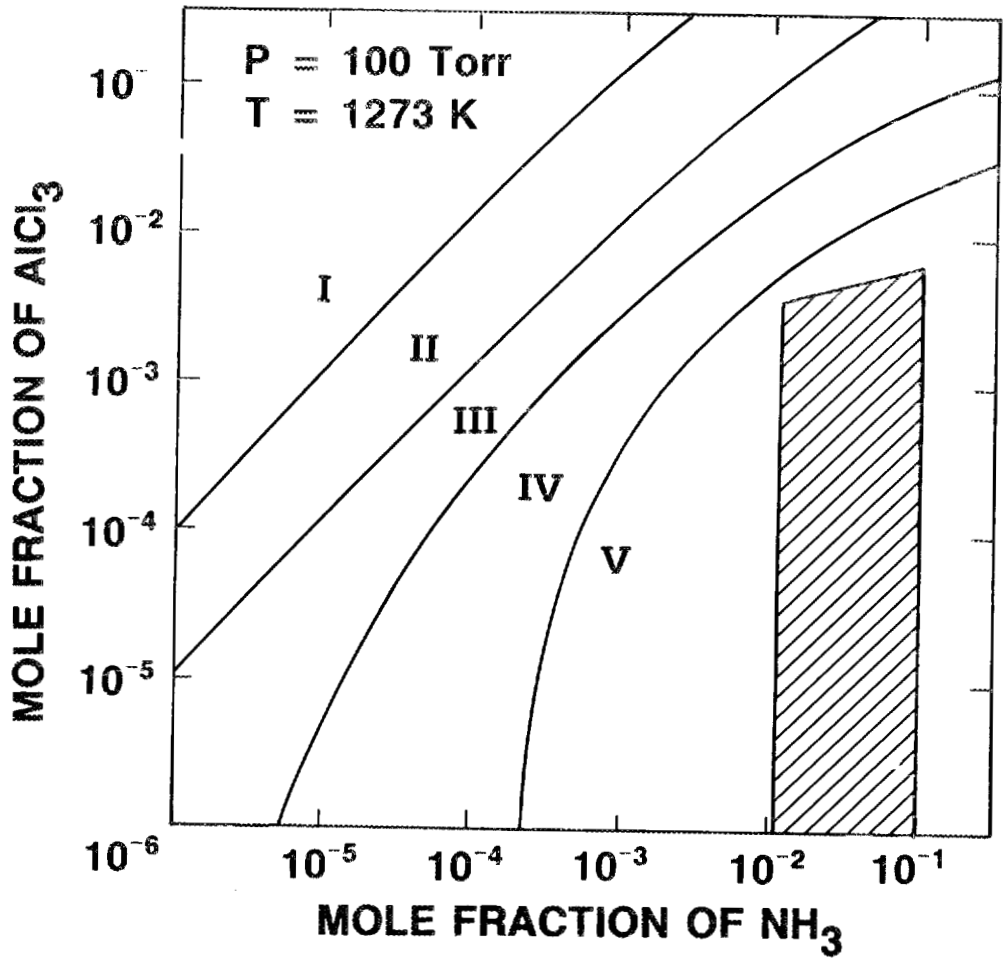

$$\eta = \text{YIELD OF AlN} = \frac{\text{No. of Moles of AlN}}{\text{Initial No. of Moles of } AlCl_3}$$

I. $\eta < 1\%$ II. $1\% < \eta < 10\%$ III. $10\% < \eta < 90\%$ IV. $90\% < \eta < 99\%$ V. $\eta > 99\%$	INLET MOLE FRACTION RANGES OF $AlCl_3$ AND NH_3 USED IN EXPERIMENTS

Figure 2: Combinations of mole fractions of $AlCl_3$ and NH_3 which give various yields of AlN from $AlCl_3$.

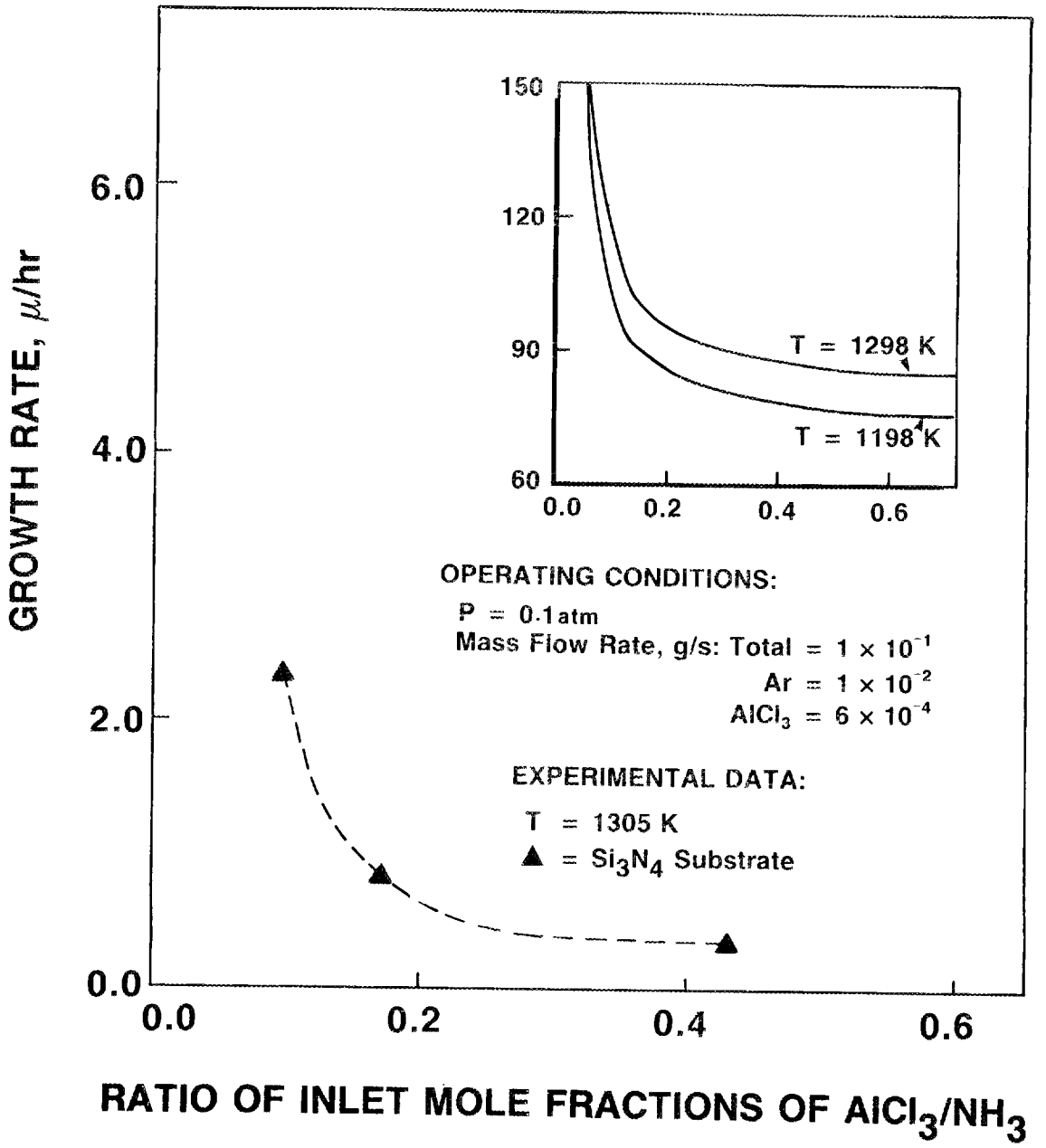

Figure 3: Experimental and theoretical growth rates of AlN.

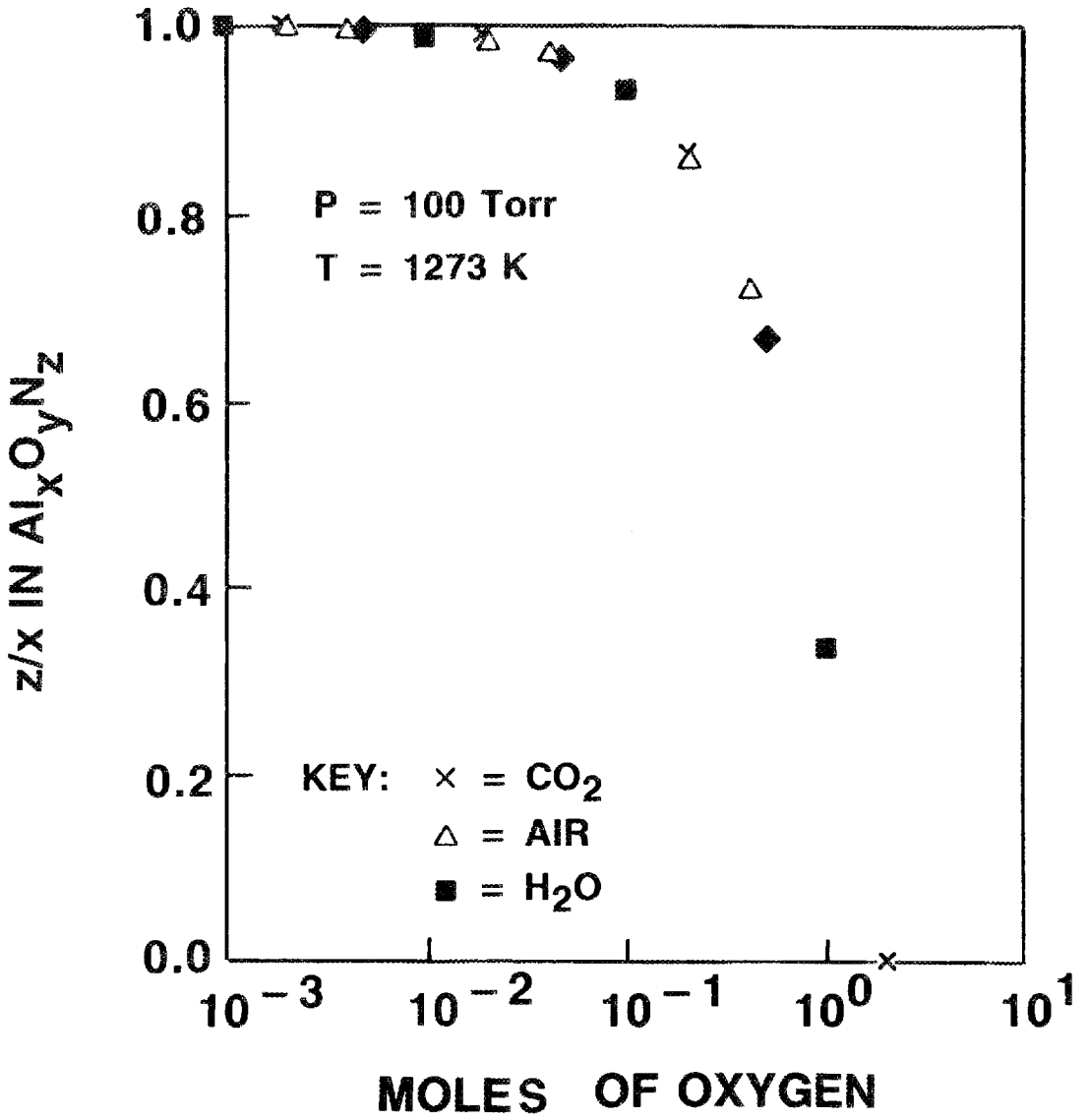

Figure 4: Extent of oxidation of AlN at equilibrium as a function of the mole fraction of oxygen in the gas. Calculations are shown for three oxygen sources: CO_2, H_2O, and air. z/x is the ratio of N to Al in aluminum oxynitride.

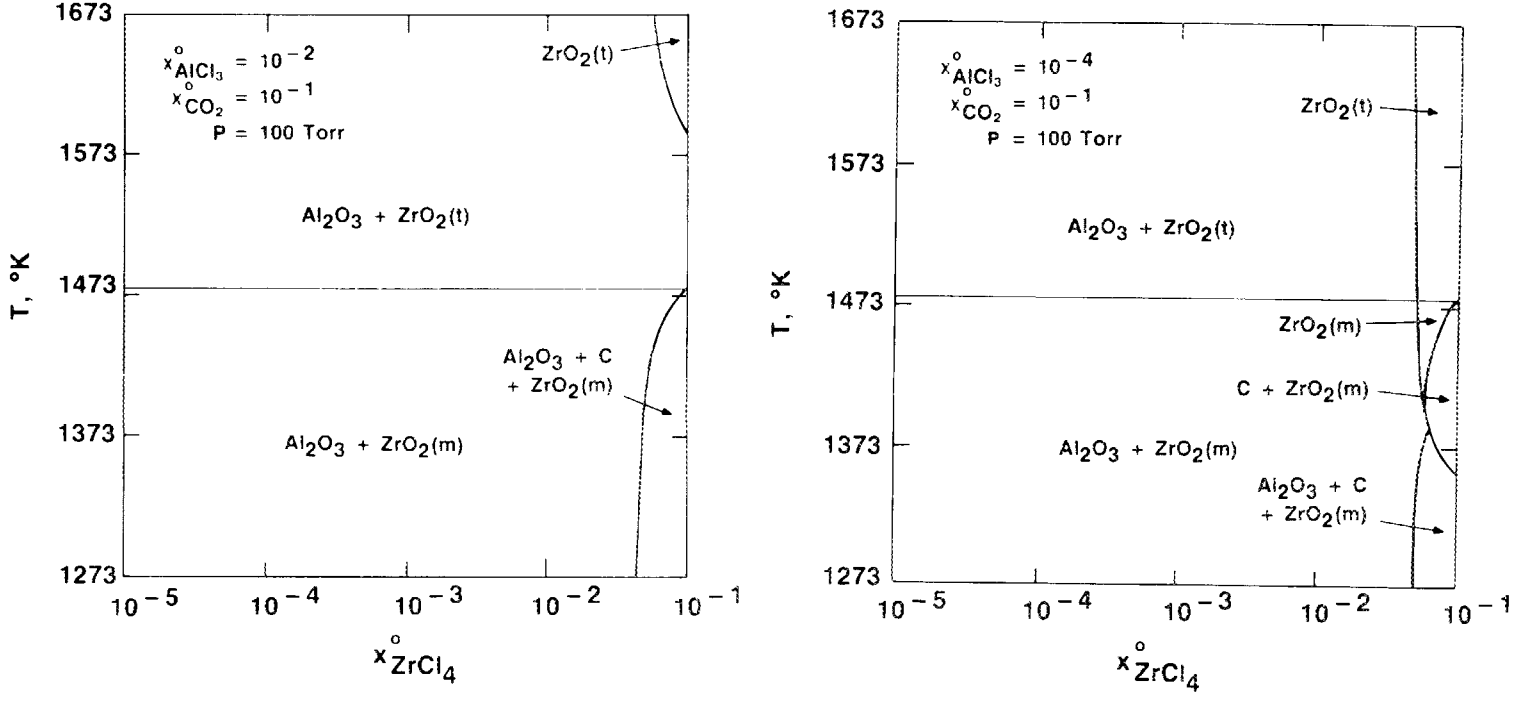

Figure 5: CVD phase diagrams of the $AlCl_3$-$ZrCl_4$-CO_2-H_2 system.

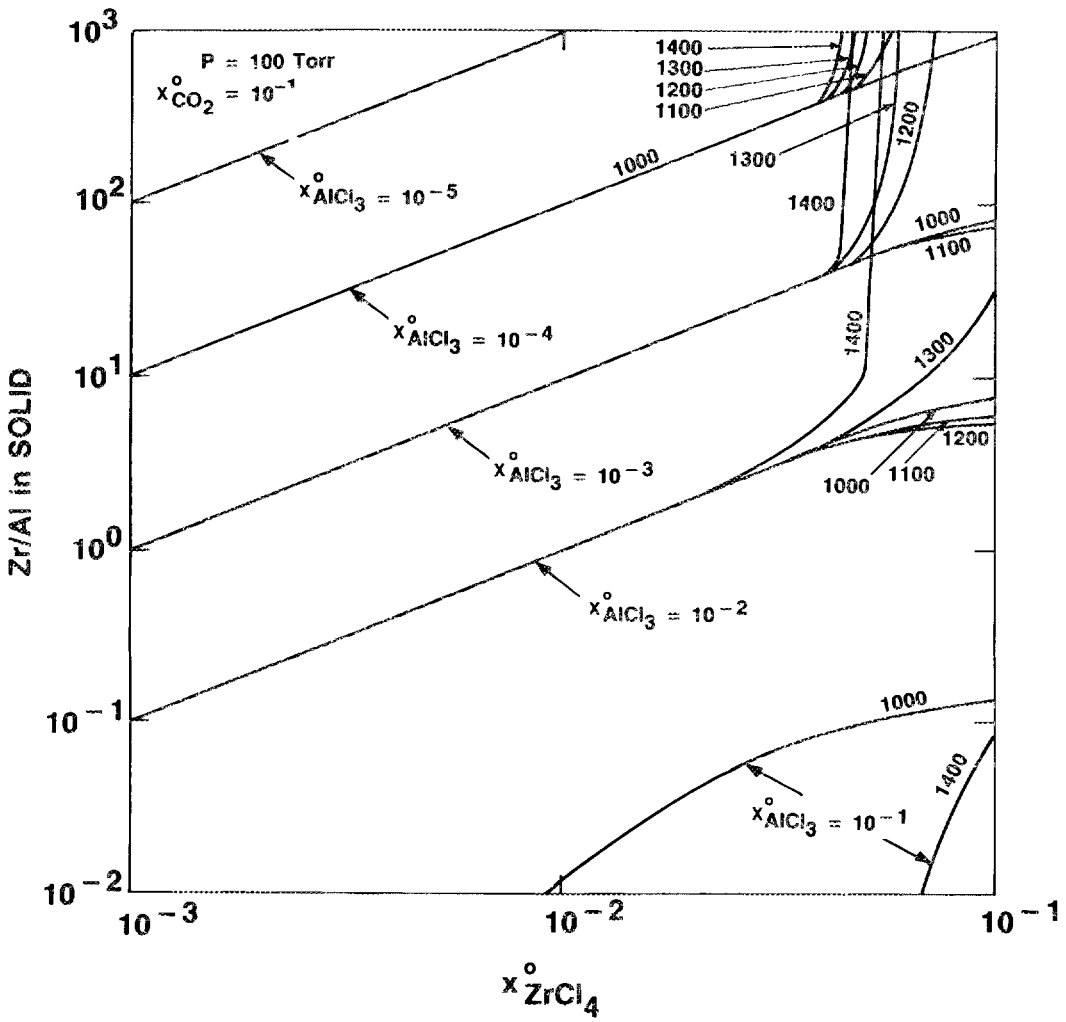

Figure 6: Predicted dependence of Zr/Al ratio in solid ZrO_2 + Al_2O_3 on initial composition and temperature

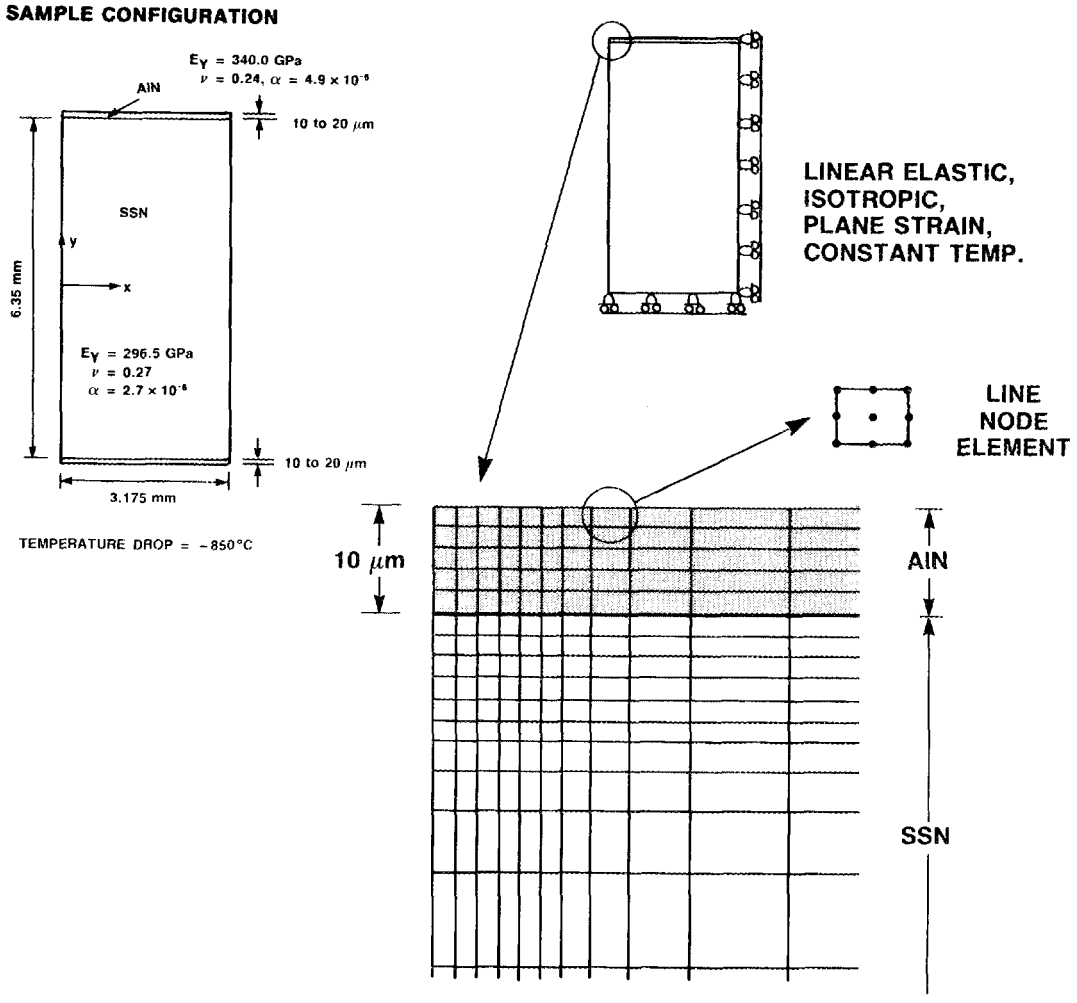

Figure 7: Schematic of substrate-coating system showing mesh used for finite element analysis. Physical properties of AlN and sintered Si_3N_4 (SSN) are listed where E_y = Young's modulus, υ = Poisson's ratio, α = thermal expansion coefficient.

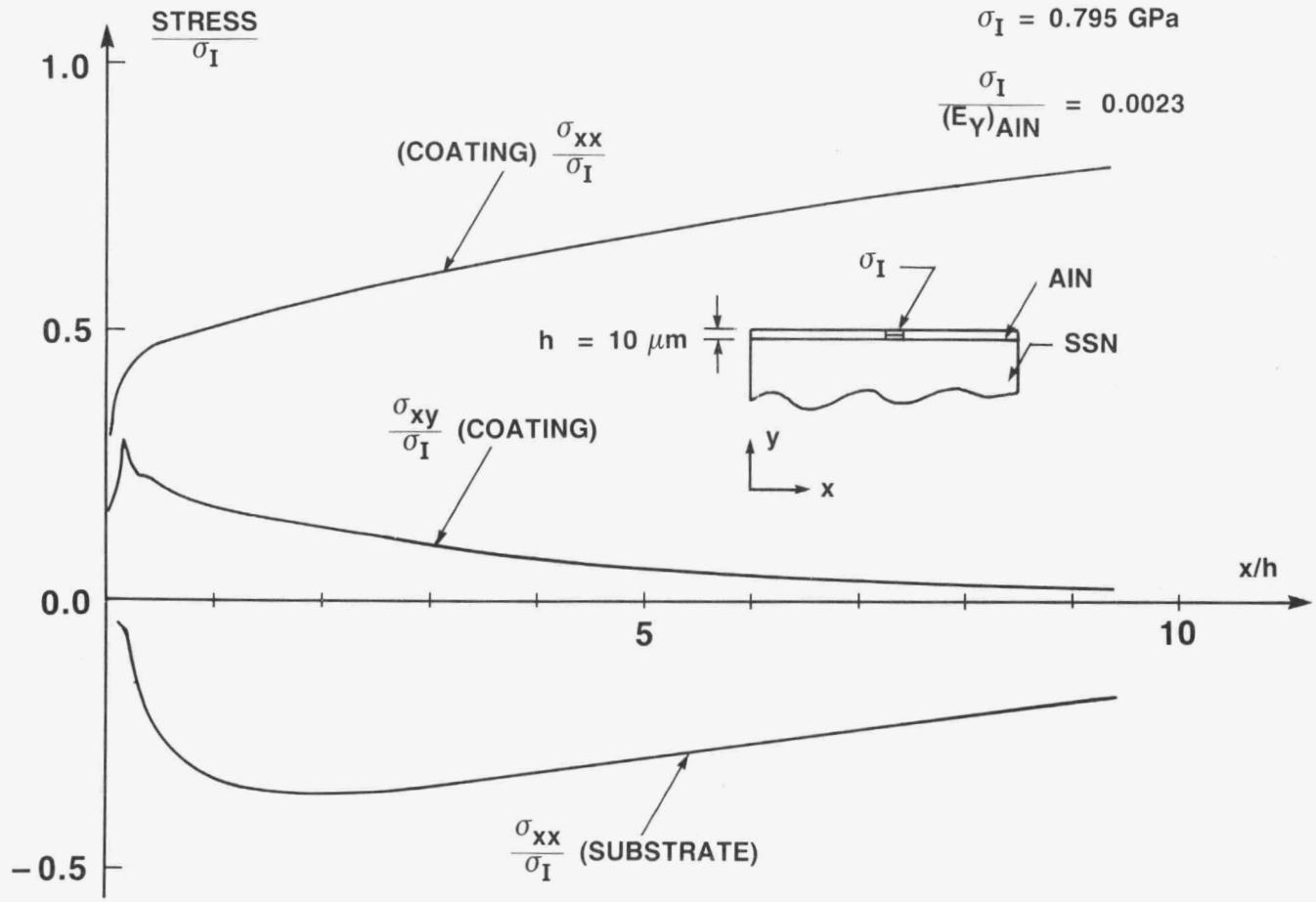

Figure 8: Residual stresses in the coating and substrate near the edge. σ_I = normal stress of AlN at center of coating, σ_{xx} = normal stress in the x direction, σ_{xy} = shear stress.

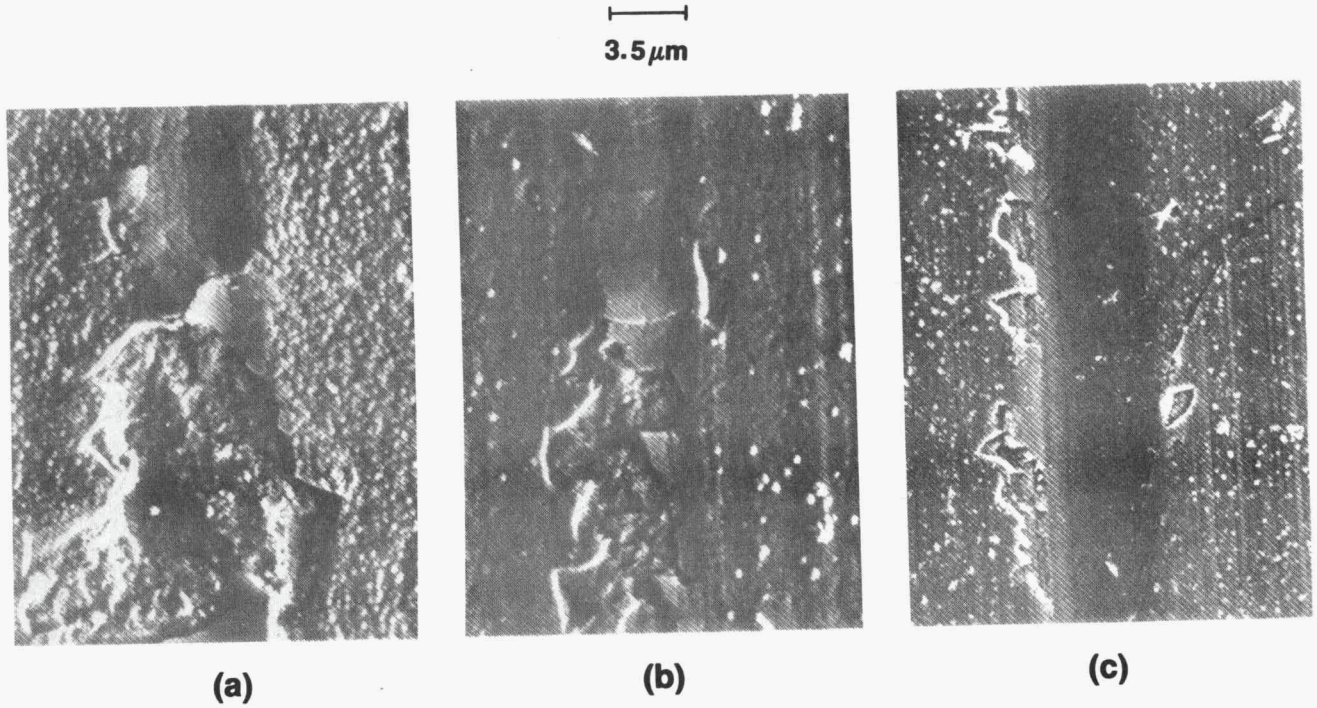

Figure 9: Photomicrographs of scratches parallel to coating/substrate interface made using a variable load scratch tester. a) AlN on RBSN, b) AlN on SSC, c) AlN on AY6(H). Coatings were deposited at 950°C, 100 torr.

1.4 JOINING

1.4.1 Ceramic-Metal Joints

Joining of Ceramics for Heat Engine Applications
M. L. Santella (Oak Ridge National Laboratory)

Objective/scope

The objective of this task is to develop strong, reliable joints containing ceramic components for applications in advanced heat engines. Currently, this work is focused on the joining of partially stabilized zirconia to nodular cast iron by brazing. Joints of this arrangement will be required for attaching monolithic pieces of partially stabilized zirconia to cast iron piston caps in order for the ceramic to provide the insulation necessary for use in low-heat-rejection diesel engines. A novel method for brazing zirconia to cast iron has already been established. The emphasis of this activity for FY 1987 was on investigating: (1) the effect of thermal aging and testing temperature on the strength of joints between zirconia and cast iron, (2) the possibilities for using alternate ceramic and metallic materials in brazed components, and (3) residual stress patterns in ceramic-to-metal braze joints using indentation techniques.

Technical progress

There was significant activity in three technical areas during this reporting period:

(1) additional room temperature shear strength data were obtained for braze joints between zirconia and either titanium or cast iron. The joints were aged at 400°C prior to testing;
(2) flexure testing of braze zirconia braze joints was begun; and
(3) several silicon nitride braze joints were metallographically analyzed, and joints of silicon nitride to either A286 steel or titanium were shear tested.

The work done in these areas is outlined in the following paragraphs.

Shear testing of MS-ZrO_2 joints

Some additional room temperature shear test data for MS-ZrO_2 to cast iron and MS-ZrO_2 to titanium joints are presented in Table 1 for active substrate joints (AS) and in Table 2 for active filler metal joints (AF). In all cases, the joints were aged in air for 120 h prior to testing. Previous data for 100 h of aging are also shown for comparison. The ZrO_2-Fe joints made by AS brazing appeared to fail by ductile shear mainly through the copper coating deposited on the cast iron. This behavior is consistent with high bond strength between the ZrO_2 and the braze filler metal. The ZrO_2-Ti joints made by AS brazing appeared to fail by ductile shear through the bond zone. In contrast, the AF joints all failed by

Table 1. Shear test results for active substrate braze joints after aging in air

Specimen	Interface	Aging	Test temperature (°C)	Shear strength (MPa)
MCB-72	ZrO_2-Fe	400°C/100 h	25	114
MCB-178				202
MCB-179				43
MCB-244	ZrO_2-Fe	400°/120 h	25	229
MCB-245				246
MCB-246				261
MCB-247				213
MCB-248				251
MCB-99	ZrO_2-Ti	400°C/100 h	25	123
MCB-169				210
MCB-170				117
MCB-249	ZrO_2-Ti	400°C/120 h	25	216
MCB-250				299
MCB-251				267
MCB-252				255
MCB-253				332

Materials:

Nilcra grade MS partially stabilized zirconia;
Grade 8003 nodular cast iron obtained from Cummins Engine Co.;
BR 604 brazing alloy supplied by Handy & Harmon Co.; and
Zirconia was vapor coated with titanium prior to brazing.

Brazing conditions:

Vacuum
Brazing temperature - 735°C

Table 2. Shear test results for active filler metal braze joints after aging in air

Specimen	Interface	Aging	Test temperature (°C)	Shear strength (MPa)
MCB-95	ZrO_2-Fe	400°C/100 h	25	61
MCB-182				180
MCB-183				150
MCB-234	ZrO_2-Fe	400°C/120 h	25	57
MCB-235				226
MCB-236				123
MCB-237				252
MCB-238				190
MCB-110	ZrO_2-Ti	400°C/100 h	25	103
MCB-184				118
MCB-185				87
MCB-239	ZrO_2-Ti	400°C/120 h	25	150
MCB-240				19
MCB-241				24
MCB-242				50
MCB-243				71

Materials:

Nilcra grade MS partially stabilized zirconia;

Grade 8003 nodular cast iron obtained from Cummins Engine Co.; and Incusil-15 ABA filler metal supplied by GTE Wesgo.

Brazing conditions:

Vacuum
Brazing temperature - 775°C

debonding at the interface between the ZrO_2 and the active braze filler metal. This mode of fracture may be partly responsible for the greater tendency for scatter in the strength data for the AF joints. Based on this testing, both processes appear to be capable of producing high strength joints. However, the shear strength data indicate that the AS brazing approach is capable of producing higher strength joints than the AF process for these particular material combinations.

Flexure testing of MS-ZrO_2 joints

Because of the difficulty of interpreting shear strength data, of relating it to other strength data, and of performing the shear strength tests at elevated temperature, flexure testing is now being used to test the strength of brazed joints. Braze joints for our initial flexure tests were made by the approach shown schematically in Fig. 1. The individual plates were 25 × 14 × 3 mm, and they were joined along the 25 mm edge. Afterward, the brazed specimens were surface ground on both faces, polished to a 1 μm diamond finish on their tensile faces, and cut into flexure test bars with dimensions of 28 × 2.5 × 2 mm and having a brazed joint in the center of each bar. Testing was done by four-point bending at a loading rate of 22.7 kg/s. The flexure test fixture had an outer span of 19.05 mm and an inner span of 6.35 mm.

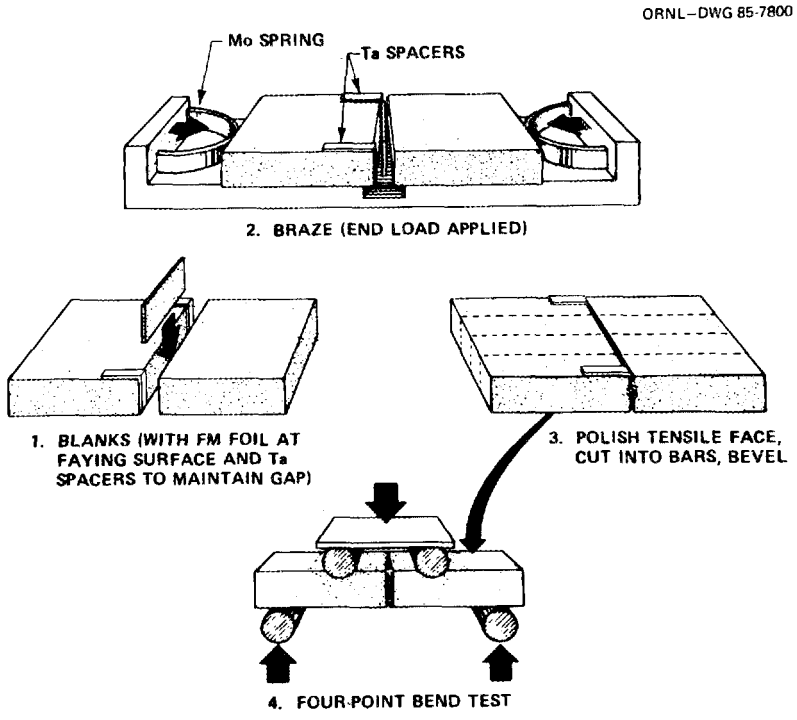

Fig. 1. Schematic drawing of the preparation of flexure test specimens from ceramic braze joints.

Two sets of strength data were produced. In one case, shown in Table 3, joints of MS-ZrO_2 brazed to itself were made and tested at room temperature, 200 and 400°C. In the other case, shown in Table 4, joints were made of MS-ZrO_2 to MS-ZrO_2, MS-ZrO_2 to nodular cast iron, and MS-ZrO_2 to titanium, and were tested at room temperature. All joints were made by active substrate brazing in vacuum at 735°C with braze alloy 604 (Ag-30Cu-10Sn).

The data in Table 3 indicate that the MS-ZrO_2 joints have strength values at 25°C that approach that of the ceramic (nominally about 600 MPa). The strength dropped considerably between 25 and 200°C, and then much less between 200 and 400°C. The strength at 400°C, however, was still quite good considering that the solidus temperature of the 604 alloy is about 620°C. Initial examination indicated that the fracture paths in the 25°C specimens were in the ZrO_2 very near the brazed interface, suggesting that the properties of the zirconia may have been degraded somewhat by interaction with the titanium vapor coating or the braze alloy. The fracture paths in the elevated temperature test specimens were mainly through the braze zone, indicating that their strength is limited by that of the filler metal or a product of the reaction of the filler metal with the titanium-vapor-coated MS-ZrO_2 surface.

The data given in Table 4 verify that the ZrO_2-ZrO_2 joints have very good room temperature strength. Fracture in these joints appeared to have initiated in the zirconia just beyond the brazed interface but then appeared to move out of the ceramic and propagate to failure by traveling along the interface. The fracture path in the ZrO_2-Ti joints was near the interface between the titanium and the 604 alloy. This suggests that a low-strength reaction layer may have formed in the joints at the titanium surface. Fracture in the ZrO_2-cast iron joints appeared to have initiated at the ZrO_2-604 interface and then moved into the ceramic as fracture proceeded, just the opposite of what happened in the ZrO_2-ZrO_2 joints. The difference in fracture path and lower strength of the ZrO_2-cast iron joints may be due to the residual stresses in the joints caused by the thermal expansion coefficient mismatch between the zirconia and the cast iron.

The fracture behavior and microstructures of these specimens are currently being analyzed in more detail.

Brazing of silicon nitride

A previous report described the results of brazing titanium-vapor-coated Si_3N_4 to A286 steel, pure titanium, and the molybdenum alloy TZM with a ductile braze filler metal (BAg-8a) at 790°C. Each of the three joints cracked in the Si_3N_4 upon cooling from the brazing temperature.

Metallographic examination indicated that the microstructures near the metal interfaces varied with the particular alloy used. However, the microstructural features at the Si_3N_4 surfaces were identical for the three joints. The titanium vapor coatings remained largely intact at their original thickness of 1 μm, and showed no sign of debonding from the Si_3N_4 surfaces in any of the joints. Microanalysis indicated that there was no significant dissolution of the titanium coatings in the BAg-8a

Table 3. Flexure test results for active substrate braze joints of MS-ZrO_2 to MS-ZrO_2

Specimen	Interface	Test temperature (°C)		Shear strength (MPa)
MCB-175	ZrO_2-ZrO_2	25		365
MCB-175	ZrO_2-ZrO_2	25		493
MCB-175	ZrO_2-ZrO_2	25		508
MCB-175	ZrO_2-ZrO_2	25		462
MCB-175	ZrO_2-ZrO_2	25		483
			Average	462
MCB-267	ZrO_2-ZrO_2	200		347
MCB-267	ZrO_2-ZrO_2	200		342
			Average	344
MCB-267	ZrO_2-ZrO_2	400		298
MCB-267	ZrO_2-ZrO_2	400		268
MCB-267	ZrO_2-ZrO_2	400		361
			Average	309

Table 4. Flexure test results for active substrate braze joints of MS-ZrO_2 to MS-ZrO_2 titanium, and nodular cast iron

Specimen	Interface	Test temperature (°C)		Shear strength (MPa)
MCB-299	ZrO_2-ZrO_2	25		571
MCB-299	ZrO_2-ZrO_2	25		532
MCB-299	ZrO_2-ZrO_2	25		493
			Average	532
MCB-298	ZrO_2-Ti	25		375
MCB-298	ZrO_2-Ti	25		469
MCB-298	ZrO_2-Ti	25		343
			Average	396
MCB-300	ZrO_2-Fe	25		380
MCB-300	ZrO_2-Fe	25		356
MCB-300	ZrO_2-Fe	25		399
MCB-300	ZrO_2-Fe	25		354
MCB-300	ZrO_2-Fe	25		369
			Average	372

filler or chemical reaction of the coatings with the Si_3N_4. The titanium coating, therefore, acted as a reaction barrier between the ceramic surface and the liquid filler metal, and the surface energy conditions that determined the extent of wetting were those established between the liquid filler metal and the titanium. A separate experiment verified the BAg-8a filler metal would not wet or bond to uncoated Si_3N_4.

Two specimens each of Si_3N_4 brazed with BAg-8a to titanium and A286 steel were shear tested at room temperature. The configuration of the specimens before testing is shown in Fig. 2. The Si_3N_4 pads were held rigidly at the edge under the cantilevered part of the metal bar, and the load was applied at the rounded "nose" of the metal bar in the direction of the cantilevered end. All of these specimens appeared to be free of cracks after brazing, presumably because of geometric factors in determining the actual level of residual stress generated by mismatches in thermal expansion coefficients. The strengths measured under this shear loading arrangement were 97 and 100 MPa for the Si_3N_4-Ti joints, and 31 and 46 MPa for the Si_3N_4-A286 joints.

The fracture paths for the Si_3N_4-Ti joints were mainly through the ceramic under the bond interface. Nugget-like fragments of Si_3N_4 remained attached to the titanium bars after testing, and the noses of the bars were slightly deformed by upsetting. One of the A286 joints fractured in a similar manner but the fracture path traveled much deeper into the Si_3N_4. The other A286 joint fractured near the interface between the steel and the solidified braze alloy, indicating poor adhesion of the BAg-8a to the A286. In neither type of joint was there an indication of

YP-3027

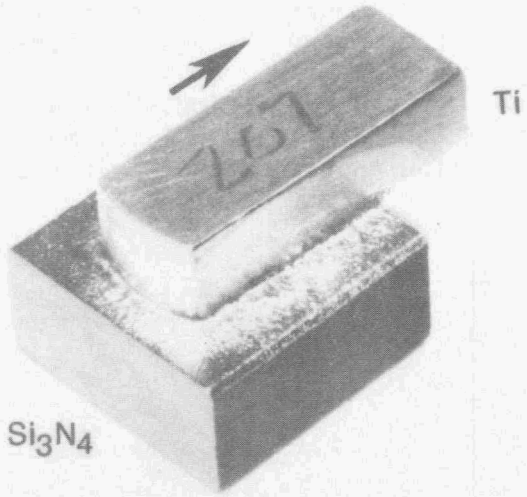

Fig. 2. Photograph of Si_3N_4-Ti joint showing spreading of the BAg-8a braze filler metal over the entire titanium-vapor-coated surface. Arrow indicates direction of loading for shear testing.

poor adhesion of the titanium vapor coating to the Si_3N_4 substrates. The measured strength values cannot be considered significant because of the residual stresses known to be in the joints, and because of the inherent difficulty of determining shear strength. The higher level of residual stress in Si_3N_4-A286 joints was probably a factor in their lower measured strength compared to the Si_3N_4-Ti joints.

Status of milestones

On schedule.

Publications

A talk entitled, "Characterization of Microstructure and Residual Stresses in Ceramic Braze Joints," by M. L. Santella and A. J. Moorhead, was presented on April 6, 1987, at the ORNL Advisory Committee Meeting.

A talk entitled, "Characterization of Interfacial Reaction Products in Ceramic Braze Joints," by M. L. Santella and A. J. Moorhead, was presented April 7, 1987, at the Spring Educational Seminar of the Milwaukee Section of ASM.

A talk entitled, "A Study of the Fracture Behavior of Ceramic Braze Joints," by M. L. Santella and A. J. Moorhead, was presented April 29, 1987, at the 89th Annual Meeting of the American Ceramic Society, Pittsburgh, PA.

A talk entitled, "Overview of Ceramic Brazing at Oak Ridge National Laboratory," by M. L. Santella, was presented September 10, 1987, at the New England Section of the American Ceramic Society, Millis, MA.

A talk entitled, "Joining of Ceramics for Heat Engine Applications," by M. L. Santella and A. J. Moorhead, was presented September 23, 1987, at the Oak Ridge National Laboratory, Metals and Ceramics Division Information Meeting, Oak Ridge, TN.

A talk entitled, "A Review of Oxide, Silicon Nitride, and Silicon Carbide Brazing," by M. L. Santella and A. J. Moorhead, was presented September 30, 1987, at the Annual North American Welding Research Seminar, Columbus, OH.

2.0 MATERIALS DESIGN METHODOLOGY

INTRODUCTION

This portion of the project is identified as project element 2 within the work breakdown structure (WBS). It contains three subelements: (1) Three-Dimensional Modeling, (2) Contact Interfaces, and (3) New Concepts. The subelements include macromodeling and micromodeling of ceramic microstructures, properties of static and dynamic interfaces between ceramics and between ceramics and alloys, and advanced statistical and design approaches for describing mechanical behavior and for employing ceramics in structural design.

The major objectives of research in Materials Design Methodology elements include determining analytical techniques for predicting structural ceramic mechanical behavior from mechanical properties and microstructure, tribological behavior at high temperatures, and improved methods for describing the fracture statistics of structural ceramics. Success in meeting these objectives will provide U.S. companies with methods for optimizing mechanical properties through microstructural control, for predicting and controlling interfacial bonding and minimizing interfacial friction, and for developing a properly descriptive statistical data base for their structural ceramics.

2.2 CONTACT INTERFACES

2.2.2 Dynamic Interfaces

Studies of Dynamic Contact of Ceramics and Alloys for Advanced Heat Engines

K. F. Dufrane and W. A. Glaeser (Battelle Columbus Division)

Objective/scope

The objective of the program is to develop an understanding of the friction and wear processes of ceramic interfaces based on experimental data. The supporting experiments are to be conducted at temperatures to 650 C under reciprocating sliding conditions reproducing the loads, speeds, and environment of the ring/cylinder interface of advanced engines. The test specimens are to be carefully characterized before and after testing to provide detailed input to the model. The results are intended to provide the basis for identifying solutions to the tribology problems limiting the development of these engines.

Technical progress

Apparatus

The apparatus developed for this program uses specimens of a simple flat-on-flat geometry, which facilitates specimen procurement, finishing, and testing. The apparatus reproduces the important operating conditions of the piston/ring interface of advanced engines. The specimen configuration and loading is shown in Figure 1. The contact surface of the ring specimen is 3.2 x 19 mm. A crown with a 32 mm radius is ground on the ring specimen to insure uniform contact. The ring specimen holders are pivoted at their centers to provide self-alignment. A chamber surrounding the specimens is used to control the atmosphere and contains heating elements to control the temperature. The exhaust from a 4500 watt diesel engine is heated to the specimen temperature and passed through the chamber to provide an atmosphere similar to that of actual diesel engine service. A summary of the testing conditions is presented in Table 1.

Materials

The compositions and sources of the various materials considered in the study are presented in Table 2. A variety of monolithic and coating materials were selected to represent various chemical compositions and materials with previously demonstrated successful sliding performance.

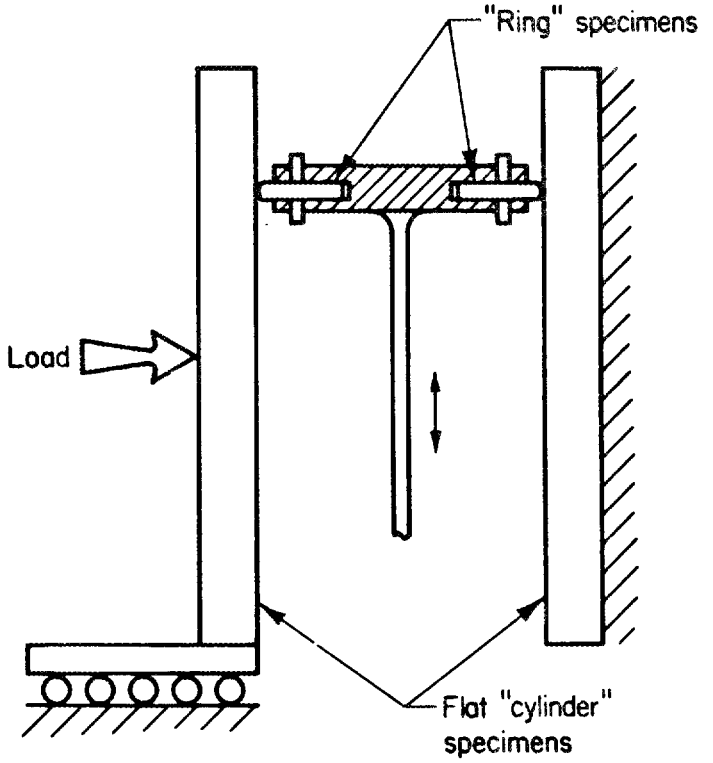

Figure 1. Test specimen configuration and loading

TABLE 1. SUMMARY OF TESTING CONDITIONS

Sliding Contact:	Dual flat-on-flat
"Cylinder" Specimens:	12.7 x 32 x 127 mm
"Ring" Specimens:	3.2 x 19 x 19 mm
"Ring" crown radius:	32 mm
Motion:	Reciprocating, 108 mm stroke
Reciprocating Speed:	500 to 1500 rpm
Average Specimen Speed:	1.8 to 5.4 m/s
Load:	to 950 N
Ring Loading:	to 50 N/mm
Atmosphere:	Diesel exhaust or other gases
Measurements:	Friction and wear (after test)

TABLE 2. CYLINDER AND RING MATERIALS

Material	Source	Manufacturer Designation	Type	Abbreviation	Nominal Composition, Weight Percent
Magnesia Partially Stabilized Zirconia	Nilcra Ceramics, Inc.	TS grade	Monolithic	MPSA	3.3 MgO, 3 HfO_2, bal ZrO_2
Yttria Partially Stabilized Zirconia	NGK-Locke, Inc.	Z-191	Monolithic	YPSZ	5.4 Y_2O_3, bal ZrO_2
Alumina Transformation Toughened Zirconia (HIP'ed)	Toya Soda Manufacturing	2Y20A	Monolithic	ATTZ	3.6 Y_2O_3, 20 Al_2O_3, bal ZrO_2
Sintered Alpha Silicon Carbide	The Carborundum Company	αSiC	Monolithic	αSiC	SiC
Silicon Nitride	Norton/TRW Ceramics	Noralide NC132	Monolithic	Si_3N_4	2W, 0.5 Mg, 0.25 Al, bal Si_3N_4
Silicon-Carbide-Whisker-Reinforced Alumina	ARCO Chemical Company	ARtuff A4AS	Fiber reinforced monolithic	SiC/Al_2O_3	SiC and Al_2O_3
Chromium Oxide Coating (AISI 1020 substrate)	Kaman Sciences Corporation	SCA-1000	drain cast coating	SCA 1000	Cr_2O_3
Gray Cast Iron	Caterpillar Cylinder Liner	---	---	CI	3.3 C, 2.3 Si, 0.7 Mn, bal Fe
Tribaloy 400 (Metallic) (AISI 410 substrate)	Stoody-Deloro Stellite	T400	plasma sprayed coating	T400	28 Mo, 34 Ni, 9 Cr, 1 Fe, 2 Si, bal Co

TABLE 2. CYLINDER AND RING MATERIALS (Continued)

Material	Source	Manufacturer Designation	Type	Abbreviation	Nominal Composition, Weight Percent
Alumina-Titania (AISI 410 substrate)	Metco	M130	plasma sprayed coating	M130	13 TiO_2, 87 Al_2O_3
Metallic (AISI 410 substrate)	Metco	M501	plasma sprayed coating	M501	30 Mo, 12 Cr, 2.5 B, 3 Fe, 0.75, bal Ni
Intermetallic (AISI 410 substrate)	Plasmadyne	P312M	plasma sprayed coating	P312M	$MoSi_2$
Metal-Bonded Chromium Carbide (AISI 1020 substrate)	Metallurgical Technologies	2090-F	plasma sprayed coating	Cr_3C_2	20 Cr_3C_2, 12 Ni, 9W, bal Cr
Chromium Oxide (AISI 1020 substrate)	Cerac	C-1225	plasma sprayed coating	Cr_2O_3	5 Cr, bal Cr_2O_3
Metal-Bonded Tungsten Carbide (AISI 1020 substrate)	Stoody-Deloro Stellite	JK114	Jet-Kote coating	WC	12 Co, bal WC
Chromium Plating (AISI 1020 substrate)	---	---	Electro-plated	Cr	Cr

Wear rate studies

Earlier experiments in the program showed that ceramics in sliding contact will require lubrication for long-term sliding applications, such as the ring/cylinder interface of advanced engines. All attempts to run the five monolithic ceramics and several plasma-sprayed coatings of ceramics and metals resulted in high friction coefficients and high wear rates. Several of the material combinations responded well both to the liquid lubrication and to lubrication with powdered molybdenum disulfide. Since lubrication provided by self-lubricating processes typically have unacceptable wear rates and dry lubricants are extremely difficult to resupply reliably, liquid lubricants are of more interest for practical engines. However, the operating temperature with liquids is limited at least to some extent by the inherent thermal stability of the liquid itself. Earlier experiments established that 310 C was too high for SDL-1, a polyalphaolefin synthetic lubricant with relatively high temperature capabilities. Experiments at 260 C were more satisfactory. Therefore, a series of experiments was conducted with various material combinations at 260 C using the polyalphaolefin to measure the relative wear performance of various material combinations.

The ring wear rates were calculated in terms of a wear coefficient to permit a direct comparison for the various material combinations obtained at different load and speed combinations. The average wear volume for the two ring specimens was used in the calculation. Since the primary wear was found to occur on the ring specimens, the wear of the ring specimens was used as the measure of performance. The wear coefficients were calculated from the Archard wear equation:

$$k = \frac{3pV}{Lx} ,$$

where:

k = wear coefficient,
p = hardness of wearing member,
V = wear volume,
L = applied load, and
x = sliding distance.

The wear coefficient can be likened to the friction coefficient in terms of being a non-dimensional proportionality constant. Values of the wear coefficient range from 10^{-1} for severe unlubricated wear to 10^{-7} or lower for the extremely low wear rates experienced under conditions of full hydrodynamic lubrication.

A summary of the friction and wear results is presented in Table 3. For a basis of comparison, the wear coefficient of the top piston ring in a conventional diesel truck engine was calculated. A wear depth of 0.25 mm was assumed for 6,000 hrs of service at an average ring loading of 18 N/mm. The resulting wear coefficient of 5×10^{-9} is very low and would be associated with hydrodynamic lubrication. It provides the overall goal for the rings in advanced engines if the longevity of current engines is to be approached. An experiment at 100 C using a chromium plated ring and cast iron cylinder specimens resulted in a wear coefficient of 8×10^{-8}. While slightly higher than the 5×10^{-9} from actual service, the result indicated that the apparatus was capable of reproducing the actual conditions sufficiently well to permit comparisons.

The best results at 260 C were obtained with ring coatings of Jet-Kote sprayed cobalt-bonded tungsten carbide (WC) and plasma sprayed Cr_2O_3. Wear coefficients of 10^{-7}, while higher than the baseline tests with chromium plated rings at 10^{-8}, indicated wear rates that could be considered in actual engine service. The improvement obtained with these materials under the deteriorated lubrication conditions at 260 C can be seen by comparing the 10^{-5} wear coefficient of chromium plated rings and cast iron cylinder specimens at 260 C. Cylinder specimens of SCA-1000 (Cr_2O_3) and silicon carbide whisker-reinforced alumina (SiC/Al_2O_3) performed well with the WC and Cr_2O_3 ring specimens. Good performance was also obtained with a monolithic Si_3N_4 ring specimen operating against a Si_3N_4 cylinder specimen having a Ceraprep surface modification treatment. The treatment resulted in a reduction in ring wear coefficient from 3×10^{-6} to 1×10^{-6}.

For comparison purposes, Table 3 also includes selected results with YPSZand chromium plated rings operating against Si_3N_4. Wear coefficients of 10^{-4} obtained in these experiments would be unsatisfactory in practical engine applications.

Status of Milestones

The program has been completed and the final report was submitted on September 30, 1987.

Publications

K. F. Dufrane and W. A. Glaeser, "Wear of Ceramics in Advanced Heat Engine Applications", Wear of Materials, 1987, ASME, New York, NY, pp. 285-291.

TABLE 3. COMPARISON OF APPROXIMATE RING WEAR COEFFICIENTS

Ring Material	Cylinder Material	Lubricant	Temperature, C	Ring Loading, N/mm	Friction Coefficient	Hardness Used in Calculation, kg/mm^2	Average Ring Wear Coefficient
Cr	Cast Iron	SAE 30	100	17.5	--	975	5×10^{-9} (a)
Cr	Cast Iron	SDL-1	100	12.3	0.03 - 0.04	975	8×10^{-8}
WC	SiC/Al_2O_3	SDL-1	260	14.5	0.04 - 0.09	2080	3×10^{-7}
WC	Cr_2O_3	SDL-1	260	13.9	0.03 - 0.08	2080	6×10^{-7}
Cr_2O_3	Cr_2O_3	SDL-1	260	13.4	0.05 - 0.08	2000	1×10^{-6}
Cr_2O_3	SiC/Al_2O_3	SDL-1	260	15.7	0.04 - 0.08	2000	1×10^{-6}
Si_3N_4	Si_3N_4 (b)	SDL-1	260	15.7	0.04 - 0.08	2000	1×10^{-6}
Si_3N_4	Si_3N_4	SDL-1	260	12.3	0.05 - 0.06	2000	3×10^{-6}
αSiC	αSiC	SAE10	20	17.0	0.04 - 0.08	2700	3×10^{-6}
Cr	Cast Iron	SDL-1	260	15.7	0.07 - 0.1	975	1×10^{-5}
Cr_3C_2	Cr_2O_3	SDL-1	260	14.0	0.13	2650	2×10^{-5}
Cr	Si_3N_4	SDL-1	260	12.3	0.14	975	1×10^{-4}
Cr	YPSZ	SDL-1	260	12.3	0.2 - 0.3	975	1×10^{-4}
YPSZ	YPSZ	SAE 10	20	12.3	0.13 - 0.16	1190	2×10^{-4}
YPSZ	YPSZ	None	540	12.3	0.3 - 0.6	1190	8×10^{-4}

(a) Typical actual diesel truck engine experience.
(b) Surface modified by Ceraprep process.

2.3 NEW CONCEPTS

Advanced Statistical Concepts of Fracture in Brittle Materials

C. A. Johnson and W. T. Tucker (General Electric Corporate Research and Development)

Objective/scope

The design and application of reliable load-bearing structural components from ceramic materials requires a detailed understanding of the statistical nature of fracture in brittle materials. The overall objective of this program is to advance the current understanding of fracture statistics, especially in the following three areas:

- Optimum testing plans and data analysis techniques.
- Consequences of time-dependent crack growth on the evolution of initial flaw distributions.
- Confidence and tolerance bounds on predictions that use the Weibull distribution function.

The studies are being carried out largely by analytical and computer simulation techniques. Actual fracture data are then used as appropriate to confirm and demonstrate the resulting data analysis techniques.

Technical progress

During the previous six month reporting period, work proceeded toward three milestones. The first milestone is a testing program to provide experimental strength data for demonstration of new methods for combining data, etc. The second is the development of Weibull estimators for combining data from multiple specimen sizes and geometries. The third milestone is an effort to develop methods for generating tolerance bounds on estimates of strengths. The following sub-sections describe the progress in each of these efforts.

1. Strength Testing

The strength testing was performed on boron-doped sintered SiC. Sintered SiC was chosen because it exhibits very clear fractographic markings when the grain size is small; its properties are reasonably homogeneous and isotropic; it is one of those ceramics being considered for use as a high temperature structural material; and it is readily available. Testing was done in six different bending configurations. The A, B and C specimen geometries of the MIL-STD-1942(MR) were used in both three and four-point bending using rolling pin fixture designs of the type specified by the testing standard. The specimen volumes vary over a factor of 64. The difference between three vs four point bending contributes another factor of approximately 10 to the effective volumes. Therefore, the data spans an effective volume range of 500-1000. Fracture data from large ranges of effective volume (or area, etc) are generally advantageous in confirming the

applicability of models (such as Weibull) and in estimating adjustable parameters and predicted behaviors.

Specimen preparation of the sintered SiC included: isopressing of spray dried beta SiC powder (with boron and carbon sintering additives) into billets with green dimensions of approximately 10 x 60 x 200 mm; sintering at approximately 2100 C in helium to a density of approximately 96 percent of theoretical; and slicing and surface grinding of specimens according to MIL-STD-1942(MR). Eight billets of SiC were used, all prepared and sintered side by side.

Six of the billets were for the size scaling study and two for a specimen location study. In the volume scaling study, each billet was cut into 6 type A, 6 type B and 6 type C specimens for a total of 108 specimens. They were divided such that 18 specimens were tested in each of the six testing configurations. Each group of 18 contained 3 specimens from each of the billets. Testing was done carefully to minimize testing errors and to maintain enough information to detect billet to billet variations, etc.

The remaining two billets were cut into a total of 30 type B specimens. The billet locations of the 30 specimens were recorded to allow a search for any location dependence of strength.

All 138 bend specimens have been tested (one specimen was accidently destroyed before testing). Analysis of the resulting strengths by analysis of variance techniques indicates no significant billet to billet variations. The following is a summary of the data when treated one geometry at a time:

Geometry	Number	Av Str (Mpa)	Std Dev (MPa)	Weibull m (Max Lik)	Sigma Zero (Mpa, mm)
3-pt A	18	388.11	33.36	14.57	347.58
4-pt A	17	312.85	34.83	9.43	342.91
3-pt B	18	350.96	31.12	12.20	373.13
4-pt B	18	302.74	29.34	11.24	388.09
3-pt C	18	325.65	21.69	16.39	374.12
4-pt C	18	283.78	22.35	14.48	391.18
4-pt B (all)	48	303.31	24.17	14.28	363.12

Low power (50X) stereo microscopy was used to identify the general location of each fracture initiating defect and to determine whether it was a surface, sub-surface, or edge related defect. Approximately 70 percent of the fracture origins were clearly associated with the as-ground tensile surfaces, 20 percent with chamfered edges, and 10 percent with sub-surface microstructural defects. Those specimens that failed from sub-surface and edge related flaws were uniformly spread through the spectrum of strengths within any one group and showed no tendency to be stronger or weaker than the average.

If all 137 specimens contain the same distribution (or distributions) of flaws, and if a model such as the Weibull model properly describes the strength variability and size scaling effects in this material, then the data

can be combined or pooled to yield better estimates of the adjustable parameters and to better confirm the validity of the model. The following section describes methods of combining data from multiple specimens sizes and geometries and then uses the SiC strength data to demonstrate the techniques.

2. Weibull Estimators for Combined Data

Problems involving estimation procedures (both point and interval) for strengths can be categorized according to the type of loading and the presence or absence of size scaling. The following four "classes" of problem have been considered:

I. Uniform tensile stress and single specimen size
II. Uniform tensile stress and multiple specimen sizes
III. Common load factor (k) and multiple specimen sizes
IV. Differing load factors and multiple specimen sizes

In each of these cases it is assumed that the Weibull distribution with a size term (volume, area or edge length) adequately describes the strength to failure according to:

$$P = 1 - e^{-\int(\sigma/\sigma_o)^m dV} \tag{1}$$

where P is the cumulative probability of failure, dV is the differential volume under a constant stress state, σ is the magnitude of that stress (at failure), m is the Weibull modulus, and σ_o is a normalizing parameter. Furthermore, it is assumed that the integral in Equation 1 can be evaluated to the form:

$$P = 1 - e^{-kV(\sigma_{max}/\sigma_o)^m} \tag{2}$$

where k is a dimensionless "load factor" describing the uniformity of the applied stress and σ_{max} is the maximum stress in the structure at the time of failure. For the case of uniform uniaxial tension (k=1), Equation 2 reduces to the form of the Weibull distribution commonly encountered in the statistical literature.

The two adjustable parameters of the distribution are derived from fracture data. For the first three "Classes" of problems described above, methods of estimating the parameters from fracture data are readily available in the literature. However, very few methods have been developed for estimating parameters for Class IV problems (1,2). During the previous reporting period, two Weibull "estimators" were developed to analyze Class IV problems of combined data. A Weibull estimator is a method or algorithm to analyze fracture data and estimate Weibull parameters. One of the new estimators is based on linear regression and the other on maximum likelihood. Both require successive approximation methods and are therefore best suited for computer analysis.

The linear regression method will be discussed and demonstrated using the SiC fracture data reviewed above. The results are plotted on Figure 1 as

log of the fracture stress vs log of the effective area (as discussed above, fractography determined that the fracture initiating defects were usually found on the specimen surface, therefore the size axis should be effective area).

The original data is included on Figure 1 as open symbols. The associated closed symbols are positioned by transforming each original effective area to the area that would be expected to yield the observed fracture strength at a probability level or quantile of 0.5. The transformation of an observed volume, V, and associated probability of failure, P, (as deduced from ranking) to a new volume, V' at a new probability of interest, P', is accomplished using:

$$V' = V \frac{\ln(1-P')}{\ln(1-P\ )} \tag{3}$$

This transform is easily derived from Equation 2 at constant stress. The transformed points of Figure 1 are all at the same probability of failure and are therefore more suitable for regression than the original data points. The linear regression line through the solid points can be used to estimate the Weibull modulus, m, since the slope of the line is an estimate of -1/m. The position of the line can be used to estimate the second parameter of the Weibull distribution, sigma zero. The two parallel lines bounding the linear regression line are estimates of the 0.1 and 0.9 quantiles. (The two parallel lines are NOT confidence bounds on estimates of the 0.5 quantile.)

The iterative nature of the linear regression estimator in Class IV problems arises because the effective areas (or volumes or lengths) of the specimens are functions of m for all loading configurations except uniform tension. Therefore the positions (and the relative positions) of both the open and closed points on Figure 1 shift horizontally as m is varied. The linear regression estimator begins by assuming an arbitrary estimate of m, then it positions and transforms the data, and performs linear regression to estimate an m. The assumed m is then iteratively modified until the assumed and estimated m's agree. An efficient algorithm for this process has been programmed that requires only four to eight iterations to determine m to greater than five significant digits for most data sets that have been analyzed.

In classical linear regression, the dependent variable is regressed on the independent variable, and the dependent variable generally contains larger random variations than the independent variable. When regression is performed on axes such as Figure 1, there is no clear resolution of which axis should be defined as independent. Therefore, the computer program carries out the iterative regression both ways. It is hoped that studies of the statistical properties of these estimators will differentiate which of the two regressions is better. It should be pointed out that for fracture data from a single specimens size and testing configuration (Class I problem), regression of the area on the fracture stress (A on S) is mathematically identical to conventional analysis on Weibull probability plots where probability is regressed on fracture stress. The regression of Figure 1 was done by regressing area on strength.

The second type of estimator developed for Class IV problems is a maximum likelihood method. The derivation parallels the derivation of a Class I estimator as published by Trustum and Jayatilaka (3) which in turn is based on maximum likelihood derivations such as those of Mann, Schafer, and Singpurwalla (4) and Lawless (5). The Class IV derivation must account for the loading factor, k, which is generally a function of the Weibull modulus. In order to evaluate the likelihood, the dependence of both k and dk/dm must be known as a function of m for every specimen geometry tested. The quantity defined as the "likelihood" is iteratively evaluated for various m values. The m value that yields the maximum for this quantity is the maximum likelihood estimate of m. The estimate of sigma zero can then be calculated without iteration. An efficient algorithm for the evaluation of maximum likelihood estimates for Class IV problems has been programmed that requires only five to ten iterations to determine m to greater than five significant digits for most data sets that have been analyzed.

A computer program to analyze fracture data and estimate Weibull parameters using the estimators and algorithms described above has been written in Fortran 77. During execution it reads a single data file with specimen geometries and strengths for each subgroup. In the current version, the program can handle uniaxial tension, 3-point and 4-point bending on rectangular or circular crossection specimens. Estimates can be done for all combinations of these geometries assuming volume, area or edge length distributed defects. The program estimates the Weibull parameters nine different ways and displays the results in table form as included in Table 1 (this table is for the SiC data discussed above). The nine estimates are displayed in nine blocks: three rows by three columns. The three rows correspond to different assumptions of defects types (volume, area or edge). The three columns correspond to different estimators (linear regression with strengths treated as the independent variable, linear regression with strength as the dependent variable, and maximum likelihood). Displayed within each block are the Weibull modulus, sigma zero (in both metric and english units), the standard error of estimate (standard deviation of the vertical displacements from the predicted line when plotted as Figure 1), and the number of iterations to reach the estimates (the original assumed m to start each iteration was five).

The standard error of estimate, SEE, can be used in class four problems to supplement fractography in determining the type of defects responsible for failure. For instance, if failure is controlled by volume distributed defects, then the SEE generated by assuming volume defects should statistically be smaller than that from area or edge length distributed defects. In the case of the results displayed in Table 1, it can be seen that the SEE's from analysis as area and edge defects are similar to each other but smaller than those from volume defects. This combined with fractographic observations suggest that scaling by surface area is preferable to volume or edge length. Similar agreement of the SEE with fractography has been seen in other experimental data sets as well as in numerous simulated data sets.

The computer program for data analysis and graphics display has been written on a DEC VAX 782, but the non-graphics portion of the code was easily ported to an IBM PC/AT (with co-processor) running Microsoft Fortran Version 4.00. No changes were necessary to the code. Using the SiC data, Table 1

was perfectly reproduced (every digit identical to that generated on the VAX). Execution time (including file read and CRT printout) on the PC/AT was approximately six seconds.

The emphasis on computational efficiency in the estimators described above arises because numerous evaluations are needed in simulation studies that are planned both for the study of statistical properties of the estimators and as one of the means of estimating confidence and tolerance bounds on Class IV problems.

3. Confidence and Tolerance Bounds.

During this reporting period the maximum likelihood and likelihood ratio methodologies have been extended to obtain confidence and tolerance bounds for Class III problems. When there is only a single test volume condition and a single component volume condition, conditional integration methods (5,6) are exact (7). For other Class III problems the integration method may also be exact (this is currently under investigation). The methodology to obtain confidence and tolerance bounds for Class IV problems is yet to be developed. Therefore, the limits on maximum likelihood analyses such as those included in Table 1 cannot be given at this time.

Recent studies indicate that employing the integration method may be useful in practical applications for Class I-III problems. Shown in Figure 2 are the results of analyzing a simulated data set consisting of 10 tensile specimens tested in each of three volumes. The solid lines are the maximum likelihood estimated 0.5 quantile (upper) and 0.05 quantile (lower) behaviors. The solid circle data points fall on curved lines that define the upper and lower bounds of the 95 percent tolerance limits on the 0.05 quantile line. For this data set, the true line (not shown) is within the confidence bounds (this should hold true, at a particular size and the given confidence level, 95 percent of the time in the long run).

Work has also begun in studying the use of likelihood ratio methodologies in obtaining confidence and tolerance bounds. Both methodologies will be validated via simulation studies and their theoretical ties investigated in the more general Class III problem. It turns out, at least for location-scale and certain other families, that there is an exact relationship (7,8) between the two methodologies. The likelihood ratio method just gives a numerical approximation to the integration approach.

Unfortunately, straightforward application of linear regression methods has not shown promise in obtaining acceptable confidence and tolerance bounds and, at this point, is not being further pursued.

References

1. C.A. Johnson and S. Prochazka, "Investigation of Ceramics for High Temperature Turbine Component," Final Report, Contract N62269-76-0243, June, 1977.

2. S.B. Batdorf and G. Sines, "Combining Data for Improved Weibull Parameter Estimation," J. Am. Ceram. Soc., 63, 214-218, (1980).

3. K. Trustrum and A. De S. Jayatilaka, "On Estimating the Weibull Modulus for a Brittle Material," J. Mater. Sci., 14, 1080-1084 (1979).

4. N.R. Mann, R. E. Schafer, and N. D. Singpurwalla, Methods for Statistical Analysis of Reliability and Life Data, John Wiley & Sons, New York, 1974.

5. J.F. Lawless, "Construction of Tolerance Bounds for the Extreme-Value and Weibull Distributions," Technometrics, 17, 255-261, 1975.

6. R.A. Fisher, "Two New Properties of Mathematical Likelihood," Proc. Royal Society A, 144, 285-307, 1934.

7. O. Barndorff-Nielson, "On a Formula for the Distribution of the Maximum Likelihood Estimator," Biometrika, 70, 343-365, 1983.

8. D. V. Hinkley, "Likelihood Inference about Location and Scale Parameters," Biometrika, 65, 253-261, 1978.

Status of Milestones

The three milestones due to be completed at the end of the third year of the program are on schedule.

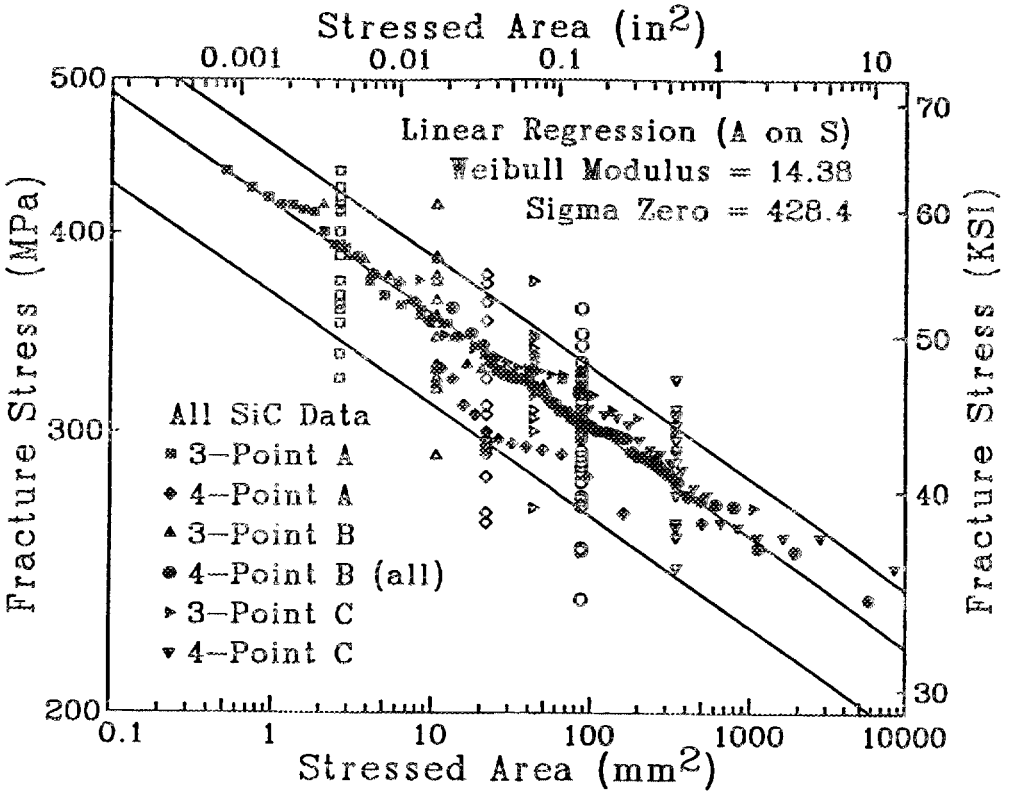

FIGURE 1: Log stress vs. log effective area for SiC fracture data.

	Linear Regression	Linear Regression	Maximum Likelihood
For Volume Defects:	(V on S)	(S on V)	
Weibull Modulus	16.178	19.304	16.429
Sigma Zero (MPa, mm)	354.215	344.107	361.614
Sigma Zero (psi, in)	28282.8	30263.5	29137.9
Std Err of Ln Stress	0.05396	0.04794	0.05811
Number of Iterations	6	6	7
For Area Defects:	(A on S)	(S on A)	
Weibull Modulus	14.380	15.667	14.216
Sigma Zero (MPa, mm)	428.381	417.188	432.146
Sigma Zero (psi, in)	39708.5	40119.5	39851.1
Std Err of Ln Stress	0.03596	0.03377	0.03682
Number of Iterations	6	6	7
For Edge Defects:	(L on S)	(S on L)	
Weibull Modulus	12.547	13.592	12.130
Sigma Zero (MPa, mm)	423.608	413.556	425.311
Sigma Zero (psi, in)	47536.8	47333.2	47309.2
Std Err of Ln Stress	0.03394	0.03231	0.03602
Number of Iterations	6	6	7

TABLE 1: Computer output from analysis of 137 SiC specimens.

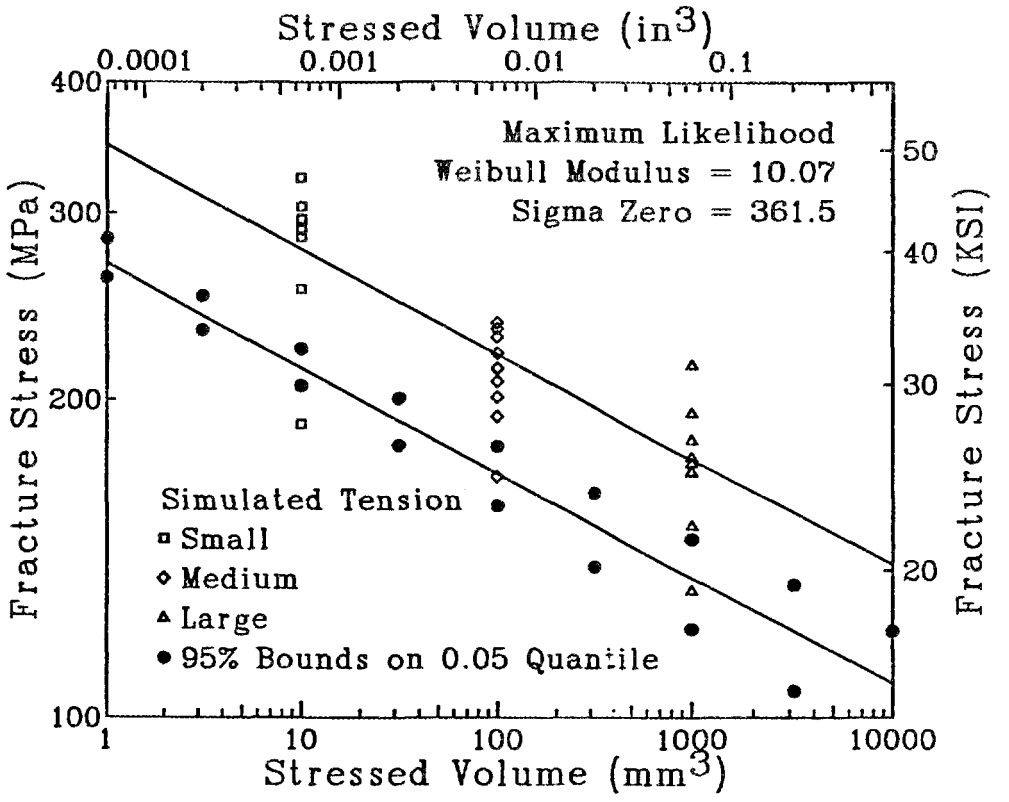

FIGURE 2: Log stress vs. log effective volume for simulated tensile data.

3.0 DATA BASE AND LIFE PREDICTION

INTRODUCTION

This portion of the project is identified as project element 3 within the work breakdown structure (WBS). It contains five subelements, including (1) Structural Qualification, (2) Time-Dependent Behavior, (3) Environmental Effects, (4) Fracture Mechanics, and (5) Nondestructive Evaluation (NDE) Development. Research conducted during this period includes activities in subelements (1), (2), and (3). Work in the Structural Qualification subelement includes proof testing, correlations with NDE results and microstructure, and application to components. Work in the Time-Dependent Behavior subelement includes studies of fatigue and creep in structural ceramics at high temperatures. Research in the Environmental Effects subelement includes study of the long-term effects of oxidation, corrosion, and erosion on the mechanical properties and microstructures of structural ceramics.

The research content of the Data Base and Life Prediction project element includes (1) experimental life testing and microstructural analysis of Si_3N_4 and SiC ceramics, (2) time-temperature strength dependence of Si_3N_4 ceramics, and (3) static fatigue behavior of PSZ ceramics.

Major objectives of research in the Data Base and Life Prediction project element are understanding and application of predictive models for structural ceramic mechanical reliability, measurement techniques for long-term mechanical property behavior in structural ceramics, and physical understanding of time-dependent mechanical failure. Success in meeting these objectives will provide U.S. companies with the tools needed for accurately predicting the mechanical reliability of ceramic heat engine components, including the effects of applied stress, time, temperature, and atmosphere on the critical ceramic properties.

3.1 STRUCTURAL QUALIFICATION

Microstructural Analysis of Structural Ceramics

B.J. Hockey and S.M. Wiederhorn
(National Bureau of Standards)

Objective/Scope

The objective of this part of the program is to identify mechanisms of failure in structural ceramics subjected to mechanical loads in various environments. Of particular interest is the damage that accumulates in structural ceramics as a consequence of high temperature exposure to environments and stresses normally present in heat engines.

Recent studies of high temperature failure of the non-oxide ceramics intended for use for heat engines indicates that for long term usage, damage accumulation will be the primary cause of specimen failure. Mechanical defects, even if present in these materials, are healed or removed by high temperature exposure so that the original defects have little influence on long term lifetime at elevated temperature. In this situation, lifetime can be determined by characterizing the nature of the damage and rate of damage accumulation in the material at elevated temperatures. In most structural ceramics of current interest, the fine grain size and chemical complexity of the microstructure precludes the use of routine characterization methods. Hence, there is a clear need for analytical transmission electron microscopy studies as an adjunct to the mechanical testing of these materials for high temperature applications.

In this project, the creep and creep-rupture behavior of several ceramic materials will be correlated with microstructural damage that occurs as a function of creep strain and rupture time. Materials to be studied include: sialons; hot-pressed silicon nitride; and sintered silicon carbide. This project will be coordinated with WBS 3.4.1.3, Tensile Creep Testing, with the ultimate goal of developing a test methodology for assuring the reliability of structural ceramics for high temperature applications.

Technical Highlights

During this period, TEM studies on siliconized silicon carbide (SOHIO KX-01) were extended to include samples that were deformed under either uniaxial tension or compression at 1300°C. These studies were aimed at determining differences in both the deformation and damage accumulation processes that exist between tension and compressive loading. Moreover, because creep curves (log $\dot{\varepsilon}$ vs log σ) for both forms of loading show an abrupt change in stress dependence (from ~4 at lower stresses to 11-14 at higher stresses),[1] the TEM studies were also arrived at determining this reason for this change in behavior.

In agreement with the earlier results - based primarily on observations on samples tested in bending - tensile deformation at

---

[1] See 3.4 Standard Tensile Test Development (NBS); this period.

1300°C invariably results in cavitation within the Si phase, which in the extreme results in the development of penetrating creep cracks, whereas compressive creep at 1300°C does not. In this regard, optical, SEM, and TEM examination of a compression sample deformed to ~1.4% strain showed no evidence for cavity formation or for microcrack formation; in tension, macro-sized cracks formation or failure typically occurred at strains below 1%. Nevertheless, aside from the formation of cavities in the silicon phase during tensile deformation (which will be described below), tensile and compressive deformation otherwise resulted in similar changes within both the silicon carbide and silicon phases. Under low stress conditions, corresponding to a stress exponent of ~4, concentric dislocation loops are found within SiC grains in the vicinity of SiC to SiC junctions. As illustrated in Figure 1, these junctions appear to be sites where adjacent SiC grains are at least tenuously self-bonded and the presence of dislocation loops (not found in the as-received state) suggests localized stress development and deformation occurs at these junctions in both tension and compression. Under these same conditions, i.e. $\dot{\epsilon} \sim \sigma^4$, evidence for deformation induced dislocations and twins are also found within the silicon phase in both tensile and compressive samples. Despite the fact that tensile creep under conditions where $\dot{\epsilon} \sim \sigma^4$ applies results in limited numbers of fully isolated cavities within the Si phase while compressive creep does not, there appeared to be no significant difference in the type or density of deformation induced defects present within either the silicon or silicon carbide phases after tensile or compressive creep.

Results from tensile and compressive creep samples tested at higher stress levels, where $\dot{\epsilon} \sim \sigma^{11-14}$ applies, could also be similarly described, again except for the occurrence of extensive cavitation in the Si phase of tensile deformed samples. Under these conditions, many of the SiC grains contain relatively high densities of dislocations which, unlike those found in the as-received state, appear confined to their slip planes (generally (0001)). The arrays of dislocations, moreover, are not just localized at SiC to SiC junctions but tend to span the entire grain, Fig. 2. This result indicates that at the high applied stress levels ($\gtrsim$ 100 MPa in tension, $\gtrsim$ 200 MPa in compression) thermally assisted dislocation slip occurs to cause at least limited shape changes in the SiC grains. As might be expected, the silicon phase in these samples also shows evidence for enhanced deformation in that it contains not only higher densities of dislocations and twins, Fig. 3, but a more uniform distribution of these defects compared to that found in samples crept at lower stress levels.

Examination of the 1300°C tensile creep samples together with a 1375°C tensile sample allowed further observations on the cavitation process. As previously reported, cavitation within the near-surface regions occurs preferentially within the thin Si layers separating adjacent SiC grains (i.e. two-grain junctions), while within the interior cavitation also involves the depletion of larger Si pockets separating multiple SiC grains. Despite numerous observations on both types of cavities, no direct correlation could be made between the presence of deformation induced defects (dislocations or twins) within either the Si phase or adjacent SiC grains and cavities. Thus while dislocation annihilation at Si to SiC interfaces or twin-twin

intersections within the Si phase may aid in cavity nucleation, there is no indication that these line or planar defects are directly involved in the growth of cavities. Instead, cavity growth appears governed by rapid diffusion processes. Moreover, many of the cavities - particularly those produced within the near surface regions of creep samples - are bounded by an amorphous layer. As illustrated in Fig. 4, this amorphous region separating the cavity from the remaining Si phase is relatively thick, and as such is quite distinct from the extremely thin amorphous layer found along the edges of holes in ion milled silicon. Furthermore, qualitative electron energy loss (EELS) analysis indicates significant concentrations of oxygen and carbon in addition to silicon. Further study of cavities developed well into the interior of tensile (or bend) creep samples or that develop in samples crept in inert atmospheres is required, however, before speculating on the possible role of oxidation and/or carbon dissolution in the cavitation process.

Status of Milestones

To date, all milestones have been met or are on target. To a large extent, the TEM analysis of creep deformation during uniaxial tensile and compressive creep as well as flexural creep is completed, and a paper describing the results is being drafted. We also anticipate completing a study of the cavitation process very soon, and this will result in another paper on cavitation and creep rupture of siliconized silicon carbide.

Publications: None.

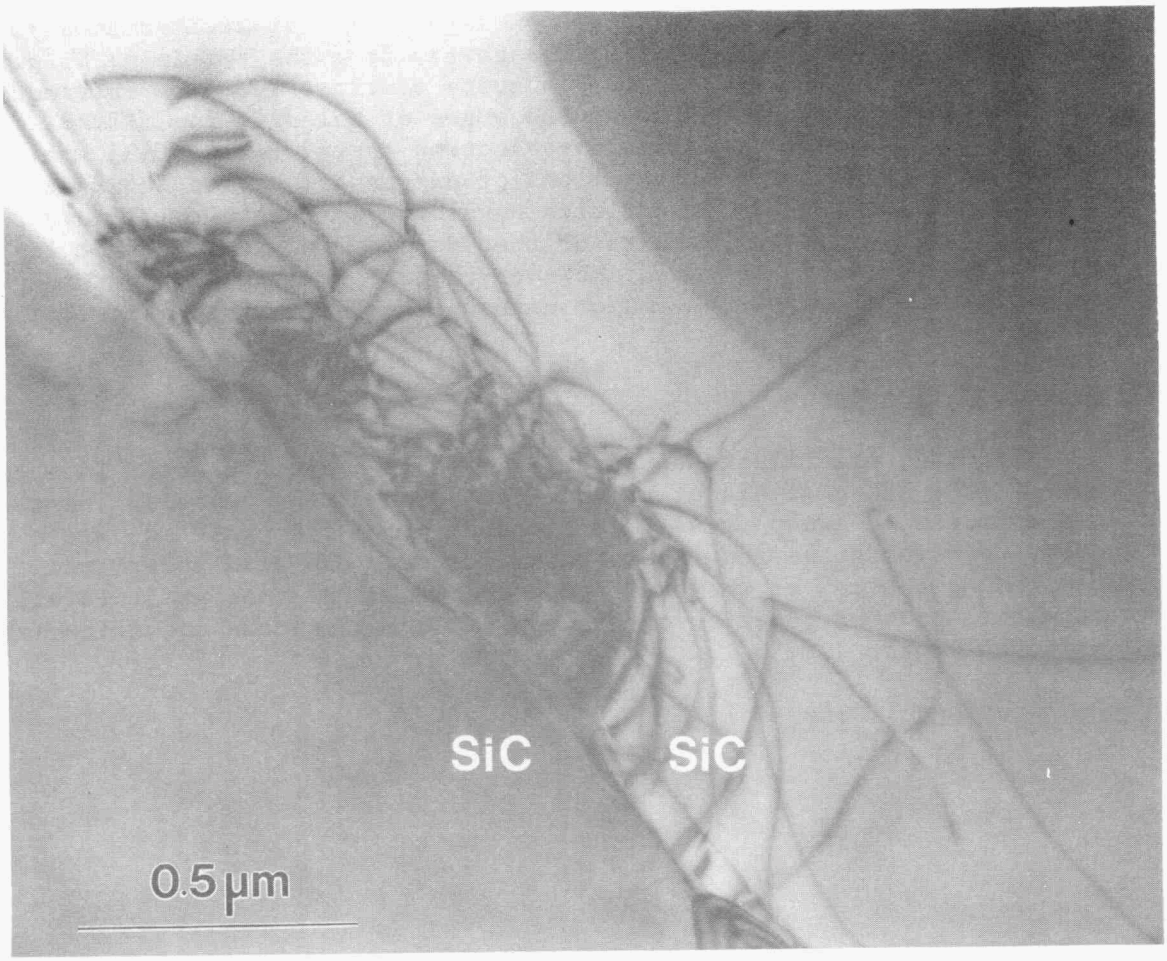

Fig. 1. Concentric dislocation loops produced in SiC grain at SiC to SiC interface. Localized deformation of contact asperities between adjacent creep at 1300°C under low stress (low strain rate) conditions.

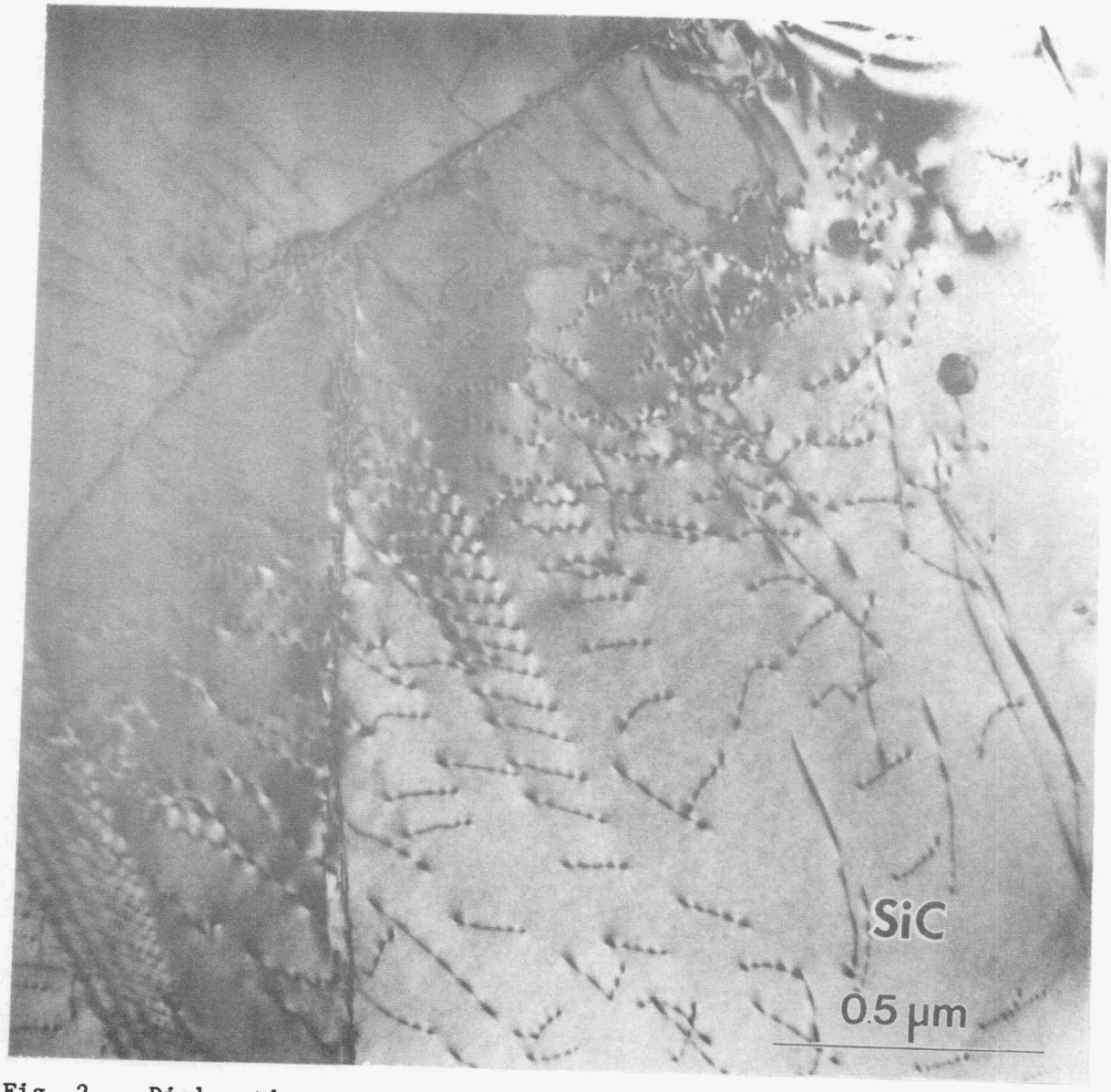

Fig. 2. Dislocation arrays situated on (0001) basal planes in α-SiC grains. Under high stress (high strain rate) conditions, tensile and compressive creep at 1300°C results in the deformation of SiC grains.

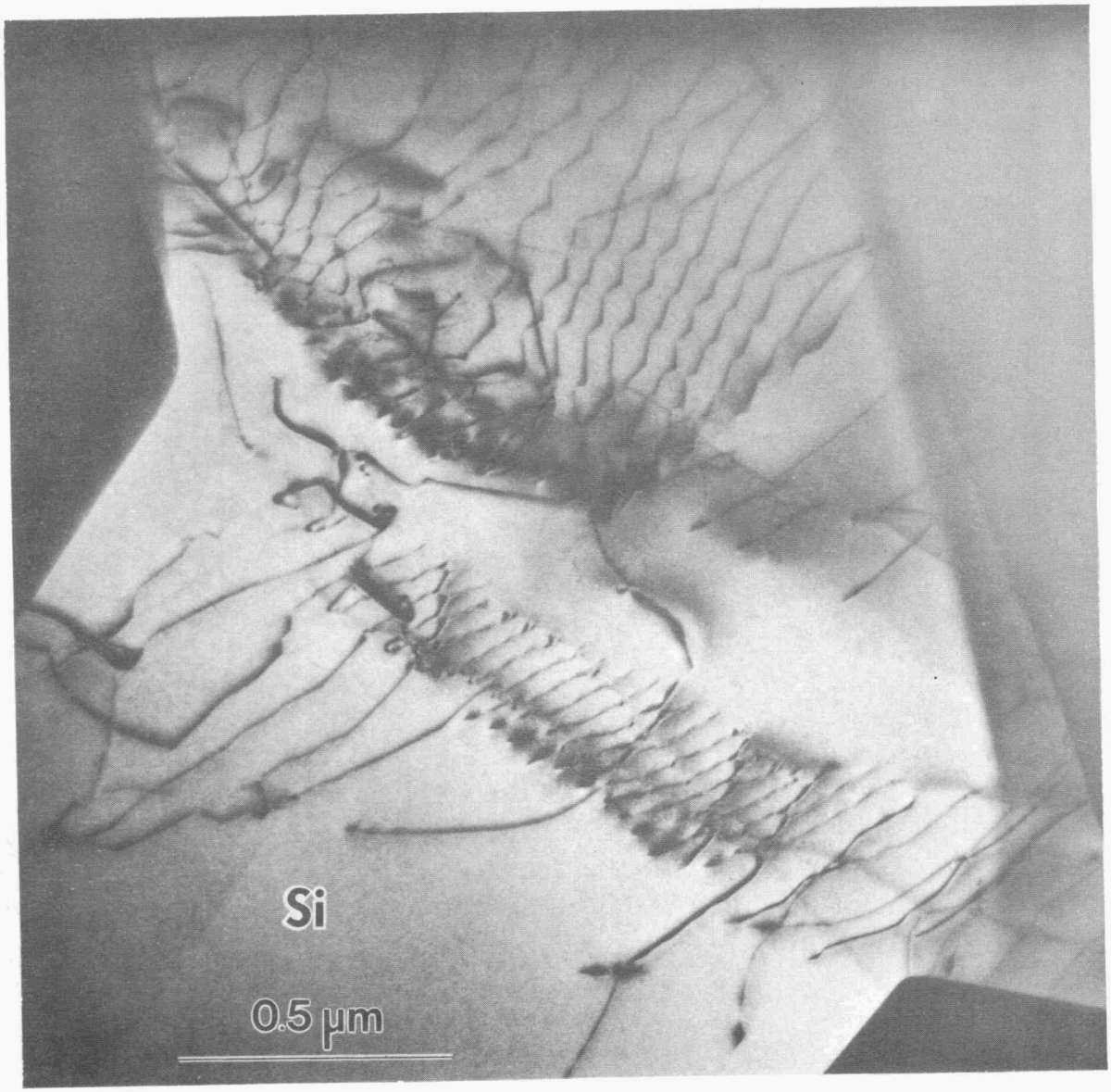

Fig. 3. High density of dislocations, largely in the form of dislocation networks, within the Si phase after compressive creep at 1300°C. Typically, much higher densities of dislocations and twins are found within the Si phase after tensile or compressive creep under high stress (high strain rate) conditions than under low stress (low strain rate).

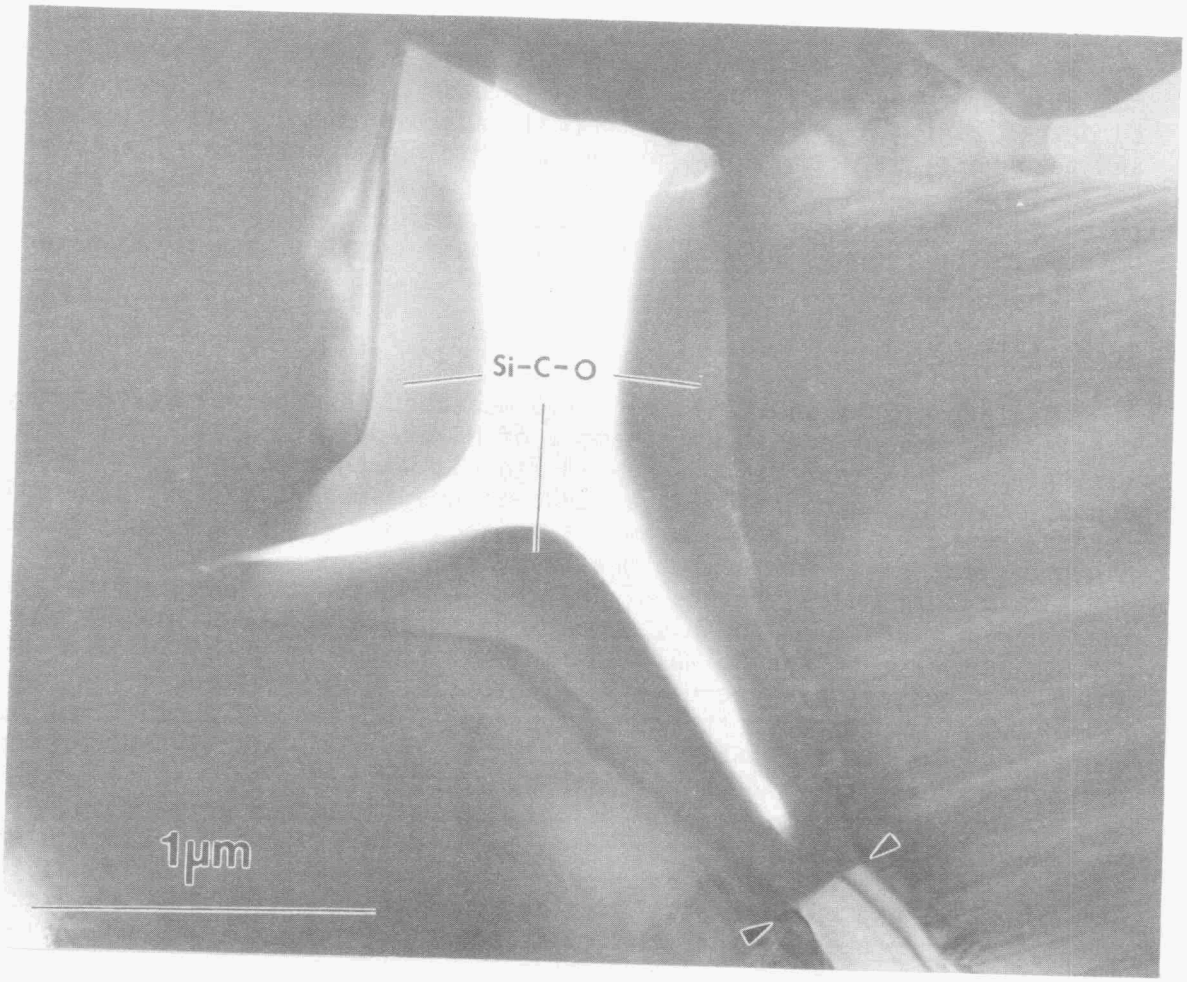

Fig. 4. Cavity produced in Si phase at multiple grain junction after tensile creep at 1375~C. Cavity is bound by amorphous silicon phase, which from EELS is found to contain significant concentrations of carbon and oxygen. Note sharp interface between amorphous phase and crystalline Si within two grain junction (arrowed).

Physical Properties of Structural Ceramics

R. K. Williams and R. S. Graves (Oak Ridge National Laboratory)

Objective/scope

The structural ceramics presently considered for use in advanced heat engine applications usually contain more than one phase and several components. The thermal conductivities of these materials are low relative to metals, and this, along with thermal expansion plus fracture strength and toughness, is a prime factor in determining suitability of a given ceramic for a particular advanced engine component. The purpose of this research is to develop an improved understanding of the factors that determine the thermal conductivities of these complex structural materials at high temperatures.

Technical progress

Taylor, Groot, and Larimore[1] have measured the thermal diffusivity, density and specific heat of a sample of MS grade partially stabilized zirconia. Their results are show in Fig. 1, which also includes thermal conductivity measurements made at ORNL on the same lot of PSZ. The difference between the two measurements is about 8%, which is within the combined uncertainties of the two measurements.

The two principal points of interest are that the results indicate that photon transport probably becomes detectable at about 1000 K, and the data do not extrapolate to zero thermal resistance at absolute zero. The 300-1000 K results vary about as expected (T^{-1}), and the deviation seen at higher temperatures corresponds to the appearance of a new heat transport mechanism. We are currently making direct thermal conductivity measurements to compare the two results at high temperatures.

In the absence of magnetic effects or point defect scattering,[2] the intermediate temperature thermal resistance data (λ^{-1}) for most insulators extrapolates to a value close to zero at absolute zero. This is not the case for PSZ, and point-defect scattering of phonons by oxygen vacancies and Mg^{+2} ions probably cause the large positive intercept shown in Fig 1.

References

1. R. E. Taylor, H. Groot, and J. Larimore, *Thermal Conductivity of Partially Stabilized Zirconia - A Report to Martin Marietta Energy Systems (ORNL)*, TPRL 649, Thermophysical Properties Research Laboratory, School of Mechanical Engineering, Purdue University (July 1987).

2. R. K. Williams, R. S. Graves, M. A. Janney, T. N. Tiegs, and D. W. Yarbrough, "The Effects of Cr_2O_3 and Fe_2O_3 Additions on the Thermal Conductivity of Al_2O_3," *J. Appl. Phys.* **61**(10), 4894 (May 1987).

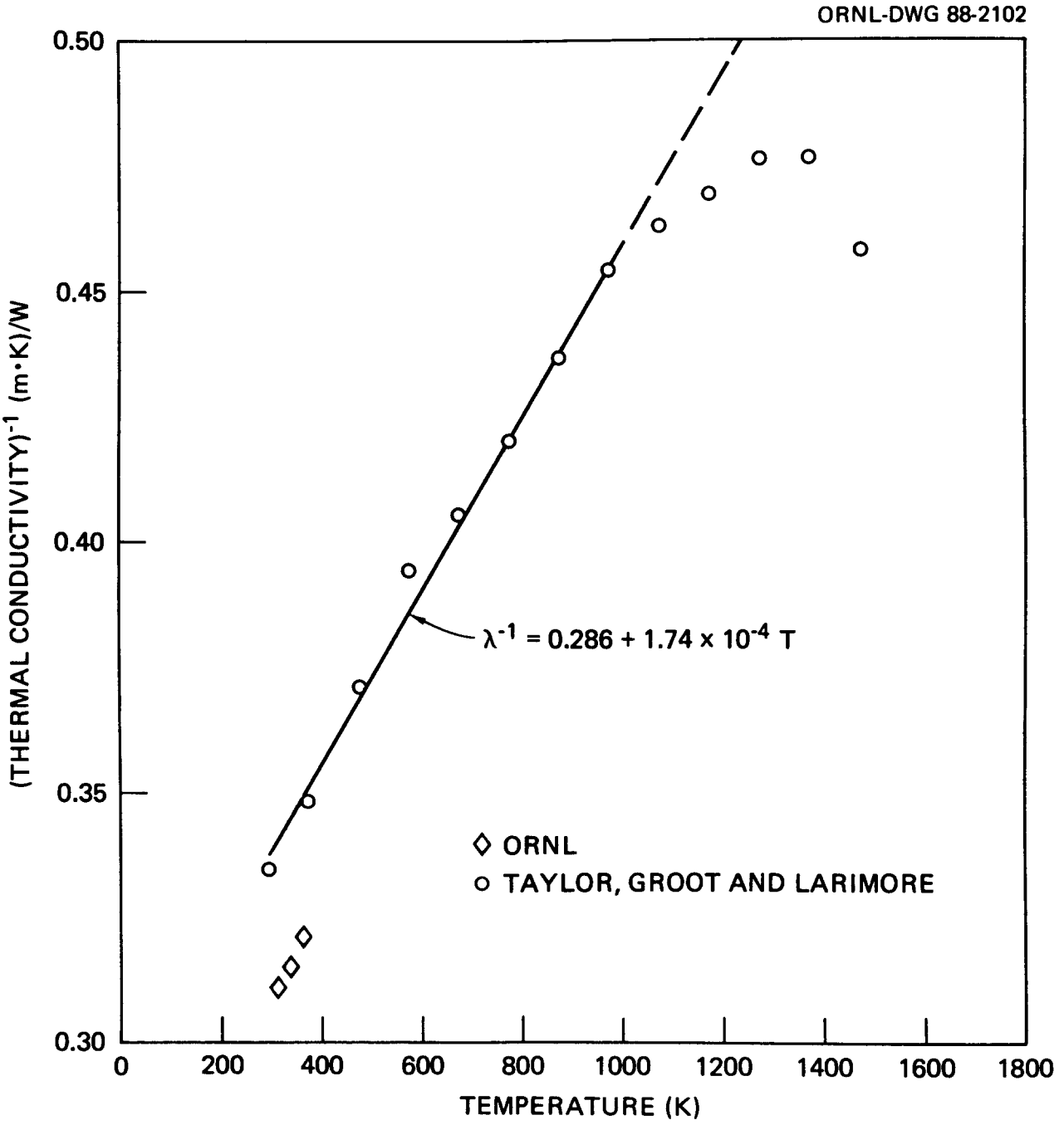
ORNL-DWG 88-2102
0.50
0.45
0.40
0.35
0.30
(THERMAL CONDUCTIVITY)$^{-1}$ (m•K)/W
0
200
400
600
800
1000
1200
1400
1600
1800
TEMPERATURE (K)
$\lambda^{-1} = 0.286 + 1.74 \times 10^{-4}$ T
◇ ORNL
○ TAYLOR, GROOT AND LARIMORE

Fig. 1.

Effect of Translucence of Engineering Ceramics on Heat Transfer in Diesel Engines

Syed Wahiduzzaman and Thomas Morel (Integral Technologies Incorporated)

Objective/scope

Ceramic materials are being used as thermal barrier materials, separating the engine metal substructure from the convective and radiative heat fluxes originating in the combustion gases. The heat transfer through the ceramic layer to the substructure will be increased by any translucence, which would allow a part of the radiation heat flux to pass through the barrier material. To quantify the effect of translucence of engineering ceramics on the heat transfer in diesel engines, Integral Technologies has conducted analytical studies using detailed computer codes which describe a realistic engine thermal environment including gas-to-wall heat fluxes, as well as the combined radiation/ conduction heat transfer through a thermal barrier layer. A detailed parametric study was carried out in which the following parameters were varied, and their effect on heat barrier effectiveness was studied: 1) material absorption coefficient, 2) material conductivity, and 3) material thickness. An analysis of the results yielded bounds on critical properties, beyond which there is a reason for concern about this effect. Also, suggestions were made for methods to control any adverse effects.

In the experimental portion of this work, data will be acquired describing the radiation properties of several engineering ceramics. The objective is to obtain the specific information needed for the analytical part of this work. This includes the absorption coefficient, scattering albedo and surface reflectivities of the materials. In order to obtain the data, specialized samples of the materials will be fabricated. Measurements of transmissivity will be obtained, and from these the desired radiation properties will be deduced using an analytical data reduction technique.

Technical progress

A technical report was prepared and sent to ORNL. This report covers the analytical work -- development of a transient heat radiation model for translucent ceramics and its application in parametric studies aimed at quantification of the effects of heat radiation from diesel flame on the effectiveness of ceramic heat barriers in engine applications.

Liaison was maintained with organizations preparing samples for the experimental portion of this program. Samples were received from ORNL and Caterpillar, others are expected from Cummins Engine Company.

Status of Milestones

Milestone 11a, model formulation, was reached in March, 1986. Milestone 11b, model development, was completed in August, 1986. Milestone 11c, material property search, was completed in December, 1986. Milestone 11e, definition of material samples, was completed in October, 1986. A report was completed and delivered to ORNL in May, 1987.

Publications

A report was submitted to ORNL on March 31, 1987. In addition, a presentation was given at a workshop:

T. Morel, "Analysis of Heat Transfer in LHR Engines: Translucence Effects in Ceramics," Workshop on Coatings for Advanced Heat Engines, Maine Maritime Academy, Castine, Maine, July 27-30, 1987.

3.2 TIME-DEPENDENT BEHAVIOR

Characterization of Transformation-Toughened Ceramics
Jeffrey J. Swab (Army Materials Technology Laboratory)

Objective/scope

Because of their unusual combination of properties, transformation toughened zirconias (TTZ) are leading candidates for cylinder liners, piston caps, head plates, valve seats and other components for the adiabatic diesel engine. These materials are age-hardened ceramic alloy systems and as such, they are likely to be susceptible to overaging and loss of strength after long times at high temperatures (i.e., close to the age-hardening temperatures). Accordingly, a task was initiated to define the extent and magnitude of the overaging (if any) at engine operating temperatures (1000-1200C) and the resulting impact on material performance.

It is also well known that Y-TZP's undergo a phenomenon at low temperatures (200-400C) which leads to decreases in strength and fracture toughness and that this phenomenon is accelerated by the presence of water. As a result, a preliminary study to try and determine the effects of this phenomenon has been included in this task.

Technical progress

The "HIP'ed" TZP from Koransha was manufactured in a reducing atmosphere, which resulted in the material having a charcoal grey color. Gross and Swain (1) confirm this coloring. Upon heat treatment at 1000C the material changed color to off white. It is believed that this is due to oxidation of the material.

The reduction during HIP'ing has an adverse affect on the high temperature performance of the material. However, this performance can be improved 2 to 3 fold by heat treating the specimens in air at 1000C for 100 hours, Figure 1. It is believed that oxygen non-stoichiometry, caused by HIP'ing in reducing atmosphere, is the direct cause of the difference in high temperature performance of the material, before and after heat treatments. Additional tests must be completed to determine the extent of oxygen non-stoichiometry.

Preliminary fracture toughness data has been obtained on the first seven (7) TZP materials. The toughness was determined by indenting the specimen with a Vickers indent and then stressing to failure in four-point bending (2). Prior to indentation all bars were lapped to a finish of 2 microinch RMS or better on one of their 4 by 50 mm faces. The value for Klc was then calculated using the following equation:

$$Klc = n_{\nu}^{R}(E/H)^{1/8}(\sigma P^{1/3})^{3/4}$$

where $n = 0.59 \pm 0.12$
E = Elastic Modulus
H = Hardness
σ = As Indented Strength
P = Indentation Load

Because each TZP material has differences in its microstructure it was decided that Klc would be determined over a range of indentation loads, Figures 2-4.

Some general trends can be seen from these figures. First, although the Hitachi TZP has excellent strength it has the lowest fracture toughness. Toshiba and NGK have the highest values of Klc and the toughness of the sintered and HIP'ed TZP from Koransha tends to increase with the length of heat treatment.

Fractography of the fracture toughness samples is now underway to determine the type of crack produced by the indent. Detailed microstructure evaluation of all TZP's has also begun. Once more information is available relationships between microstructure and properties will be drawn.

Also during this period an examination of the high temperature fast fracture of four (4) of the best TZP's has been started. The four TZP's are Hitachi "1985", NGK-Locke Z-191 and the Sintered and HIP'ed versions from Koransha. These materials were selected based on their as-received strength and ability to retain that strength after high temperature aging. Flexure strength will be measured at 700, 850 and 1000C. Table 1 lists the results to date.

TABLE 1

	25C	700C
NGK Z-191		
Characteristic MOR (MPa)	873	428
Weibull Number	15.2	7.1
Mean MOR (MPa)	884	400
Standard Deviation	65	55
Hitachi "1985"		
Characteristic MOR (MPa)	1169	438
Weibull Number	3.6	12.2
Mean MOR (MPa)	1045	463
Standard Deviation	265	42

Koransha HIP'ed

Characteristic MOR (MPa)	1261	669
Weibull Number	8.8	3.9
Mean MOR (MPa)	1192	595
Standard Deviation	140	107

Koransha Sintered

Characteristic MOR (MPa)	640	329
Weibull Number	9.5	12.8
Mean MOR (MPa)	608	316
Standard Deviation	75	27

NOTE: 30 samples were used in the 25C strength measurement but only 10 will be used at the other temperatures.

It can be seen that for all TZP's the fracture strength at 700C was approximately 50% of the room temperature strength.

Status of Milestones:

The in-house technical report, authored by Lise Schioler, is now available.

Communications/Visitors/Travel:

Attended the 89th Annual Meeting and Exposition of the American Ceramic Society and presented two papers.

Traveled to Oak Ridge National Laboratory, 21 July 1987, for program review and presentation of technical results and planning of future work.

Visited by Dr. Ed Lilley and Dr. Gulio Rossi of Norton, Co. Discussed the possibility of a co-operative effort in the area of Zirconia. The paper work has been started to initiate this effort but it will take time to work out the details.

Visited Prof. Gary Leatherman at Worcester Polytechnic Institute. Prof. Leatherman is doing the detailed microstructure evaluation of the TZP materials under the terms of a Short Term Analytical Services (STAS) program. This has just started and there is no data available at this time.

Problems Encountered:

Due to a severe shortage of in-house personnel in the area of metallography, detailed microstructural evaluation of the TZP materials has been delayed.

Publications:

Swab, J.J., "Evaluation of Advanced Transformation Toughened Zirconia", Proceedings of the Twenty-Fourth Automotive Technology Development Contractors' Coordination Meeting, Dearborn, MI, Oct 27-30, 1986, Published by the Society of Automotive Engineers, Warrendale, PA, July 1987.

Swab, J.J., "Evaluation of Commercially Available Transformation Toughened Zirconias", ADVANCED STRUCTURAL CERAMICS, ed, P.F. Becher, M.V. Swain, and S. Somiya, Materials Research Society Symposia Proceedings, Vol 78, p137-146, 1987.

REFERENCES:

1. Gross, V. and Swain, M.V., "Mechanical Properties and Microstructure of Sintered and Hot Isostatically Pressed Yttria-Partially-Stabilised Zirconia (Y-PSZ)", J. Austr. Ceram. Soc., 22, [1] (1986) p1-12.

2. Chantikul, P., Anstis, G.R., Lawn, B.R. and Marshall, D.B., "A Critical Evaluation of Indentation Techniques for Measuring Fracture Toughness: II", J. Am. Ceram. Soc., 64 [9] 1981, p539-543.

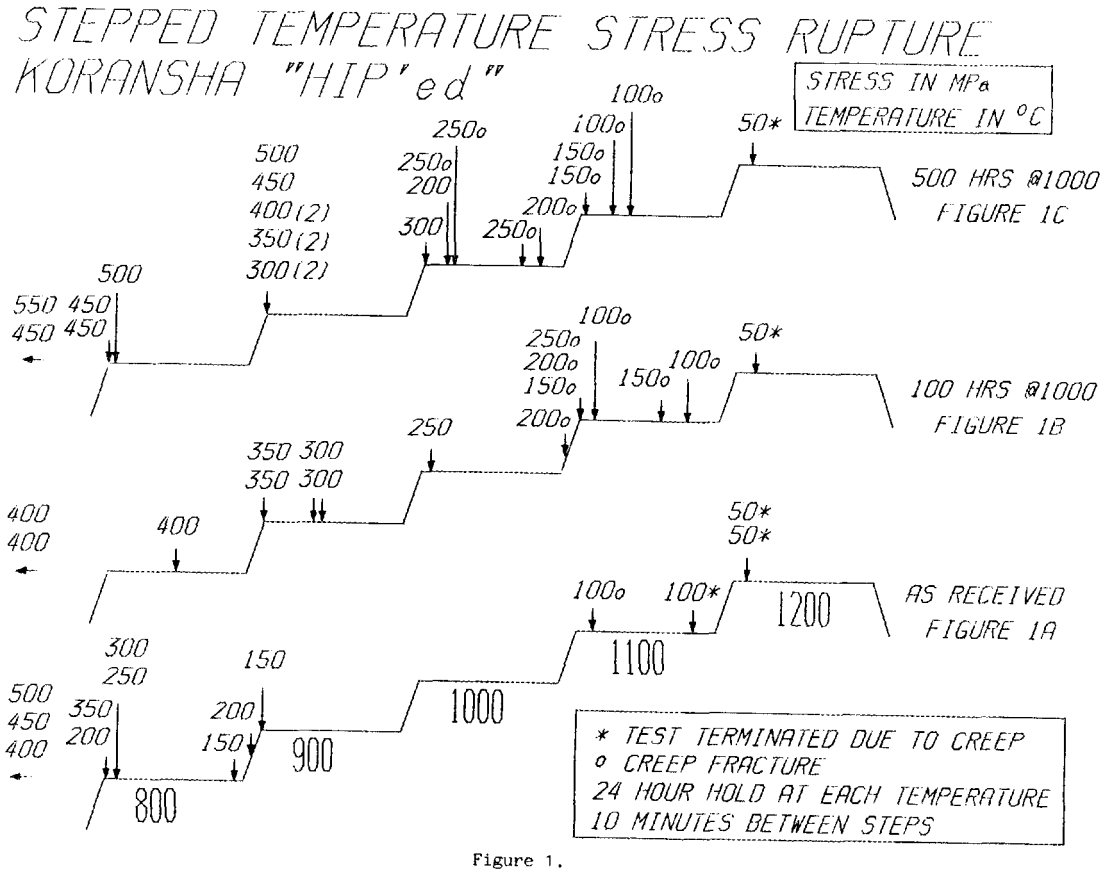

Figure 1.

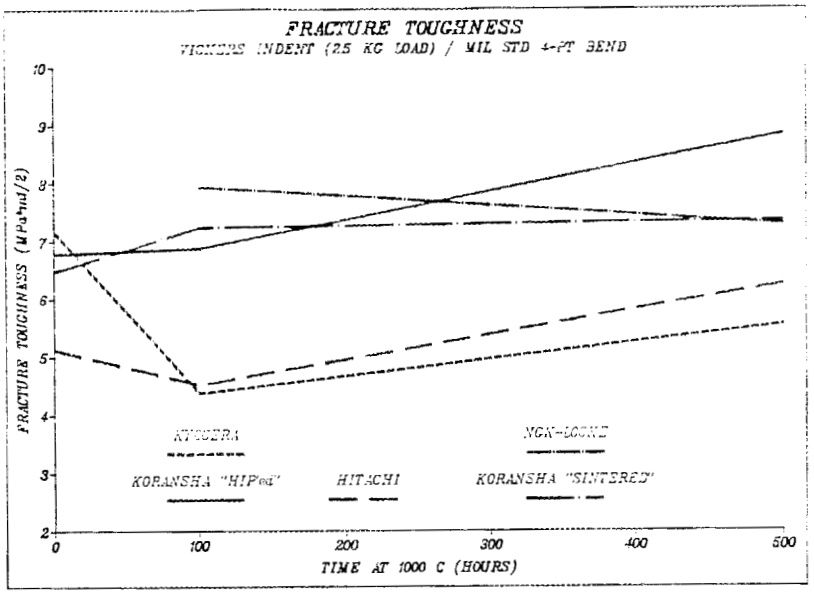

Figure 2

Figure 3

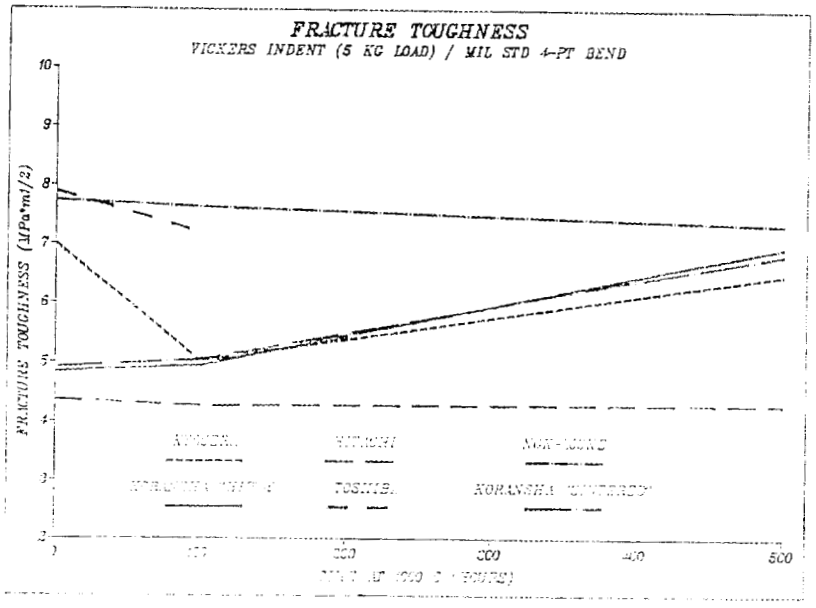

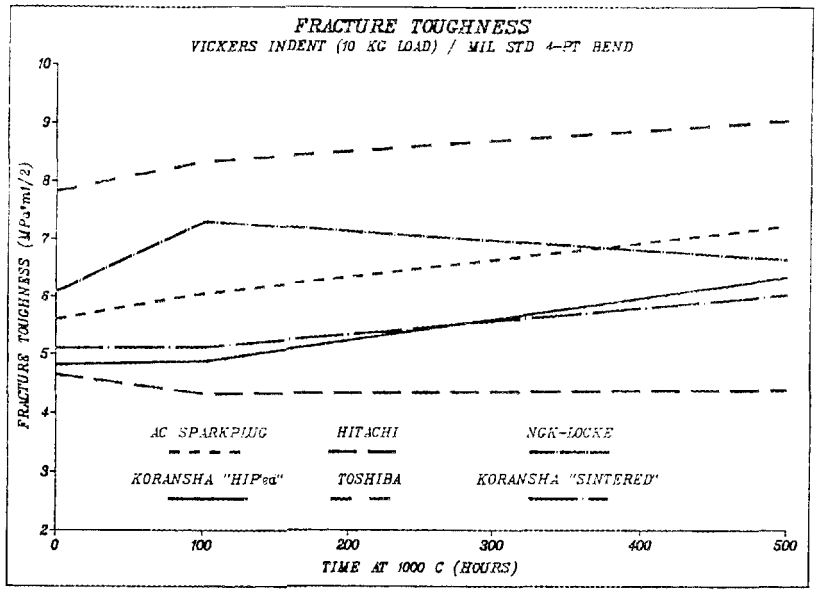
FRACTURE TOUGHNESS
VICKERS INDENT (10 KG LOAD) / MIL STD 4-PT BEND
FRACTURE TOUGHNESS (MPa*m1/2)
10
9
8
7
6
5
4
3
2
0
100
200
300
400
500
TIME AT 1000 C (HOURS)
AC SPARKPLUG
HITACHI
NGK-LOCKE
KORANSHA "HIPed"
TOSHIBA
KORANSHA "SINTERED"

Figure 4.

Fracture Behavior of Toughened Ceramics

P. F. Becher, T. N. Tiegs and W. H. Warwick (Oak Ridge National Laboratory)

Objective/scope

Because of their excellent toughness, oxide ceramics such as partially stabilized zirconia (PSZ), dispersion-toughened alumina (DTA), and whisker-reinforced ceramics are prime candidates for many diesel engine components. The enhanced toughness of the PSZ and DTA materials is thought to be due to a stress-induced transformation (of the dispersed tetragonal ZrO_2 phase) which requires additional energy for catastrophic fracture to occur. However, these materials are still susceptible to slow crack growth and thus strength degradation. Also there is limited evidence that at temperatures above 700°C, time-dependent aging effects can reduce the concentration of the phase involved in the transformation process, leading to significant losses in toughness and strength. It is essential that mechanisms responsible for both the slow crack growth and aging behavior be well understood. Similarly, the toughening behavior in whisker-reinforced ceramics and their high-temperature performance must be evaluated to develop materials for particular applications.

In response to these needs, studies have been initiated to examine toughening and fatigue properties of transformation-toughened and whisker-reinforced materials. Particular emphasis has been placed on understanding the effect of microstructure on processes responsible for time-dependent variations in toughness and high-temperature strength. In addition, fundamental insight into the slow crack growth behavior associated with these materials is being obtained.

Technical progress

Previous studies have examined the critical fracture strength and long-term strength behavior at elevated temperatures in air of fine grained (1-2 μm) alumina reinforced with 20 vol % silicon carbide whiskers (ARCO). The long-term strength studies involved subjecting flexure bars to an applied stress equal to two-thirds the critical fracture strength at the temperature of interest for selected time periods and then increasing the stress until fracture occurred. It was found that under these conditions [interrupted static fatigue IFS)], the retained fracture strengths increased with increasing time of exposure to the applied stress in the range of 800 to 1100°C. At 1200°C, the retained fracture strengths decreased.

These tests were conducted at a fixed applied stress/critical fracture strength ratio of 2:3 and tests were initiated to examine the effects of various applied stress levels. These studies can be used to describe the lifetime versus applied stress behavior and define the mechanisms leading to strength changes. This is especially critical in the temperature range of 1100 to 1200°C where a transition from stable/improved retained strengths to strength degradation with time was observed in the earlier IFS-type tests.

Flexure bars of the alumina-20 vol % silicon carbide whisker composite materials were prepared and surface finished with a 180-grit resinoid bonded diamond surface grinding wheel as in previous studies. Samples were tested in four-point flexure using inner and outer spans of 6.35 and 19.05 mm under constant applied stress conditions in air to determine times to failure at selected applied stresses and temperatures. These latter tests can be used in combination with the previous IFS results to determine the constant stress (static fatigue/creep rupture) response of materials at any desired temperature. At elevated temperatures, such fatigue behavior can be a result of slow crack growth by diffusion, crack blunting by diffusion or surface reactions, or crack generation/growth by creep cavitation. Typically, diffusive crack growth occurs when the creep strain rate exhibits a linear dependence on the applied stress. Cavitation processes generally are observed when the creep strain rate exhibits a (applied stress)n dependence where n equals 2 or greater.

The results for the fatigue behavior (from both IFS and static fatigue/creep rupture tests) of the alumina-20 vol % silicon carbide whisker composites are illustrated in Fig. 1. The results are given as a log-log plot of the time to failure as a function of the applied stress for samples tested at 1200 and 1100°C. The salient features of these plots are (1) the change in slope of the log stress-log time plots for 1100 and 1200°C and (2) the transition from stress dependent time to failure to a region where failure does not occur at 1100°C. The latter feature observed at 1100°C is a result of crack blunting which occurs when the applied stress is decreased below a critical level. The results at 1100°C suggest that slow crack growth by diffusion may be occurring above this critical stress level. Thus, the critical stress level will be defined by the competitive interaction of diffusive crack growth and crack blunting.

The greater applied stress sensitivity of the time to failures at 1200°C versus that at 1100°C is seen to be a result of the initiation of creep cavitation processes at 1200°C. Previous results showed that crack generation which will be associated with cavitation and cavity growth and coalescence does occur in this material at 1200°C and above.[1] Also, separate studies show that the steady state creep strain rates exhibit a (applied stress)n dependence with n equal to 2. Such creep behavior can be attributed to grain boundary sliding which is not fully accommodated, which leads to cavitation. Thus, the change in the applied stress-life time behavior at 1200°C and above apparently is a result of the initiation of creep cavitation and crack generation processes.

Discussions were held with Prof. R. F. Davis of North Carolina State University who has conducted compressive creep studies of SiC whisker-reinforced (20 vol %) mullite and mullite samples which were provided by ORNL. The commercial mullite powders used to fabricate these composites are known to contain an excess of silica, and thus the composites contain a glassy phase at the matrix grain boundaries and whisker-matrix interfaces. Our previous studies had shown that a comparable SiC whisker-reinforced mullite composite retained their fracture strength in four-point flexure to temperatures of at least 1200°C in air. At 1400°C, the

ORNL-DWG 88-2121

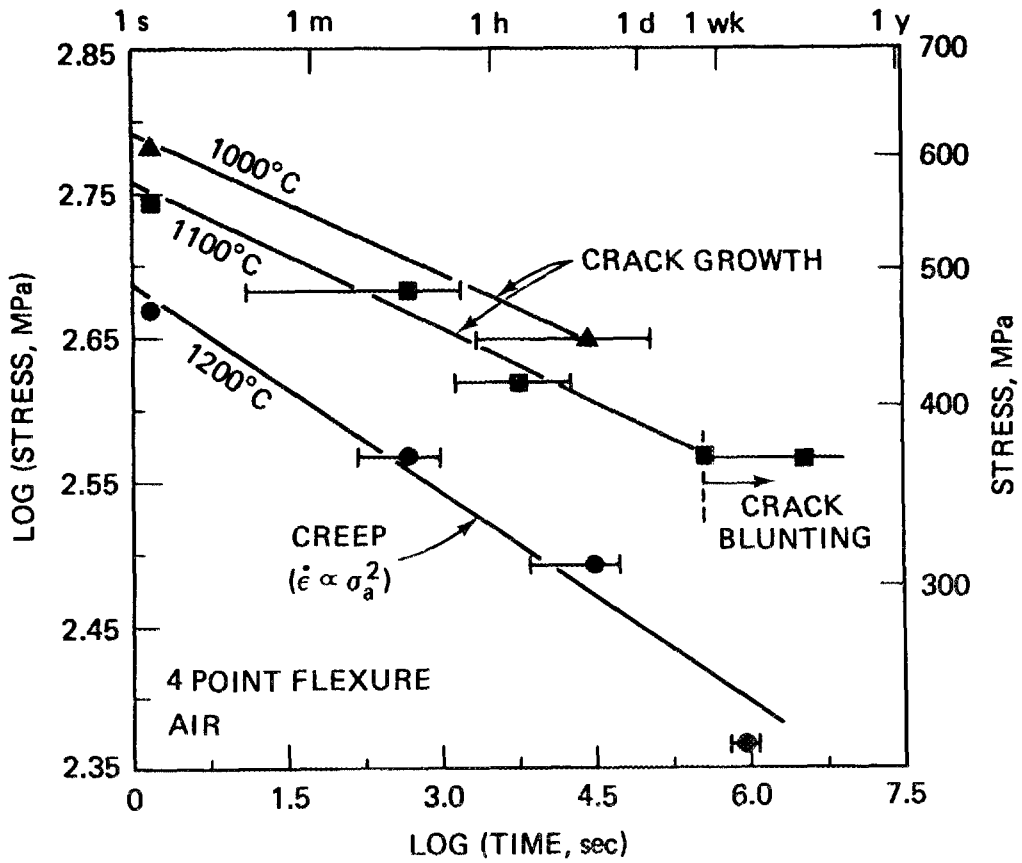

Fig. 1. Time to failure dependence on the applied stress level for alumina-20 vol % silicon carbide whisker composites tested in air at 1100 and 1200°C. Note at 1100°C there is a transition from slow crack growth behavior (i.e., increase in time to failure with decrease in stress) to crack blunting (i.e., indicated by no failure). At 1200°C, the composite exhibits time to failure dependence on the applied stress which is greater than that observed at 1100°C. This is consistent with observations of the initiation of creep cavitation and crack generation at 1200°C.

fracture strength is significantly decreased. Similar decreases in the flexural fracture strength of SiC whisker-reinforced (20 vol %) aluminas which occurred above 1100°C were shown to be related to the onset of creep and creep damage processes.[1] Similar behavior was thus expected in the mullite-based composite above 1200°C, and the presence of glassy grain boundary and interface phase(s) would be expected to promote creep. Note that mullite ceramics which are essentially free of glassy grain boundary phases exhibit the greatest creep resistance observed in oxide ceramics.[2]

Preliminary results by Prof. Davis show that the creep deformation in the SiC whisker-reinforced mullite is a result of viscous flow of the glassy phase at temperatures of ~1175°C to ~1425°C in argon. Creep at ~1360°C results in the formation of cavities at whisker-matrix and

whisker-whisker interfaces containing the glassy phase; however, above this temperature cavities are not observed, as the viscosity of the glass phase is quite low. The creep resistance is improved by whisker reinforcement as compared to the unreinforced mullite. Based on independent studies by Prof. Davis, elimination of the glass phase will provide an increase in the creep resistance of the mullite composites.

Status of milestones

On schedule.

Publications

1. P. F. Becher and T. N. Tiegs, "Temperature Dependence of Strengthening by Whisker Reinforcement: SiC Whisker Reinforced Alumina in Air," *J. Am. Ceram. Soc.*, in press (1987).

2. T. N. Tiegs and P. F. Becher, "Thermal Shock Behavior of an Alumina-SiC Whisker Composite," *J. Am. Ceram. Soc.* **70**(5), C-109–11 (1987).

References

1. P. F. Becher and T. N. Tiegs, "Temperature Dependence of Strengthening by Whisker Reinforcement: SiC Whisker Reinforced Alumina in Air," *J. Am. Ceram. Soc.*, in press (1987).
2. P. A. Lessing, R. S. Gordon, and K. S. Mazdiyasni, "Creep of Polycrystalline Mullite," *J. Am. Ceram. Soc.* **58**(3-4), 149 (1975).

Cyclic Fatigue of Toughened Ceramics

K. C. Liu and C. R. Brinkman (Oak Ridge National Laboratory)

Objective/scope

The objective of this task activity is to develop, design, fabricate, and demonstrate the capability to perform tension-tension dynamic fatigue testing on a uniaxially-loaded ceramic specimen at elevated temperatures.

Three areas of research have been identified as the main thrust of this task: (1) design, fabrication, and demonstration of a load train column that truly aligns with the line of specimen loading; (2) development of a simple specimen grip that can effectively link the load train and test specimen without complicating the specimen geometry and, hence, minimize the cost of the test specimen; and (3) design and analysis of a specimen for tensile cyclic fatigue testing.

Technical progress

Exploratory tensile cyclic fatigue testing has been successfully conducted for two commercial ceramics tested at elevated temperatures as high as 1200°C. A first ceramic material selected for this experiment is a commercial grade of sintered silicon nitride (SNW-1000) obtained from GTE Wesgo Division. A second is a MgO partially stabilized zirconia (MgO-PSZ, TS Grade) engineered by NILCRA of Australia for maximum thermal shock resistance.

Specimen and experimental details

Buttonhead tensile specimens as shown in Fig. 1 were used. Si_3N_4 specimens were made from near-shape blanks and MgO-PSZ specimens from solid round bars. The finished specimens have a uniform gage-section of 6.3 mm (0.25 in.) in diameter by 25.4 mm (1 in.) gage length. The gage surface was finished by diamond-wheel grinding along the longitudinal axis to 16 rms; no polishing was given to the gage surface. Specimens were heated by an induction heater as described in a previous report.[1] Specimen temperature was measured by a two-color pyrometer. Strain was measured directly on the gage-section of the specimens using a mechanical extensometer capable of accurate strain measurement at high temperatures. Tensile loading was applied at a ramp rate of 70 MPa (10 ksi) per second. Cyclic loading was controlled by a triangular wave form at a rate of 0.5 Hz, as shown in wave form I of Fig. 2. Some specimens were tested using wave form II schematically illustrated in Fig. 2 also. This method of testing, called "coaxing," is used in metal alloy fatigue testing to raise the fatigue endurance limit. The specimen is cycled from low stress to high stress loading in multiple steps.

Test results of Si_3N_4 (GTE Wesgo SNW - 1000)

A complete summary of test results for this material is given in Table 1 and data are plotted in Fig. 3. Closed symbols used in Fig. 3 indicate the lifetimes of specimens subjected to the constant-amplitude cyclic loading (wave form I). Open symbols indicate the terminal points of

YP-4559

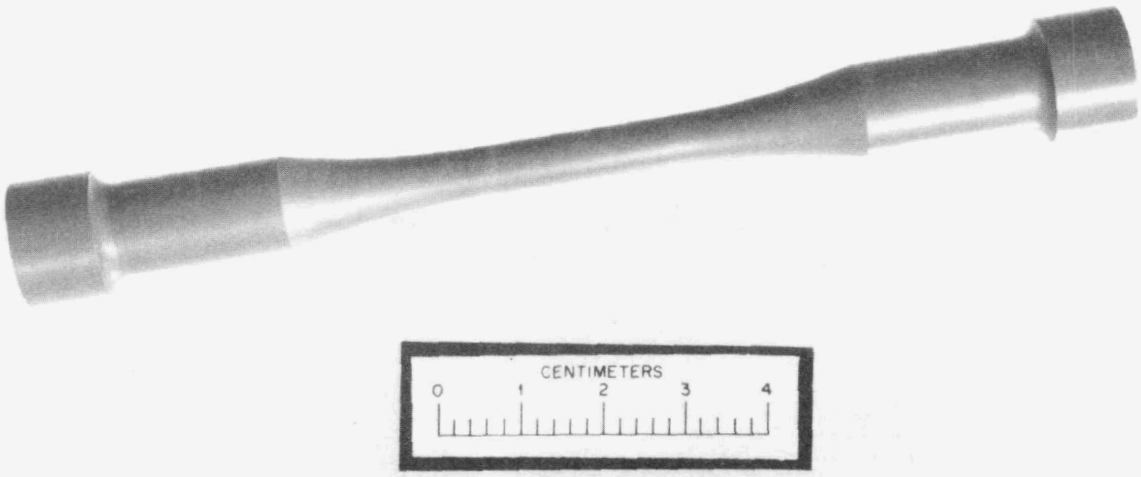

Fig. 1. Buttonhead tensile fatigue specimens of Si_3N_4.

ORNL-DWG 88-2114

Wave Form I:
Constant Amplitude Loading

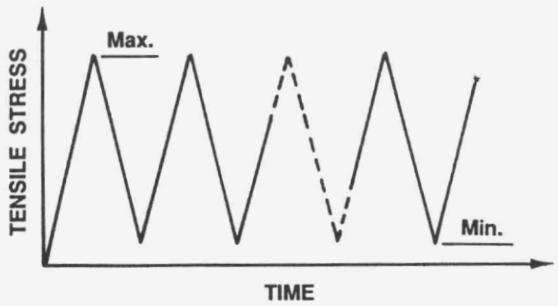

Stress Ratio (R = min./max. stress) = 0.1
Frequency, f = 0.5 Hz

Wave Form II:
Increasing Multiple-Step Loading
(coaxing)

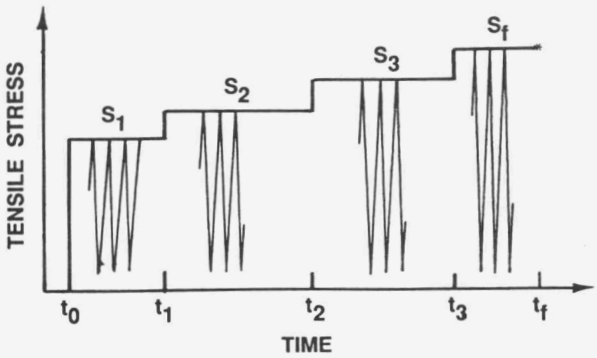

Fig. 2. Wave forms used in tension/tension cyclic fatigue testing.

Table 1. Results of tensile and cyclic fatigue tests of GTE Wesgo SNW-1000 silicon nitride at 1000, 1100, and 1200°C

Specimen number	Modulus of elasticity, GPa (10^6 psi)	Tensile strength, MPa (ksi)	Cyclic stress to failure, MPa (ksi)	Intermediate cyclic stress, MPa (ksi)	Cycles at intermediate cyclic loading	Cycles to failure	Total test time (h)
			Test Temperature at 1000°C				
13	265 (38.4)	450 (65.3)				1	0
14		462 (67.0)				1	0
15	246 (35.6)	502 (72.8)				1	0
16			457 (66.3)			1,107	0.6
17	252 (36.5)			439 (63.6)	40,700	-	-
				456 (66.1)	14,810	-	-
			474 (68.3)			102	30.9
GTE		641 (92.9)[a]					
			Test Temperature at 1100°C				
1	-	446 (64.7)				1	0
2	217 (31.5)	449 (65.2)[b]				1	0
3	-		348 (50.5)			115,138	64.0
4	248 (35.9)		404 (58.7)			301,025	167.2
5	236 (34.2)		418 (60.6)			6	0
6	229 (33.2)		402 (58.3)			2,054	1.1
GTE		~527 (76.4)[a]					
			Test Temperature at 1200°C				
7	-	240 (34.8)				1	0
8	147 (21.3)	255 (37)				1	0
9	165 (23.9)		204 (29.6)			22	0
10	-	195 (28.3)				1	0
11				142 (20.6)	46,100	-	-
				184 (26.7)	89,864	-	-
				199 (28.8)	141,361	-	-
			213 (30.8)			24,340	167.6
12			183 (26.5)			179	0.1
18			141 (20.5)			620	0.3
19			142 (20.5)			54,438	30.2
GTE		413 (59.9)[a]					

[a]Flexural strength determined by four-point-bend tests; data obtained from GTE Publication 5M-86.

[b]Indicates the stress at the gage section. The average stress on the fracture surface that occurred outside the gage section was 397 MPa (57.6 ksi).

ORNL-DWG 88-2115

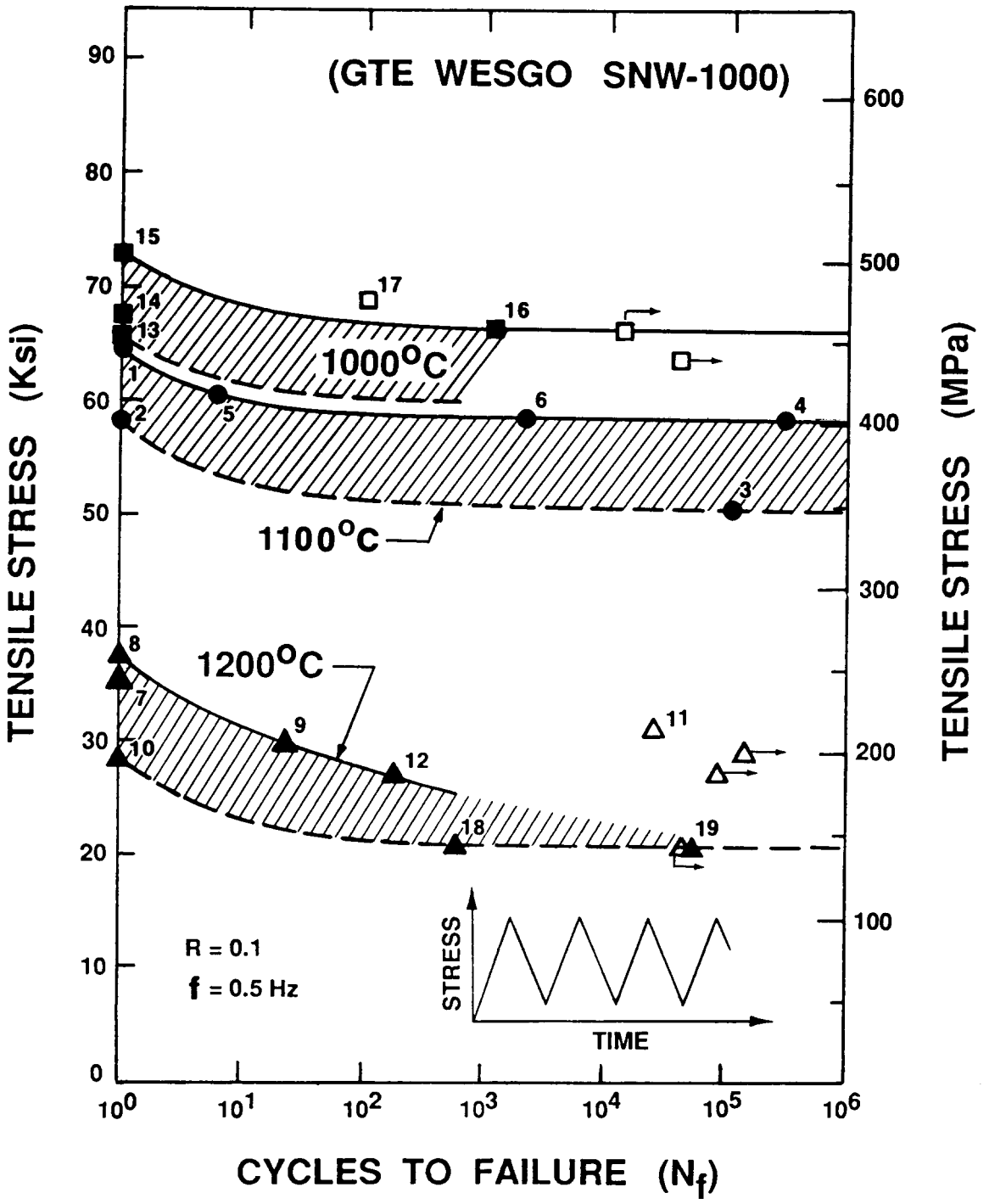

Fig. 3. Tension/tension cyclic fatigue of silicon nitride (GTE Wesgo, SNW-1000) at elevated temperatures. Tensile fast fracture tests are considered to have failed in a single cycle as shown in the diagram.

each intermediate cyclic loading segment of wave form II. The arrowhead attached to the open symbols indicates that failure had not occurred when the test was terminated at the indicated conditions. Tensile fast fractures were considered to have occurred in a single cycle and therefore the data were plotted accordingly. To best describe the fatigue behavior of this material, the test data for each temperature group are bracketed by two fatigue curves, as shown in Fig. 3. The solid line approximates the upper bound and the broken line the lower bound, separated by a scatter band. Practically speaking, all the data points fall closely on the boundaries of the scatter bands, except specimens 11 and 17, which fall above the upper bound. Reasons for the high fatigue performance in these specimens are not well known at this time. Therefore, detailed discussions will be deferred until the ongoing microstructural studies are completed. A plausible explanation is that these two specimens were fatigue tested in multiple steps using wave form II, whereas others were fatigue tested using wave form I. Available data indicate that the fatigue curves for 1000 and 1100°C are very flat in the high cycle range. However, the behavior beyond the test data remains undefined and might be modified by environmental interaction. The fatigue behavior at 1200°C are clearly different from that at the lower temperatures. Reasons for the differences will be discussed in the appropriate section that follows.

Comparisons are made between the average ORNL-measured tensile strength values and the GTE-measured flexural strength values determined by four-point bending, as shown in Fig. 4. The differences between the two sets of data are about 26, 18, and 44% at 1000, 1100, and 1200°C, respectively. The values of elastic moduli tabulated in Table 1 were determined from the stress-strain curves which reveal that this material behaves virtually elastic at temperatures below 1100°C, but it exhibits some plasticity at 1200°C at stress levels above 150 MPa (21.8 ksi).

Figure 4 further indicates that the tensile strength and fatigue behavior of this silicon nitride are strongly dependent on temperatures above 1000°C. Below 1000°C the tensile strength is believed to be nearly constant based on recent room temperature test results obtained by North Carolina A & T University, also reported in a later section of this report. The decrease in tensile strength is rather moderate, i.e., about 10%, as the temperature increases to 1100°C. However, there was a sharp drop-off in tensile strength, i.e., about 50%, as the temperature increased to 1200°C. The influence of temperature on the fatigue behavior is very similar to that described above because the fatigue curves were determined relative to the tensile strength.

Plastic strain rachetting (accumulation of incremental plasticity) was observed when specimen 9 was cycled to 165 MPa (23.9 ksi), which clearly exceeded the elastic range. To avoid cyclic failure by the strain rachetting, specimen 11 was cycled initially to 142 MPa (20.6 ksi), slightly below the approximate elastic stress range. There was perceptible accumulation of the plastic strain by rachetting at the beginning of the stress cycling, but the specimen showed shakedown behavior, i.e., apparent hardening, before it completed 46,100 cycles. This behavior is very similar to that observed in cyclic fatigue of many metal alloys, generally referred to as strain hardening. The cyclic stress was then increased to 184 MPa (26.7 ksi) and cycled for another 89,864 cycles

ORNL-DWG 88-2116

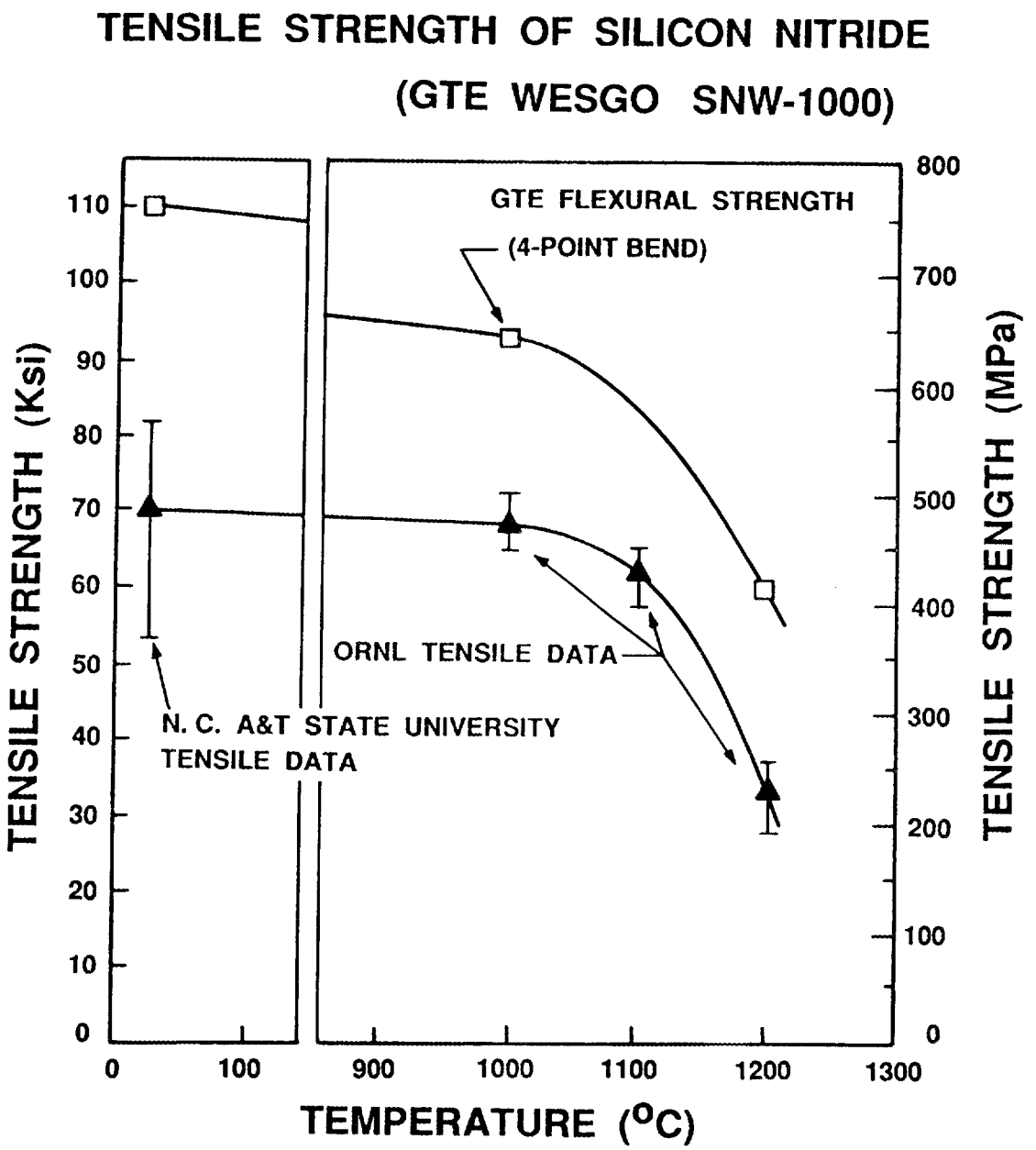

Fig. 4. Comparison of four-point-bend flexure strength and uniaxially determined tensile strength of Si_3N_4 at room and elevated temperatures.

without fatigue failure. During the second step loading, some plastic strain rachetting was again noticed during the first few hundred cycles. A similar observation was again made when the cyclic load was increased to 199 MPa (28.8 ksi), which was about equal to the lowest tensile fracture strength among the three tensile tests at 1200°C. After cycling for 141,361 cycles with no apparent indication of imminent fatigue failure, the cyclic stress was raised to 213 MPa (30.8 ksi). The specimen finally failed at 24,340 cycles. We speculate that the high fatigue performance exhibited by specimen 11 could be the result of the strain hardening or coaxing effect. Efforts to reproduce the result of specimen 11 were made using specimens 18 and 19, but were futile in each case as the data points indicated in Fig. 3. In summary, this is an obvious reason why the fatigue of this material at 1200°C behaves differently from that at the lower temperatures.

Specimen 17 was tested in three ascending steps. The initial cyclic loading was selected not to exceed the lowest tensile fracture strength among specimens 13, 14, and 15, tested at 1000°C. After successfully passing the first 40,000 cycles, the load was increased to about the fracture strength of specimen 14 and run for another 15,000 cycles. It finally failed in fatigue at cycle 102 and 474 MPa (68.3 ksi). Hardly any rachetting behavior was noticed in this case because the test was run at 1000°C. Nevertheless, specimen 17 exhibits higher fatigue performance than the upper-bound curve, indicating a possible coaxing effect.

Optical inspections indicate that all the fractures were originated from the internal porosity. Typical fracture morphology is shown in Figs. 5 and 6 for specimens 13 and 17, respectively. We found there are little differences in fracture morphology between the two specimens except that the crack mirror zone is slightly larger for the fatigue-induced fracture. Cavities are filled with silicon-rich whiskers grown from the cavity wall. A large crystal, visible in Fig. 6(*b*), near the edge of the fractured void is believed to be yttria. No fracture was observed to have occurred from the surface defects, suggesting that the tests are successful and the data are reliable.

Test results of MgO-PSZ (NILCRA, TS Grade)

A total of 16 specimens were tested to date at room and elevated temperatures up to 1000°C. Test results are summarized in Table 2 and data are plotted in Figs. 7 and 8. For the sake of clarity, 400°C and 1000°C data are plotted in Fig. 8.

Because the number of test data is very limited, the fatigue behavior of the material at each test temperature is approximated by a scatter band. The data scatter is more obvious for the data groups at room temperature and 400°C. It is not clear if this is attributed to the transformation toughening effect activated by the tensile and cyclic stress loading. The fatigue curves for 800 and 1000°C cannot be well defined because they lack data points in the intermediate-cycle range.

A slight hint of plastic deformation was noticed for this material tested at 800° and 1000°C. However, plastic strain rachetting was perceptible when the specimen was cycled for several thousand times. Test results for specimens 1, 6, and 14 show that it is possible to raise the

M26083

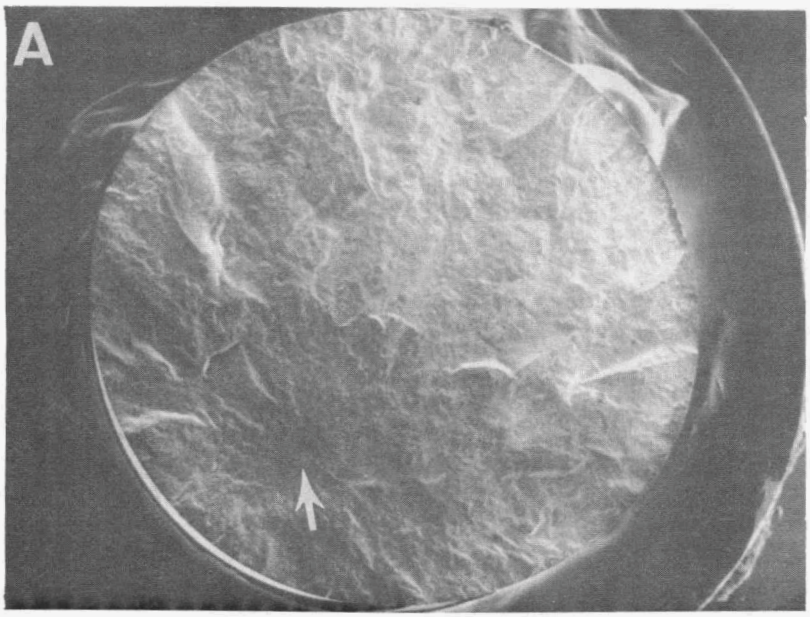

1000 μm

M26086

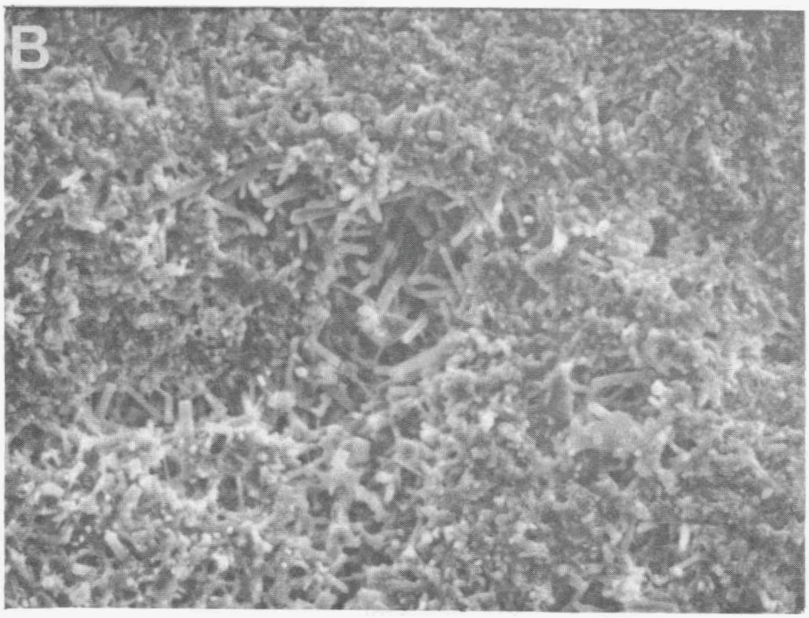

10 μm

Fig. 5. Fracture surface of specimen 13 tested in pure tension at 1000°C. (*a*) Fracture origin is seen at the center of the penny-shaped plateau. (*b*) A magnified view of the fracture initiation site showing the cavity filled with whiskers.

M26101

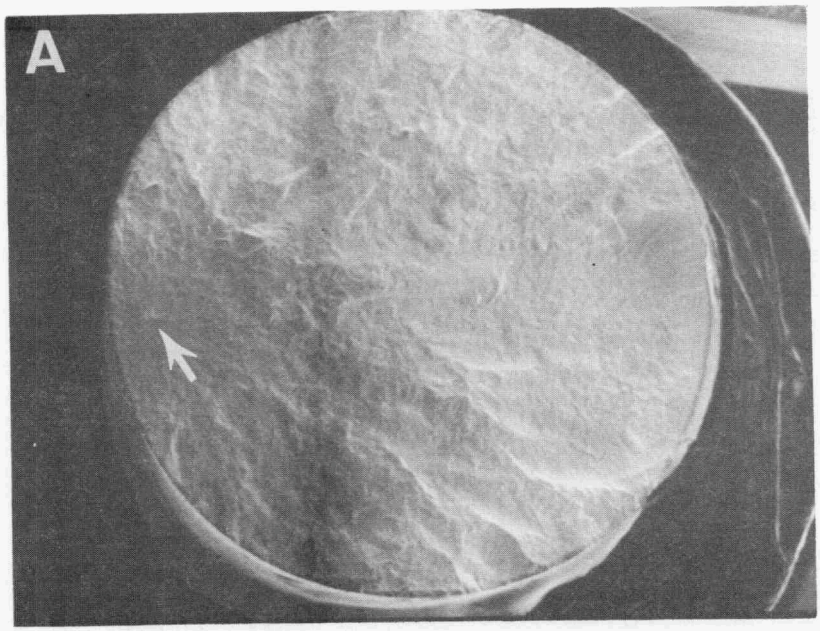

1000 μm

M26103

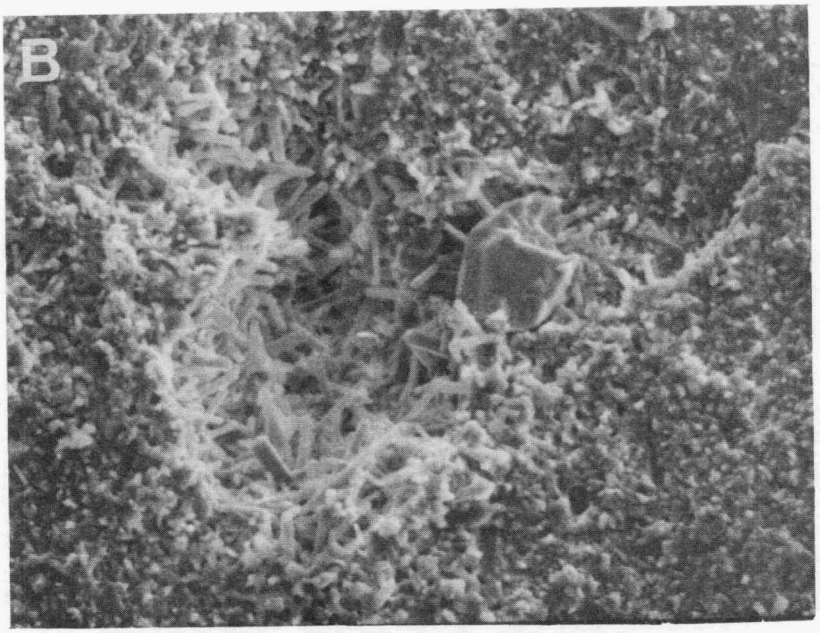

10 μm

Fig. 6. Fracture surface of cyclically fatigued specimen 17 tested at 1000°C. (*a*) The arrowhead indicates the location of fracture origin. (*b*) A high magnification view of the fracture origin showing a large fractured crystal high in yttrium content.

Table 2. Results of tensile and cyclic fatigue tests of NILCRA's MgO-PSZ at elevated temperatures

Specimen number	Modulus of elasticity, GPa (10^6 psi)	Tensile strength, MPa (ksi)	Cyclic stress to failure, MPa (ksi)	Intermediate cyclic stress, MPa (ksi)	Cycles at intermediate cyclic loading	Cycles to failure	Total test time (h)
			Test at Room Temperature				
15		326 (47.4)				1	0
16		448 (65.0)				1	0
			Test Temperature at 400°C				
7		376 (54.5)				1	0
8		314 (45.5)				1	0
9			336 (48.8)			1,209	0.7
10	150 (21.7)		328 (47.5)			13	0
11	156 (22.7)		314 (45.5)			5	0
			Test Temperature at 800°C				
2	167 (24.3)	292 (42.3)				1	0
3	156 (22.6)	269 (38.9)				1	0
4	148 (21.4)		279 (40.4)			3	0
5	156 (22.6)		254 (36.9)			2	0
6	160 (23.2)			241 (35.0)	45,126		
				260 (37.7)	124,946		
				279 (40.4)	88,970		
			295 (42.7)			90,837	194.4
1	159 (23.1)			235 (34.0)	77,071		
				256 (37.1)	48,709		
				271 (39.3)	132,555		
				287 (41.7)	88,970		
			300 (43.5)			30	193.0
			Test Temperature at 1000°C				
12	148 (21.5)	244 (35.3)				1	0
13	145 (21.0)	253 (36.7)				1	0
14	147 (21.3)			212 (30.7)	49,120		
				228 (33.1)	82,315		
				242 (35.1)	129,036		
				254 (36.8)	43,725		
			270 (39.2)			40,979	191.8

ORNL-DWG 88-2117

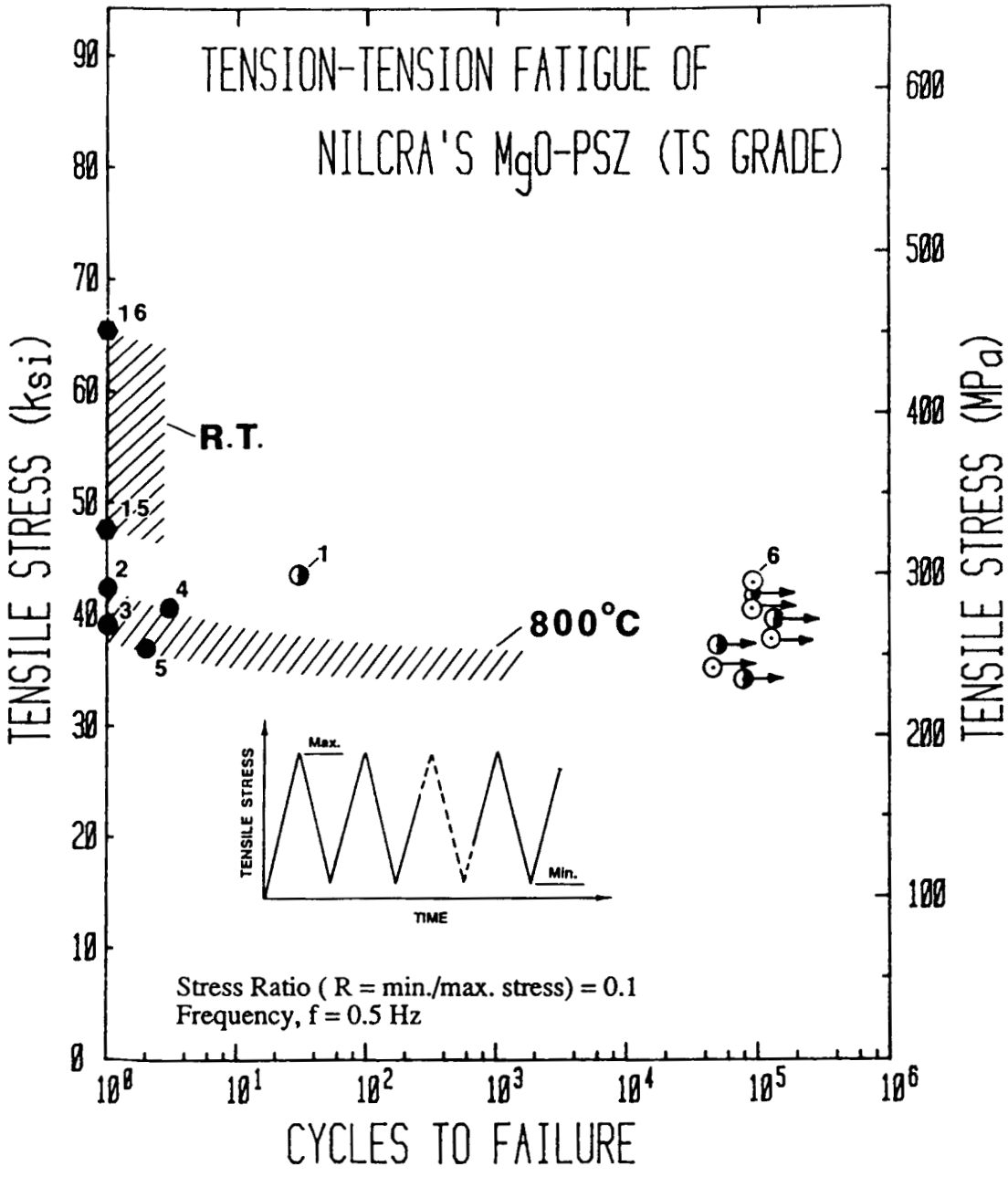

Fig. 7. Tensile strength and fatigue behavior of MgO-PSZ tested at room temperature and 800°C. Attached to the symbols are specimen numbers.

ORNL-DWG 88-2118

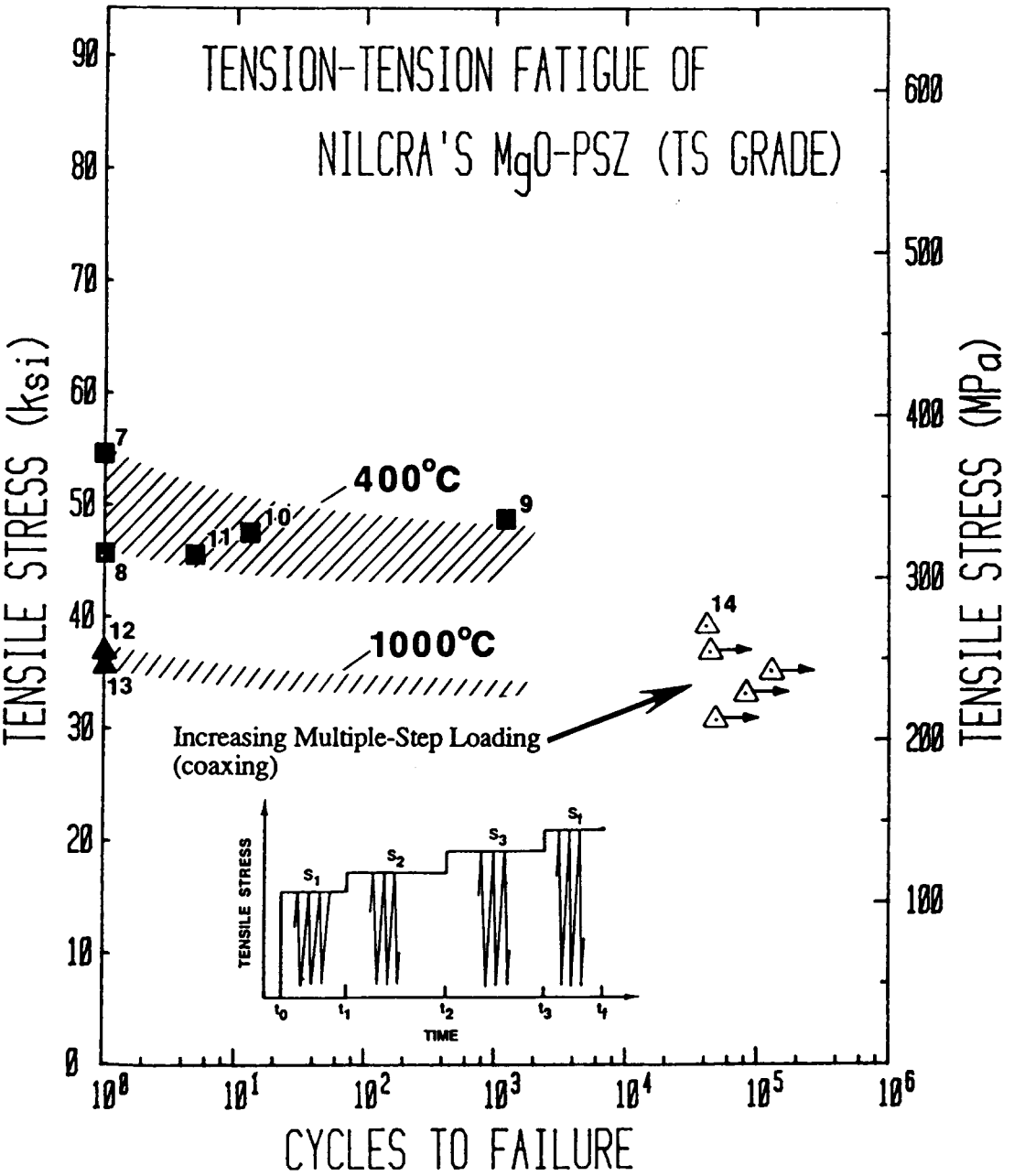

Fig. 8. Tensile strength and fatigue behavior of MgO-PSZ tested at 400°C and 1000°C.

fatigue strength of this material by the method of coaxing. In all cases, the fatigue strength exceeded the maximum tensile strength determined by the uniaxial monotonic loading, as shown in Figs. 7 and 8.

Comparisons were made between the ORNL tensile data and the four-point-bend flexural strength data reported by the supplier, as shown in Fig. 9. It clearly suggests that both sets of data can be well correlated. In both cases, the strength values are shown to be a function of temperature. However, the flexural strength is more sensitive to temperature change than the uniaxial tensile strength. As a result, both strength data merge closer to each other as temperature increases. Finally, the gap decreases to about 10% of the flexural strength at 1000°C. Note also that the data scatter for the tensile strength decreases as temperature increases.

Fracture surfaces of the tested specimens are being examined by optical and scanning electron microscopy; five specimens have been investigated to date and the work is continuing. It appears that there are no significant differences in fracture morphology between tensile fast fractured and cyclically fatigue-fractured specimens tested at 800°C. We found that all the fractures initiated from internal process flaws. Besides, this material contains a large population of microvoids uniformly distributed in the matrix as well as grain boundaries. Cleavage-like transgranular fractures were observed in the region near the fracture initiation site. The fracture morphology changes to a mixed mode of transgranular and intergranular fractures in the region away from the fracture origin.

Important findings and observations

Results of cyclic fatigue testing at high temperatures show that it is possible to raise the fatigue strength of Si_3N_4 as well as MgO-PSZ by precycling from low stress to high stress loading in multiple steps.

Status of milestones

Milestone 321404, concerning preliminary elevated temperature fatigue tests on advanced ceramic materials, was completed on July 31, 1987, as scheduled.

Publications

K. C. Liu, "Self-aligning Hydraulic Piston Assembly For Tensile Testing Of Ceramic," U.S. patent 4,686,860, August 17, 1987.

K. C. Liu, "Dynamic Tensile Cyclic Fatigue of Si_3N_4," extended abstract for 1987 Automotive Technology Development Contractor's Coordination Meeting, Dearborn, Michigan, October 28–29, 1987.

Reference

1. K. C. Liu and C. R. Brinkman, "Tensile Cyclic Fatigue of Alumina at Room and Elevated Temperatures," pp. 191–200 in *Proceedings of the 24th Automotive Technology Development Contractors' Coordination Meeting*, Dearborn, Michigan, October 27–30, 1986.

ORNL-DWG 88-2119

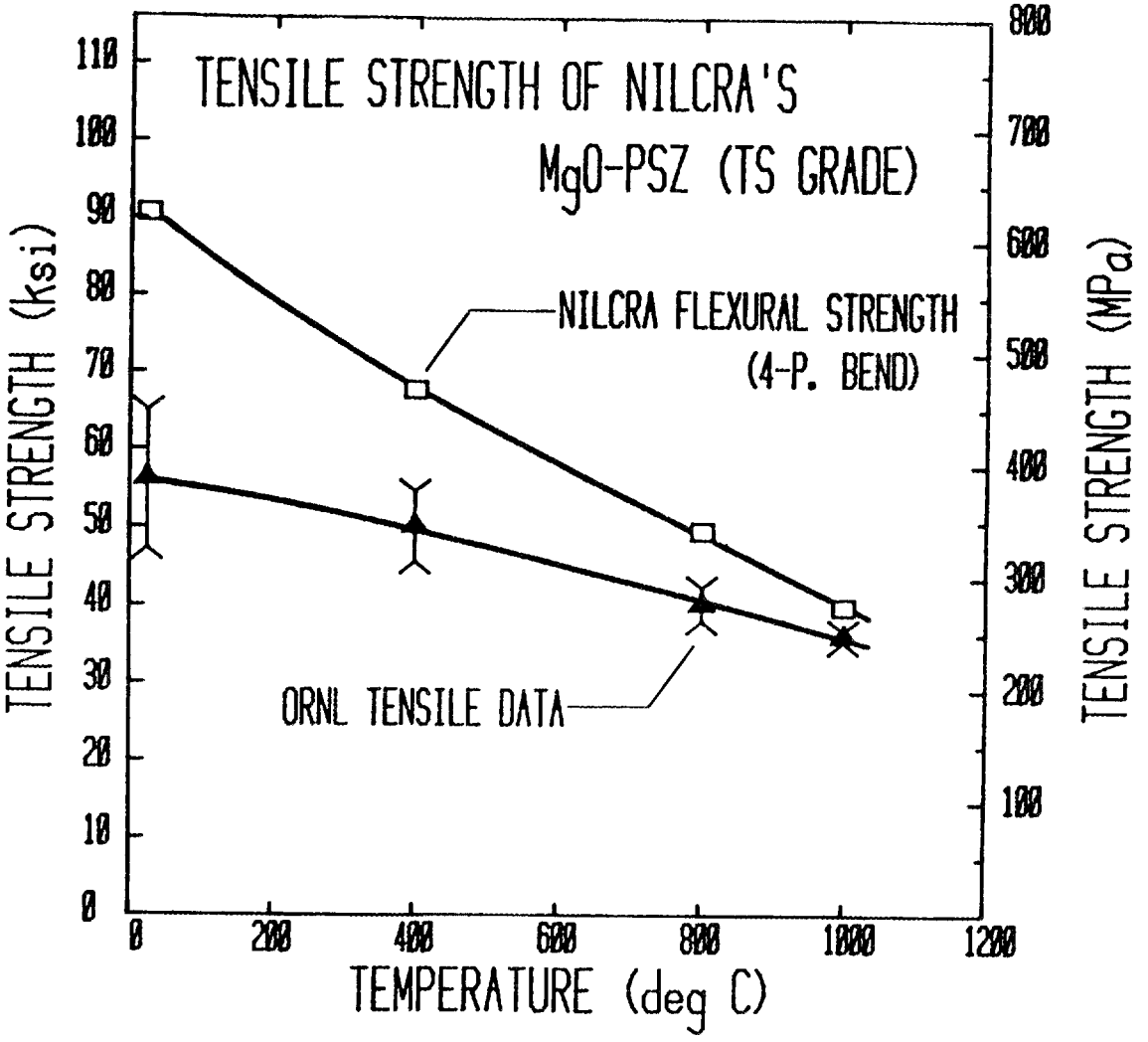

Fig. 9. Comparison of four-point-bend flexural strength and uniaxially determined tensile strength of MgO-PSZ at room and elevated temperatures.

3.3 ENVIRONMENTAL EFFECTS

Static Fatigue Behavior of Toughened Ceramics

M. K. Ferber (University of Illinois)

Objective/Scope

The objective of this program is to study the long-term mechanical stability of toughened ceramics for diesel engine applications. Materials under current investigation include (1) 2 varieties of an MgO partially stabilized zirconia (Mg-PSZ), (2) a yttria partially stabilized zirconia (Y-PSZ), and (3) a SiC whisker reinforced alumina. The work is divided into two tasks. The first involves the measurement of the time-dependent strength behavior of ceramic flexure-bar samples as a function of temperature and applied stress using the Interrupted Fatigue (I.F.) method. In the second task, the microstructures of selected I.F. specimens are characterized using SEM and TEM. In the case of the zirconia samples, x-ray diffraction and dilatometry studies are conducted to examine changes in their transformation behavior resulting from the high-temperature exposure.

Technical Progress

(a) Interrupted Fatigue Testing

The fatigue behavior was determined using the Interrupted Fatigue (I.F.) technique in which the four-point bend strength S_f was measured as a function of time (t), temperature (T), and applied stress (σ_a). This method has several advantages over conventional static fatigue testing. First, since time is a controllable quantity, problems associated with an unpredictable fatigue life (as in the case of static fatigue) are avoided. In the present study, this feature allowed for periodic examination of test specimens so that changes in both the microstructure and phase assemblage could be ascertained. A second advantage is that processes responsible for both strength degradation and strength enhancement can be readily distinguished.[1]

All testing was conducted in a specially designed Flexure Test System (F.T.S.) capable of holding up to three bend samples. The general layout of the F.T.S. is shown in Fig. 1. The Test Frame contains the hardware for applying mechanical forces to each of three samples which are supported by aluminum oxide (Al_2O_3) four-point bend fixtures.[a] The loads are generated by pneumatically driven air cylinders located at the top of the support frame. These loads are transmitted into the hot zone of the furnace through Al_2O_3 rods . Each of the bottom three Al_2O_3 rods are also attached to a load cell which monitors the applied force as a function of time. Water-cooled adapters connect the aluminum oxide rams to both the load cells and the air cylinders. The computer monitors the load on each specimen and provides necessary adjustments in the air pressure (via the electro-pneumatic transducer) such

---

[a] The F.T.S. design is based on a similar system originally developed by S. M. Wiederhorn and N. J. Tighe of the National Bureau of Standards.

that the desired stress level is maintained. Following the designated exposure time, the samples are fractured using a prescribed loading rate (345 KPa/s in the present study).

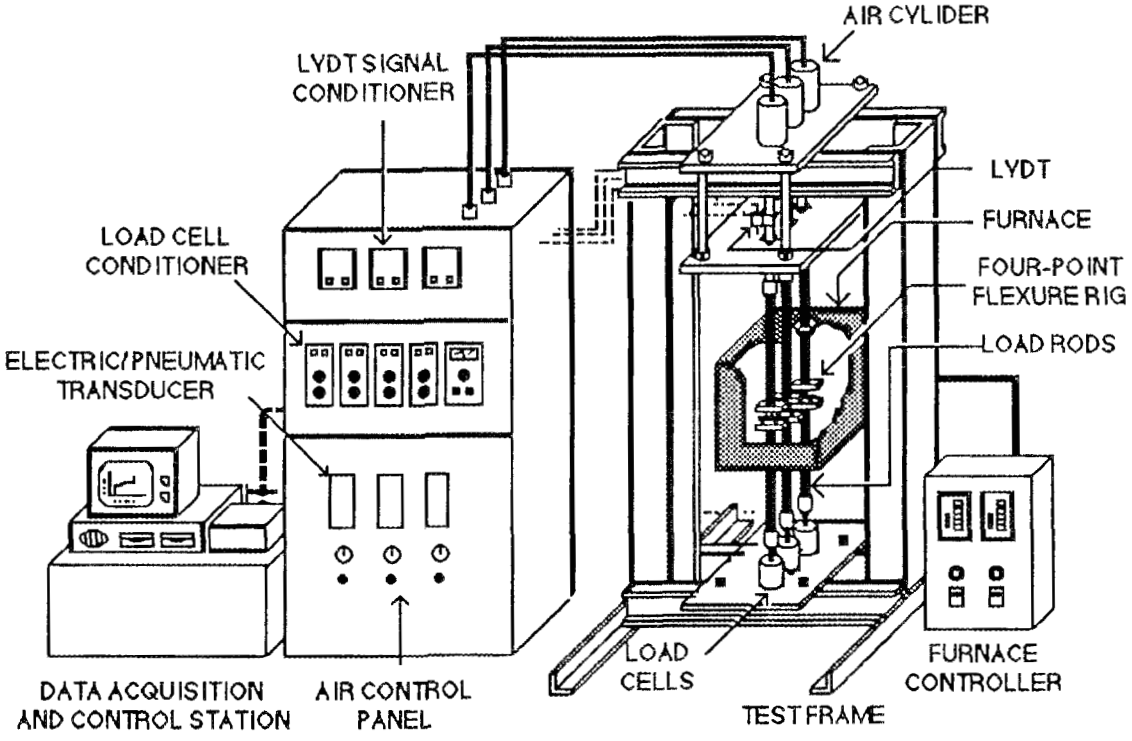

Figure 1. I.F. testing was conducted in specially designed Flexure Test System in which loads are applied pneumatically.

(b) MgO PSZ Ceramics

Although I.F. tests involving the MgO-PSZ materials were completed during the last reporting period, additional dilatometer aging studies were conducted in order to better understand the eutectoid decomposition process. As discussed previously,[2] the time-dependent strength behavior for the Mg-PSZ ceramic[b] designated TS-PSZ (thermal shock grade) tested at 800 and 1000°C exhibited a strong dependence upon the applied stress. In particular, the application of stress promoted both strengthening and weakening processes depending upon time and temperature. The strengthening tendency was most prominent at 1000°C. X-ray data gave evidence that this effect was related to a preferential generation of the eutectoid decomposition phase along the tensile surface. Recent aging studies conducted at 1100°C [3-6] have shown that the eutectoid decomposition of the MgO-stabilized (c) matrix can occur via two

[b] Manufactured by Nilcra Ceramics, USA Office, Glendale Heights, Illinois.

reactions:

$$Mg\text{-}ZrO_2\ (c) \rightarrow ZrO_2\ (m) + MgO \quad (T=1000°C) \qquad (1)$$

and

$$Mg\text{-}ZrO_2\ (c) \rightarrow ZrO_2\ (t) + MgO \quad (T=1000°C) \qquad (2a)$$

$$ZrO_2\ (t) \rightarrow ZrO_2\ (m) \qquad \text{(upon cooling).} \qquad (2b)$$

The results of the additional dilatometer aging studies conducted at 1000°C are illustrated in Figure 2. During the 336 h exposure there was a modest volume increase which is consistent with the decomposition reaction in Eq. 2a. This result suggests that in the absence of any significant applied stress, the (c) matrix phase decomposed directly to the ZrO_2 (t) phase. TheZrO_2 (m) observed at room temperature was apparently a consequence of the reaction in Eq. 2b. Therefore, it is possible that in I.F. tests involving samples subjected to mechanical loads, the ZrO_2 (t) $\rightarrow$ ZrO_2 (m) transition was triggered within the highly stressed regions leading to the generation of compressive stresses. Such behavior could explain the strengthening trends observed at 1000°C. It should be noted that the phase variations resulting from the stress-induced (m) generation would not be observed at room temperature since any ZrO_2 (t) would transform upon cooling.

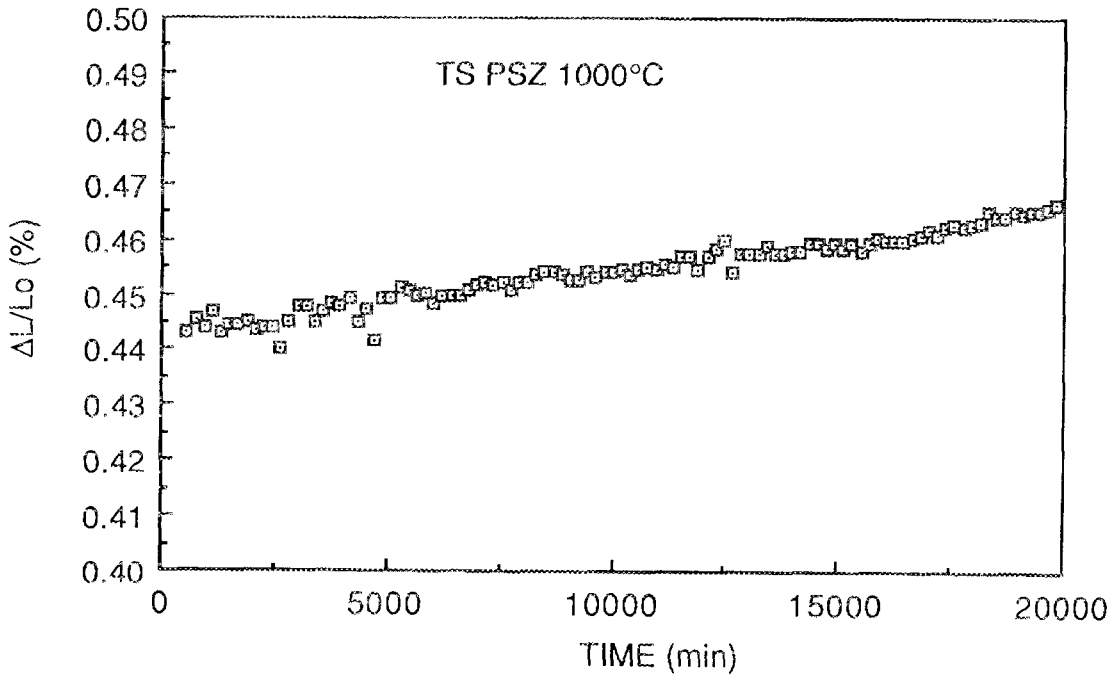

Figure 2. The TS PSZ exposed at 1000°C under no stress conditions exhibited a modest volume increase with time.

(c) SiC/Alumina Composite

The I.F. testing of the SiC/alumina* composite was completed this reporting period. The results for the 1000°C tests conducted at 0, 60, and 70% stress levels are shown in Fig. 3a. The strength S_f of the unstressed samples exhibited a short-term maximum during the first 336 h of exposure and then increased slightly at t =1008 h. Although a similar time dependency was observed for the 60 and 70% stress level tests, S_f at a given exposure time increased with increasing applied stress. At the 80% level, S_f decreased rapidly with time (Fig. 3b) giving rise to premature failure. This behavior was apparently due to slow crack growth effects.

Preliminary SEM studies of fractured surfaces indicated that a whisker pullout mechanism was operative for all exposure times considered. In addition, visual observations revealed the presence of a light colored surface phase on samples exposed for t >336 h. This phase was identified as mullite in previous studies by Kriven.[7] High temperature x-ray analyses are now underway.

(d) Y_2O_3 Stabilized Zirconia

I.F. studies involving the Y_2O_3 stabilized zirconia* were initiated this reporting period. Preliminary testing indicated that the strength (S_f) of this material dropped significantly as the temperature was increased (Fig. 4). For example, S_f at 25°C was approximately 850 MPa while S_f at 1000°C was 200 MPa. This behavior, which parallels that for the the MgO PSZ, can be attributed to the increase in the (t) stability with temperature. This increased stability lowers the effectiveness of transformation toughening in these materials.

As shown in Fig. 5, the strength of yttria partially stabilized zirconia exposed at 800°C was relatively insensitive to time and applied stress level. This behavior was similar to that for the MgO PSZ. Consequently, these materials exhibit little susceptibility to slow crack growth effects at elevated temperatures.

Status of Milestones

No Milestones.

Communications/Visitors/Travel

None.

Problems Encountered

No problems were encountered.

---

* Supplied by Terry Tiegs, Oak Ridge National Laboratory, Oak Ridge, TN.

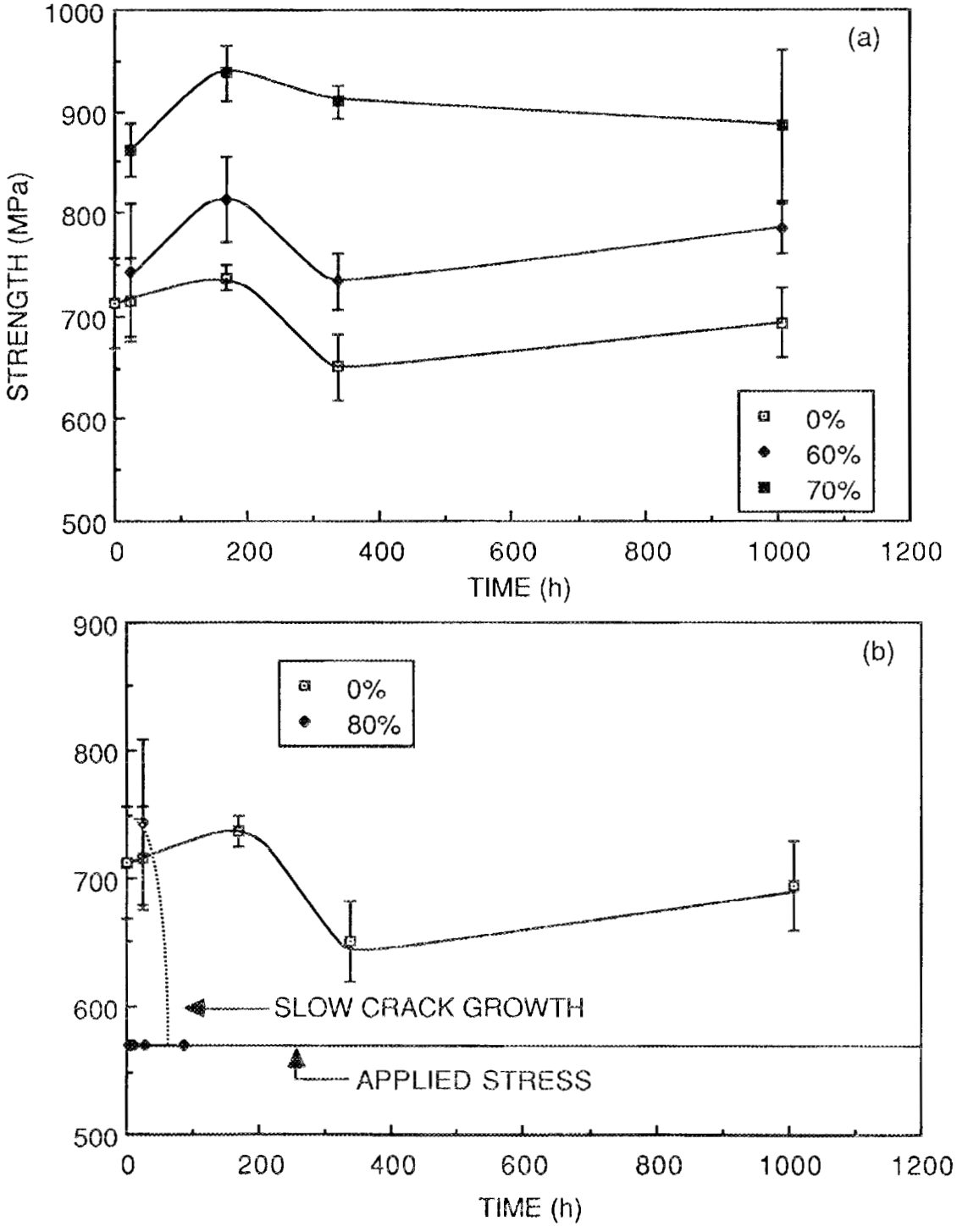

Figure 3. The strength of SiC whisker-reinforced alumina exposed at 1000°C increased as the stress level increased from 0 to 70% (a). At the 80% level (b), S_f decreased with time due apparently to slow crack growth effects.

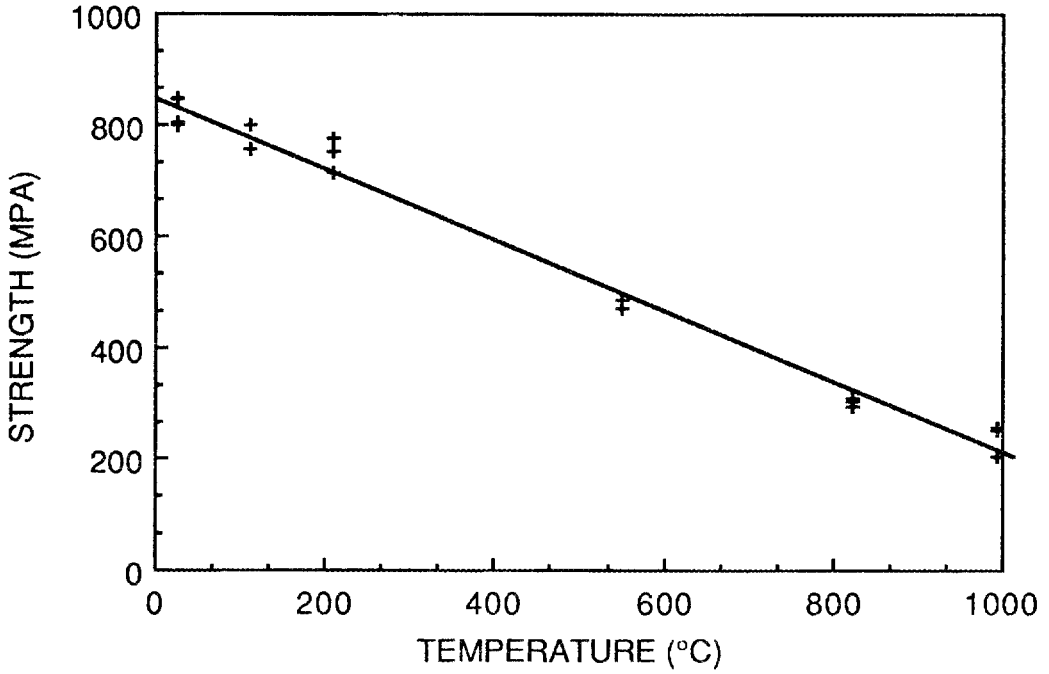

Figure 4. The strength of yttria partially stabilized zirconia decreased with increasing temperature.

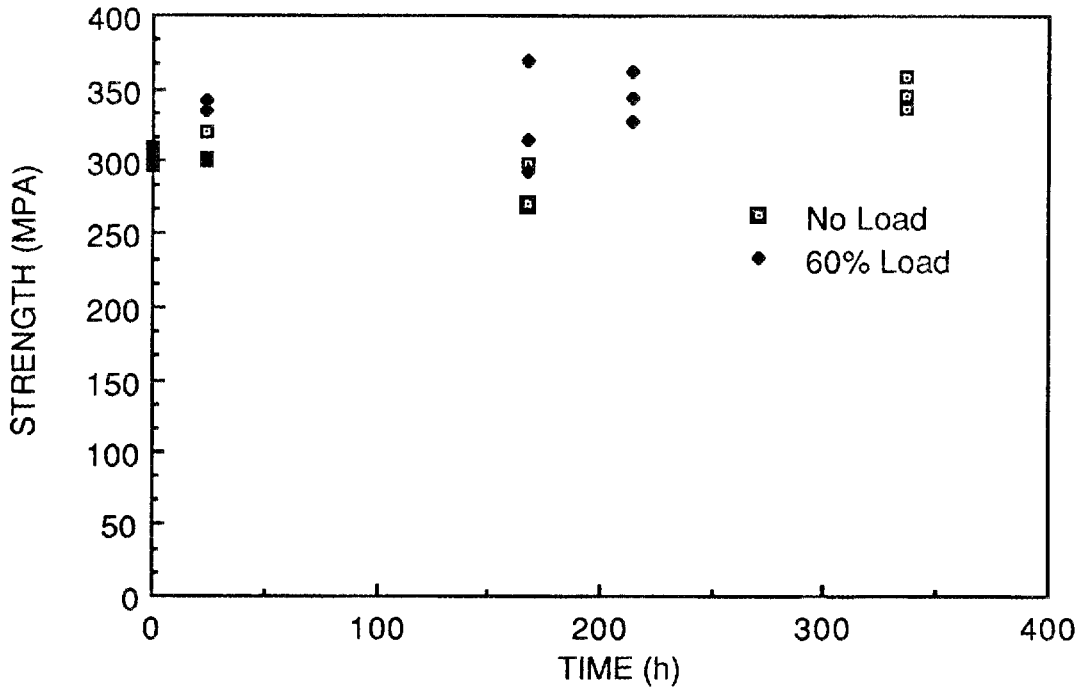

Figure 5. The strength of yttria partially stabilized zirconia exposed at 800°C was relatively insensitive to time and applied stress level.

Publications

A paper entitled," Fatigue Behavior of Partially Stabilized Zirconia, " was published in the *Proceedings of the Twenty-Fourth Automotive Technology Development Contractors' Coordination Meeting* .

References

1. S. M. Wiederhorn, "A Probabilistic Framework for Structural ceramics "; pp. 197-226 in *Fracture Mechanics of Ceramics*, Vol 5., eds. R. C. Bradt, A. G. Evans, D. P. H. Hasselman, and F. F. Lange. Plenum, New York, 1983.

2. M. K. Ferber and T. Hine, "Fatigue Behavior of Partially Stabilized Zirconia Ceramics,to be published in Proceedings of the Twenty-Fourth Automotive Technology Development Contractors' Coordination Meeting, Society of Automotive Engineers, Warrendale, PA.

3. R. Hannink and M. Swain, "Magnesia-Partially Stabilized Zirconia: The Influence of Heat Treatment on Thermomechanical Properties,"*J. Aust. Ceram. Soc.* **18** (2), pp. 53-62 (1983).

4. R. Hannink and R. Garvie, "Sub-eutectoid Aged Mg-PSZ Alloy with Enhanced Thermal Upshock Resistance,"*J. Mater. Sci.* **17** , pp.1637-43 (1982).

5. R. Hannink, "Microstructural Development of Sub-eutectoid Aged Mg-ZrO_2 Alloys,"*J. Mater. Sci.* **18** , pp.457-70 (1982).

6. M. V. Swain, R. C. Garvie, R. H. J. Hannink, "Influence of Thermal Decomposition on the Mechanical Properties of Magnesia-Stabilized Cubic Zirconia,"*J. Am. Ceram. Soc.* **66** (5), pp. 358-62 (1983).

7. W. M. Kriven, G. Van Teneloo, T. N. Tiegs and P. F. Becher, "Effect of High Temperature Oxidation on the Microstructure and Mechanical Properties of Whisker-Reinforced Ceramics, " published in *Proc. Int'l Symposium on Ceramic Microstructures '86* , edited by J. A. Pask, Plenum Press (in press).

Environmental Effects in Toughened Ceramics - Norman L. Hecht
(University of Dayton)

Objectives/scope

In January 1987 the ORNL sponsored project investigating the Environmental Effects in Toughened Ceramics at the UDRI was extended to investigate SiC and Si_3N_4 ceramics for heat engine applications. Three materials (two Si_3N_4 and one SiC) were selected for characterization and evaluation. The test protocol used was based on the characterization procedures developed in our initial project, designed to investigate the environmental effects in toughened ceramics. Microstructure, chemistry, physical characteristics, and mechanical properties at 25° and 1450°C were investigated.

Background

As part of this investigation a literature review was conducted. This review concentrated on the proceedings and agendas for technical meetings concerned with the development of ceramics for heat engine applications. In addition, a limited number of source documents, government reports, and articles in the open literature were reviewed. A compilation of the documents reviewed is presented in the references.

Since the late 1960's an extensive effort has been underway for the development of ceramic materials for use in heat engine applications. Major emphasis has been placed on silicon nitride (Si_3N_4) and silicon carbide (SiC) ceramics. More recently, attention has focused on SiC and Si_3N_4 composites. The development of SiC whisker reinforced Si_3N_4, Al_2O_3, and Al_2O_3 SiO_2 matrix composites has also been reported at several recent meetings [14,49,51], however, little property data are available for these materials.

Property data

The investigation and development of SiC and Si_3N_4 materials for heat engine applications dates back to the late 1960's, and in the ensuing years a significant body of literature concerning these materials has accumulated. From the literature review it became apparent that a significant number of SiC and Si_3N_4 ceramics have been studied. The compositions identified in the literature include both experimental and commercially available materials which were developed primarily for high temperature structural applications. A significant portion of the literature cited describes characterization studies performed and the property values obtained. However, these studies were not always systematically conducted, the test methods were not always well documented, and the reporting procedures varied. In addition, material suppliers frequently altered compositions and manufacturing processes in efforts to improve material behavior. Unfortunately, the material designations were not always altered to reflect these changes. As a result, the property data available in the literature are incomplete and somewhat inconsistent.

The works of Larsen and Adams [31-34], Quinn [53,54], Helms, et al. [26], and Richardson and Lindberg [44-46,57] were particularly valuable in providing property data for a large number of these ceramics. Unfortunately, the majority of reported property data has not been collected and organized into a central data base.

The SiC and Si_3N_4 ceramics can generally be categorized by the methods used for their fabrication. Hot pressing, sintering, and reaction sintering (siliconizing or nitriding) processes are used for preparing these SiC and Si_3N_4 ceramics. The identification and brief description of the generalized process typical for each category is presented in Table 1. The specific materials referenced in the literature review are listed in Table 2 according to the fabrication categories described in Table 1. The materials identified have been the subjet of a variety of characterization studies.

The properties and behavior of the SiC and Si_3N_4 ceramics have been measured and studied by a variety of test methods and in a number of different environments. Microstructure, density, elastic modulus, coefficient of thermal expansion, thermal conductivity, flexure strength, fracture toughness, creep, stress rupture, and oxidation behavior were the properties most frequently reported. Room temperature physical and mechanical properties have been measured for almost all of the materials cited. Properties have also been measured for some of these materials to temperatures in excess of 1400°C.

In addition, a number of studies have been conducted on the behavior of various SiC and Si_3N_4 ceramics in simulated engine environments. The effects of mechanical stress, thermal shock, thermal and mechanical cycling, and exposure to erosion and corrosion conditions in heat engines (water vapor, oxygen, sulfur, sodium salts, and other combustion gas contaminants) have been investigated. The results of the exposure studies in simulated engine environments have been reported in the proceedings of a number of workshops and conferences on heat engines and heat engine materials. However, this was not the main objective of our literature review. Our emphasis was on specific material characterization and property measurement information.

Property data available for the various SiC and Si_3N_4 ceramics were compiled and consolidated according to fabrication category. The compilation is presented in Table 3 which provides both the mean and range of values reported for the different specific materials categories. Flexure strength, tensile strength, and elastic modulus property values are repored at both room temperature and 1400°C. It should be noted that several materials failed prior to reaching 1400°C.

The creep data compiled are for steady state conditions (type II creep) and follows the relationship:

$$\dot{\varepsilon} = A^{n} e^{-Qc/RT} \quad (1)$$

where: $\dot{\varepsilon}$ = creep rate

A,n = process constants

Q_c = activation energy

RT = gas constant and temperature.

Flexure creep behavior for a variety of Si_3N_4 and SiC ceramics was plotted by Larsen et al. (31) and is reproduced in Figure 1.

From the data compiled it can be seen that a considerable range of property values has been reported for the individual materials within any single process category. This wide range of values is probably due to the variations in chemical composition, starting powder size and morphology, and variations in the processing procedure used by the different material manufacturers. The large number of compositions and process variations are due, in part, to efforts to improve specific SiC and Si_3N_4 products.

At room temperature the hot pressed Si_3N_4 and SiC materials have the highest strength. Although this trend may not always continue at the higher temperatures. In general, the SiC materials retain a greater fraction of their strength at elevated temperature and have somewhat better resistance to oxidation. The SiC materials also have greater creep resistance. The Si_3N_4 materials have lower coefficients of expansion and slightly higher fracture toughness.

The fracture origin of room temperature flexure specimens is reported to result from three sources: inclusions (or very large grains), pores, machining flaws, or a combination of these features. At elevated temperatures (above 1200°C) fracture origins usually occurred at oxidation pits, inclusions, machining flaws, or a combination of these features. At temperatures above 1200°C fracture behavior tends to be time dependent. Although the data in the literature are somewhat conflicting, time dependent failure is reported for both Si_3N_4 and SiC. However, it appears to be more dominant for Si_3N_4 (31). Subcritical crack growth, stress corrosion, and creep rupture

are the primary mechanisms identified for time dependent strength reduction. The particular mechanisms active for any specific material depend on the chemical composition and the environmental conditions present.

Static and dynamic fatigue property measurements

A number of different test methods can be used to investigate the occurrence of slow crack growth (subcritical crack growth) in ceramics. Both the double cantilever beam and double torsion test methods measure slow crack growth directly using large fracture-mechanics specimens into which a macro crack, larger than any natural flaws, is introduced and tracked. Static fatigue (tensile stress rupture) and dynamic fatigue (differential strain rate flexure) are used to measure slow crack growth indirectly.

Static fatigue measures slow crack growth by the application of static tensile loads below the known instantaneous failure load at a constant temperature. Temperature, load, and time to tensile specimen fracture are recorded. Static fatigue testing requires a significant number of tensile test specimens at a variety of temperatures and stresses.

In the case of dynamic fatigue several (3-4) different load rates (crosshead speeds) are used to measure the flexure strength at the temperature of interest. The flexure strength is measured by 4 point flexure testing. If slow crack growth has occurred, the flexure strength (σ_f) measured is higher at the higher stressing rates ($\dot{\sigma}$). The time to failure (specimen life time) can be determined by analysis of the strength-time curve using least-squares curve fitting techniques.

The median strength at a constant applied stress rate is

$$\sigma f^{N+1} = B(N+1)\, \sigma_o^{N-2}\, \dot{\sigma} \qquad (2)$$

where

$$B = \frac{2}{AY^2 K_{Ic}^{N-2}(N-2)} \qquad (3)$$

Y is a geometric factor related to flaw shape, and K_{Ic} is the critical stress intensity and is either known or measured independently. σ_o is the inert strength measured at a very rapid loading rate in an inert environment. Equation (2) can be written in the form:

$$\ln \sigma_f = \frac{\ln\dot{\sigma}}{N+1} + \left(\frac{\ln B(N+1) + (N-2) \ln \sigma_o}{N+1}\right) \qquad (4)$$

A linear regression analysis of $\ln\sigma_f$ and $\ln\dot{\sigma}$ can be performed if the fracture stress is measured at two or more stress rates. This analysis will yield estimates of the slope and intercept from which N and B can be calculated. The time to failure t_f can be determined from the relationship:

$$\ln t_f = \ln B + \left(\frac{N-2}{m}\right)\left(\ln \ln \frac{1}{1-F} - M_o \ln S_o\right) - N \ln \sigma_a \qquad (5)$$

where F = failure probability

M_o = Weibull modulus of the inert strength distribution

m = Weibull modulus

So = scaling parameter for the inert strength distribution

σ_a = the applied strength for a service application.

Although both the static and dynamic fatigue test methods are indirect, they measure slow crack growth of the inherent microflaws in the materials of interest. Due to concerns about the sensitivity differences between these two methods (22-24), it is desirable that both indirect measurement methods be used to study time dependent strength degradation.

Mechanical testing protocol

The procedures used to prepare test specimens for property evaluation are quite critical. Machining direction and surface finish can have a significant effect on the mechanical strength measured. Flexure strengths are lower when the tensile surface is not well polished or when the grinding and polishing performed is in a perpendicular direction to the applied tensile stress. On the average, the flexure strength increases about 15% when grinding and polishing operations are performed in a longitudinal direction (parallel) to the applied tensile stress. It was also found that the measured flexure strength increased when the edges of the tensile surface were chamfered. The use of beveled or rounded edges along the longitudinal direction reduced the effects of edge flaws (chips, etc.) and point stress concentrations along the specimen edges (65).

Reliability values reported also varied considerably, with Weibull shape parameter (m) ranging from 6 to 25. However, the majority of values reported were in the 8 to 12 range for the ceramics studied with the modulus increasing at the higher test temperatures (above 1200°C).

An examination of the data shown in Table 3 indicates considerable scatter in the data reported for the different material properties measured and significant gaps in the property data available for the SiC and Si_3N_4 ceramics. It is also apparent that the property values reported are based on limited data and lack a high degree of confidence. Most noticeable is the limited amount of tensile strength data reported in the literature. Measuring the tensile strength of brittle materials, particularly at elevated temperatures, presents a number of experimental difficulties and is expensive. The most serious problem encountered in uniaxial tension testing is eccentric loading. The bending which results due to eccentric loading can cause a significant increase in the maximum stress in the test

specimen. Until recently, the generally accepted approach has been to measure flexure strength of ceramics rather than tensile strength because of these problems.

From the data in the literature, it appears that the reported tensile strength values range from 0.5 to 0.8 of the flexure strength of any specific ceramic system and averages 0.64 [14,15,57]. Unfortunately, much of the reported data does not specify whether the flexure measurements were made by three or four point bend testing. In addition, specimens tested in uniaxial tension are more likely to fail from internal (bulk) flaws, while specimens tested in flexure tend to fail from surface flaws. For initial estimates, the tensile strength can be assumed to be 0.5 of the measured four point bend strength, however, the actual correlation is very material specific. Due to the uncertainty of the correlation between flexure and tensile data, valid tensile strength data at the use temperatures are critically needed for detailed design of heat engine components.

The correlation between the property values obtained for test bars prepared from billets compared to test bars prepared from actual components for heat engines is not well established, and the variations in strength associated with scale-up are not well understood. A reliable correlation between bulk material properties and actual component properties is an important design factor for economical quality assurance and reliability.

Work plan

For this investigation three materials were selected for evaluation:

1. Norton/TRW . . . . . Si_3N_4 . . XL144
2. GTE . . . . . Si_3N_4 . . PY6
3. Sohio Engineering Materials . . SiC . . Hexoloy α-SiC

A brief description of these three materials and the manufacturers property data are compiled in Table 4. For our initial studies rectangular test bars 5.1 x 0.64 x 0.32 cm (2 x 0.25 x 0.125 in) were required. Upon receipt of the test specimens they were visually inspected and then machined into the appropriate configuration and dimensions. The tensile surface of all test bars were ground and polished and the long edges of the tensile surface were chamfered.

The characterization protocol used to evaluate the three candidate materials are outlined in Table 5. Flexure strength measurements were made at room temperature (25°C) and at 1450°C using an Instron Universal Testing Machine (Model 1123). The flexure tests at 1450°C were conducted in an ATS #3320 high temperature furnace. Flexure strength was measured using a four point bend test fixture shown in Figure 2. For the room temperature testing the bend fixture was made of steel and for the 1450°C testing the bend fixture was made of SiC. Fracture origin was determined by optical microscope (Nikon Epiphot Metallograph) and SEM (JOEL/SM - 840 with EG&G Ortec System 5000 Micronanalysis System). The flexure strength values obtained were evaluated by Weibull analysis. Maximum likelihood estimates of the shape parameter, m (modulus), and the scale parameter, S_0 (the 63rd percentile for the distribution of breaking strength) were determined. Upper and lower bounds at the 90% confidence limits were also calculated.

The elastic modulus of three representative specimens of each candidate material was measured by a Grindo-Sonic (Model MR3ST) Transient Impulse/Elastic Modulus Apparatus. Hardness was measured on five representative samples from each candidate material using a Vickers microindent hardness tester.

The microstructure and chemistry of the three candidate materials were also studied. Polished sections from representative specimens were viewed by optical microscope (Nikon Epiphot) and freshly fractured sections were viewed by scanning electron microscope (JOEL JSM-840). X-ray fluorescence (EDXA) spectra were obtained using the EG&G Ortec System 5000 attached to the JSM-840. Specimens tested

at 25°C and specimens tested to 1450°C were examined. Similar specimens were also examined by x-ray diffraction (GE-XRD6).

In addition, representative specimens of GTE PY6, Noralide XL144, and Hexoloy-αSiC were examined using high resolution scanning Auger spectroscpy (JOEL JAMP-30). Each specimen was freshly fractured in air, rapidly mounted on a specimen holder, and inserted into the JAMP-30 instrument which maintained an operational pressure during analysis of less than 9×10^{-10} Torr. The specimens were not coated with a gold overlayer to prevent charging.

For each specimen, at least three regions were selected which appeared relatively flat and were free from any visible anomalies, for wide area analysis. A 100 micrometer beam was used for the Auger analysis in these selected regions. Auger spectra taken in this way most closely represent the average surface composition.

After the general regions were analyzed, the fracture surface of each specimen was probed with a beam diameter of less than 1 μm to determine the local composition of regions of interest. Regions which appeared brighter or darker than normal in the secondary electron images were selected. Depths of 5 to 10 nanometers were probed in these analyses. Spectral data were reduced using relative sensitivity factors based on literature values.

The silicon nitride specimens were examined with a 3 to 5 keV electron beam at currents ranging from about 0.2 to 0.7 microamps. The fracture surfaces were tilted about 60° to the beam probe. No visible evidence of beam damage was observed under these experimental conditions.

The Hexoloy silicon carbide was examined using a 10 keV beam with beam currents between .5 and 1 microamp. This specimen was also tilted at least 60° to the beam probe to eliminate charging of the uncoated surface.

Fracture toughness was measured for the three materials by two different techniques; the controlled flaw method and the micro indent

method. It was intended that fracture toughness would also be measured by double cantilever beam (DCB), however, the GTE PY6 billets available were not the appropriate size to prepare test specimens of the correct dimensions. In addition, the UDRI did not have the required cutting tool to prepare DCB specimens. This equipment is on order and should be received shortly. When the cutting tool is received, specimens will be prepared and tested. The DCB test results will be submitted in a supplemental report.

In the controlled surface flaw method either a Knoop or Vickers diamond indenter is used to produce a small crack (micro flaw) of controlled size in the tensile surface of a bend bar of the material to be tested. It is anticipated that the indent serves as the critical flaw when the bar is tested in flexure using three point loading. The bend bars are flat and have a good surface polish prior to indentation. The load is applied with the point of the diamond as close to the center of the bend bar as possible using loads from 500 g to 2 kg. After indentation, the length of the long diagonal is measured with a calibrated eyepiece. The specimens are carefully marked before indenting to ensure that the top knife edge is aligned directly over the microhardness indentation flaw when the three point flexure fixture is used.

For the fracture toughness determination to be made, normal three point loading fixtures are used on an Instron universal testing machine with a load recorder. The indented side (tensile surface) is placed face down on the lower loading points, and the top knife edge is located directly over the indent crack. Crosshead speed is rapid to eliminate or substantially reduce any slow crack growth. The two specimen halves are retrieved after breaking for flaw observation and measurement. Fracture toughness (K_{Ic}) is determined by the relationship:

$$K_{Ic} = 2.06\ \sigma_f \sqrt{c/\pi} \qquad (6)$$

where σ_f = flexure strength MPa
c = the radial crack extension (m)

The microindentation technique uses a Vicker's indenter to measure fracture toughness. Toughness is determined by the length of the radial crack produced by the indenter. The specimen surface is carefully prepared by grinding, polishing, and annealing to remove surface stresses. The radical crack extension ($\hat{c}$) is measured in the optical microscope with a calibrated eyepiece. The length of the diagonal of the indent is also measured in an optical microscope to obtain $\hat{a}$ one half the diagonal indent distance.

K_{Ic} can be estimated from the data using:

$$K_{Ic} = (\hat{c}/\hat{a})^{-3/2} \left(\frac{H}{E\theta}\right)^{2/5} \frac{H\sqrt{a}}{\theta} \qquad (7)$$

or

$$K_{Ic} = 0.15\ k\ (\hat{c}/\hat{a})^{-3/2} \frac{H\sqrt{a}}{\theta} \qquad (8)$$

where $\theta \approx 3$ (constraint factor), $k \approx 3.2$ (correction for free surface), H is the measured hardness, $\hat{a}$ is one-half the indent diagonal, and $\hat{c}$ is the radical crack extension.

During the course of our project, we also obtained test specimens of a Sialon material from Sohio and a vapor deposited SiC from CVD Inc. at no cost. The specimens obtained were used to conduct limited characterization studies. The results of these evaluations are presented in Appendix I.

Technical progress and discussion of results

The density, elastic modulus, and hardness values measured for the three candidate materials are presented in Tables 6 through 8. The density measurements indicate that all three materials are approximately 99% of the calculated theoretical density. The average density, elastic modulus, and hardness measurements were within the published range of values reported for these materials, however, the hardness values measured were slightly lower than the average value reported.

The optical micrographs of the as-received materials are presented in Figures 3 through 5. SEM photomicrographs of the flexure tested material at 25°C and 1450°C are presented in Figures 6 through 23. The EDXA spectra obtained from the candidate materials after flexure testing at 25°C and 1450°C are presented in Figures 24 through 32. A comparison of the EDXA spectra for the GTE PY6 and Noralide XL144 is shown in Figure 33. The X-ray diffraction patterns obtained from the as-received material and after flexure testing at 1450°C are presented in Figures 34 through 39 and in Tables 9 through 14.

The results of the flexure strength measurements for the three candidate materials at 25°C and 1450°C are presented in Tables 15 through 20. The results of the Weibull analysis for the flexure test data are presented in Tables 21 through 23 and in Figures 40 through 45.

The room temperature flexure strength values obtained for α-SiC were in good agreement with the published values. However, the strength values measured for the PY6 material were about 10% higher than published values and the strength values for the XL144 material were about 30% lower than manufacturers published values. The flexure strengths measured for all three materials at 1450°C are more than 30% higher than the average strength values published for these materials. The two Si_3N_4 materials tested at 1450°C were observed to have undergone considerable oxidation when examined after testing. The α-SiC specimens did not appear to have undergone any observable oxidation. It is estimated that during flexure strength testing at 1450°C the test specimens are above 1000°C for about four hours. From the XRD analysis it was found that both cristobalite and $Y_2Si_2O_3$ formed on the surface of the Si_3N_4 test specimens.

The objectives in conducting the flexure strength tests were (a) to characterize the distributions of ultimate strengths for the material-temperature combinations, (b) to determine the first order effect of temperature on ultimate strength for the materials, and (c) to compare the ultimate strength distributions for the silicon nitride materials (GTE PY6 and Noralide). Tables 15-20 presented the ultimate

strengths obtained in the tests of each combination of type of material and temperature.

The data of each set were adequately modeled by both the normal and the Weibull distributions. The Weibull moduli ranged from about 8 to 12 with the estimate of the modulus for the Noralide at 25°C being somewhat smaller. The average ultimate strength for the Hexoloy was significantly larger at 1450°C than at 25°C. Average strength decreased with temperature for the silicon nitrides with the amount of decrease depending on the material. The average strength of the GTE PY6 was significantly larger than that of the Noralide at 25°C but the opposite trend existed at 1450°C.

The observed ultimate strengths were characterized assuming both normal and Weibull distributions for modeling the variation in the data. The data from each material-temperature combination was tested to determine if either distribution could be rejected as a possible model. Neither distribution could be rejected for any of the data sets. This is not a surprising result since a sample of size 10 is small for testing hypotheses concerning distributional models. An example of the fit of the distributions was shown in Figures 40 and 41 which presented sample cumulative distribution functions plotted on normal and Weibull probability paper, respectively, for the Hexoloy specimens at 25°C. A perfect cumulative normal or Weibull would plot as a straight line on these plots.

The normal distribution is completely characterized by the population mean and standard deviation. The estimates of these parameters from the observed strengths are tabulated in Tables 15 through 20. Also included in Tables 15 through 20 are 95 percent confidence bounds on the average strengths for each combination of material and temperature.

The Weibull distribution is characterized by the Weibull modulus or shape parameter (m) and the characteristic strength or scale parameter (S_o). Maximum likelihood estimates of these parameters were obtained for each data set and are presented in Table 21. Also included in Table 21 are the 90 percent confidence intervals for both

the modulus and the characteristic lives. The Weibull modulus is inversely proportional to the degree of variability in a data set.

The effect of temperature on ultimate strength for each material was investigated by testing for a change in mean strength between temperatures. Figures 42, 43, and 44 present plots of the observed strengths versus temperature. In the silicon carbide (Hexoloy) specimens, the ultimate strengths were significantly higher at 1450°C than they were at 25°C. The opposite was true for the silicon nitride specimens, since the strengths were significantly less at 1450°C than at 25°C for the Noralide and PY6 specimens. The statistics upon which these conclusions are based are presented in Table 22.

The ultimate strengths of the silicon nitrides (Noralide-XL144 and GTE-PY6) were compared by means of an analysis of variance of the complete factorial experiment that was conducted on these materials. The analysis of variance table is presented in Table 23. The interaction between material and temperature was statistically significant which means that the observed change (decrease) in strength between the two temperatures for the PY6 was significantly larger than that observed for the Noralide. Figure 45 is a plot of the average strength of each material as a function of temperature and displays these changes in average strength. Since the ultimate strength of the materials depends on the temperature at which the tests were performed, neither of the materials can be selected as having greater strength. At 25°C, the PY6 specimens had a significantly greater average strength than the Noralide specimens. At 1450°C, the PY6 specimens had a significantly lower average strength than the Noralide specimens.

Fracture origin was determined by optical microscope and SEM. The photomicrographs of typical fracture sites for the 25°C and 1450°C tested specimens are shown in Figures 46 through 48. Examination of the fractured test bars showed that at room temperature all of the Hexoloy specimens failed due to tensile surface flaws. The PY6 and XL144 materials failed at both tensile surface and edge flaws. At 1450°C it was observed that the Hexoloy specimens failed at tensile

surface and edge flaws and the PY6 material failed at tensile surface, edge, and subsurface flaws. The XL144 material tested at 1450°C failed primarily due to tensile surface flaws, however, two of the test specimens failed at edge flaws and one specimen failed at a subsurface inclusion. It was further observed that failure initiation for the PY6 material at elevated temperature was frequently at a surface or subsurface inclusion (see Figures 49 and 50). The inclusion failure site shown in Figure 50 was examined by EDXA and found to contain Fe, Cr, and Cu contaminates (see Figure 51).

Similar inclusions were also observed on the surface of untested PY6 specimens. A typical inclusion is shown in Figure 52. This inclusion was also examined by EDXA and found to contain Mo (see Figure 53). The presence of Mo and Fe inclusions in sintered Si_3N_4 materials has been reported by Helms, et al.,[26] Larsen,[31] and Pasto.[43] Inclusions were also observed in the Norton Noralide XL144 material. EDXA spectra of inclusions found in the specimens tested at 20°C and 1450°C are presented in Figures 54 and 55.

The identification of these metallic inclusions in the Si_3N_4 specimens has prompted us to re-examine specimens from all three vendors more extensively. In addition to the SEM and EDXA analysis representative samples were examined by the JOEL JAMP-30 scanning Auger microprobe. The typical spectra obtained for the PY6 material is shown in Figure 56. Typical spectra for the Noralide XL144 and Sohio Hexoloy α-SiC are shown in Figures 57 and 58. Table 24 presents the data from three regions on a freshly fractured PY6 Si_3N_4 surface. Table 25 shows the results from six additional regions on this PY6 specimen. Table 26 presents the data from three regions on a freshly fractured Noralide XL144, and Table 27 shows the data obtained from seven other regions on the same specimens. Table 28 presents the data from four regions of a freshly fractured Hexoloy α-SiC, and Table 29 shows the data from six additional regions from the same specimen.

The presence of carbon and oxygen is readily apparent from the data for PY6 in Table 24. Traces of boron were found on the surface of the material. The peak shape of carbon suggests a noncarbon form

of carbon present in this material. Table 25, which tabulates the results from six selected regions on the PY6 specimen, shows significant point to point variation in concentration of all the elements detected. Because of peak interferences with silicon and boron, the presence of yttrium could not be unambiguously confirmed.

Efforts were made to sputter this surface with 3 keV argon to determine wheher the oxide was just on the surface. It was difficult to obtain an Auger spectrum from the sputtered surface due to charging effects after sputtering. There was some evidence, however, which suggests that the oxide is not primarily a surface oxide.

Atomic compositions calculated from the Auger data and presented in Table 26 are very similar to those obtained for the GTE PY6 specimen but with a smaller degree of element variation.

The carbon contained in the Noralide specimen was a noncarbide form as indicated by the Auger peak shape. Some boron was also observed in almost every region studied. The oxygen observed is distributed throughout the material and is not chemisorbed oxygen. Although no complete Auger spectra were acquired after sputtering, indications were that the oxygen level was not reduced as a result of sputtering.

As reported in Figure 28, it appears that a carbon rich silicon carbide surface was observed which contains about 12% oxygen. The carbon peak exhibited the characteristic carbide peak shape which is well documented in the literature. Auger signal from any noncarbide carbon would most probably be masked by the carbide peak.

Data from the six regions reported in Table 29 appear quite similar to the data presented in Table 28. An inclusion about 20 μm in diameter was observed in the SiC specimen and appears to be a noncarbide form of carbon. Secondly, a peak occurred near 380 eV which could indicate the presence of either nitrogen or cadmium. Because this was a minor peak, it could not be positively identified by its shape. Our best estimate is that it is probably nitrogen. However, more work would be required using elemental standards to make a more positive identification.

Further comments about regions 9, 10, and 11 described in Table 29 are necessary. The Auger spectrum from region 9 represents the composition of a flat on a grain. The spectrum from region 10 was taken from a grain boundary. The calculated compositions from both regions are nearly identical. The atomic compositions reported for region 11, Table 29, are from a region which was argon ion etched for two minutes. The oxygen concentration did not decrease as it should have if it were a chemisorbed oxygen specie. A slight increase in oxygen was observed which suggests that perhaps some surface carbon was removed. It can be concluded that the oxygen seen on this freshly fractured surface is a bulk oxide residing in a carbon rich silicon carbide material. Further investigation would be necessary with x-ray photoelectron spectroscopy to determine the oxidation states of the constituent elements in this material.

The use of Raman spectroscopy to evaluate Si_3N_4 ceramics was also investigated. Three GTE specimens and one Norton specimen were studied. The laser Raman microprobe used had a pulsed doubled Nd:YAG laser. In addition to the Chromatix Model 1000 laser system, the facility had an optical focusing and collection system, a dispersive system, and an electronic detection system. Microprobe optics provide spatial resolutions down to 1 μm which will allow spectra from individual grains to be recorded. The spectra obtained for this study were all taken with the microprobe using an illuminated area of about 5 μm by 20 μm.

The specimens selected for evaluation were:

GTE No. 17 (tested at 1450°C)
GTE No. 23 (tested at 1450°C)
GTE No. 56 (as-received)
Noralide XL144 No. 8 (as-received)

The spectra from all four specimens (see Figures 59 through 68) show three lines in the low frequency region around 200 cm^{-1} which are attributable to lattice modes. Additional lines, probably also originating from lattice modes, can be seen weakly in the 400-450 cm^{-1}

region. There is a large variation in the strengths of the broad background spectrum in the four samples relative to the strength of the lines near 200 cm^{-1}. The background is considerably higher in the GTE specimen No. 56 than in the other samples. This could be due to the presence of an amorphous phase in the sample.

The spectra in the 500-1300 cm^{-1} region show extraordinary variations. There is a basic pattern reported by other workers of six lines located at approximately 615, 730, 860, 925, 935, and 1045 cm^{-1} which can be seen in the spectra of all four samples. There are, however, wide variations in the relative strenghs and the appearance of additional lines or features. Typically, lines in the region above 500 or 600 cm^{-1} in Raman spectra of solids are due to internal vibrations of molecular groups such as carbonates, nitrates, etc. This implies that these samples either contain a molecular crystalline phase or there are molecular species present.

The features observed in the spectrum of the GTE specimen No. 23 is rather dramatic in the 1300-3800 cm^{-1} region. Here strong lines in the CO and NO stretch region around 1800 cm^{-1} are seen. This frequency region is often associated with metal carbonyl (M-CO) and metal nitrosyl (M-NO) complexes. The vibration is that of the stretching of the double or triple bond of the CO or NO species. Similar features are not observed in the spectra for GTE specimen No. 17 which was exposed to the same high temperature environment.

Although oxygen stretch frequencies can extend out to 2400 cm^{-1}, modes that occur beyond this range can only be due to molecular groups containing light atoms, primarily hydrogen. The lines near 3400 cm^{-1} in the spectrum for GTE No. 23 almost certainly are due to a hydroxide (OH). As can be seen, the GTE specimen No. 17 showed none of these features.

It is quite evident from this limited investigation that these samples provide Raman spectra that is quite rich for study. The purpose of this effort was to generate a large range of spectra rather than to optimize the recording of specific features. Clearly a detailed study would utilize optimized scans of the desired features.

The results of the thermal expansion measurements are presented in Table 30, and typical thermal expansion curves are presented in Figures 69 through 71. The results of the fracture toughness (K_{Ic}) measurements are presented in Tables 31 through 33. Typical indents are shown in Figures 72 through 74. For the PY6 and XL144 materials an indent load of 2.6 kg was used. However, for the α-SiC material a load of 500 grams was used. The higher loading weights crushed the α-SiC specimens and the lower loading weight had to be used to obtain acceptable indents.

The coefficients of thermal expansion measured for both Si_3N_4 materials were in close agreement with published values for these materials. However, the average coefficient measured for α-SiC was more than 17% higher than reported for this material. The standard deviation calculated for the SiC material was relatively small (about 7-1/2%), however, the standard deviation calculated for the two Si_3N_4 materials were significantly higher (about 16%). In addition, the retesting of the Si_3N_4 specimens resulted in substantial differences in measured coefficients of expansion. This difference may be due to oxidation of the test specimen during the initial test cycle. The coefficient of thermal expansion tended to decrease when measured during the second test cycle for the Si_3N_4 material. Based on a single data point it would appear that the measured coefficient stabilizes after the first test cycle.

The fracture toughness values measured by microindent tended to be higher than the toughness values measured by the controlled flaw method. However, almost all the values measured were lower than published or reported by the manufacturer.

Conclusions

This project provided a limited evaluation for three candidate SiC/Si_3N_4 materials. From the results obtained it can be concluded that:

(1) In general, the property values measured were in agreement with published values for these materials.

(2) Based on the data obtained it would appear that the Hexoloy α-SiC material offers the most promise for extended structural application at elevated temperatures (1450°C).

(3) This project also provided important insights into the procedures for effective property evaluation of the SiC and Si_3N_4 ceramics;

a. It is desirable to use more test specimens (25) per test temperature for strength measurements. It is also desirable to measure strength at three or four different temperatures.

b. To obtain consistant values for coefficient of thermal expansion it is desirable to measure each test specimen three times.

c. Chemical analysis and identification of inclusions is imperative.

d. Since the potential application for these materials is for use at extended times in oxidizing environments at high temperature (1400°C), it is important to measure the mechanical strength under these conditions. It is probably desirable to monitor mechanical strength at elevated temperature (1400°C) after significant exposure (hundreds of hours) under nominal loading.

References

1. Alliegro, R. A. and S. H. Coes. "Reaction Bonded Silicon Carbide and Silicon Nitride for Gas Turbine Applications," ASME 72-GT-20, 1972.

2. Alliegro, R. A. and M. L. Torti. Gas Turbine International, 30-36, January/February 1973.

3. G. Bandyopadhyay, K. W. French, and C. L. Quackenbush. "Injection Molded Silicon Nitride for Engine Applications: Fabrication and Properties," presented at Automotive Technology Development Contracts Coordination Meeting, Nov. 14-17, 1983, Dearborn, MI.

4. Bradt, R. C. Pennsylvania State University, NASA-CR-165325, April 1984.

5. Burke, J. J., A. E. Gorum, and R. N. Katz, eds. "Ceramics for High Performance Applications;" Brook Hill Publ. Co.: Chestnut Hill, MA, 1974.

6. Burke, J. J., A. E. Gorum, and R. N. Katz, eds. "Ceramics for High Performance Applications-II;" Brook Hill Publ. Co.: Chestnut Hill, MA, 1978.

7. Ceramic Industry, 20-23, March 1986.

8. "Ceramics Based on Silicon Nitride," Nature, 238, July 21, 1972.

9. Davidge, R. W., G. Tappin, and J. R. McLaren. Powder Metallurgy International, 8(3), 110-114, 1976.

10. Dutta, S., R. W. Rice, H. C. Graham, and M. C. Mendiratta. Journal of Materials Science, 15, 2183-2191, 1980.

11. Edington, J. W., D. J. Rawcliffe, and J. L. Henshall. Powder Metallurgy International, 7, 82-96, May 1975.

12. 11th Annual Conf. on Composites & Advanced Ceramic Materials, Cocoa Beach, FL, American Ceramic Society, 1987.

13. The Engineers Handbook on Silicon Nitride, GTE Precision Materials, GTE Products Corp., Royal Oak, MI.

14. "Engineering Property Data on Selected Ceramics, Volume I, Nitrides," Metals and Ceramics Information Center, Battelle, MCIC-HB-07-Vol. I, March 1976.

15. "Engineering Property Data on Selected Ceramics, Volume II, Carbides," Metals and Ceramics Information Center, Battelle, MCIC-HB-07-Vol. II, August 1979.

16. Fairbanks, J. W. and R. W. Rice. Columbus, OH, MCIC Report/MCIC-78-36, March 1978.

17. Godfrey, D. J. Metals and Materials, 2, 305-311, October 1968.

18. Godfrey, D. J. In "Proceedings of the British Ceramic Society," 22, 1-25, 1973.

19. Godfrey, D. J. "Silicon Nitride Ceramics for Engineering Applications," SAE paper 740238, 1974.

20. Govila, R. K. Fracture and Intermediate Temperature Instability in Yttria-Doped Hot-Pressed Silicon Nitrides, Am. Ceram. Soc. Bull., 65(9), 1287-92, 1986.

21. Govila, R. K. Strength characterization of yttri-doped sintered silicon nitride, J. of Mat. Sci., 20, 4345-4353, 1985.

22. Govila, R. K. Pheonmenology of fracture in sintered alpha silicon carbide, J. of Mat. Sci., 19, 2111-2120, 1984.

23. Govila, R. K. High temperature uniqxial tensile stress rupture strength of sintered alpha SiC, J. of Mat. Sci., 18, 1967-1976, 1983.

24. Govila, R. K. Uniaxial Tensile and Flexural Stress Rupture Strength of Hot-Pressed Si_3N_4, January 1982.

25. Govila, R. K., K. R. Kinsman, and P. Beardmore. Phenomenology of fracture in hot-pressed silicon nitride, J. of Mat. Sci., 14, 1095-1102, 1979.

26. Helms, H. E., P. W. Heitman, L. C. Lindgren, and S. R. Thrasher. Ceramic Applications in Turbine Engines, Noyes Publications, New Jersey.

27. Johnson, D. R., et al. "Ceramic Technology for Advanced Heat Engines Project," CONF-8410103-5, n.d.

28. Johnson, D. R. "Ceramic Technology for Advanced Heat Engines Project Semiannual Progress Report for Period October 1983-March 1984," ORNL/TM-9466, December 1984.

29. Kamo, R. and W. Bryzik. "Ceramics in Heat Engines," SAE paper 790645, 1979.

30. Lange, F. F. "Strong, High-Temperature Ceramics," AD775218, February 6, 1974.

31. Larsen, D. C. and J. W. Adams. "Property Screening and Evaluation of Ceramic Turbine Materials," ADA 142739, April 1984.

32. Larsen, R. P. and L. R. Johnson. Argonne, IL, ANL/CNSV-47, August 1984.

33. Larsen, R. P., ed. Proc. of the 22nd Automotive Technology Development Contractors' Coordination Meeting, Dearborn, MI, November 1984.

34. Larsen, D. C., et al. "Evidence of Strength Degradation by Subcritical Crack Growth in SiC and Si_3N_4," in Fracture Mechanics of Ceramics, Vol. 6, Evans, A. G., et al., Plenum Press, New York, 1984.

35. Lenoe, E. M., R. N. Katz, and J. J. Burke, eds. "Ceramics for High Performance Applications-III-Reliability," Plenum Press: New York, 1983.

36. Matthews, M. C. and D. R. Johnson. "Ceramic Technology for Advanced Heat Engines Project Semiannual Progress Report for Period April 1984-September 1984," ORNL/TM-9497, February 1985.

37. ME Staff Report. Mechanical Engineering, 64-67, July 1985.

38. Mueller, J. I., A. S. Kobayashi, and W. D. Scott, eds. "Design with Brittle Materials," University of Washington: Seattle, WA, 1979.

39. Neil, J. T. Materials Engineering, 99(3), 1984.

40. Neil, J. T., K. W. French, C. L. Quackenbush, and J. T. Smith. "Fabrication of Turbine Components and Properties of Sintered Silicon Nitride," ASME Paper #82-GT-252 (1982).

41. Pasto, A. E. In "Ceramic Engineering and Science Proceedings," 5, 385-396, May/June 1984.

42. Pasto, A. E. Journal of the American Ceramic Society, 67(9), September 1984.

43. Pasto, A. E., J. T. Neil, and C. L. Quackenbush. "Microstructural Effects Influencing Strength of Sintered Silicon Nitride," to be published in Proc. of International Conf. on Ultrastructure Processing of Ceramics, Glasses, and Composites (1984).

44. Preprints of the 24th Automotive Technology Development Contractors' Coordination Meeting, SAE CONF-861002, Dearborn, MI, 1986.

45. Proceedings of the 22nd Automotive Technology Development Contractors' Coordination Meeting, SAE P-155, Dearborn, MI, 1984.

46. Proceedings of the 23rd Automotive Technology Development Contractors' Coordination Meeting, SAE P-165, Dearborn, MI, 1985.

47. Quackenbush, C. L. and J. T. Smith. "Sintering, Microstructure, and Properties of Si_3N_4- and SiC-Based Structural Ceramics," ASME Paper #81-GT-220 (1981).

48. Quackenbush, C. L. "Silicon Nitride at GTE," GTE Labs Profile, Vol. 1 (1979), pp. 6-10.

49. Quackenbush, C. L., K. W. French, and J. T. Neil. "Fabrication of Sinterable Silicon Nitride by Injection Molding," presented at Automotive Technology Development Contractor Coordination Meeting, Oct. 26-29, 1981, Dearborn, MI.

50. Quackenbush, C. L., J. T. Smith, and J. T. Neil. "Oxidation in the Si_3N_4-Y_2O_3-SiO_2 Systems," presented at the Automotive Technology Development Contractor Coordination Meeting, Nov. 11-14, 1980, Dearborn, MI.

51. Quackenbush, C. L. and J. T. Smith. "Phase Effects in Silicon Nitride Containing Y_2O_3 or CeO_2:II, Oxidation," Bull. Am. Ceramic, 59(5)533-7 (1980).

52. Quackenbush, C. L., J. T. Smith, J. T. Neil, and K. W. French. "Sintering Properties, and Fabrication of Si_3N_4 + Y_2O_3 Based Ceramics," Progress in Nitrogen Ceramics, ed. by F. L. Riley, pp. 669-682 (1983).

53. Quinn, G. D. "Characterization of Turbine Ceramics After Long-Term Environmental Exposure," Report No. AMMRC-TR-80-15, Army Materials and Mechanics Research Center, April 1980.

54. Quinn, G. D. and J. B. Quinn. "Slow Crack Growth in Hot Pressed Silicon Nitride," in Fracture Mechanics of Ceramics, Vol. 6, Evans, A. G., et al., Plenum Press, New York, 1984.

55. Regan, R. E., W. A. Baginski, and C. A. Krier. Ceramic Bulletin, 46(5), 502-508, 1967.

56. "Reliability of Ceramics for Heat Engine Applications," Natl. Materials Advisory Board, NMAB-357, 1980.

57. Richerson, D. W. "Modern Ceramic Engineering - Properties, Processing, and Use in Design," Marcel Dekker, Inc., New York and Basel.

58. Smith, J. T. and C. L. Quackenbush. "A Study of Sintered Silicon Nitride Compositions with Y_2O_3 and Al_2O_3 Densification Additives," Proc. Int. Symp. Factors Densification and Sintering Oxide Nonoxide Ceramics, pp. 426-442, Japan (1978).

59. Smith, J. T. and C. L. Quackenbush. "Phase Effects in Silicon Nitride Containing Y_2O_3 or CeO_2: I, Strength," Bull. Am. Ceram. Soc. 59 (5) 529-532, 537 (1980).

60. Smothers, W. J., ed. Ceramic Engineering and Science Proceedings, 6(7-8), 1985.

61. Smothers, W. J., ed. Ceramic Engineering and Science Proceedings, 7(7-8), 1986.

62. Stambler, I. Research and Development, 58, May 1986.

63. Stern, K. H. "Oxidation of Silicon, Silicon Carbide (SiC) and Silicon Nitride (Si_3N_4);" NRLM 5774, June 4, 1986.

64. Thomas, H. L. Research and Development, 70-72, July 1986.

65. Thomas, M. B., et al. "Effect of Machining Parameters on the Surface Finish and Strength of Hot Pressed Silicon Nitride," THERM Incorporated, Ithaca, NY, n.d.

66. Torti, M. L., G. Q. Weaver, and D. W. Richerson. "Hot Pressed Silicon Nitride for Gas Turbine Applications," ASME 72-GT-19, 1972.

67. Wachtman, J. B. and M. G. McLaren. Manufacturing Engineering, 56-63, February 1985.

68. Wessel, D. The Wall Street Journal, 27, November 8, 1985.

69. Westwood, A. R. C. and J. P. Skalny. Advanced Ceramic Materials, 1(1), 21,25,35, 1986.

70. Woods, M. E. and I. Oda. "PSZ Ceramics for Adiabatic Engine Components," SAE paper 820429, 1982.

Table 1. Classification of Si_3N_4 and SiC Ceramics by Process

Si_3N_4

1. Hot Pressed Si_3N_4 (HPSN) - α - Si_3N_4 powder (minus 325 mesh) fabricated by uniaxial or isostatic hot pressing. Additives such as MgO, Y_2O_3, ZrO_2, CeO_2, and $SiBeN_2$ are used to enhance densification. The powder mixtures are usually milled then consolidated at pressures of 25-30 MPa and temperatures at or in excess of 1750°C for 1-2 hours. The final product is predominantly β Si_3N_4 and is close to 100% dense.
2. Sintered Si_3N_4 (SSN) - Slip casting, injection molding, and other conventional forming techniques are used to form Si_3N_4 powder and sintering aids prior to pressureless sintering.
3. Reaction Bonded Si_3N_4 (RBSN) - These materials, which are also termed reaction-sintered, are fabricated by a number of different Si powder consolidation processes and are subsequently nitrided. In the initial stage of a multi-stage fabrication process a Si metal preform is prepared. Slip casting, dry pressing, flame spraying, injection molding, or some other forming process is used to produce the green body. In the second stage the green preform is nitrided in an atmosphere of pure N_2 or N_2 and H_2 at a temperature of 1200°C. Prior to final nitriding at 1400°C, the component can be machined. Densities of 75-80% of theoretical are typically obtained for these materials.

SiC

1. Hot Pressed SiC (HPSC) - A minus 325 mesh SiC powder blended with small additions of Al_2O_3, Fe_2O_3, or B to aid densification is prepared for hot pressing by blending and milling. The prepared powders are typically hot pressed at pressures from 25-30 MPa at a temperature of 2150°C for 1-2 hours. Densities of close to 100% are usually obtained.
2. Sintered SiC (SSC) - α and β SiC are prepared by conventional forming and pressureless sintering. Additions of B and C are added to aid densification. Slip casting, extrusion, and dry pressing forming techniques aer used. Sintering is normally carried out at 2150°C for 1-2 hours in an Ar environment. Final densities tend to range between 96-98% of theoretical.
3. Reaction Sintered SiC (RSSC) - Also termed reaction bonded or siliconized SiC and for certain fabrication processes recrystallized SiC. A mixture of SiC powder, graphite, and a plasticiser are formed into a green body. The forming processes used include extrusion and dry pressing. In the initial thermal treatment the plasticiser is burned out or pyrolyzed to a carbon char. Si metal in the liquid or vapor state is introduced into the green body to react with the graphite powder to form SiC which reaction sinters the fabrication component. Excess Si is usually left to fill voids in the material. An alternate method is the infiltration of Si liquid into carbon or graphite fiber preforms.

Table 2. Materials Evaluated in the Literature Reviewed

A. Hot-Pressed Si_3N_4

- Norton NC-132 HP-Si_3N_4 (1% MgO)
- Norton NCX-34 HP-Si_3N_4 (8% Y_2O_3)
- Harbison-Walker HP-Si_3N_4 (10% CeO_2)
- Kyocera SN-3 HP-Si_3N_4 (4% MgO, 5% Al_2O_3)
- Naval Research Laboratory HP-Si_3N_4 (4-16 wt % ZrO_2)
- AFML Developmental HP-Si_3N_4 (CeO_2 and BN Additives)
- Ceradyne Ceralloy 147A, HP-Si_3N_4 (1% MgO)
- Ceradyne Ceralloy 147Y, HP-Si_3N_4 (15% Y_2O_3)
- Ceradyne Ceralloy 147Y-1, HP-Si_3N_4 (8% Y_2O_3)
- Fiber Materials HP-Si_3N_4 (4% MgO)
- Toshiba HP-Si_3N_4 (4% Y_2O_3, 3% Al_2O_3)
- Toshiba HP-Si_3N_4 (3% Y_2O_3, 4% Al_2O_3, SiO_2)
- Westinghouse HP-Si_3N_4 (4% Y_2O_3, SiO_2)
- NASA/AVCO/Norton HP-Si_3N_4 (10% ZrO_2)
- Norton NC-110 HP-Si_3N_4 (MgO + CaO impurities) (1972)
- Norton NC-136 HP-Si_3N_4 (1975)
- Battelle HIP-Si_3N_4 (5% Y_2O_3)

B. Sintered Si_3N_4

- Kyocera SN-250 Sintered Si_3N_4
- GE-Sintered Si_3N_4 (1982)
- Kyocera SN-205 Sintered Si_3N_4 (5% MgO, 9% Al_2O_3)
- Kyocera SN-201 Sintered Si_3N_4 (4% MgO, 7% Al_2O_3)
- GTE Sintered Si_3N_4 (6% Y_2O_3) (AY6-1983)
- AiResearch Sintered Si_3N_4 (8% Y_2O_3, 4% Al_2O_3)
- Rocketdyne SN-50 Sintered Si_3N_4 (6% Y_2O_3, 4% Al_2O_3)
- Rocketdyne SN-104 and SN-46 Sintered Si_3N_4 (14% Y_2O_3, 7% SiO_2)
- NGK (SN-50)/NGK (SN-82) Sintered Si_3N_4
- Ford RM20 Sintered Si_3N_4 (1984)
- ACC Code 2-Sintered Si_3N_4
- Toshiba Sintered Si_3N_4

Table 2. Materials Evaluated in the Literature Reviewed (continued)

C. Reaction Sintered Si_3N_4

- o 1976 Norton NC-350 RS-Si_3N_4
- o Kawecki-Berylco RS-Si_3N_4
- o Ford Injection Molded RS-Si_3N_4 (2,7)
- o AiResearch Slip Cast RS-Si_3N_4 (Airceram RBN-101)
- o Raytheon Isopressed RS-Si_3N_4
- o Indussa/Nippon Denko RS-Si_3N_4
- o AiResearch Injection Molded RS-Si_3N_4 (Airceram RBN-122)
- o 1979 Norton NC-350 RS-Si_3N_4
- o Annawerk Ceranox NR-115H RS-Si_3N_4
- o Associated Engineering Developments (AED) Nitrasil RS-Si_3N_4
- o Georgia Tech RS-Si_3N_4
- o AME RS-Si_3N_4
- o AiResearch RBN-104 RS-Si_3N_4

D. Hot-Pressed SiC

- o Norton NC-203 HP-SiC ($\approx$2% Al_2O_3)
- o Ceradyne Ceralloy 146A, HP-SiC (2% Al_2O_3)
- o Ceradyne Ceralloy 146I, HP-SiC (2% B_4C)
- o AVCO-HP-SiC
- o ACE-HP-SiC

E. Sintered SiC

- o General Electric Sintered β-SiC
- o Carborundum Sintered α-SiC (1977 vintage)
- o Kyocera SC-201, Sintered β-SiC (1980 vintage)
- o Carborundum 1981 SASC (Hexoloy SX-05)
- o ESK Sintered SiC

Table 2. Materials Evaluated in the Literature Reviewed (concluded)

F. Reaction Sintered SiC (Siliconized)

- Norton NC-433-Si/SiC (1976)
- Norton NC-435 Si/SiC
- UKAEA/BNF Refel Si/SiC (diamond-ground and as-processed)
- Norton NC-430 Si/SiC
- Norton NC-400 Si/SiC
- Coors Si/SiC (1979, SC-1)
- Coors Si/SiC (1981 and 1982, SC-2)
- General Electric Silcomp Si/SiC (Grade CC)/(Grade CRC)
- University of Michigan SiC (1984-pyrolyzed polymer infiltrated with Si)

Table 3. Summary of Reported Property Values for Si_3N_4 and SiC

Material Type	Density (g/cc)	MOR_{RT} (MPa)	MOR_{1400} (MPa)	TS_{RT} (MPa)	TS_{1400} (MPa)	E_{RT} (GPa)	E_{1400} (GPa)	K_{Ic} RT (MPa$\sqrt{m}$)	α-20°-1000°C (10^{-6}/°C)	O_2 Behavior Weight Gain (%)/1000 hrs.	Creep Data n	Creep Data Q_c kcal/mol
HPSN	3.18	750	300*	375	150	300	175	4.8+	3.3	0.75	1.2	110
(range)	3.07-3.37	450-1100	0-600	---	---	250-325	175-250	2.8-6.6	3-3.9	.05-2.5	0.5-2.3	
SSN	3.13	415	70	---	---	245	---	4.3	3.5	0.2	1.1	114
(range)	2.8-3.4	275-840	0-700	---	---	195-315	---	3-5.6	---	---		
RSSN	2.4	200	250	170	140	175	155	3.6	2.9	1.5	1.7	82
(range)	2.0-2.8	50-300	0-400	70-210	---	100-220	120-200	---	2.5-3.1	.10-2.6		
HPSC	3.23	500	300	200	35-150	440	380	3.9	4.55	0.3	0.9	--
(range)	3.2-3.3	300-800	175-575	---	---	430-450	---	3-4	4.3-5.4	.1-.6		
SSC	3.1	375	380	---	---	395	372	4	4.5	0.1	1.1	230
(range)	3.0-3.2	275-535	240-450	---	---	375-420	300-400	2.5-6.5	4.4-4.8	.01-.25		
RSSC	3.0	310	190	77	---	360	275	---	4.33	0.1	1.6	235
(range)	2.9-3.1	175-450	70-450	---	---	350-375	200-320	---	4.3-4.4	.06-.16		

*Above 1200°C dynamic fatigue shows slow crack growth.

+K_{Ic} increases at temperatures above 1000°C.

MOR = Flexure Strength
TS = Tensile Strength
E = Young's Modulus
K_{Ic} = Fracture Toughness
Q_c = Activation Energy
n = Creep Constant (slope)
RT = Room Temperature
α = Coefficient of Thermal Expansion

Table 4. Reported Characterization Information for Candidate Materials

Material	Fabrication Method	Chemistry	MOR_{RT} MPa	MOR_{1400} MPa	Elastic Modulus GPa	Fracture Toughness MPa·$\sqrt{m}$	Hardness kg/mm²	Coefficient Thermal Expansion 10^{-6}/°C(20-1000°)	Grain Size µm
GTE PY6	Injection Molded and Hipped	βSi_3N_4+6 w/o Y_2O_3 Trace-Al, Fe, Mo	550-950 (800)	70-275	245-290	4-4.5	-	3.5	.5-3
Sohio Hexoloy	Pressureless Sintered (formed by pressing injection or isostatic forming)	αSiC+.5 β Trace-Al, Fe, Ti, β	300-350	370-380	300	4	2740	4.5	2-8
Norton XL144	Hot Pressed	βSi_3N_4 - no other data	770	300-350	370-395	4-4.5	1600	3.5	3-5

Table 5. Characterization Protocol

Measurement	Technique/Conditions	Number of Specimens
Microstructure	SEM/Optical Microscope	3
Chemistry	XRD/EDXA, Auger	3
Density	Immersion at 25°C	5
Hardness	Microhardness at 25°C	5
Thermal Expansion[+]	Temp. Range 25-1450°C	4
Fracture Toughness[*]	Microindent and DCB at 25°C	10
Flexure Strength[x]	At 25° and 1450°C	10/10
Elastic Modulus	Sonic Velocity	3

[+]Thermal expansion will be measured on four specimens no less than two times for at least three of the specimens from 25° to 1450°C using a Theta Industries Dilatronic II (Model 6024) in order to determine if expansion hysteresis effects are present.

[*]Fracture toughness will be measured by microindentation, controlled flaw and double cantilever beam techniques and a comparison of the toughness values will be made.

[x]Flexure strength will be measured in four-point flexure with an outer span of 3.81 cm (1.50 in), an inner span of 1.91 cm (0.75 in), and a specimen cross section of 0.64 x 0.32 cm (0.250 x 0.125 in), with specimens loaded at a rate of 0.051 cm/min (0.020 in/min), 10 specimens will be used at each test condition.

Table 6. Density Measurements

GTE-PY6	
Specimen Number	Density (g/cc)
1	3.25
9	3.25
26	3.24
33	3.25
66	3.22
Average	3.24

Hexoloy -α- SiC	
Specimen Number	Density (g/cc)
1-1	3.17
1-2	3.17
1-3	3.17
1-4	3.17
1-5	3.17
Average	3.17

Noralide xL144	
Specimen Number	Density (g/cc)
1	3.23
2	3.23
3	3.23
4	3.23
5	3.23
Average	3.23

Table 7. Sonic Modulus

GTE PY6

Specimen No.	Av. Modulus GPa
83	290
92	294
94	294
	Av. 293 (42.4 x 10^6 psi)

Hexoloy-α-SiC

Specimen No.	Av. Modulus GPa
5-4	426
5-5	429
5-6	427
	Av. 427 (61.9 x 10^6 psi)

Noralide XL144

Specimen No.	Av. Modulus GPa
28	312
29	316
30	314
	Av. 314 (45.5 x 10^6 psi)

Table 8. Microhardness

GTE PY6

Specimen No.	Vickers Hardness (kg/mm^2)
5	1386
56	1489
66	1440
73	1484
95	1491
	1458 (st. dev. 118)

Hexoloy-α-SiC

Specimen No.	Vickers Hardness (kg/mm^2)
1-3	2611
1-4	2524
1-5	2638
3-9	2611
3-10	2558
	2588 (st. dev. 80)

Noralide XL144

Specimen No.	Vickers Hardness (kg/mm^2)
1	1367
3	1440
4	1437
8	1419
10	1441
	1421 (st. dev. 52)

Table 9. X-Ray Diffraction Analysis for GTE PY6 As Received

2θ	D - Spacing	Intensity (I/I_{max} = 100)	Crystal Phase
23.4	3.801	29	β[+]
26.5	3.363	6	?α[*]
27.1	3.290	82	β
29.7	3.013	6	?Y[#]
33.9	2.659	88	β
36.1	2.488	100	β
37.1	2.426	6	-
37.6	2.392	6	-
39.0	2.312	12	β
41.5	2.178	29	β
48.05	1.901	12	β
50.0	1.826	18	β
52.2	1.752	41	β
58.0	1.591	18	β

[+]β - β phase Si_3N_4

[*]α - α phase Si_3N_4

[#]Y - $Y_2Si_2O_7$

Table 10. X-Ray Diffraction Analysis For GTE PY6 After Testing At 1450°C

2θ	D - Spacing	Intensity (I/I_{max} = 100)	Crystal Phase
21.95	4.05	92	C*
23.4	3.802	27	β+
26.5	3.364	1	?α#
27.1	3.291	94	β
27.75	3.215	6	Yx
28.4	3.145	4	C
29.5	3.028	3	Y
31.45	2.845	11	C
33.7	2.66	85	β
36.1	2.488	100	β
39.05	2.307	11	Y
41.45	2.179	36	β

*C - cristobalite

+β - β phase Si_3N_4

#α - α phase Si_3N_4

xY - $Y_2Si_2O_7$

Table 11. X-Ray Diffraction Analysis For Norton Noralide XL-144 As Received

2θ	D - Spacing	Intensity (I/I_{max} = 100)	Crystal Phase
23.55	3.778	29	β*
27.25	3.273	97	β
33.85	2.648	39	β
36.25	2.478	100	β
39.2	2.298	6	β
41.6	2.171	13	β
48.05	1.894	11	β
50.1	1.821	12	β
52.4	1.746	24	β
58.15	1.587	11	β

*β - β phase Si_3N

Table 12. X-Ray Diffraction Analysis For Norton Noralide XL144 After Testing At 1450°C

2θ	D - Spacing	Intensity (I/I_{max} = 100)	Crystal Phase
21.95	4.05	24	C[+]
23.4	3.802	25	β[*]
27.1	3.291	97	β
27.7	3.221	6	Y[#]
29.45	3.033	8	Y
31.45	2.845	1	C
32.75	2.735	1	-
33.25	2.695	5	-
33.7	2.66	33	β
36.1	2.488	100	β
39.0	2.31	4	β
39.7	2.271	1	Y
41.45	2.179	13	β

[+]C - cristobalite

[*]β - β phase Si_3N_4

[#]Y - $Y_2Si_2O_7$

Table 13. X-Ray Diffraction Analysis For Sohio Hexoloy -α-SiC As Received

2θ	D - Spacing	Intensity (I/I_{max} = 100)	Crystal Phase
24.9	3.555	3	-
26.75	3.339	1	-
34.2	2.618	25	α*
34.95	2.564	4	-
35.75	2.508	100	α
38.25	2.350	31	α
41.5	2.173	13	α
45.4	1.996	6	α
55.0	1.675	7	α
60+	1.535	60	α

*α - α phase SiC

Table 14. X-Ray Diffraction Analysis For Sohio Hexoloy-α-SiC After Testing At 1450°C

2θ	D - Spacing	Intensity (I/I_{max} = 100)	Crystal Phase
22	4.041	9	C*
34.2	2.622	33	α#
34.95	2.568	8	α
35.75	2.512	100	α
38.25	2.353	36	α
41.5	2.176	17	α
45.4	1.998	8	α

*C - cristobalite

#α - α phase SiC

Table 15. Measured Flexure Strength Of Sohio Hexoloy SA-α-SiC At 25°C

SPECIMEN NUMBER	WIDTH (in)	THICKNESS (in)	LOAD (lbs)	ULTIMATE STRENGTH MPa	ksi
1-1	0.2452	0.1220	158	336	48.7
1-2	0.2455	0.1224	135	285	41.3
1-3	0.2452	0.1225	154	325	47.1
1-4	0.2453	0.1226	132	278	40.3
1-5	0.2454	0.1225	166	350	50.7
3-6	0.2454	0.1228	147	308	44.7
3-7	0.2453	0.1221	191	405	58.8
3-8	0.2453	0.1215	138	296	42.9
3-9	0.2454	0.1228	181	379	55.0
3-10	0.2451	0.1231	167	349	50.6
			Average	331	48.0
			Stdev.	41	6.0
		95% confidence limits on mean		302-360	44-52

Table 16. Measured Flexure Strength Of Sohio Hexoloy SA-α-SiC At 1450°C

SPECIMEN NUMBER	WIDTH (in)	THICKNESS (in)	LOAD (lbs)	ULTIMATE STRENGTH MPa	ksi
5-1	0.2438	0.1220	218	466	67.6
5-2	0.2439	0.1225	278	589	85.5
5-3	0.2448	0.1221	277	589	85.4
3-4	0.2454	0.1232	227	473	68.6
3-5	0.2457	0.1236	252	521	75.5
1-6	0.2455	0.1225	236	497	72.1
1-7	0.2453	0.1235	238	493	71.6
1-8	0.2455	0.1226	230	483	70.1
1-9	0.2455	0.1231	212	442	64.1
1-10	0.2455	0.1228	214	448	65.0
			Average	500	72.5
			Stdev.	52	7.6
			95% confidence limits on mean	463-538	67-78

Table 17. Measured Flexure Strength Of GTE Silicon Nitride, PY6 At 25°C

SPECIMEN NUMBER	WIDTH (in)	THICKNESS (in)	LOAD (lbs)	ULTIMATE STRENGTH MPa	ksi
1	0.2427	0.1230	319	674	97.7
5	0.2425	0.1231	290	612	88.8
9	0.2424	0.1224	273	583	84.6
26	0.2434	0.1235	328	685	99.4
33	0.2435	0.1216	348	750	108.7
56	0.2427	0.1219	273	587	85.2
66	0.2428	0.1222	337	721	104.6
73	0.2433	0.1214	314	679	98.5
76	0.2387	0.1159	232	561	81.4
95	0.2425	0.1230	265	560	81.3
			Average	641	93.0
			Stdev.	69	10.0
			95% confidence limits on mean	592-691	86-100

Table 18. Measured Flexure Strength Of GTE Silicon Nitride, PY6 At 1450°C

SPECIMEN NUMBER	WIDTH (in)	THICKNESS (in)	LOAD (lbs)	ULTIMATE STRENGTH MPa	ksi
6	0.2125	0.1167	169	453	65.7
13	0.2437	0.1168	132	308	44.7
17	0.2444	0.1154	193	460	66.7
23	0.2408	0.1185	177	406	58.9
24	0.2376	0.1162	180	435	63.1
43	0.2394	0.1176	185	433	62.9
48	0.2401	0.1176	133	311	45.1
53	0.2388	0.1147	109	269	39.0
61	0.2391	0.1158	175	423	61.4
67	0.2400	0.1181	185	429	62.2
			Average	393	57.0
			Stdev.	69	10.0
			95% confidence limits on mean	343-442	50-64

Table 19. Measured Flexure Strength Of Norton Si_3N_4 Noralide XL144 At 25°C

SPECIMEN NUMBER	WIDTH (in)	THICKNESS (in)	LOAD (lbs)	ULTIMATE STRENGTH MPa	ksi
1	0.2439	0.1236	217	452	65.5
3	0.2439	0.1236	252	525	76.1
4	0.2419	0.1239	291	608	88.2
5	0.2438	0.1234	241	504	73.0
7	0.2440	0.1238	349	724	105.0
8	0.2454	0.1241	210	431	62.5
9	0.2438	0.1237	283	588	85.3
10	0.2432	0.1240	227	471	68.3
11	0.2448	0.1240	216	445	64.6
12	0.2438	0.1234	302	631	91.5
			Average	538	78.0
			Stdev.	97	14.0
			95% confidence limits on mean	467-607	68-88

Table 20. Measured Flexure Strength Of Norton Si_3N_4 Noralide XL144 At 1450°C

SPECIMEN NUMBER	WIDTH (in)	THICKNESS (in)	LOAD (lbs)	ULTIMATE STRENGTH MPa	ksi
13	0.2443	0.1246	242	495	71.8
14	0.2440	0.1238	214	444	64.4
16	0.2448	0.1240	172	354	51.4
17	0.2428	0.1244	207	427	62.0
19	0.2411	0.1243	238	496	71.9
21	0.2424	0.1243	182	377	54.7
22	0.2420	0.1242	222	461	66.9
23	0.2425	0.1243	249	516	74.8
25	0.2415	0.1263	237	477	69.2
27	0.2432	0.1248	236	483	70.1
			Average	453	65.7
			Stdev.	53	7.7
			95% confidence limits on mean	415-491	60-71

Table 21. Summary Of Weibull Analysis Results

Material Designation	Test Temp.(°C)	Average Strength (MPa)	Shape Parameter ($\hat{M}$)	Scale Parameter ($\hat{So}$)	Confidence Bounds M LCL*	M UCL+	So LCL	So UCL
GTE PY6	25	641	10.80	671	5.94	14.69	632	714
GTE PY6	1450	393	8.30	419	4.57	11.25	388	454
Hexoloy SiC	25	331	8.90	349	4.90	12.10	342	376
Hexoloy SiC	1450	500	9.88	524	5.43	13.44	490	560
Norton XL144	25	538	6.06	578	3.33	8.24	520	645
Norton XL144	1450	453	12.02	474	6.61	16.35	449	501

*LCL - lower confidence limit.

+UCL - upper confidence limit.

Table 22. Comparison Of Average Strengths Between Temperatures For Each Material

A. HEXOLOY

SOURCE	DF	SS	MS	F
FACTOR	1	142805	142805	64.60
ERROR	18	39788	2210	
TOTAL	19	182593		

LEVEL	N	MEAN	STDEV
HEX25	10	331.10	41.10
HEX1450	10	500.10	52.26

POOLED STDEV = 47.02

```
INDIVIDUAL 95 PCT CI'S FOR MEAN
BASED ON POOLED STDEV
--------+---------+---------+-------
 (---*----)
                          (---*----)
--------+---------+---------+-------
     350       420       490
```

B. GTE PY6

SOURCE	DF	SS	MS	F
FACTOR	1	308761	308761	64.64
ERROR	18	85974	4776	
TOTAL	19	394735		

LEVEL	N	MEAN	STDEV
PY625	10	641.20	68.99
PY61450	10	392.70	69.24

POOLED STDEV = 69.11

```
INDIVIDUAL 95 PCT CI'S FOR MEAN
BASED ON POOLED STDEV
------+---------+---------+---------
                          (---*----)
 (---*----)
------+---------+---------+---------
   400       500       600       700
```

C. NORALIDE XL144

SOURCE	DF	SS	MS	F
FACTOR	1	36040	36040	5.93
ERROR	18	109409	6078	
TOTAL	19	145449		

LEVEL	N	MEAN	STDEV
NORT25	10	537.90	96.58
NORT1450	10	453.00	53.18

POOLED STDEV = 77.96

```
INDIVIDUAL 95 PCT CI'S FOR MEAN
BASED ON POOLED STDEV
----+---------+---------+---------
                 (--------*--------)
 (--------*--------)
----+---------+---------+---------+
 420       480       540       600
```

Table 23. Analysis of Variance of Ultimate Strengths for GTE PY6 and Noralide by Temperature

Source of Variation	Degrees of Freedom	Mean Square Error	F Ratio
Temperature	1	2777889	51.2
Material	1	4623	8.5
T x M	1	66912	12.3
Error	36	5427	
Total	39		

Standard error for comparing average of 10 specimens:

$$\frac{5427}{10} = 23.3 \text{ MPa}$$

Table 24. Composition of Freshly Fractured Surface of GTE PY6 Silicon Nitride

Region	Si	B	C	N	O
#1	42.5	T*	3.6	31.1	22.8
#2	37.4	T	4.7	34.4	23.5
#3	31.9	---	3.9	35.0	29.2

*Trace amount

Table 25. Composition of Features of Interest on Freshly Fractures GTE PY6 Silicon Nitride

Region	Si	B	C	N	O	Ni
#4	T	11.4	19.5	42.3	26.7	---
#5	26.2	T	19.9	30.5	21.4	2
#6	39.1	---	5.6	31.8	23.5	---
#7	41.3	---	10.5	25.7	22.5	---
#8	17.1	---	9.5	42.8	30.6	---
#9	37.2	T	4.4	31.1	27.3	---

Table 26. Composition of Freshly Fractured Noralide Silicon Nitride

Region	Si	B	C	N	O
#1	35.8	-	3.8	36.0	24.4
#2	35.6	1.2	3.9	34.1	25.3
#3	30.9	T	4.4	36.1	28.6

Table 27. Composition of Features of Interest on Noralide Silicon Nitride Fracture Surface

Region	Si	B	C	N	O
#4	35.4	T	4.5	32.8	27.3
#5	31.8	2.9	5.6	31.5	28.2
#6	33.9	T	5.1	34.8	26.1
#7	33.3	-	5.5	34.8	26.4
#8	25.9	4.2	10.9	33.4	25.6
#9	28.0	2.2	7.6	35.7	26.4
#10	28.7	-	6.8	36.2	28.2

Table 28. Composition of Freshly Fractured Hexoloy Silicon Carbide

Region	Si	B	C	O
#1	27.6	1.2	59.1	12.1
#2	27.4	1.1	59.7	11.8
#3	26.8	1.3	59.3	12.6
#4	27.9	1.2	58.7	12.3

Table 29. Composition of Regions of Interest on Hexoloy Silicon Carbide Fractured Surface

Region	Si	B	C	O
#5	26.6	2.1	60.7	10.7
#6	27.4	-	58.6	14.0
#7	27.9	T	57.7	14.4
#9	25.6	-	61.2	13.2
#10	25.8	-	61.7	12.5
#11	26.1	1.3	57.3	15.2

Table 30. Thermal Expansion Test Results

MATERIAL	SPECIMEN NUMBER	TEMP (°C)	C.T.E. ($X10^{-6}$)
Noralide XL144 Norton Si_3N_4	6	1460	3.3
	18	1200	4.0
		1250	3.6
	20	1465	2.9
		1475	3.3
	26	1450	4.2
		1450	2.7
		Average	3.4
		Stdev.	0.5
PY6 GTE Si_3N_4	32	1450	4.2
		1480	3.0
	39	1425	4.3
		1450	2.8
		1450	2.9
	63	1390	4.0
		1475	3.0
	83	1460	3.3
		Average	3.4
		Stdev.	0.6
Hexoloy SA Sohio SiC	3-1	1460	5.2
		1460	5.1
	5-7	1465	5.9
		1475	5.2
	5-9	1465	5.8
		1475	5.0
	5-10	1410	5.7
		Average	5.4
		Stdev.	0.4

Table 31. Fracture Toughness Results for GTE PY6

Specimen Number	Load (lbs)	Crack Length (μm)	Av. K_{Ic} by Micro-indent (MPa·√m) (av. indent diag. ≈55 μm)	K_{Ic} by controlled flaw (MPa·√m)
1	115	94.8	6.1	3.2
3	112	82.8		3.0
4	102	89.5		2.8
10	119	79.8		3.1
				3

Table 32. Fracture Toughness Results for Noralide XL144

Specimen Number	Load (lbs)	Crack Length (μm)	Av. K_{Ic} by Micro-indent (MPa·√m) (av. indent diag. ≈52 μm)	K_{Ic} by controlled flaw (MPa·√m)
1	97	130	3.8	3.1
3	91	108		2.7
4	128	93		3.5
10	113	97		3.1
				3.1

Table 33. Fracture Toughness Results for Hexoloy-α-SiC

Specimen Number	Load (lbs)	Crack Length (μm)	Av. K_{Ic} by Micro-indent (MPa·√m) (av. indent diag. ≈20 μm)	K_{Ic} by controlled flaw (MPa·√m)
2	84	60	2.55	invalid fracture
3	110	50		2.2
4	95	60		invalid fracture
9	64	54		1.4
10	99	66		2.3
				2

APPENDIX 1

ADDITIONAL MATERIAL CHARACTERIZATION STUDIES

During the course of this project, we obtained two additional materials for limited characterization. CVD Inc. provided us with a SiC prepared by chemical vapor deposition, and Sohio Engineered Materials provided us with a "Sylon 102" material. Ten test specimens of SiC were provided for our first evaluation. This material was used for flexure strength measurements at 25°C and 1450°C. In addition, material was provided for fracture toughness, hardness, Young's modulus, and Poisson's ratio. The results of these evaluations are summarized in Table 1A.

Table 1A. Summary of Characterization Studies for CVD SiC Material

1.	Hardness (Vickers - 500 gm load)	2600 kg/mm^2
2.	Young's Modulus (sonic measurement)	470 GPa
3.	Poisson's Ratio	0.23
4.	Flexure Strength @ 25°C (4 pt. bend)	554 MPa
5.	Standard Deviation	120 MPa
6.	Flexure Strength @ 1450°C (4 pt. bend)	556 MPa
7.	Standard Deviation	27.6 MPa
8.	Fracture Toughness (microindent)	2.6 $MPa\sqrt{m}$

Sohio Engineered Materials Inc. provided us with a billet of their SiAlON material "Sylon 102" for evaluation. Flexure strength, Young's Modulus, density, microstructure, and chemistry were

investigated. Flexure strengths were measured at 25°C, 1400°C, and 1200°C. At 1400°C the materials tested underwent severe oxidation and retained only 10% of their room temperature flexure strength. The materials tested at 1200°C were not greatly affected by the oxidizing environment and retained a significant fraction of their room temperature strength. A summary of the property values measured for the "Sylon 102" material is presented in Table IB. Photomicrographs of test specimens fractured at 25°C and 1200°C are presented in Figures A through D. EDXA spectra of specimens tested at 25°C are presented in Figure E.

Table IB. Summary of Property Measurement Data for Sylon 102

1.	Density	3.21 g/cc
2.	Young's Modulus	311 GPa
3.	Flexure Strength @ 25°C	672 MPa
4.	Standard Deviation	51 MPa
5.	Flexure Strength @ 1200°C	319 MPa
6.	Standard Deviation	17 MPa

The results of these preliminary evaluations show that the CVD SiC has good flexure strength at both room temperature and 1450°C. An average flexure strength of 550 MPa is significantly higher than is reported for SiC prepared by any other processing methods. The CVD SiC also shows good hardness and good oxidation resistance. However, the measured fractured toughness was somewhat lower than

usually reported for SiC. The Sylon 102 material showed good room temperature flexure strength with a relatively narrow standard deviation. However, the poor oxidation resistance observed would appear to limit its high temperature use to below 1200°C.

Figure E. EDXA spectrum of Sylon 102 as-received.

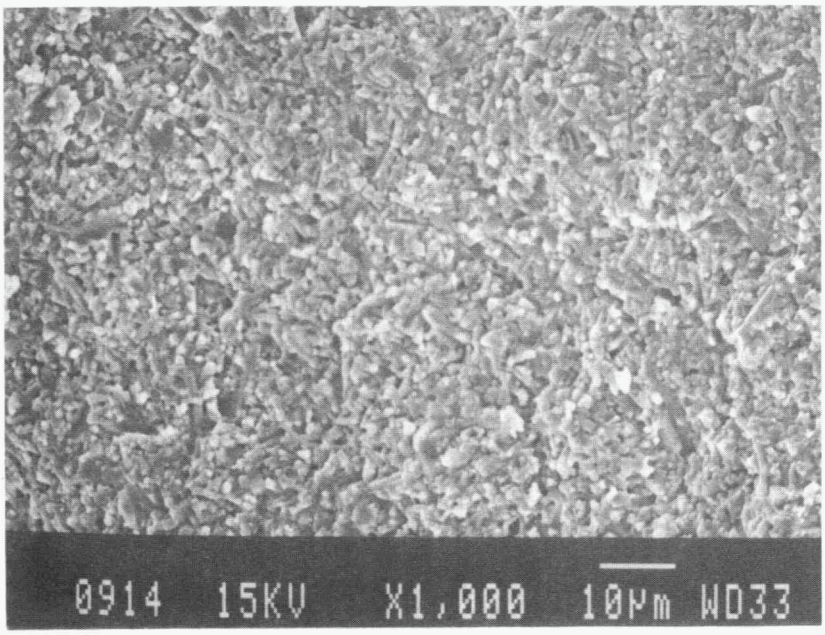

Figure A. SEM photomicrograph of Sylon 102 as received.

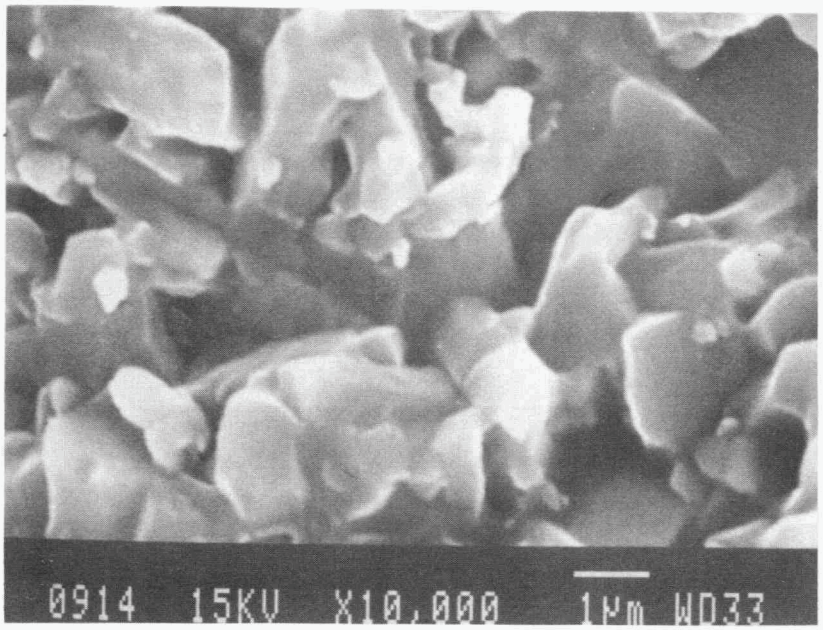

Figure B. SEM photomicrograph of Sylon 102 as received.

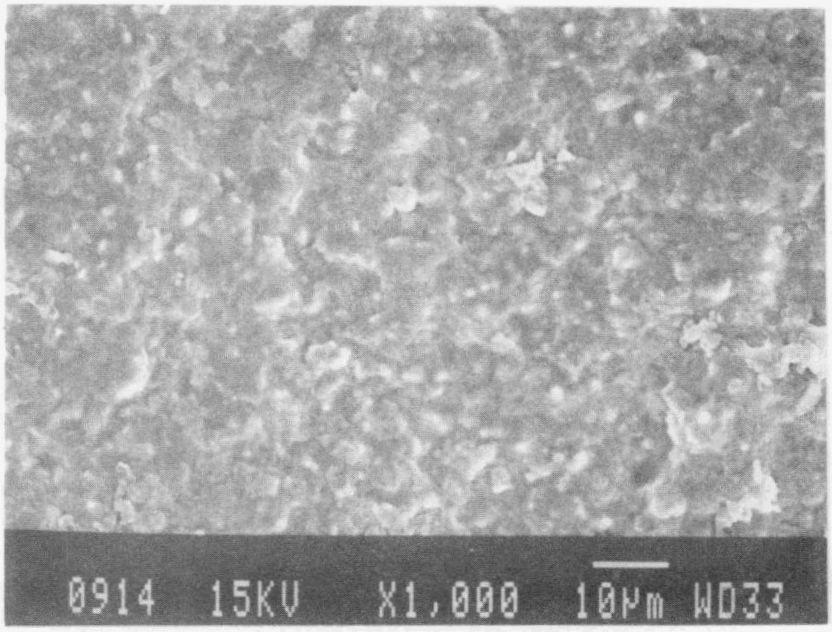

Figure C. SEM photomicrograph of Sylon 102 tested to 1200°C.

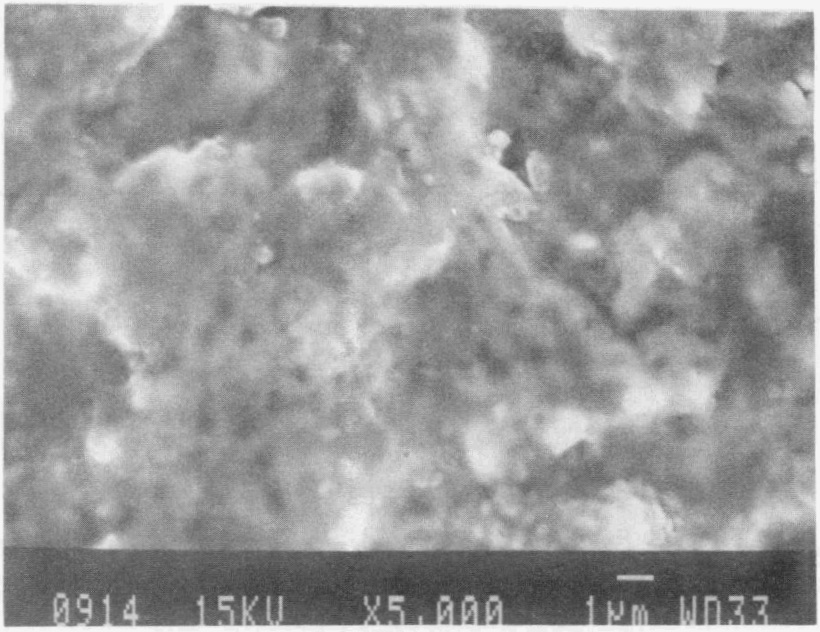

Figure D. SEM photomicrograph of Sylon 102 tested to 1200°C.

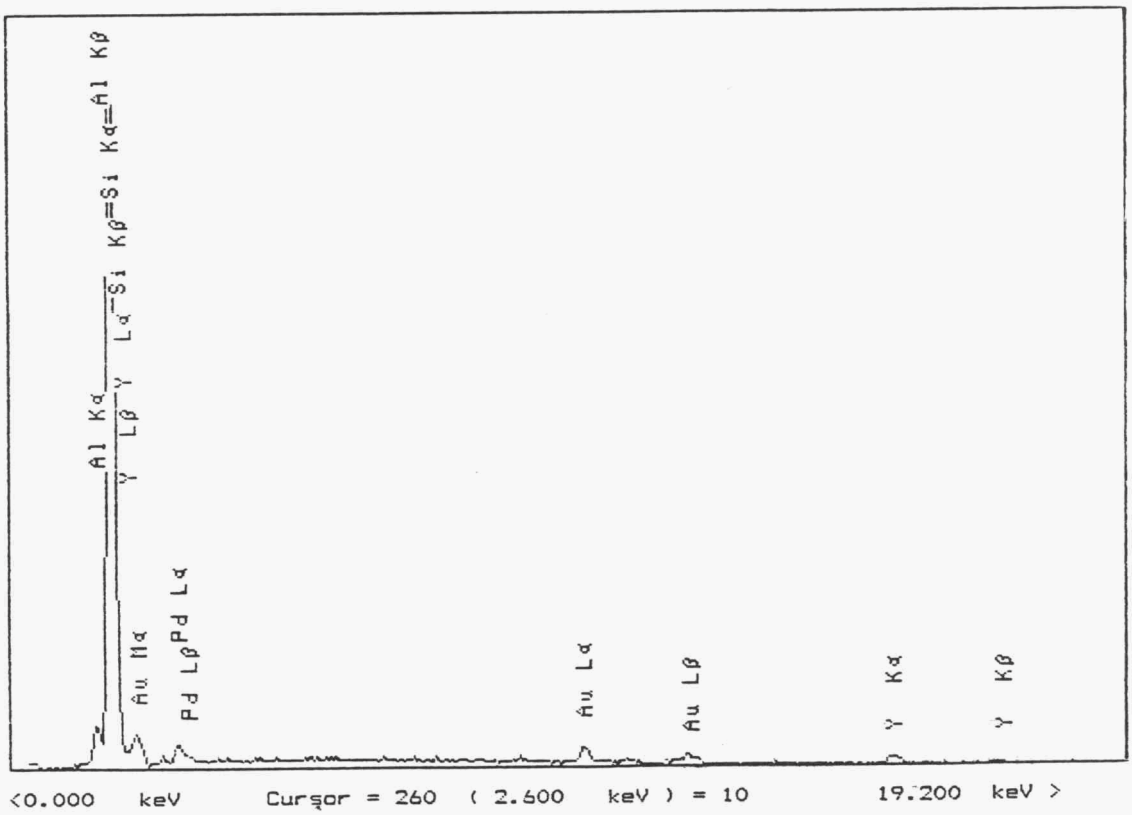

Figure E. EDXA spectrum of Sylon 102 as received.

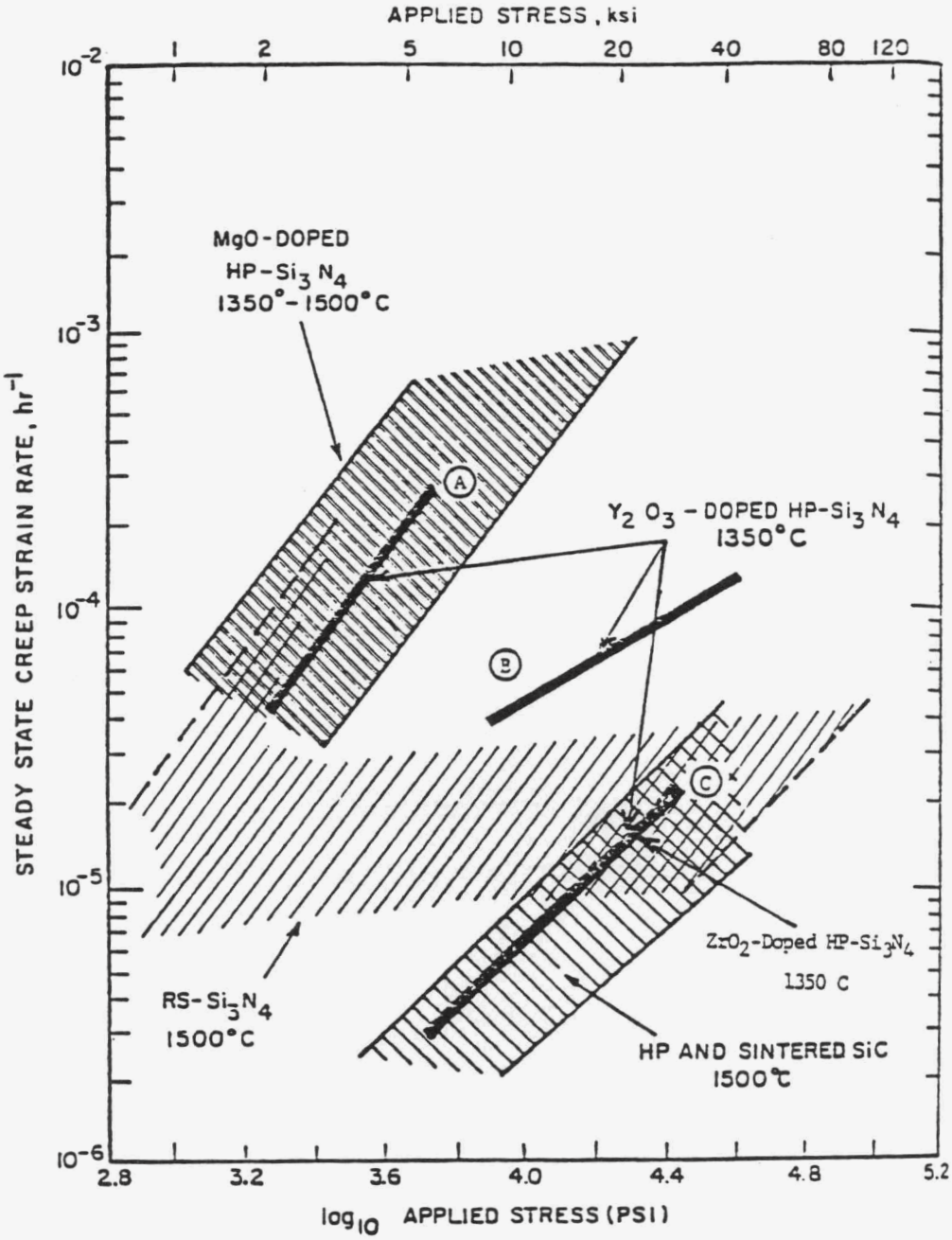

Figure 1. Flexure creep behavior of various Si_3N_4 and SiC materials.[31]

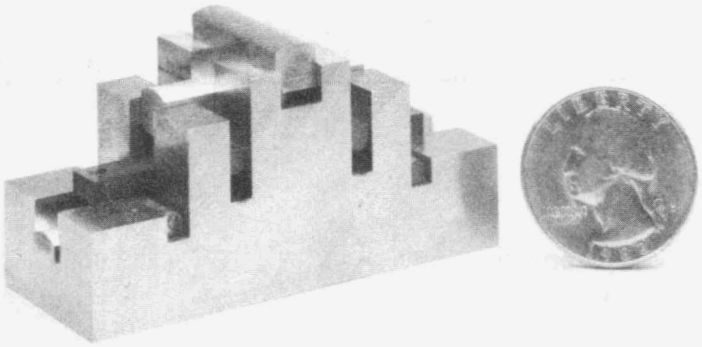

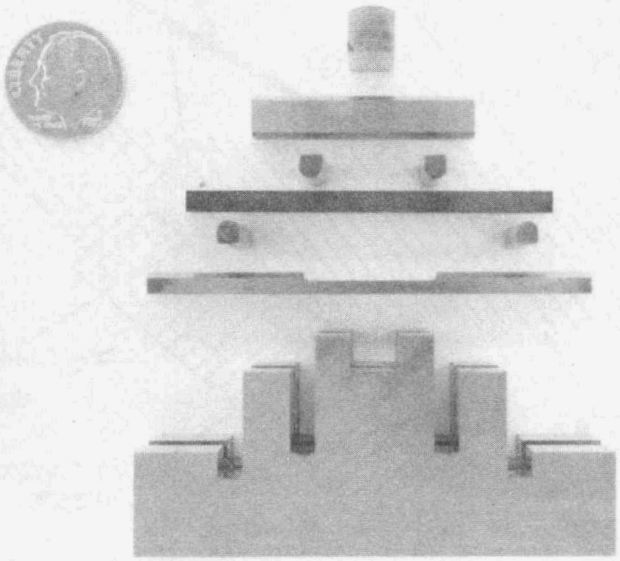

Figure 2. The four point bend fixture for flexure testing.

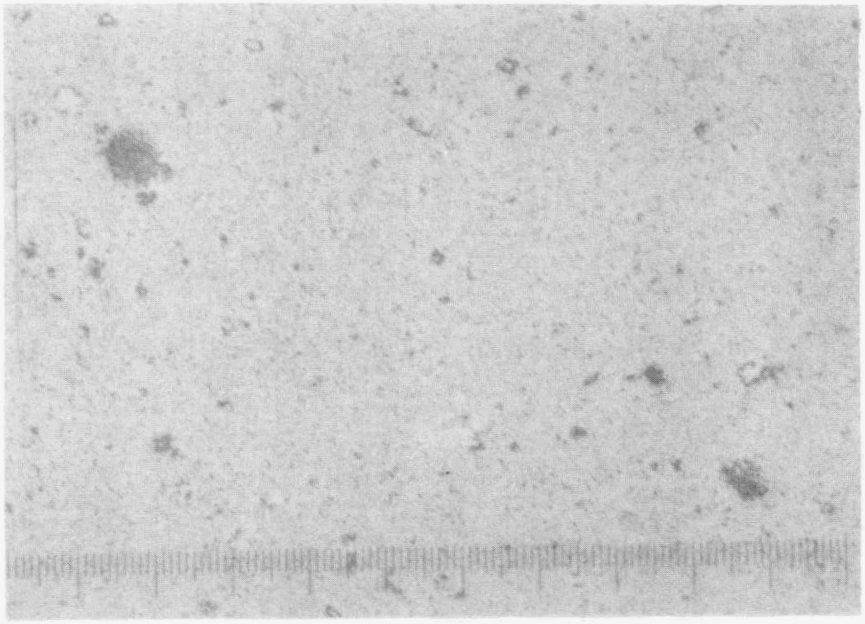

minor division = 2.5 μm

Figure 3. Optical microscope photomicrograph of the Sohio-Hexoloy α-SiC material.

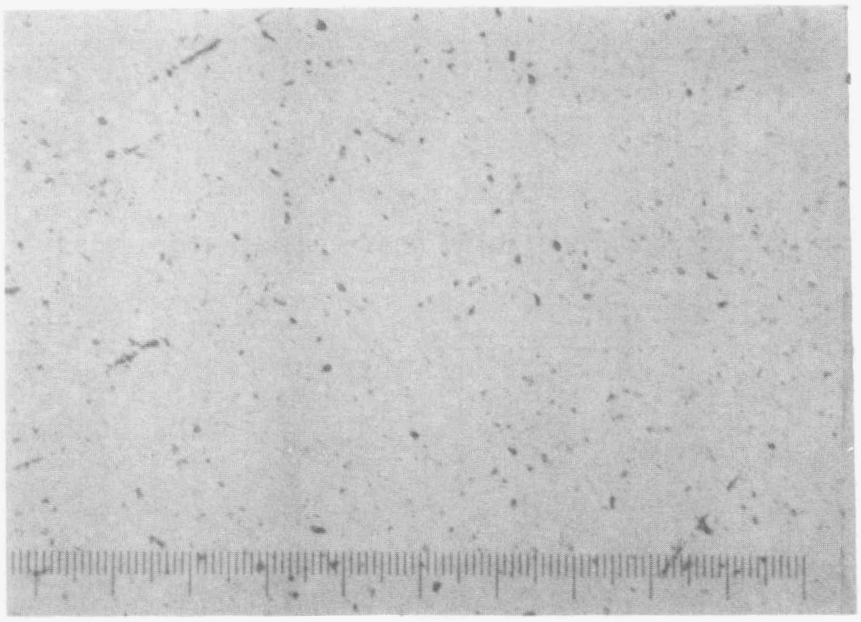

minor division = 2.5 μm

Figure 4. Optical microscope photomicrograph of the GTE PY6 material.

10 μm

Figure 5. Norton Noralide XL144 heat treated and etched in HF at 1000X.

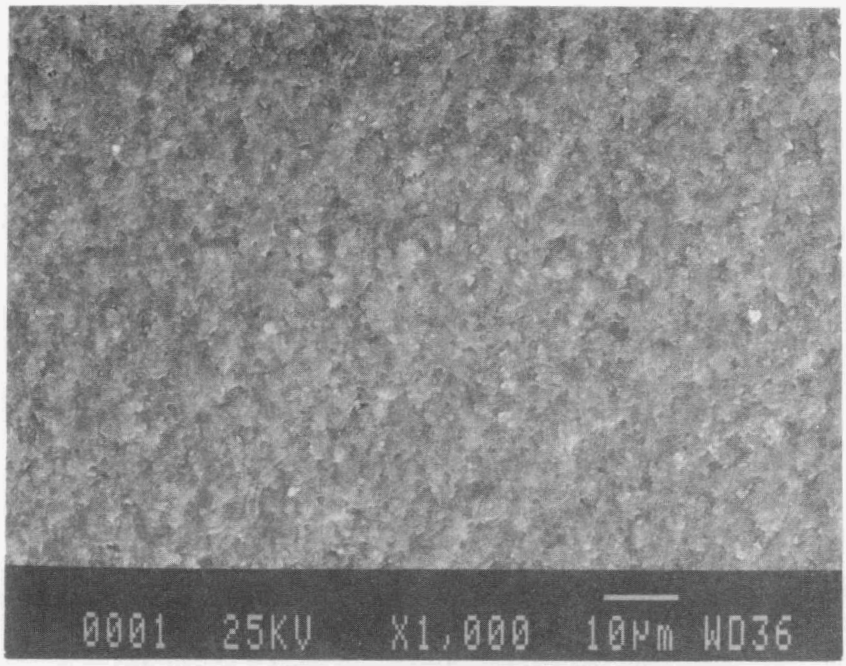

Figure 6. SEM photograph of a GTE PY6 specimen.

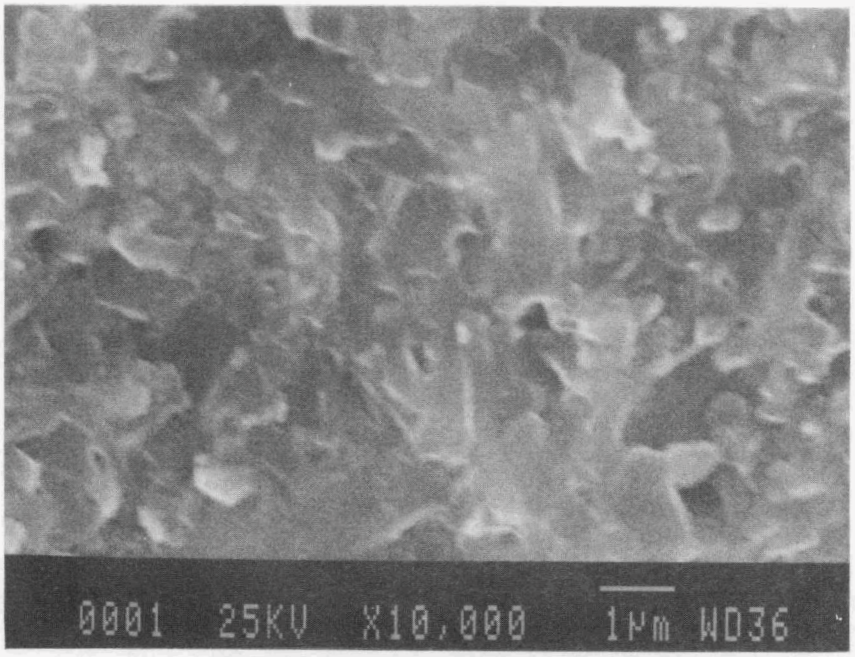

Figure 7. SEM photograph of a GTE PY6 specimen.

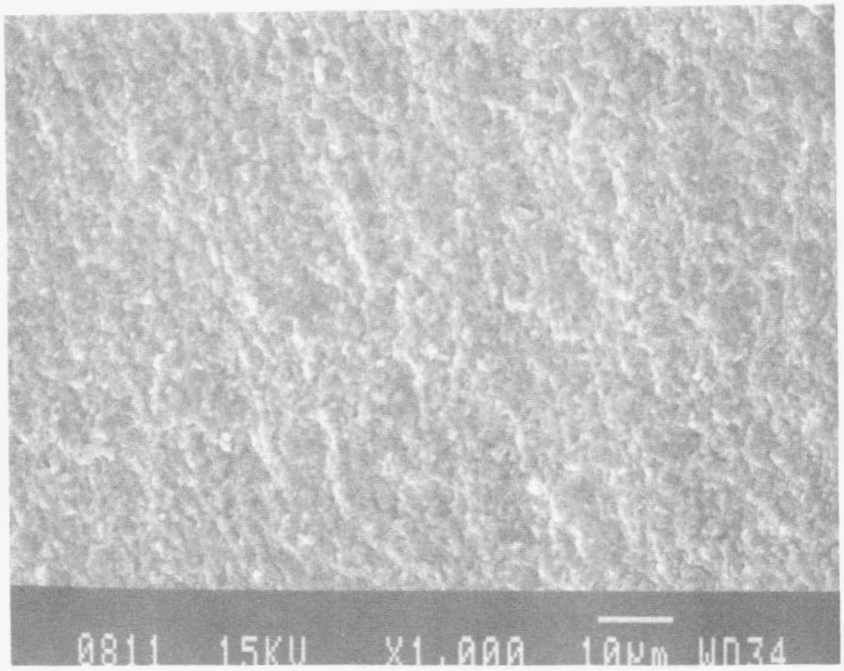

Figure 8. SEM photomicrograph of an etched GTE PY6 specimen.

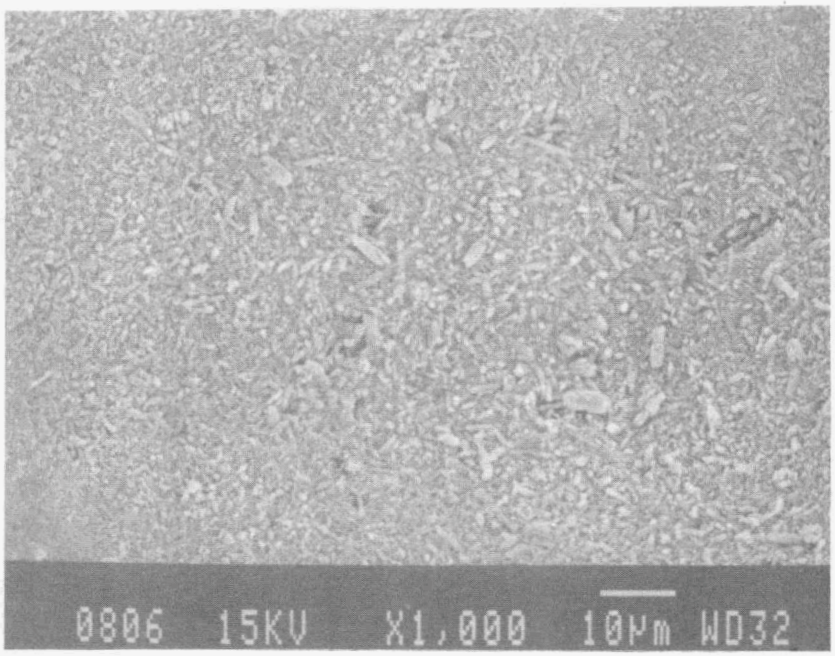

Figure 9. SEM photomicrograph of a GTE PY6 specimen tested at 1450°C.

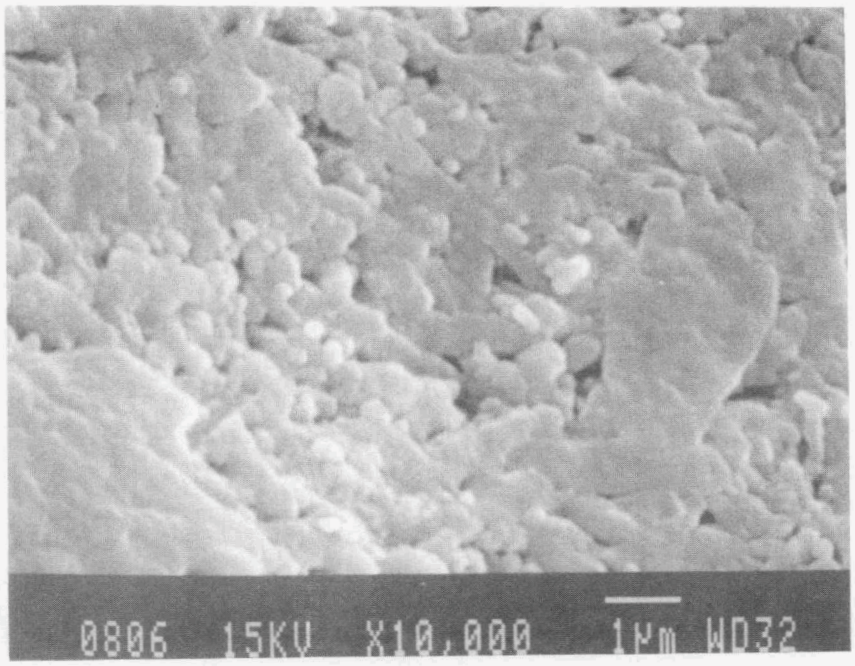

Figure 10. SEM photomicrograph of a GTE PY6 specimen tested at 1450°C.

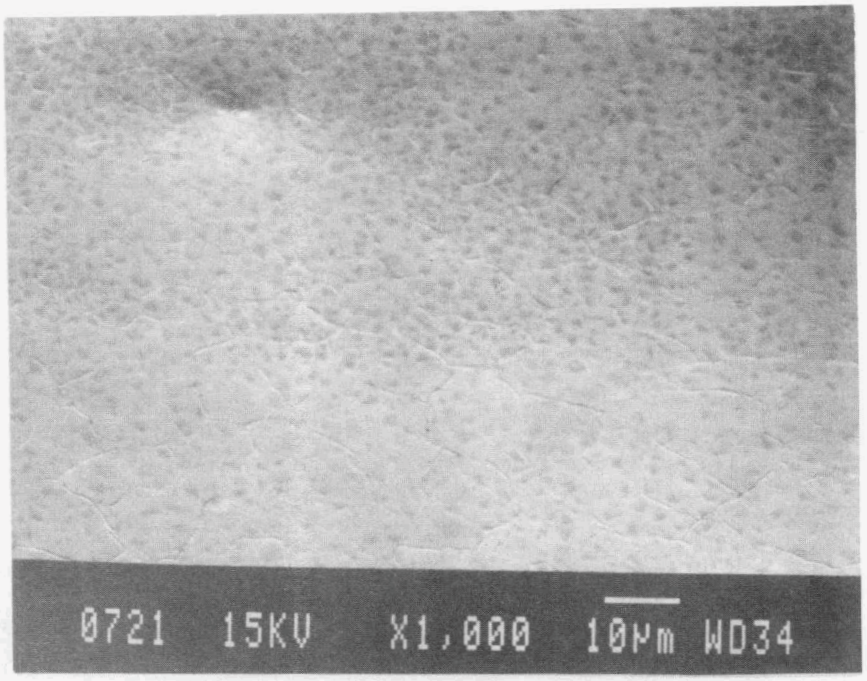

Figure 11. SEM photomicrograph of the glass surface of a GTE PY6 specimen tested at 1450°C.

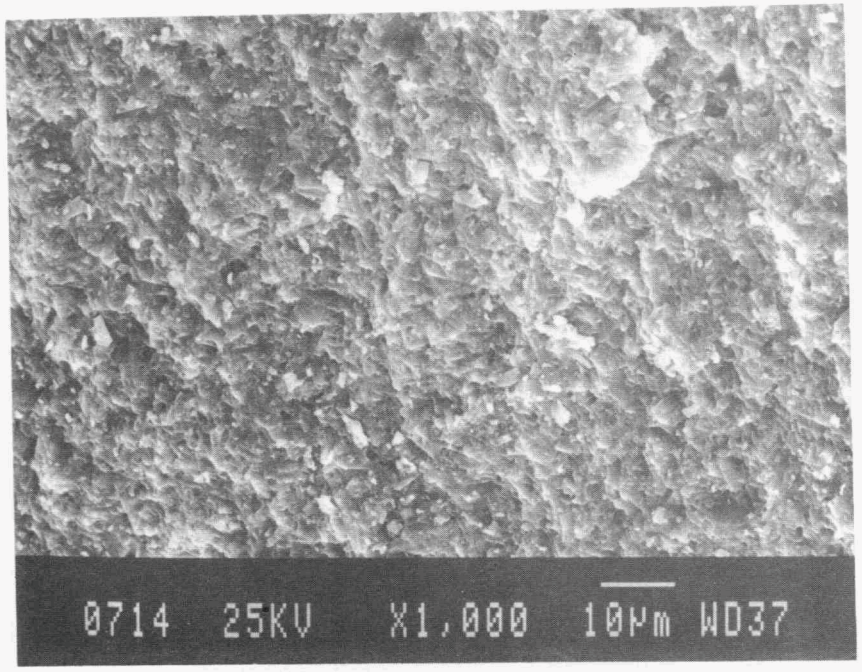

Figure 12. SEM photomicrograph of a Norton Noralide XL144 specimen.

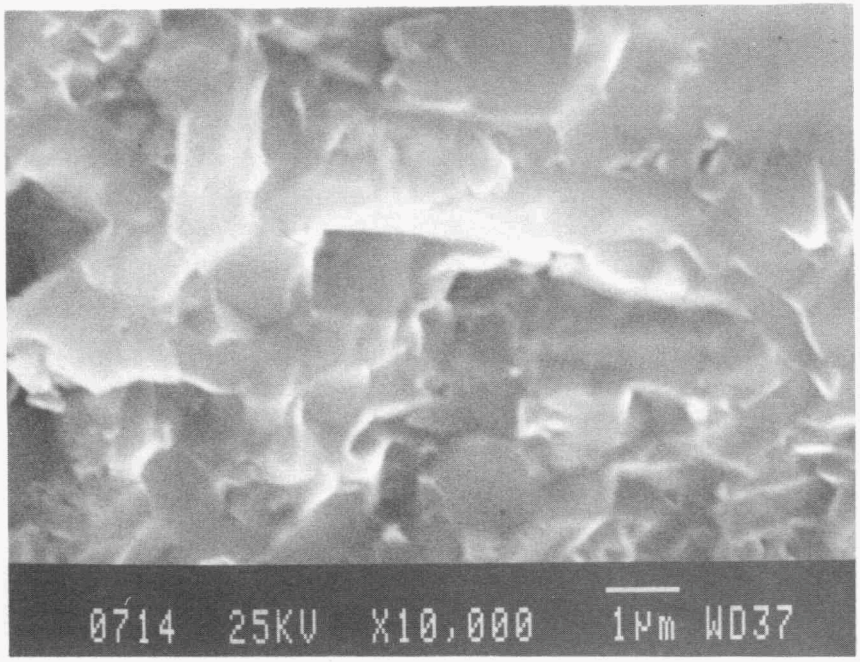

Figure 13. SEM photomicrograph of a Norton Noralide XL144 specimen.

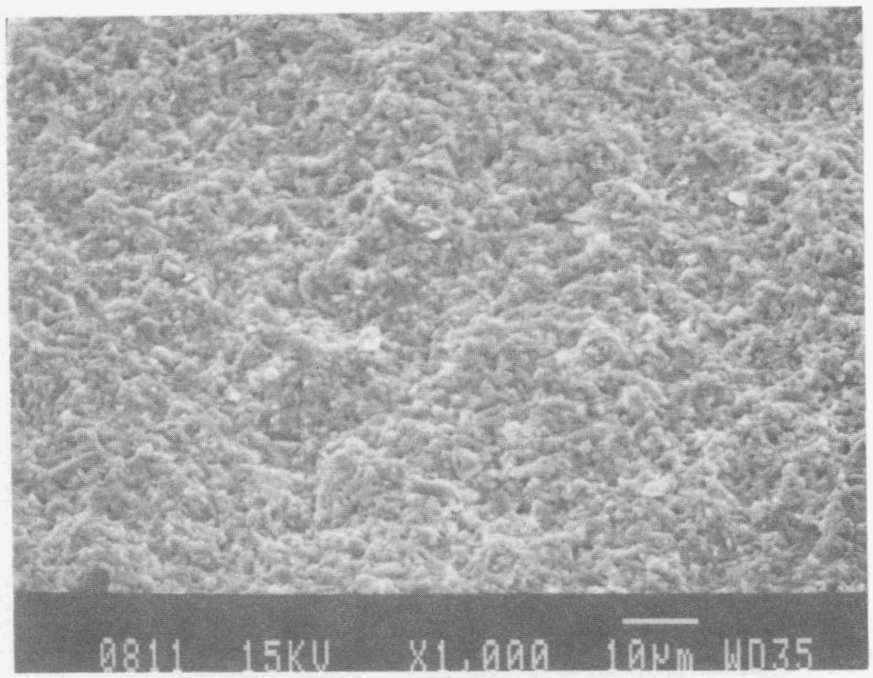

Figure 14. SEM photomicrograph of an etched Norton Noralide XL144 specimen.

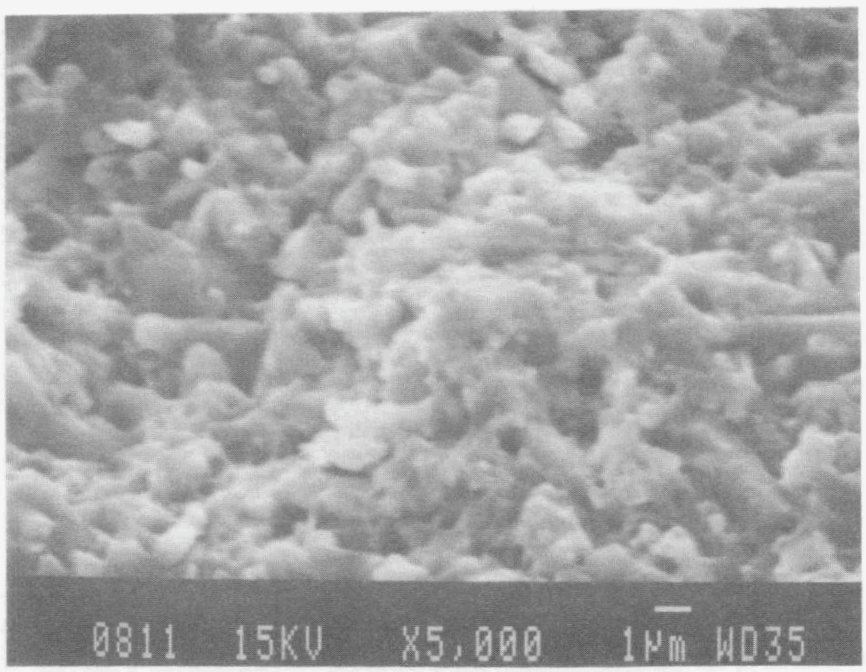

Figure 15. SEM photomicrograph of an etched Norton Noralide XL144 specimen.

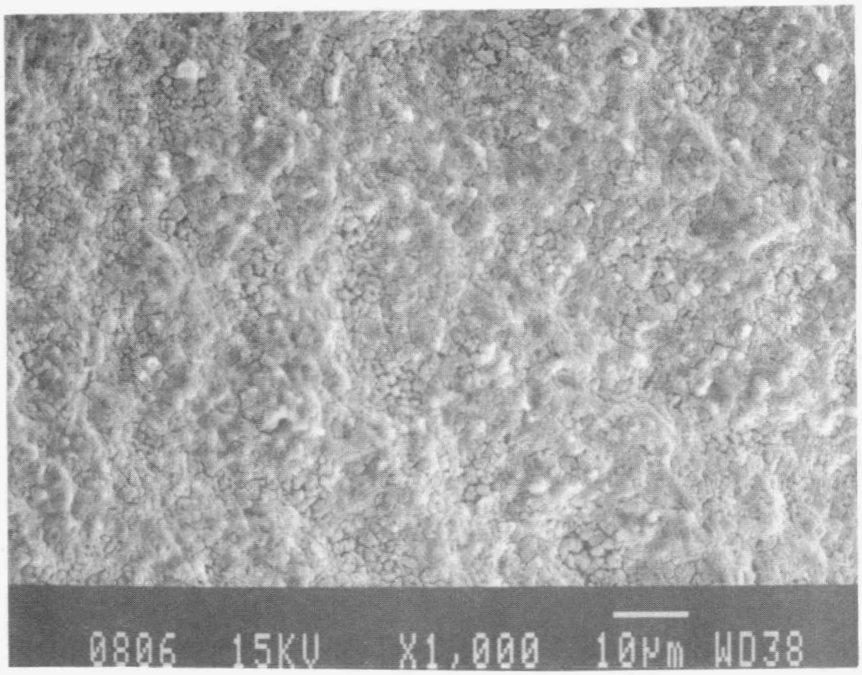

Figure 16. SEM photomicrograph of a Norton Noralide XL144 specimen tested at 1450°C.

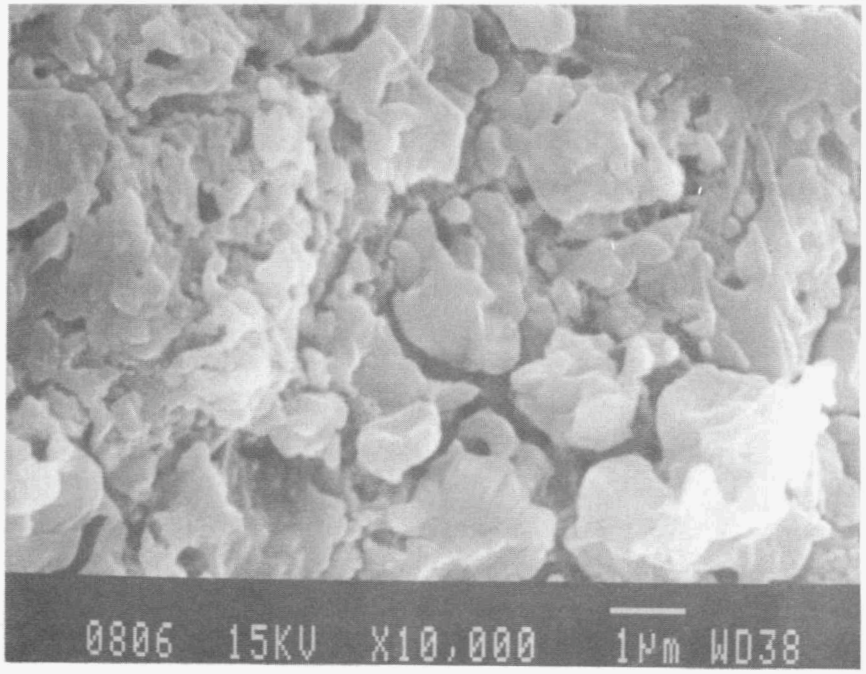

Figure 17. SEM photomicrograph of a Norton Noralide XL144 specimen tested at 1450°C.

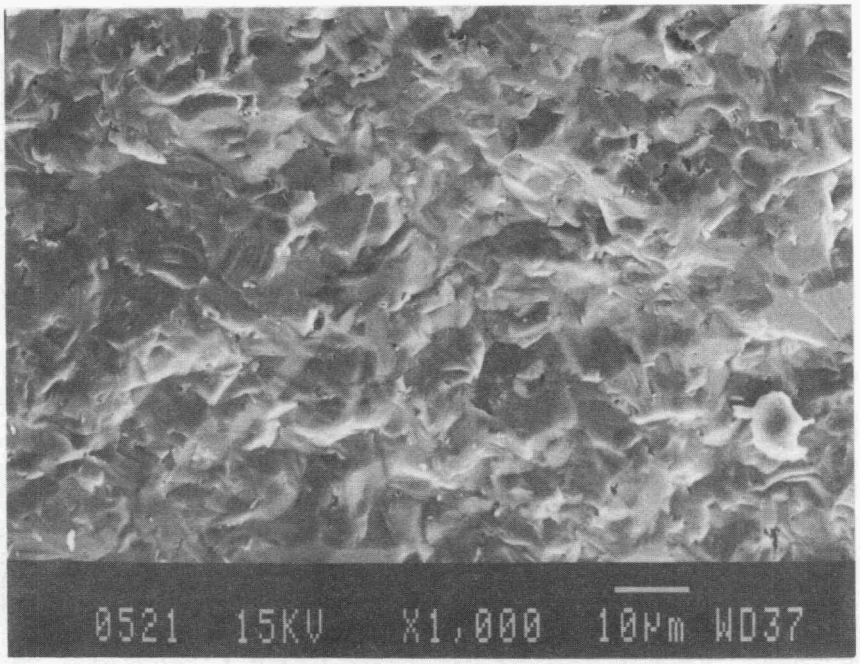

Figure 18. SEM photomicrograph of a Sohio Hexoloy SA specimen.

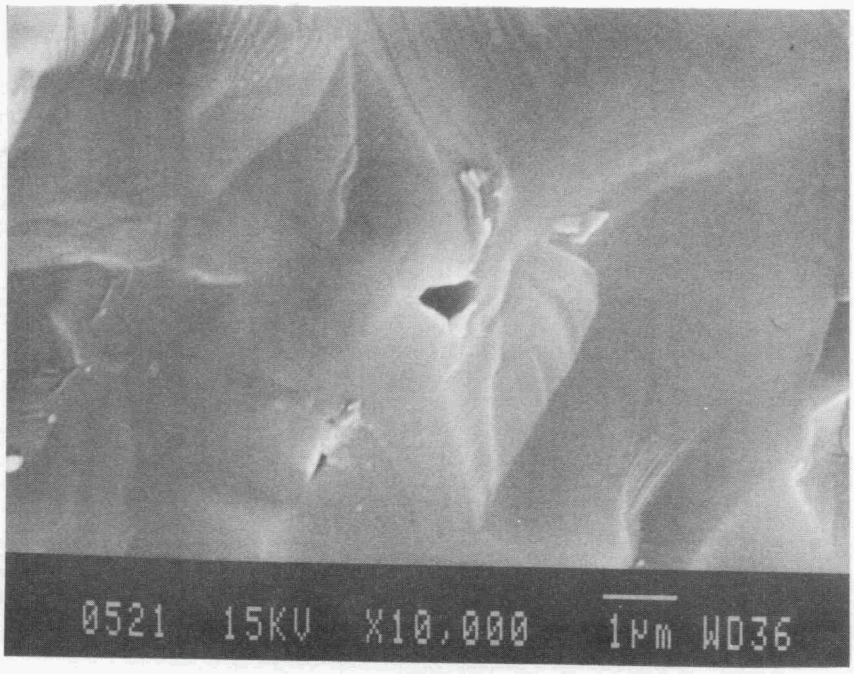

Figure 19. SEM photomicrograph of a Sohio Hexoloy SA specimen.

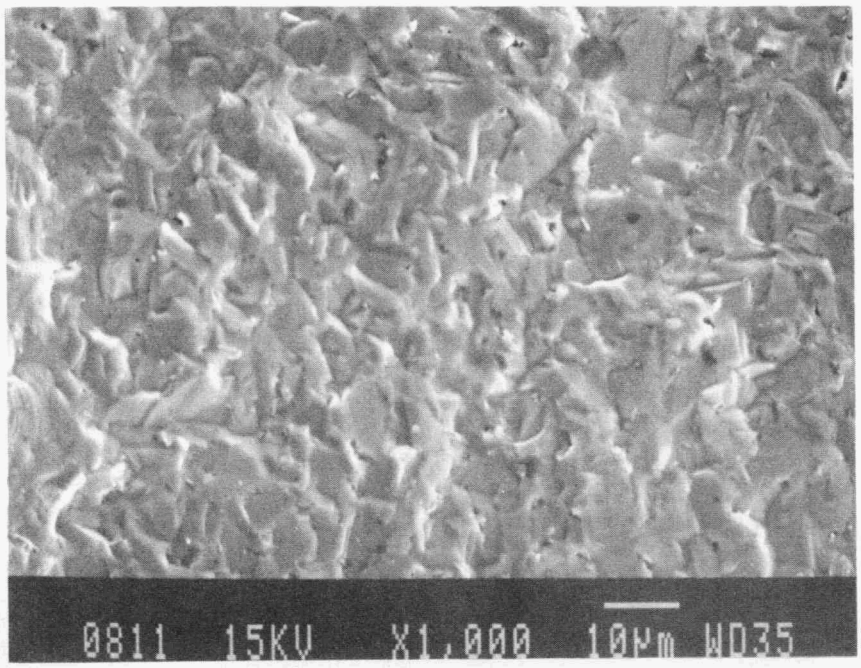

Figure 20. SEM photomicrograph of an etched Sohio Hexoloy SA specimen.

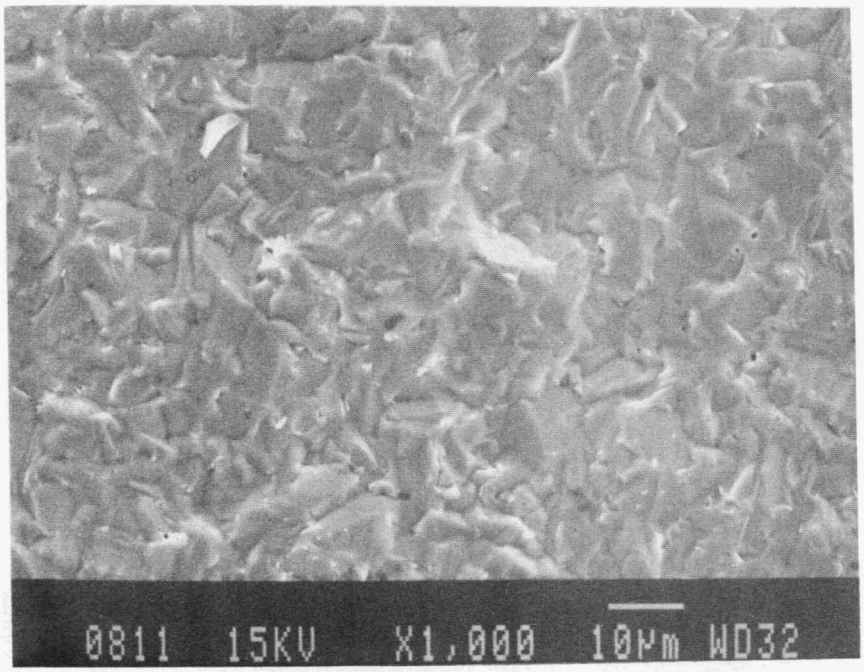

Figure 21. SEM photomicrograph of a Sohio Hexoloy SA specimen tested at 1450°C.

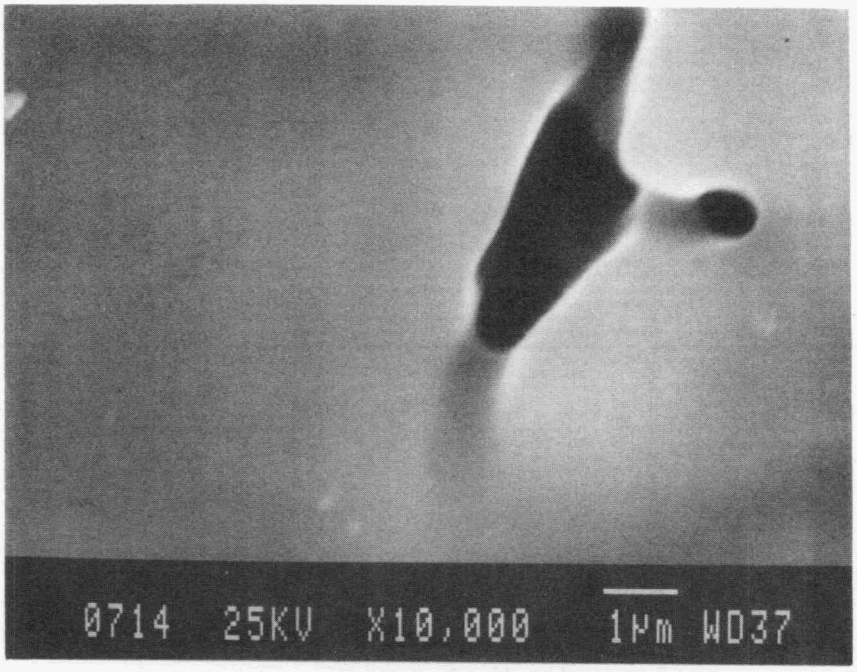

Figure 22. SEM photomicrograph of a Sohio Hexoloy SA specimen tested at 1450°C.

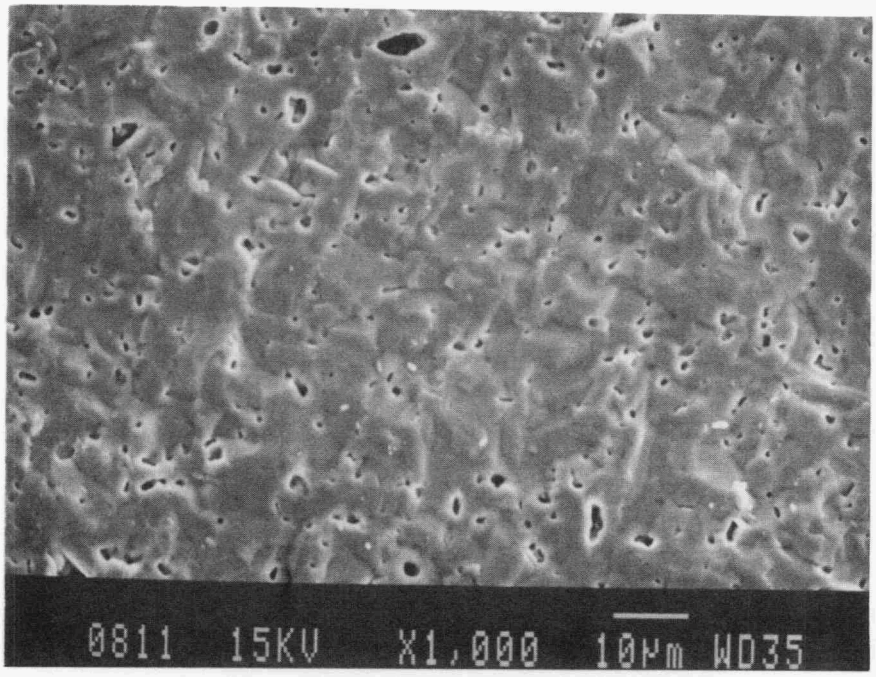

Figure 23. SEM photomicrograph of an etched Sohio Hexoloy SA specimen tested at 1450°C.

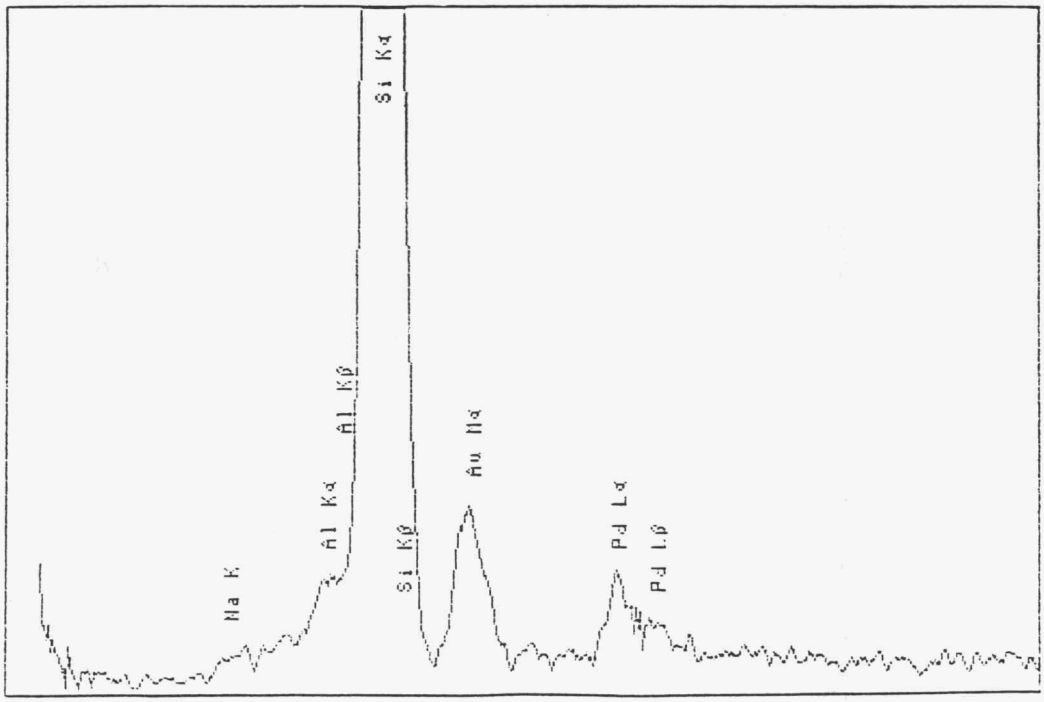

Figure 24. Typical EDXA spectra for Sohio Hexoloy α-SiC.

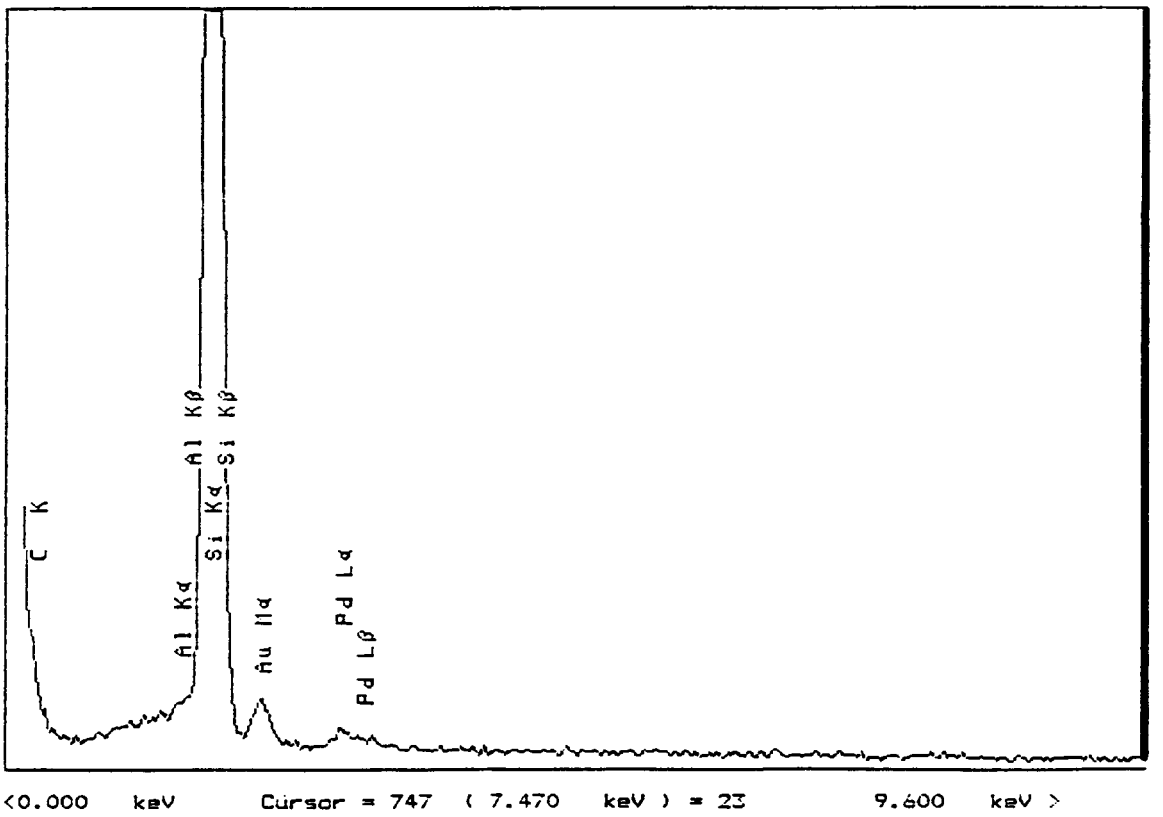

Figure 25. Typical EDXA spectra for Sohio Hexoloy α-SiC.

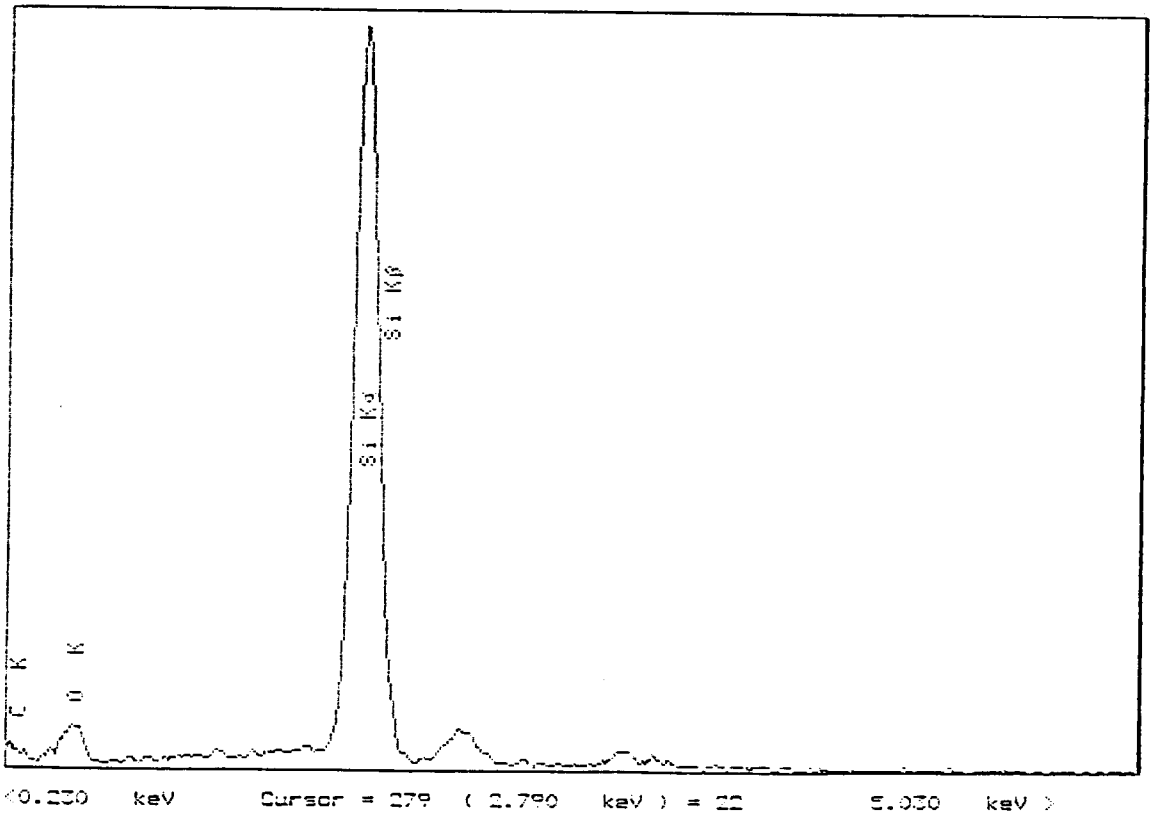

Figure 26. Typical EDXA spectra for Sohio Hexoloy α-SiC tested at 1450°C.

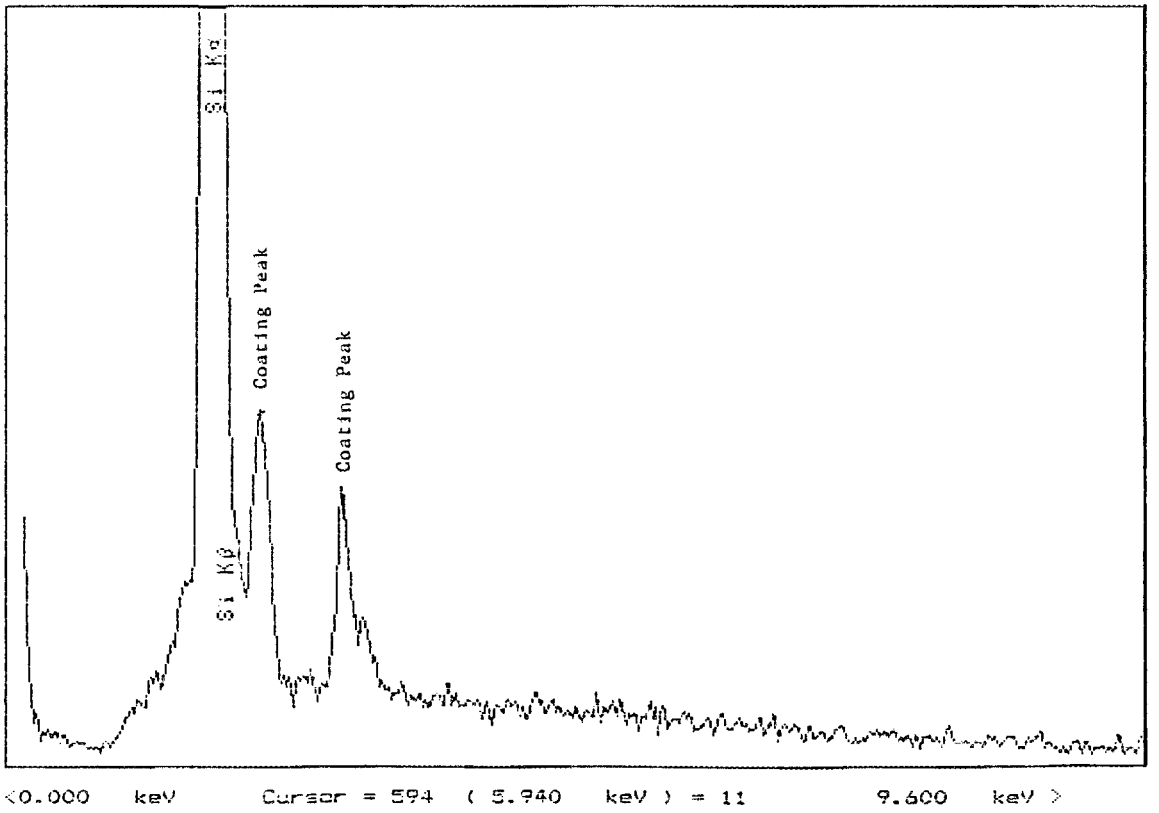

Figure 27. Typical EDXA spectra for GTE PY6 material.

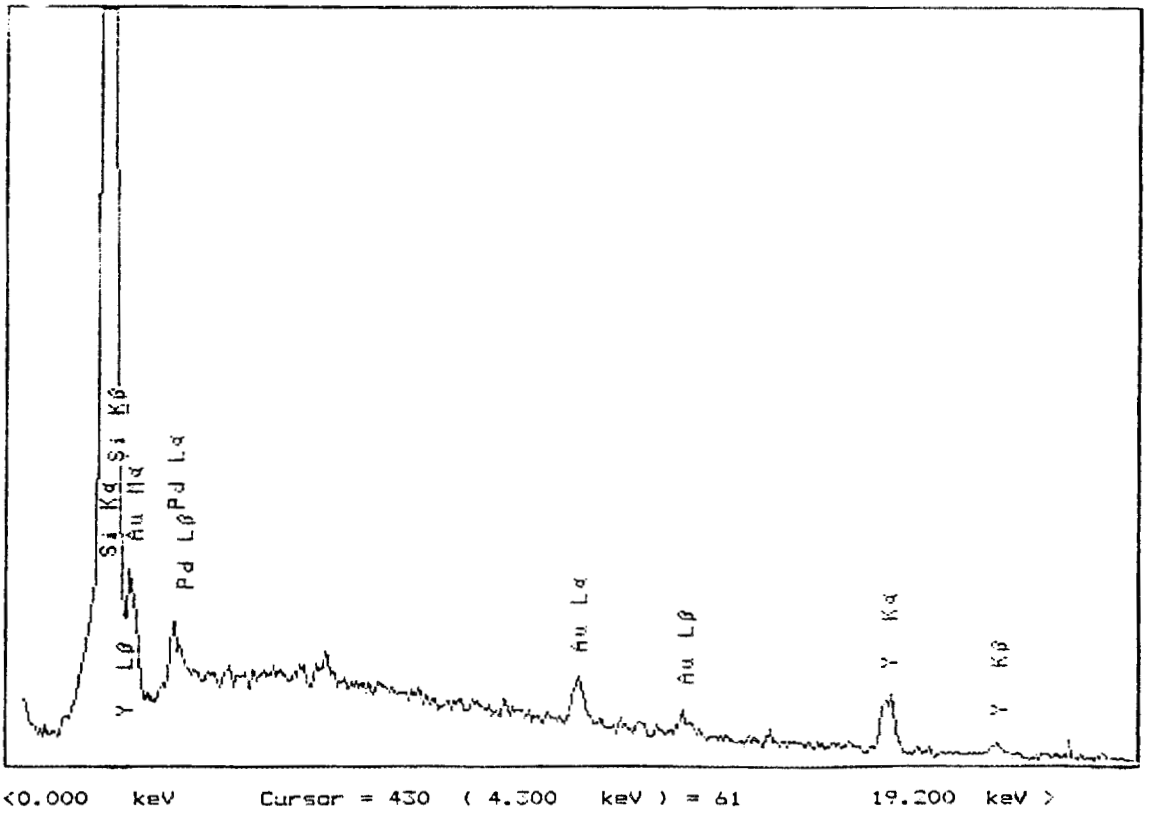

Figure 28. Typical EDXA spectra for GTE PY6 material.

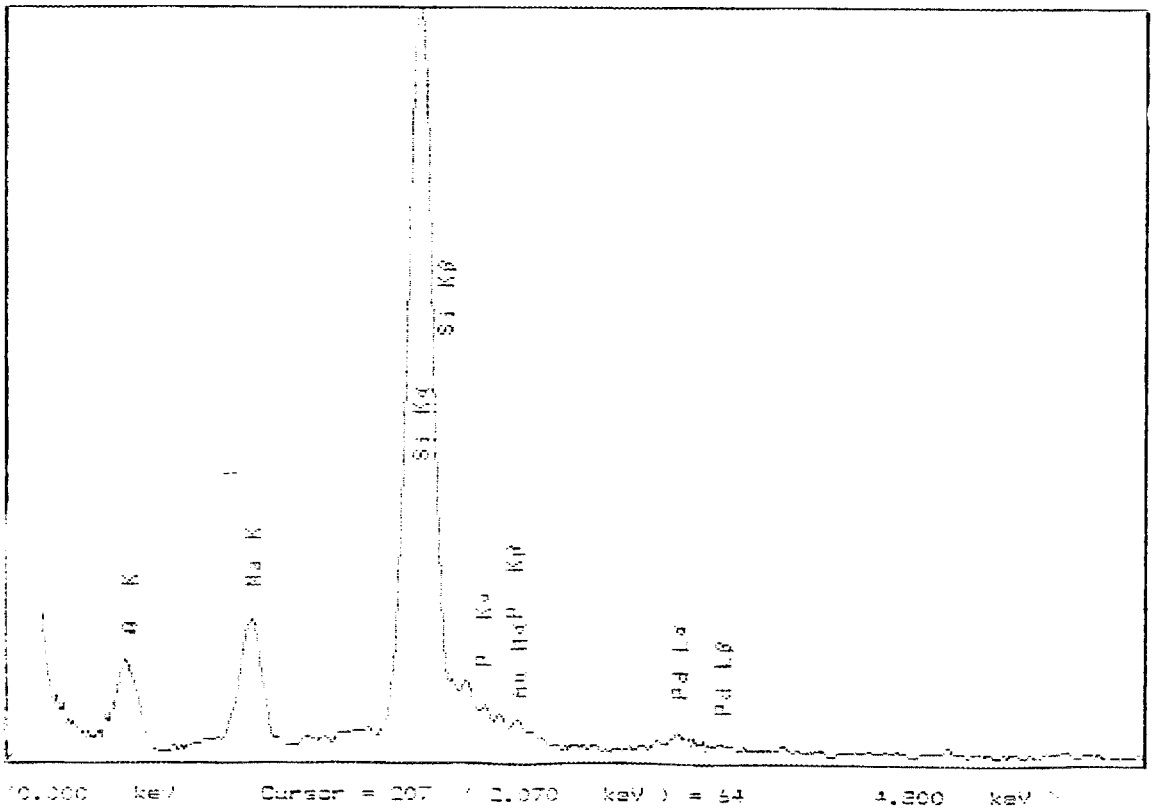

Figure 29. Typical EDXA spectra for GTE PY6 material tested at 1450°C.

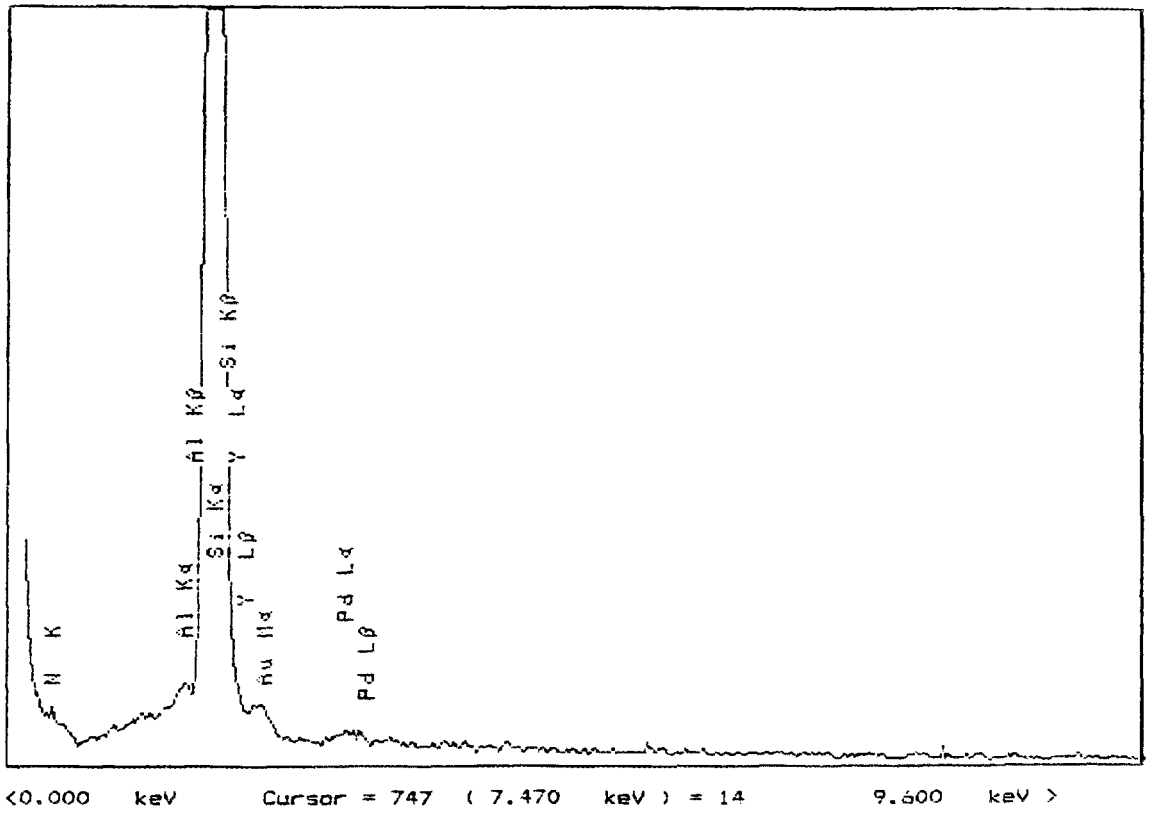

Figure 30. Typical EDXA spectra for Noralide XL144 material.

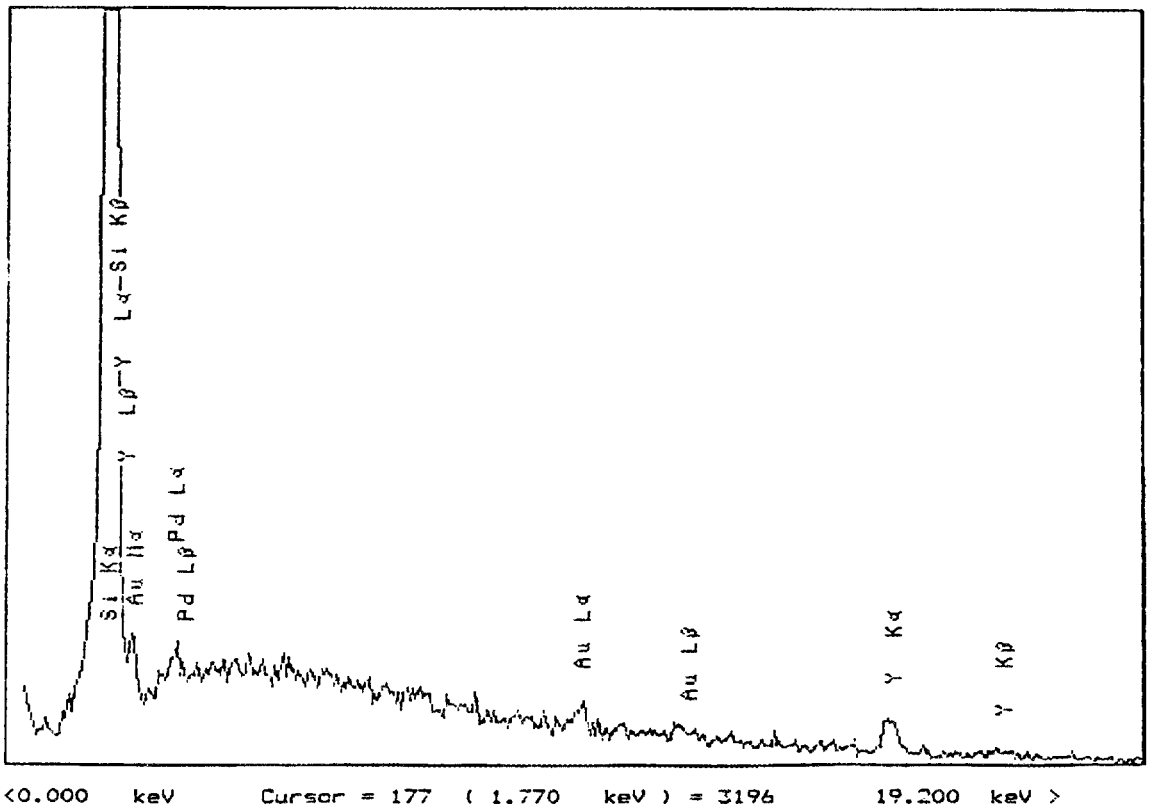

Figure 31. Typical EDXA spectra for Noralide XL144 material.

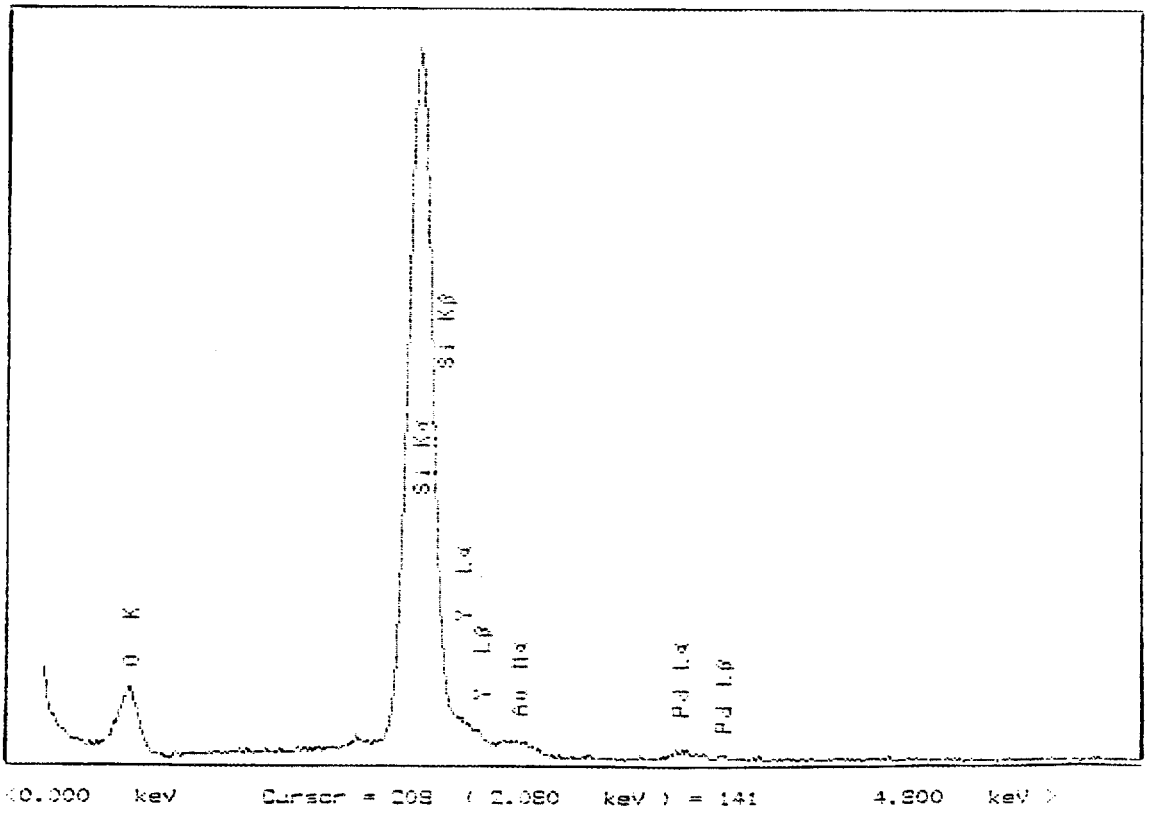

Figure 32. Typical EDXA spectra for Noralide XL144 material tested at 1450°C.

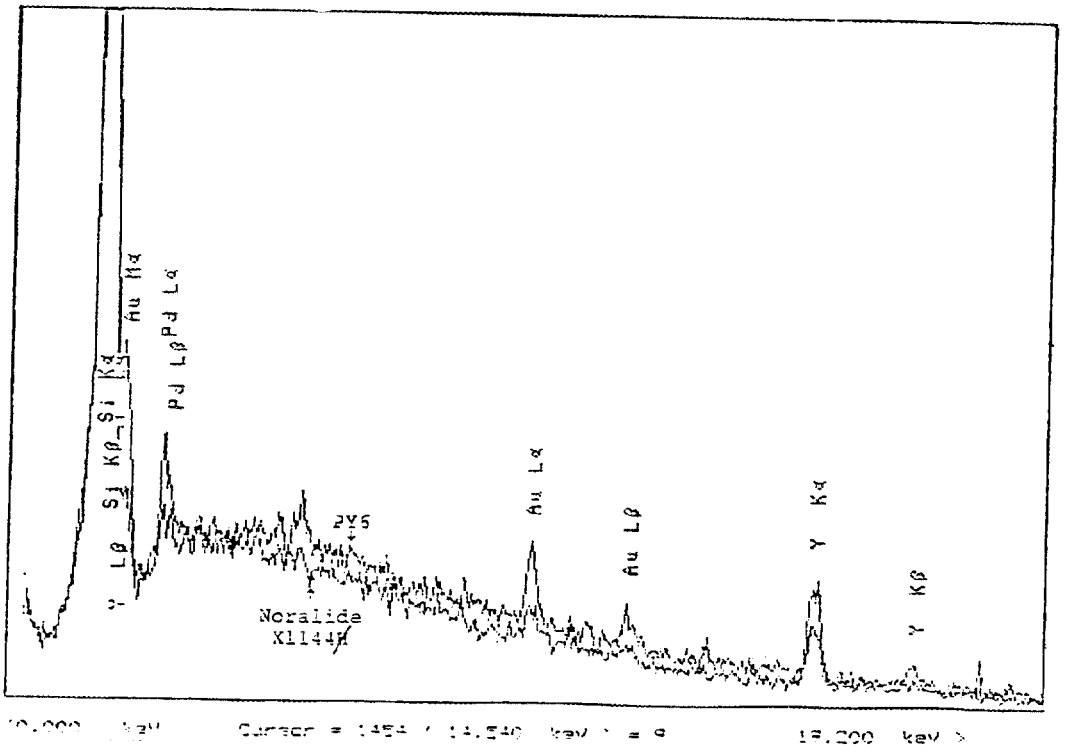

Figure 33. Comparison of typical EDXA spectra for GTE PY6 and Noralide XL144.

Figure 34. Typical x-ray diffraction pattern for Hexoloy-α-SiC.

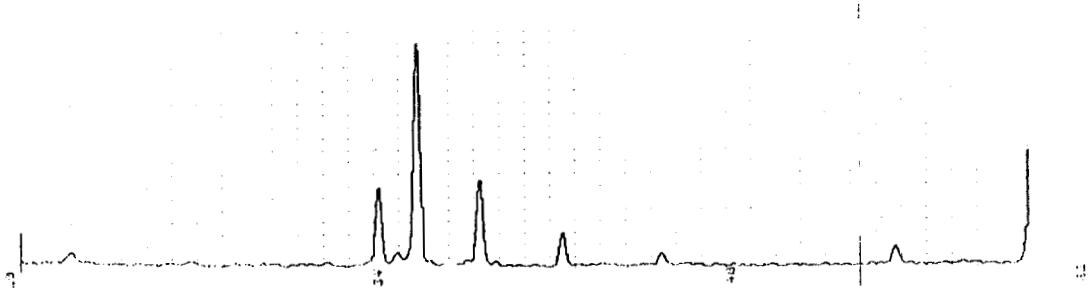

Figure 35. Typical x-ray diffraction pattern for Hexoloy-α-SiC tested at 1450°C.

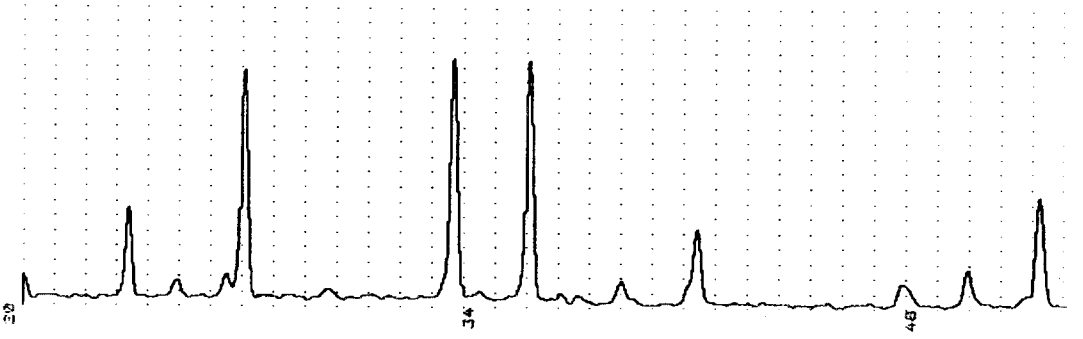

Figure 36. Typical x-ray diffraction pattern for GTE PY6.

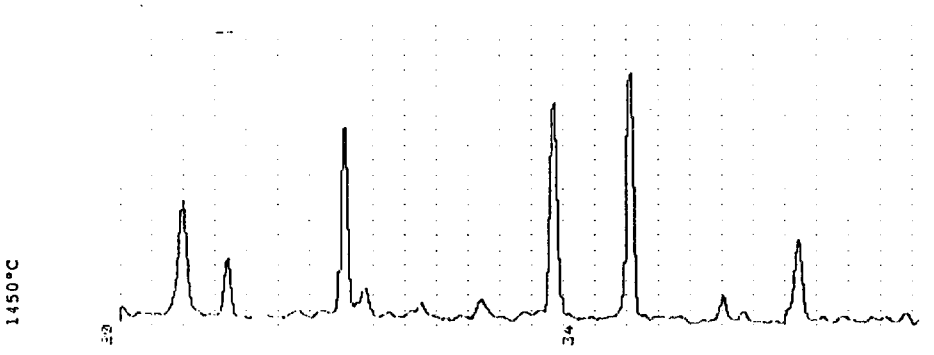

Figure 37. Typical x-ray diffraction pattern for GTE PY6 tested at 1450°C.

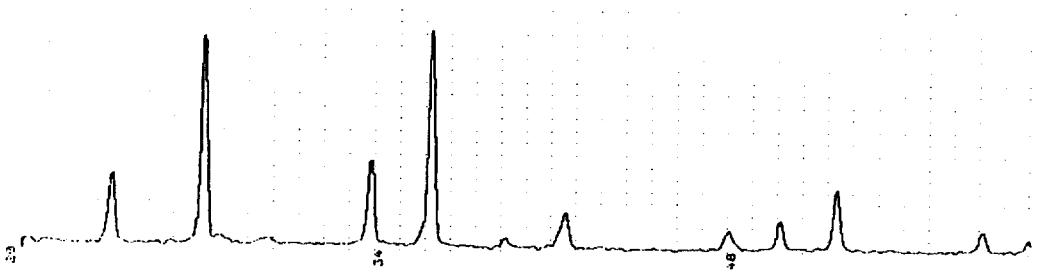

Figure 38. Typical x-ray diffraction pattern for Noralide XL144.

Figure 39. Typical x-ray diffraction for Noralide XL144 tested at 1450°C.

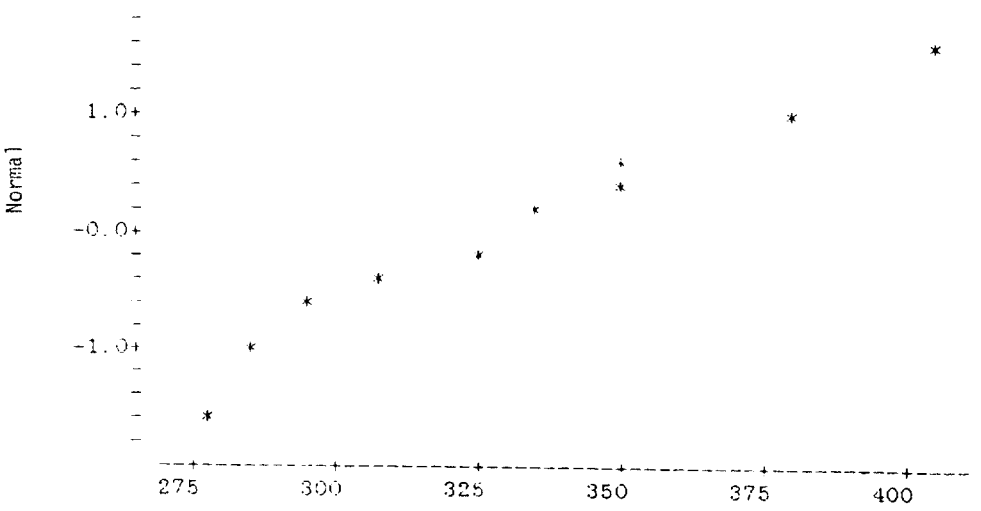

Figure 40. Normal distribution plot of a Hexoloy-α-SiC at 25°C.

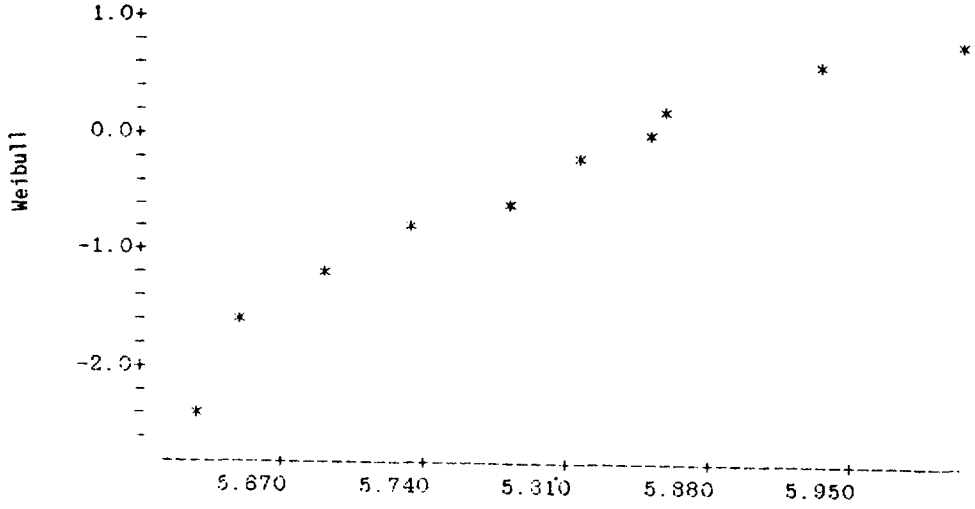

Figure 41. Weibull distribution plot for Hexoloy-α-SiC at 25°C.

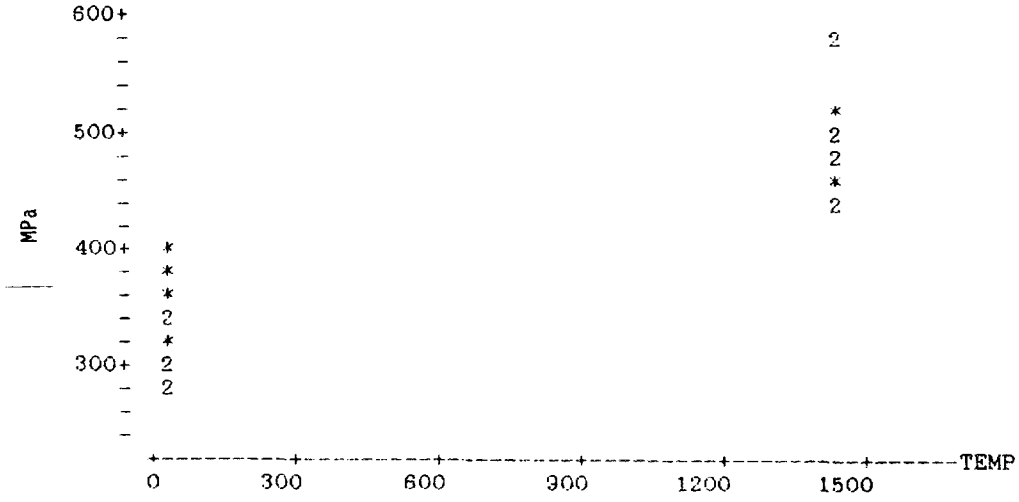

Figure 42. Observed ultimate strengths versus temperature (°C) for Hexoloy-α-SiC.

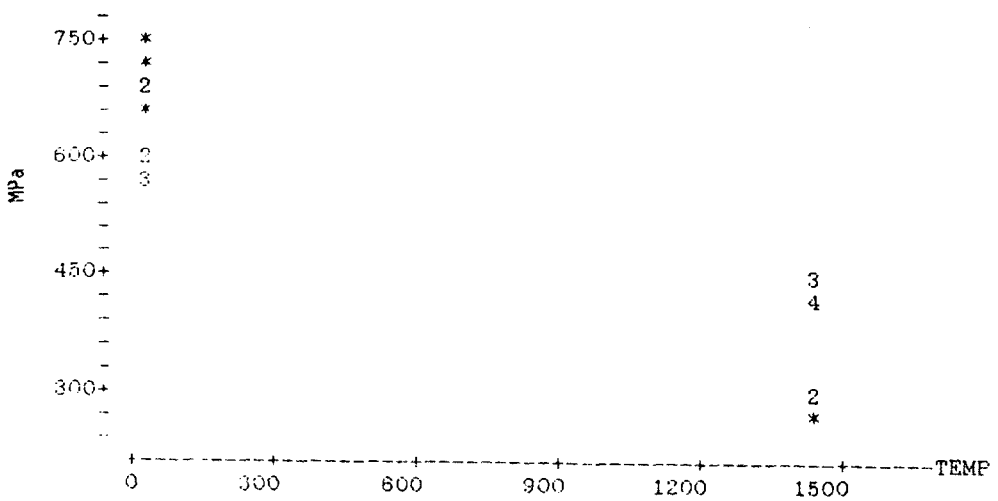

Figure 43. Observed ultimate strengths versus temperature (°C) for GTE PY6.

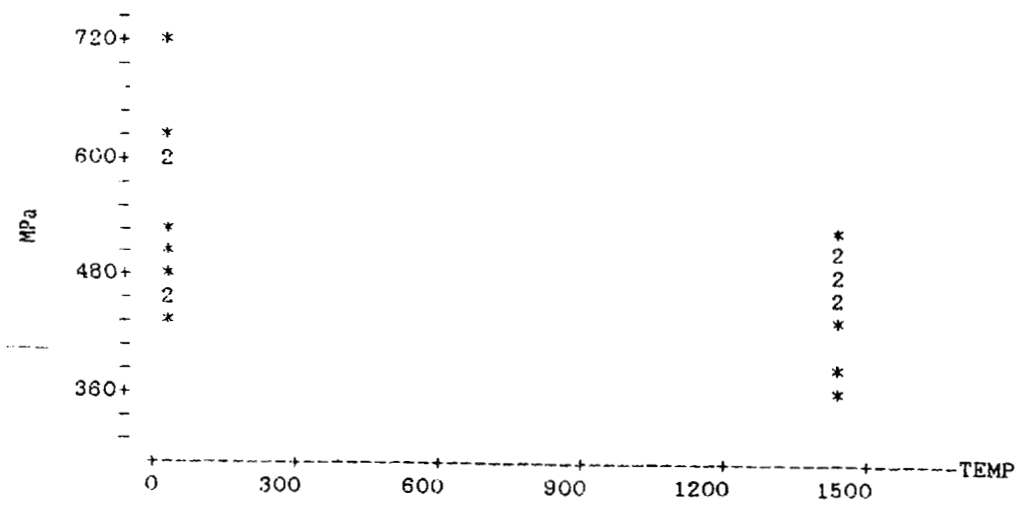

Figure 44. Observed ultimate strengths versus temperature (°C) for Noralide XL144.

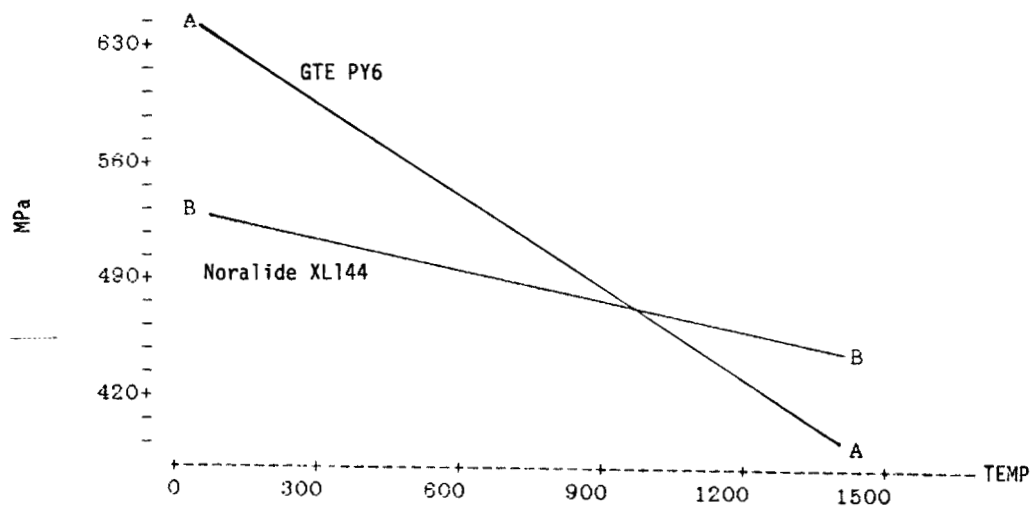

Figure 45. Average strength versus temperature (°C) for GTE PY6 and Noralide XL144.

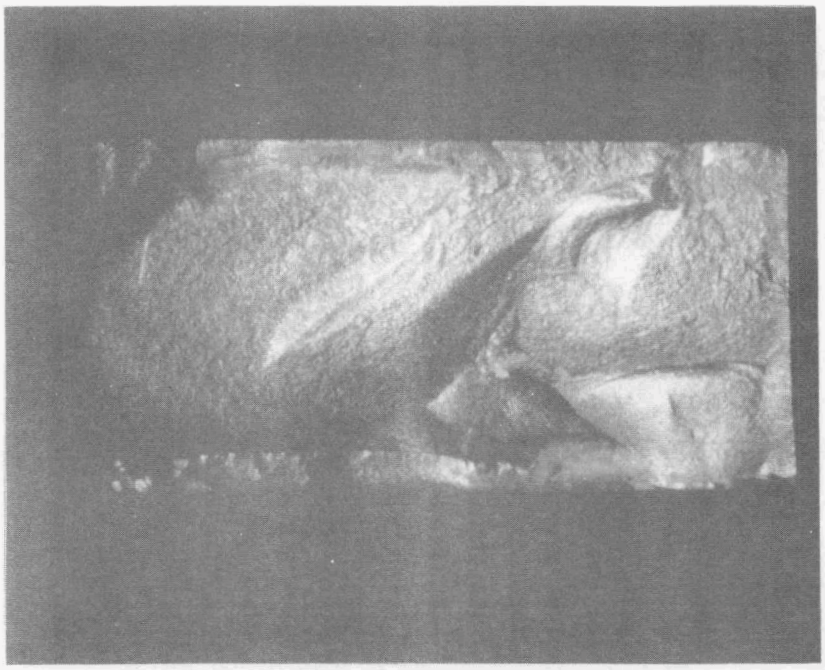

a) specimen tested at 25°C

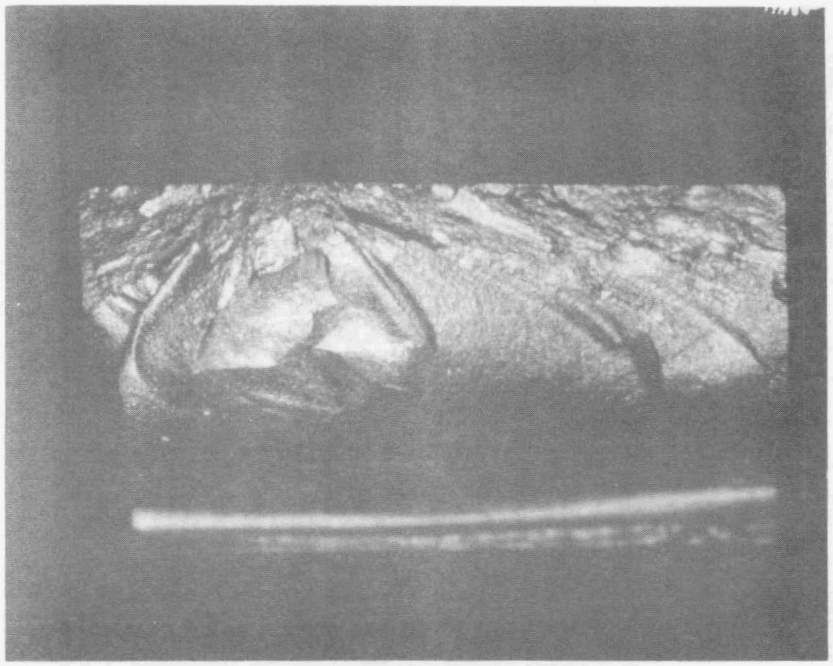

b) specimen tested at 1450°C

Figure 46. Fracture surface of Hexoloy-α-SiC.

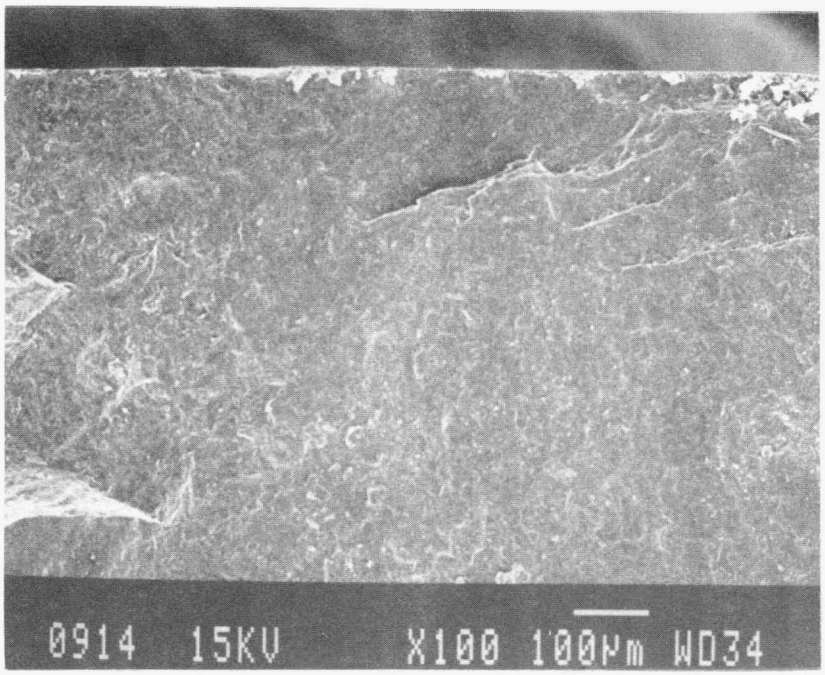

c) specimen tested at 25°C

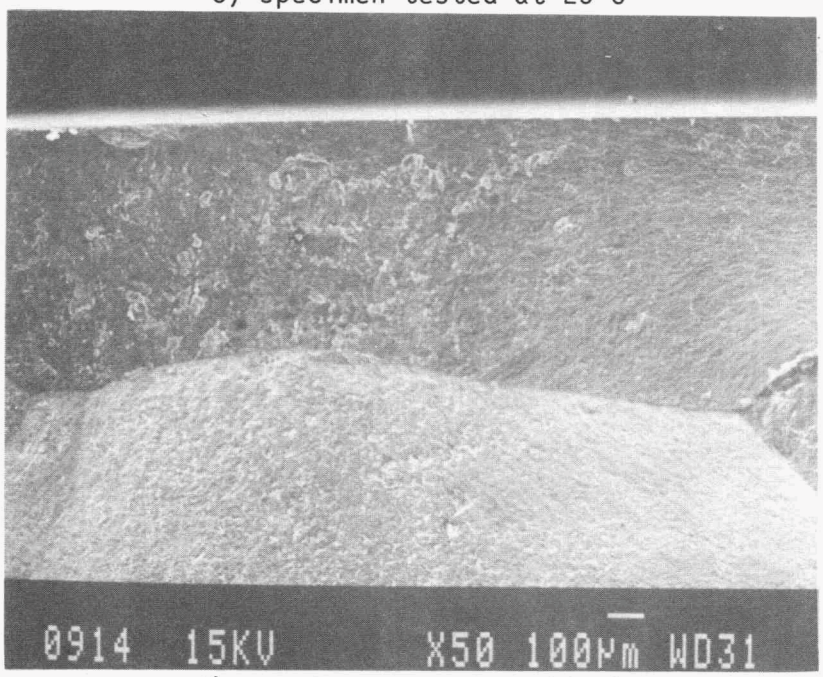

d) specimen tested at 1450°C

Figure 46. Fracture surface of Hexoloy-α-SiC (concluded).

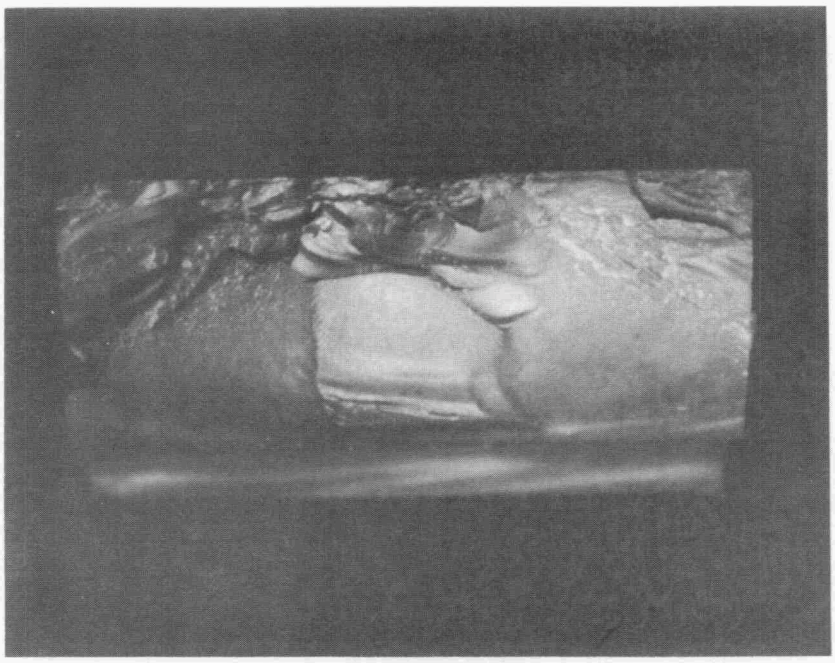

a) specimen tested at 25°C

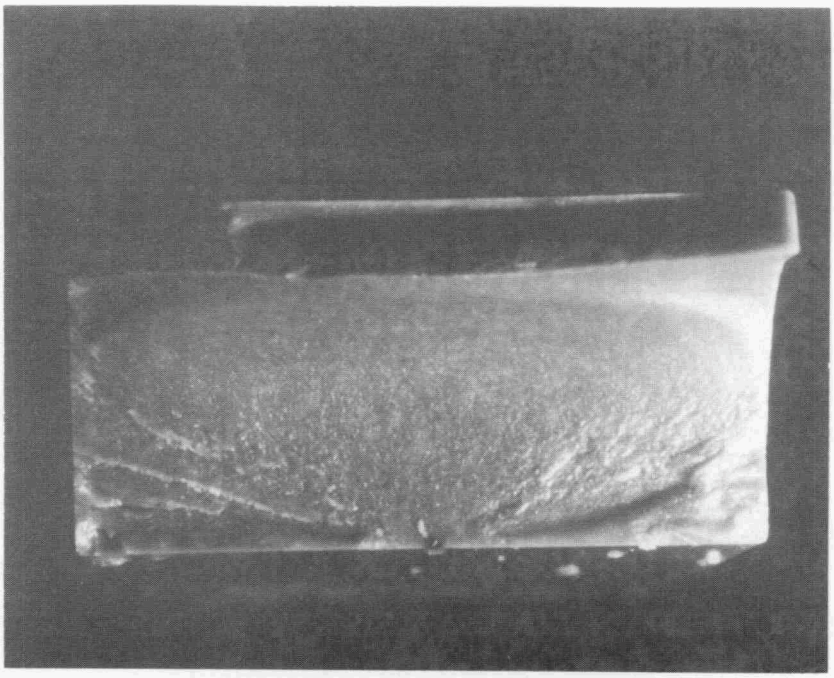

b) specimen tested at 1450°C

Figure 47. Fracture surface of GTE PY6.

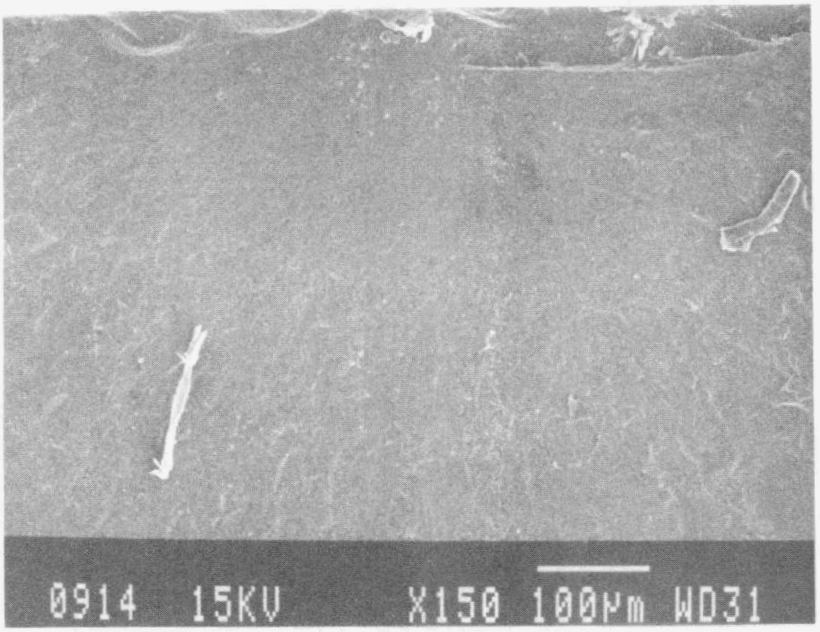

c) specimen tested at 25°C

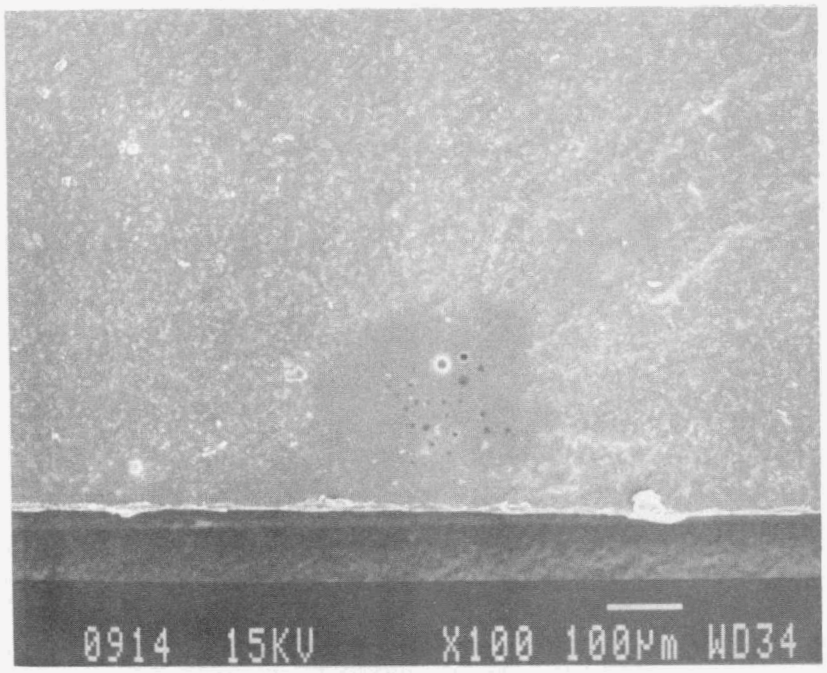

d) specimen tested at 1450°C

Figure 47. Fracture surface of GTE PY6 (concluded).

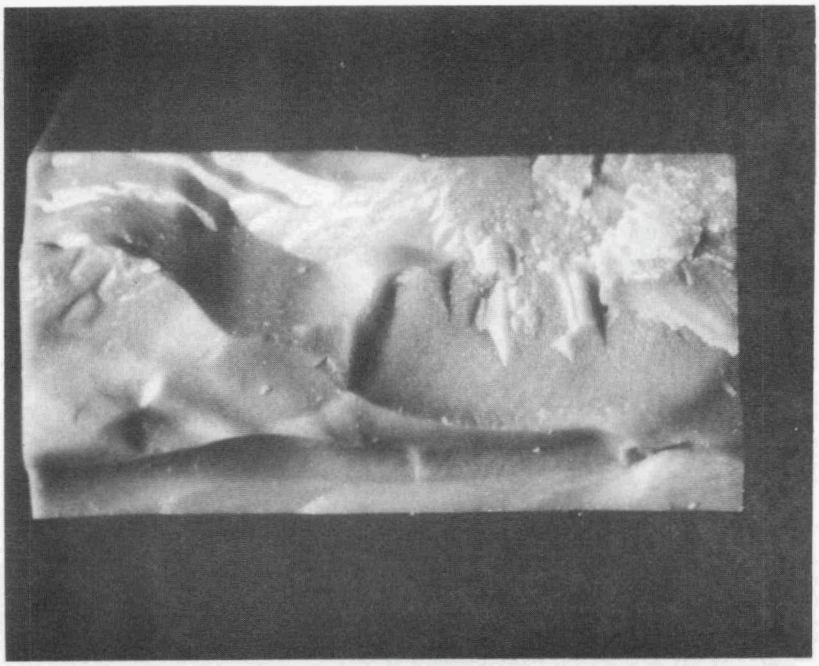

a) specimen tested at 25°C

b) specimen tested at 1450°C

Figure 48. Fracture surface of Noralide XL144.

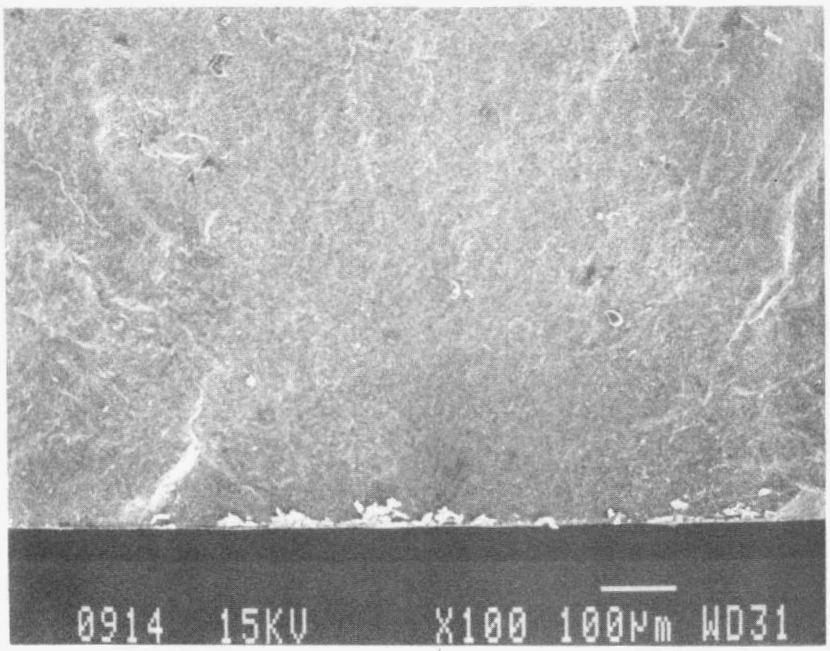

c) specimen tested at 25°C

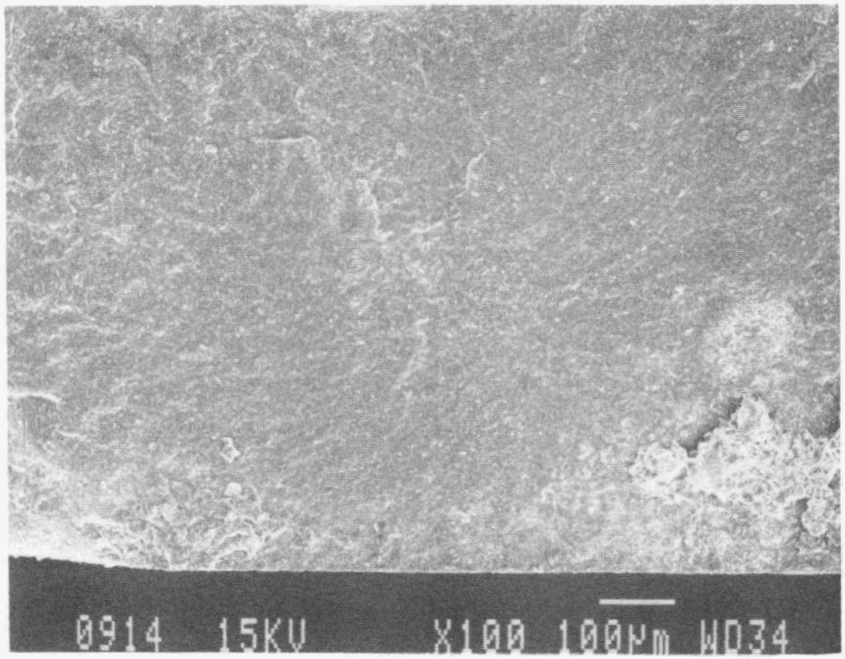

d) specimen tested at 1450°C

Figure 48. Fracture surface of Noralide XL144 (concluded).

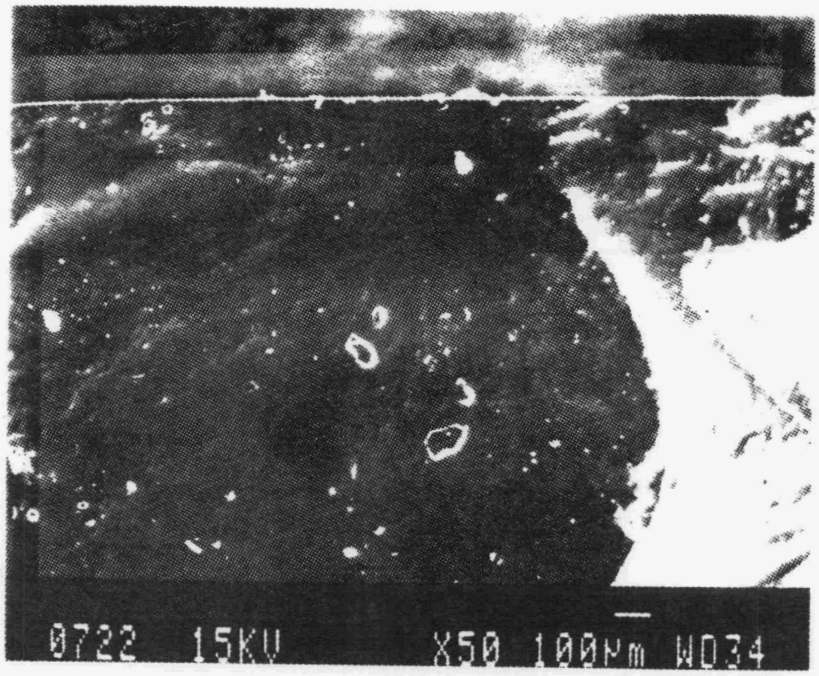

Figure 49. Fracture surface of PY6 specimen tested at 1450°C (fracture initiated at inclusion).

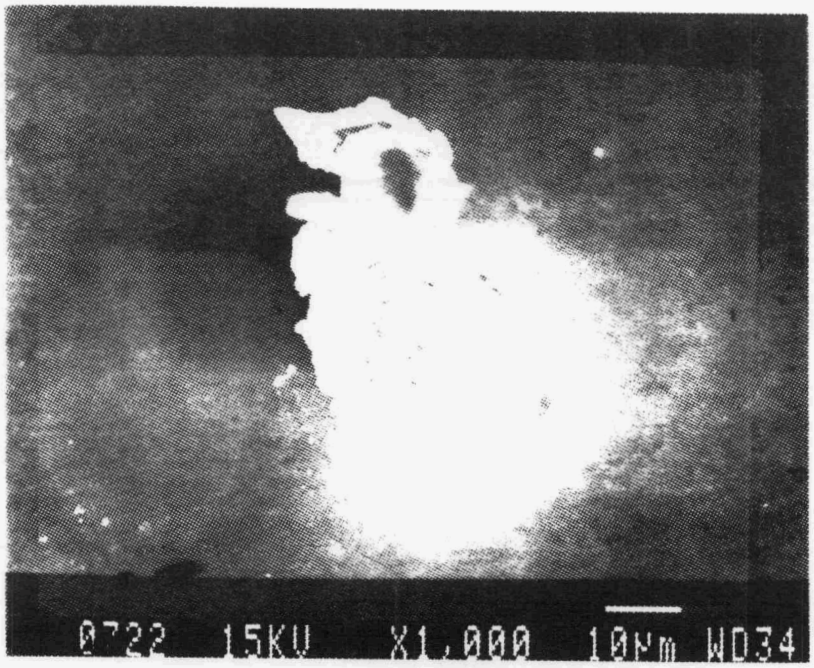

Figure 50. Inclusion at fracture site.

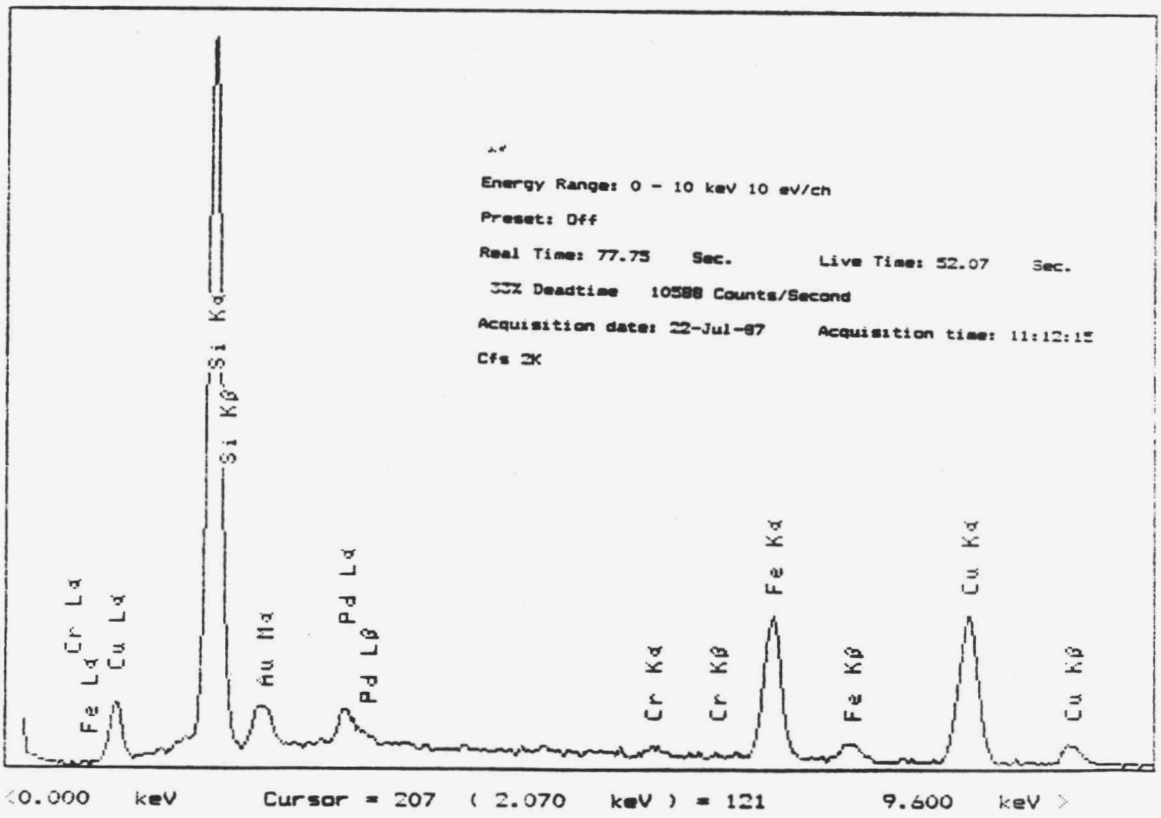

Figure 51. EDXA scan of the inclusion found in the GTE PY6 specimen.

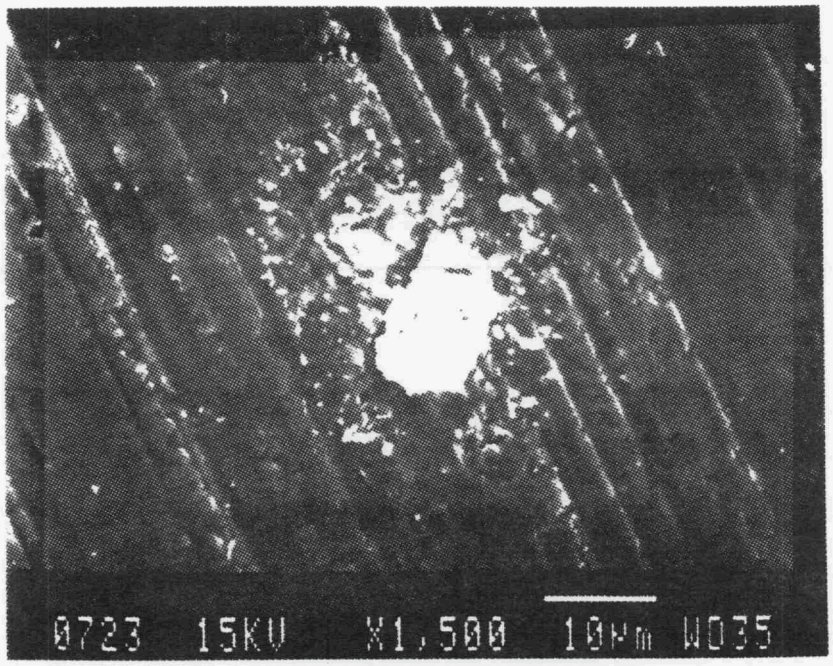

Figure 52. Inclusion on surface of an untested PY6 specimen.

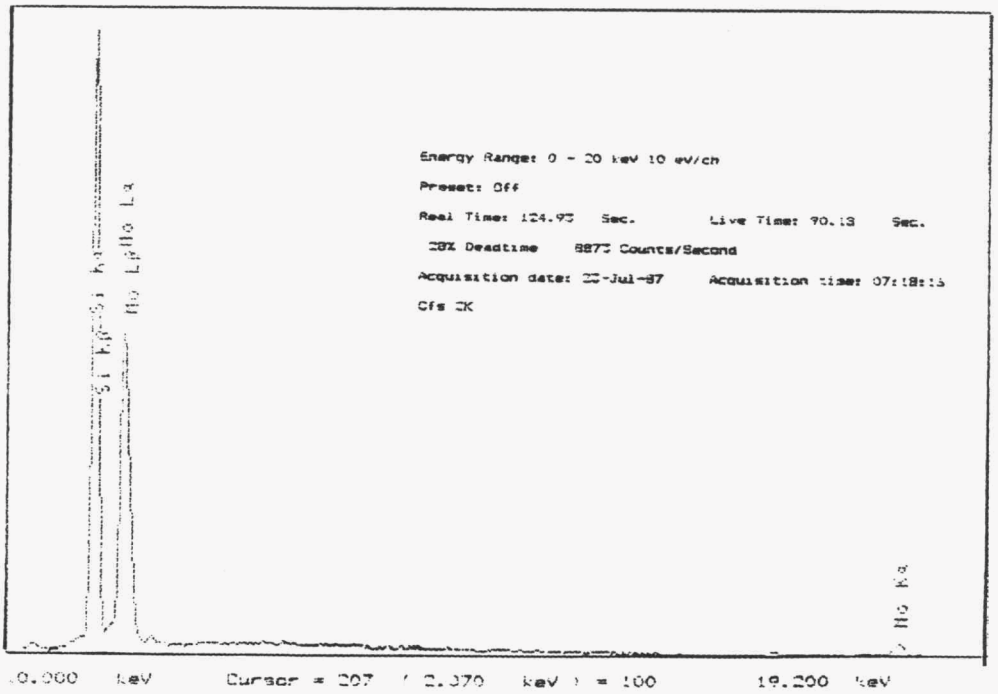

Figure 53. EDXA scan of an inclusion found in the untested GTE PY6 specimen.

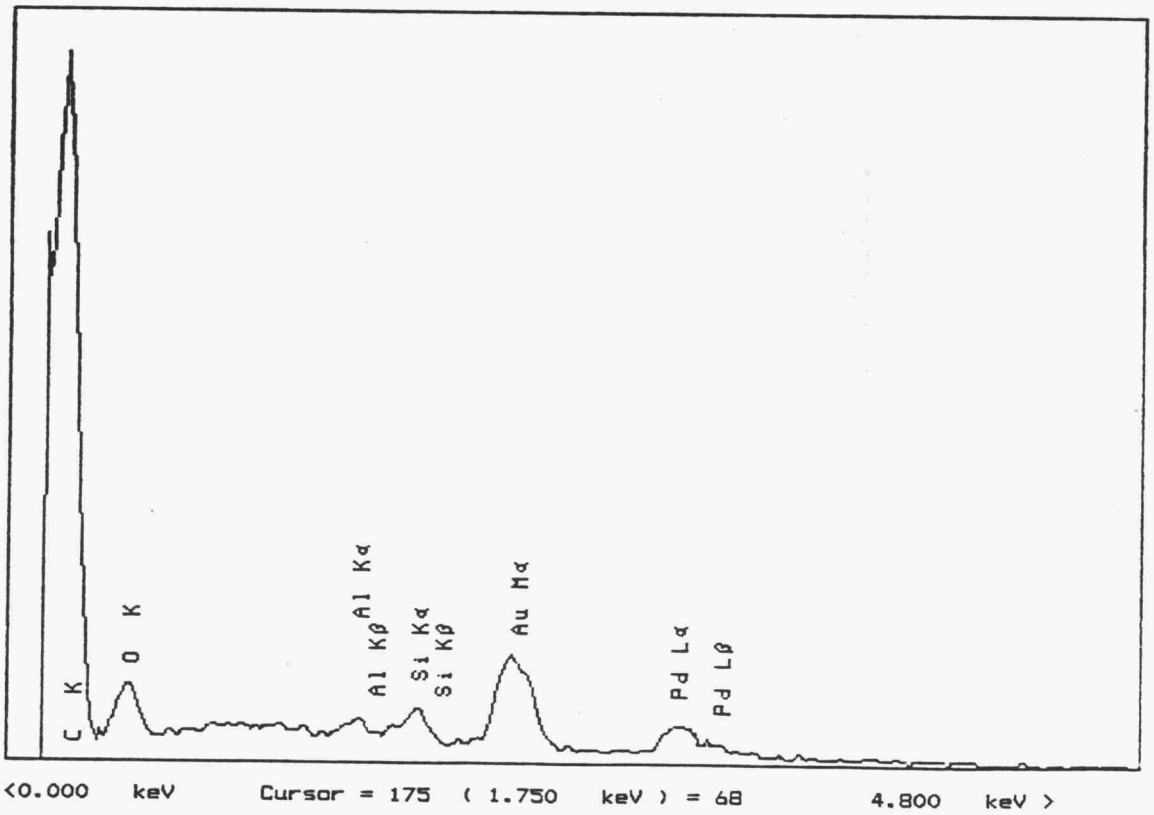

Figure 54. Inclusion found in an untested Noralide XL144.

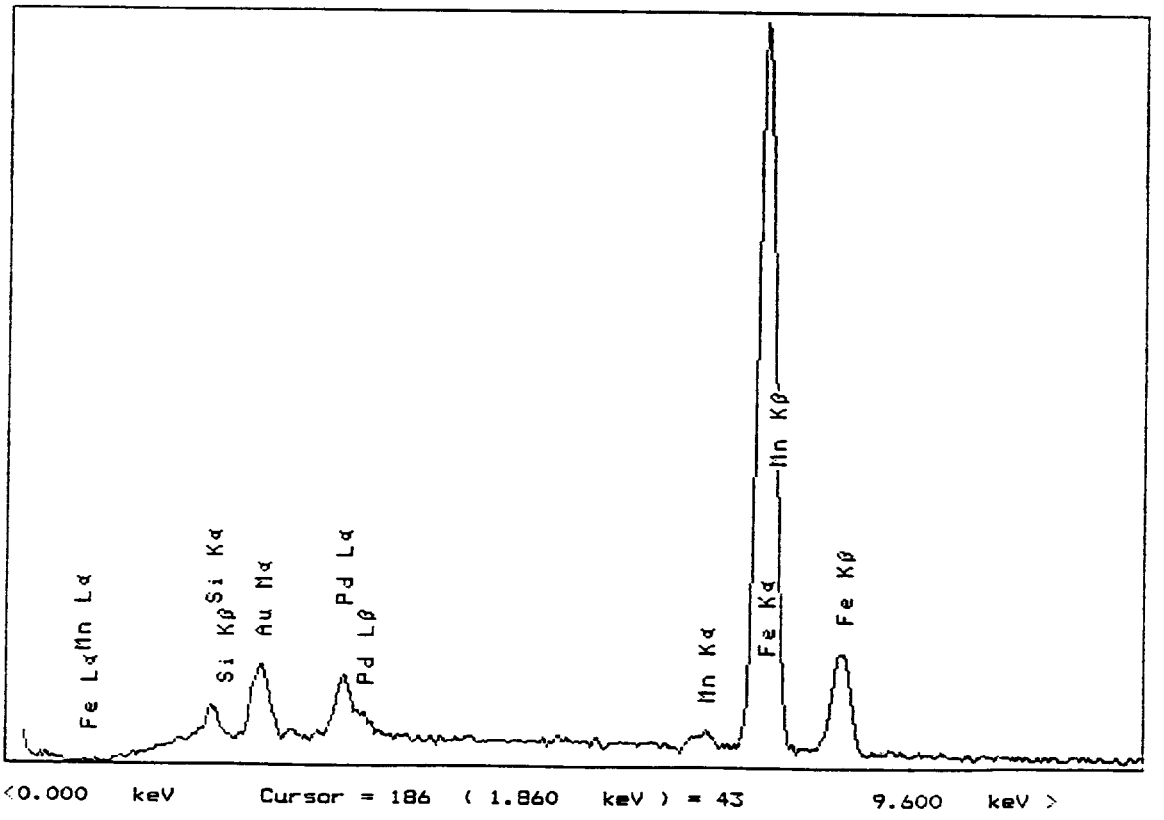

Figure 55. Inclusion found in Noralide XL144 tested at 1450°C.

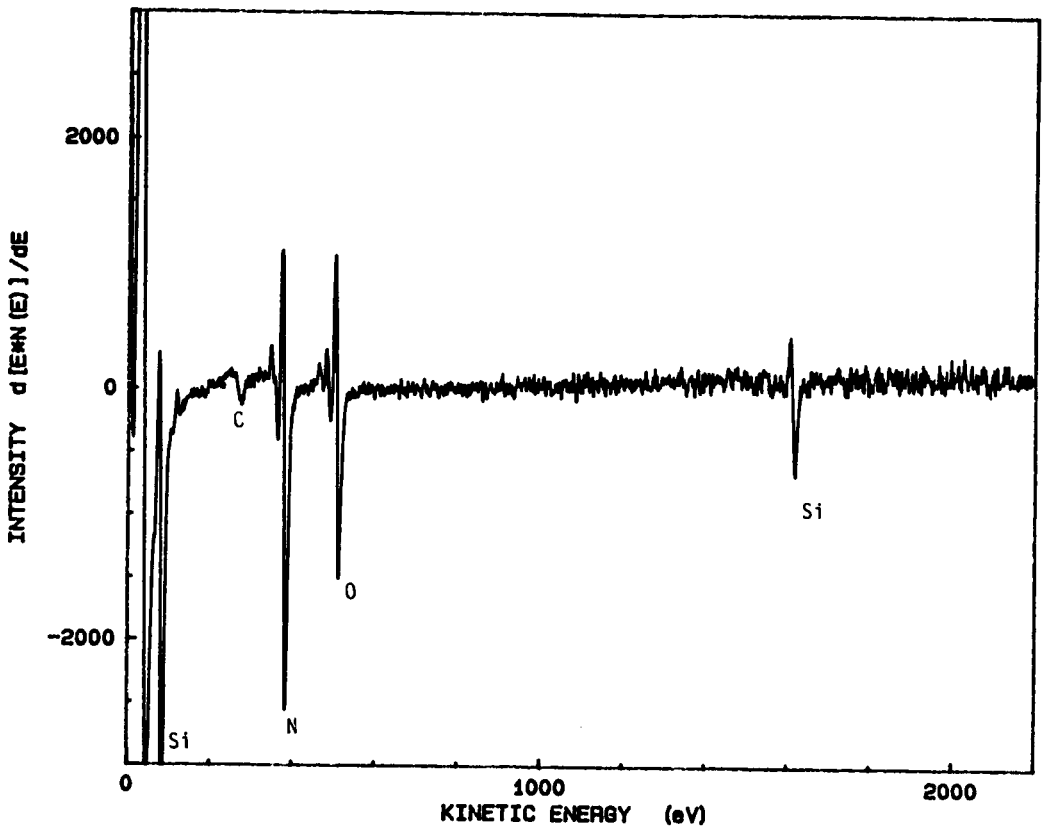

Figure 56. GTE PY6 fracture surface region #2.

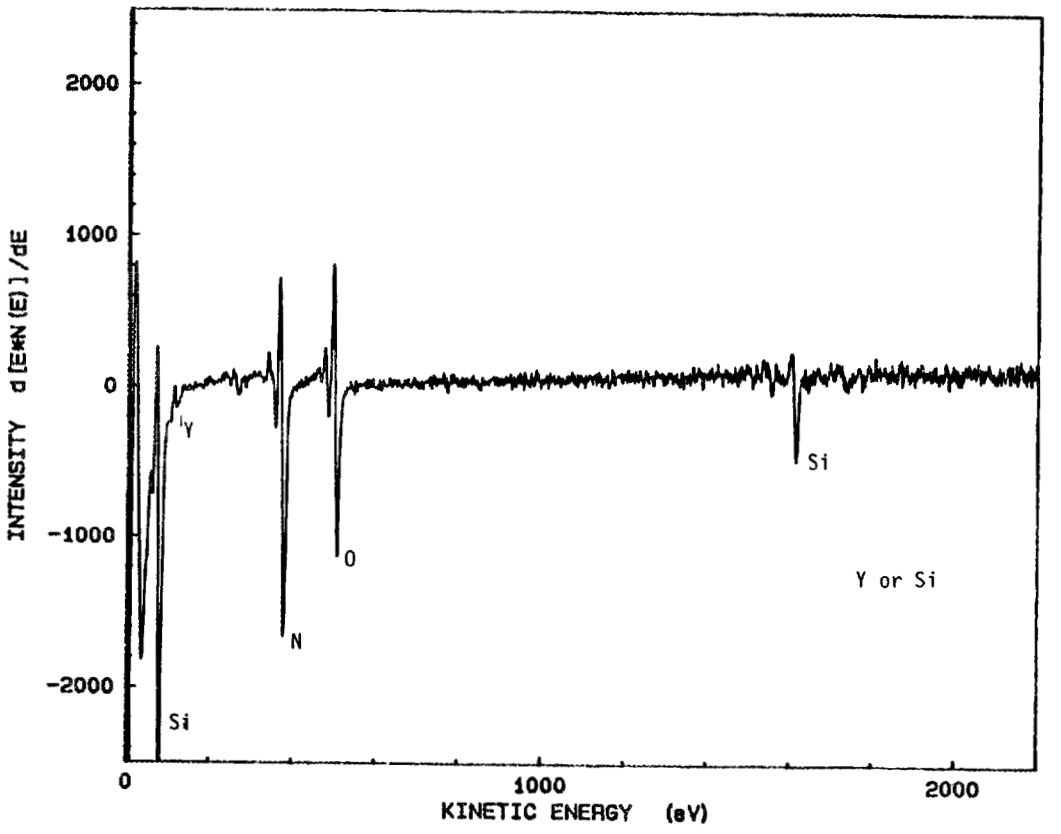

Figure 57. Noralide XL144 fracture surface region #3.

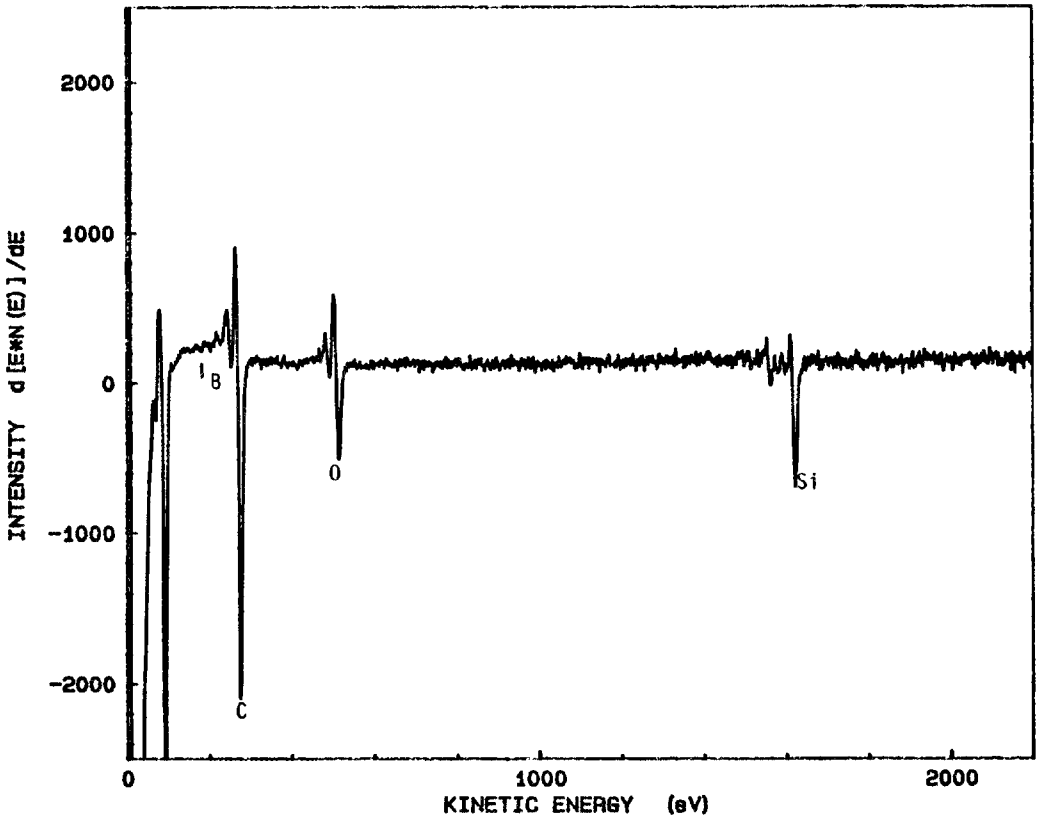

Figure 58. Hexoloy-α-SiC region #2.

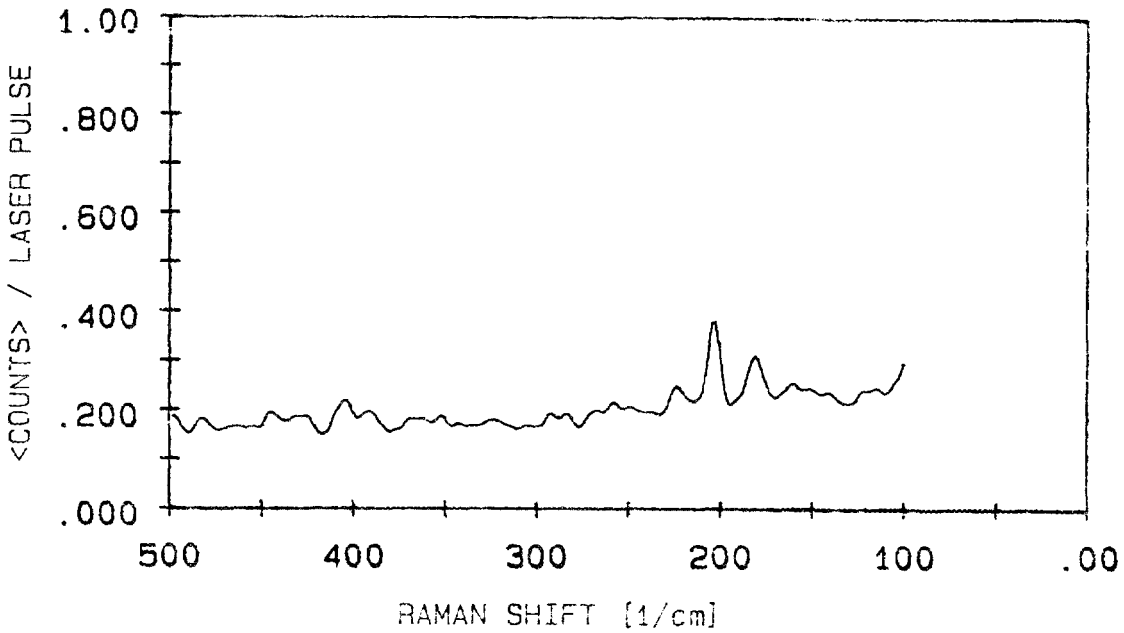

Figure 59. Raman spectra for GTE PY6 as received specimen 56 from 0-500 cm^{-1}.

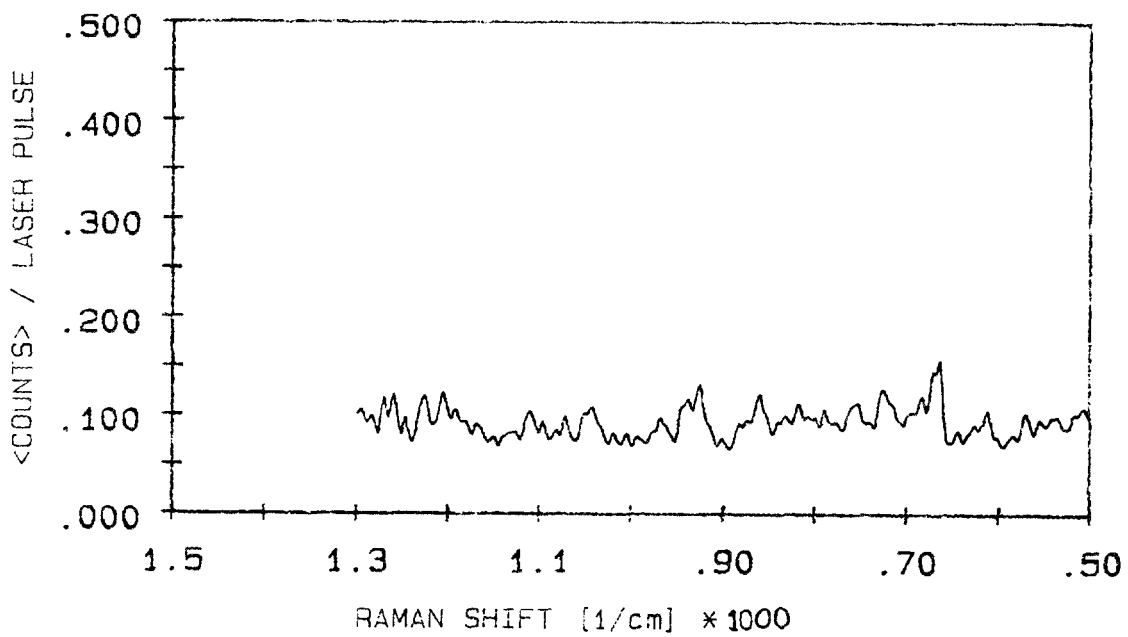

Figure 60. Raman spectra for GTE PY6 as received specimen 56 from 500-1500 cm^{-1}.

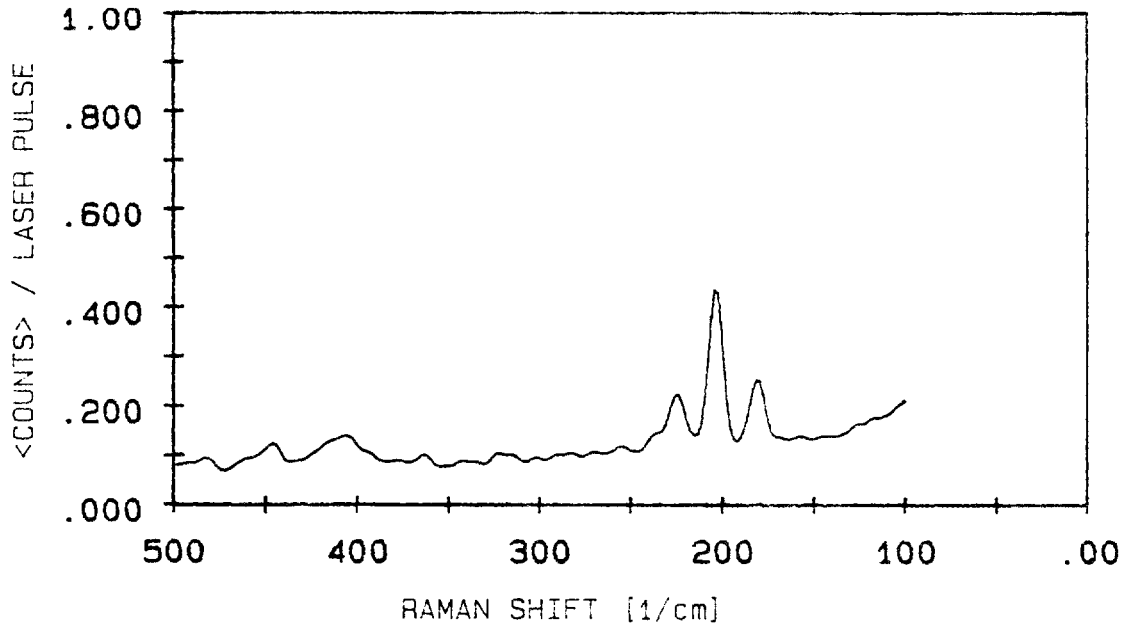

Figure 61. Raman spectra for GTE PY6 specimen 17 after testing to 1450°C from 0-500 cm^{-1}.

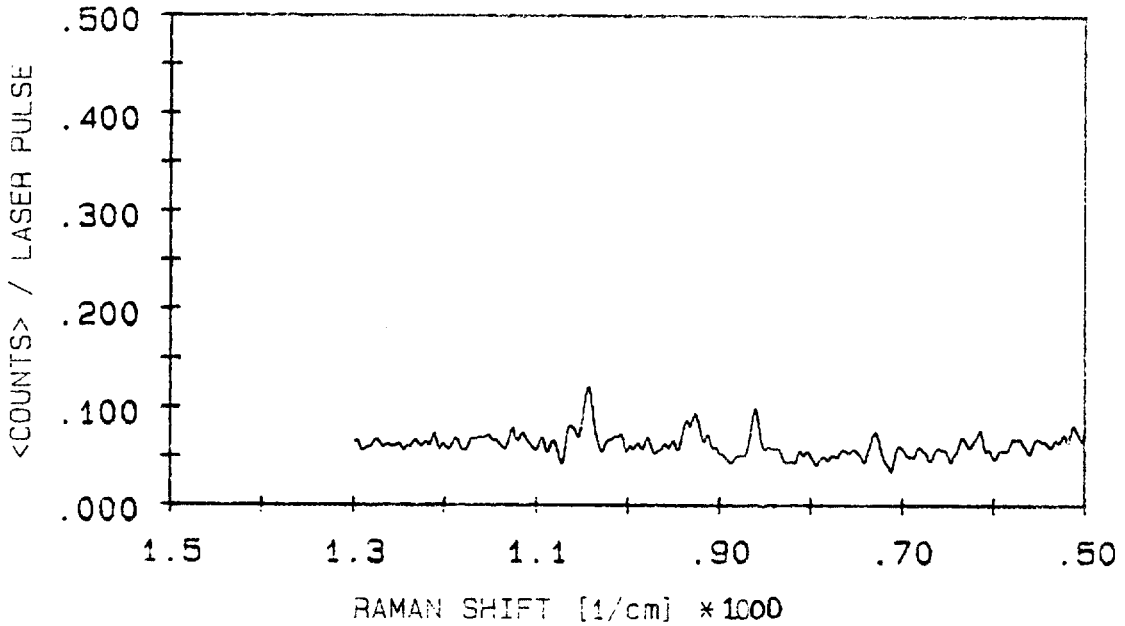

Figure 62. Raman spectra for GTE PY6 specimen 17 after testing to 1450°C from 500-1500 cm^{-1}.

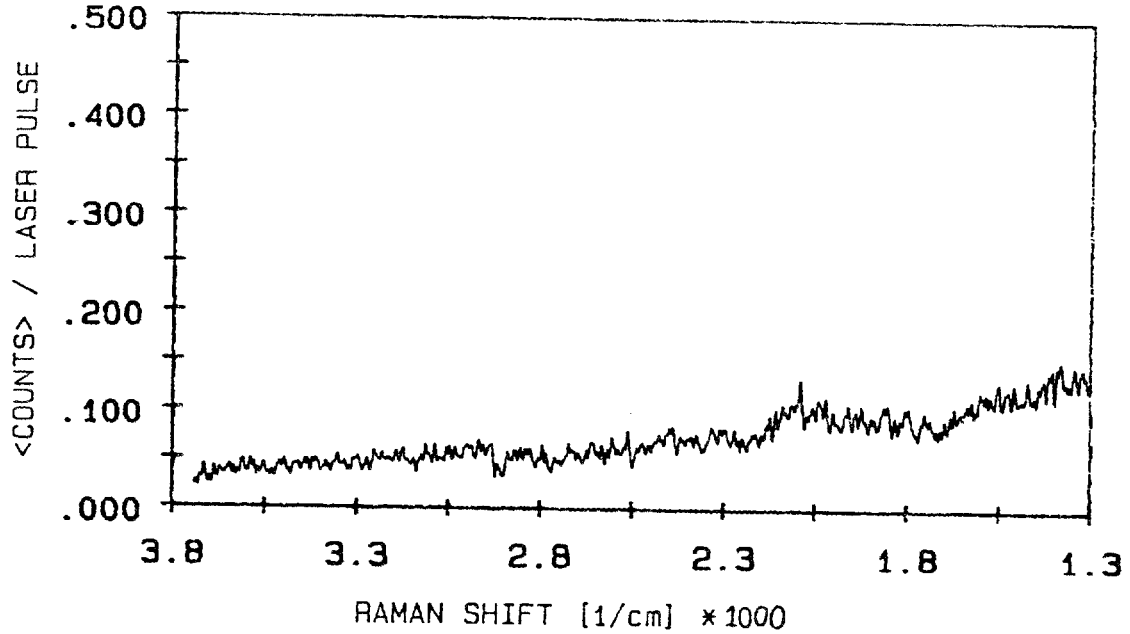

Figure 63. Raman spectra for GTE PY6 specimen 17 after testing to 1450°C from 1300-3800 cm^{-1}.

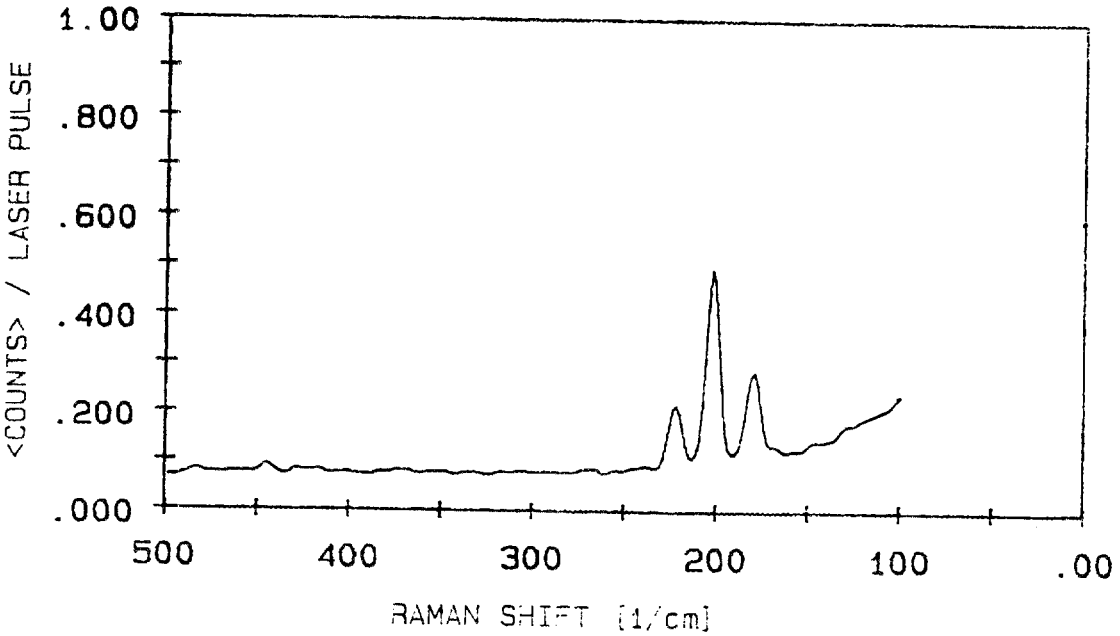

Figure 64. Raman spectra for GTE PY6 specimen 23 after testing to 1450°C from 0-500 cm^{-1}.

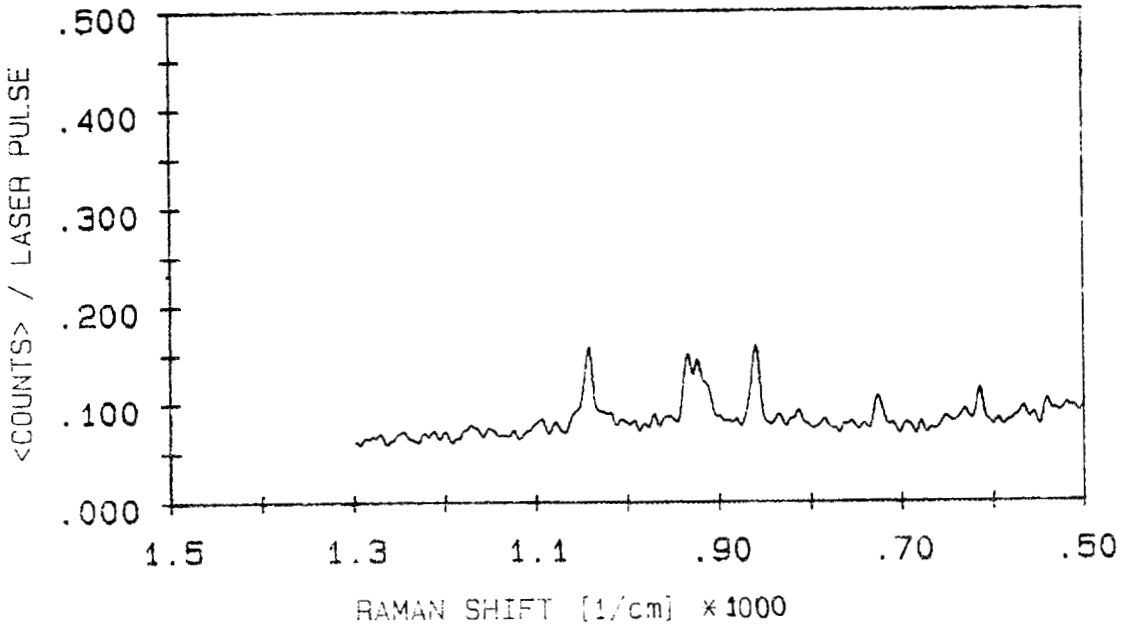

Figure 65. Raman spectra for GTE PY6 specimen 23 after testing to 1450°C from 500-1500 cm^{-1}.

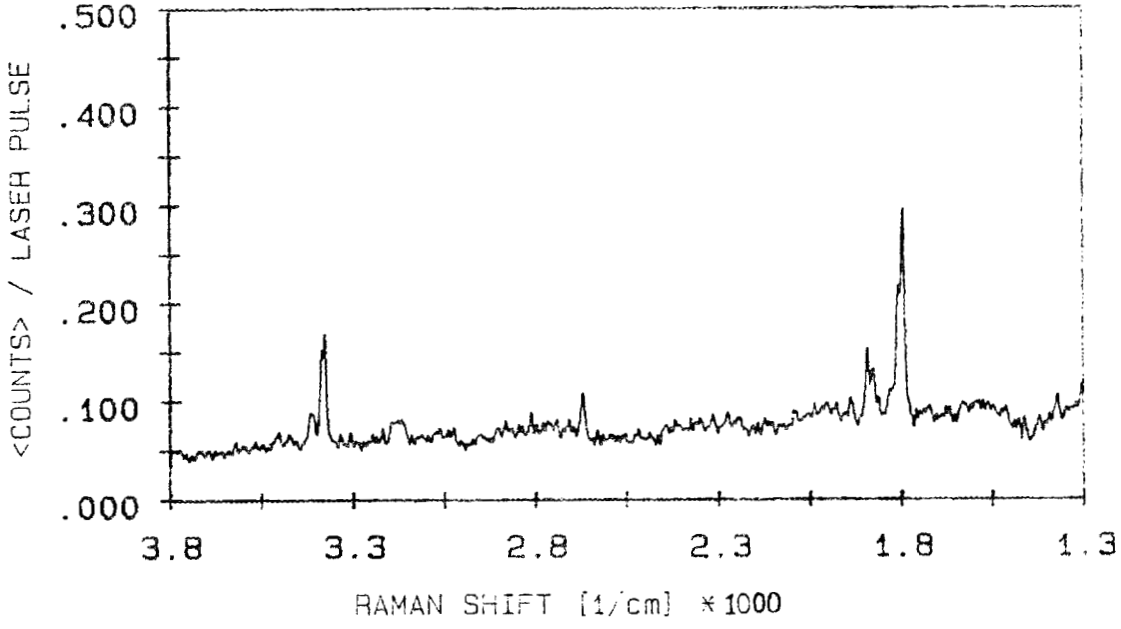

Figure 66. Raman spectra for GTE PY6 specimen 23 after testing to 1450°C from 1300-3800 cm^{-1}.

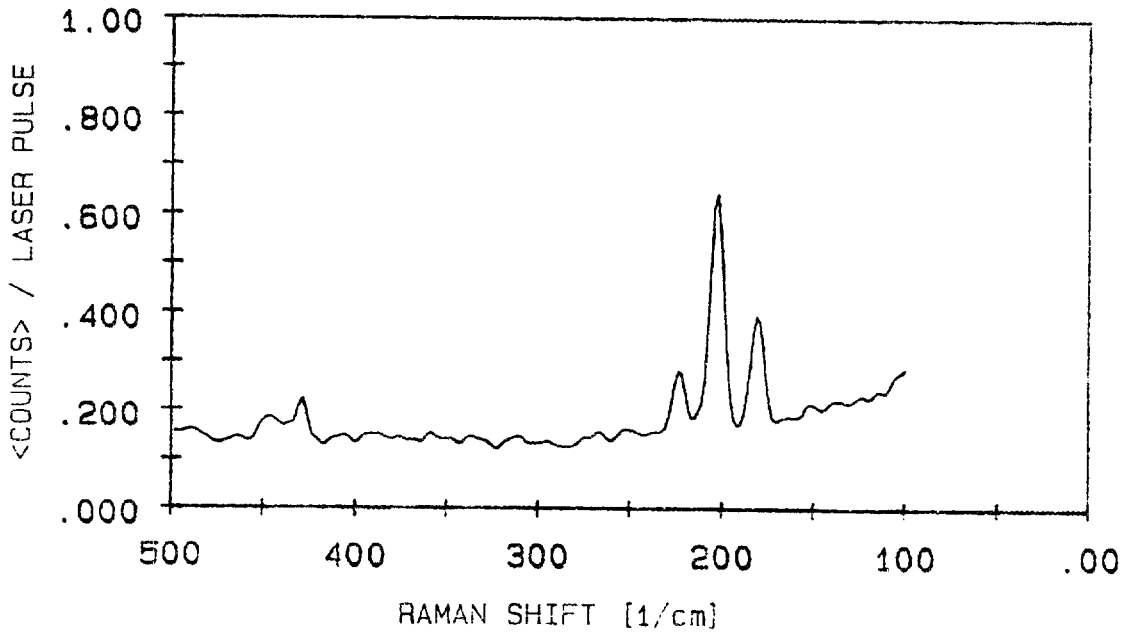

Figure 67. Raman spectra for Noralide XL144 as received specimen 8 from 0-500 cm^{-1}.

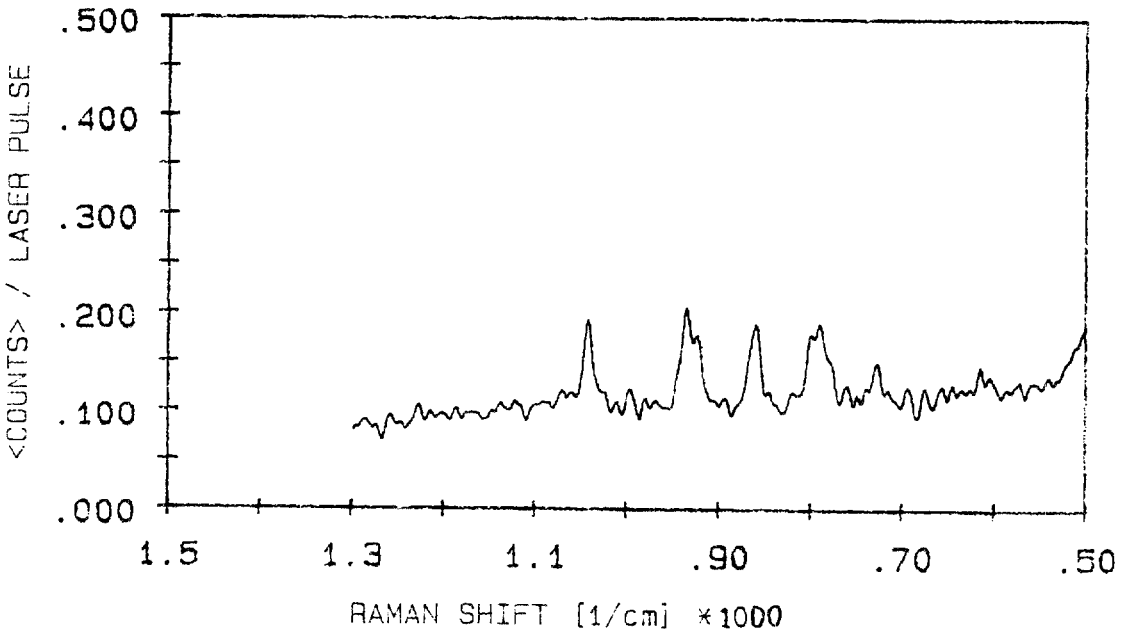

Figure 68. Raman spectra for Noralide XL144 as received specimen 8 from 500-1500 cm^{-1}.

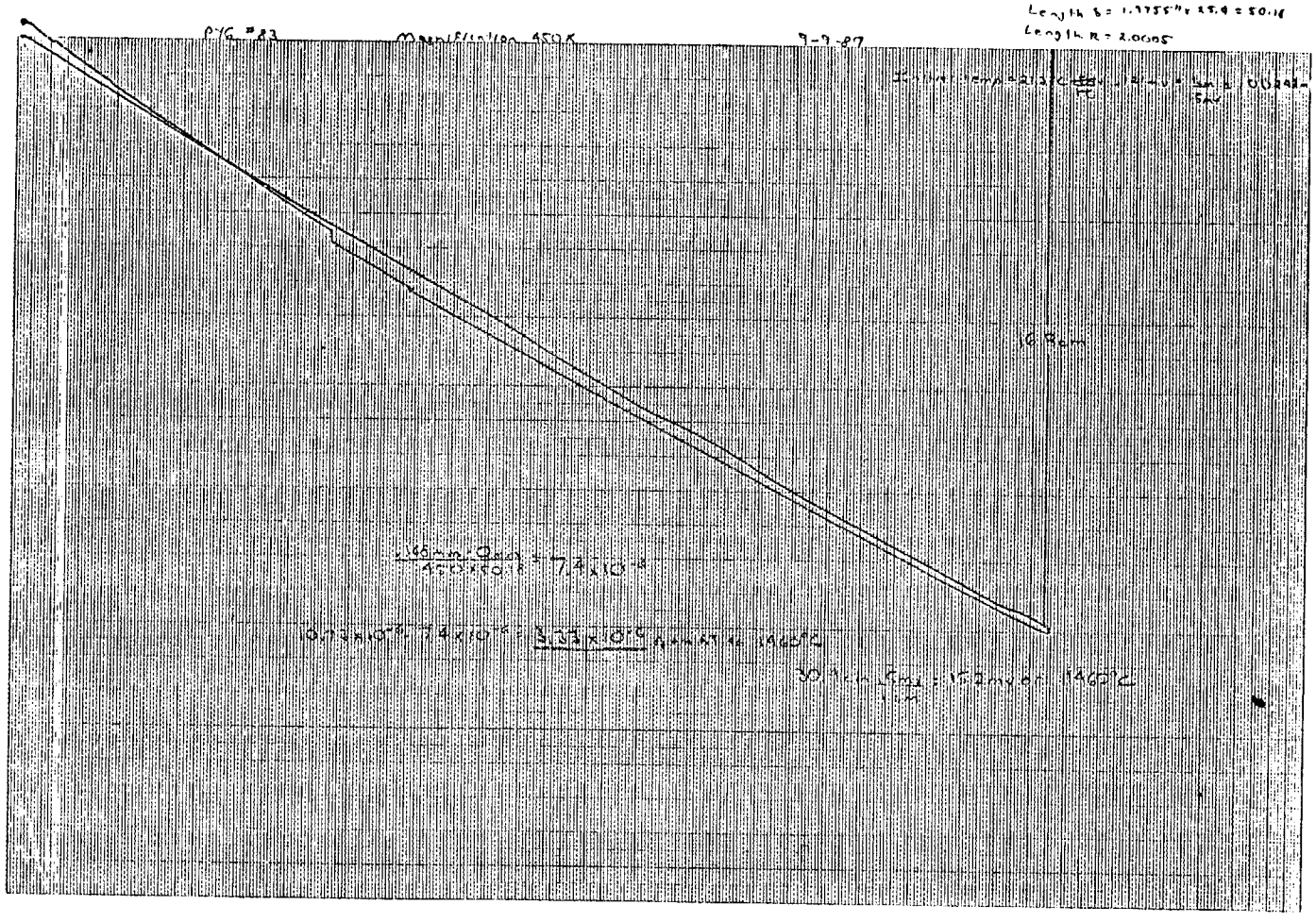

Figure 69. Typical thermal expansion curve recorded for GTE PY6.

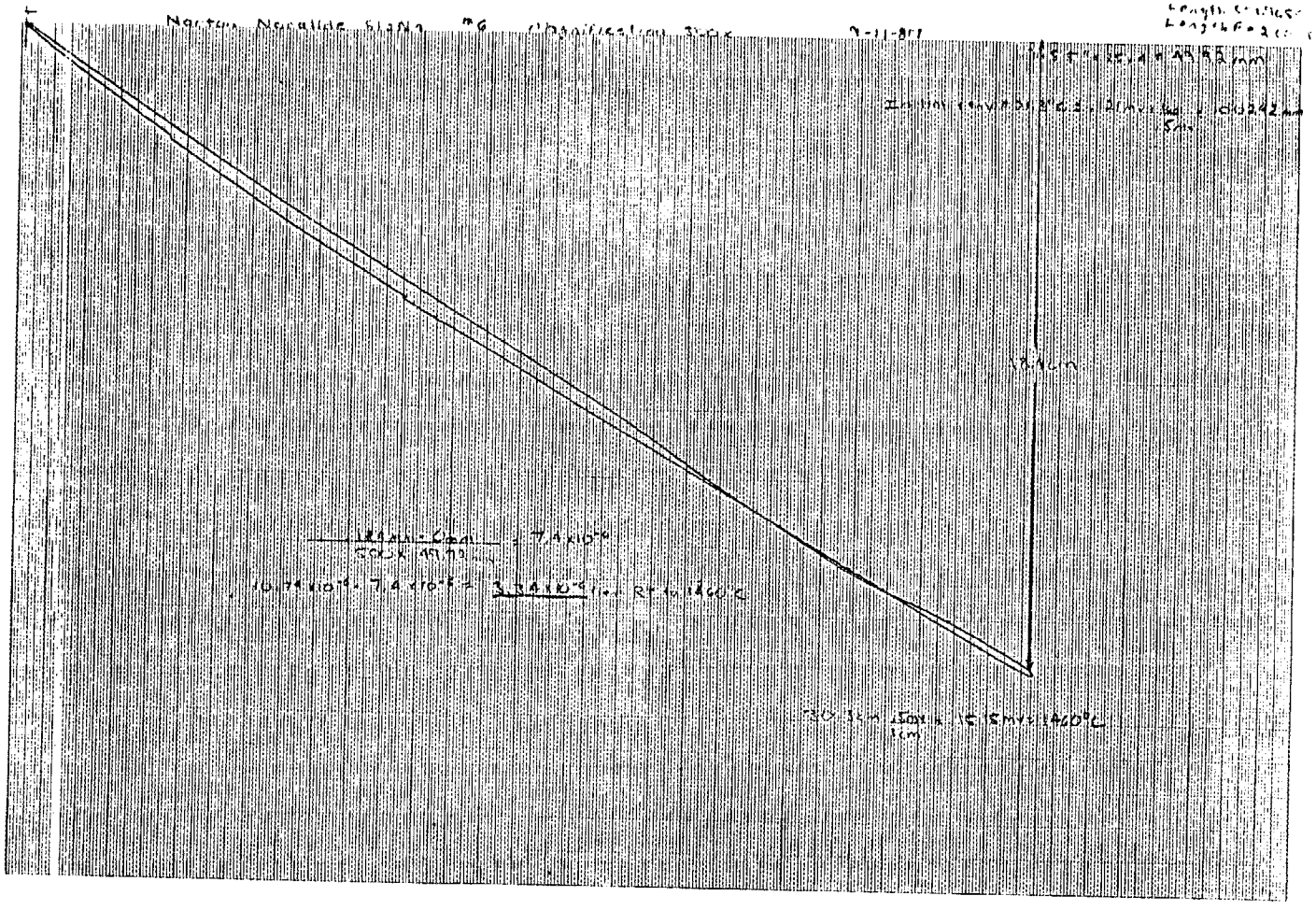

Figure 70. Typical thermal expansion curve recorded for Noralide XL144.

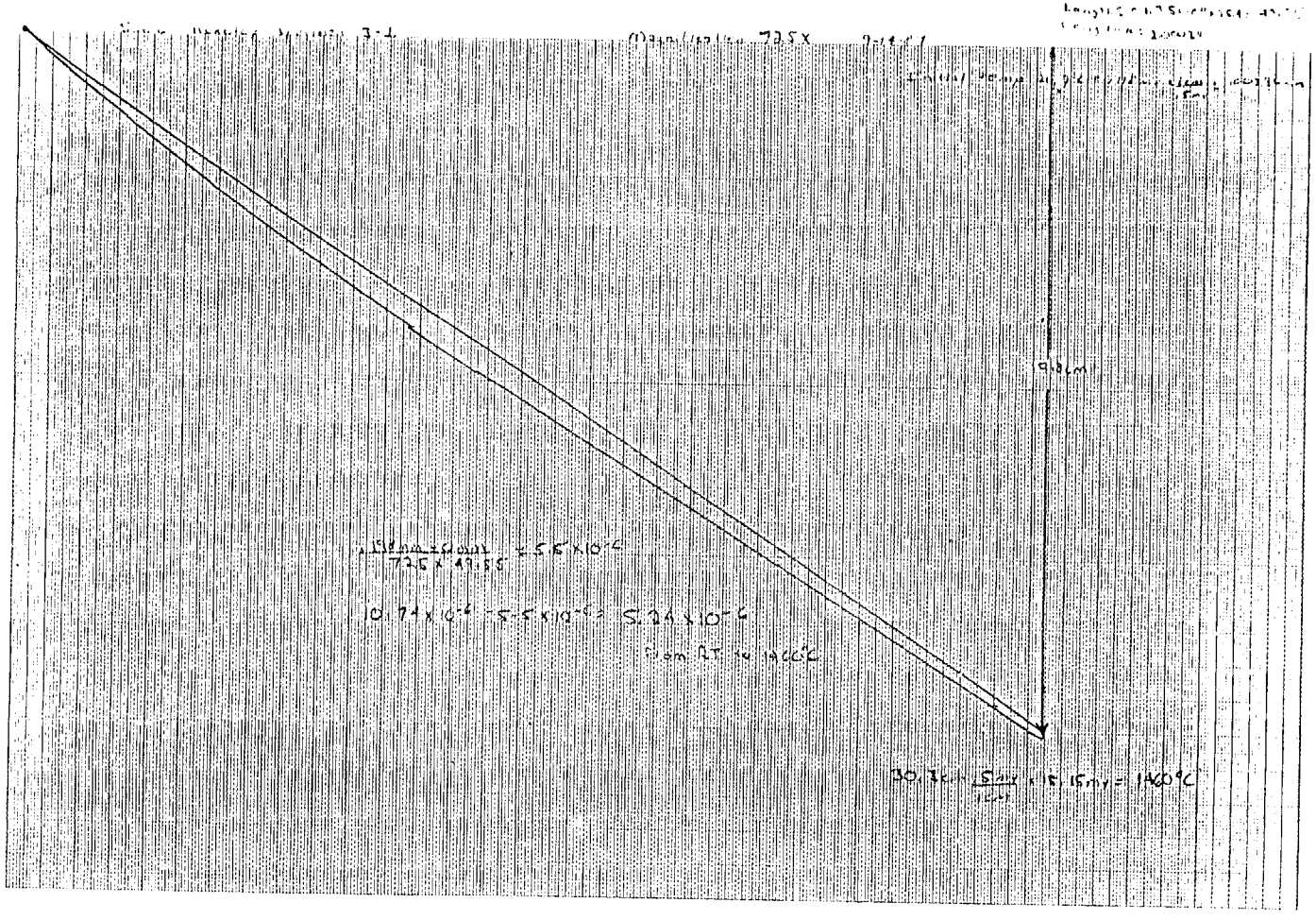

Figure 71. Typical thermal expansion curve recorded for Hexoloy-α-SiC.

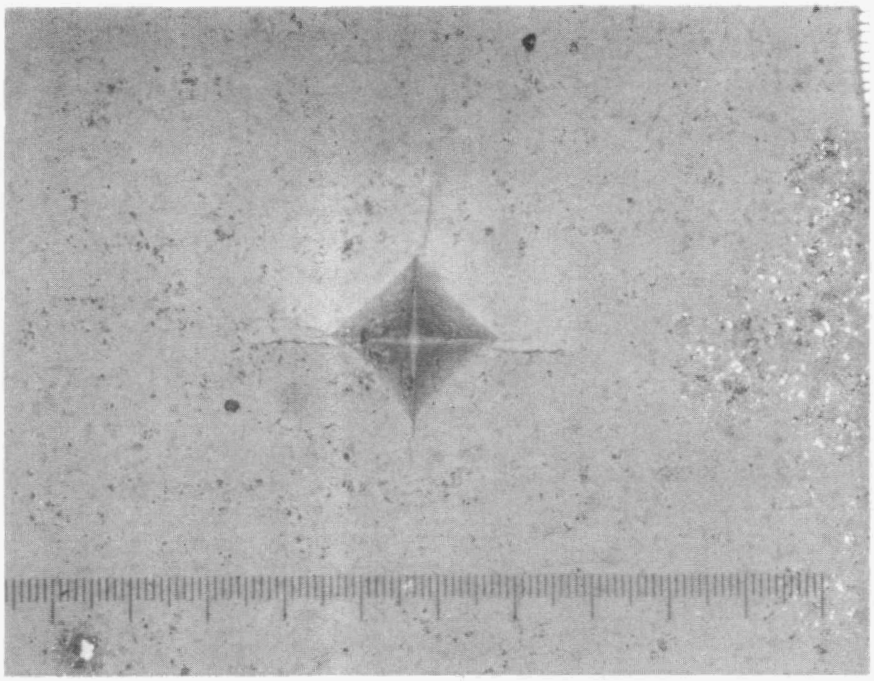

Figure 72. Typical indent for GTE PY6.

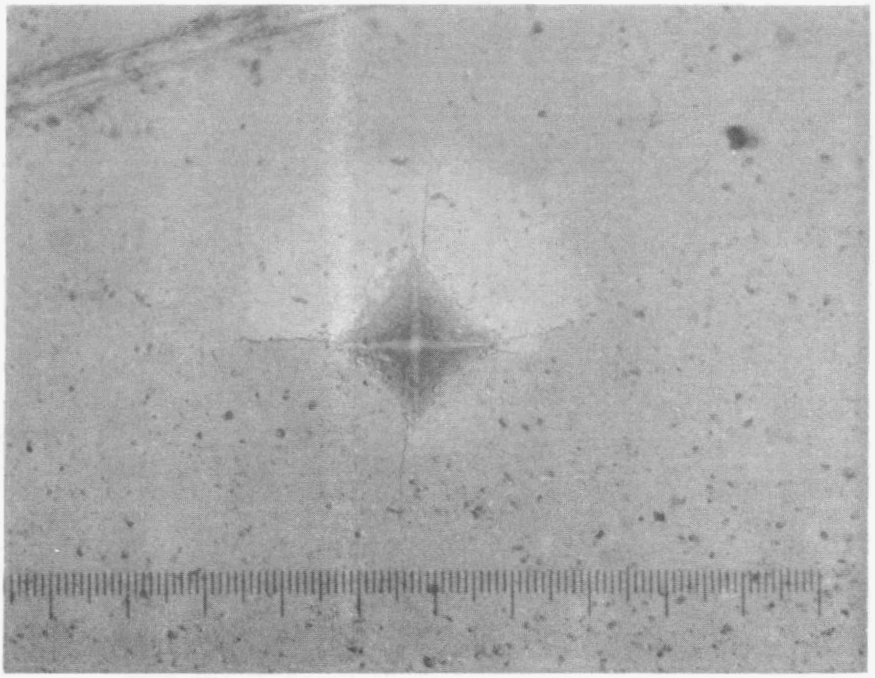

Figure 73. Typical indent for Noralide XL144.

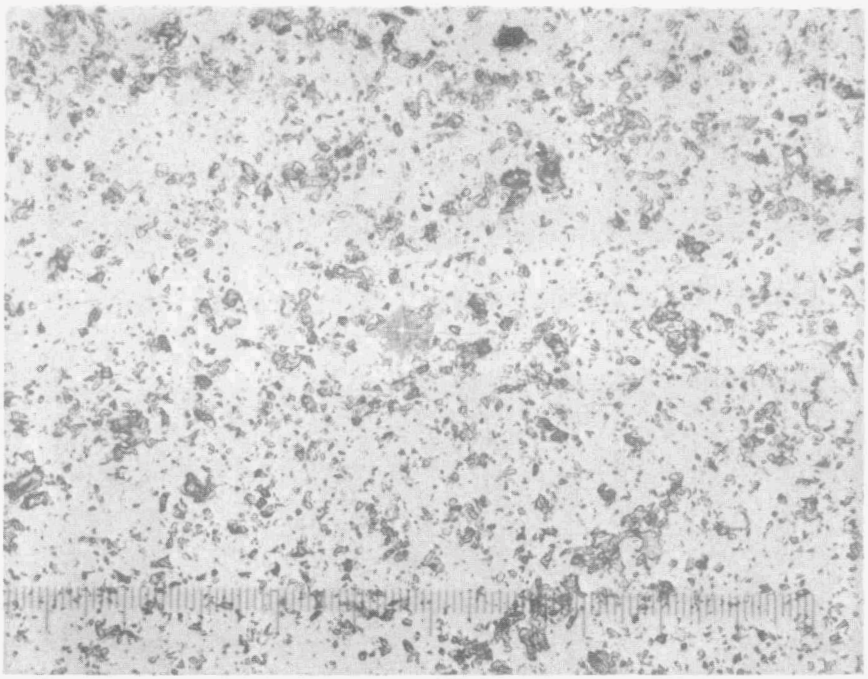

Figure 74. Typical indent for Hexoloy-α-SiC.

3.4 FRACTURE MECHANICS

Improved Methods for Measuring the Fracture Resistance of Structural Ceramics

R. C. Bradt and A. S. Kobayashi (University of Washington)

No report submitted.

Testing and Evaluation of Advanced Ceramics at High Temperature in Uniaxial Tension

J. Sankar, V.S. Avva, and R. Vaidyanathan (North Carolina A & T State University)

Objectives/Scope

The purpose of this effort will be to test and evaluate advanced ceramic materials at temperatures up to 1500°C in uniaxial tension. Testing may include fast fracture strength, stepped static fatigue strength, and cyclic fatigue strength, along with analysis of fracture surfaces by scanning electron microscopy. This effort will comprise the following tasks:

- Task 1. Specifications for Testing Machine and Controls + (Procurement)
- Task 2. Identification of Test Material (s) + (Procurement of specimens)
- Task 3. Identification of Test specimen configuration
- Task 4. Specifications for Testing grips and Extensometer + (Procurement)
- Task 5. Specifications for Testing Furnace and Controls + (Procurement)
- Task 6. Development of Test Plan
- Task 7. Room Temperature and High Temperature Tensile Testing
- Task 8. Reporting (Periodic)
- Task 9. Final Report

It is anticipated that this two (2) year program will help in understanding the behavior of ceramic materials at very high temperatures in uniaxial tension.

Technical Progress

Aluminum oxide (samples manufactured by Coors Porcelain Company and supplied by Ken Liu of ORNL) and SNW-1000 Silicon nitride (samples manufactured and supplied by GTE Wesgo division) were tested in uniaxial tension during the reporting period. Three stressing rates of approx. 450 MPa (65 Ksi), 900 MPa (130 Ksi), and 2100 MPa (305 Ksi) per minute were used for the silicon nitride samples and two stressing rates of approx. 225 MPa (32.5 Ksi), and 485 MPa (70 Ksi) per minute were used for the alumina samples. The alumina samples had a nominal gage section diameter of 1/4 in. with a 1 in. gage length. The silicon nitride samples had a nominal gage section diameter of 6 mm and a gage length of 25 mm. Tests were performed in the load control mode using the tension testing program provided by MTS Corporation. Silicon nitride samples were drawn from 2 batches, batch #1 consisting of 6 samples and batch #2 consisting of 12 samples. A total of 3 alumina samples and 18 silicon nitride samples were tested during this reporting period.

Table 1 summarises the test results for alumina samples (AD 998 and AD 94). Table 2 thru 4 summarises the uniaxial tensile test results for SNW-1000 silicon nitride obtained at stressing rates of 450 MPa/min, 900 MPa/min, and 2100 MPa/min respectively. Fig. 1 shows the Engineering

Table 1. Tension Test Results for alumina at room temperature tested at stressing rates of 220 MPa/min and 440 MPa/min.

Sample #	Tensile Strength MPa(Ksi)	Strain at Fracture %	Duration of Test Min:Sec	Remarks
1	256.18(37.15)	0.042	1:10	AD 998(220 MPa/min)
2	254.62(36.93)	0.0414	1:05	AD 998(220 MPa/min)
3	306.52(44.46)	0.0794	0:38	AD 94 (440 MPa/min)

Table 2. Tension test results for silicon nitride SNW-1000 tested at room temperature, at a stressing rate of 450 MPa/Min.

Sample #	Tensile Strength MPa(Ksi)	Strain at Fracture %	Duration of Test Min:Sec	Remarks
4	532.21(76.21)	0.18	1:09	#1 of batch #1
5	516.92(74.97)	0.128	1:06	#2 of Batch #1
6	499.65(72.47)	0.165	1:04	#3 of batch #1
7	504.21(73.12)	0.1852	1:05	#4 of batch #1
8	553.13(80.22)	0.1828	1:12	#5 of batch #1
9	438.98(63.67)	0.1484	0:57	#6 of batch #1
10	468.70(67.98)	0.1461	1:00	#1 of batch #2
11	447.51(64.90)	0.1392	0:57	#2 of batch #2

Note:

1. Batch #1 samples were dark grey and batch #2 samples were light grey tinged with yellow/green spots.

Table 3. Tension test results for silicon nitride SNW-1000 tested at room temperature, at a stressing rate of 900 MPa/Min.

Sample #	Tensile Strength MPa(Ksi)	Strain at Fracture %	Duration of Test Min:Sec	Remarks
12	373.27(54.14)	0.1236	0:24	#3 of batch #2
13	399.66(57.96)	0.1208	0:26	#4 of batch #2
14	559.11(81.10)	0.1708	0:36	#5 of batch #2
15	406.52(58.96)	0.1324	0:27	#6 of batch #2
16	352.72(51.16)	0.1040	0:23	#7 of batch #2

Note:

1. Batch #1 samples were dark grey and batch #2 samples were light grey tinged with yellow/green spots.

Table 4. Tension test Results for silicon nitride SNW-1000 tested at room temperature, at a stressing rate of 2100 MPa/Min.

Sample #	Tensile Strength MPa(Ksi)	Strain at Fracture %	Duration of Test Min:Sec	Remarks
17	594.20(86.18)	0.1952	0:17	#8 of batch #2
18	481.691(69.86)	0.1492	0:15	#9 of batch #2
19	551.02(79.92)	0.1836	0:16	#10 of batch #2
20	502.52(72.88)	0.1664	0:15	#11 of batch #2
21	516.60(74.92)	0.1800	0:17	#12 of batch #2

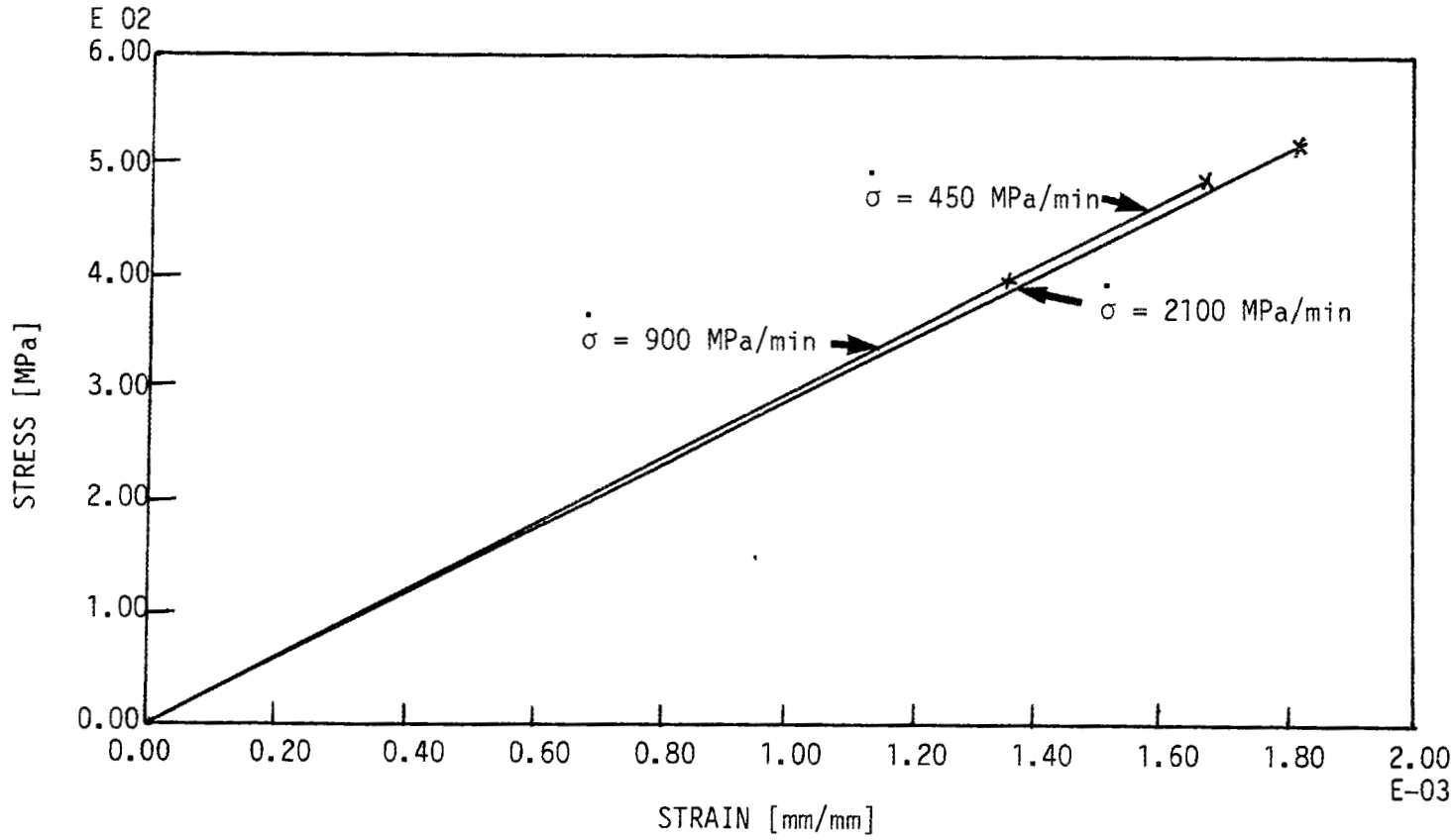

Fig. 1 Engineering stress-strain data for 3 typical samples of GTE SNW-1000 silicon nitride tested at different stressing rates.

stress-strain data obtained for 3 typical samples of SNW-1000 tested at stressing rates of 450 MPa/min, 900 MPa/min and 2100 MPa/min respectively. Fig. 2 shows a typical silicon nitride sample and Fig. 3 shows a fractured silicon nitride sample. Fig. 4 shows the SEM fractograph of a typical silicon nitride sample along with the fracture initiation point. X-Ray microanalysis of the fracture surface indicated the presence of silicon and aluminum rich particles on the fracture surface. These particles also show traces of a number of extraneous elements like Fe, C, Zn, Cl and O_2 indicating that the particles may have a complex alumino-silicate structure. Figures 5-6 show the presence of these particles. SEM analysis of the fracture surface further indicates the presence of a number of voids which appear to have coalesced during the fracture process. Fig. 7 shows the presence of a number of voids on the fracture surface. Figures 8-9 are magnified images of the voids in Fig. 7. Fig. 10 is a magnified image of a void which shows the presence of whiskers inside the void. Fig. 11 which is a gamma controlled image of a void also shows the presence of whiskers inside the void.

Detailed analysis of the test data, fractography and X-Ray microanalysis of the fracture initiation points are currently underway.

Status of Milestones

Tasks 1-4 are complete. Room temperature testing of silicon nitride is complete. The high temperature furnace is expected to arrive by the middle of November 1987. The next batch of samples are also expected to arrive by the middle of November 1987 and testing at high temperature will start as soon as the furnace arrives.

Communications/Visitors/Travel

J. Sankar and R. Vaidyanathan visited ORNL on Oct. 9, 1987 for technical discussions and analysis of the SEM data of room temp. tested silicon nitride. Two A & T undergraduate students also accompanied the visit.

Publications

1. R. Vaidyanathan, J. Sankar, V.S. Avva, "Testing and Evaluation of Silicon nitride in uniaxial tension at room temperature", paper to be presented at the 25th Automotive Technology Development Contractor's Coordination meeting, Dearborn, Michigan, October 1987.

References

None

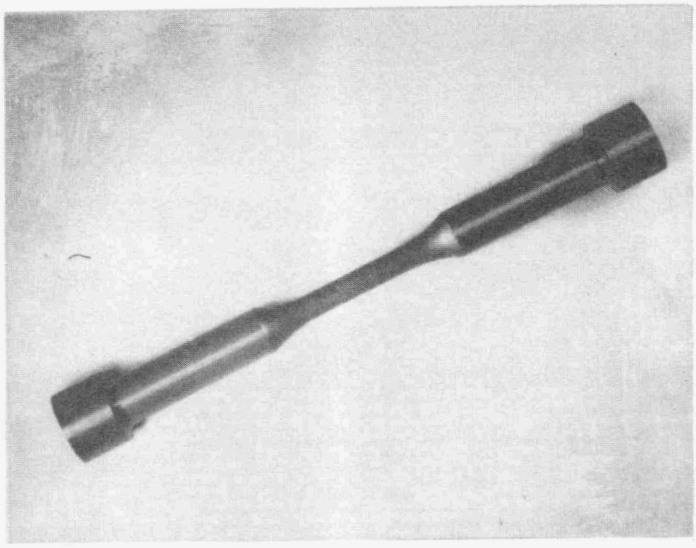

Fig. 2. A Typical Silicon Nitride sample.

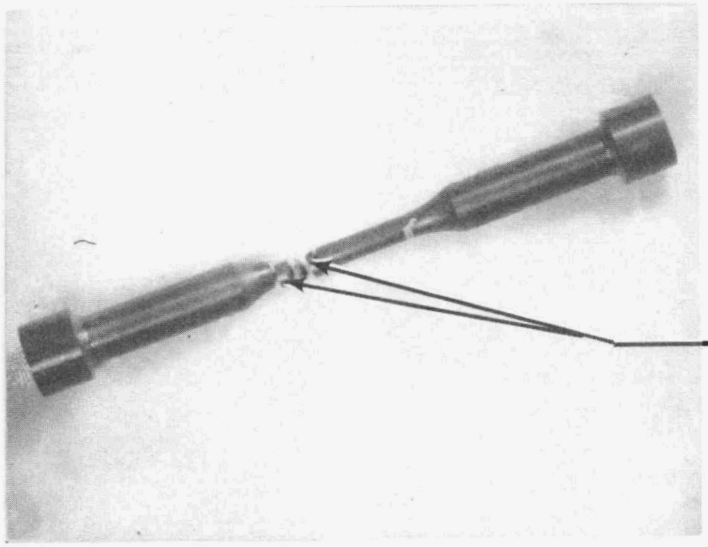

Fig. 3. Areas of a Silicon Nitride sample sectioned for Fracture surface analysis.

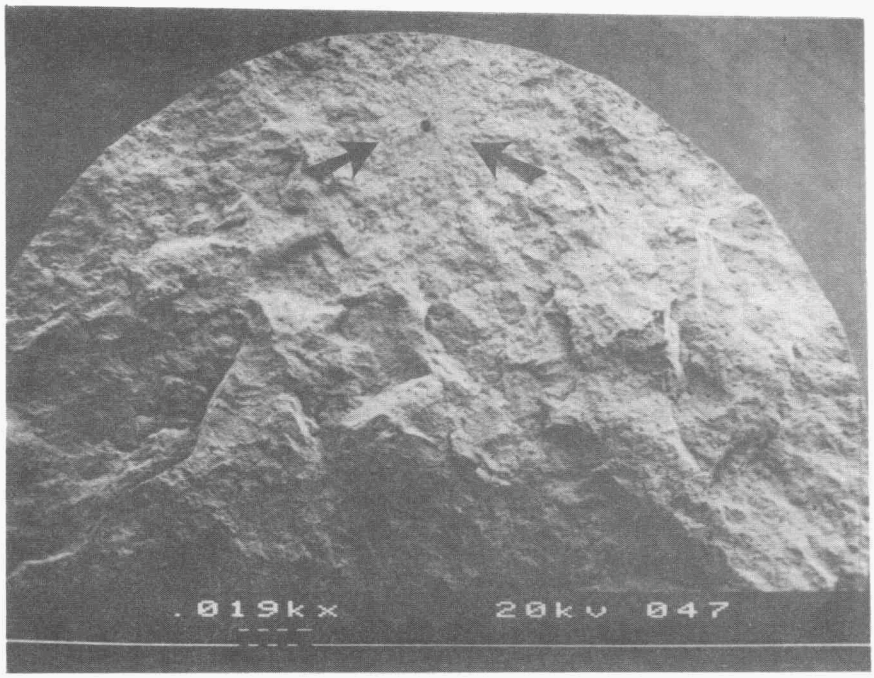

Fig. 4 SEM fractograph of a typical silicon nitride sample along with the fracture initiation point.

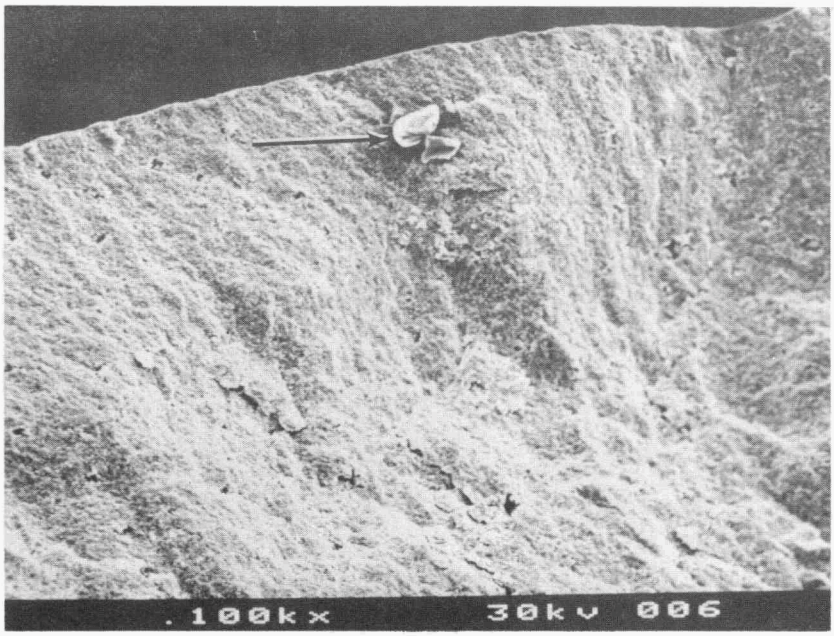

Fig. 5 SEM fractograph showing the presence of silicon rich inclusions on the fracture surface.(marked by arrows)

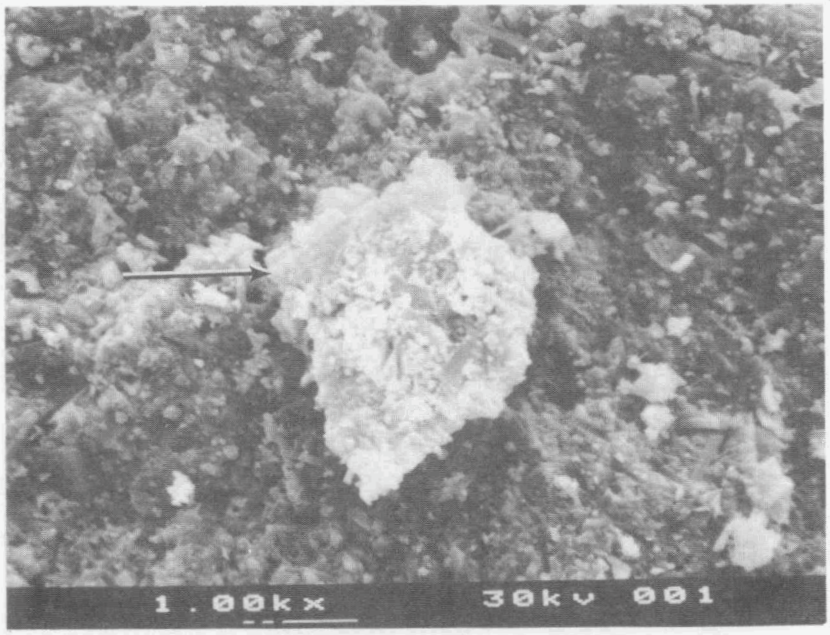

Fig. 6 Presence of silicon rich inclusions shown by fractograph (marked by arrow).

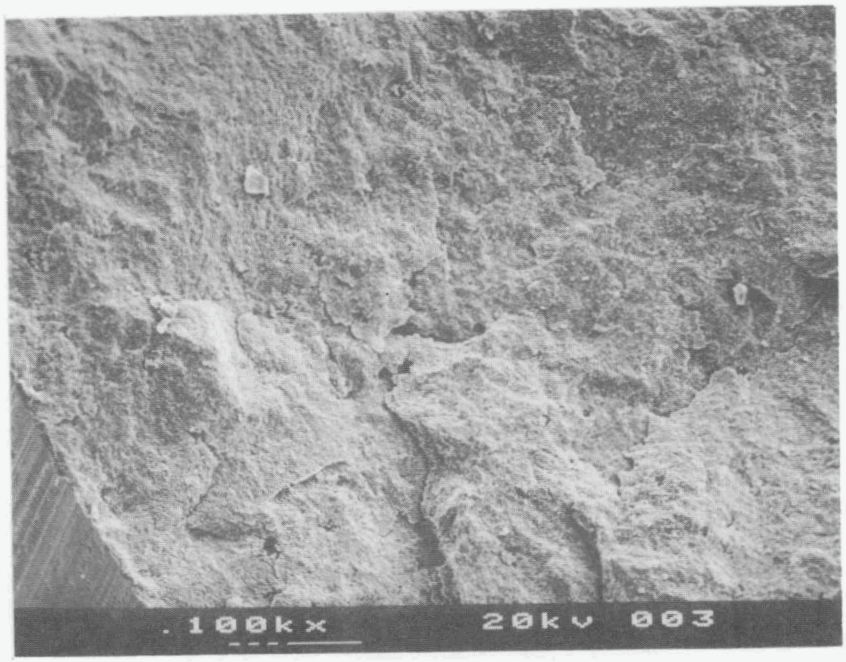

Fig. 7 SEM fractograph showing a large number of voids on the fracture surface.

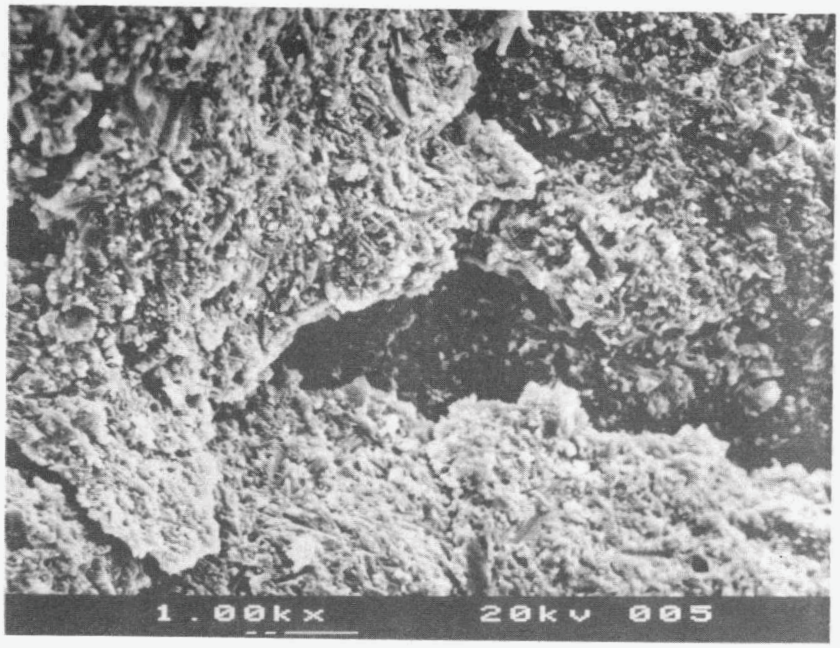

Fig. 8 Close up view of the voids in Fig. 7

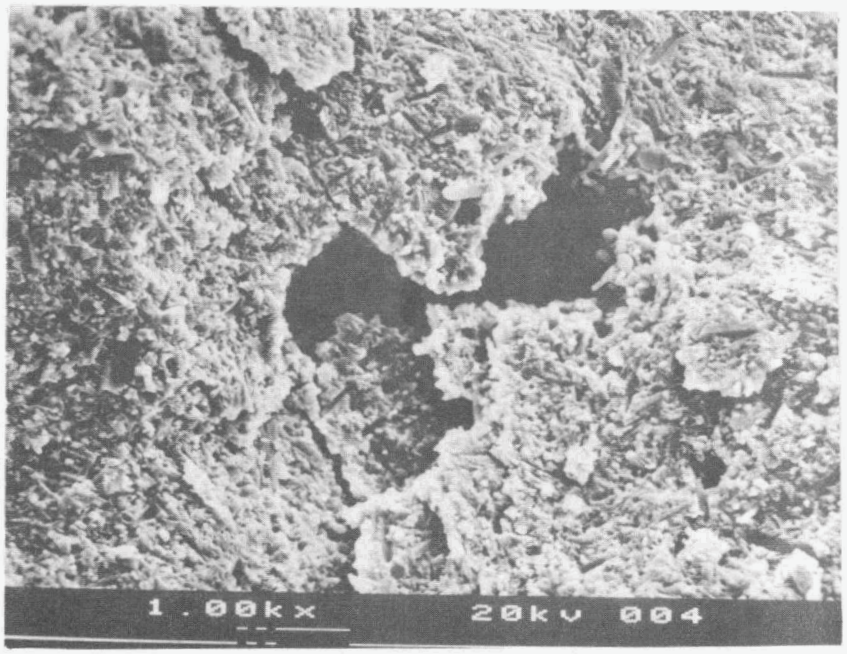

Fig. 9 Close up view of the voids from Fig. 7. Note the presence of whiskers near the void.

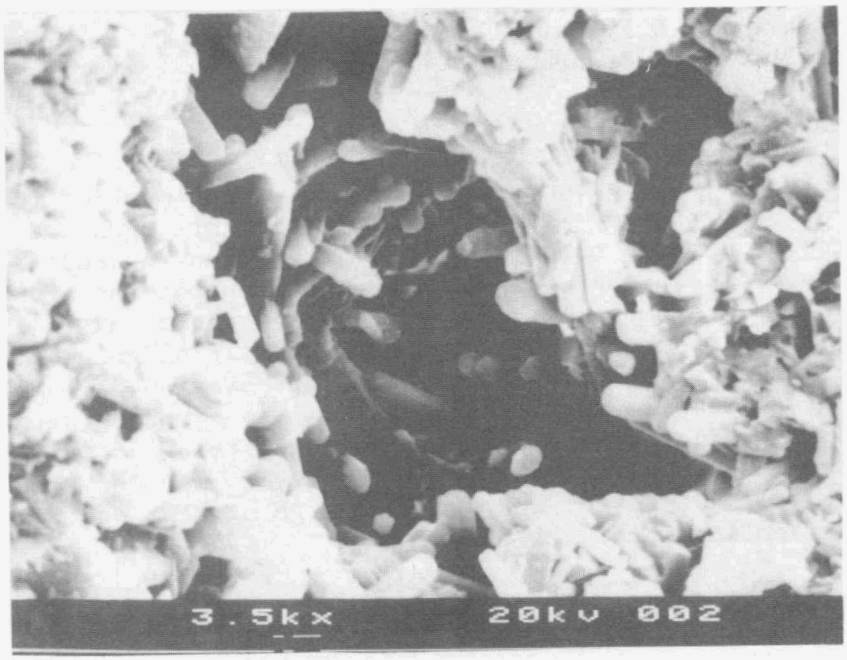

Fig. 10. Magnified image of a void showing the presence of whiskers inside the void.

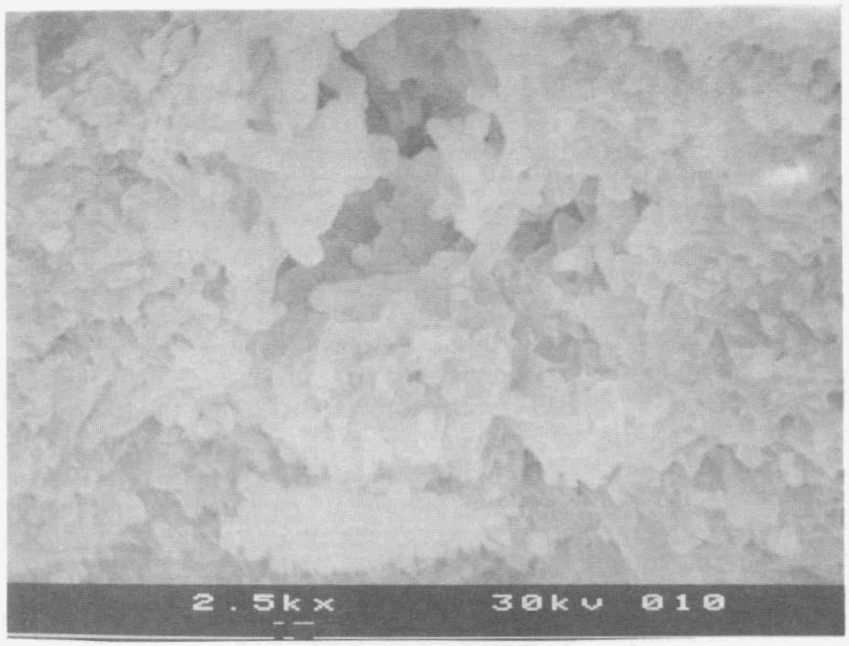

Fig. 11. Gamma controlled SEM image of a void showing the presence of whiskers inside the void.

Standard Tensile Test Development

S. M. Wiederhorn, D.F. Carroll, T.-J. Chuang and D. E. Roberts
(National Bureau of Standards)

Objective/Scope:

This project is concerned with the development of test equipment and test procedures for measuring the tensile strength and creep resistance of ceramic materials at elevated temperatures. Inexpensive techniques of measuring creep at elevated temperatures are being developed and are being used to characterize the mechanical behavior of structural ceramics. The test methods use self aligning fixtures, and simple grinding techniques for specimen preparation. Creep data obtained with tensile test techniques will be compared with data obtained using flexure and compressive creep techniques. The ultimate goal of the project is to assist in the development of a reliable data base that can be used for structural design of heat engines for vehicular applications.

Technical Highlights

During the past 6 months, experimental work on the creep behavior of reaction bonded silicon carbide in both tensile and compressive loading at 1300°C has been completed. As noted in earlier reports, steady state creep is reached early in both modes of loading such that almost the entire creep behavior within the strain regime studied (0 to 3 percent strain) can be described by steady state creep. In tension the steady state mode is maintained almost to failure, in compression to ≈3 percent strain. These results suggest that the creep behavior of this material can be defined reasonable accurately by the steady state creep rate.

In the present study the creep rate in both tension and compression can be described by bimodal curves on a logarithmic plot of creep rate versus applied stress figure 1. As can be seen, the slope of the curves has a slope of ≈4 at low values of the applied stress, and ≈11-14 at high values of the applied stress. The curve for compressive creep occurs at a much higher value of the applied stress than the one for tensile creep which indicates that creep in tension is much easier for this material than creep in compression. The slope of the curves at low stresses, ≈4, suggests a dislocation mechanism as the controlling factor for creep. Dislocation motion is observed in the composite material during creep supporting this supposition. At high tensile stresses, cavitation occurs in the silicon phase of the composite, suggesting damage accumulation in the form of cavitation as the main cause for the increased slope of the creep rate curve. This effect of cavitation on the creep behavior has been shown by Carroll and Tressler [1] to quantitatively account for the increase in the slope of the creep rate curve.

The increase of the slope of the curves in compression also suggests a damage mechanism to account for the increase of the creep

rate as a function of applied stress. Examination of the microstructure of deformed specimens by both optical and transmission electron microscopy gives no indication of cavity formation under compressive loading. This observation suggests that if a damage mechanism controls the creep rate, then the damage does not lead to cavity formation, and most probably is not dilatational. It is suspected that any damage that occurs is due to the generation of shear faults within the material. Shear faults have been observed by other authors and in vitreous bonded aluminum oxide [2].

The difference in creep behavior in tension and compression has been analyzed by other authors, and explained on the basis of a volume expansion caused by cavitation at grain boundaries, or dilation as a consequence of the creep process. Thus, Birch, Wilshire and Godfrey [3] attributed their results in reaction bonded silicon nitride to grain boundary sliding accompanied by microcrack formation. Microcrack formation was considered necessary to accommodate the sliding, and since crack formation depends on the development of tensile stresses across the grain boundary, cracks form more easily in tension than in compression, and the creep rate in tension is enhanced over that in compression.

Morrell and Ashbee [4] in their study of glass ceramics assumed creep to be confined to the remnant glass matrix surrounding elastic silicate crystals. Dilation of the glass-ceramic composite, accompanied by cavitation of the glass and percolation of the glass through the composite were suggested as the primary determinants of the creep behavior. Since dilation and cavitation both involve a volume expansion, creep will be retarded by compressive stresses, which result in a net positive pressure throughout the solid. Conversely, creep is enhanced by tensile stresses for the same magnitude of imposed stress.

The susceptibility of a composite to creep will also depend on the sign of the stress if both the particles and matrix are independently interconnected. Such structures introduce an asymmetry into the creep process as a consequence of the mechanical behavior of the more rigid of the two phases. For the present study, it is clearly necessary to either deform, or fracture the contact points between silicon carbide grains if deformation of the composite is to occur. Because contact between the silicon carbide grains is tenuous, contact points between grains of silicon carbide are expected to be at a high stress and consequently to rupture readily in tension, leaving the silicon to carry the tensile load. Hence, in tension, creep occurs primarily by deformation of the silicon phase. In compression, however, the silicon carbide network will be supported by the surrounding silicon so as to prevent buckling of the network, thus necessitating deformation of the silicon carbide network for creep to occur. Deformation is expected to occur preferentially at the contact sites between the silicon carbide particles, where the stresses are the highest, and since silicon carbide is more difficult to deform than silicon, the creep rate in compression is expected to be less than that in tension for a given stress level. The stress exponent ≈ 4, obtained in compression is consistent with the suggestion that creep is controlled by deformation of the silicon carbide. Frictional forces resulting from the sliding of the silicon carbide particles over one another may also play a role in the

deformation process. Because these forces increase with compressive loading, frictional forces will effectively increase the stress required for deformation in compression over that required in tension.

To test the possibility that creep in compression is controlled by deformation of the silicon carbide, a specimen of reaction bonded silicon carbide was subjected to creep at 150 MPa both above and below the melting point of silicon (1410°C). If, as suggested above, creep were controlled by deformation of the silicon carbide, then the creep rate would be expected to be unaffected by the melting of the silicon. As the temperature was increased, a continuous increase in the creep rate would be expected, as determined by the temperature sensitivity of the creep rate below the melting point of the silicon. To test this thesis, data were obtained at temperatures of 1390°C and 1430°C, i.e. 20°C above and 20°C below the melting point of the silicon. Data obtained in this experiment are shown in figure 2. As can be seen on this Arrhenius plot, data collected at 1300, 1390 and 1430°C lie on a straight line, suggesting that the mechanism of deformation above the melting point of the silicon is essentially the same as that below the melting point of the silicon. Furthermore, since silicon is an inviscid liquid above its melting point, it is not expected to carry its share of the load at 1430°C. The fact that the reaction bonded silicon carbide supports the load and creeps at a predicted rate above the melting point of the silicon, supports the thesis that creep in compression is determined by deformation of the silicon carbide grains. By contrast, a similar experiment performed in tension indicates a complete loss in specimen strength once the melting temperature of the silicon has been exceeded. This finding is similar to that reported earlier by Vaandrager and Pharr [5] on alpha brass containing a liquid grain boundary phase. Here too melting of the grain boundary phase had no effect on the creep rate, when measured in compression.

Status of Milestones

341301 One paper has been published on test techniques used to study creep in tension, two others are currently under review by the American Ceramic Society.

Publications

1. T.-J. Chuang and S.M. Wiederhorn, "Damage-Enhanced Creep in a Siliconized Silicon Carbide: Mechanics of Deformation," J. Am. Ceram. Soc. submitted.

2. S.M. Wiederhorn, D.E. Roberts, T.-J. Chuang and L Chuck, "Damage Enhanced Creep in a Siliconized Silicon Carbide: Phenomenology," J. Am. Ceram. Soc. Submitted.

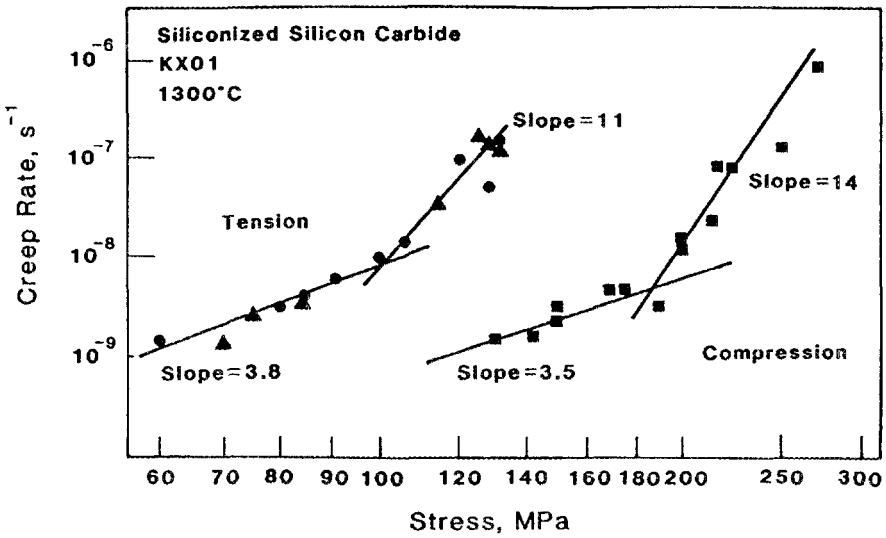

1. Stress dependence of the creep rate as a function of the applied stress. The creep data is bimodal; the slope at low stresses approximately one-third that obtained at high stresses. The data obtained in tension using the clothespin design apparatus (▲) appear to fall within the scatter of the data obtained using the pin and clevis apparatus (●). In compression (■) the creep data also follow a bimodal curve. The high and low stress portions of the compressive creep curve lie roughly parallel to the equivalent portions of the tensile creep curve.

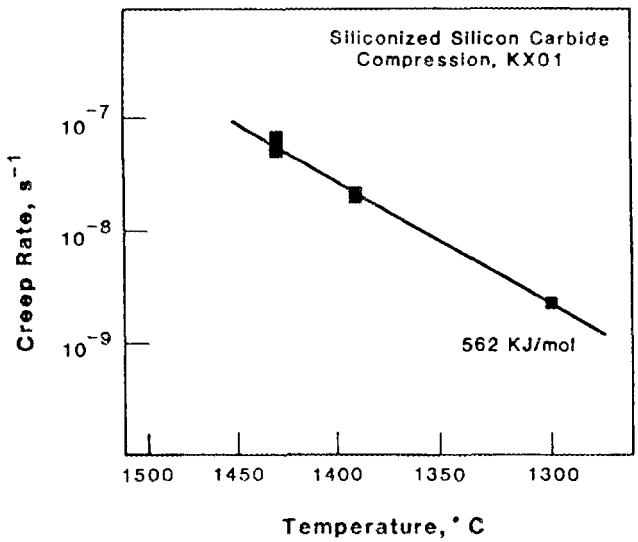

2. Creep data collected on reaction bonded silicon carbide below and above the melting point of silicon. The data lie on a straight line suggesting that the mechanism of creep just below the melting point of the silicon is the same as that controlling creep below the melting point of the silicon. The apparent activation energy for the process, ≈562 KJ/Mol, is approximately of the same magnitude as that obtained by Carter and Davis [6], ≈711 KJ/mol, on a different grade of reaction bonded silicon carbide. These author's data were all obtained above the melting point of silicon.

References

1. D.F. Carroll and R.E. Tressler, "Effect of Creep Damage on the Tensile Creep Behavior of a Siliconized Silicon Carbide," to be published.

2. D.R. Clarke, "High Temperature Deformation of a Polycrystalline Alumina Containing an Intergranular Glass Phase," J. Mater. Sci. 20, 1321-32 (1985)

3. J.M. Birch, B. Wilshire and D.J. Godfrey, "Deformation and Fracture Processes During Creep of Reaction Bonded and Hot Pressed Silicon Nitride," Proc. Brit. Ceram. Soc. 26, 141-54 (1978).

4. R. Morrell and K.H.G. Ashbee, "High Temperature Creep of Lithium Zinc Silicate Glass-Ceramics, Part 1, General Behavior and Creep Mechanisms," J. Mater. Sci. 8, 1253-1270 (1973).

5. B.L. Vaandrager and G.M. Pharr, "Creep of Alpha Brass Containing a Liquid Grain Boundary Phase," Scripta Met. 18, 1337-39 (1984).

6. C.H. Carter, Jr. and R.F. Davis, "Kinetics and Mechanisms of High-Temperature Creep in Silicon Carbide: I, Reaction Bonded," J. Am. Ceram. Soc. 67, 409-417 (1984).

3.5 NONDESTRUCTIVE EVALUATION DEVELOPMENT

Nondestructive Characterization
R. W. McClung (Oak Ridge National Laboratory)

Objective/scope

The purpose of this program is to conduct nondestructive evaluation (NDE) development directed at identifying approaches for quantitative determination of conditions (including both properties and flaws) in ceramics that affect the structural performance. Those materials that have been seriously considered for application in advanced heat engines are all brittle materials whose fracture is affected by structural features with dimensions on the order of the dimensions of their microstructures. This work seeks to characterize those features using high-frequency ultrasonics and radiography to detect, size, and locate critical flaws and to measure nondestructively the elastic properties of the host material.

Technical progress

Ultrasonics – W. A. Simpson, Jr., and K. V. Cook

Ultrasonic studies in this reporting period included development of techniques and evaluation of monolithic and whisker-reinforced ceramic composites, surface wave techniques on IEA silicon nitride modulus of rupture (MOR) bars, several ultrasonic approaches on partially stabilized zirconia (PSZ) MOR bars, and silicon nitride MOR bars with varying particle diameters.

Monolithic and composite ceramic billets. We completed the ultrasonic characterization of three ceramic billets obtained from an outside ceramics supplier. Two of these billets, one alumina and the other silicon nitride, were reinforced with silicon carbide whiskers. The third sample was a monolithic silicon nitride. As expected, the monolithic material yielded only a few ultrasonic indications comparable in size and intensity to those from voids on the order of 25 to 50 μm in diameter. The whisker-toughened materials, however, both showed evidence of whisker clumping, with the silicon nitride sample being particularly affected. Figure 1 shows this sample with numerous whisker clumps. The alumina sample also contained numerous indications, which, in size, intensity, and shape, are comparable to the scattering from 100-μm-diam voids.

A material transfer curve (elastic wave attenuation vs frequency) was also obtained on each of the billets, and, as with samples produced at ORNL, the attenuation in the whisker-toughened material was measurably higher than in the monolithic sample. We had previously noted this behavior for alumina when fiber clumping is present, but this is the first opportunity that we have had to examine whisker-toughened silicon nitride. For all three billets, however, the ultrasonic attenuation in the range 20 to 100 MHz was very low and increased linearly with frequency, indicating that scattering losses (from the microstructure) are not important in this wavelength region. Figures 2 and 3 show the transfer curve results on the monolithic and whisker-toughened silicon nitride, respectively. Note that

ORNL-DWG 87-5593

Fig. 1. Detection of whisker clumps in a whisker-toughened silicon nitride.

the linear coefficient of attenuation increased by a factor of about two between these samples.

Surface-wave techniques on IEA MOR bars. As part of our work in inspecting the IEA silicon nitride MOR bars, we have fabricated surface wave standards by dph indentation of the surface. This approach produces cracks whose size is dependent on the load applied and whose theoretical profile is half-penny shaped. Loads ranging from 2 to 10 kg were used to produce a test sample. Microscopic examination of the surface indicated that no discernible cracking was generated at the lower load limit, while cracks about 200 μm long were produced by the 10-kg load. Although the presence of machining marks tended to obscure the cracks that were directed along the axis of the bar, in a few cases these longitudinally oriented cracks could be seen and were found to be comparable to the transversely oriented cracks, thus indicating that there was little or no residual surface stress.

The surface wave standard was examined ultrasonically using a 50-MHz focused transducer to produce a high-frequency Rayleigh wave. Optimum generation of the surface wave was found to occur when the axis of the transducer was inclined at approximately the Rayleigh angle and when the focal point was at or just below the surface of the sample. (Although the maximum signal was generated when the transducer focus was located at the

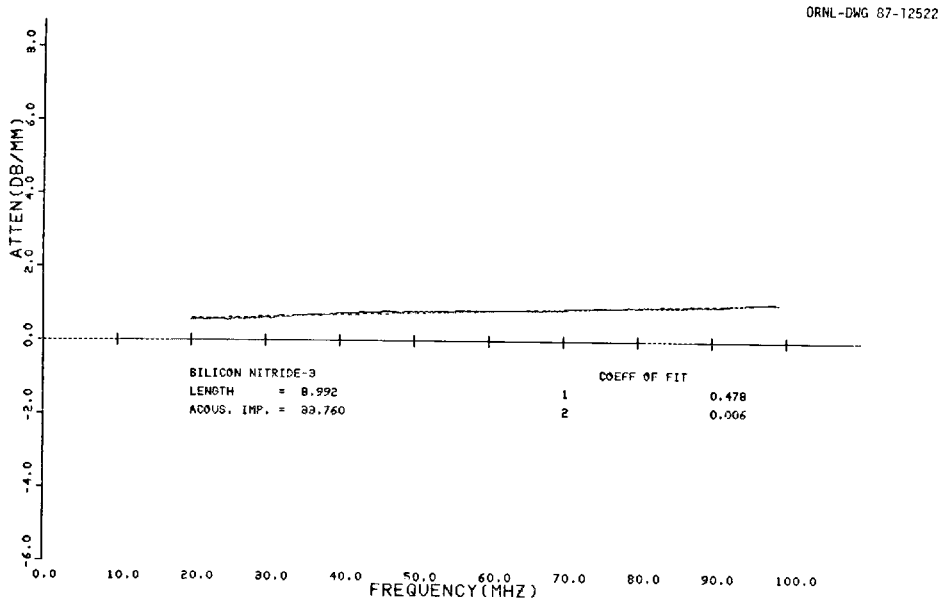

Fig. 2. Transfer curve on a monolithic silicon nitride.

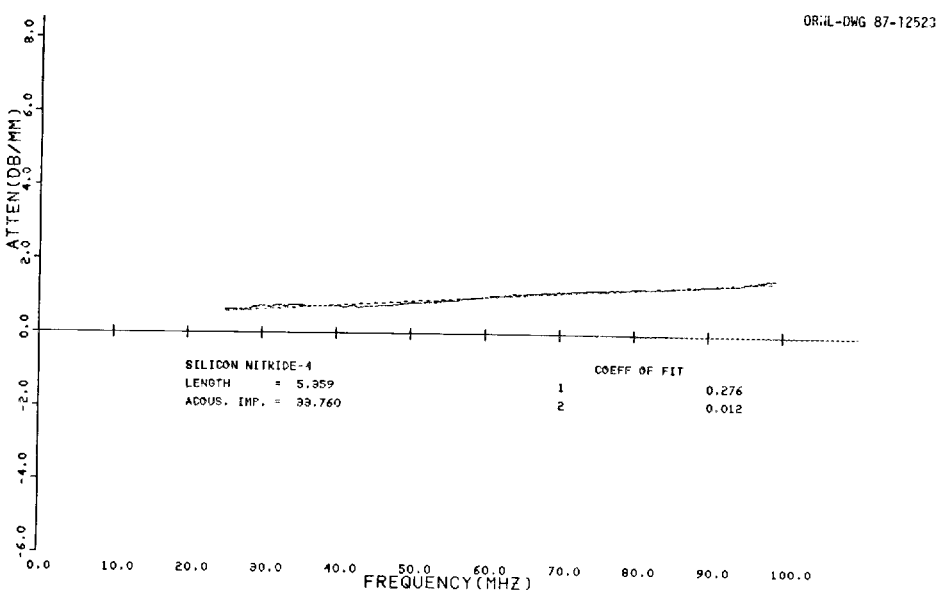

Fig. 3. Transfer curve on a whisker-toughened silicon nitride.

sample surface, the surface-generated noise was also much worse for this arrangement. The best signal-to-noise ratio was thus obtained when the focus lay slightly below the surface.) Under these conditions, the losses in the water column reduced the frequency of maximum amplitude in the transducer response to about 35 MHz.

Inspection of the dph standard indicated that the 10-kg load cracks could be detected easily. Those produced by the 8- and 6-kg loads were also detected with correspondingly smaller signal-to-noise ratios. Surface noise produced by the relatively rough surface finish of these bars appears to be the limiting factor in detecting small surface cracks, since the Rayleigh wave amplitude (actually a leaky Rayleigh wave because of the water coupling) decreases rapidly with distance from the crack. Thus one needs to gate very close to the surface-generated signal for maximum sensitivity, and this signal is relatively diffuse for rough surfaces. Nevertheless, the detection of the 10-kg load cracks seems adequate, since these cracks are only about one wavelength deep for a 35-MHz surface wave.

Ultrasonic studies on PSZ MOR bars. We have completed ultrasonic examination on 157 PSZ MOR bars. A number of tests, designed to detect the presence of critical flaws and to characterize the microstructure of the material, were performed on each bar. A full volumetric inspection for flaws was performed at 50 MHz, as were a surface-wave inspection on the surface which would be in tension during flexure tests, a qualitative back-surface signal amplitude test, and a measurement of the absolute attenuation as a function of frequency. Several of the bars contained demonstrable flaws, as detected by either the volumetric or surface-wave tests. However, the majority of the samples yielded no indications for any of the flaw tests. No estimate of the size was made for those flaws which were detected, but the conditions of the test were such that flaws having diameters of perhaps 75 μm and larger would be detected. The standard, which was scanned with each group of bars inspected, contained a fabricated 125-μm void which was easily detected.

For the surface-wave tests, a standard was created by dph indentation of one surface using a load of 8 kg. In this material, the resulting crack is poorly defined and oriented along local grain boundaries rather than along the diagonal of the indentation. This results in a much poorer standard and one in which the subsurface profile of the crack is not known. The length of the cracks was measured by microscope and found to be about 150 μm. Because of the problems with dph indentation in zirconia, a 125-μm-diam hole 100 μm deep was also drilled in the inspection surface. Although this target should present a smaller scattering cross section to the surface wave than a well-formed penny-shaped crack of 150 μm in diameter, in fact it gave a much larger indication than the dph indentations. All four standards were easily discernible, however.

The absolute attenuation as a function of frequency was measured for 91 of the bars. Although we have the capability of determining this quantity over the range of 1 to 150 MHz, the scattering losses in the PSZ become excessive above about 50 MHz and are minimal below about 20 MHz. For this reason, the measurement of attenuation was restricted to the range 20 to 50 MHz. For all the bars, if α/f^2, where α is the measured attenuation and f is the frequency, is plotted as a function of f^2, a

straight line of virtually zero slope results, indicating nearly perfect square-law scattering. This is precisely what one would expect in this frequency range from a coarse-grained material. At the low end of the frequency range, the plot begins to diverge from a straight line, indicating the increasing importance of a linear damping term and a constant absorption term. Each of these terms is available individually for correlation with the destructive results.

Four of the bars were exposed to the combustion environment of a diesel engine for 100 h following ultrasonic evaluation. They were then returned for reexamination. As expected, no additional indications were seen in the flaw tests, and the previously detected indications had not changed. When the attenuation was measured, however, there was a noticeable and uniform change in the result. Detailed comparison of the data indicated that the quadratic coefficient of loss was unchanged for all four bars. Since this term results from scattering losses and is indicative of the average grain size, it is not surprising that it was unaltered. The absorption and damping terms, however, were changed for all four bars, with the former term increasing and the latter decreasing. The net result was to lower the total high-frequency attenuation in all cases. We do not yet know what properties of the samples have been altered, but we are investigating this phenomenon. Figure 4 shows the transfer curve obtained on one of these bars following exposure to the combustion environment.

Fifty-five of the bars have been broken by four-point bending. The breaking load, and thus maximum tensile stress, is available for each of these bars. The bars are currently undergoing fractography to determine if the initiating source can be determined. Only for two of these samples, however, have we thus far received data indicating the location of the break. Examination of our flaw data, both volumetric and surface, shows no indications at the location of the rupture for these two bars. Since several of the indications detected in other bars appear to originate from sources larger than 100 μm, it will be interesting to see if these are indeed the initiating events.

We have examined the relationship between our attenuation data and the maximum stress at rupture for the 55 broken bars. Since the quadratic term in our data should correlate with average grain size, there should be correlation between this term and the rupture stress only if the latter correlates with grain size. As expected, in the present case there is no apparent relationship between these variables. We have also examined the constant and linear terms in the attenuation data, both of which exhibit considerably more variation than the quadratic terms. Although we have not completed the analysis, there is no obvious correlation between then coefficients and the rupture stress. The only correlation noted thus far is that between the attenuation and thermal history described above.

If, as we believe, the failure in these PSZ bars is dominated by the presence of demonstrable flaws, then the flaw data that we have obtained will be the most meaningful of the information collected in this case. The quadratic attenuation data will not be affected by the presence of a single flaw, or even by a low-density aggregation of flaws. We do not yet know the physical significance of a variation in the other attenuation

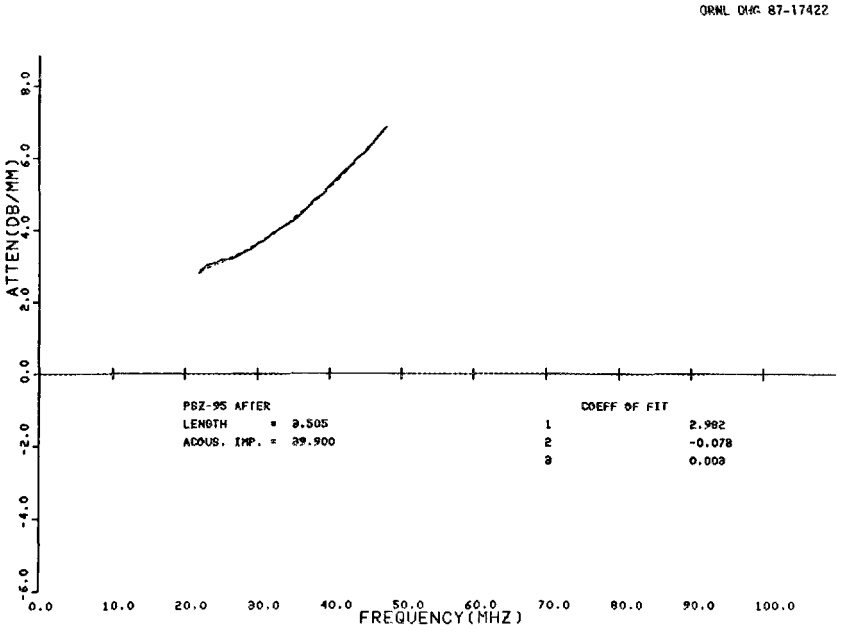

Fig. 4. Transfer curve on a partially stabilized zirconia specimen.

terms, however, but we have recently reported[1] a possible correlation between these terms and the presence of whisker clumping in whisker-reinforced ceramics.

Silicon nitride MOR bars with varying particle diameters. We have obtained several samples of silicon nitride MOR bars containing silicon carbide particles of various diameters from 2.3 to 16.9 μm. The breaking strength of these bars exhibited a very pronounced dependence on the particulate diameter with the strength increasing until a diameter of 3.2 μm was reached and then declining rapidly thereafter. We have obtained attenuation data on the 2.3-, 3.2-, and 16.9-μm samples, and the data show a marked change between the latter and the first two. Figures 5 and 6 show the results on the 2.3- and 16.9-μm particulate diameter samples, respectively. While the smaller particulate diameter samples show only a linear (no scattering) loss characteristic with frequency, the 16.9-μm sample exhibits much higher attenuation which is predominantly quadratic. This loss is much higher than one would expect from such small particles, and the possibility exists that the sample contains severe microcracking to which the attenuation is responding. If so, then our nondestructive results may correlate well with the fracture data. We are currently collecting attenuation data on the intermediate particle size samples.

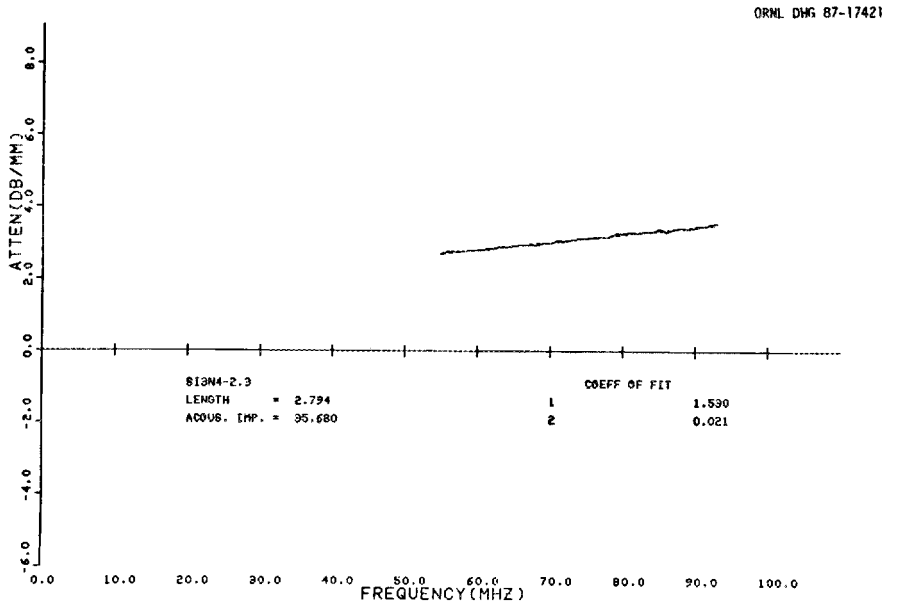

Fig. 5. Transfer curve on a silicon nitride sample containing 2.3-μm silicon carbide particles.

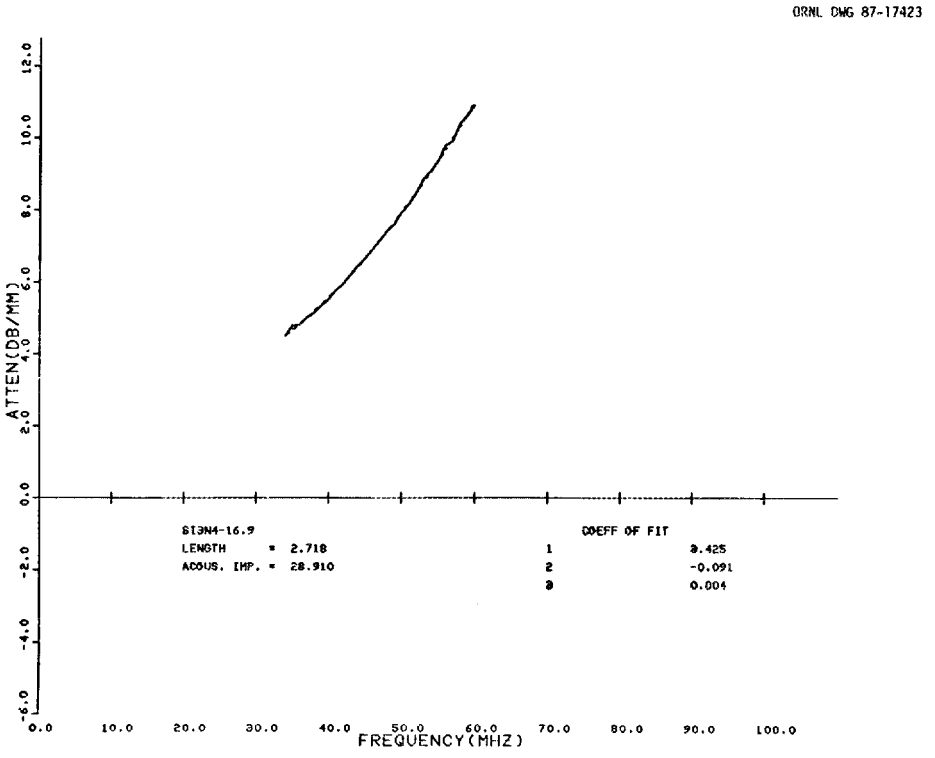

Fig. 6. Transfer curve on a silicon nitride sample containing 16.9-μm silicon carbide particles.

Radiography — B. E. Foster

Radiographic studies have included visits to facilities for X-ray computed tomography and development and application of techniques for PSZ MOR and tensile specimens and IEA silicon nitride MOR bars.

Computed tomography. Visits were made to a user and supplier of computed tomographic equipment for discussions and demonstration of equipment to determine the sensitivity and resolution that could be obtained on ceramic MOR bars and other specimens.

Four MOR bars containing flat-bottom holes with diameters of 75, 100, 125, and 250 μm and depths from 10 to 70 μm, another section of silicon nitride (12.6 mm thick) containing flat-bottom holes with diameters of 125, 250, and 375 μm and depths of 50 to 375 μm, and a 10-cm cube of Plexiglas containing a flat-bottom hole with a diameter and depth of 375 μm were used for the evaluations. This combination of samples represented an equivalent penetrameter sensitivity of 0.26 to 4.2% and permitted assessment of sensitivity and resolution of the equipment.

At the user installation (Kennedy Space Center) in April, energies from 200 to 300 kV, various beam intensities, different sample orientations, and several different image processing techniques were used, but none of the holes in the MOR bars were imaged. The problem was related to the minimum beam slice thickness and width that could be utilized with this equipment which was obtained for inspection of large rocket sections. During the visit, it was learned that a high-resolution detector system was under development by the manufacturer of this equipment [Scientific Measurement Systems (SMS)].

A visit was made to SMS in May with the same complement of samples. The equipment evaluated is marketed by SMS as model 101 and had been in operation only a few days. Features included a Seifert 300-kV X-ray tube, fan beam slice thickness variable from 0.25 to 10 mm (set at 0.3 mm), a high-resolution detector system, a sample handling mechanism providing translation in two orthogonal directions in the horizontal plane and rotation about the vertical axis, a Micro Vax II computer and array processor, and proprietary software developed by SMS.

Energies from 125 to 300 kV, various beam intensities, different sample orientations, and several image processing techniques were used. The 0.26% hole in the Plexiglas and two holes (2.1 and 1.0%) in the 12.6-mm silicon nitride sample were imaged. This is the best imaging noted thus far with the various tomographic systems.

SMS has recently developed a higher sensitivity detector for energies in the range of 30 to 420 kV yielding a factor of 20 increase in efficiency over the present detectors in that range. Installation and checkout of the new detectors was anticipated for late June or early July.

A return visit was made to Scientific Measurement Systems in September to evaluate their computed tomography equipment modified by the inclusion of a recently developed high-resolution detector system. Features now include the Siefert 300-kV X-ray tube, fan beam slice thickness variable from 0.25 to 1 mm (set at 0.25 mm), and the high-resolution detector system (including the newly developed high-efficiency

proprietary detector simply labeled as a BGO detector). The rest of the system was the same.

The complement of samples used for the evaluation included four MOR bars noted earlier and one section (6.3 mm thick, 24 mm wide, and 49 mm long) of silicon nitride containing four flat-bottom holes with diameters of 375, 250, 125, and 125 μm and respective depths of 375, 125, 125, and 75 μm, which was glued to a second section with similar dimensions using cyanoacrylate ("Zip Grip"), providing a sample thickness of 12.6 mm with internal holes and equivalent penetrameter sensitivities of 2.1 to 0.5%.

Energies from 200 to 300 kV, various beam intensities, different sample orientations, and several image processing techniques were used. All four holes were imaged in the 12.6-mm-thick silicon nitride sample using the equipment in the computed tomography mode for an equivalent penetrameter sensitivity of 0.5%. The equipment was used in the digital radiography mode for the MOR bars with successful imaging of the 100-μm-diam, 37-μm-deep hole for an equivalent penetrameter sensitivity of 1.5%. The larger diameter and deeper holes were also imaged. This is the best imaging noted thus far with the various tomographic systems.

IEA MOR bars. A visit was made to Allison Gas Turbine, Division of General Motors, to use their microfocus X-ray equipment (manufactured by Fein Focus in Germany) for projection radiography of 112 silicon nitride flexure bars from the SNW-1000 IEA Annex-II Project. An X-ray energy of 75 kV, 0.25-mA beam current, 400-s exposure, and a projection magnification of ~5× was used. Most of the indications previously detected with contact radiography were noted but no additional ones were located.

PSZ MOR bars and tensile specimens. The PSZ MOR bars noted in the ultrasonic section were radiographed in two orientations arbitrarily noted as 0 (with the radiation beam passing through the 0.138-in. thickness) and 90 (with the radiation beam passing through the 0.178-in. thickness). An X-ray energy of 115 kV was used for the thin sections and 120 kV for the thick sections. The other exposure conditions (beam current, 13 ma; time, 10.5 min; filtration, 0.010 in. copper; cassette loading, PbO screens with type M film; and film-to-focal distance, 52 in.) were held constant for all thicknesses.

A few irregularly shaped voids with a maximum dimension of 0.25 to 1 mm (0.010 to 0.040 in.) were noted in the samples (less than 10 total). A chipped corner and a thickness reduction were noted in two other samples.

Two PSZ tensile bars were obtained for the initiation of radiographic studies of optimum techniques for evaluation of the circular cross-section specimens. Preliminary masks to reduce radiation undercut and scatter were machined. A contact radiographic technique was developed (including the antiscattering masks and a standard) for the tensile specimens with a gage thickness of 6.3 mm (0.250 in.). The standard contained three flat-bottom holes with diameters of 250, 125, and 75 μm with respective depths of 125, 65, and 33 μm in the gage section. These holes represented equivalent penetrameter sensitivities of 2.0, 1.0, and 0.6%.

We were able to image the two larger holes (representing 1.0 and 2.0% sensitivity) using an X-ray energy of 150 kV, a beam current of 10 mA, and an exposure time of 8 min with type-M X-ray film.

Reference

1. W. A. Simpson, Jr., and R. W. McClung, "NDE of Advanced Structural Ceramics," to be published in proceedings of Conference on Nondestructive Testing of High-Performance Ceramics, Boston, August 25-27, 1987.

Status of milestones

Milestone 351101 was completed on schedule.

Publications

W. A. Simpson, Jr., presented a paper entitled "NDE of Advanced Structural Ceramics," and R. W. McClung presented a paper entitled "Needs Assessment for NDT and Characterization of Ceramics: Assessment of Inspection Technology for Green State and Sintered Ceramics," at the Conference on Nondestructive Testing of High-Performance Ceramics in Boston. Manuscripts were prepared and will appear in the proceedings of the meeting.

Computed Tomography - W. A. Ellingson, M. W. Vannier, and H. C. Yeh
(Argonne National Laboratory)

Objective/scope

The purpose of this program is to develop X-ray computed tomographic (CT) imaging for application to structural ceramic materials. This technique has the potential for mapping density distributions, detecting and sizing high- and low-density inclusions, and detecting cracks in green-state and densified ceramics. CT imaging is capable of interrogating the full volume of a component, and is non-contacting. It is also relatively insensitive to part shape and thus can be used to inspect components with complex shapes such as turbocharger rotors, rotor shrouds, and large turbine blades.

Technical progress

Technical effort in this program has centered on two main activities: correction for beam hardening (BH) and development of calibration phantoms. During the current reporting period, we focused on applying dual-energy software BH correction methods to sets of densified and green-state Si_3N_4 specimens made especially for us by the Norton Advanced Ceramics Company. In addition, Freon TF was experimented with as a calibration fluid.

The dual-energy software package[1-4] was evaluated on a set of five green-state Si_3N_4 cold-pressed cylinders (64, 51, 38, 26, and 13 mm diameter; heights of 46, 37, 28, 20, and 9 mm, respectively) and a set of densified Si_3N_4 specimens of the same size. Theoretical optimum-energy calculations[5-8] have shown that for a 50-mm-diam green-state Si_3N_4 specimen, the optimum incident photon energy for maximum sensitivity to thickness change should be near 55 keV, as shown in Fig. 1. However, use of the dual-energy software package allows collection of equivalent monoenergetic photon data; by statistical analysis of individual images, optimum energy can be determined, as shown in Fig. 2.

Figure 3 shows a set of equivalent 50- to 125-keV monoenergetic photon images of a 105-mm-diam polyethylene bottle filled with Freon TF. Previous work had established that Freon TF had a mass attenuation coefficient close to that of green-state Si_3N_4, as shown in Fig. 4. A region within each of the images in Fig. 3 was analyzed statistically for noise. Thus, a statistical noise level as a function of equivalent photon energy could be obtained. Figure 5 shows such a plot for the 51-mm-diam Si_3N_4 test cylinder and Fig. 6 shows the data for the 105-mm-diam Freon TF test specimen. The theoretical optimum energy is about 55 keV for the Si_3N_4 (see Fig. 1) and about 70 keV for 105 mm of Freon TF. The experimental data show values of about 75 and 80 keV, respectively. This level of agreement(within about 20 keV for the Si_3N_4 and 10 keV for the Freon TF) clearly shows the potential of the dual-energy approach for quantitative densitometry studies and significant reduction of beam hardening.

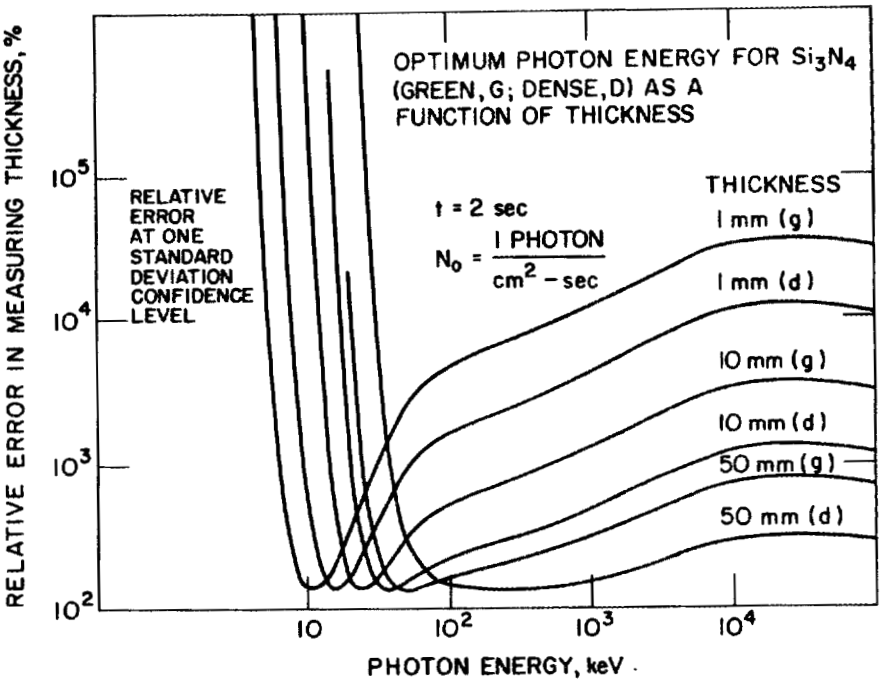

Fig. 1. Theoretical Optimum Incident Photon Energy as a Function of Energy for Green and Dense Si_3N_4 Specimens of Various Thicknesses.

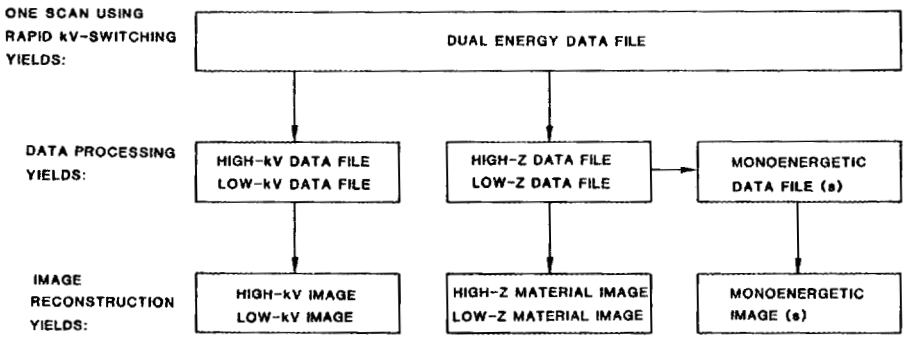

Fig. 2. Process Scheme for Dual-Energy CT Data Obtained with Siemens Somatom DR-H Scanner.

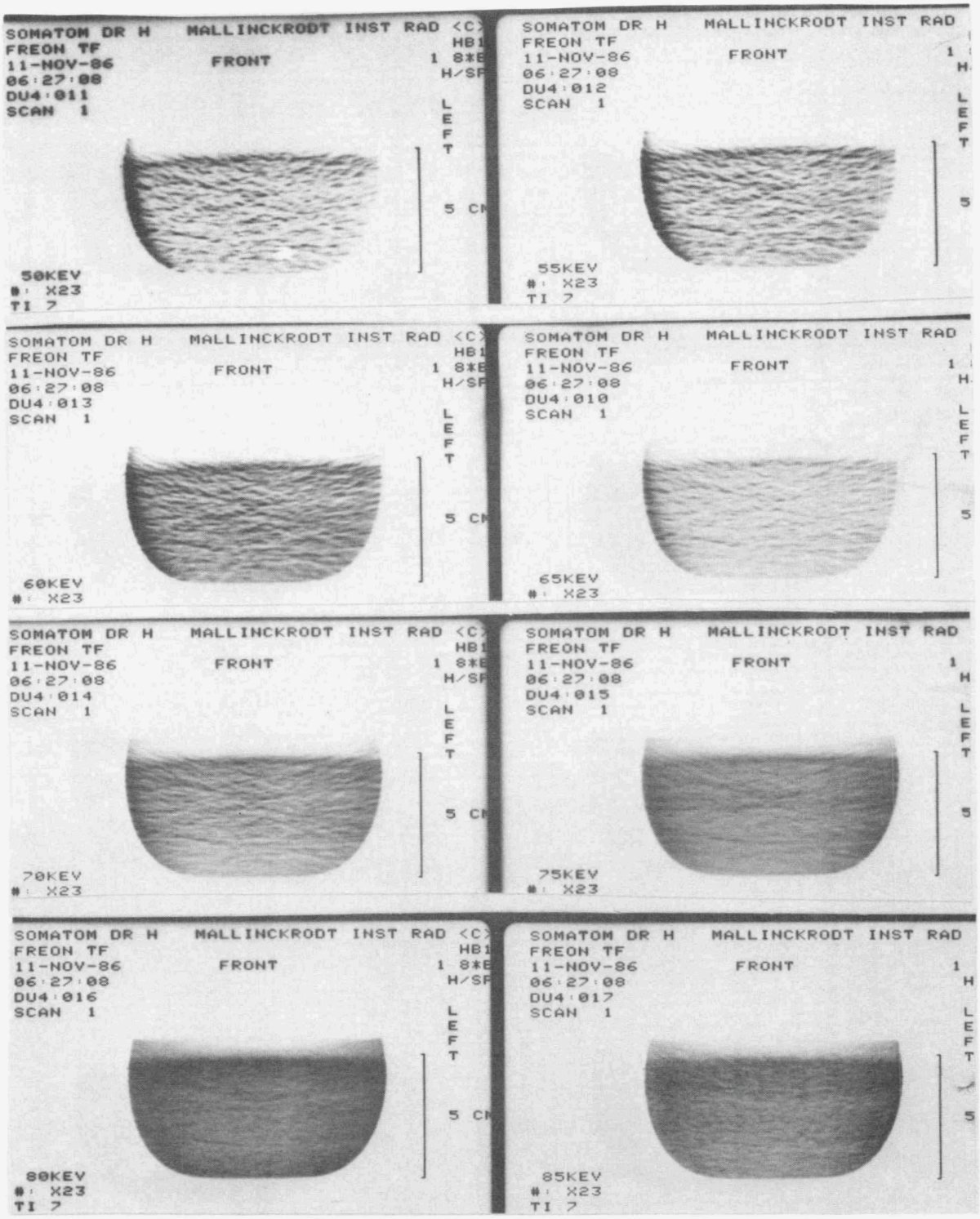

Fig. 3. Set of Equivalent Monoenergetic-Photon Images of a 105-mm-diam Bottle of Freon TF. The same dual-energy raw data set was reconstructed at 5-keV increments from 50 to 125 keV.

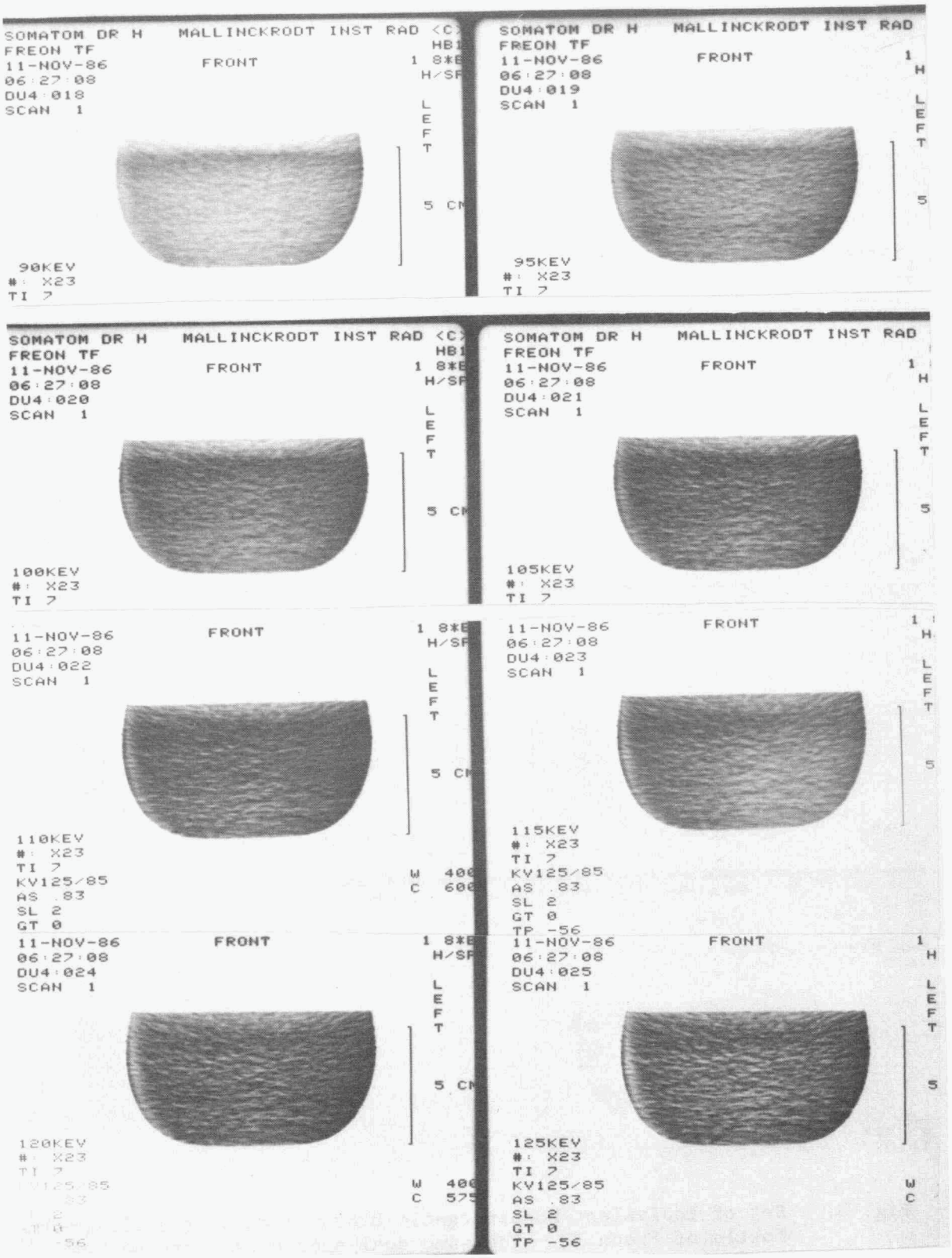

Fig. 3 (continued)

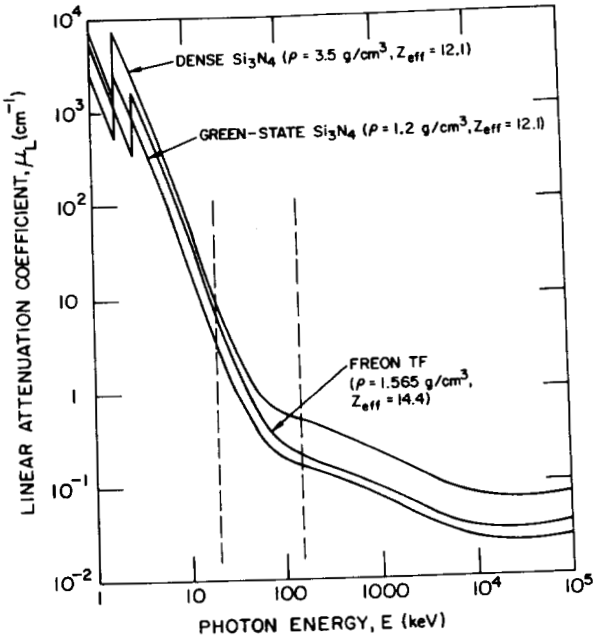

Fig. 4. Linear Attenuation Coefficient of Green and Dense Si_3N_4 and a Potential Calibration Fluid, Freon TF.

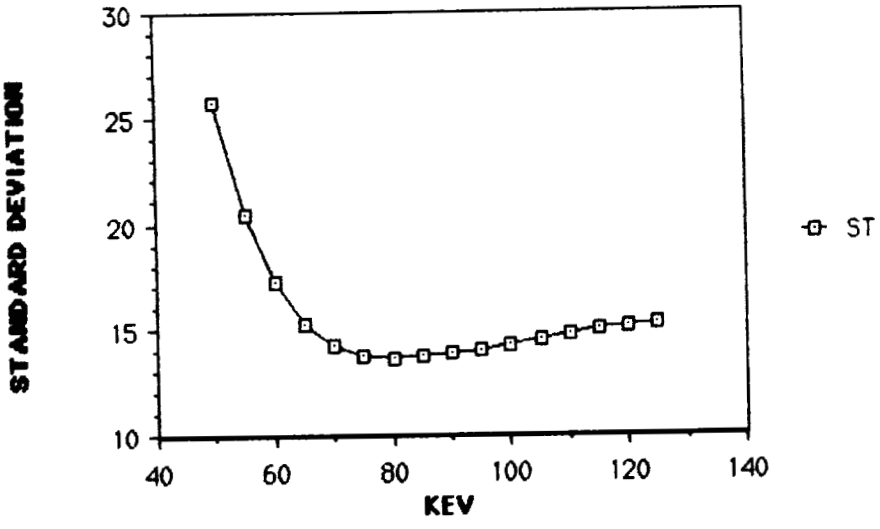

Fig. 5. Experimentally Obtained Optimum Incident Photon Energy for a 51-mm-diam Green-State Si_3N_4 Sample.

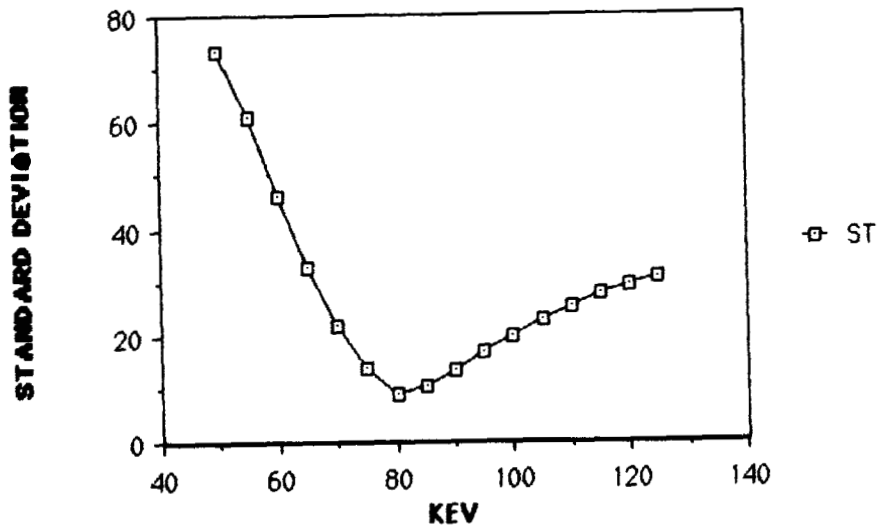

Fig. 6. Experimentally Obtained Optimum Incident Photon Energy for a 105-mm-diam Freon TF Sample.

Status of milestones

All milestones are on schedule.

References

1. W. A. Kalendar, W. H. Perlman, J. R. Vetter, and E. Klotz, "Evaluation of a Prototype Dual-Energy Computed Tomographic Apparatus: I. Phantom Studies," Med. Phys. 13(6), 334-339 (May-June 1986).

2. A. J. Coleman and M. Sinclair, "A Beam Hardening Correction Using Dual-Energy Computed Tomography," Phys. Med. Biol. 30(11), 1251-1256 (1985).

3. R. E. Alvarez and A. Macovski, "Energy-Selective Reconstruction X-Ray Computerized Tomography," Phys. Med. Biol. 21, 733-744 (1976).

4. L. A. Lehmann, R. E. Alvarez, A. Macovski, and W. R. Brody, "Generalized Image Combinations in Dual kVp Digital Radiography," Med. Phys. 8, 659-667 (1981).

5. E. Segal and W. A. Ellingson, "Beam-Hardening Correction Methods for Polychromatic X-Ray CT Scanners Used to Characterize Structural Ceramics," to be published in the Proceedings of the 2nd Intl. Symposium on the Nondestructive Characterization of Materials, Montreal, Canada, July 21-23, 1986.

6. E. Segal, W. A. Ellingson, Y. Segal, and I. Zmora, "A Linearization Beam-Hardening Correction Method for X-Ray Computed Tomographic Imaging of Structural Ceramics," to be published in the Proceedings of the Review of Progress in Quantitative NDE, La Jolla, CA, August 3-8, 1986.

7. W. A. Ellingson and E. Segal, "Computed Tomography," pp. 326-339 in Ceramic Technology for Advanced Heat Engines Project Semiannual Progress Report for Period October 1985-March 1986, ORNL/TM-10079, Oak Ridge National Laboratory, Oak Ridge, Tenn., August 1986.

8. W. A. Ellingson, E. Segal, and M. W. Vannier, "Computed Tomography," in Ceramic Technology for Advanced Heat Engines Project Semiannual Progress Report for Period April-September 1986, ORNL/TM-10308, Oak Ridge National Laboratory, Oak Ridge, Tenn., in press.

4.0 TECHNOLOGY TRANSFER

4.1 TECHNOLOGY TRANSFER

4.1.1 Technology Transfer

Technology Transfer
D. R. Johnson (Oak Ridge National Laboratory)

Technology transfer in the Ceramic Technology Project is accomplished by a number of mechanisms including the following:

Trade shows. A portable display describing the program has been built and used at several trade shows and technical meetings, most recently at the Annual Meeting of the American Ceramic Society, April 26-30, 1987, in Cincinnati, Ohio.

Newsletter. A Ceramic Technology Newsletter is published regularly and sent to a large distribution.

Reports. Semiannual technical reports, which include contributions by all participants in the program, are published and sent to a large distribution. Informal bimonthly management and technical reports are distributed to the participants in the program. Open-literature reports are required of all research and development participants.

Direct Assistance. Direct assistance is provided to subcontractors in the program via access to unique characterization and testing facilities at the Oak Ridge National Laboratory.

Workshops. Topical workshops are held on subjects of vital concern to our community.

International Cooperation. Our program is actively involved in and supportive of the cooperative work being done by researchers in West Germany, Sweden, and the United States under an agreement with the International Energy Agency. That work, ultimately aimed at development of international standards, includes physical, morphological, and microstructural characterization of ceramic powders and dense ceramic bodies, and mechanical characterization of dense ceramics. Detailed planning and procurement of ceramic powders and flexural test bars have been accomplished. Exchange of preliminary data on ceramic and powder characterization results has been started by those laboratories participating.

IEA Annex II Management
V. J. Tennery (Oak Ridge National Laboratory)

Objective/scope

The IEA Annex II agreement between the United States, the Federal Republic of Germany, and Sweden on structural ceramics is directed to cooperative research and development oriented to the identification and adoption of standardized methods for characterizing these materials. This agreement includes four subtasks: (1) information exchange, (2) ceramic powder characterization, (3) ceramic chemistry and structural characterization, and (4) ceramic mechanical property characterization. Each country is providing selected ceramic powders and sintered structural ceramics for use in the research work in Subtasks 2, 3, and 4 in all three participating countries. Participating laboratories in all three countries have agreed to share all resulting data with the purpose of using the knowledge gained from the work for developing standard measurement methods for characterizing ceramic powders and sintered structural ceramics.

The lack of such standard measurement methods has been an impediment to the evolution and development of structural ceramics, both from the point of view of both the manufacturer and the user. This Annex II agreement was conceived to accelerate the development of standard methods for determining important properties of these evolving materials.

In the United States, many companies and their research staffs have agreed to contribute significant resources in performing the required measurements. For example, in Subtask 2, 12 laboratories are participating; in Subtask 3, 7 laboratories are participating; and in Subtask 4, 8 laboratories are participating.

The research in Subtask 2 includes five ceramic powders which are being studied in the initial phase of this subtask. For Subtasks 3 and 4, three sintered ceramics are being studied, including one from each of the three countries. The ceramic from the United States is a silicon nitride, SNW-1000 from GTE-Wesgo; that from Germany is a hipped SiC from ESK Kempton; and that from Sweden is a silicon nitride from ASEA Cerama.

Technical progress

The major technical status changes since the last semiannual report are reviewed briefly:

Subtask 2
Ceramic Powder Characterization

The U.S. National Bureau of Standards (NBS) is distributing all ceramic powders for Annex II; the first was a zirconia from Toyosoda in Japan, while the second is a silicon nitride from L. C. Stark from the Federal Republic of Germany. Sealed specimens of the zirconia were distributed to participants in all three countries by the NBS in January 1987. Similarly specimens of the nitride powder, identified as LC-10, were distributed during this reporting period. Distribution of this

powder required powder riffling, plus filling and sealing of approximately 2400 vials. Flame sealing was accomplished by the end of May. This powder was distributed by the NBS in late June. Preliminary results obtained from some of the U.S. participants in this subtask indicated that the zirconia powder has a bimodal character, which complicates the analysis of particle size and other properties. Discussions have been initiated among the U.S. participants to decide how to best quantify the data for this powder. On September 15 and 16, a workshop for U.S. participants in this subtask was held at the NBS to determine the status of data acquisition and to prepare plans for the U.S. participation in the international Subtask 2 working group meeting to be held in Orlando on November 5 and 6. This meeting was attended by representatives of 10 industrial firms or government laboratories. Subsequent to the meeting on September 15 and 16, the U.S. participants decided to hold another U.S. working group meeting the evening of November 4 in Orlando to prepare for the full working group meeting scheduled for November 5 and 6.

Subtasks 3 and 4
Ceramic Chemical, Structural, and Mechanical Characterization

ESK Silicon Carbide from the Federal Republic of Germany

The SiC bars from Germany to be studied in the United States were received at ORNL in October 1986, and were distributed to the five U.S. participating laboratories on November 25.

ASEA Cerama Silicon Nitride from Sweden

The entire complement of 1200 ASEA Cerama silicon nitride bars were received at ORNL on May 2, 1987. These bars were machined from sintered billets in the United States, and it was therefore unexpectedly necessary for staff at ORNL to randomize all of these bars, and repackage them in preparation for distribution to all participating laboratories in the three countries. The randomizing was accomplished using a random number generator and a discrete uniform distribution function. Of these 1200 bars, 170 were distributed to Subtask 3 participants, and 880 were distributed to Subtask 4 participants. The remaining 150 bars are held at ORNL in the IEA Annex II archive. The 1050 bars were distributed from ORNL on June 24, 1987.

GTE-Wesgo Silicon Nitride from the United States

The final shipment of GTE-Wesgo SNW-1000 silicon nitride bars were received at ORNL on July 10, 1987. The first shipment was received at ORNL on January 8, 1987. The total complement of bars having the German metric dimensions included 1526 specimens. ORNL staff had to repackage each bar into an individual container, and the entire population was then randomized using a random number generator and a discrete uniform distribution function. Of these 1526 bars, 170 were distributed to Subtask 3 participants, and 1120 were distributed to Subtask 4 participants. The remaining 236 bars are held at ORNL in the IEA Annex II archive. The 1290 bars were distributed from ORNL on August 5, 1987.

Subtask 3 Results
ESK Silicon Carbide

A total of 80 of the ESK silicon carbide bars were distributed in sets of 10 bars each to eight U.S. laboratories in January 1987. LOTUS templates were distributed earlier to all U.S. participants for use in reporting and sharing data in this subtask. Some preliminary results were obtained during this period. Basically, they indicate that intra-laboratory measurements of density provide reasonably consistent results, with standard deviations of about 0.008 or less among a set of values for the same ceramic material. Very limited data have been received for major or minor elemental analyses of any of these ceramics. The data available from some of the U.S. laboratories for the ESK silicon carbide indicate an average Si value of 68.10% with a standard deviation of 1.7. Only three carbon analyses have been received for the carbide, and these have an average of 29.45 wt % with a standard deviation of 0.19.

ASEA Cerama Silicon Nitride and GTE-Wesgo Silicon Nitride

In support of the work in Subtask 3, sets of 10 bars of the ASEA silicon nitride and GTE-Wesgo silicon nitride were sent by ORNL to six laboratories in Germany, three in Sweden, and to eight in the United States. For the ASEA silicon nitride, only one Si analysis has been received, which was from a U.S. laboratory, and this value was 56.62 wt %.

Subtask 4 Results
ESK Silicon Carbide

In support of the work in Subtask 4, 400 of the ESK silicon carbide bars were distributed by ORNL in November 1986 to the five U.S. participating laboratories. An additional 200 bars which are the international archive for this material are held at ORNL. Results for the 395 ESK silicon carbide bars fractured in the five U.S. laboratories were discussed in the previous report. The other two materials were distributed as indicated previously in this report.

A report entitled, *Analysis of Flexural Strength Data For ESK Silicon Carbide Measured In The United States, IEA Annex II, Subtask 4*, was completed and will be provided to all attendees of the IEA Annex II Working Group meeting scheduled for October 26, 1987, in Dearborn, Michigan. The Maximum Likelihood Analysis technique has been demonstrated to be superior in determining the Weibull modulus (alpha or m) compared to the Least Squares or linear regression technique often used in the United States. Furthermore, Kolmogorov-Smirnov statistics were demonstrated as being very useful in testing these flexural strength data sets for determining their "fit" with proposed Weibull distribution functions.

In summary, the results show that the flexure strength of the ESK silicon carbide evaluated in the United States could not be definitively identified as being from a Weibull distribution. For example, the critical Kolmogorov-Smirnov statistic DN for most of the five data sets as well as the combined U.S. data set for 395 specimens is about the same when tested against the "best fit" Weibull and Gaussian distributions. This is

illustrated in Table 1. Similarly, the critical statistic of Little et al. for distribution fitting for the five U.S. data sets for the German silicon carbide does not allow an obvious choice between these alternative distributions for this ceramic material. This fact is illustrated in Table 2, where for a two-tailed test at a significance level of 0.10, the value of DN for almost all of the data sets for either distribution function is less than the value of the critical statistic.

Fracture strength results from the United States, Sweden, and Germany for the ESK silicon carbide are shown in Table 3, in which values for the Weibull shape parameter alpha (or m), the average strength, the standard deviation, and the number of specimens in each data set are shown for the ESK silicon carbide. These results clearly show that there is some reasonable level of consistency for the average strength and standard deviations for strength sets determined by a number of different laboratories in three different countries for the same ceramic material. Analysis of some of the results shown in Table 3 give the following results for the Weibull shape parameter, which is typically considered the most difficult mechanical behavior descriptor to determine with consistency. These results are shown in Table 4. These data show that the maximum variation observed among the four data sets in Table 4, for the maximum likelihood estimators for the Weibull shape parameter occurs between the U.S. set with N = 395, with alpha = 6.41 and a Std. Dev. = 0.87, and the Swedish set with N = 155, with alpha = 6.94 and a Std. Dev. = 1.14. The grand average for this parameter for the individual data sets for the entire set with N = 837 is alpha = 6.62 and a Std. Dev. = 0.97.

The complete U.S. fracture strength data files for the ESK silicon carbide in the form of complete calculated LOTUS templates which are distributed by ORNL were sent to both Germany and Sweden on September 16, 1987. The Swedish data were received September 18.

In addition to these measurements, each participating laboratory is performing fractography analysis on selected specimens from the weakest, medium strength, and strongest specimens from that laboratory's bar sets. These results will be provided to ORNL, as they become available.

Status of milestones

On schedule.

Publications

1. V. J. Tennery, *Analysis of Flexural Strength Data for ESK Silicon Carbide Measured in the United States, IEA ANNEX II, Subtask 4*, prepared for distribution to all participants in Subtask 4 at the international working group meeting scheduled for October 26, 1987, in Dearborn, Michigan.

Table 1. Kolmogorov-Smirnov goodness-of-fit statistics for six flexure strength data sets of ESK silicon carbide for the Weibull and Gaussian distributions (best fit cases)

	GTE Labs	SOHIO	Allison Turbine	NASA Lewis	Garrett Turbine
			Weibull distribution		
D+	0.048534	0.071237	0.079603	0.063649	0.080716
D-	0.053023	0.098843	0.068261	0.047503	0.065303
DN	0.053023	0.098843	0.079603	0.063649	0.080716
			Statistics for 395 specimens of silicon carbide		
			D+ 0.030714		
			D- 0.021805		
			DN 0.030714		
			Gaussian distribution		
D+	0.042599	0.072969	0.058625	0.057190	0.052407
D-	0.083762	0.137694	0.043479	0.071997	0.101982
DN	0.083762	0.137694	0.058625	0.071997	0.101982
			Statistics for 395 specimens of silicon carbide		
			D+ 0.023259		
			D- 0.039989		
			DN 0.039989		

Table 2. Kolmogorov-Smirnov statistics for six flexure strength data sets tested against the Weibull and Gaussian distribution functions

ESK silicon carbide

	GTE Labs	SOHIO	Allison Turbine	NASA Lewis	Garrett Turbine
N	75	80	80	80	80
Weibull					
D+	0.0485337	0.0712365	0.0796028	0.0636489	0.0775842
D-	0.0530226	0.0988428	0.0682612	0.0475029	0.0700930
Gaussian					
D+	0.0425987	0.0729686	0.0586251	0.0571902	0.0524070
D-	0.0837623	0.137694	0.0434794	0.0719972	0.1019821
D(Critical) accept null hypothesis if D ≤ D(Critical)					
D(Crit.)	0.12355	0.11962	0.11962	0.11962	0.11962

Where D(Critical) = $1.07/\sqrt{N}$ for two-tailed test with $\alpha = 0.10$ for all 395 specimens:

Weibull	
D+	0.0307144
D-	0.0218048
Gaussian	
D+	0.0232593
D-	0.0399889
D(Critical) for $\alpha = 0.10$	0.058869

Table 3. Flexure strength results and analysis of data from the three countries in IEA Annex II

ESK silicon carbide

United States

	Laboratory				
	GTE	SOHIO	ALLISON	NASA	GTEC
m(ML)	7.16	6.82	4.91	6.59	6.60
m(LS)	7.33	6.04	5.70	6.78	6.75
STR.AVG.	506.91	482.11	468.69	519.23	516.50
STD.DEV.	81.81	88.07	99.45	90.28	90.54
N	75	80	80	80	80

Germany

	Laboratory				
	KFK	LONZA	DATEN ISD	KFA IRW	MAN TECH
m(ML)	7.15	5.97	5.24	6.76	8.33
m(LS)	7.20	5.81	4.37	6.85	8.22
STR.AVG.	490.05	500.73	503.94	509.85	514.98
STD.DEV.	80.17	99.06	117.76	82.67	73.55
N	60	60	60	48	59

Sweden

	Laboratory	
	SSRI	SANDVIK
m(ML)	6.13	7.74
m(LS)	6.10	7.23
STR.AVG.	470.41	442.18
STD.DEV.	90.05	69.08
N	75	80

Definitions:

m(ML) = Maximum likelihood estimator for Weibull shape parameter
m(LS) = Least Squares estimator for Weibull shape parameter
STR.AVG. = Average strength in MPa
STD.DEV. = Nonbiased standard deviation of flexure strength
N = Number of specimens in the data set

Table 4. Comparison of Weibull shape parameter, α, determined in three participating countries in the IEA Annex II agreement

ESK silicon carbide
(maximum likelihood estimators only)

	United States	Sweden	Germany	All countries combined
α (or m)[a] (Avg.)	6.41	6.94	6.69	6.62
STD.DEV.	0.87	1.14	1.18	0.97
N	395	155	287	837

[a]Weibull parameter values are averages of individual laboratory data sets.

Definitions:

STD.DEV. = Nonbiased standard deviation of the flexure strength
N = Number of specimens in the data set

Standard Reference Materials

A. L. Dragoo, D. B. Minor, C. R. Robbins, J. F. Kelly, and J. P. Cline
(National Bureau of Standards)

Objective/Scope

Ceramics have been successfully employed in engines on a demonstration basis. The successful manufacture and use of ceramics in advanced engines depends on the development of reliable materials that will withstand high, rapidly varying thermal stress loads. Improvement in the characterization of ceramic starting powders is a critical factor in achieving reliable ceramic materials for engine applications. The production and utilization of such powders require characterization methods and property standards for quality assurance.

The objectives of the NBS program are (1) to assist with the division and distribution of five ceramic starting powders for an international round-robin on powder characterization; (2) to provide reliable data on physical (dimensional), chemical and phase characteristics of two silicon nitride powders: a reference and a test powder; and (3) to conduct statistical assessment and modeling of round-robin data. This program is directed toward a critical assessment of powder characterization methodology and toward establishment of a basis for the evaluation of fine powder precursors for ceramic processing. This work will examine and compare by a variety of statistical means the various measurement methodologies employed in the round-robin and the correlations among the various parameters and characteristics evaluated. The results of the round-robin are expected to provide the basis for identifying measurements for which Standard Reference Materials are needed and to provide property and statistical data which will serve the development of internationally accepted standards.

Technical Progress

The technical progress covered in this report includes descriptions of work on the preparation of powder samples for the IEA/ANNEX II round-robin and of the analysis of round-robin data.

Division, Distribution and Certification of Ceramic Starting Powders. During the current reporting period two powders silicon nitride powders were riffled, bottled, flame-sealed in glass tubes and distributed to the participants in IEA/ANNEX II Subtask 2 round-robin on powder characterization. These powders consisted of one powder (H.C. Starck LC-10[a]) to be used as a reference powder and a powder

---

[a] Certain commercial equipment, instruments, or materials are identified in this report in order to adequately specify the experimental procedure. Such identification does not imply recommendation or endorsement by the National Bureau of Standards, nor does it imply that the materials or equipment identified are necessarily the best available for the purpose.

(Ube) to be used as one of the four test powders in the round-robin. Final riffling of a silicon powder will begin by mid-November. The procedures used to riffle and package these powders followed closely those that were used to prepare the zirconia powder which was described in previous reports. 1976 flame-sealed vials of the reference powder were prepared, of which 1902 were labeled. 1538 flame-sealed vials of the test powder were prepared, of which 1487 were labeled. Unlabeled vials consisted of vials for which the outer glass tube had failed after flame-sealing. These samples were distributed as preliminary samples. Homogeneity of the powders were verified by surface area and particle size analysis. Extensive physical and chemical analyses of these two silicon nitride powders are planned.

Data Analysis. Analysis of data from the IEA/Annex II powder characterization round-robin have entailed the following tasks:

(1) entry of data received for zirconia (ZYO) and silicon nitride reference (SNR) samples into a Lotus 123 database;
(2) revision of 123 template for data entry;
(3) development of procedure for electronic transfer to 123-based files to the central computer facility at the National Bureau of Standards;
(4) graphical analysis of data to examine precision and correlation between methods;
(5) development of general analysis procedure for estimation of particle size statistics.

(1) Data entry

All U.S. data for zirconia samples have been entered in the following categories: median particle size (D_{50}) or experimentally computed average particle size values; other physical properties, including surface area, tap density, bulk density and Fisher sub-sieve size; and chemical properties, including bulk chemistry, major, minor and trace impurities, and phase composition. Data from U.S. participants for SNR samples have been entered for median or computed average particle size values. Data from European participants was not received in time for this report.

(2) Revision of Lotus 123 template

A previously created Lotus 123 template was used for initial data entry; however, it soon became apparent that revision of the template was necessary to make it more efficient, to change the data categories and to obtain more ROM-space for data. Consequently, a number of menues and macros were eliminated. The revised template was used for entry of particle size data and was adapted for other physical property data and for chemical property data. Data was categorized with respect to experimental method. Methods included in the templates for Particle Size, Other Physical Properties and Chemical Properties are summarized

in Tables 1, 2 and 3, respectively. Elimination of some remaining "bugs" will be carried out before the templates are distributed to the participants in the round-robin.

(3) Electronic transfer of Lotus 123 files to central computer

Transfer of 123 spreadsheet to the NBS central computer facility was carried out by writing a Lotus 123 spreadsheet into several ASCII files. This process was expedited by division of a spreadsheet into several "pages," each of which is no more than 80 characters wide. The length of a page is determined by the length of the spreadsheet.

To write a page into a ASCII file using the Lotus 123 command /PF

is entered; the range is specified to correspond to the page of interest; and the Options category is entered so that the subcategories "Other," "Unformatted" can be selected. The ASCII files are stored on 5-1/4 floppy diskettes and conveniently read electronically into the central computer.

(4) Graphical analysis of data

As first step in the analysis of the data various portions of the data was plotted using dataplotting routines resident on the central computer. Plots were generated to examine the scatter of the data for given class of measurements and to compare different methods of measurement. Results of the graphical analysis of the data were presented at meeting working group for IEA/Annex II Subtask 2, at Orlando, Florida, on November 5.

(5) General analysis procedure for particle size statistics

Particle size distribution data received for the ZYO samples indicated the particle size distribution was not simply lognormal. Consequently, although several methods, such as gravitational sedigraph, yielded analog plots of the cumulative size distribution from which median (D_{50}) values for the particle size could be instantly read, these values could not be taken as approximations for the geometric mean. Similarly, calculation of the geometric standard deviation using the assumption of lognormality also was no longer valid. Therefore, the problem of finding an integral approximations for these two statistics in terms of the cumulative distribution was solved. Estimates of these two statistics are obtained from empirical data by replacing the integrals with the appropriate summations over the data.

The experimental results are typically expressed in terms of the cumulative size distribution which can be represented as the function G(z), where z is the transformed size given by the expression

$$z = \ln(x) \tag{1}$$

and x is the particle size. The domain of x is 0 to ∞, whereas the domain of z is $-\infty$ to ∞. An expression for the geometric mean, x_g, is obtained as an integral expression over G(z) by splitting the single integral over the entire range of z at z_o, to yield

$$\ln(x_g) = Z_o - \int_{-\infty}^{z_o} G(z)dz + \int_{z_o}^{\infty} [1-G(z)]dz \qquad (2)$$

The parameter z_o defines the scale for x, and $z_o = 0$ may be conveniently taken so that $x_o = 1$. To estimate x_g the integrals are replaced by summations with equal intervals, ∂z. An expression for the variance, $\sigma_g{}^2$, can be obtained in a similar manner, with the result

$$\ln(\sigma_g{}^2) = 2\{-\int_{-\infty}^{z_o} zG(z)dz + \int_{z_o}^{\infty} [1-G(z)]dz\} - [\ln(x_g)]^2, \qquad (3)$$

where it is assumed that $\lim_{z\to-\infty} z^2G(z) = 0$ and $\lim_{z\to\infty} z^2[G(z)-1] = 0$.

Application of this method is illustrated here for the cumulative particle size data shown in Figure 1. The analysis of this data is illustrated in Figure 2. The analysis consists of the following steps:

(1) Generate a column of log(x) values. This can be done convenient using the Lotus 123 command, /DF. An interval of 0.05 was used here.
(2) Calculate a column of x values, corresponding to the Equivalent Spherical Diameter on the data graph in Figure 1. The x values can calculated with Lotus 123 by using the function @EXP(log(x) cell*2.3026) to calculate x from each log(x) cell.
(3) Read off the Cumulative Mass Percent (CMP) from the experimental graph for each x value.
(4) If the cumulative distribution does not extend to 0, an extrapolation is required. This is illustrated in the lower portion of Figure 2, where the CMP values were obtained by a linear extrapolation with respect to log(x).
(5) Evaluate the quantities

$$(1-c)\partial z \ , \ 0.00<\log(x)<\log(x_{max})$$
$$c\partial z \ , \ \log(x_{min})<\log(x)<0.00$$
$$z(1-c)\partial z \ , \ 0.00<\log(x)<\log(x_{max})$$
$$zc\partial z \ , \ \log(x_{min})<\log(x)<0.00$$

where c=CMP/100, z=log(x)*2.3026 and ∂z=0.05*2.3026.
(6) Sum each of the quantities over the appropriate range of log(x).
(7) The geometric mean is estimated by

$$\ln(x_g) = \sum(1-c)\partial z - \sum c\partial z$$

and the standard deviation by

$$\ln(s_g{}^2) = 2\sum z(1-c)\partial z - 2\sum zc\partial z - [\ln(x_g)]^2 \quad .$$

The results are summarized in Table 4. The geometric mean and standard deviation are compared respectively with the median, D_{50} and the ratio D_{84}/D_{50}. The ratio D_{84}/D_{50} is equal to the geometric standard deviation if the condition of lognormality applies. For the powder considered here, which has two significant, well-resolved modes, the median and the geometric mean do not differ by a large amount, but the presence of the significant second mode at the coarse particle sizes invalidates the use of the ratio to estimate the geometric standard deviation.

Status of Milestones

Milestones were discussed with the project monitor and new milestones were drafted. Both silicon nitride powders have been packaged and distributed to the participants in the round-robin. Preparation of samples of the remaining two powders is proceeding on schedule.

Publications

A manuscript entitled "Powder Characterization Methods--Future Needs," coauthored by A. L. Dragoo and S. M. Hsu, was submitted in conjunction with an invited lecture which was given at the ICAMT Workshop II, in Nagoya, Japan on March 10.

TABLE 1

METHOD CODE AND WEIGHTING FACTORS

CODE	METHOD
1	Sieving
2	Air Classification - Counters
3	Air Classification - Mass Detectors
4	Chromatographic - Hydrodynamic
5	Chromatographic - Field Flow
6	Sensing Zone - Light Blockage
7	Sensing Zone - Electrical
8	Microscopy/Image Analysis
9	Sedimentation - Gravity
10	Sedimentation - Centrifugal
11	Sedimentation - Ultracentrifugal
12	Light Scattering - Angular
13	Light Scattering - Diffraction
14	Light Scattering - Turbidity
15	Light Scattering - Quasi-Elastic
16	Surface Methods

TABLE 2

METHODS AND CODES FOR PHYSICAL PROPERTY DATA

CODE	METHOD
1	Single Point Surface Area
2	3-Point Surface Area
3	Tap Density
4	He gas pycnometer
5	Liquid pycnometer, water
6	Liquid pycnometer, hydrocar
7	XRD, crystal parameter
8	Fisher Sub-Sieve Size
9	Optical Microscopy
10	SEM
11	TEM
12	X-ray Line Broadening
13	Density, Hg Intrusion
14	Porosity, Hg Intrusion

TABLE 3

METHODS AND CODES FOR CHEMICAL DATA

CODE	METHOD
1	Atomic absorption/emission (AA/AE), flame
2	Inductively Coupled Plasma (ICP)
3	Ion Chromatography
4	Specific Ion Electrode
5	Mass Spectro
6	Liquid pycnometer, hydrocar
7	XRD, crystal parameter
8	Fisher Sub-Sieve Size
9	Optical Microscopy
10	SEM
11	TEM
12	X-ray Line Broadening
13	Density, Hg Intrusion
14	Porosity, Hg Intrusion

Table 4. Particle size distribution for zirconia test powder; units are in μm.

Central Tendency		Spread	
Geom. Mean x_g	Median D_{50}	Geom. Std. Dev. s_g	D_{84}/D_{50}
0.311	0.205	2.469	9.02

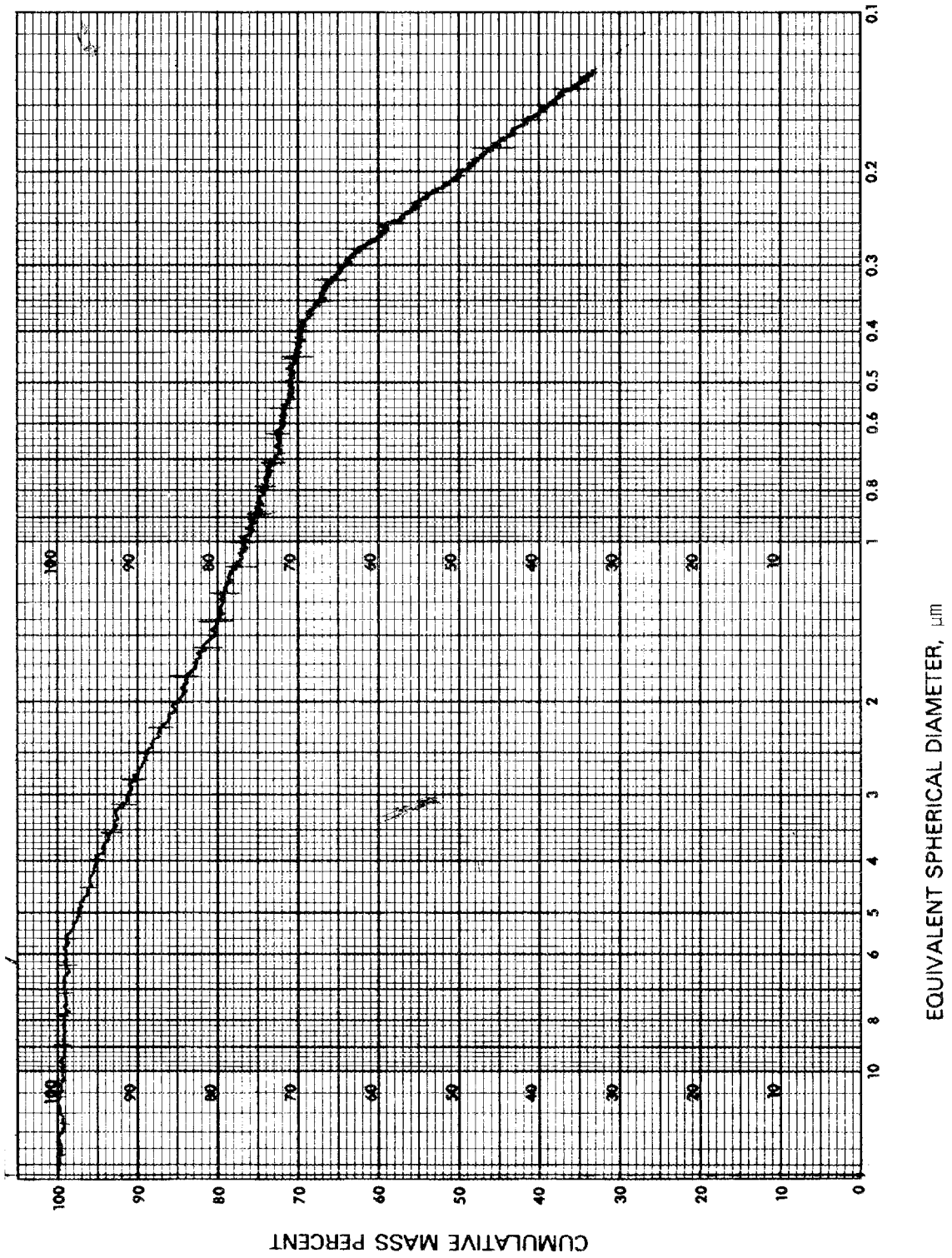

Figure 1. Cumulative particle size distribution (in Mass Percent) vs. Equivalent Spherical Diameter (μm) for a zirconia test powder.

Form 500/42701

SIZE	LOG SIZE	CMP	c(z) = C(z)/100 (1-c)dz	c	z(1-c)dz	zcdz
14.13	1.15	99.80	0.00069		0.00183	
12.59	1.10	99.00	0.00058		0.00146	
11.22	1.05	100.00	0.00046		0.00111	
10.00	1.00	99.20	0.00104		0.00239	
8.91	0.95	99.00	0.00115		0.00252	
7.94	0.90	99.00	0.00115		0.00239	
7.08	0.85	99.00	0.00115		0.00225	
6.31	0.80	99.00	0.00127		0.00233	
5.62	0.75	98.80	0.00219		0.00378	
5.01	0.70	97.40	0.00380		0.00612	
4.47	0.65	96.00	0.00507		0.00758	
1.78	0.25	83.80	0.01992		0.01147	
1.58	0.20	81.60	0.02210		0.01018	
1.41	0.15	80.00	0.02360		0.00815	
1.26	0.10	79.00	0.02498		0.00575	
1.12	0.05	77.60	0.02625		0.00302	
1.00	-0.00	76.80	0.02763	0.08750	-0.00000	-0.00000
0.89	-0.05	75.20		0.08589		-0.00989
0.79	-0.10	74.00		0.08474		-0.01951
0.71	-0.15	73.20		0.08381		-0.02895
0.63	-0.20	72.40		0.08301		-0.03823
0.56	-0.25	71.80		0.08220		-0.04732
0.13	-0.90	32.40	EXTRAP.	0.03477		-0.07205
0.11	-0.95	28.00	EXTRAP.	0.02976		-0.06510
0.10	-1.00	23.70	EXTRAP.	0.02481		-0.05713
0.09	-1.05	19.40	EXTRAP.	0.01980		-0.04788
0.08	-1.10	15.00	EXTRAP.	0.01482		-0.03753
0.07	-1.15	10.74	EXTRAP.	0.00987		-0.02613
0.06	-1.20	6.40	EXTRAP.	0.00484		-0.01336
0.06	-1.25	2.00	EXTRAP.	0.00115		-0.00331
0.05	-1.30	0.00	EXTRAP.	0.00000		0.00000
0.04	-1.35	0.00	EXTRAP.			

SUMS-M1	0.25398	1.42156		
LN(XG)	-1.16758			
XG	0.31112			
SUMS-M2			0.15944	-1.42601
LN(SG^2)	1.80765			
SG^2	6.09612			
SG	2.46903			

Figure 2. Analysis of particle size distribution from Figure 1 to estimate geometric mean, x_g, and standard deviation, s_g; dimensions in μm.

INTERNAL DISTRIBUTION

1-2. Central Research Library
3. Document Reference Section
4-5. Laboratory Records Department
6. Laboratory Records, ORNL RC
7. ORNL Patent Section
8. S. Baik
9. R. L. Beatty
10. P. F. Becher
11. J. Bentley
12. T. M. Besmann
13. A. Bleier
14. E. E. Bloom
15. K. W. Boling
16. W. D. Bond
17. R. A. Bradley
18. C. R. Brinkman
19. V. R. Bullington
20. A. J. Caputo
21. R. S. Carlsmith
22. P. T. Carlson
23. J. A. Carpenter, Jr.
24. J. V. Cathcart
25. R. H. Cooper
26. S. A. David
27. J. H. DeVan
28. W. P. Eatherly
29. J. I. Federer
30. W. Fulkerson
31. R. L. Graves
32. D. L. Greene
33. M. A. Janney
34-38. D. R. Johnson
39. R. R. Judkins
40. M. A. Karnitz
41. M. P. Kertesz
42. T. B. Lindemer
43. K. C. Liu
44. E. L. Long, Jr.
45. W. D. Manly
46. R. W. McClung
47. D. L. McElroy
48. A. J. Moorhead
49. J. L. Rich
50. C. R. Richmond
51. J M Robbins
52. M. W. Rosenthal
53. M. L. Santella
54-77. A. C. Schaffhauser
78. J. H. Schneibel
79. J. L. Scott
80. G. M. Slaughter
81. E. J. Soderstrom
82. D. P. Stinton
83. R. W. Swindeman
84. V. J. Tennery
85-87. P. T. Thornton
88. T. N. Tiegs
89. J. R. Weir, Jr.
90. F. W. Wiffen
91. R. K. Williams
92. C. S. Yust
93. A. Zucker

EXTERNAL DISTRIBUTION

94. Donald F. Adams
University of Wyoming
Laramie, WY 82071

95. Jane W. Adams
Corning Glass Works
Corning, NY 14831

96. Donald J. Adrian
High Velocity Corporation
701 Scarboro Road
Oak Ridge, TN 37830

97. Bruce J. Agle
Sundstrand Corporation
Turbomach Division
4400 Ruffin Road
Post Office Box 85757
San Diego, CA 92138-5757

98. Richard T. Alpaugh
U.S. Department of Energy
Forrestal Building CE-151
1000 Independence Avenue
Washington, DC 20585

99. H. Arbabi
Brunel University
Uxbridge Middlesex
United Kingdom UB8 3PH

100. V. S. Avva
North Carolina Agricultural & Technical State University
Greensboro, NC 27411

101. John M. Bailey
Caterpillar Tractor Company
100 N.E. Adams
Peoria, IL 61629

102. Murray Bailey
NASA Lewis Research Center
21000 Brookpark Road
MS: 77-6
Cleveland, OH 44135

103. R. R. Baker
Ceradyne, Inc.
3169 Red Hill Avenue
Costa Mesa, CA 92626

104. J. Gary Baldoni
GTE Laboratories, Inc.
40 Sylvan Road
Waltham, MA 02254

105. A. L. Bement, Jr.
TRW, Inc.
23555 Euclid Avenue
Cleveland, OH 44117

106. M. Bentele
Xamag, Inc.
259 Melville Avenue
Fairfield, CT 06430

107. Clifton G. Bergeron
University of Illinois
105 South Goodwin Avenue
204 Ceramics Building
Urbana, IL 61801

108. William D. Bjorndahl
TRW, Inc.
One Space Park
Building 01, Room 2060
Redondo Beach, CA 90278

109. James A. Black
American Matrix, Inc.
118 Sherlake Drive
Knoxville, TN 37922

110. Keith Blandford
Boride Products, Inc.
2879 Aero Park Drive
Traverse City, MI 49684

111. John Blum
Norton Company
High Performance Ceramics
Goddard Road
Northboro, MA 01532-1545

112. Paul N. Blumberg
Integral Technologies Inc.
415 East Plaza Drive
Westmont, IL 60559

113. Wolfgang D. G. Boecker
Standard Oil Engineered Materials Co.
Post Office Box 832
Niagara Falls, NY 14302

114. Han Juergen Bossmeyer
BMW Technologies, Inc.
800 South Street
Waltham, MA 02154

115. Raymond J. Bratton
Westinghouse Electric Corp.
1310 Beulah Road
Pittsburgh, PA 15235

116. Catherine E. Brown
E. 1. DuPont de Nemours & Co.
Wilmington, DE 19898

117. J. J. Brown
Virginia Polytechnic Institute and State University
Blacksburg, VA 24061

118. W. Bryzik
U.S. Army Tank Automotive Command
Warren, MI 48090

119. S. T. Buljan
GTE Laboratories, Inc.
40 Sylvan Road
Waltham, MA 02254

120. John M. Byrne, Jr.
PPG Industries, Inc.
One PPG Place
Pittsburgh, PA 15272

121. Donald J. Campbell
Air Force Wright Aeronautical Laboratory
AFWAL/POX
Wright-Patterson AFB, OH 45433

122. Roger Cannon
Rutgers University
Post Office Box 909
Bowser Road
Piscataway, NJ 08855-0909

123. Harry W. Carpenter
19945 Acre Street
Northridge, CA 91324

124. David Carruthers
Garrett Turbine Engine Company
111 South 34th Street
Post Office Box 5217
Phoenix, AZ 85010

125. Jere G. Castor
Garrett Turbine Engine Co.
111 South 34th Street
Post Office Box 5217
Phoenix, AZ 85010

126. Se-Tak Chang
Sundstrand Corporation
Turbomach Division
4400 Ruffin Road
San Diego, CA 92138-5757

127. R. J. Charles
General Electric Company
Post Office Box 8
Schenectady, NY 12301

128. En-sheng Chen
B&C Engineering Research
13906 Dentwood Drive
Houston, TX 77014

129. Albert A. Chesnes
U.S. Department of Energy
Forrestal Building CE-151
1000 Independence Avenue
Washington, DC 20585

130. Frank Childs
EG&G, Inc.
Post Office Box 1625
Idaho Falls, ID 83415

131. Gilbert Y. Chin
Bell Telephone Laboratories
Murray Hill, NJ 07974

132. Melvin H. Chiogioji
U.S. Department of Energy
Forrestal Building CE-15
1000 Independence Avenue, SW
Washington, DC 20585

133. William J. Chmura
The Torrington Company
59 Field Street
Torrington, CT 06790

134. Eugene V. Clark
Turbine Metal Technology, Inc.
7327 Elmo Street
Tujunga, CA 91042-2204

135. William L. Cleary
ORI, Inc.
1375 Piccard Drive
Rockville, MD 20850

136. Jack L. Clem
J. M. Huber Corporation
Post Office Box 2831
Borger, TX 79008-2831

137. Philip R. Compton
National Aeronautics and Space Administration
Washington, DC 20546

138. Harry E. Cook
Chrysler Motors Corporation
1200 Chrysler Drive
Highland Park, MI 48288-1118

139. Stephen Copley
University of Southern California
Los Angeles, CA 90089-0241

140. John A. Coppola
Standard Oil Engineered Materials Company
Structural Ceramics Division
Bldg. 91-2
Post Office Box 1054
Niagara Falls, NY 14302

141. Normand D. Corbin
Norton Company
High Performance Ceramics
Goddard Road
Northboro, MA 01532-1545

142. David M. Corneille
The Garrett Corporation
One First National Plaza
Suite 1900
Dayton, OH 45402

143. Charles H. Craig
Defense Technology Security Administration
400 Army-Navy Drive, Suite 300
Arlington, VA 22202

144. William J. Croft
U.S. Army Materials Technology Laboratory
Arsenal Street
Watertown, MA 02172

145. Gary M. Crosbie
Ford Motor Company
Room S-2079
Post Office Box 2053
Dearborn, MI 48121

146. Floyd W. Crouse, Jr.
U.S. Department of Energy
Morgantown Energy Technology Center
Post Office Box 880
Morgantown, WV 26505

147. Raymond Cutler
Ceramatec, Inc.
163 West 1700 South
Salt Lake City, UT 84115

148. David A. Dalman
The Dow Chemical Company
Midland, MI 48640

149. James I. Dalton
Reynolds Metals Company
Fourth and Canal Streets
Post Office Box 27003
Richmond, VA 23261

150. Stephen C. Danforth
Rutgers University
Post Office Box 909
Bowser Road
Piscataway, NJ 08854

151. Stanley J. Dapkunas
National Bureau of Standards
Gaithersburg, MD 20899

152. Robert F. Davis
North Carolina State University
232 Riddick Laboratory
Box 7907
Raleigh, NC 27695

153. Evelyn M. DeLiso
Rutgers University
Post Office Box 909
Bowser Road
Piscataway, NJ 08854

154. Alan L. Dragoo
National Bureau of Standards
Gaithersburg, MD 20899

155. Keith F. Dufrane
Battelle Columbus Laboratories
505 King Avenue
Columbus, OH 43201

156. Edmund M. Dunn
GTE Laboratories Inc.
40 Sylvan Road
Waltham, MA 02254

157. Jeremy D. Dunning
Indiana Memorial Union 662
Indiana University
Bloomington, IN 47405

158. Dr. Sunil Dutta
NASA Lewis Research Center
MS: 49-3
Cleveland, OH 44135

159. Paul N. Dyer
Air Products and Chemicals, Inc.
Post Office Box 538
Allentown, PA 18105

160. Robert J. Eagan
Sandia National Laboratories
Department 1840
Post Office Box 5800
Albuquerque, NM 87185

161. Christopher A. Ebel
Norton Company
High Performance Ceramics
Goddard Road
Northboro, MA 01532-1545

162. J. J. Eberhardt
U.S. Department of Energy
Forrestal Building CE-12
1000 Independence Avenue, S.W.
Washington, DC 20585

163. E. E. Ecklund
U.S. Department of Energy
Forrestal Building CE-151
1000 Independence Avenue
Washington, DC 20585

164. William A. Ellingson
Argonne National Laboratory
9700 South Cass Avenue
Argonne, IL 60439

165. Graydon A. Elliott
U.S. Army Research and Technology Laboratory
Fort Eustis, VA 23604

166. A. Erdely
26 Av. Gore des Eaux-Vives
1208 Geneva
Switzerland

167. Charles D. Estes
U.S. Senate
Washington, DC 20510

168. Peggy Evanich
National Aeronautics and Space Administration
Washington, DC 20546

169. Anthony G. Evans
University of California
Santa Barbara, CA 93106

170. Robert C. Evans
NASA Lewis Research Center
21000 Brookpark Road
Cleveland, OH 44135

171. Katherine T. Faber
Ohio State University
2041 College Road
Columbus, OH 43210

172. John W. Fairbanks
U.S. Department of Energy
Forrestal Building CE-151
1000 Independence Avenue
Washington, DC 20585

173. Larry Farrell
Babcock and Wilcox
Old Forrest Road
Lynchburg, VA 24505

174. H. W. Foglesong
Dow Corning Corporation
3901 South Saginaw Road
Midland, MI 48640

175. Thomas F. Foltz
Avco Corporation
Two Industrial Avenue
Lowell, MA 01851

176. Robert G. Frank
Technology Assessment Group
10793 Bentley Pass Lane
Cincinnati, OH 45140

177. Douglas W. Freitag
LTV Aerospace and Defense Co.
Post Office Box 225907
MS: TH-85
Dallas, TX 75265

178. George E. Gazza
U.S. Army Materials Technology Laboratory
Arsenal Street
Watertown, MA 02172

179. Charles M. Gilmore
The George Washington University
Washington, DC 20052

180. Paul Glance
Concept Analysis
950 Stephenson Highway
Troy, MI 48007-7013

181. Fred M. Glaser
U.S. Department of Energy
Washington, DC 20545

182. Joseph W. Glatz
Naval Air Propulsion Test Center
Box 7176, PE 34
Trenton, NJ 08628

183. W. M. Goldberger
Superior Graphite Company
2175 East Broad Street
Columbus, OH 43209

184. Stephen T. Gonczy
Allied Signal Research Center
50 UOP Plaza
Des Plaines, IL 60016-6187

185. Robert J. Gottschall
U.S. Department of Energy
Washington, DC 20545

186. Dr. Earl Graham
Cleveland State University
Uclid Avenue at East 24th St.
Cleveland, OH 44115

187. Kenneth Green
Coors Ceramics Company
17750 West 32nd Street
Golden, CO 80401

188. Lance E. Groseclose
General Motors Corporation
Post Office Box 420
Indianapolis, IN 46206-0420

189. T. D. Gulden
GA Technologies, Inc.
Post Office Box 81608
San Diego, CA 92138

190. P. Ulf Gummeson
Hoeganaes
River Road and Taylors Lane
Riverton, NJ 08077

191. M. D. Gurney
NIPER
Post Office Box 2128
Bartlesville, OK 74005

192. John P. Gyekenyesi
NASA Lewis Research Center
21000 Brookpark Road
Cleveland, OH 44135

193. J. J. Habeeb
Esso Petroleum Canada
Post Office Box 3022
Sarina, Ontario
Canada N7T 7MI

194. H. T. Hahn
Pennsylvania State University
227 Hammond Building
University Park, PA 16802

195. Nabil S. Hakim
General Motors Corporation
36880 Ecorse Road
Romulus, MI 48174

196. John W. Halloran
Ceramic Process Systems
840 Memorial Drive
Cambridge, MA 02139-3758

197. R. A. Harmon
25 Schalren Drive
Latham, NY 12110

198. Stephen D. Hartline
Norton Company
High Performance Ceramics
Goddard Road
Northboro, MA 01532-1545

199. Willard E. Hauth
Dow Corning Corporation
3901 South Siginaw Road
Midland, MI 48640

200. Kevin L. Haynes
McDonnell Douglas Astronautics Company
Box 516 E456/HQ/3N/MS329
Saint Louis, MO 63166

201. Norman L. Hecht
University of Dayton Research Institute
300 College Park
Dayton, OH 45469-0001

202. S. S. Hecker
Los Alamos National Laboratory
Post Office Box 1663
Los Alamos, NM 87545

203. Peter W. Heitman
General Motors Corporation
Post Office Box 420, W-5
Indianapolis, IN 46206-0420

204. Richard L. Helferich
The Duriron Company, Inc.
Post Office Box 1145
Dayton, OH 45401

205. H. E. Helms
General Motors Corporation
Post Office Box 420
Indianapolis, IN 46206-0420

206. Thomas L. Henson
GTE Products Corporation
Hawes Street
Towanda, PA 18848-0504

207. Thomas P. Herbell
NASA Lewis Research Center
21000 Brookpark Road
MS: 49-3
Cleveland, OH 44135

208. Hendrik Heystek
Bureau of Mines
Tuscaloosa Research Center
Post Office Box L
University, AL 35486

209. Robert V. Hillery
General Electric Company
One Neumann Way
Post Office Box 156301
Cincinnati, OH 45215

210. Jonathan W. Hinton
Standard Oil Engineered Materials Company
Structural Ceramics Division
Post Office Box 1054
Niagara Falls, NY 14302

211. Stephen M. Hsu
National Bureau of Standards
Gaithersburg, MD 20899

212. Harold A. Huckins
Princeton Advanced Technology, Inc.
56 Finley Road
Princeton, NJ 08540

213. Fred Huettic
Advanced Ceramic Technology, Inc.
17 Deerfield Road
East Brunswick, NJ 08816

214. O. Richard Hughes
Celanese Research Company
86 Morris Avenue
Summit, NJ 07901

215. Joseph E. Hunter, Jr.
General Motors Corporation
12 Mile and Mound Roads
Warren, MI 48090-9055

216. Louis C. Ianniello
U.S. Department of Energy
Washington, DC 20545

217. Robert H. Insley
Champion Spark Plug Company
20000 Conner Avenue
Detroit, MI 48234

218. D. M. Jacques
Norton Company
HPC Library
Goddard Road
Northboro, MA 01532-1545

219. Curt A. Johnson
General Electric Company
Post Office Box 8
Schenectady, NY 12301

220. Douglas C. Johnson
Sundstrand Corporation
4400 Ruffin Road
Post Office Box 85757
San Diego, CA 92138-5757

221. Larry Johnson
Argonne National Laboratory
Building 362
9700 South Cass Avenue
Argonne, IL 60439

222. R. A. Johnson
General Motors Corporation
Post Office Box 420
Indianapolis, IN 46206-0420

223. L. A. Joo
Great Lakes Research Corp.
Post Office Box 1031
Elizabethton, TN 37643

224. A. David Joseph
Sealed Power Corporation
100 Terrace Plaza
Muskegon, MI 49443

225. Roy Kamo
Adiabatics, Inc.
630 South Mapleton
Columbus, IN 47201

226. Allan Katz
Air Force Wright Aeronautical Laboratory
Materials Laboratory
Wright-Patterson AFB, OH 45433

227. R. N. Katz
U.S. Army Materials Technology Laboratory
Arsenal Street
Watertown, MA 02172

228. P. Victor Kelsey
Aluminum Company of America
Alcoa Technical Center B
Alcoa Center, PA 15061

229. Frederick L. Kennard, III
General Motors Corporation
1300 North Dort Highway
Flint, MI 48556

230. J. R. Kidwell
Garrett Turbine Engine Company
111 South 34th Street
Post Office Box 5217
Phoenix, AZ 85010

231. Max Klein
Gas Research Institute
8600 West Bryn Mawr Avenue
Chicago, IL 60631

232. C. E. Knapp
Norton Company
8001 Daly Street
Niagara Falls, Ontario
Canada

233. A. S. Kobayashi
University of Washington
Seattle, WA 98195

234. David M. Kotchick
AiResearch Manufacturing Co.
2525 West 190th Street
Torrance, CA 90509

235. Bruce Kramer
George Washington University
Washington, DC 20052

236. Saunders B. Kramer
U.S. Department of Energy
Forrestal Building CE-151
1000 Independence Avenue
Washington, DC 20585

237. D. M. Kreiner
Garrett Turbine Engine Company
111 South 34th Street
Post Office Box 5217
Phoenix, AZ 85010

238. Pieter Krijgsman
Ceramic Design Int. Hold., Ltd.
Post Office Box 68
8050 AB Hattem
The Netherlands

239. W. J. Lackey
Georgia Tech Research Institute
Atlanta, GA 30332

240. Everett A. Lake
Air Force Wright Aeronautical Laboratory
AFWAL/POOS
Wright-Patterson AFB, OH 45433

241. Hari S. Lamba
General Motors Corporation
Electro-Motive Division
LaGrange, IL 60525

242. James Lankford
Southwest Research Institute
6220 Culebra Road
P.O. Drawer 28510
San Antonio, TX 78284

243. John G. Lanning
Corning Glass Works
Corning, NY 14831

244. David C. Larsen
Corning Glass Works
Sullivan Park, FR-51
Corning, NY 14831

245. Dr. S. K. Lau
Standard Oil Engineered
Materials Company
Technology Division
Box 832
Niagara Falls, NY 14302

246. Harry A. Lawler
Standard Oil Engineered
Materials Company
Structural Ceramics Division
Building 91-2
Post Office Box 1054
Niagara Falls, NY 14302

247. Alan Lawley
Drexel University
Philadelphia, PA 19104

248. Daniel Lee
Temescon
2850 7th Street
Berkeley, CA 94710

249. June-Gunn Lee
Korea Advanced Institute of
Science and Technology
Post Office Box 131
Dong Dac Mun, Seoul
Korea

250. E. M. Lenoe
Air Force Office of
Scientific Research
APO San Francisco, CA 96503

251. Stanley R. Levine
NASA Lewis Research Center
21000 Brookpark Road
Cleveland, OH 44135

252. David Lewis
Naval Research Laboratory
4555 Overlook Avenue, S.W.
Washington, DC 20375

253. Winston W. Liang
AMERCOM, Inc.
8948 Fullbright Avenue
Chatsworth, CA 91311

254. Bill Long
Babcock and Wilcox
Post Office Box 1260
Lynchburg, VA 24505

255. L. A. Lott
EG&G, Inc.
Post Office Box 1625
Idaho Falls, ID 83415

256. Bryan K. Luftglass
Chem Systems, Inc.
303 South Broadway
Tarrytown, NY 10591

257. Michael J. Lynch
General Electric Company
Post Office Box 414, 7B-36
Milwaukee, WI 53201

258. James W. MacBeth
Standard Oil Engineered
Materials Company
Structural Ceramics Division
Box 1054
Niagara Falls, NY 14302

259. Vincent L. Magnotta
Air Products and Chemicals,
Inc.
Post Office Box 538
Allentown, PA 18105

260. Tai-il Mah
Universal Energy Systems
4401 Dayton-Xenia Road
Dayton, OH 45432

261. L. Manes
Commission of the European
Communities
Ispra Establishment
1-21020 Ispra (Varese)
Italy

262. Gerald R. Martin
Fleetguard, Inc.
Cookeville, TN 38501

263. Dr. John L. Mason
The Garrett Corporation
2525 West 190th Street
Torrance, CA 90509

264. J. McCauley
U.S. Army Materials Technology Laboratory
DRXMR-MC
Arsenal Street
Watertown, MA 02172-0001

265. William J. McDonough
U.S. Department of Energy
Room 5G-030A
Forrestal Building CE-151
1000 Independence Avenue
Washington, DC 20585

266. Bryan J. McEntire
Norton Company
TRW Ceramics
Goddard Road
Northboro, MA 01532-1545

267. Thomas D. McGee
Iowa State University
Ames, IA 50011

268. H. Christopher McGowan
Advanced Ceramic Technology, Inc.
17 Deerfield Road
East Brunswick, NJ 08816

269. Malcolm G. McLaren
Rutgers University
Post Office Box 909
Bowser Road
Piscataway, NJ 08854

270. Brian L. Mehosky
Standard Oil Engineered Materials Company
4440 Warrensville Center Road
Cleveland, OH 44128

271. P. K. Mehrotra
Kennametal, Inc.
Post Office Box 639
Greensburg, PA 15601

272. Joseph J. Meindl
Reynolds International, Inc.
Post Office Box 27002
6603 West Broad Street
Richmond, VA 23261

273. D. Messier
U.S. Army Materials Technology Laboratory
DRXMR-MC
Arsenal Street
Watertown, MA 02172

274. Arthur G. Metcalfe
Solar Turbines, Inc.
2200 Pacific Highway
Post Office Box 80966
San Diego, CA 92138

275. Thomas N. Meyer
Aluminum Company of America
Alcoa Technical Center
Alcoa Center, PA 15069

276. W. Miloscia
Standard Oil Engineered Materials Company
4440 Warrensville Center Road
Cleveland, OH 44128

277. Bill Moehle
Ethyl Corporation
451 Florida Avenue, Ethyl Tower
Baton Rouge, LA 70801

278. Helen Moeller
Babcock and Wilcox
Post Office Box 11165
Lynchburg, VA 24506-1165

279. Frederick E. Moreno
Turbo Energy Systems, Inc.
350 Second Street, Suite 5
Los Altos, CA 94022

280. Peter E. D. Morgan
Rockwell International
1049 Camino Dos Rios
Post Office Box 1085
Thousand Oaks, CA 91360

281. Solomon Musikant
General Electric Company
Post Office Box 8555
MS: U-1219
Philadelphia, PA 19101

282. Pero Nannelli
Pennwalt Corporation
900 First Avenue
Post Office Box C
King of Prussia, PA 19406-0018

283. Robert M. Neilson, Jr.
EG&G Idaho, Inc.
Post Office Box 1625
Idaho Falls, ID 83415

284. William D. Nix
Stanford University
Stanford, CA 94305

285. Richard D. Nixdorf
American Matrix, Inc.
118 Sherlake Drive
Knoxville, TN 37922

286. Brian M. O'Connor
The Lubrizol Corporation
29400 Lakeland Boulevard
Wickliffe, OH 44092

287. W. Richard Ott
Alfred University
Alfred, NY 14802

288. Muktesh Paliwal
GTE Products Corporation
Hawes Street
Towanda, PA 18848-0504

289. Hayne Palmour III
North Carolina State University
2158 Burlington Engineering Laboratories
Post Office Box 5995
Raleigh, NC 27607

290. Joseph N. Panzarino
Norton Company
Goddard Road
Northboro, MA 01532-1545

291. Pellegrino Papa
Corning Glass Works
Corning, NY 14831

292. James G. Paschal
Reynolds Metals Company
Post Office Box 76154
Atlanta, GA 30358

293. Arvid E. Pasto
GTE Laboratories, Inc.
40 Sylvan Road
Waltham, MA 02254

294. Donald O. Patten
Norton Company
High Performance Ceramics
Goddard Road
Northboro, MA 01532-1545

295. James W. Patten
Cummins Engine Company, Inc.
Box 3005, Mail Code 50183
Columbus, IN 47202-3005

296. Timothy M. Pattison
Textron Lycoming
MS: LSM1
550 Main Street
Stratford, CT 06497

297. Robert A. Penty
Eastman Kodak Company
901 Elmgrove Road
Rochester, NY 14650

298. Gary R. Peterson
U.S. Department of Energy
785 DOE Place
Idaho Falls, ID 83402

299. R. Byron Pipes
University of Delaware
2001 Spencer Laboratory
Newark, DE 19716

300. Robert C. Pohanka
Office of Naval Research
Code 431
800 North Quincy Street
Arlington, VA 22217

301. Stephen C. Pred
ICD Group, Inc.
1100 Valley Brook Avenue
Lyndhurst, NJ 07071

302. Karl M. Prewo
United Technologies Corp.
Silver Lane, MS: 24
East Hartford, CT 06108

303. Hubert B. Probst
NASA Lewis Research Center
21000 Brookpark Road
Cleveland, OH 44135

304. Carr Lane Quackenbush
Norton Company
High Performance Ceramics
Goddard Road
Northboro. MA 01532-1545

305. Brian Quigy
National Aeronautics and Space Administration
Washington, DC 20546

306. George Quinn
U.S. Army Materials Technology Laboratory
Arsenal Street
Watertown, MA 02172

307. Dennis T. Quinto
Kennametal, Inc.
Post Office Box 639
Greensburg, PA 15601

308. S. Venkat Raman
Air Products and Chemicals, Inc.
Post Office Box 538
Allentown, PA 18105

309. Dennis Readey
Ohio State University
2041 College Road
Columbus, OH 43210

310. Robert R. Reeber
U.S. Army Research Office
Post Office Box 12211
Research Triangle Park, NC 27709

311. K. L. Reifsnider
Virginia Polytechnic Institute and State University
Blacksburg, VA 24061

312. Paul Rempes
Champion Spark Plug Company
20000 Conner Avenue
Detroit, MI 48234

313. T. M. Resetar
U.S. Army Materials Technology Laboratory
DAXMA-MC
Arsenal Street
Watertown, MA 02172

314. K. T. Rhee
Rutgers University
Post Office Box 909
Bowser Road
Piscataway, NJ 08854

315. Roy W. Rice
W. R. Grace and Company
7379 Route 32
Columbus, MD 21044

316. David W. Richerson
Ceramatec, Inc.
163 West 1700 South
Salt Lake City, UT 84115

317. Paul Rieth
Ferro Corporation
661 Willet Road
Buffalo, NY 14218-9990

318. Michael A. Rigdon
Institute for Defense Analyses
1801 Beauregard Street
Alexandria, VA 22311

319. John E. Ritter, Jr.
University of Massachusetts
Amherst, MA 01003

320. Giulio A. Rossi
Norton Company
High Performance Ceramics
Goddard Road
Northboro, MA 01532-1545

321. Barry R. Rossing
Lanxide Corporation
Tralee Industrial Park
Newark, DE 19711

322. David J. Rowcliffe
SRI International
333 Ravenswood Avenue
Menlo Park, CA 94025

323. Donald W. Roy
Coors Ceramics Company
17750 West 32nd Street
Golden, CO 80401

324. Bruce Rubinger
Gobal
50 Milk Street, 15th Floor
Boston, MA 02109

325. Robert Ruh
Air Force Wright Aeronautical Laboratory
Materials Laboratory AFWAL/MLLM
Wright-Patterson AFB, OH 45433

326. Robert J. Russell, Sr.
Norton Company
High Performance Ceramics
Goddard Road
Northboro, MA 01532-1545

327. George P. Safol
Westinghouse Electric Corp.
Pittsburgh, PA 15235

328. J. Sankar
North Carolina Agricultural & Technical State University
Greensboro, NC 27411

329. Maxine Savitz
Garrett Ceramic Components Division
19800 South Venice
Torrance, CA 90509

330. Richard Schapery
Texas A&M University
College Station, TX 77843

331. J. L. Schienle
Garrett Turbine Engine Company
111 South 34th Street
Post Office Box 5217
Phoenix, AZ 85034

332. L. J. Schioler
Aerojet Tech Systems Company
Post Office Box 13222
Dept. 9990, Bldg. 2001
Sacramento, CA 95813

333. Richard A. Schmidt
Battelle Columbus Laboratories
505 King Avenue
Columbus, OH, 43201-2693

334. Arnie Schneck
Deere and Company Technical Center
Post Office Box 128
Wood-Ridge, NJ 07075

335. Matthew Schreiner
Gas Research Institute
8600 West Bryn Mawr Avenue
Chicago, IL 60631

336. John Schuldies
Industrial Ceramic Technology, Inc.
37 Enterprise Drive
Ann Arbor, MI 48103

337–356. R. B. Schulz
U.S. Department of Energy
Forrestal Building CE-151
1000 Independence Avenue
Washington, DC 20585

357. Wesley J. C. Schuster
Thermo Electron Corporation
115 Eames Street
Post Office Box 340
Wilmington, MA 01887

358. Murray A. Schwartz
Bureau of Mines
2401 Eye Street, N.W.
Washington, DC 20241

359. Douglas B. Schwarz
The Dow Chemical Company
52 Building
Midland, MI 48674

360. Thomas M. Sebestyen
U.S. Army Tank Automotive Command
AMSTA-RGRT
Warren, MI 48397-5000

361. Brian Seegmiller
Coors Ceramics Company
17750 West 32nd Street
Golden, CO 80401

362. S. G. Seshadri
Standard Oil Engineered Materials Company
Post Office Box 832
Niagara Falls, NY 14302

363. Peter T. B. Shaffer
Advanced Refractory Technologies, Inc.
699 Hertel Avenue
Buffalo, NY 14207

364. Maurice E. Shank
United Technologies Corp.
East Hartford, CT 06108

365. Laurel M. Sheppard
Advanced Materials and Processes
Route 87
Metals Park, OH 44073

366. Dinesh K. Shetty
The University of Utah
Salt Lake City, UT 84112

367. Jack D. Sibold
Coors Ceramics Company
17750 West 32nd Street
Golden, CO 80401

368. Neal Sigmon
U.S. House of Representatives
Rayburn Building, Room B308
Washington, DC 20515

369. Richard Silberglitt
Quest Research Corporation
1651 Old Meadow Road
McLean, VA 22102

370. Maurice J. Sinnott
University of Michigan
438 West Engineering Building
Ann Arbor, MI 48109

371. S. R. Skaggs
Los Alamos National Laboratory
Post Office Box 1663
Los Alamos, NM 87545

372. J. Thomas Smith
GTE Laboratories, Inc.
40 Sylvan Road
Waltham, MA 02254

373. Jay R. Smyth
Garrett Turbine Engine Co.
Post Office Box 5217
MS: 93-172/1302-2K
Phoenix, AZ 85010

374. Rafal Sobotowski
Standard Oil Engineered Materials Company
3092 Broadway Avenue
Cleveland, OH 44115

375. Thomas M. Sopko
Lubrizol Enterprises, Inc.
29400 Lakeland Boulevard
Wickliffe, OH 44092

376. Boyd W. Sorenson
Du Pont Company
Bldg. 304
Experimental Station
Wilmington, DE 19898

377. Dr. Richard M. Spriggs
Center for Advanced Ceramic Technology
New York State College of Ceramics at Alfred University
Alfred, NY 14802

378. M. Srinivasan
Standard Oil Engineered Materials Company
Post Office Box 832
Niagara Falls, NY 14302

379. Gordon L. Starr
Cummins Engine Company, Inc.
Box 3005, Mail Code 50183
Columbus, IN 47202-3005

380. Harold L. Stocker
General Motors Corporation
Post Office Box 420, T-23
Indinapolis, IN 46206-0420

381. Roger Storm
Standard Oil Engineered Materials Company
Post Office Box 832
Niagara Falls, NY 14302

382. E. E. Strain
Garrett Turbine Engine Company
111 South 34th Street
Post Office Box 5217
MS: 301-2N
Phoenix, AZ 85010

383. Thomas N. Strom
NASA Lewis Research Center
21000 Brookpark Road, 77-6
Cleveland, OH 44135

384. Jerry Strong
Albright & Wilson
Post Office Box 26229
Richmond, VA 23260

385. Richard Suddeth
Boeing Motor Airplane Company
Post Office Box 7730
MS: K-76-67
Wichita, KS 67277

386. Paul Sutor
Midwest Research Institute
425 Volker Boulevard
Kansas City, MO 64116

387. J. J. Swab
U.S. Army Materials Technology Laboratory
Arsenal Street
Watertown, MA 02172

388. John W. Swain, Jr.
PCK Technology Division
15424 Garrison Lane
Southgate, MI 48915

389. Lewis Swank
Ford Motor Company
Post Office Box 2053
Building SRL, Room S2023
Dearborn, MI 48121

390. Stephen R. Tan
ICI Advanced Materials
Post Office Box 11
The Heath, Runcorn
Cheshire
England WA7 4QE

391. Anthony C. Taylor
U.S. House of Representatives
Rayburn Building, Room 2321
Washington, DC 20515

392. W. H. Thielbahr
U.S. Department of Energy
550 2nd Street
Idaho Falls, ID 83401

393. John K. Tien
Columbia University
1137 S.W. Mudd Building
New York, NY 10027

394. T. Y. Tien
University of Michigan
Dow Building
Ann Arbor, MI 48109-2136

395. Julian M. Tishkoff
Air Force Office of
Scientific Research
(AFOSR/WC) Bolling AFB
Washington, DC 20332

396. Louis E. Toth
National Science Foundation
1800 G Street, N.W.
Washington, DC 20550

397. Richard E. Tressler
Pennsylvania State University
201 Steidle Building
University Park, PA 16802

398. Donald R. Uhlmann
Massachusetts Institute of
Technology
77 Massachusetts Avenue
Cambridge, MA 02139

399. Edward C. Van Reuth
Technology Strategies, Inc.
10722 Shingle Oak Court
Burke, VA 22015

400. Thomas Vasilos
Avco Corporation
201 Towell Street
Wilmington, MA 01887

401. V. Venkateswaran
Standard Oil Engineered
Materials Company
Post Office Box 832
Niagara Falls, NY 14302

402. John B. Wachtman, Jr.
Rutgers University
Post Office Box 909
Bowser Road
Piscataway, NJ 08854

403. Richard B. Wallace
General Motors Corporation
36880 Ecorse Road
Romulus, MI 48174

404. Harlan L. Watson
U.S. House of Representatives
Rayburn Building, Suite 2321
Washington, DC 20515

405. John D. Watson
BHP Research & New Technology
Melbourne Research Laboratories
245 Wellington Road
Mulgrave, Victoria 3170
Australia

406. Albert R. C. Westwood
Martin Marietta Laboratories
1450 South Rolling Road
Baltimore, MD 21227

407. Thomas J. Whalen
Ford Motor Company
Dearborn, MI 48121

408. Sheldon M. Wiederhorn
National Bureau of Standards
Gaithersburg, MD 20899

409. James C. Williams
Carnegie-Mellon University
Schenley Park
Pittsburgh, PA 15213

410. Roger R. Wills
TRW, Inc.
Valve Division
1455 East 185th Street
Cleveland, OH 44110

411. J. M. Wimmer
Garrett Turbine Engine Co.
111 South 34th Street
Post Office Box 5217
Phoenix, AZ 85010

412. David Wirth
Coors Ceramics Company
17750 West 32nd Street
Golden, CO 80401

413. Thomas J. Wissing
Eaton Corporation
26201 Northwestern Highway
Post Office Box 766
Southfield, MI 48037

414. Dale Wittmer
Southern Illinois University
at Carbondale
Department of Mechanical Eng.
and Energy Processes
Carbondale, IL 62901

415. George W. Wolter
Howmet Turbine Components Corp.
699 Benston Road
Whitehall, MI 49461

416. James C. Wood
NASA Lewis Research Center
21000 Brookpark Road
MS: 500-210
Cleveland, OH 44135

417. Roger P. Worthen
Eaton Corporation
26201 Northwestern Highway
Post Office Box 766
Southfield, MI 48076

418. Hun C. Yeh
Ceramic Processing Company
19800 Van Ness Avenue
Torrance, CA 90509

419. Thomas M. Yonushonis
Cummins Engine Company, Inc.
Box 3005, Mail Code 50183
Columbus, IN 47202-3005

420. Don Zabierek
Air Force Wright Aeronautical Laboratory
AFWAL/POTC
Wright-Patterson AFB, OH 45433

421. Charles Zeh
U.S. Department of Energy
Post Office Box 880
Morgantown, WV 26505

422. Anne Marie Zerega
U.S. Department of Energy
Forrestal Building CE-15
1000 Independence Avenue
Washington, DC 20585

423. Martin Zlotnick
Nichols Research Corporation
Suite 200
8618 Westwood Center Drive
Vienna, VA 22180-2222

424. Klaus M. Zwilsky
National Research Council
2101 Constitution Avenue
Washington, DC 20418

425. Department of Energy
Oak Ridge Operations Office
Assistant Manager for Energy Research and Development
PO Box E
Oak Ridge, TN 37831

426–435. Department of Energy
Office of Scientific and Technical Information
Office of Information Services
PO Box 62
Oak Ridge, TN 37831

For distribution by microfiche as shown in DOE/TIC-4500, Distribution Category UC-95.

☆U.S. GOVERNMENT PRINTING OFFICE 1988—548-118/601